DOE-ER-0313/35
Distribution
Categories
UC-423, -424

FUSION MATERIALS
SEMIANNUAL PROGRESS REPORT
FOR THE PERIOD ENDING
December 31, 2003

Prepared for
DOE Office of Fusion Energy Sciences
(AT 60 20 10 0)

DATE PUBLISHED: APRIL 2004

Prepared for
OAK RIDGE NATIONAL LABORATORY
Oak Ridge, Tennessee 37831
Managed by
UT-Battelle, LLC
For the
U.S. DEPARTMENT OF ENERGY

FOREWORD

This is the thirty-fifth in a series of semiannual technical progress reports on fusion materials science activities supported by the Fusion Energy Sciences Program of the U.S. Department of Energy. This report focuses on research addressing the effects on materials properties and performance from exposure to the neutronic, thermal, and chemical environments anticipated in the chambers of fusion experiments and energy systems. This research is a major element of the national effort to establish the materials knowledge base of an economically and environmentally attractive fusion energy source. Research activities on issues related to the interaction of materials with plasmas are reported separately.

The results reported are the product of a national effort involving a number of national laboratories and universities. A large fraction of this work, particularly in relation to fission reactor irradiations, is carried out collaboratively with partners in Japan, Russia, and the European Union. The purpose of this series of reports is to provide a working technical record for the use of program participants, and to provide a means of communicating the efforts of fusion materials scientists to the broader fusion community, both nationally and worldwide.

This report has been compiled and edited under the guidance of R. L. Klueh and Teresa Roe, Oak Ridge National Laboratory. Their efforts, and the efforts of the many persons who made technical contributions, are gratefully acknowledged.

S. E. Berk
Facilities and Enabling Technologies Division
Office of Fusion Energy Sciences

TABLE OF CONTENTS

1.0 VANADIUM ALLOYS

FABRICATION OF CREEP TUBING FROM THE US AND NIFS HEATS OF V-4Cr-4Ti—A. F. Rowcliffe, D. T. Hoelzer, and M. L. Grossbeck (Oak Ridge National Laboratory)

OBJECTIVE

Utilize commercial-scale processing to fabricate small-diameter, thin-wall tubing from plate stock of V-4Cr-4Ti for both the US program heat no.832665 and the NIFS-HEAT-2 and produce sufficient tubing to meet the programmatic needs for investigating creep behavior in both lithium and vacuum environments and for carrying out irradiation creep measurements.

SUMMARY

Previous attempts at commercial–scale processing to fabricate thin-wall tubing from the V-4Cr-4Ti alloy resulted in extensive surface cracking and a doubling of the oxygen content during multiple intermediate anneals in a vacuum of 1-4 x 10^{-4} torr. An improved procedure was developed to fabricate tubing from both the US program heat and the NIFS-HEAT-2. Although the intermediate vacuum was improved by an order-of-magnitude, the oxidation rate was increased by a factor of ~3, resulting in an unacceptably high oxygen level of ~1700 wppm in the finished tubing. It is shown that under the poorer vacuum conditions, oxygen diffusion to the interior is inhibited by the formation of an oxide film whereas under the improved vacuum conditions, oxygen diffuses rapidly into the tube wall unimpeded by an oxide film .Internal oxidation proceeds by the formation of an oxygen-rich globular Ti(CON) phase. This process is reversed during exposure to liquid lithium at 800-1000ºC. A two–stage heat treatment in liquid lithium was developed which lowered the oxygen content to ~700 wppm and resulted in a uniform grain size distribution with 12-15 grains across the tube wall. This technique was used to produce a set of creep tubes from both heats to be used in the HFIR-RB-17J irradiation experiment.

PROGRESS AND STATUS

Introduction

Determination of the thermal and irradiation creep properties of the heats of V-4Cr-4Ti procured in both the US and in Japan is carried out utilizing a pressurized creep tube specimen measuring 25.4mm long, with a 4.57mm outside diameter and a wall thickness of 0.25mm. Because of the high solubility and rapid mobility of oxygen in this material, maintaining the desired chemical and microstructural characteristics of the alloy during the fabrication of thin sections presents a difficult technological challenge. In 1995, the US fusion program procured some 6 meters of tubing of the US heat No. 832665 with Century Tubes Inc. of San Diego as the primary sub-contractor [1].This effort (Batch A), met with mixed success since a large fraction of the tubing developed cracks at both surfaces which were frequently linked through the wall via a band of severe macroscopic deformation. In addition to the cracking problems the levels of interstitials were also increased significantly during processing; carbon increased from 80 to 300 wppm, oxygen increased from 310 to 700 wppm, (nitrogen remained fairly constant). Relatively crack-free sections of tubing were selected by visual inspection and were used for a series of creep tests in both in vacuum and liquid Li environments [2] and also used to develop irradiation creep data in experiments conducted in the ATR [1], and in the HFIR [3].

Two small heats of V-4Cr-4Ti with low levels of interstitials (~350wppm) were produced in Japan under the direction of the National Institute for Fusion Sciences (NIFS). A limited quantity of creep tubing was prepared from the NIFS-HEAT-2 material using a three-directional rolling process [4]. The problems encountered with surface cracking and interstitial pick-up were somewhat less severe than those experienced with Batch A of the US heat. Based upon the experience with these two tubing campaigns, a new procedure was developed and applied to the production of ~10meters of finished tubing from both the US heat and the NIFS-HEAT-2 materials.

Revisions to Fabrication Procedure

A number of changes were made to the Batch A procedure [5] which may be summarized as follows;

a) The intermediate heat treatments for Batch A were carried out by a commercial vendor (Vendor A), using a tube furnace operating with a vacuum in the range 1-4 x 10^{-4} torr. For Batch B a different vendor was specified (Vendor B) operating a large oven furnace with a vacuum in the range1-10 x 10^{-6} torr.

b) It was conjectured that the surface cracking encountered with the Batch A tubing resulted from a combination of high surface oxygen levels picked up during the annealing cycle and the high stresses imposed by the relatively large reductions in area (>40%) imposed during the draw cycle. Accordingly for Batch B, it was specified that the reduction in area (R/A) per cycle should not exceed 30% for the final 6 stages. Because of this change, it was necessary to utilize 12 drawing and annealing cycles followed by a final 26% R/A to reach final dimensions compared with the 9 drawing and annealing cycles followed by a final 45% R/A to final dimensions used for Batch A.

c) A more rigorous cleaning operation was introduced for the removal of the die lubricant prior to annealing. Following this cleaning, a less aggressive acid cleaning was adopted consisting of a 30 sec. treatment with 20%HNO_3 + 10%HF + 70% H_2O compared with the 5 min treatment with 20% HNO_3 + 20% HF + 60% H_2O used during Batch A processing.

d) Problems were encountered with the bonding of the Ti wrap to the tubing surface during Batch A. For Batch B, gettering was achieved using a tent consisting of multiple layers of clean Ta foil.

These procedures and the modifications are fully documented in Refs [5,6].

Characterization of Batch B Tubing

Interstitial pick-up

Archive samples for chemical analysis and metallography were obtained after each draw cycle and after each anneal. (For Batch A only the initial and final interstitial analyses were obtained).The interstitial analyses for Batch B are summarized for both heats in Table 1.

Table 1. Chemical analyses (wppm) for Batch B tubing

Anneal No.	Wall (mm)	U.S. Heat			NIFS Heat		
		C	O	N	C	O	N
BLANK	4.87	119	331	88	59	130	156
1	4.87	134	346	93	63	152	132
2	4.32						
3	3.50						
4	2.85						
5	2.13	169	403	92	85	219	140
6	1.52	119	511	94			
7	1.22	155	494	101	90	378	148
8	0.99	179	637				
9	0.81						
10	0.64				223	741	210
11	0.48	264	994	133	253	879	206
12	0.38						
13	0.31	457	1745	170	390	1675	211

Because of the order-of –magnitude improvement in the vacuum conditions it was expected that the level of interstitial pick-up would be lower for Batch B than for Batch A. Contrary to these expectations, the pick-up of oxygen accelerated rapidly during the final stages and eventually exceeded the final oxygen content of Batch A tubing by more than a factor of two. During the last two anneals the oxygen content of both heats approximately doubled to reach 1745 wppm for the US heat and 1675 wppm for the NIFS heat. Significant increases also occurred in carbon and nitrogen levels. The oxygen analysis data for each anneal cycle closely tracked the increasing surface area:volume ratio (SAV) of the tubing as shown in Fig. 1 for the US heat. (For tubing, the SAV=2/t, where t is the wall thickness). The NIFS heat showed identical behavior [6].

Microstructure

During the early stages of processing the recrystallized microstructures were uniform across the tube wall. The recrystallized grain size of the NIFS heat was ~50 microns whereas the US heat contained a much higher fraction of small grains (5-10 microns) and an average grain size of ~28 microns. These grain size differences were probably related to differences in the number density and distribution of Ti(CON) particles in the initial plate materials. A more detailed discussion of the microstructural differences between the two heats and details of the type and frequency of surface defects may be found in [5,6].

As the number of anneals increased, a near-surface zone developed which etched differently and was characterized by very fine irregularly-shaped grains. After the tenth anneal, when the oxygen concentrations had increased to 950 and 741wppm in the US and NIFS heats respectively, the surface zones were 40-50 microns thick. After a final draw of ~26% R/A, tubing samples were recrystallized in a laboratory furnace at 1000ºC in a vacuum of $<10^{-6}$ torr. The recrystallized microstructures for both heats were very similar with an inhomogeneous irregular grain structure, due to extensive grain boundary pinning during recrystallization, and with surface zones characterized by very fine grains extending 60-70 microns in from the OD surface and 30-40 microns in from the ID surface. In spite of the high oxygen concentrations, there was no generalized surface cracking.

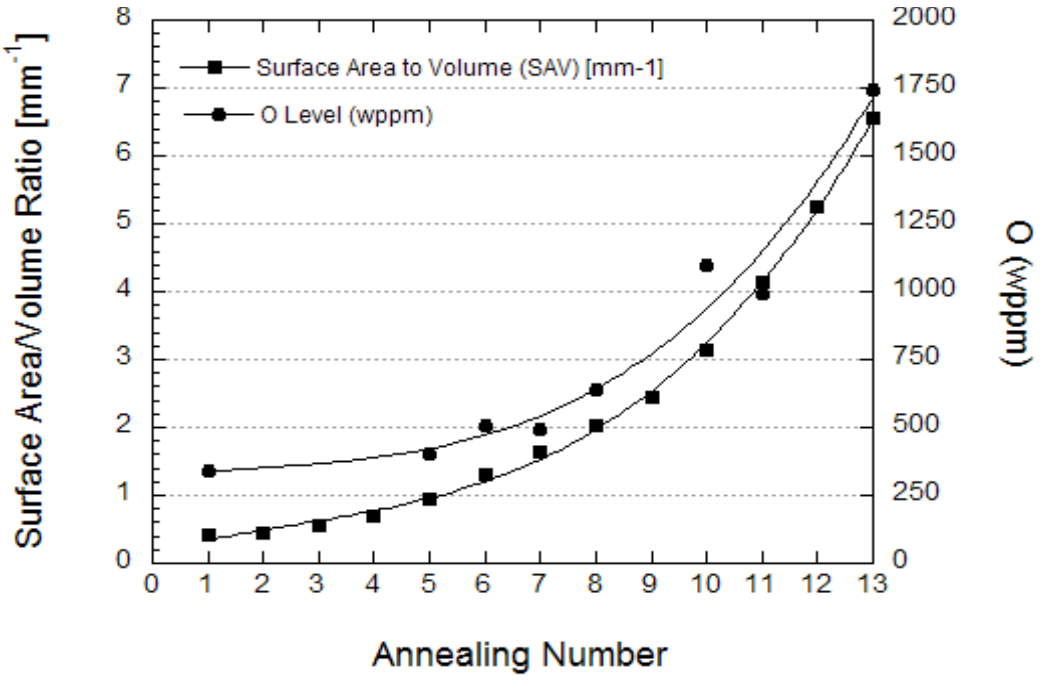

Fig. 1. Oxygen concentration and SAV ratio versus annealing cycle for Batch B (US Heat).

The nature of the surface oxidation zones was examined further using a scanning-Auger system. The results indicated that a process of internal oxidation was occurring with the formation of Ti(CON) particles with sizes in the range 0.1-0.5 microns, with the number density of particles increasing towards the surfaces. Grain growth in the surface zone was severely restricted due to grain boundary pinning by the particles (Fig. 2). Auger analyses showed that the preponderance of oxygen was associated with the particles and that there were no significant differences between the oxygen concentrations in matrix regions located near the center of the tube wall and the matrix regions near the surfaces.

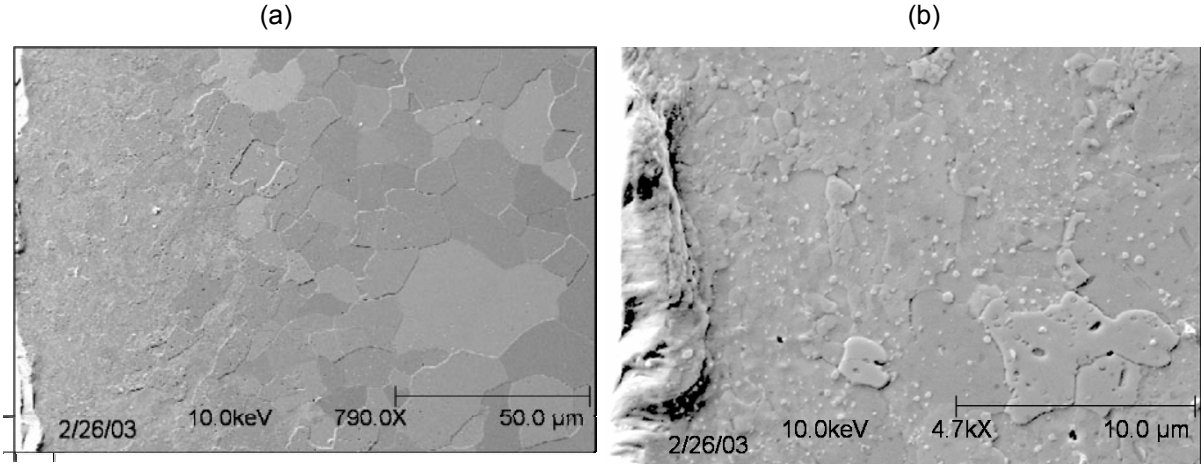

Fig. 2. SEM micrographs of the US heat of tubing following the tenth anneal showing (a) the changes in grain size from surface to the interior of the tube wall and (b) the increase in number density of TiCON particles near the surface region

Oxygen Removal

The high oxygen content and inhomogeneous microstructure of the finished tubing made it unacceptable for the fabrication of specimens for irradiation creep experiments and it was decided to lower the oxygen content by exposing the creep specimens prior to pressurization to a liquid Li environment at 800ºC-1000ºC. Based upon a series of trial exposures [6], a double treatment was defined in which the cold-worked tubing was exposed initially to Li at 800ºC for 168 hrs. During this treatment, dissolution of the surface zone Ti(CON) particles occurred as oxygen transferred to the Li and the overall oxygen content was reduced to ~1100 wppm. At this temperature, which is below the recrystallization temperature, recovery was impeded by the relatively high concentration of oxygen. The temperature was then increased to 1000ºC for a further 1 hour to further reduce the oxygen concentration. Sufficient stored energy was retained following the 800ºC treatment to effect full recrystallization during the 1000ºC treatment. Because of the reduction in the concentration of surface zone Ti(CON) particles which occurred at 800ºC, the final grain size distribution was uniform with approximately 12-15 grains across the tube wall (Fig 3). The double treatment was effective in reducing the oxygen concentrations to acceptable levels of ~700wppm for both heats. Fig. 4 shows the interstitial concentrations measured in the creep specimens of the U.S. Heat following the various conditions of exposure in Li.

Fabrication of Pressurized Creep Tubes for HFIR-RB-17J

Test matrix

The HFIR-RB-17J test matrix for the pressurized creep tube (PCT) specimens is shown in Table 2. It consists of a total of 28 PCT specimens of V-4Cr-4Ti; 14 specimens were fabricated from the U.S. Heat 832665 and the Japanese NIFS-1 Heat. Two subcapsules containing 7 PCT specimens from both heats will be irradiated at 450ºC and 600ºC.

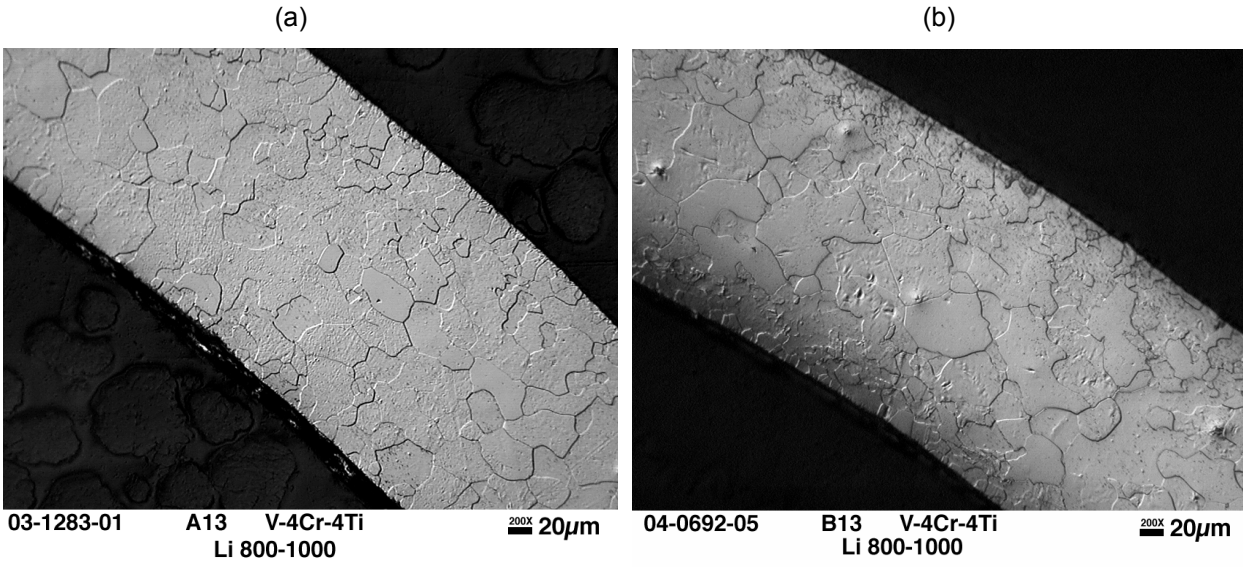

Fig. 3. Light micrographs showing the microstructure of the creep tube specimens of the: (a) U.S. Heat and (b) NIFS Heat after the double exposure to Li at 800ºC for 168 hrs followed by 1 hr at 1000ºC.

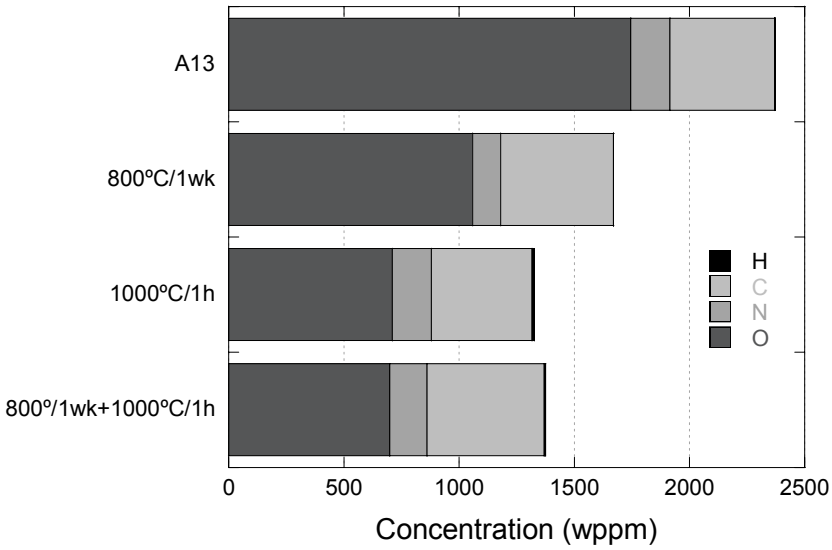

Fig. 4. A summary of the interstitial concentrations measured in the Batch B tube (US Heat) following various conditions of exposure to molten Li.

Li treatments

Twenty-three creep tube specimens were machined from the Batch B drawn tubing of V-4Cr-4Ti from the U.S. Heat 832665 and the Japanese NIFS-1 Heat. These specimens were 25.4 mm in length and were exposed to molten Li for lowering the oxygen concentration. The specimens were placed in liquid Li in a TZM alloy retort, located inside a glove box with high purity Ar atmosphere. The moisture, oxygen, and nitrogen levels are below 1 ppm in the glove box using a continuously operating molecular sieve/copper purification system and Ti-sponge column that is heated to 850ºC. The creep tubes were placed in the retort at a temperature of ~200ºC and then sealed using a Nb-1Zr gasket between mating knife-edge

Table 2. Test matrix of PCT specimens in HFIR-RB-17J irradiation experiment

Material	Temperature	
	450ºC	600ºC
U.S. Heat	7	7
NIFS-1 Heat	7	7

flanges. The temperature of the retort was then raised to 800ºC and the creep tubes were held for 168 hrs. Following this treatment, the temperature was raised to 1000ºC and the tubes were held for 1 hour, and then subsequently removed from the Li.

A cleaning procedure was used to remove the residual Li that solidified on the surface of the creep tubes. The first step consisted of removing the tubes from the glove box and soaking them in a beaker containing liquid anhydrous ammonia until most of the Li was removed. The tubes were then soaked in ethanol, followed by water. This procedure minimized the contamination of the tubes by hydrogen, which was confirmed by chemical analysis (Fig. 4).

Specimen Assembly and Dimensions

The creep tube specimens were individually fitted to end caps that were machined from the U.S. Heat of V-4Cr-4Ti and engraved with specimen identification codes. The wall thickness of each tube was measured in three azimuthal locations at approximately 6 mm from both ends using a tube wall micrometer. Table 3 shows the measured average wall thickness and standard deviation for the creep tubes. The end caps were electron-beam welded to the creep tubes, followed by annealing at 1000ºC for 1 hr in vacuum. The creep tube specimens were then measured using a laser profilometer. A total of 500 measurements were made in a helical pattern near the central 12.7 mm of the tubes to a precision of ±250nm. The average tube diameter was calculated from the central 300 measurements. Two measurements were recorded for each specimen.

Fill Pressures

The creep tube specimens were pressurized with He to several different pressures for the HFIR-RB-17J experiment. The specimens were placed in a pressure chamber, which was then pressurized at the desired pressure of He. A 0.20 mm diameter hole was machined into one endcap welded on the tube that allowed the internal pressure of the creep tube to equilibrate with the external pressure in the chamber. A 0.127 mm diameter wire of vanadium was inserted in the end cap hole and sealed with a laser welder. The pressurized creep tubes were leak tested using a helium leak detector and then measured using the laser profilometry, making three measurements on each tube. Table 4 shows the fill pressures of specimens that were included in HFIR-RB-17J experiment.

Discussion of Oxidation Behavior During Processing

The increase in oxygen for each annealing stage for Batch B tubing may be estimated from Fig 1 and plotted against the SAV ratio of the tubing at each stage, (Fig 5). For Batch A tubing only the initial and final oxygen analyses are known. Assuming that the oxygen content followed the same curve as the increasing SAV ratio as it did for Batch B, then we can estimate the incremental change in oxygen for each anneal and also plot these data in Fig 5. A comparison of the slopes of the two lines indicates that the oxygen pick-up rate was approximately three times more rapid for Batch B when the measured vacuum in the furnace chamber ranged from10^{-5} to 10^{-6} torr, than it was for Batch A (1 - 4 x 10^{-4} torr.)

A number of possible differences between the two batches were eliminated as being significant factors in this surprising result. The surface condition of the tubing was similar for both batches since the tubes

Table 3. Wall thickness measurements of un-pressurized creep tube specimens

U.S. Heat			Japanese NIFS-1 Heat		
Specimen I.D.	Average (mm)	Standard Deviation	Specimen I.D.	Average (mm)	Standard Deviation
UB00	0.259	0.005	UN00	0.247	0.010
UB01	0.241	0.002	UN01	0.256	0.008
UB02	0.253	0.003	UN02	0.246	0.004
UB03	0.224	0.006	UN03	0.246	0.004
UB04	0.258	0.005	UN04	0.247	0.005
UB05	0.251	0.001	UN05	0.247	0.002
UB06	0.255	0.003	UN06	0.250	0.003
UB07	0.259	0.004	UN07	0.250	0.001
UB08	0.251	0.004	UN08	0.249	0.003
UB09	0.257	0.012	UN09	0.248	0.003
UB10	0.247	0.004	UN10	0.247	0.003
UB11	0.254	0.007	UN11	0.244	0.004
UB12	0.252	0.007	UN12	0.248	0.007
UB13	0.249	0.004	UN13	0.246	0.003
UB14	0.254	0.004	UN14	0.246	0.004
UB15	0.252	0.003	UN15	0.252	0.002
UB16	0.258	0.004	UN16	0.246	0.005
UB17	0.262	0.002	UN17	0.247	0.003
UB18	0.252	0.004	UN18	0.239	0.003
UB19	0.257	0.003	UN19	0.243	0.003
UB20	0.263	0.008	UN20	0.241	0.003
UB21	0.257	0.004	UN21	0.243	0.001
UB22	0.258	0.003	UN22	0.250	0.005

were drawn by the same vendor. Batch A utilized a Ti getter-wrap whereas Ta was used for Batch B. However trial anneals at Vendor B with US heat tubing using Ta or Ti produced essentially the same level of oxygen pick-up. Differences in vacuum measurement techniques and furnace geometry between the two vendors were also discounted.

Since archive material from Batch A was not available, a section of the US heat tubing with a wall thickness 0.5mm was annealed at 1000ºC for 30min at Vendor A using the same furnace and vacuum conditions utilized during the earlier processing of Batch A (1-4 x 10^{-4} torr.) An identical sample, using the same wrap of Ta plus Ti foil was similarly annealed at Vendor B (1-2 x 10^{-5} torr.) The anneal carried out at the lower vacuum at Vendor A resulted in the formation of a visible oxide film whereas a visible oxide film did not form under the higher vacuum conditions at Vendor B It was found that this oxide film could be completely removed by subjecting the tubing to the 5 min acid cleaning procedure used for Batch A.

A possible explanation of the observed differences in the rate of increase in the bulk oxygen concentration between the two batches may be found in the work of Pint and DiStefano [7] who studied the oxidation kinetics of the US heat of V-4Cr-4Ti at 600-700ºC under partial pressures of oxygen in the range 10^{-3}-10^{-6} Pa (10^{-5}-10^{-8} torr). It was found that at 700ºC for example, oxidation followed linear kinetics at very low oxygen partial pressures (10^{-4}-10^{-6} Pa) without formation of a visible oxide film

Table 4. Helium pressurization data of creep tube specimens in the HFIR-RB-17J experiment

Tube		Irradiation	Hoop Stress	Fill Pressure
U.S. Heat	NIFS Heat	Temperature (ºC)	(MPa)	(Psig)
UB13	UN20	450	0	0
UB17	UN00	450	60	453
UB02	UN03	450	100	752
UB05	UN09	450	120	902
UB09	UN16	450	120	902
UB16	UN14	450	180	1350
UB04	UN07	450	200	1499
UB00	UN19	600	0	0
UB15	UN08	600	30	195
UB08	UN13	600	60	381
UB12	UN01	600	120	754
UB03	UN12	600	120	754
UB06	UN02	600	180	1126
UB10	UN11	600	200	1251

whereas at higher pressures, deviations from linearity were observed. The linear-parabolic behavior at 10^{-3} Pa was attributed to the formation of a surface oxide which inhibited oxygen diffusion into the substrate and under these conditions specimen surfaces became discolored by the formation of a visible oxide film. At 700ºC, the transition to an oxide film- limited oxidation regime occurred between 10^{-4} and10^{-3} Pa partial pressure of oxygen. Using tensile ductility measurements, it was shown that the surface oxide film formed a very effective barrier to the diffusion of oxygen into the interior.

Based on these observations, it is proposed that the origin of the unexpected increase in the overall oxygen pick-up rate which occurred under the improved vacuum conditions utilized for Batch B is related to a change in the oxidation mode. In the lower vacuum regime (Batch A), the formation of an oxide film inhibited internal oxidation and during subsequent prolonged acid cleaning, the oxide film, and hence a major fraction of the absorbed oxygen was removed prior to the next anneal. In contrast, the Batch B tubing was annealed in a regime where linear kinetics prevailed and the rate of internal oxidation was not inhibited by the formation of an oxide film. Further scanning–Auger analysis is in progress to quantify this hypothesis.

During commercial-scale processing of thick-sections of vanadium alloys, oxygen pick-up may be controlled satisfactorily by annealing in a sub-linear oxidation regime and removing the oxide film by acid cleaning at each stage. However for thin sections (< 0.5-0.8mm) this approach increases the risks of developing surface cracking. It is preferable to avoid the formation of surface oxide films and operate in the linear oxidation regime during intermediate anneals. However, since un-impeded oxygen diffusion into the bulk is rapid the furnace vacuum needs to be maintained in the 10^{-6}-10^{-7} torr regime.

Conclusions

1. Changes to the procedure for commercial-scale processing of thin-wall tubing of V-4Cr-4Ti were effective in reducing the incidence of surface cracking; however the rate of internal oxidation of the tubing increased by a factor of ~3 in spite of the improvement to the vacuum conditions by an order-of-magnitude.

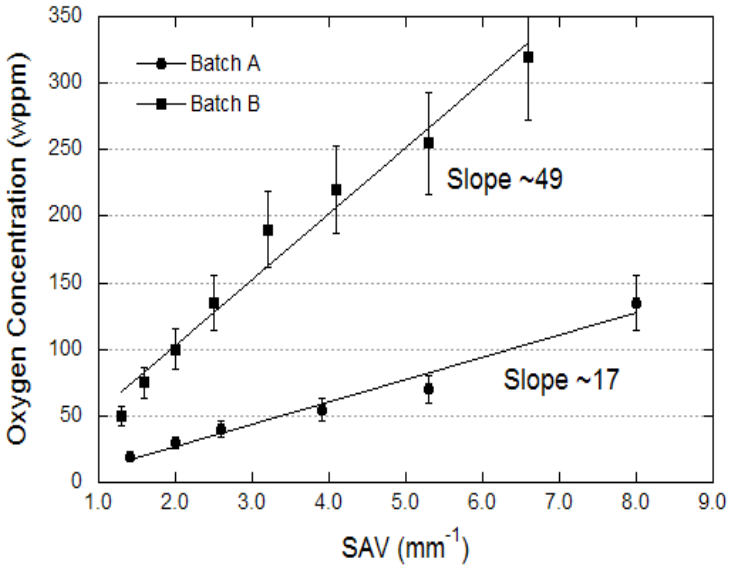

Fig. 5. Incremental oxygen increase for Batch A and Batch B tubing

2. Under the improved intermediate annealing vacuum conditions, the evidence suggests that oxygen diffusion was un-impeded by a surface oxide film and rapid internal oxidation occurred. Under the previously used lower vacuum conditions, oxygen diffusion into the bulk was limited by the formation of a visible oxide film; this oxide film was removed after each anneal by aggressive acid cleaning and as a result, the effective rate of oxygen pick-up was lower by a factor of ~3.

3 The internal oxidation process involved the formation of an oxygen-rich phase of the globular type of Ti(CON) phase; this process was reversed by exposure to liquid lithium at 800ºC and 1000ºC.

4. A two stage heat treatment in liquid lithium was developed which lowered the oxygen content in the final cold drawn tubing for both heats from ~1700wppm to ~700wppm and simultaneously produced a uniform recrystallized microstructure with 12-15 grains across the tube wall. This procedure was used to prepare the specimens for the irradiation creep test matrix in the HFIR-RB-17J experiment

Acknowledgements

The authors wish to acknowledge the outstanding technical support provided by L.T. Gibson and M.J. Gardner.

References

[1] H. Tsai, M. C. Billone, R. V. Strain, and D. L. Smith, Fusion Materials semi-Annual Report DOE/ER-0310/23 (December 1997) 149.

[2] M. L. Grossbeck, R. J. Kurtz, L. T. Gibson, and M. J. Gardner, Fusion Semi-Annual Progress Report DOE/ER-0310/32 (June 2002) 26.

[3] H. Tsai, M. C. Billone, T. S. Bray, and D. L. Smith, Fusion Materials Semi-Annual Progress Report DOE/ER-0310/27 (December 1999) 65.

[4] T. Nagasaka, T. Muroga, and T. Iikbo, Development of Tubing Technique for High-Purity Low Activation Vanadium Alloys, ANS Winter Meeting, Washington DC (November 2002).

[5] A. F. Rowcliffe, W. R. Johnson, and D. T. Hoelzer, Fusion Materials Semi-Annual Progress Report DOE/ER-0310/ 33 (December 2002) 7-21.

[6] A. F. Rowcliffe, D. T. Hoelzer, W. R.Johnson, and C. Young, Fusion Materials Semi-Annual Progress Report DOE-0310/34 (June 2003) 6-21.

[7] B. A. Pint and J. R. Distefano, Oxygen Embrittlement of Vanadium Alloys With and Without Surface Oxide Formation, J. Nucl. Mater 307-311 (2002) 560-565.

2.0 CERAMIC COMPOSITE MATERIALS

COMPATIBILITY OF CVD SIC WITH PB-LI AT 800°-1100°C—B. A. Pint, L. D. Chitwood, and J. R. DiStefano (Oak Ridge National Laboratory, USA)

OBJECTIVE

The objective of this task is to assess the long-term, high-temperature compatibility of SiC/SiC composites and Pb-Li. One proposed fusion reactor concept uses SiC/SiC composites with a self-cooled Pb-17Li blanket. One attractive feature of ceramic composites is their high temperature capabilities (≥1000°C). However, there is no compatibility data above 800°C for this system. As the first step in the evaluation process, monolithic SiC was exposed to Pb-17Li in capsule tests at 800°-1100°C.

SUMMARY

Static Pb-17Li capsule tests were performed on monolithic SiC specimens. To avoid unwanted reactions with Pb-Li, the SiC specimens were contained in SiC capsules. After 1000h at 800°C, no wetting was observed between Pb-Li and SiC and therefore no chemical attack would be expected. At 1100°C, there was evidence of only limited wetting after 1000h. After cleaning the specimens, no mass change was measurable at either temperature suggesting that SiC is compatible with static Pb-17Li to at least 1100°C.

PROGRESS AND STATUS

Introduction

Among the proposed fusion reactor concepts, silicon carbide composites are a structural material option that is thought to allow the highest reactor operating temperature (1000°-1100°C) and thus the highest operating efficiency.[1,2] Both the TAURO and ARIES-AT proposals have Pb-17at.%Li self-cooled blankets which are attractive because the Pb-17Li acts as coolant, neutron multiplier and tritium breeder.[3] (The eutectic Pb-Li composition was chosen because it has a low melting point of 235°C.) Present assessments of the materials feasibility for these concepts are incomplete because there is little information available on the high temperature compatibility of SiC with Pb-Li at temperatures of 800°C and higher. In a static exposure at 427°C, SiC composites (but not monolithic SiC) dissolved in unalloyed Li.[4,5] However, the activity of Li in Pb-17Li is greatly reduced (1.2×10^{-4} at 500°C)[6] suggesting that compatibility would be better with the eutectic. Previous results at 800°C have shown limited reaction between Pb-17Li and SiC composites.[7,8] Other work has examined the compatibility of SiC and its composites with ceramic breeding materials for He-cooled concepts.[9]

In order to obtain information about SiC compatibility with Pb-17Li at 800°-1100°C, static capsule experiments were conducted with specimens of high-purity CVD SiC. These experiments used high-purity monolithic SiC instead of composites as a first step towards evaluating SiC compatibility to avoid the microstructural and microchemistry complexities of composites and due to the better compatibility found for monolithic material compared to SiC/SiC composites in Li.[4] Capsules were exposed for 1000h at 800°, 1000° and 1100°C.

Experimental Procedure

Proper execution of the experiment is a critical part of this type of test, particularly at the high temperatures of interest. In order to isolate the specimen-liquid metal system and avoid additional contamination of the liquid metal during the test, it is preferable to perform a capsule test in a sealed (i.e. welded) refractory metal inner capsule which is then placed in a secondary, oxidation- resistant outer capsule to prevent the refractory metal capsule from oxidizing during the test. Refractory metals are relatively inert to Li in this

temperature range.[10] This type of capsule experiment has been successfully used in testing ceramics in Li.[11] A Mo inner capsule appears to be inert to Li at temperatures ≤800°C, and is expected to be compatible with Pb-Li.[12] However, Mo_2C (-77.4kJ/mol) is more stable than SiC (-45.6kJ/mol) at 823°C.[13] Therefore, a Mo capsule could affect the corrosion process, similar to the increased corrosion observed when vanadium alloy capsules were used for AlN samples exposed to Li.[11] (No problems were reported with Mo capsules at ≤800°C but higher temperatures may be a problem, including the formation of a Pb-Mo-C phase.[8]) Thus, for this experiment, a SiC inner crucible was used to contain the Pb-Li and then this unsealed, but lidded crucible was placed inside a Mo secondary capsule that was sealed by arc welding, Figure 1. The Pb-Li composition was obtained by adding appropriate amounts of 99.999% purity Pb shot and pieces of high purity unalloyed Li (140 ppmw N)[11] to the SiC crucible. To hold the SiC specimen in place at the bottom of the SiC capsule during the test, a SiC holder was used. The lid of the SiC capsule was held closed with a 0.25mm diameter Mo wire fed through the lid of the Mo capsule and welded in place during assembly. The outer oxidation resistant capsule was type 304 stainless steel or type 600 Inconel. The various capsules and crucibles were loaded and sealed in a high-purity argon glove box using gas-tungsten-arc welding. In order to ease specimen removal, at the end of the high temperature exposure the entire assembly was inverted so that the Pb-Li would drain away from the SiC specimen, Figure 1b.

The high purity (99.9995%) CVD β-SiC specimens were manufactured by Rohm and Haas Company Advanced Materials (Woburn, MA) and had dimensions of 3 x 8 x 12 mm and a density of 3.21g/cm^3. Specimen mass was measured before and after exposure on a Mettler-Toledo balance with an accuracy of ±0.02mg. The sealed capsules were exposed in laboratory air for 1000h at 800°, 1000° and 1100°C in resistively heated box furnaces with a thermocouple positioned near the capsule. After exposure, cleaning

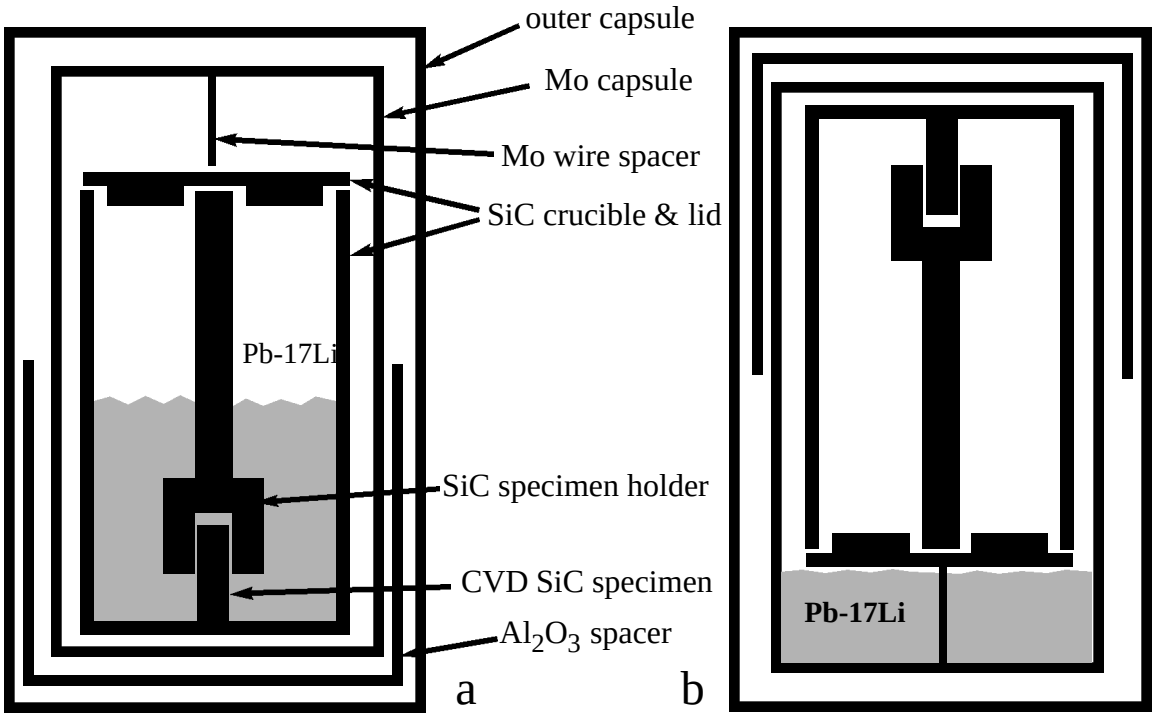

Figure 1. Schematic of the capsule test (a) during loading and at temperature and (b) after test. The outer capsule is stainless steel or a Ni-base Inconel alloy. The secondary capsule is Mo and the inner capsule and specimen holder are SiC. The capsule is inverted at the end of the test to allow the Pb-Li to flow away from the SiC specimen and crucible. An alumina spacer was used at 1100°C.

of the specimen was a significant issue. Various techniques have been suggested in the literature, including a mixture of acetic acid, hydrogen peroxide and ethanol;[14] just acetic acid and hydrogen peroxide;[5] stoichiometric amounts of nitric acid;[12] and immersion in low temperature liquid Li followed by Li removal in alcohol or water.[15] The first method was used in this study with the specimen immersed for 24h. After exposure, specimens were characterized by Auger electron spectroscopy (AES) and x-ray photoelectron spectroscopy (XPS).

Results

The capsule exposed for 1000h at 800°C was opened and disassembled in the argon glove box, Figure 2. Surprisingly, all of the SiC parts and the specimen were almost clean of liquid metal which had drained into the Mo capsule and solidified after the capsule was inverted (Figure 1b). The clean crucible, holder and specimen suggest that Pb-Li did not wet SiC under these conditions. (For capsule exposures in Li, the ceramic specimens and capsule remain covered with a layer of Li after exposures at 400°-800°C.[11]) No change in the specimen appearance was observed after cleaning; although a small amount of powdery black residue was left on the specimen surface. No change in the specimen mass was measurable and the original shiny surface finish was still visible. The specimen was analyzed by XPS and weak Pb and Li signals were detected on the surface but only a layer of C was detected by AES.

During exposure at 1000°C, the capsule system failed causing catastrophic oxidation of the stainless steel and Mo capsules and oxidizing the Pb-Li as well as the SiC parts. The problem was likely caused by a solid state reaction between the stainless steel outer capsule and the Mo secondary capsule. To avoid this problem at 1100°C, an Inconel outer capsule was used and an alumina spacer was included between the Mo and Inconel capsules, Figure 1. The 1000°C test is being repeated.

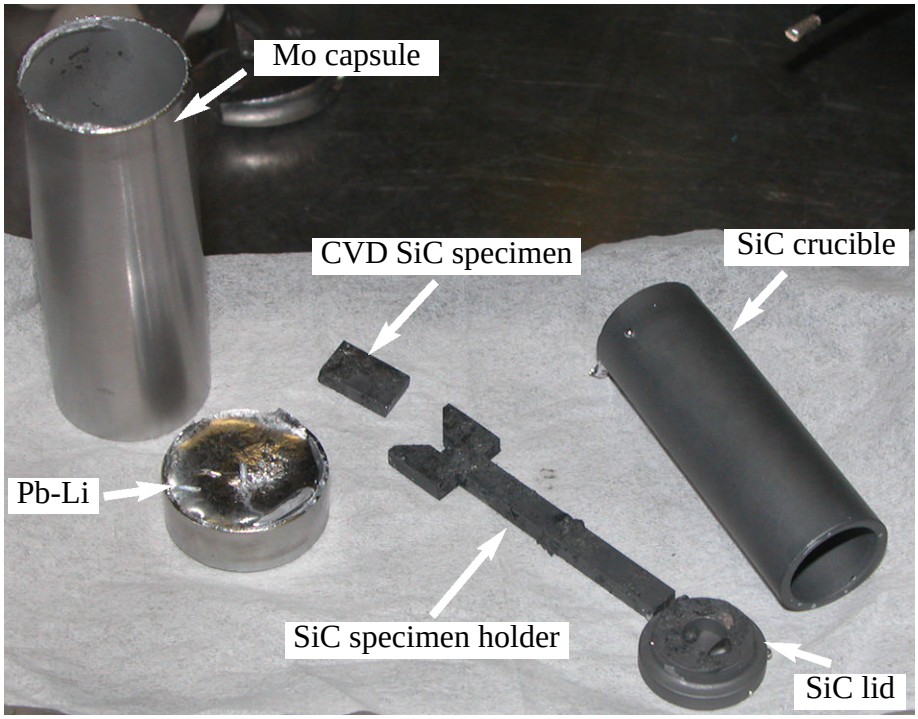

Figure 2. Photograph of the components inside the glove box immediately after disassembly of the 1000h, 800°C capsule test. Note that all of the components came out clean because the Pb-Li did not wet SiC at this temperature.

When the capsule exposed for 1000h at 1100°C was opened in the glove box, the SiC parts had a similar appearance as those exposed at 800°C. In this case, the Mo capsule was more brittle and shattered during opening as did the SiC crucible, Figure 3. The Pb-Li drained away from the specimen leaving only a few small patches of metal on the specimen and holder. Before cleaning, the specimen mass had increased by 18mg. However, after 24h in the cleaning solution, there was no measurable change in specimen mass from the original mass. Again there was a black residue on the surface, but the original surface finish could be seen. Further characterization is being performed on this specimen.

Discussion

In agreement with previous static-type experiments, no degradation was noted by exposing SiC in Pb-17Li at 800°C.[7,8] The indication of no wetting at this temperature is important because a lack of wetting precludes any chemical attack.[16] Some limited wetting may have occurred at 1100°C. However, only a few thin patches of metal were left on the specimen after the test and the crucible and holder were relatively free of metal. Observations with stainless steel and mercury indicate that there can be an extended incubation period to develop wetting.[16] Therefore, wetting observations may be dependent on the exposure time. A direct assessment of wetting behavior in this system including the temperature where wetting begins could provide important information about the upper temperature limit for compatibility between SiC and Pb-17Li. However, the high temperatures, high vapor pressure of Li and other experimental difficulties with wetting experiments[17] make this a difficult experiment to perform.

More complete characterization of the SiC specimens is being conducted. Also, the chemistry of the Pb-Li after the tests is being determined. Additional experiments will be performed on monolithic SiC and SiC composites in order to determine the compatibility of fibers and, especially, the fiber-matrix interface which can be susceptible to enhanced corrosion.[18,19] However, it is anticipated that a dense CVD SiC seal coat will cover the outer layer of any SiC composite components.

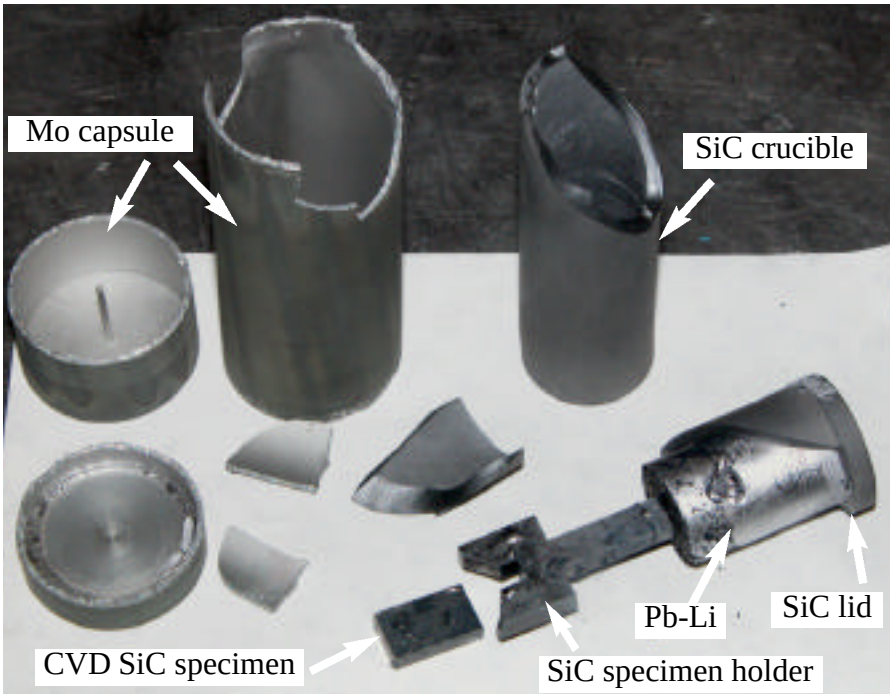

Figure 3. Photograph of the components inside the glove box immediately after disassembly of the 1000h, 1100°C capsule test. The Mo and SiC crucibles broke during disassembly.

References

[1] A. Hasegawa, A. Kohyama, R. H. Jones, L. L. Snead, B. Riccardi, and P. Fenici, J. Nucl. Mater. 283-287 (2000) 128.
[2] R. H. Jones, L. Giancarli, A. Hasegawa, Y. Katoh, A. Kohyama, B. Riccardi, L. L. Snead, and W. J. Weber, J. Nucl. Mater. 307-311 (2002) 1057.
[3] A. R. Raffray et al., Fusion Eng. Des. 55 (2001) 55.
[4] T. Terai, T. Yoneoka, and S. Tanaka, unpublished research 2000 from reference #2.
[5] T. Yoneoka, S. Tanaka, and T. Terai, Mater. Trans. 42 (2001) 1019.
[6] P. Hubberstey, J. Nucl. Mater. 247 (1997) 208.
[7] F. Barbier, Ph. Deloffre, and A. Terlain, J. Nucl. Mater. 307-311 (2002) 1351.
[8] H. Kleykamp, J. Nucl. Mater. 321 (2003) 170.
[9] H. Kleykamp, J. Nucl. Mater. 283-287 (2000) 1385.
[10] E. E. Hoffman, J. H. DeVan, and J. R. DiStefano, in Evolution of Refractory Metals and Alloys, Eds. E. N. C. Dalder, T. Grobstein, and C. S. Olsen, TMS, Warrendale, PA (1994), 137.
[11] B. A. Pint, J. H. DeVan, and J. R. DiStefano, J. Nucl. Mater. 307-311 (2002) 1344.
[12] H. Feuerstein, H. Gräbner, J. Oschinski, and S. Horn, J. Nucl. Mater. 233-237 (1996) 1383.
[13] M. W. Chase, C. A. Davies, J. R. Downey, D. J. Frurip, R. A. McDonald, and A. N. Syverud, JANAF Thermochemical Tables, 3rd Edition, Amer. Inst. Physics, New York, NY (1985).
[14] G. Benamati, C. Fazio, and I. Ricapito, J. Nucl. Mater. 307-11 (2002) 1391.
[15] P. F. Tortorelli, J. Nucl. Mater. 191-194 (1992) 965.
[16] S. J. Pawel, Report # ORNL/TM-2002/280, Oak Ridge National Laboratory, Oak Ridge, TN.
[17] P. Protsenko, A. Terlain, M. Jeymond, and N. Eustathopoulos, J. Nucl. Mater. 307-311 (2002) 1396.
[18] P. F. Tortorelli, S. Nijhawan, L. Riester, and R. A. Lowden, Ceram. Eng. Sci. Proc. 14 (1993) 358.
[19] K. N. Lee and N. S. Jacobson, J. Am. Ceram. Soc. 78 (1995) 711.

EFFECTS OF IRRADIATION AND POST IRRADIATION ANNEALING ON THE THERMAL CONDUCTIVITY/ DIFFUSIVITY OF MONOLITHIC SIC AND SIC/SIC COMPOSITES—G. E. Youngblood, D. J. Senor, and R. H. Jones (Pacific Northwest National Laboratory)*

Extended abstract of a paper submitted to the Journal of Nuclear Materials as part of the proceedings of the 11th International Conference on Fusion Reactor Materials, Kyoto, Japan, December 7-12, 2003.

EXTENDED ABSTRACT

Laser flash thermal diffusivity measurements were made on high-purity monolithic CVD-SiC (impurity concentration <5 wppm) and 2D f-SiC/PyC/ICVI-SiC composite samples (plain weave Hi-Nicalon™ fabric layers with 0-90 layup made by the isothermal chemical vapor infiltration process and with either a "thick" 1.0 μm or a "thin" 0.11 μm PyC fiber coating) before and after irradiation in the HFIR reactor (250 to 800°C, 4-8 dpa-SiC) and after post-irradiation annealing composite samples to 1200°C.

Thermal conductivity in SiC is controlled by phonon transport. Point defects introduced into SiC during neutron irradiation are effective scattering centers for phonons, and as a consequence the thermal conductivity is sharply reduced. For irradiation temperatures below ~800°C, the accumulation of point defects (in SiC mostly single or small clusters of interstitials and isolated vacancies) saturates when the interstitial-vacancy recombination rate equals the defect production rate. For saturation conditions, the relative reduction in the SiC thermal conductivity decreases in a manner similar to its swelling reduction with increasing irradiation temperature. Examination of SiC swelling data at various irradiation temperatures and doses indicates that saturation occurs for ~2 dpa-SiC at 200°C and decreases continuously to ~0.4 dpa-SiC at 800°C. Based on a model that assumes a uniform distribution of the phonon scattering defects, the calculated defect concentration for unirradiated CVD-SiC was less than 1 appm, which is consistent with the manufacturer's value of <5 wppm impurities. The defect concentrations estimated for the irradiated CVD-SiC samples decreased continuously from ~25,000 to 940 appm as the irradiation temperature increased from 252 to 800°C. The small intrinsic defect concentration in comparison to the rather large extrinsic irradiation-induced defect concentrations illustrates why CVD-SiC makes an ideal irradiation damage monitor.

in Figure 1, the temperature dependence of K_{ir}/K_o, the ratio of the irradiated-to-unirradiated thermal conductivity values measured at the irradiation temperature, is graphically presented. The general trend that the K_{ir}/K_o-ratio increases as the irradiation temperature increases reflects the relative dominance of temperature independent point defect phonon scattering in the lower temperature range, while the temperature dependent phonon-phonon scattering becomes relatively more important with increasing temperature. The curve for high-purity CVD-SiC represents a lower limit for SiC-based materials with K_{ir}/K_o ~ 0.05 at 200°C and only gradually increasing up to ~0.12 by 800°C. For irradiation temperatures above 800°C, an apparent transition occurs where the K_{ir}/K_o-curve turns upward with an increasing slope until at 1100°C the ratio is ~0.6. Above ~800°C, the defect structure formed by the highly mobile irradiation-induced interstitials must become relatively coherent with the surrounding SiC matrix and presents less effective phonon scattering centers. Furthermore, above 800-1000°C the equivalent dose required for saturation also appears to "turn around" and starts to increase with increasing dose as evidenced by the dose dependence at ≈1 dpa observed at 1100°C.

In Figure 2, the measured thermal diffusivity $\alpha(T)$-values for the Hi-Nicalon™ composite with the "thick" PyC interface are presented for various conditions. When the PyC interfaces were removed by oxidation, the α-values dramatically decreased to about 40% of their as-received values. Such a large degradation indicates that entire fiber bundles (including the SiC matrix material contained within the bundles) were separated (thermally decoupled) from the surrounding SiC matrix. For the irradiated and annealed

*Pacific Northwest National Laboratory (PNNL) is operated for the U.S. Department of Energy by Battelle Memorial Institute under contract DE-AC06-76RLO-1830.

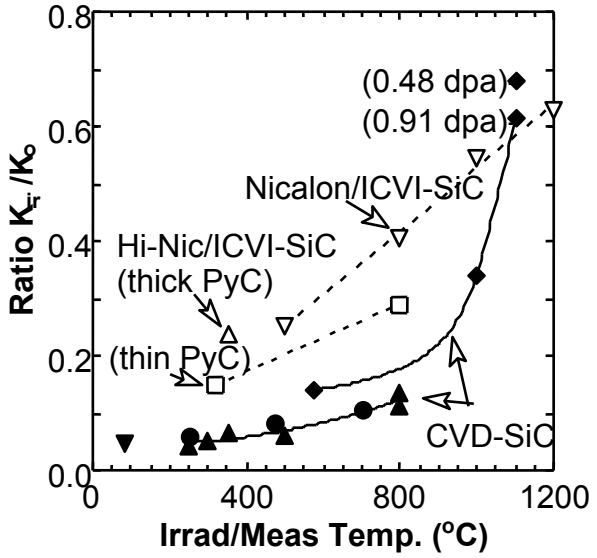

Figure 1. Ratio K_{ir}/K_o for high-purity CVD-SiC and SiC and for 2D f-SiC/SiC composites.

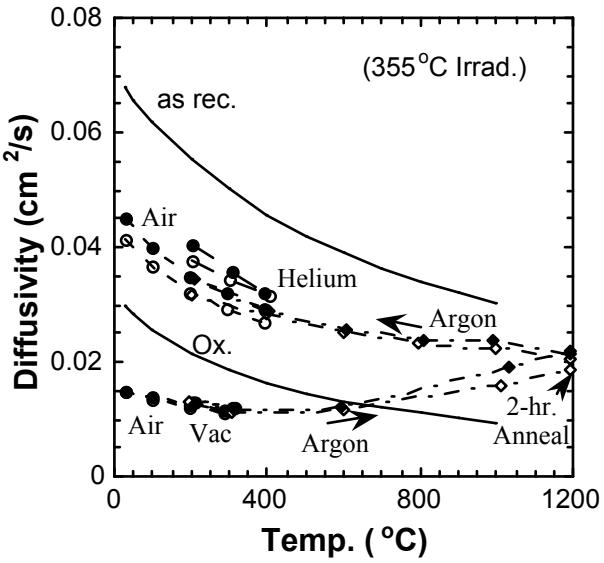

Figure 2. Thermal diffusivity of 2D Nicalon/ICVI-SiC composites with a "thick" PyC interface for various unirradiated (solid lines) and irradiated and/or annealed (dashed lines) conditions.

conditions, close agreement of the α(T)-values made in vacuum, argon or air just after irradiation indicate that at this point physical fiber/matrix (f/m) separations did not exist even though the matrix was expected to swell ~0.8% and the Hi-Nicalon™ fiber was expected to shrink ~1.7%. Apparently, the radial swelling in the irradiated PyC fiber coating compensated somewhat for the differential shrinkage-swelling between the f/m components, and significant f/m thermal decoupling didn't occur. In contrast, when the Hi-Nicalon™ composite with a "thin" PyC interface was irradiated at 330 or at 800°C and then taken through the same measurement and annealing sequence, the α(T)-values were substantially different in different atmospheres just after irradiation (data not shown). For this case, radial swelling in the irradiated "thin" PYC interface was insufficient to close the f/m separations and at least partial f/m thermal decoupling occurred. However, after annealing to 1200°C and cooling to the irradiation temperature, substantial f/m debonding (or decoupling) occurred for both cases due to permanent net shrinkage in the fiber and the PyC interface components.

A thermal conductivity model based on composite constituent properties as well as microstructural and architectural variables was used to predict α(T)-values for the irradiated composites. The predictions closely matched the observed magnitudes and slopes of the measured α(T)-values after irradiation. Input to the model required that the major contribution to K_{eff} for the irradiated and annealed Hi-Nicalon composites was the conductivity of a still-continuous SiC matrix, which indicates that the major cause of the degradation in K_{eff} was the accumulation of the irradiation-induced point defects in the matrix constituent.

For the unirradiated Hi-Nicalon/PyC/ICVI-SiC composites, the K_{eff}-values calculated from the α(T)-data ranged from a maximum 15 W/mK at 200°C down to 8-10 W/mK at 1000°C. Then from estimated K_{ir}/K_o-values for these composites (also shown in Figure 1), K_{ir}(T) values can also be estimated.

Acknowledgements

The irradiation tests were performed as part of the U.S./Japan JUPITER fusion materials collaboration.

MODELING THE TRANSVERSE THERMAL CONDUCTIVITY OF 2D-SIC$_F$/SIC COMPOSITES MADE WITH WOVEN FABRIC—G. E. Youngblood, D. J. Senor, and R. H. Jones (Pacific Northwest National Laboratory)*

Oral presented at the American Nuclear Society Winter Meeting, November 17-21, 2002, in the topical session on Technology of Fusion Energy. A paper by the same title is scheduled to be published in Fusion Science and Technology, June 2004.

EXTENDED ABSTRACT

The hierarchical two-layer (H2L) model was developed to describe the effective transverse thermal conductivity (K_{eff}) of a 2D-SiC$_f$/SiC composite plate made from stacked and infiltrated woven fabric layers in terms of constituent properties and microstructural and architectural variables. The model includes the effects of fiber-matrix interfacial conductance, high fiber packing fractions within individual tows and the non-uniform nature of 2D fabric/matrix layers that usually include a significant amount of interlayer porosity. Previously, H2L model K_{eff}-predictions were compared to measured values for two versions of 2D Hi-Nicalon™/PyC/ICVI-SiC composite, one with a "thin" (0.11 μm) and the other with a "thick" (1.04 μm) pyrocarbon (PyC) fiber coating, and for a 2D Tyranno™ SA/"thin" PyC/FCVI-SIC composite. In this study, H2L model K_{eff}-predictions were compared to measured values for a 2D-SiC$_f$/SiC composite made using the ICVI-process with Hi-Nicalon™ type S fabric and a "thin" PyC fiber coating. The values of K_{eff} determined for the latter composite were significantly greater than the K_{eff}-values determined for the composites made with either the Hi-Nicalon™or the Tyranno™ SA fabrics. Differences in K_{eff}-values were expected for the different fiber types, but major differences also were due to observed microstructural and architectural variations between the composite systems, and as predicted by the H2L model.

Based on the results for the four different 2D-SiC$_f$/SiC systems examined, we concluded that the H2L model realistically describes how K_{eff} depends upon constituent, structural, microstructural and architectural variables for typical 2D composites made by chemical vapor infiltration (CVI). Using the H2L model and directly measured K_{eff}- and K_f-values, the fiber PyC coating K_c-values for these four composite systems, when assumed to be the same, were predicted to range from ≈28 W/mK at RT, increase to a maximum 34 W/mK at about 300°C, then continuously decrease to ≈ 28 W/mK at 1000°C. Likewise, the "intrinsic" K_m-values of the ICVI-SiC matrix were predicted to decrease continuously from ≈40 W/mK at RT to 18-20 W/mK at 1000°C. The corresponding K_m-values for the FCVI-SiC matrix were predicted to be somewhat less, ≈28 W/mK at RT decreasing to ≈15 W/mK at 1000°C.

Recent fusion reactor power core design concepts utilizing continuous fiber-reinforced SiC$_f$/SiC composite as a structural material require a K_{eff} ≈15-20 W/mK during operation in the temperature range 600-1000°C [1]. Based on observed degradation limits for irradiated SiC$_f$/SiC composite, to meet current fusion thermal conductivity goals we estimate that candidate SiC$_f$/SiC composites should have unirradiated K_{eff}-values of 43 and 27 W/mK minimum at 600°C and 1000°C, respectively. Current commercially available composites made by CVI-processing with Hi-Nicalon™ SiC fabric exhibit K_{eff}-values at 600°C and 1000°C of only about 11 and 9 W/mK, respectively, values which are much lower than design goals.

In Figure 1, measured K_{eff}-values for a SiC$_f$/SiC composite system made by the CVI-process with near stoichiometric SiC fiber (Hi-Nicalon™ type S) are shown along with H2L model predictions of K_{eff} for a hypothetical and an "optimized" composite both made by the CVI-process, but with Tyranno™ SA fibers. Also shown in this figure are our projected minimum fusion K_{eff}-goals for SiC$_f$/SiC within a 600-1000°C window. Clearly, the K_{eff}-values for currently available 2D-SiC/SiC composite systems and even for a hypothetical "optimized" system fall far short of fusion power core design goals.

*Pacific Northwest National Laboratory (PNNL) is operated for the U.S. Department of Energy by Battelle Memorial Institute under contract DE-AC06-76RLO-1830.

For the following reasons, it does not appear likely that the current minimum fusion K_{eff}-goals can be attained for even an optimized 2D SiC_f/SiC composite system made with woven fabrics with a CVI-SiC fabricated matrix. The Tyranno™ SA fiber has relatively high purity and is crystalline, and has about as high a value of K_f achievable for a SiC-type fiber. The ICVI-SiC matrix is high-purity crystalline SiC with a minimum amount of internal microporosity and a favorable grain crystalline microstructure for producing relatively high K_m-values. A certain amount of macroporosity, both within the fiber bundles and between the fabric layers, is necessary for gas exchange as part of the CVI-process, and likely cannot be reduced beyond that obtained using the isothermal process. Using satin weave fabric with a 0-90 lay-up likely results in the most favorable macroporosity shape factor for a 2D alternating fabric-matrix layer architecture. The f/m interfaces for the examined CVI-processed systems were all well bonded, so the interfacial conductance was already high enough to not have a degrading effect on K_{eff}. Overall, it appears that the margin of improvement in K_{eff} required to meet the minimum fusion K_{eff}-goals is just too large (on the order of doubling even the optimized K_{eff}-values) to be met by any minor improvements potentially possible through CVI-fabrication, structural or architectural methods. Unless design considerations allow adjustment of the minimum fusion K_{eff}-goals downward, it appears prudent for the fusion community to emphasize other methods for continued efforts to develop a SiC_f/SiC composite suitable to meet the fusion thermal conductivity goals.

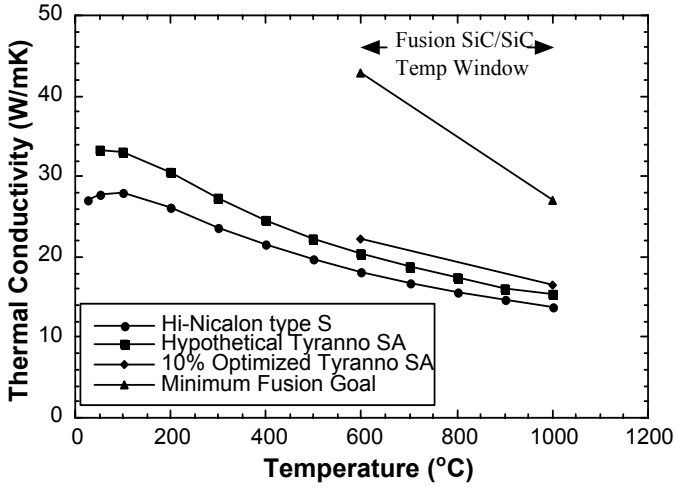

Figure 1. H2L model predictions of K_{eff} for a hypothetical Tyranno™ SA composite system and a 10% optimized Tyranno™ SA system compared to measured K_{eff}-values for the Hi-Nicalon™ type S composite system and to our projected minimum K_{eff} fusion goals for unirradiated SiC_f/SiC, 43 and 27 W/mK at 600 and 1000°C, respectively.

References

[1] A. R. Raffray, R. Jones, G. Aiello, M. Billone, L. Giancarli, H. Golfier, A. Hasegawa, Y. Katoh, A. Kohyama, S. Nishio, B. Riccardi, and M. S. Tillack, Design and material issues for high performance SiC_f/SiC-based fusion power cores, Fusion Eng. and Design 55 (2001) 55.

A MODEL STRESS ANALYSIS OF SWELLING IN SIC/SIC COMPOSITES AS A FUNCTION OF FIBER TYPE AND CARBON INTERPHASE STRUCTURE—C. H. Henager, Jr. (Pacific Northwest National Laboratory), E. A. Le (University of Washington), and R. H. Jones (Pacific Northwest National Laboratory)*

OBJECTIVE

The objective of this task is to develop and validate a numerical model of swelling-induced stresses in SiC composites with Hi-Nicalon and Type-S ceramic fibers and having a pyrocarbon interphase to determine which pyrocarbon interphase results in the lowest stresses due to irradiation.

EXTENDED ABSTRACT

A continuous fiber composite was simulated by four concentric cylinders (consisting of fiber, fiber/matrix interphase coating, matrix, and surrounding composite) to explore composite stresses when irradiation swelling of the various components is included as a function of neutron dose. SiC Type-S and Hi-Nicalon fibers and three types of transversely isotropic carbons for the fiber coating were considered. Radiation swelling terms were added by using parametric fits to strain (swelling) as a function of dose for the various materials. The swelling of β-SiC and Type-S fibers for different temperatures [1, 2] was fit using linear swelling versus time and the swelling is assumed to be linearly dependent on dose up to a critical dose, which then saturates at constant swelling; the saturation dose being temperature dependent. For Hi-Nicalon fibers, fiber density as a function of neutron dose was converted to fiber strain. The data of Kaae [3] were used for the swelling of three pyrolytic carbons, denoted as high-density isotropic carbon (HDIC), low-density isotropic carbon, and high-density slightly anisotropic carbon.

Six different cases were studied under simulated neutron irradiation at 1000°C using a dose rate of 0.44 dpa/year. Values of the model domain radii were chosen to match microstructural information for CVI SiC/SiC composites. The fiber coating thickness was 0.15 μm which is representative of pyrocarbon coating thicknesses. One case considered a 1-μm thick HDIC fiber coating on Type-S fiber. The stresses were computed out to 8 dpa. Composites containing Hi-Nicalon fibers reach 1 GPa radial tensile stresses at the fiber-coating interface at 1 dpa, large enough to cause interfacial debonding due to differential swelling between the Hi-Nicalon fiber and the SiC matrix. These large stresses occur at the interface regardless of the type of pyrocarbon coating. The observation of interfacial debonding in irradiated Hi-Nicalon fiber composites validates this finding of the model. Composites containing Type-S fiber have no differential swelling stresses developing between the fiber and matrix. Differential swelling of the various carbon coatings causes small values of radial stresses (ranging from 65 to 280 MPa) at the fiber/coating interface, allowing retention of fiber/matrix bonding up to significant neutron doses. In particular, the HDIC pyrocarbon interphase shows excellent irradiation stability and results in low interfacial stresses in the simulation. Although no detailed study of the pyrocarbon interphase of irradiated SiC/SiC with Type-S fiber has been conducted, the lack of debonding after irradiation has been observed. Since the carbon interphase swelling determines the radial debonding stresses for the Type-S fiber materials, interphase tailoring can be explored to control composite properties by controlling the coating deposition process. Changing the coating thickness from 0.15 μm to 1 μm increases radial stresses at the fiber-coating interface. This result suggests that thinner coatings can lead to improved radiation resistance.

References

[1] R. J. Price, Nucl. Technol. 35 (1977) 320.
[2] R. Scholz, J. Nucl. Mater. 258-263 (1998) 1533.
[3] J. L. Kaae, Nuclear Technol. 35 (1977) 359.

*Pacific Northwest National Laboratory (PNNL) is operated for the U.S. Department of Energy by Battelle Memorial Institute under contract DE-AC06-76RLO-1830.

HELIUM EFFECT ON IRRADIATED MICROSTRUCTURES AND PROPERTIES IN SiC/SiC COMPOSITES—Y. Katoh (Oak Ridge National Laboratory), S. Kondo, K. Ozawa, K. H. Park, and A. Kohyama (Kyoto University)

OBJECTIVE

The objective of this report is to summarize recent efforts for understanding the effects of helium on irradiated microstructures and properties in silicon carbide and its composites in fusion environments by using a technique of dual-beam charged particle irradiation.

SUMMARY

Synergistic effects of displacement damage production and helium implantation are being extensively studied. Recent progress can be highlighted:

- Major progress is achieved in comprehensive understanding of microstructural development in SiC during irradiation to very high doses up to very high temperatures.
- Substantial understanding of void swelling behavior of SiC in the presence of helium is provided.
- Superior irradiation stability of an advanced fiber-matrix interphase is demonstrated.
- Helium-related potential issues for the Generation-III SiC fibers are identified.
- Understanding of irradiation-induced toughening and the underlying mechanism is advanced.

PROGRESS AND STATUS

Technical issues related to potential helium effects in SiC and SiC/SiC composites for fusion in-vessel structural applications are identified and summarized in Table 1 [1]. Among the anticipated issues, potential helium-assisted enhancement in point-defect swelling and thermal conductivity degradation may force up the low temperature application limit of the materials of these classes. On the other hand, the enhanced cavity swelling may lower the limits of highest temperature and lifetime fluence in high temperature regimes of design window. Potential detrimental effects on interphase stability, irradiation creep and matrix fracture toughness may affect the materials performance at all temperatures.

Microstructural Development under Dual-beam Irradiation

The experiment was performed using chemically vapor deposited (CVD) SiC (Roam & Haas Co., Philadelphia, PA) as samples at DuET dual beam static accelerators facility, Kyoto University, Japan. Irradiation temperatures, displacement damage rate, and helium co-implantation rates were 873~1673K, ~$1x10^{-3}$ dpa/s, and 0/60 appm He/dpa, respectively.

At 1273K, ‘black spot’ defects and small dislocation loops developed at very high density. In the dual-beam irradiation case, the initial ‘black spot’ microstructure appeared substantially finer than in the single-beam case. As the number density of ‘black spot’ defects increased with the increasing dose, they tended to align to form planer agglomerates, and eventually collapsed into planer defects. At 1673K, without helium, the initial ‘black spot’ features developed into large planer defects on <111> family planes before the fluence level reached 30dpa. When helium was present, dislocation networks and fine helium bubbles developed instead of the planer defects by 30dpa.

Table 1. Potential helium effects in irradiation properties of SiC and SiC/SiC composites

Enhanced point-defect swelling	- Potentially significant at intermediate temperatures. - Comprehensive data available from a dual-beam ion irradiation experiment.
Cavity-swelling	- Potentially significant at >1000C at very high fluence levels. - Cavity formation occurs in high purity crystalline SiC when helium atoms are present.
Enhanced thermal conductivity degradation	- Potentially significant at intermediate temperatures. - Experimental data not published.
Fracture toughness modification	- Potentially significant at all temperatures. - Fracture toughness of SiC may either be enhanced or be degraded and may consequently influence composite strength.
Enhanced interphase instability	- Potentially significant at all temperatures. - Microstructural damage accumulation and amorphization are promoted by helium in PyC interphase. - Helium cavity precipitation on PyC-SiC boundaries.
Enhanced irradiation creep	- Potentially significant at all temperatures. - Very significant dislocation evolution acceleration and/or modification by helium.
Accelerated amorphization	- Anticipated only at < ~150C.

Cavities (voids and bubbles) were not observed in CVD-SiC irradiated with self ions only at 1273~1673K. During dual-beam irradiation at T>~1273K, relatively large cavities developed preferably on grain boundaries, subgrain boundaries and twin boundaries. These cavities grew in size with the increasing dose. Tiny bubbles became visible within matrix at very high concentration at T>~1473K. Size distribution of the matrix bubbles remained unchanged up to ~100dpa. Large coarse cavities were found, both on grain boundaries and within matrix, in the subsurface regions of 1673K dual-beam irradiated samples. This indicates that a long-range helium transport has occurred toward the free surface by diffusion on grain boundaries and/or along network dislocations.

As a conclusion, helium co-implantation at 60 appm He/dpa significantly modified the irradiated microstructure in cubic SiC. The observation is summarized in Figure 1. Helium influenced evolution of all types of defects as well as introduced new type of defects in irradiated SiC. Drastic microstructural modifications by helium occurred at T>~1073K, at which vacancies are mobile. Void swelling, high temperature creep, and thermal conductivity shall be affected by helium through vacancy-related mechanisms. Many of the underlying mechanisms for the observed helium effects on microstructural defect evolution are not sufficiently understood. Nature of some defect features is not yet known, either. The interaction of helium with development of dislocation microstructures seems to be the key issues for better understanding the helium effects. Details will be published in Reference [2].

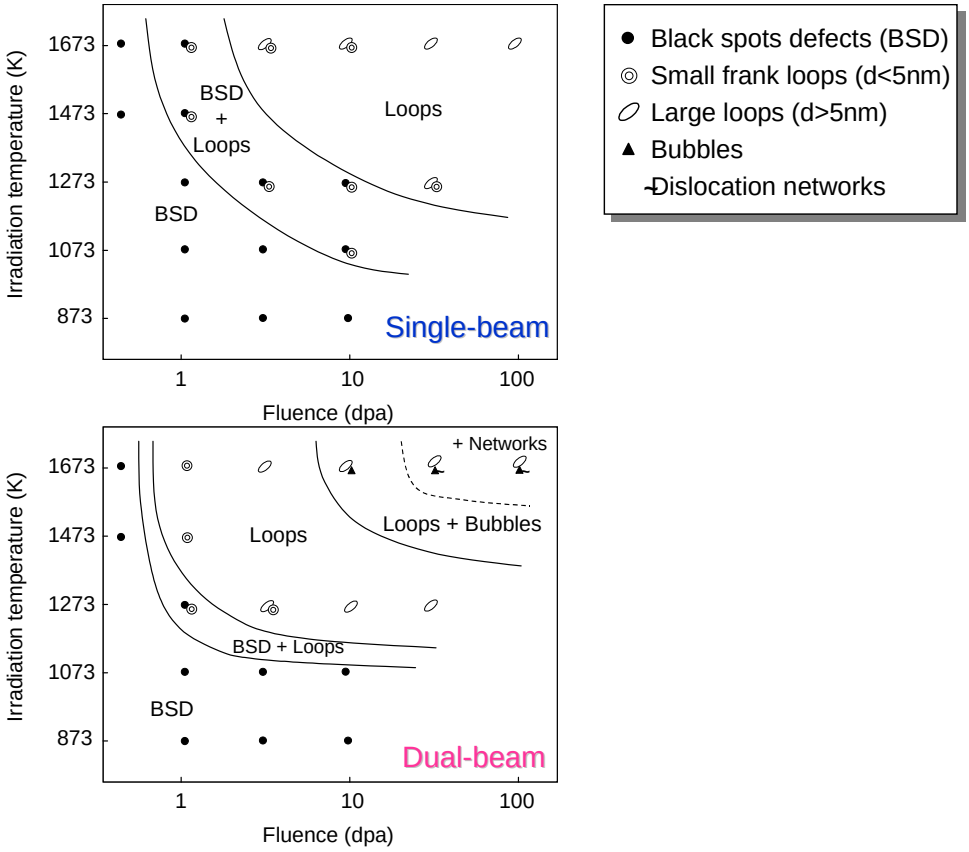

Figure 1. A preliminary overview of helium effect on microstructural development in CVD-SiC during ion irradiation.

Helium Effect on Swelling Behavior

The experiment was performed in a way similar to the previous section, while irradiation temperatures and helium co-implantation rates were 333~1673K and 0/60/1000 appm He/dpa, respectively, for the purpose of swelling determination. Macroscopic swelling was measured by precision surface profilometry [3]. Void swelling was determined based on graphical analysis to cavity images on transmission electron micrographs.

In the ‘point defect swelling’ regime, saturated ion-induced swelling agreed well with recent neutron data and post-neutron irradiation annealing data at T<~1273K. At T>~1273K, ion irradiation causes enhanced swelling due probably to dose rate effect and implantation effect. Helium seems to have enhanced swelling significantly at 673~1073K, as shown in Figure 2. The swelling enhancement observed in this temperature range seems to be too significant for the implanted amount of helium. It is preferred that this result is confirmed by additional experiments.

Void swelling was identified at temperatures higher than ~1273K. The fluence-dependent void swelling curves, which can be seen in Figure 3, seem to be consisting of incubation, transient and steady-state

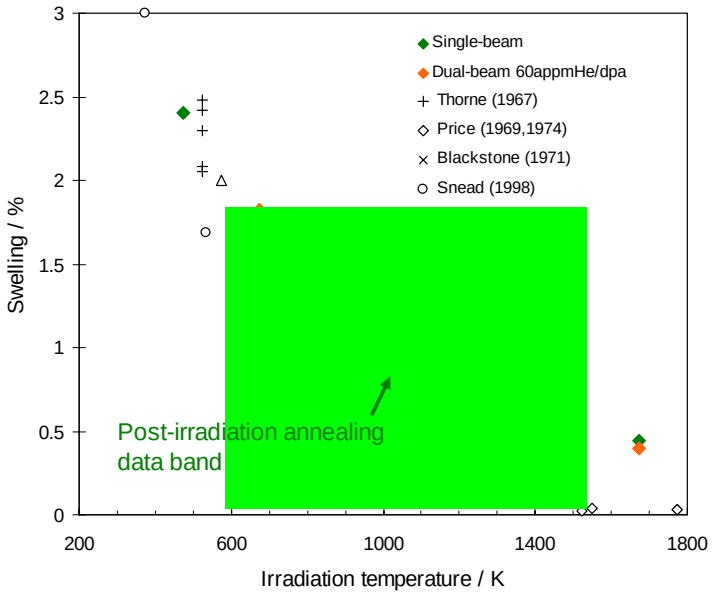

Figure 2. Irradiation temperature dependence of macroscopic swelling of ion-irradiated CVD-SiC with and without helium co-implantation at 60 appm He/dpa. The amount of swelling was measured by surface profilometry.

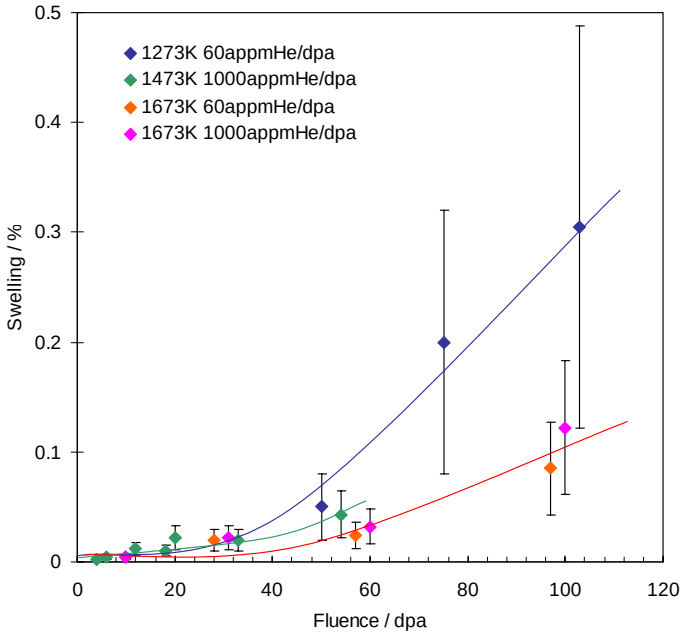

Figure 3. Fluence dependence of cavity swelling in CVD-SiC during dual-beam ion irradiation. The amount of swelling was estimated from TEM micrographs.

regimes, as is common in metals and metallic alloys. The extent of void swelling appeared relatively small. Temperature dependence of steady-state swelling rate can not be discussed from these data, primarily because the transport of helium to free surfaces must significantly be affecting data for 1673K, as discussed in the previous section.

References

[1] Y. Katoh, A. Kohyama, T. Hinoki, and L. L. Snead, Fusion Science and Technology 44 (2003) 155.
[2] S. Kondo, Y. Katoh, and A. Kohyama*, Interaction of Dislocation Development with Helium in Silicon Carbide*, presented at the 11th International Conference on Fusion Reactor Materials, December 7-12, 2003, Kyoto, Japan.
[3] Y. Katoh, H. Kishimoto, and A. Kohyama, J. Nucl. Mater. 307-311 (2002) 1221.

SiC/SiC COMPOSITES THROUGH TRANSIENT EUTECTIC-PHASE ROUTE FOR FUSION APPLICATIONS—Y. Katoh (Oak Ridge National Laboratory), A. Kohyama, T. Nozawa (Kyoto University), and M. Sato (Ube Industries, Ltd.)

Paper was presented at the 11th International Conference on Fusion Reactor Materials, December 7-12, 2003, Kyoto, Japan, and it will be published in the conference proceedings in the *Journal of Nuclear Material.*

EXTENDED ABSTRACT

Innovative SiC/SiC composites, which possess properties substantially more attractive than conventional SiC/SiC composites, were developed through a processing technique named nano-infiltration and transient eutectic-phase (NITE) process. Representative baseline properties of lab-grade NITE SiC/SiC composite is presented and compared with those suggested for design analysis of SiC/SiC-based power plant for the long term in Table 1. The demonstrated superior strength properties, thermal conductivity, hermeticity, surface smoothness and elevated temperature stability are attributed primarily to the near full-density crystalline SiC matrix. The elevated temperature stability expectedly enables the application of permanent joining and refractory coating techniques which have not been considered for the conventional SiC/SiC composites. Some of those techniques have been demonstrated and others are being studied.

Table 1. Representative properties of NITE SiC/SiC as compared with those suggested for design analysis of SiC/SiC-based power plants for the long term

Key SiC/SiC properties	Suggested value[1]	NITE (lab grade)
Density	~3000 kg/m^3	2800~3000 kg/m^3
Porosity	~5 %	3~6 %
Young's modulus	200~300 GPa	190~220 GPa
Thermal expansion coefficient	4 x 10^{-6} K^{-1}	3.3~4.7 x 10^{-6} K^{-1} (20~1000°C)
Thermal conductivity through thickness	~20 W/m-K	17~29 W/m-K (20°C)* 15~20 W/m-K (1000°C)*
Maximum allowable combined stress	~190 MPa	~150 MPa**
Cost	$\leq$ $400/kg	~$5000/kg***

*Unirradiated

**2/3 of tensile proportional limit stress

***Rough estimate for a 10kg batch of cross-plied composite

Pilot industrial grade materials of NITE SiC/SiC composite were produced in a variety of shapes and sizes. The industrial process is still under development and therefore the material properties for such grade are not yet comparable with those for the lab-grade. However, the pilot grade components have been demonstrating much improved performances over the conventional SiC/SiC composites.

Fundamental and applied research are still being extensively conducted for the purposes of further improvement and tailorability of material properties and reduced cost of industrial material production.

3.0 FERRITIC/MARTENSITIC STEELS AND ODS STEELS

ANALYSIS OF EXTRACTION RESIDUE OF HFIR 11J-IRRADIATED RAFS—H. Tanigawa (Japan Atomic Energy Research Institute), H. Sakasegawa (Kyoto University), S. J. Zinkle, R. L. Klueh (Oak Ridge National Laboratory), and A. Kohyama (Kyoto University)

OBJECTIVE

The objective of this work is to analyze the precipitation behavior of irradiated reduced-activation ferritic/martensitic steels (RAFs) by measuring the weight change of extraction residue.

SUMMARY

Extraction residue was made from several HFIR 11J-irradiated RAFs, and the mass change was measured to investigate the irradiation-enhanced change in precipitation. Two different types of filter with coarse and fine pores were used in order to separate the difference of irradiation effects between larger and smaller precipitates. Unirradiated specimens were examined as well. Results suggest that during irradiation the mass of larger precipitates increased in F82H-IEA, Ni-doped F82H, JLF-1 and ORNL9Cr, fine precipitates disappeared in JLF-1, and fine precipitates increased in Ni-doped F82H.

PROGRESS AND STATUS

Introduction

Measuring the mass change of extraction residue is the common technique to investigate the state of precipitates in R&D of steels. Until now this technique has not been used for the analysis of precipitation in irradiated steels, because of the expected practical difficulty in performing this technique. As for this, the irradiation effect on precipitation has been examined by observing TEM thin film or extraction replica samples [1,2]. The information obtained by this TEM observation is limited to the very local 2D information, and it is very difficult to obtain the overall tendency on precipitation changes with high statistical accuracy. Therefore, it is desirable to obtain a more accurate assessment on precipitation behavior, and such information could be obtained if the mass changes of extraction residue after irradiation could be determined.

It was reported that RAFs irradiated in HFIR 11J (5dpa/573K) show a variety of hardening and DBTT shifts [3]. TEM microstructure observation on these specimens revealed that the dislocation microstructure of these irradiated RAFs did not show a big enough difference to explain the difference in mechanical properties [4]. To look for the possibility that the precipitation was affected by the irradiation and caused these mechanical property differences, precipitates were extracted from 11J-irradiated RAFs to investigate the changes in precipitation after irradiation. Unirradiated (normalized-and-tempered) specimens were also measured for comparison.

Experimental

The material used for irradiation was IEA-modified F82H (F82H-IEA) and another heat treatment of F82H designated HT2 (F82H HT2), ORNL9Cr-2WVTa (ORNL9Cr), JLF-1 HFIR heat (JLF-1) and a 2% natural Ni-doped F82H (F82H+2Ni). Details of the chemical compositions and the heat treatments are shown in another report [3]. Irradiation was performed in the Oak Ridge National Laboratory (ORNL) High Flux Isotope Reactor (HFIR) up to 5 dpa at 573K in the removable beryllium (RB) position. Specimens selected to be used were 1/3-size Charpy specimens. Unirradiated specimens of all materials were also used for comparison.

The precipitates were extracted electrochemically in a solution containing 10% hydrochloric acid in methanol at a potential of about 1.5V with respect to the platinum electrode. The specimen was slightly polished before extraction to remove surface microstructure. The filters used for vacuum filtering are a

coarse filter (pore size 1μm) and a fine filter (pore size 200nm). The mass of the specimen and filter were measured with an accuracy of ±0.1 mg before and after extraction.

Results and Discussion

The mass of extracted residue before and after irradiation is shown in Fig. 1. Here the mass of residue obtained with the coarse filter (column denoted "Large") is interpreted as the value corresponding to the mass of large precipitates, and the difference of mass obtained with fine filter and coarse filter (column denoted "Small") is interpreted as that of the fine precipitates. These results indicate (1) the mass of larger precipitates increased in F82H-IEA, F82H+2Ni, JLF-1 and ORNL9Cr, (2) no mass change in F82H HT2, (3) small precipitates disappeared in JLF-1, and (4) small precipitates increased in F82H+2Ni. These results suggest that there is an apparent effect of irradiation on precipitation except for F82H HT2, even if irradiated only at 573K to 5dpa.

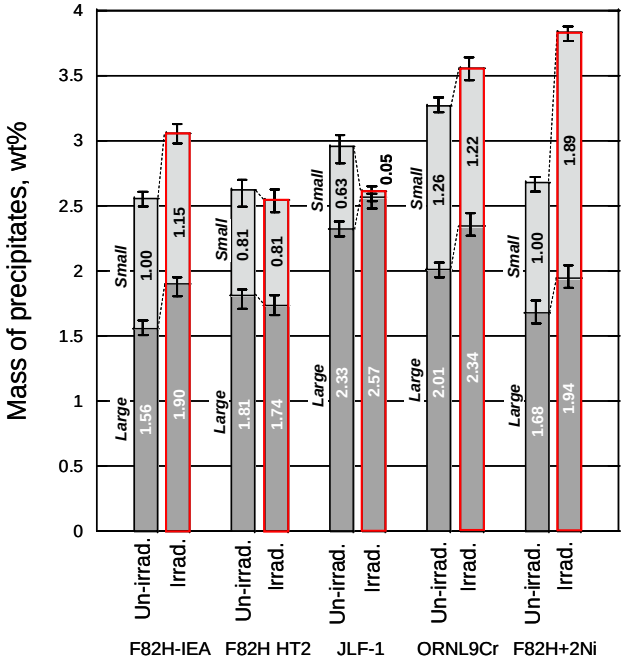

Fig. 1. Mass of extracted residue of unirradiated and irradiated RAFs extracted with coarse filter (Large) and fine filter (Large+Small). Number in the columns shows the actual wt% values of corresponding columns.

It is also worth noting that these increases of precipitate mass have good correlation with hardening, as shown in Fig. 2, i.e., the increases of yield stress of all RAFs except F82H-IEA are on the linear trend against the increase of precipitate mass. The reason that F82H-IEA is off this trend could be explained as the effect of the difference of prior austenite grain (PAG) size, since F82H-IEA has a large PAG size (ASTM grain size 3) than the other RAFs (ASTM grain size 7~8).This suggest the possibility that this irradiation-enhanced precipitation might cause additional irradiation hardening. Further analysis of this relationship will be performed in near future.

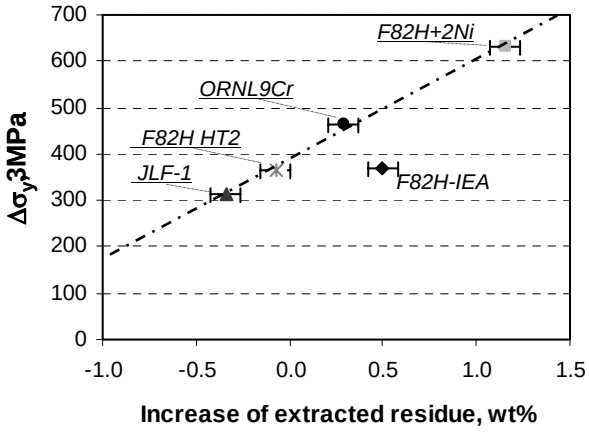

Fig. 2. Irradiation hardening plotted against the mass changes of precipitates of each RAFs.

SUMMARY AND CONCLUSIONS

Extraction residue was obtained from HFIR-11J irradiated RAFs, and the mass change was measured to investigate the irradiation-enhanced change in precipitation. Two different types of filter with coarse and fine pores were used in order to separate the difference of irradiation effects between larger precipitate and the smaller precipitate. Unirradiated specimens were examined as well. The following is a summary of the important conclusions:

(1) The mass of larger precipitates increased in F82H-IEA, F82H+2Ni, JLF-1 and ORNL9Cr after irradiation.
(2) The fine precipitates disappeared in JLF-1 after irradiation.
(3) The fine precipitates increased in F82H+2Ni after irradiation.
(4) Correlation between irradiation hardening and the mass change of precipitates was suggested.

Acknowledgements

The authors would like to thank Mr. J.L. Bailey and J.W. Jones for their help on preparing specimens for this experiment. This research was sponsored by the Japan Atomic Energy Research Institute and the Office of Fusion Energy Sciences, US Department of Energy under contract DE-ACO5-00OR22725 with UT-Battelle.

References

[1] A. Kimura and H. Matsui, J. Nucl. Mater. 212-215 (1994) 701.
[2] J. J. Kai and R. L. Klueh, J. Nucl. Mater. 230 (1996) 116.
[3] H. Tanigawa, M. A. Sokolov, K. Shiba, and R. L. Klueh, Fusion Sci. Tech. 44 (2003) 206.
[4] N. Hashimoto, H. Tanigawa, M. Ando, and M. A. Sokolov, in this progress report.

ANALYSIS OF Ta-RICH MX PRECIPITATES IN RAFS—H. Tanigawa (Japan Atomic Energy Research Institute), H. Sakasegawa (Kyoto University), N. Hashimoto, S. J. Zinkle, and R. L. Klueh (Oak Ridge National Laboratory), and A. Kohyama (Kyoto University)

OBJECTIVE

The objective of this work is to analyze the precipitate distribution with emphasis on Ta-rich MX precipitate in reduced-activation ferritic/martensitic steels (RAFs) by observing the extraction replica samples with TEM and SEM.

SUMMARY

Extraction replica samples were prepared from F82H-IEA, F82H HT2, JLF-1 and ORNL9Cr to analyze the precipitate distribution. The samples were examined to obtain precipitate size distribution with TEM and to analyze chemical composition distribution with SEM. Back-scattered electron imaging was found to be the effective way to separate Ta-rich precipitate from other precipitates. Results showed that most of the precipitates were $M_{23}C_6$, and the shape is a round ellipsoid in F82H-IEA and HT2, but was a long ellipsoid in JFL-1 and ORNL9Cr. It was also found that MX precipitates were few and large and contain Ti in F82H-IEA and HT2, but a lot of fine MX precipitates without Ti were observed in JLF-1 and ORNL9Cr.

PROGRESS AND STATUS

Introduction

Using extraction replica samples for precipitate analysis is the typical method for the investigation of precipitation in irradiated steels. The critical point of this method is the fact that the area to be analyzed for its chemical composition tends to be limited to a few tenths of a micron (generally less than 10μm) square. This limitation makes it difficult to find minor precipitates such as MX, and it also makes it difficult to increase the statistical accuracy. In this study, FE-SEM and TEM were used for the observation of replica samples to analyze a wider region. A new technique to detect Ta-rich precipitates was proposed.

Experimental

Materials used in these experiments are IEA-modified F82H (F82H-IEA), another heat treatment of F82H (F82H HT2), ORNL9Cr-2WVTa (ORNL9Cr) and JLF-1 HFIR heat (JLF-1). The details of these steels were shown in another paper [1]. Extraction replicas were made from the cross section of 1/3CVN specimens. The specimen surface was first mechanically polished and then electropolished with 8% sulfuric acid, 1% hydrofluoric acid, and methanol before etching. Then the surface was electroetched with 10% hydrochloric acid in methanol and carbon coated to make the replica. The replica was removed by weak electroetching and collected in dilute ethanol on a mesh.

TEM (JEOL 2000FX) and FE-SEM (Philips XL30FEG) was used for the analyses of replica samples. FE-SEM operated at 15kV was used for observation with a secondary electron (SE) imaging mode and with a back-scattered electron (BSE) imaging mode, and it was used for chemical analysis with X-ray energy-dispersive spectrometry (XEDS) system. The XEDS mapping was done for 10 μm square areas with a resolution of 80 nm and 3.0 s dwell time per spot.

Results and Discussion

Fig. 1 shows the typical TEM images of replica samples of each RAFs around a triple point of a prior austenitic grain. It shows that; (1) number density of precipitates in JLF-1 and ORNL9Cr is larger than that of in F82H-IEA and F82H HT2, (2) precipitates in JLF-1 are larger than those of other RAFs, and (3) precipitates in JLF-1 and ORNL9Cr had relatively longer ellipsoid shape compared to those of F82H-IEA and F82H HT2. The tendency suggested in (1) and (2) coincides with the results obtained from extraction residue samples [2].

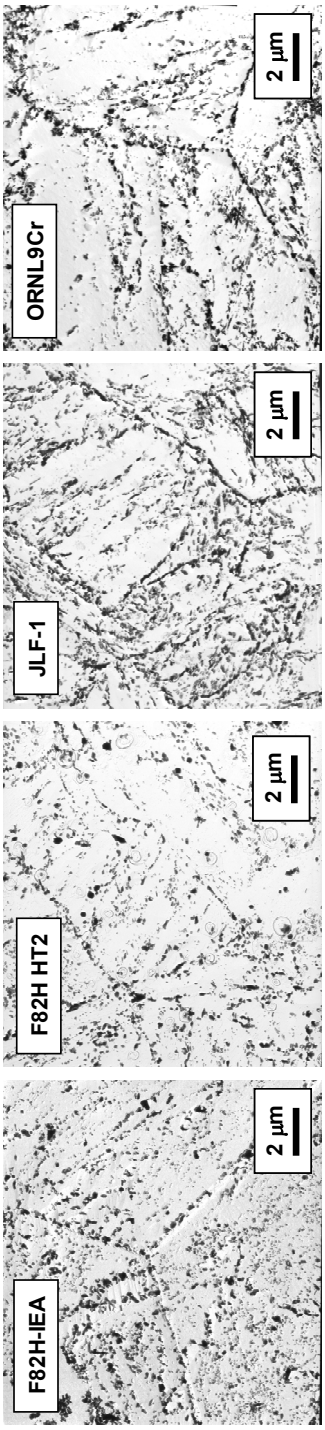

Fig. 1. TEM bright field images of replica samples made from each RAFs.

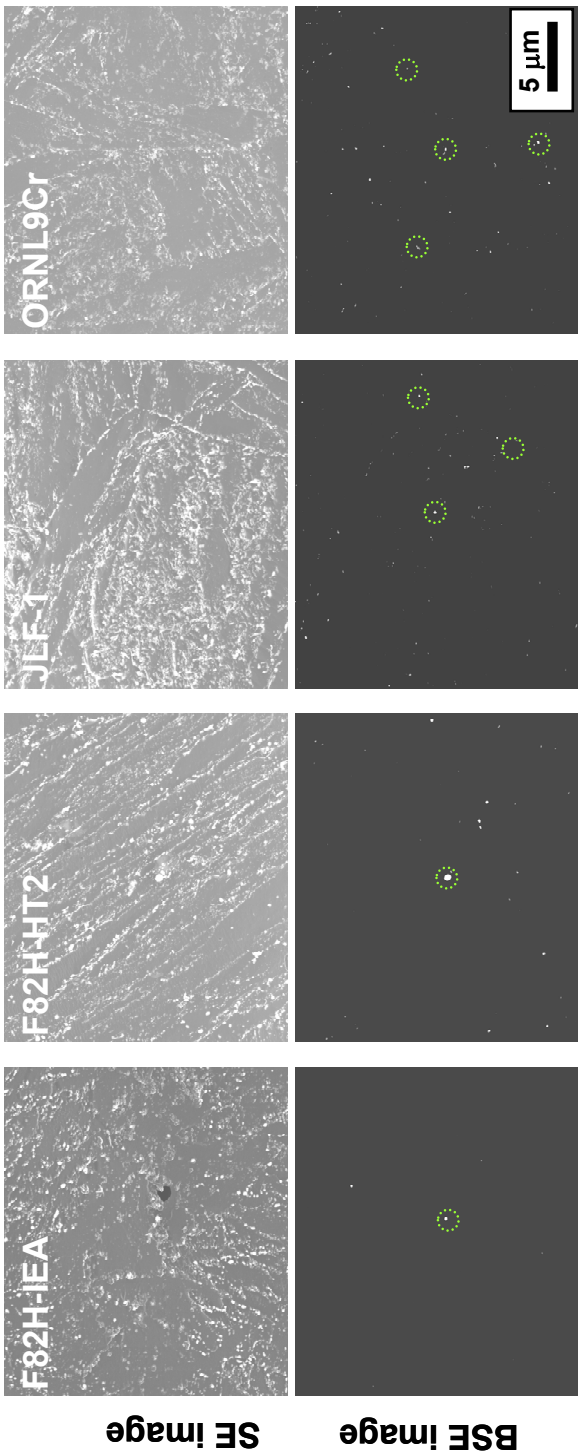

Fig. 2. Secondary electron (SE) and back-scatted electron (BSE) images of replica samples made from each RAFs. Green dotted circles in BSE images indicate the MX precipitates.

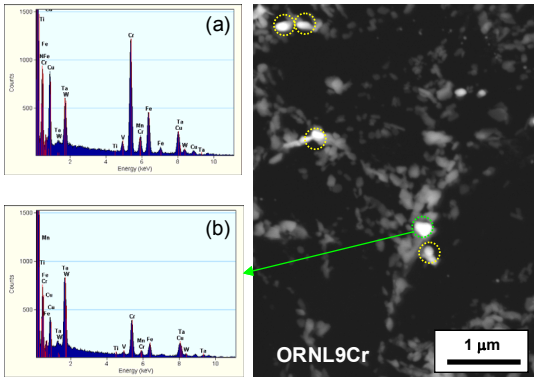

Fig. 3. High contrast BSE images of replica sample from ORNL9Cr. (a) shows EDS peaks from dark contrast precipitates or bright precipitates encircled by a dotted yellow line, and (b) shows the peaks from bright precipitate encircled by a dotted green line.

Fig. 2 shows the SE and BSE images of replica samples of each RAFs. The BSE image with high contrast condition gave a bright image of some precipitates. EDS mapping suggested that most of the precipitates are Cr rich, i.e., $M_{23}C_6$ (M; Cr, W, Fe) precipitates. XEDS analyses on each of those bright imaged precipitates revealed that some of the precipitates contain tantalum, i.e., MX (M;Ta,V,Ti :X ; C, N) precipitates, and others are large or double-layered $M_{23}C_6$ precipitates (Fig. 3). This is similar to Z-contrast images usually obtained by HAADF (high-angle annular dark field) imaging in STEM. Fig. 4 shows the number density and average size of MX precipitates (white arrows in Fig. 2). The result suggests that large, spherical-shaped and a low number density of MX precipitates were observed in F82H-IEA and F82H HT2, but small and a relatively high number density of MX precipitates were observed in JLF-1 and ORNL9Cr. A high density of MX precipitates in JLF-1 and ORNL9Cr is quite reasonable as those steels have higher Ta (0.07 and 0.09 wt%, respectively) compared to that of F82H (0.02wt%). It should be noted that all MX precipitates in F82H contain Ti. This is also reasonable as F82H contains a relatively higher Ti (0.01wt%) compared to the other RAFs. It is known that Ti forms Ti(C,N) that is stable at high temperature (~1473K), and Ti(C,N) could become the nucleus of MX precipitates [3]. Therefore, it could be concluded that Ti (Ti(C,N)) contributed to the formation and stabilization of large MX precipitates in F82H.

It should be noted that about 1/3 of the MX precipitates in ORNL9Cr were accompanied by Mo- and Mn-rich precipitates. Fig. 5 shows how the

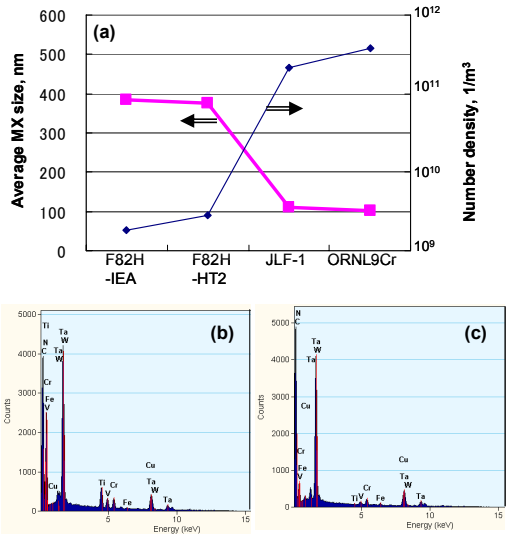

Fig. 4. (a)Number density and average size of MX (TaC) precipitates of each RAFs, (b) typical EDX peaks obtained from MX precipitates in F82H-IEA and F82H HT2, and (c) those from JLF-1 and ORNL9Cr.

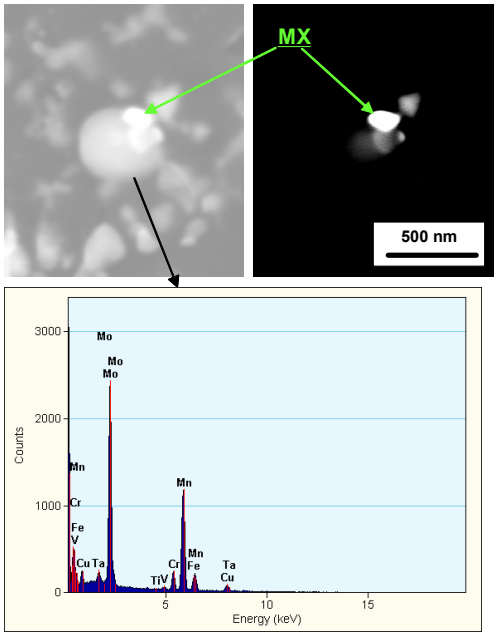

Fig. 5. Mo- and Mn-rich precipitate observed next to MX precipitates in ORNL9Cr.

large (~400nm diameter) and spherical-shaped Mo/Mn-rich precipitates were usually located just below the MX precipitates. This type of precipitate is not expected, as Mo and Mn are generally believed to be included in $M_{23}C_6$ or in the matrix as solute, and it has not been reported to form this type of precipitate. Further analyses on this will be conducted in the future.

SUMMARY AND CONCLUSIONS

Extraction replica samples were prepared from F82H-IEA, F82H HT2, JLF-1 and ORNL9Cr to analyze the precipitate distribution. The samples were examined to obtain precipitate size distribution with TEM, and to analyze chemical composition distribution with SEM. The following is a summary of the important observations and conclusions:

(1) Results show that most of the precipitates are $M_{23}C_6$ with a round ellipsoid shape in F82H-IEA and HT2, but with a long ellipsoid shape in JFL-1 and ORNL9Cr.
(2) Back-scattered electron imaging was found to be the effective way to separate Ta-rich precipitate from other precipitates.
(3) MX precipitates were few and large and contain Ti in F82H-IEA and HT2, but a lot of fine MX precipitates without Ti were observed in JLF-1 and ORNL9Cr.
(4) About 1/3 of MX precipitates in ORNL9Cr were found to be accompanied by large and spherical-shaped Mo/Mn-rich precipitates.

Acknowledgements

The authors would like to thank Mr. J.L. Bailey and J.W. Jones for their help on preparing specimens for this experiment. This research was sponsored by the Japan Atomic Energy Research Institute and the Office of Fusion Energy Sciences, US Department of Energy under contract DE-ACO5-00OR22725 with UT-Battelle.

References

[1] H. Tanigawa, M. A. Sokolov, K. Shiba, and R. L. Klueh, Fusion Sci. Tech. 44 (2003) 206.
[2] H. Tanigawa, H. Sakasegawa, S. J. Zinkle, R. L. Klueh, and A. Kohyama, in this semiannual report.
[3] M. Tamura, K. Shinozuka, K. Masamura, K. Ishikawa, and S. Sugimoto, 258-263 (1998) 1158.

X-RAY DIFFRACTION ANALYSIS ON PRECIPITATES OF 11J IRRADIATED RAFS—H. Tanigawa (Japan Atomic Energy Research Institute), H. Sakasegawa (Kyoto University), E. A. Payzant, S. J. Zinkle, and R. L. Klueh (Oak Ridge National Laboratory), and A. Kohyama (Kyoto University)

OBJECTIVE

The objective of this work is to analyze the precipitation behavior of irradiated reduced activation ferritic/martensitic steels (RAFs) by X-ray diffraction (XRD) analysis.

SUMMARY

XRD analyses were performed on the extraction residue of HFIR 11J-irradiated RAFs to investigate the overall precipitate character. Un-irradiated and aged specimens were examined as well. Results suggested that the distinctive peaks of $M_{23}C_6$ (M; Cr, Fe, W) were observed on all specimens. Peaks possibly related to MX (M;Ta,Ti,V : X ; C, N) were observed on the specimens extracted from un-irradiated JLF-1 and ORNL9Cr, but those peaks were not observed on irradiated specimens.

PROGRESS AND STATUS

Introduction

XRD analysis on an extraction residue specimen is the commonly used technique to analyze the precipitate characteristics on the R&D of steels in an irradiation-free condition. This technique has not been used for irradiated steels because of the practical limitation on making and handling the neutron - irradiated specimens. Transmission electron microscope (TEM) observation on thin film specimens or on extraction replica specimens is the most commonly used technique for precipitate analysis [1,2]. The conclusion obtained from TEM thin film and extraction replica specimens is that the results usually represent a very local microstructure, and it requires a lot of work to obtain a certain level of statistical reliability on the results. In order to cover the above problem, the authors decided to develop the extraction residue procedure to perform XRD analysis on irradiated steels.

In this study, XRD analyses were performed on the extraction residue of HFIR 11J-irradiated RAFs, which showed a variety of brittleness-hardness combination, to investigate the overall precipitate character. The un-irradiated and aged RAFs were also examined for comparison.

Experimental

The material used was IEA-modified F82H (F82H-IEA). Base metal with two heat treatment variations (standard IEA heat treatment and another heat treatment designated HT2) was irradiated. ORNL9Cr-2WVTa (ORNL9Cr), JLF-1 HFIR heat (JLF-1) and 2% natural Ni-doped F82H (F82H+2Ni) were also irradiated for comparison. Details of the chemical compositions and the heat treatments are shown in other reports [3,4]. Irradiation was performed in the Oak Ridge National Laboratory (ORNL) High Flux Isotope Reactor (HFIR) up to 5 dpa at 573K in the removable beryllium (RB) position. Specimens selected to be used were the 1/3-size Charpy specimens. Unirradiated (normalized-and-tempered) specimens of all materials and aged specimens of ORNL9Cr (873K for 10k h) were also used for comparison. The extraction residue from these specimens was collected on a filter with 200 nm pore size [5].

Samples were analyzed using PANalytical X'Pert Pro MPD x-ray diffractometer with a Ni-filtered Cu K-alpha radiation source at 45kV and 40mA. The diffractometer was configured with an incident beam multilayer mirror optic and diffracted beam parallel plate collimator, which yield parallel beam optics and thereby minimize sample surface displacement errors (mainly associated with sample mounting). Axial divergence limiting Soller slits were used on both the incident and diffracted beam, and the detector was a gas proportional counter. The fine powders were examined as-deposited on the filter materials and radiological safety requirements necessitated covering the powders with a thin film of Mylar (6.35μm thick)

to prevent possible contamination of the system (Fig. 1). Consequently the relatively weak sample diffraction data was combined with diffraction from the Mylar and the filter. The diffraction data were analyzed using Jade version 6.5 software [Materials Data Inc., Livermore, CA].

Results and Discussion

Fig. 2 shows the raw peaks obtained from irradiated F82H-IEA, Mylar, background, filter, and the processed peaks of irradiated F82H-IEA. Background peak was obtained by extremely lowered X-ray energy. It is clear that there is no effect on the result from radiation, though the sample has an activity about 20mR/hr at contact. Mylar has a large wide peak at 18 degrees, but this does not affect the results as we used the peaks above 30 degrees for analyses. The filter has several distinctive peaks above 30 degrees. The peaks are matched to manganese phosphorus nitride (Mn_2PN_3). These peaks were removed from the original scan by subtracting the appropriately scaled diffraction pattern of the filter itself.

Fig. 3 shows the results of peaks from the extracted residue of unirradiated and irradiated RAFs. It revealed that the majority of precipitates are $M_{23}C_6$ type (denoted with diamond mark) for all as-prepared and irradiated steels. The 3 distinctive peaks (denoted with triangle) are observed on as-prepared JLF-1 and ORNL9Cr, and those peaks are not detected on irradiated specimens. There is no exact match pattern for those peaks, but the best match is for the TaC peaks. This supposition is quite reasonable as a high number density of Ta-rich precipitates is observed on these steels [6]. The reason for this peak offsets would be that TaC is usually present as MX precipitate (M; Ta, V, Ti : X; C, N). This disappearance of MX peaks is a very distinctive feature of the irradiation effect, because MX precipitate itself is thermodynamically stable at 573K.

The stability of MX precipitate in the unirradiated condition was suggested from the peaks of aged ORNL9Cr (Fig. 4), as MX peaks are still obvious even after 873K for 10k h aging. It should be noted that the peaks of aged ORNL9Cr also show that they have Laves phase (Fe_2W) in their residue, and this is very common in this type of steel.

The other feature obtained from Fig. 3 is the decrease of the $M_{23}C_6$ peaks of F82H-2Ni after irradiation. The weight of the residue itself was increased, as shown in other reports [6], so this change could be interpreted as

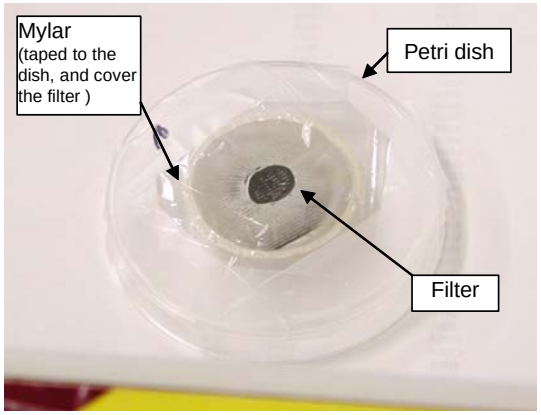

Fig. 1. Prepared status of the extraction residue sample of irradiated steels for XRD analyses.

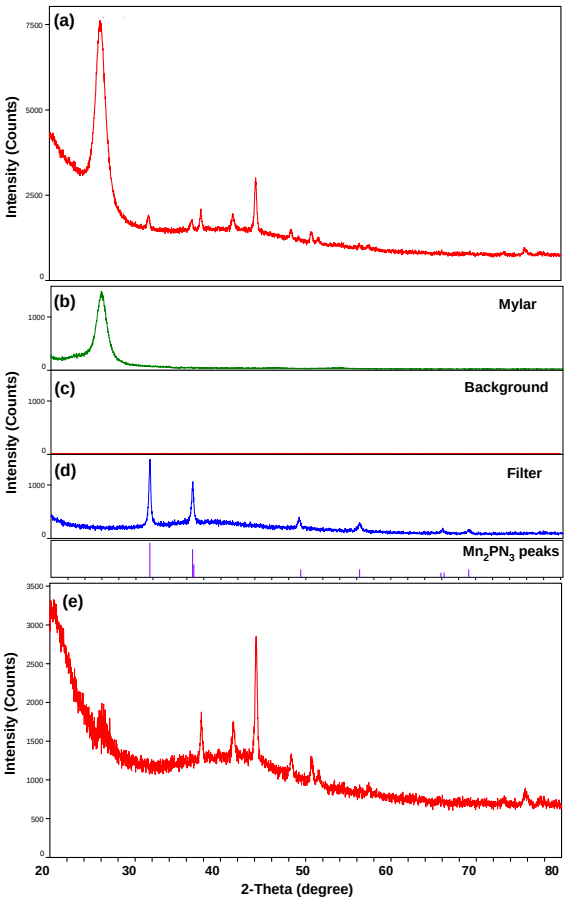

Fig. 2. Raw XRD peaks of (a) irradiated F82H-IEA, (b) Mylar, (c) background, (d) filter, with (e) processed peaks of (a).

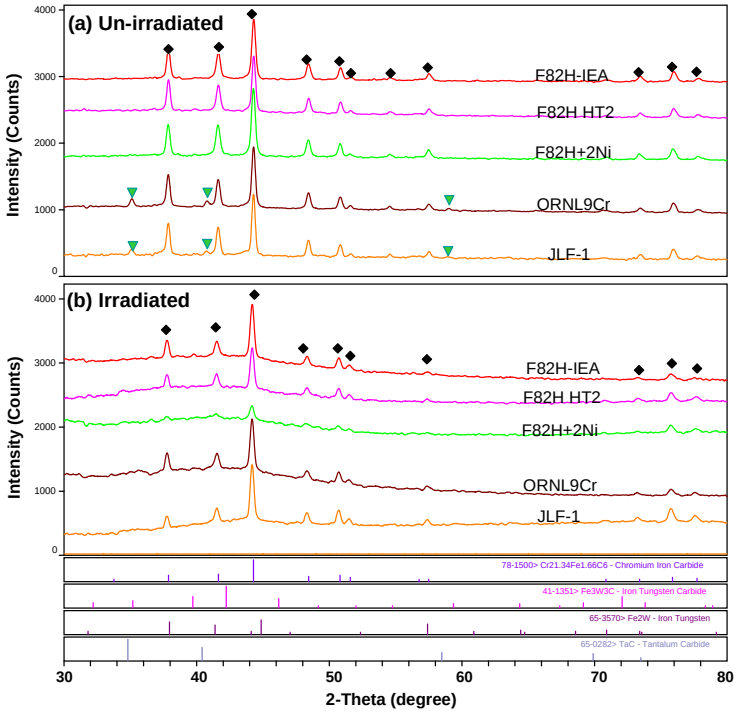

Fig. 3. XRD peaks of extracted residue from un-irradiated and irradiated RAFs. Peaks marked with diamond correspond to the peaks from $M_{23}C_6$, and with triangles correspond to peaks from MX (TaC).

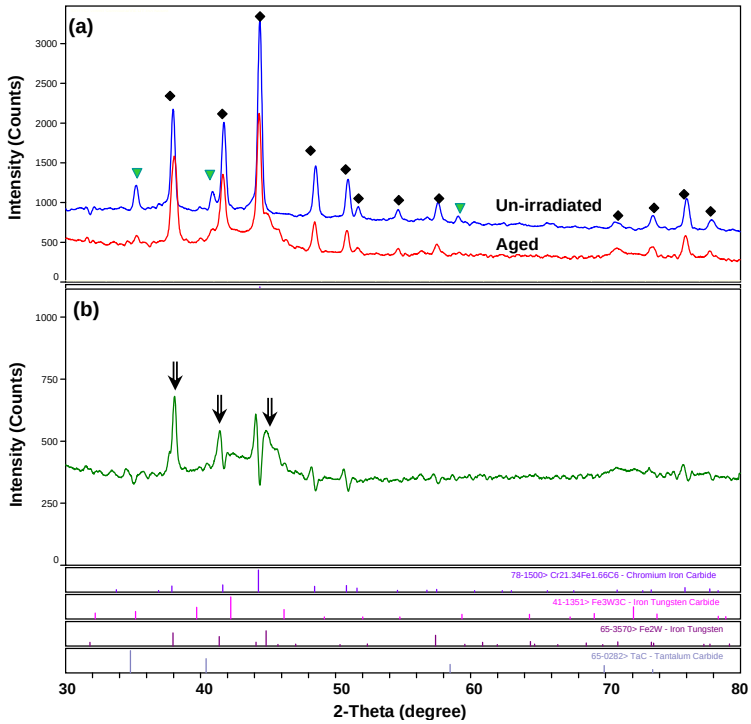

Fig. 4. XRD peaks of (a) un-irradiated and aged ORNL9Cr and (b) peaks obtained by subtracting the peaks of un-irradiated ORNL9Cr from peaks in (a). Black arrows suggest the peaks correspond to Laves (Fe_2W) phase.

the average size decrease of $M_{23}C_6$. It also should e noted that the peaks of all irradiated specimens tended to have broad and shallow peaks with the median of about 42 degrees. This might be related to the peaks from fine particles of M_6C (Fe_3W_3C), as its highest peak located at 42 degrees. This suggests the possibility that fine M_6C (M; Fe, W, Cr: nominally Fe_3W_3C) may be present. Further investigation on these changes will be performed by detailed TEM observation.

SUMMARY AND CONCLUSIONS

XRD analyses were performed on the extraction residue of HFIR 11J-irradiated RAFs to investigate the overall precipitate character. Unirradiated and aged specimens were examined as well. The following is a summary of the important observations and conclusions:

(1) The most distinctive peaks are of $M_{23}C_6$ (M; Cr, Fe, W) on all specimens.
(2) Peaks possibly related to MX precipitates were observed on the residue from un-irradiated JLF-1 and ORNL9Cr, but those peaks were not observed on irradiated specimens of those steels.
(3) The above peaks are observed on 873K 10k h aged ORNL9Cr.
(4) This disappearance of MX peaks is probably the effect of irradiation.
(5) The decrease of peak intensity after irradiation was observed on Ni-doped steel, and the relation to the average particle size decrease was suggested.
(6) The possibility of the presence of fine M_6C in the irradiated steels was suggested.

Acknowledgements

The authors would like to thank J.L Baily and P.S. Tedder for preparing irradiated specimens for this experiment. This research was sponsored by the Japan Atomic Energy Research Institute and the Office of Fusion Energy Sciences, US Department of Energy under contract DE-AC05-96OR22464 with UT-Battelle.

References

[1] A. Kimura and H. Matsui, J. Nucl. Mater. 212-215 (1994) 701.
[2] J. J. Kai and R. L. Klueh, J. Nucl. Mater. 230 (1996) 116.
[3] H. Tanigawa, M. A. Sokolov, K. Shiba, and R. L. Klueh, Fusion Sci. Tech. 44 (2003) 206.
[4] K. Shiba, M. Suzuki, and A. Hishinuma, J. Nucl. Mater. 233-237 (1996) 309.
[5] H. Tanigawa, H. Sakasegawa, S. J. Zinkle, R. L. Klueh, and A. Kohyama, in this progress report.
[6] H. Tanigawa, H. Sakasegawa, N. Hashimoto, S. J. Zinkle, R. L. Klueh, and A. Kohyama, in this progress report.

COMPARISON OF MICROSTRUCTURE BETWEEN NEUTRON-IRRADIATED REDUCED-ACTIVATION FERRITIC/MARTENSITIC STEELS, F82H-IEA, JLF-1 AND ORNL9CR—

N. Hashimoto (Oak Ridge National Laboratory), H. Tanigawa (Japan Atomic Energy Research Institute), M. Ando (JAERI), T. Sawai (JAERI), K. Shiba (JAERI), and R.L. Klueh (ORNL)

OBJECTIVE

To clarify the mechanisms of the difference in Charpy impact properties between F82H-IEA, JLF-1, and ORNL9Cr steels after irradiation, TEM microstructural analysis was performed.

SUMMARY

Transmission electron microscopy (TEM) specimens of F82H-IEA, F82H HT2, JLF-1, and ORNL9Cr steels were prepared from miniature Charpy specimens irradiated up to 5 dpa at 573K by using the Focused Ion Beam (FIB) technique in order to determine the mechanisms that cause the difference in Charpy impact properties. TEM microstructural analysis was performed with emphasis on dislocation structure and precipitate distribution. The TEM specimens indicated no significant difference on dislocation microstructures, such as dislocation loop size and density, in the steels. While precipitate's distribution of each steel was somewhat different in their size and density, larger precipitates were observed on prior austenite grain (PAG) boundaries and martensite packet boundaries of F82H-IEA and F82H HT2 compared to JLF-1 and ORNL9Cr. TEM analysis also suggested that ORNL9Cr had the finest grain structure, and F82H had a coarse grain structure. The microstructure of the deformed region of irradiated F82H-IEA contained dislocation channels. This suggests that dislocation channeling could be the dominant deformation mechanism in the RAFs, resulting in the loss of strain-hardening capacity.

PROGRESS AND STATUS

Introduction

Since ferritic/martensitic steels have several advantages based upon their resistance to void swelling, good thermal stress resistance, and well-established commercial production and fabrication technologies, reduced-activation ferritic/martensitic steels (RAFs) have been developed as candidate materials for structural applications in fusion energy systems. In a previous study, it was reported that ORNL9Cr-2WVTa and JLF-1 (Fe-9Cr-2W-V-Ta-N) steels showed smaller ductile-brittle transition temperature (DBTT) shifts compared to IEA-modified F82H (Fe-8Cr-2W-V-Ta) after neutron irradiation up to 5 dpa at 573K. This difference in DBTT shift could not be interpreted as an effect of irradiation hardening. To clarify the mechanisms of the difference in Charpy impact property between these steels, microstructure analyses by transmission electron microscopy (TEM) were performed.

Experimental Procedure

The materials used were IEA modified F82H with its standard heat treatment and an alternate heat treatment (HT2), JLF-1, and ORNL9Cr-2WVTa. The compositions and the heat treatments are given in Table 1. Miniature Charpy specimens of these steels were irradiated up to 5 dpa at 573K in HFIR RB-11J capsule with europium thermal neutron shields for neutron spectrum tailoring. TEM specimens were prepared from the miniature Charpy specimens by using the FIB processor (Hitach FB-2000A) with a microsampling system at Japan Atomic Energy Research Institute (JAERI). FIB fabrication can provide the optimum sample taken from a proper area of bulk specimen and less magnetic field samples to be handled just as nonmagnetic materials. The Low Energy Gun Milling (LEG) was carried out at JAERI for 4

all specimens to remove damage by fabrication. The FIBed samples were examined using a JEM-2000FX (LaB6) transmission electron microscope at ORNL.

Table 1 Chemical compositions of the steel used in this experiment

	C	Cr	W	V	Ta	Ti	N
F82H-IEA	0.11	7.7	2.00	0.16	0.02	0.01	0.008
JLF-1	0.1	8.9	1.95	0.20	0.09	0.002	0.023
ORNL9Cr	0.1	8.8	1.97	0.18	0.065	-	0.023

Heat treatment:		
	F82H-IEA	1313K/40min/AC + 1023K/1hr
	F82H HT2	NT + 1193K/1hr/AC + 1023K/1hr
	JLF-1	1323K/1hr/AC + 1053K/1hr
	ORNL9Cr	1323K/1hr/AC + 1023K/1hr

Results and Discussion

Before TEM examination of the irradiated steels, microstructures of unirradiated (normalized-and-tempered) F82H-IEA, F82H HT2, JLF-1, and ORNL9Cr were examined by exraction replica [1] and TEM in order to investigate grain size, distribution and chemical composition of precipitates. In all the steels, precipitates on prior austenite grain (PAG) boundaries were mainly $M_{23}C_6$; the average size in F82H-IEA, F82H HT2, JLF-1, and ORNL9Cr is 103, 106, 123, and 111 nm, respectively. Also, there were a few MX-type precipitates in F82H-IEA and F82H HT2, which were Ti-rich. A lot of fine MX precipitates without Ti were found in ORNL9Cr and JLF-1. Furthermore, F82H-IEA had large PAGs and martensite packets, the other steel's PAGs were relatively smaller than F82H-IEA.

Fig. 1 shows typical microstructures of F82H-IEA, F82H HT2, JLF-1, and ORNL9Cr irradiated up to 5 dpa at 573K using the diffraction condition: **B**=001, ***g***=110 and (***g***,***5g***). The TEM specimens indicated irradiation-induced dislocation loops with a high number density in all the steels, although there was no significant difference on dislocation microstructures, such as size and number density, between the steels. Also, the size of PAG and packets of the steels were not changed by the irradiation.

In all the steels, precipitates on PAG boundaries were mainly $M_{23}C_6$, and it seemed that irradiation-enhanced precipitation had occurred. Precipitate's distribution of each steel showed some difference in size; relatively larger precipitates were observed on PAG boundaries and packet boundaries of F82H-IEA and F82H HT2 compared to JLF-1 and ORNL9Cr. On the other hand, fine precipitates observed in the unirradiated specimens were not found in the irradiated JLF-1 and ORNL9Cr steels. The results of exraction residue and XRD experiments [1] suggested that the MX precipitates (probably TaC) disappeared after irradiation, and a similar phenomenon (dissolution of TaC) was reported in ion-irradiated Fe-0.2Ta-0.015C alloy [2]. Estimation of fracture stress with the modified Griffith equation [1] indicated a possibility that dissolution of Ta in MX precipitates could lead to an increase of the surface energy and the fracture stress, resulting in the low DBTT of the irradiated JLF-1 and ORNL9Cr.

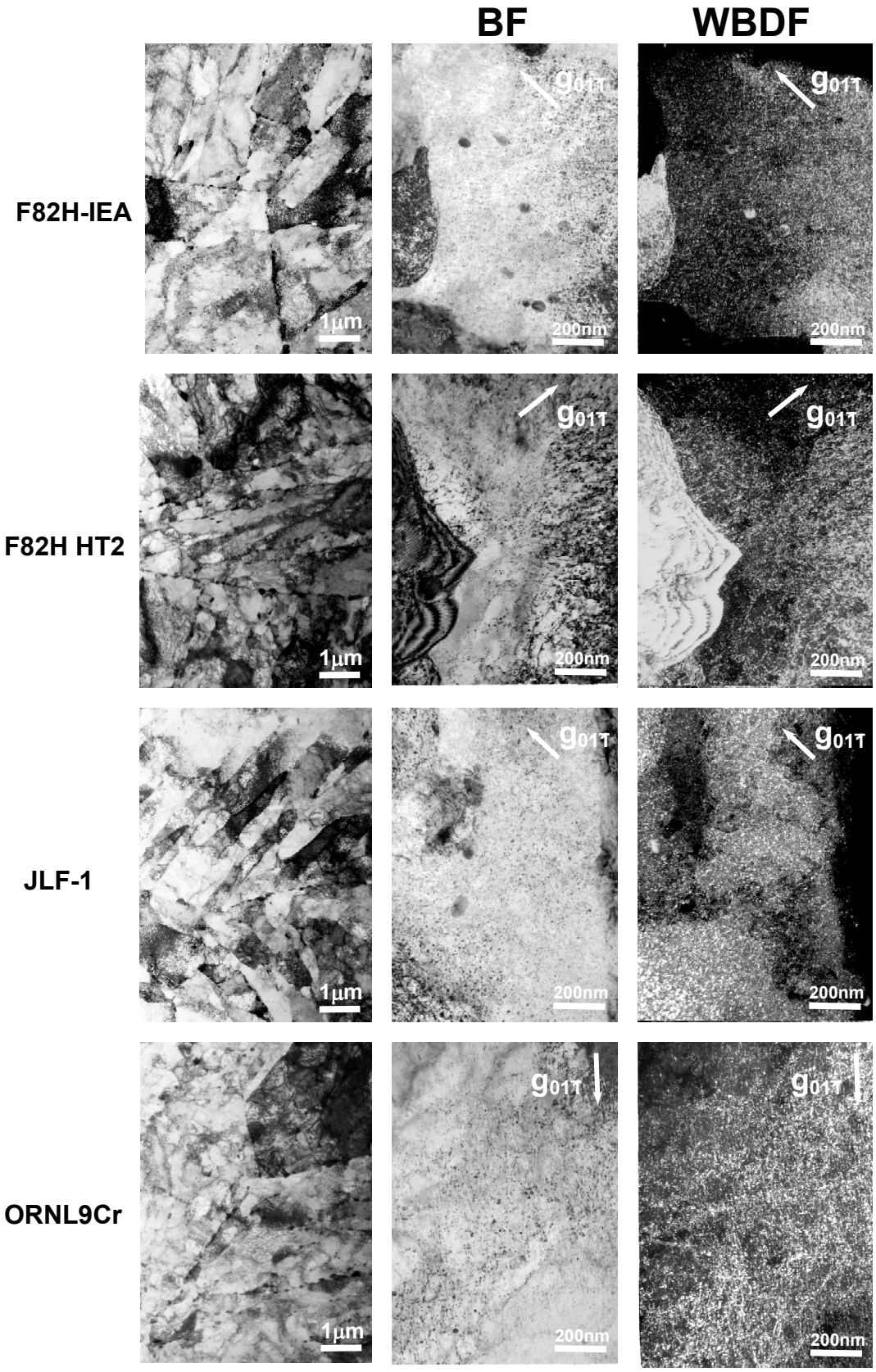

Fig. 1. Typical microstructures of F82H-IEA, F82H HT2, JLF-1, and ORNL9Cr irradiated up to 5 dpa at 573K using the diffraction condition: **B**=001, ***g***=110 and (***g***,***5g***).

Acknowledgements

This research was sponsored by the Japan Atomic Energy Research Institute and the Office of Fusion Energy Sciences, US Department Energy under contract No DE-AC05-96OR22464 with UT-Battelle, LLC.

References

1. H. Tanigawa, N. Hashimoto, M. Ando, H. Sakasegawa, R. L. Klueh, M. A. Sokolov, K. Shiba, T. Sawai, S. Jitsukawa, and A. Kohyama, Proceedings of the 11th International Conference of Fusion Reactor Materials, Kyoto (2003).
2. H. Tanigawa et al., unpublished research.

UPDATE ON FRACTURE TOUGHNESS VARIABILITY IN F82H—D. S. Gelles (Pacific Northwest National Laboratory)* and Mikhail A. Sokolov (Oak Ridge National Laboratory)

OBJECTIVE

The objective of this effort is to better understand the fracture toughness response of low activation ferritic steel F82H.

SUMMARY

The fracture toughness database for F82H displays some anomalous behavior associated with the center of the 25 mm thick plate. Metallographic carbide etchant reveals larger particles dispersed through the 25 mm thick F82H plate. The particles are found to be rich in Ta and O. Size distribution measurements indicate no enhancement at the center of the plate. However, the spatial distribution is affected so that large particles are more often located next to other large particles in the center of the plate. A mechanism is proposed that promotes easy crack nucleation between large tantalum oxide particles.

PROGRESS AND STATUS

Introduction

As described previously [1], fracture toughness measurements of 25 mm F82H plate are showing indications of non-uniform behavior as a function of thickness [2]. The purpose of the present effort is to continue to identify the microstructure features that may be responsible for this fracture toughness degradation.

Experimental Procedure

Specimens previously prepared for metallographic examination have been re-etched using Vilella's etch, and examined metallographically and by scanning electron microscopy (using a JEM-840 Scanning Electron Microscope (SEM) operating at 20 KeV equipped with a backscatter detector.) Images were stored and quantified digitally.

Results

Metallography

Both transverse and longitudinal etched samples showed large individual equiaxed particles fairly uniformly distributed. A portion of the transverse section was selected for detailed study and is shown in Figure 1a. The section was approximately 6.8 x 25 mm (the full thickness of the plate). Any large carbides found were photographed with positions recorded. Examples of some of the largest particles found are shown in Figures 1b) through g), with the corresponding micrograph numbers superimposed on Figure 1a) to show the location of each particle. The particles are often slightly elongated in the rolling direction of the plate, are often (but not always) associated with prior-austenite grain boundaries, and are usually isolated away from other particles.

*Pacific Northwest National Laboratory (PNNL) is operated for the U.S. Department of Energy by Battelle Memorial Institute under contract DE-AC06-76RLO-1830.

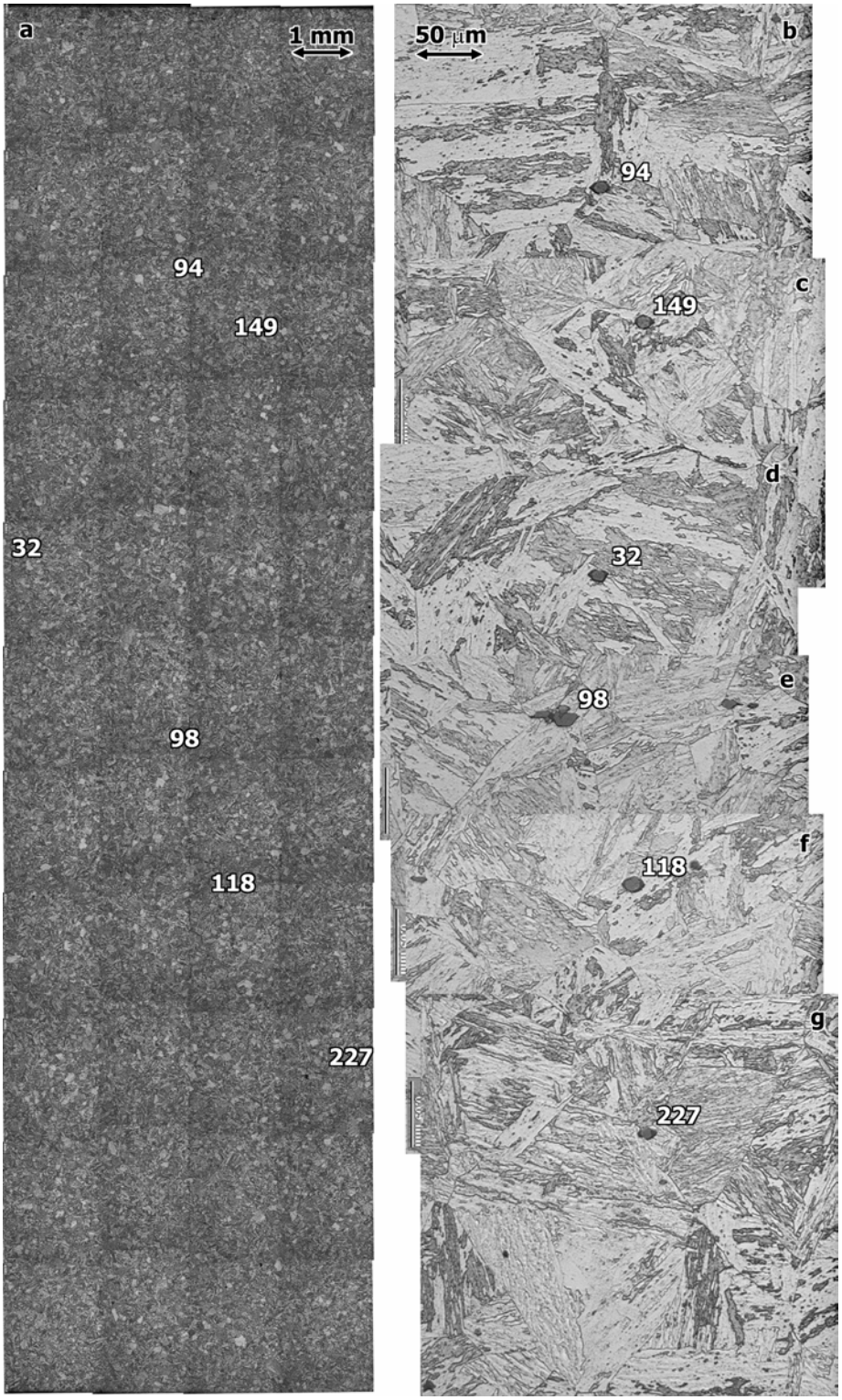

Figure 1. Transverse section etched microstructure of F82H plate showing in a) a mosaic of the microstructure across the full width of the 25 mm plate and in b) through g) some of the largest particles found. The numbers shown refer to the micrograph numbers, with positions indicated in a).

The micrographs containing particles were measured to provide approximate particle diameters for 480 particles, and these particle sizes have been plotted as a function of position from one of the surfaces in order to identify any non-uniformity in the distribution. The plot is shown in Figure 2. From Figure 2 it is apparent the particles range in size form 2 to 12 m with a fairly uniform distribution as a function of distance from the surface. Smaller particles were present but were not measured. It can be argued that few of the larger particles were less than 5 mm from the surface, but at issue is whether an explanation can be found for lower fracture toughness in the middle 5 mm of the plate. Therefore, it is concluded that reduced fracture toughness in the center of the 25 mm plate cannot be ascribed to variations in the size of these large particles.

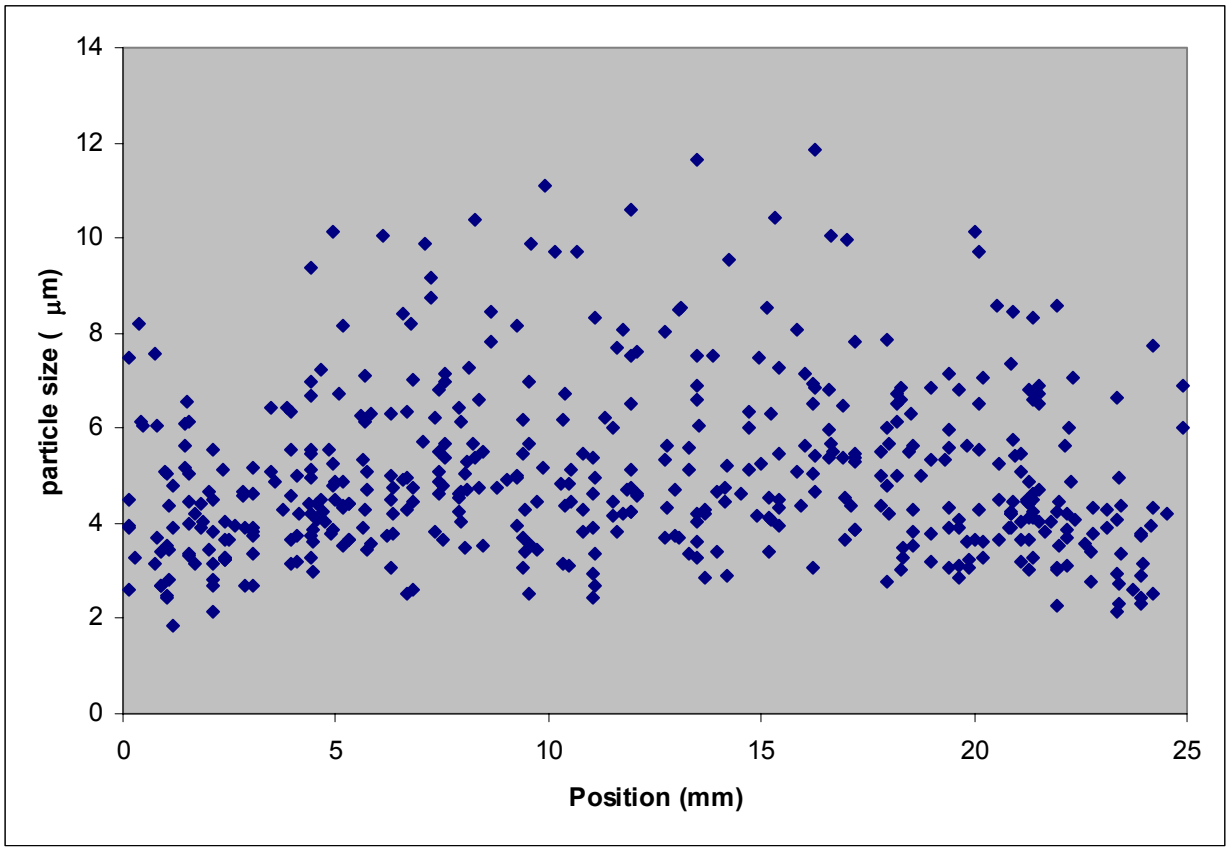

Figure 2. Particle size as a function of position in the 25 mm plate of F82H.

The particle size distribution for particles measured is shown in Figure 3. The largest fraction of the particles was in the range 3.5 to 4.5 μm. Based on a spherical approximation, the areal fraction of particles that were measured in the region shown in Figure 1a) was 0.10%, indicating that the volume fraction for these particles is only 0.1%.

However, in the course of examination, it became apparent that particles tended to clump, but clumping was generally restricted to the center of the plate. This tendency can be noted in Figure 1e) showing a line or stringer of particles 13.5 mm from the top surface. To the left and below the numerals “98”, a clumping of particles can be identified. Other examples of such clumping selected from the entire transverse section sample are provided at higher magnification in Figure 4. Examples 4a), 4e) and 4f) were from the area selected for examination, and therefore the larger particles shown are from outside the area shown in Figure 1a). All were found in the center of the plate. It therefore is apparent that particles had a greater tendency for clumping in the center of the plate.

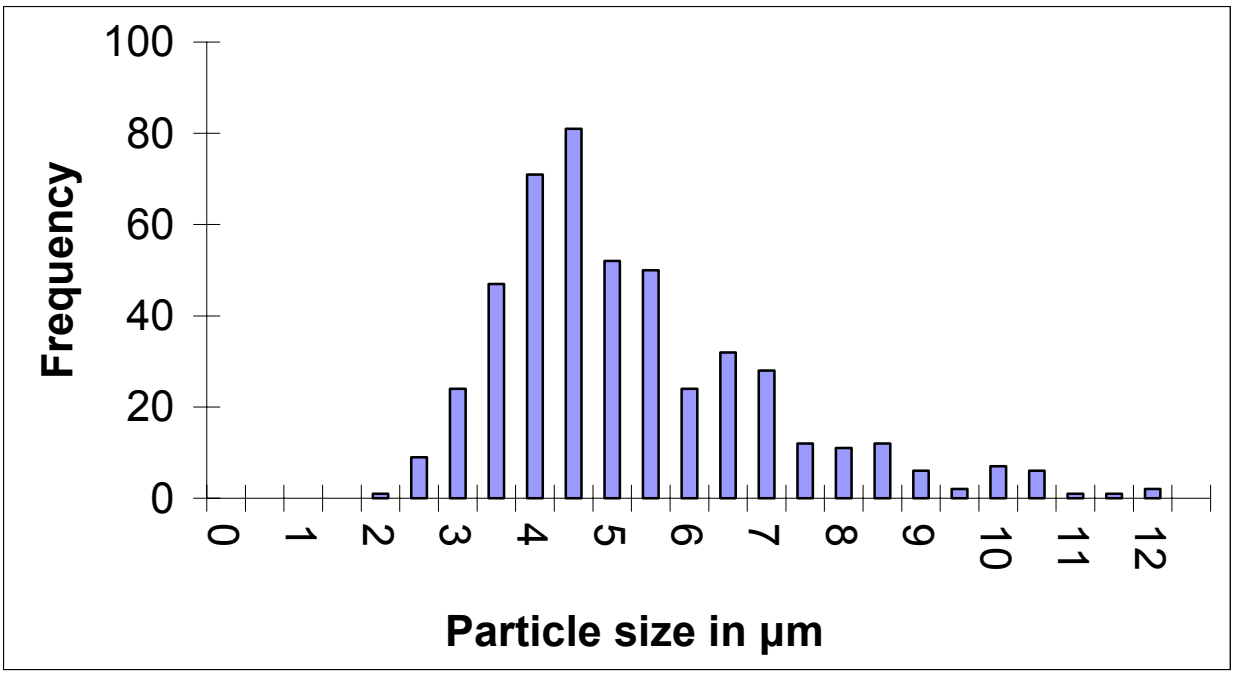

Figure 3. Particle size distribution.

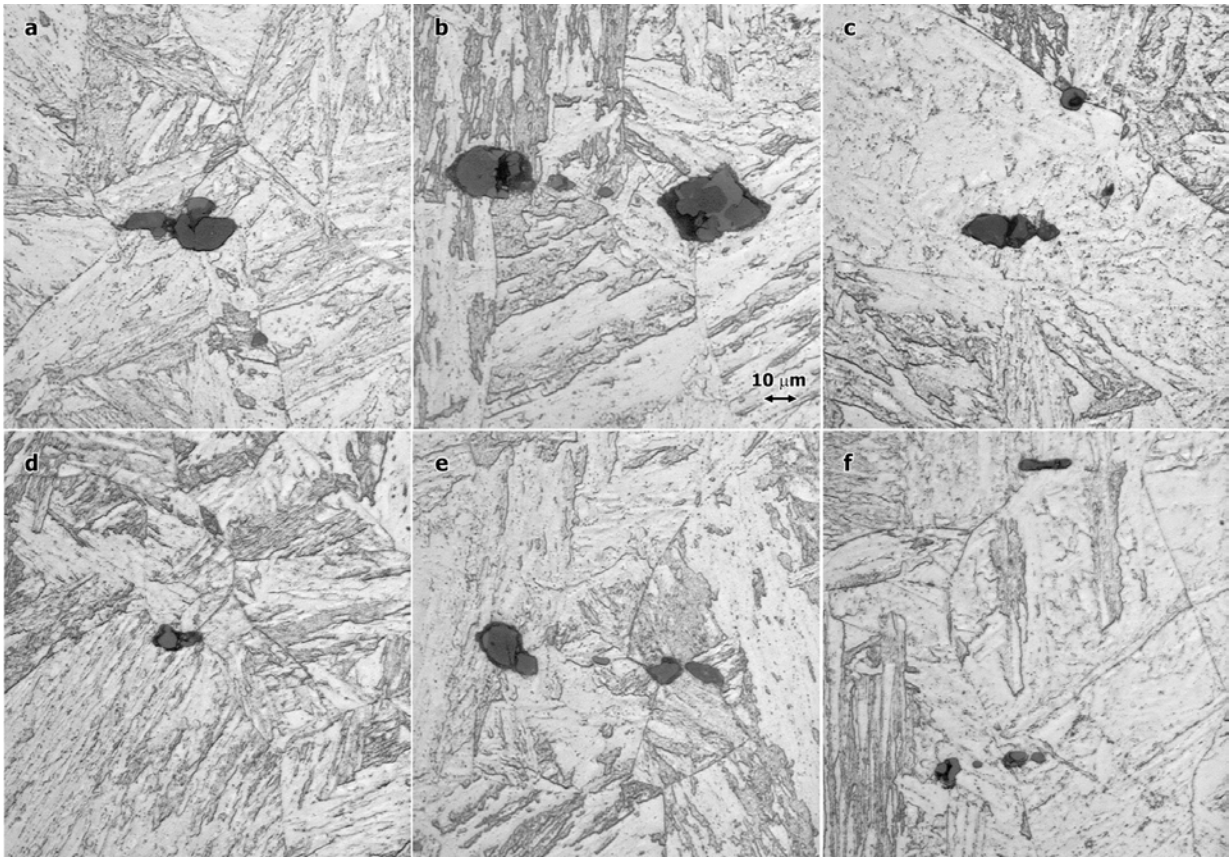

Figure 4. Higher magnification examples of clumped particles.

Scanning Electron Microscopy

The longitudinal section was examined by SEM to determine the chemical nature of the particles. Particles appeared as bright features in backscatter mode, but low magnification images did not contain sufficient resolution to map the distribution of particles. Examples of particles in backscatter mode over a range of magnifications are shown in Figure 5. Note that brightness in backscatter mode indicates higher atomic number. Figure 5c) provides another example of particle clumping. Five particles were selected for compositional analysis and x-ray spectra for two containing the lowest Fe content are provided in Figure 6. The spectra show high Ta and varying levels of Ti. Also, O is at higher levels than C. Therefore, these particles can best be described as tantalum oxide. A best estimate of the composition of the particles is Ta-6.8Cr-10.8Ti-4.0V-4.9Fe-1.7Al (metal content in weight percent) and Ta-9.9C-20.9O-4.7Cr-7.3Ti-2.7V-3.4Fe-0.7Al (total content in weight percent) so Ta levels are on the order of 73% of the metal content (and as high as 79% when Ti is low). As Al is not intentionally added in F82H, it is possible that the Al levels measured arise from alumina contamination, the grinding media.

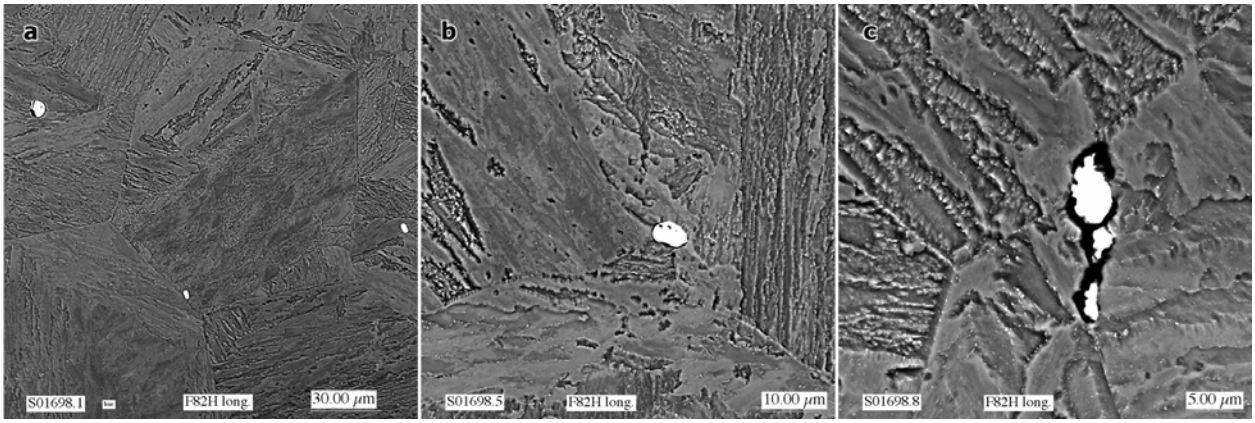

Figure 5. SEM images of particles shown in backscatter mode.

Discussion

After carbide etching, metallographic examination reveals the presence of large tantalum oxide particles in 25 mm plate of F82H produced by JAERI. The particles are approximately 4 μm in diameter but some exceed 12 μm and are slightly elongated in the rolling direction. Note that the 25 mm plate of F82H (heat 5753) contains 0.04 weight percent Ta, in moderate agreement with the estimated volume fraction of 0.1% for the measured tantalum oxide particles [3]. However, particles are uniformly distributed. Therefore, an explanation for reduced fracture toughness cannot be based just on the presence of these large particles. However, clumping of such particles, as appears to be the case particularly in the center of the plate, provides a possible explanation. It can be expected that under plastic strain, undeformable closely spaced particles should easily create insipient cracks between them because insufficient plasticity between particles is available to take up the deformation.

F

This raises interesting questions about the applicability of Ta additions to martensitic steels in order to promote improved fracture toughness by controlling prior austenite grain size. However, it can be anticipated that clumping of tantalum oxide particles can be reduced by further processing, and perhaps by improvements in melting practice.

Conclusions

Reduced fracture toughness observed in the central portion of 25 mm F82H plate may be attributed to clumped tantalum oxide particles. Therefore, it may be possible to mitigate the problem by elimination of tantalum, or improving melting and/or processes practices.

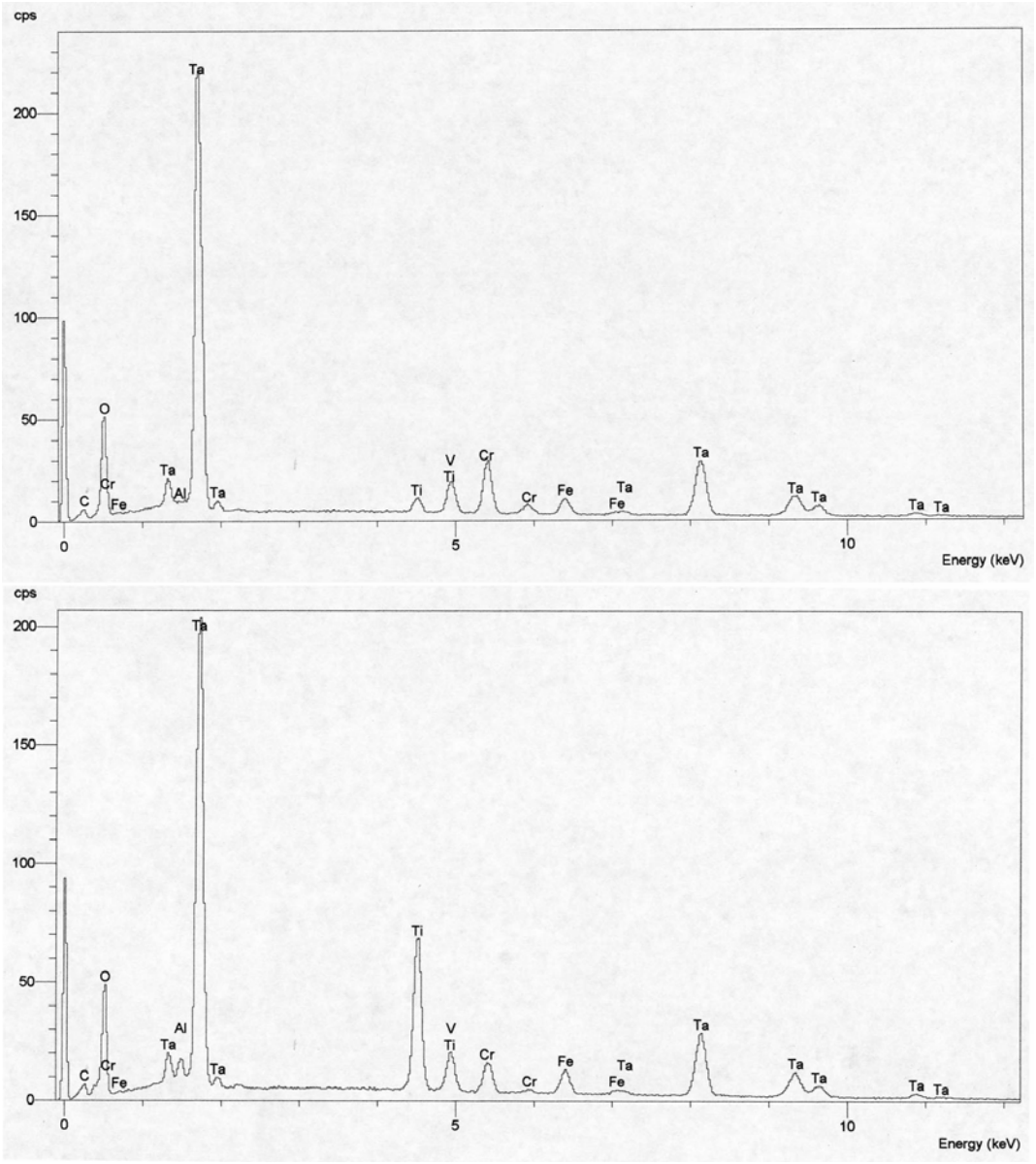

Figure 6. Two examples of x-ray spectra from large particles in 25 mm F82H plate.

Future Work

The effort will be continued as opportunities become available.

References

[1] D. S. Gelles and M. A. Sokolov in DOE/ER-0313/34 (2003).
[2] K. Wallin, A. Laukkanen, and S. Tähtinen in Small Specimen Test Techniques: Fourth Volume, ASTM STP 1418, Eds. M. A. Sokolov, J. D. Landes, and G. E. Lucas (ASTM International, West Conshohocken, PA, 2002) 33.
[3] IEA Summary Report A in the IEA Reduced Activation Ferritic Steel Data Base for F82H compiled by K. Shiba (2003).

A MASTER CURVE ANALYSIS OF F82H USING STATISTICAL AND CONSTRAINT LOSS SIZE ADJUSTMENTS OF SMALL SPECIMEN DATA—G. R. Odette, T. Yamamoto, H. Kishimoto, W. J. Yang, and G. E. Lucas (University of California, Santa Barbara), M. Sokolov (Oak Ridge National Laboratory), P. Spätig (CRPP EPFL, Switzerland), and J.-W. Rensman (NRG Petten, The Netherlands)

OBJECTIVE

The objective of this work was to assemble a database on the fracture toughness of the IEA heat of F82H normalized and ≈ 8Cr tempered martensitic steel and to assess the consistency of the data with the master curve method of establishing unirradiated reference toughness temperature curves.

SUMMARY

We assembled a fracture toughness database for the IEA heat of F82H based on a variety of specimen sizes with an ASTM E1921 nominal master curve (MC) reference temperature, T_o = -119±3°C. However, the data are not well represented by a MC. T_o decreases systematically with a decreasing deformation limit M_{lim} starting at ≈ 200, which is much higher than the E1921 censoring limit of 30, indicating large constraint loss in small specimens. The small scale yielding T_o at high M_{lim} is ≈ -98±5°C. While, the scatter is somewhat larger than predicted, after model-based adjustments for the effects of constraint loss, the data are in reasonably good agreement with a MC with a T_o = -98°C. This supports to use of MC methods to characterize irradiation embrittlement, as long as both constraint loss effects are properly accounted for. Finally, we note various issues, including sources of the possible excess scatter, which remain to be fully assessed.

PROGRESS AND STATUS

Introduction

One of the key challenges facing the development of ≈ 8Cr normalized and tempered martensitic steels (TMS) for fusion applications is irradiation embrittlement. Embrittlement is best characterized in terms of fracture toughness-temperature curves, $K_{Jc}(T)$. Measuring fracture toughness requires pre-cracked specimens subject to strict size and geometry requirements. Various versions of the master curve (MC) method, described in the next section [1-4], greatly reduce fracture toughness testing requirements in terms of both the size and number of specimens. This is critical since embrittlement depends on the combination of a large number of variables and there are very severe restrictions on irradiation volumes that can be accessed, particularly at high dose and with good control of specimen temperatures.

However, use of small specimens demands that the issue of size effects be addressed directly [1,3,5-11]. The sources of such size effects and approaches to accounting for them are described in the next section. We focus on the issue of determining a toughness temperature curve, $K_{Jr}(T)$, for the IEA F82H reference heat. Previous studies suggested that there was considerable variability in the $K_{Jr}(T)$ data for this heat, presumably associated with heterogeneities in the underlying microstructure, suggesting that a single MC can not represent IEA F82H. However, size effects were not fully assessed in the previous studies, confounding this conclusion. In order to evaluate the applicability of the MC method to TMS, a physically based method is used to adjust for size effects in the IEA F82H database and we assess the agreement of the adjusted data with a single MC.

Background, Master Curve and Specimen Size and Geometry Effects on Fracture Toughness

Various MC methods *assume* there is a universal invariant toughness temperature curve shape, $K_{Jc}(T-T_o)$, or small family of shapes, in the cleavage transition regime that can be indexed on an absolute temperature (T) scale by a reference temperature (T_o) at a median reference toughness of 100 MPa√m [1-4]. The American Society for Testing and Materials (ASTM) E1921 Standard MC is given by [2]

$$K_{Jc}(T-T_o) = 30 + 70[0.019(T-T_o)]\ (MPa\sqrt{m}). \quad (1)$$

T_o can be measured using a relatively small number of relatively small specimens. The Master Curve-Shifts Method (MC-ΔT) [1,3], adjusts the reference T_o for the alloy in the unirradiated condition with a set of temperature shifts (ΔT_o) to account for the loading rate [1] and irradiation embrittlement [1,3,4,6]. The effects of specimen size and geometry can also be treated in terms of a ΔT_o and adjusted MC shapes [1,3,5]. Large ΔT_o may control the lifetime of fusion reactor structures. However, the ΔT_o that accounts for shallow surface cracks in thin-walled structures has a large negative value, thus may mitigate the effects of embrittlement [3].

The various ΔT_o can be independently measured and modeled. For example, at irradiation temperatures below about 400°C, the ΔT_o for embrittlement can be related the irradiation hardening, measured in tensile ($\Delta\sigma_y$) or microhardness tests [1,4,6]. Further, models that relate $\Delta\sigma_y$ to metallurgical and irradiation variables derived from fits to the large tensile test database can also be used to help model ΔT_o [1,3,4,6]. Multiscale models can also be used to relate $\Delta\sigma_y$, hence ΔT_o, to irradiation-induced microstructural evolutions, as well as to guide the development of radiation resistant alloys [3].

There is a large and growing body of data on the fracture toughness of TMS in the unirradiated and, to a lesser extent, irradiated conditions. However, these data represent a wide range of test specimen sizes and types [10-14]. Size and specimen geometry are known to influence the measured values of fracture toughness, K_{Jm}. Indeed, fracture toughness is an intrinsic, geometry and size-independent material property, K_{Jr}, only for very restricted reference conditions of a cracked-body (specimen or structure). Thus in order to assess the applicability of the MC method to TMS, it is necessary to properly account for size/geometry effects and to develop methods to transfer the measured K_{Jm} data to the intrinsic property at a reference condition, K_{Jr} (1,3,5-11), as well as to transfer the K_{Jr} to conditions pertinent to a cracked structure [1,3].

Two different size-effects must be considered. Constraint loss (CL) effects occur when the specimen ligament length, b, and/or thickness, B, are no longer small with respect to the dimension of the plastic zone of the crack [1,3,5-11]. Note that the ligament length is defined as b = W – a, where a is the crack length and W is the width of the specimen. Tri-axial constraint elevates the normal stress near the crack tip, σ_{22}, to values of 3 to 5 times σ_y. Any CL lowers σ_{22}, hence, a higher K_{Jm} is needed for cleavage fracture compared to the K_{Jc} for plane strain, deeply cracked specimens, loaded in bending under small-scale yielding (SSY) conditions.

K_{Jm} and K_{Jc} also increase with a decreasing volume of material under the high σ_{22} stress field near a crack tip [2,3,7-9]. This derives from the fact that cleavage occurs when a critical $\sigma_{22} = \sigma^*$ encompasses a sufficient volume of material to cause the formation and propagation of a microcrack from a broken, brittle trigger-particle, like a large grain boundary carbide. The trigger-particles have statistical size and spatial distributions; hence, they act in a way that is similar to a distribution of the strengths of the links in a long chain. Thus, cleavage is a statistical, weakest-link process, and this has two important consequences. The first is that there is an inherently large specimen-to-specimen scatter in K_{Jm} and K_{Jc}. Second, as noted above, K_{Jm} and K_{Jc} increase as the specimen thickness or crack front length, B, hence stressed volume, decreases. We refer to this as the statistical stressed volume (SSV) effect. The stressed volume scales with BK_J^4 under SSY conditions.

In order to decouple the SSV from CL effects, we recently carried out a single-variable experiment on a large matrix of a/W ≈ 0.5, 3-point bend specimens, with a wide range of B (8 to 254mm) and W (6 to 50 mm) [3,7-9]. The pre-cracked specimens were fabricated from a large plate section of the unused Shoreham A533B reactor pressure vessel. Eight specimens were tested at T = -91°C and a constant loading rate for each B-W combination. The baseline B-W matrix was complimented by a large number of fracture tests using 1T compact tension and pre-cracked full and sub-sized Charpy specimens, as well as small bend bars with shallow, a/W ≈ 0.2, pre-cracks. Tensile tests and optical metallography were also

carried out to characterize the constitutive properties and basic microstructure of the steel; and the fracture surfaces were characterized by scanning electron microscopy.

The B-W database showed that CL occurs at loading levels well below the current E1921 censoring limit, defined at $M = b\sigma_y E'/K_{Jm}^2 > M_{lim} = 30$ [2]. However, the data also clearly show a SSV effect that is reasonably consistent with the scaling law in E1921 [2],

$$K_{Jr} = (K_{Jc} - K_{Jmin})(B/B_r)^{-1/4}. \quad (2)$$

Here B_r is a reference thickness of 25.4 mm. This expression reflects the stressed volume scaling as BK_J^4, modified by the assumption that cleavage only occurs above a minimum K_{Jmin}, taken as 20 MPa$\sqrt{m}$ in E1921 [2].

The single-variable B-W database was successfully analyzed with calibrated micromechanically-based three-dimensional (3D) finite element (FE) CL models [7-9]. The models were used to separate CL and SSV effects. The models compute the theoretical ratio of the large-scale yielding (LSY) to SSY loading ratio, $[K_{lsy}/K_{ssy}]$, that produce the same local crack tip stress field conditions. One model was based on a local fracture criterion that assumes that cleavage occurs when the $\sigma_{22} = \sigma^*$ stress contour encompasses a critical average in-plane area, A*, of the fracture process zone in front of the crack tip. The model was used to evaluate $[K_{lsy}/K_{ssy}]$ for the Shoreham steel constitutive law as a function of B/W, b, σ^*/σ_y and K_{lsy}, where $K_{Jc} = K_{Jm}/[K_{lsy}/K_{ssy}]$ is evaluated at $K_{lsy} = K_{Jm}$. The calibration of σ^* involved fitting a σ^*-A* $K_{Jc}(T)$ model [1,3,4,7-9] to an independent set of high constraint (≈ SSY) K_{Jc} data. Equation 2 was used to adjust K_{Jc} to a reference K_{Jr} for B = 25.4 mm. Another approach to evaluating $[K_{lsy}/K_{Jc}]$ based on a self-calibrated Weibull stress statistical model gave very similar results [9].

The adjusted K_{Jr} for the B-W Shoreham matrix formed a very self-consistent data population with expected statistical properties and a T_o = -84±5°C. The adjustment procedure was also applied to the other UCSB Shoreham data, as well as a large set of K_{Jm} data for the same Shoreham plate section reported by Joyce and Tregoning, for a variety of standard specimens tested over a wide range of temperatures [3,8,9]. Remarkably, the entire Shoreham K_{Jr} database (445 data points) was well represented by a single MC with an ASTM E1921 T_o = -85±5°C. Of course, the T_o of the individual subsets of data varied somewhat, but generally fell within the expected statistical distribution and only 22 of the 445 data points fell outside the 5 to 95% confidence interval.

A K_{Jm} Database for the IEA Heat of F82H and Adjustment to K_{Jr}

The CL and SSV method described above were used to adjust the K_{Jm} IEA F82H database that we have assembled, currently composed of 219 data points. The K_{Jm} data represent a wide range of bend bar and compact tension specimen sizes from research programs at UCSB [10,11], ORNL [12], VTT [13] and NRG [14]. Figure 1 shows the K_{Jm} data that has been only adjusted for SSV size-effects based on Equation 2 to a reference B_r = 25.4 mm, K_{Jmr}, based on the ASTM E1921 Standard; but these data have not been adjusted for CL effects. The MC and the 5 and 95% confidence interval curves based on a ASTM E1921 analysis of the K_{Jmr} data, that yielded a T_o ≈ -119±3°C, are also shown. A large number of data points fall outside the 5 and 95% confidence interval; and at higher temperatures many fall below the 5% bound. Thus the K_{Jmr} data are not well represented by a single MC with T_o = -119°C.

Figure 2 illustrates the strong effect of CL loss on the IEA F82H database. Here we plot the E1921 T_o excluding K_{Jm} data with M below a variable censoring limit, M_{lim}, which has a nominal value of 30 in the ASTM Standard. Above M_{lim} ≈ 200 for the T_o plateaus at a SSY value of ≈ -98±5°C. However, T_o decreases below a value of M_{lim} ≈ 200, at a deformation level that is much lower at the E1921 limit of 30. Thus an E1921 analysis results in a highly non-conservative, small specimen T_o bias of ≈ -21°C.

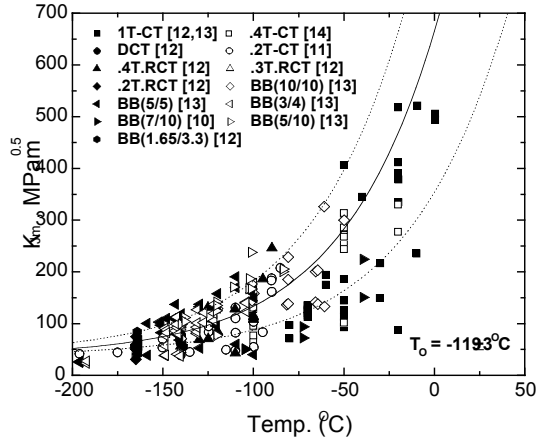

Figure 1. The F82H K_{Jmr} data versus temperature after a SSV (Equation 2) but with no CL adjustment and the median, 5% and 95% confidence interval toughness-temperature curves for the E1921 T_o = -119±3°C.

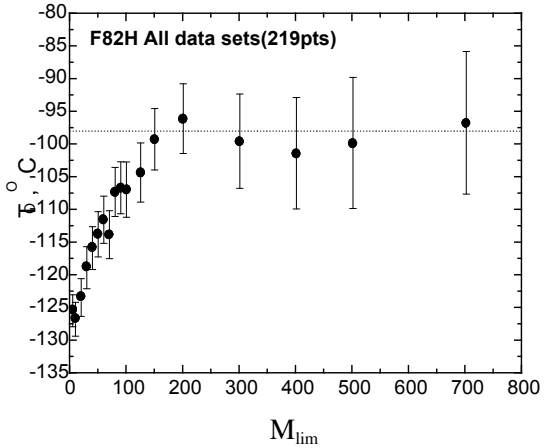

Figure 2. ASTM E1921 multiple temperature analysis T_o versus M_{lim} for the IEA F82H database, showing large effects of constraint loss and a SSY T_o ≈ 98±5°C at M_{lim} > 200.

The CL adjustment procedure was calibrated to the IEA heat of F82H by fitting the $K_{Jc}(T)$ model to a set of high constraint (≈ SSY) data based on a preliminary estimate of T_o ≈ - 94°C[1], yielding □* ≈ 2100±100 MPa for A* = 2.5x10^{-8} m^2. The CL and SSV adjusted K_{Jr} data are shown in Figure 3, along with the corresponding MC and the 5 and 95% confidence interval curves based on a multiple-temperature ASTM E1921 analysis that yielded a T_o ≈ -103°±3°C. This is reasonably consistent the best estimate T_o = -98±5°C based on the M_{lim} analysis, but reflects a slight residual small specimen bias that will be discussed below.

[1]Note the CL analysis was carried out prior to the multi-temperature T_o evaluation shown in Figure 3. The preliminary T_o = -94°C estimate was largely based on the results of data from the largest 1T CT specimens. Re-analysis based on □* for a T_o = -98°C would be possible, but this would not result in a significant change in the conclusions.

Figure 4 plots the differences between the adjusted K_{Jr} data and the MC median toughness, K_{Jo}, as a function of temperature for T_o = -98°C. The MC 5 and 95% confidence interval curves are also shown, along with average K_{Jr}- K_{Jo}, and the corresponding standard deviations, in small intervals around common test temperatures. At lower temperatures the adjusted K_{Jr} data are slightly biased to the low side of K_{Jo}. This negative bias decreases at higher temperatures where the data become reasonably well centered, with the average deviations scattering about K_{Jr}- K_{Jo} = 0. However, a total of 34 data points fall below the nominal 5% and 22 above the 95% confidence interval limits, respectively. This is ≈ 2.5 times the number (≈ 22) of data points expected to fall outside the 5 to 95% confidence interval. However, it is noted that most of these excess deviations are relative small.

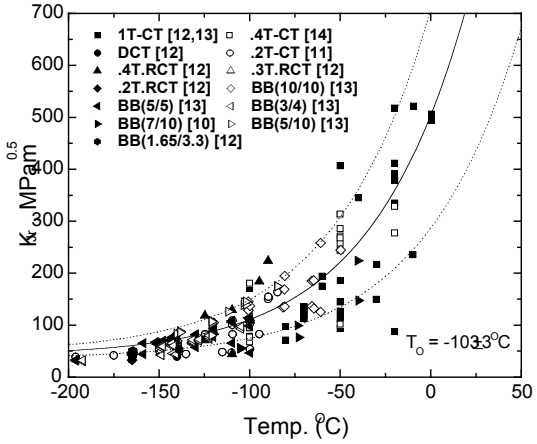

Figure 3. The F82H K_{Jr} data versus temperature after a SSV and CL adjustment and the median, 5% and 95% confidence interval toughness-temperature curves for the E1921 T_o = -103±3°C.

As highlighted by the arrows, examination of Figure 4 suggests that the CL and SSV model may slightly over-adjust the K_{Jm} data for very small specimen at low temperature and slightly under-adjust K_{Jm} at higher temperatures around and above T_o. This leads to a slightly lower T_o = -103°C for the adjusted K_{Jr} database, compared to the T_o = -98°C found in the M_{lim} analysis. This is not surprising, since in bending dominated crack tip fields, the [K_{lsy}/K_{ssy}] adjustments are larger at lower $\square^*/\square_y$. Since $\square_y$ increases with decreasing temperature, $\square^*/\square_y$ decreases. Thus the model may tend to over-adjust the measured data at low temperature and under-adjust at the higher temperatures. In addition, the applicability of SSV adjustments of low temperature data is questionable; indeed, SSV adjustments of data near or on the lower shelf regime are not recommended in the E1921. Further, this assessment assumes that the shape and lower shelf toughness of the MC described by Equation 1 is precisely applicable to TMS, which may not be the case. Other issues that are not completely resolved relate to the physical basis for and value of K_{min} = 20 MPa$\sqrt{m}$, and assumptions leading the nominal confidence limits specified in the E1921 Standard. Finally, the excess scatter may in part be due to material heterogeneity for different IEA F82H plate sections and section thicknesses or thickness locations. Such heterogeneity may be have the largest impact on the 25.4 mm specimens, with a full though-plate thickness crack, that may sample the lowest toughness microstructure at the center-plane of the plate. We plan to carry out additional research directly aimed at resolving these issues.

However, the issue of possible excess scatter aside, it is clear that the adjusted K_{Jr} data are in generally good agreement with a single MC with T_o = -98±5°C MC. Thus there can be considerable confidence in $\square T_o$ evaluations, including for irradiation embrittlement, based on the MC-$\square$T method using a sufficient number of small specimens, provided that size effects are properly accounted for. However, assessing the $\square T_o$ for irradiation embrittlement raises some additional issues. First, the effect of reduced strain hardening on increased CL in irradiated specimens must be carefully quantified. Second, while results to

date are promising [6], the effects of irradiation on the shape of the MC for large $\Delta\sigma_y$ and ΔT_o are not fully understood.

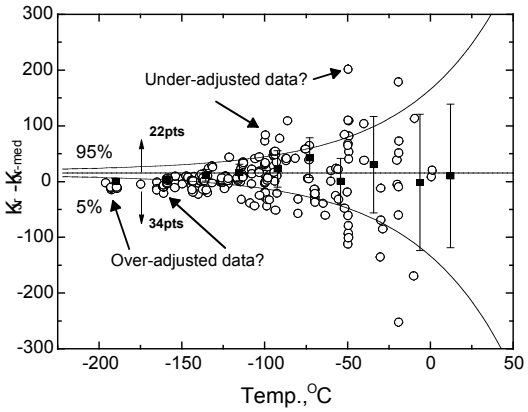

Figure 4. K_{Jr} - K_{Jo} as a function of temperature and the corresponding 5 and 95% confidence interval curves for T_o = -98°C. The square symbols and error bars are the average and one standard deviation K_{Jr} - K_{Jo} for groups of data over small test temperature intervals. The arrows indicate data that may be under-adjusted leading to a slightly lower T_o = -103°C.

Summary and Conclusions

We have assembled a database on the fracture toughness of the IEA heat of F82H. The database, currently composed of 219 data points, is based a wide variety of compact tension and bend bar specimen sizes. ASTM E1921 evaluation of this database yielded a T_o = -119±3°C. However, the data are not well represented by a single MC. In the past, these deviations have raised questions about the applicability of the MC based methods to TMS, or were attributed to material heterogeneity.

However, T_o is sensitive to the assumed deformation limit, M_{lim}, specified in E1921 as 30; and T_o decreases systematically with decreasing M_{lim} starting at a much higher value ≈ 200 due to constraint loss. At higher M_{lim} >200, T_o reaches a SSY plateau of ≈ 98±5°C. Thus we applied a calibrated size-adjustment procedure, which accounts for constraint loss effects that are controlled by the specimen size, as well as statistical effects of B. An E1921 analysis of the fully adjusted toughness database gave a T_o = 103±4°C, close to the result of the M_{lim} analysis; and the adjusted K_{Jr} data are in reasonably good agreement with a MC with T_o = -98°C. However, the scatter was somewhat larger than predicted, with ≈ 25% of the data points falling outside the estimated 5 to 95% confidence interval. Nevertheless, the excess deviations were generally small and can in part be linked to the approximate adjustment model. The data generally seemed to be slightly over-adjusted at very low temperatures and slightly under-adjusted at temperatures around T_o and above. Finally, we describe a number of issues that are not fully resolved, including possible excess scatter. However, the results of this study lend strong support to the use of MC-type methods in characterizing the effects of irradiation and other variables on the toughness temperature curves of TMS.

Future Research

We will continue to add and analyze additional data on the IEA F82H as it becomes available. We will also extend the database to include other ≈ 8Cr TMS including Eurofer98 and irradiated alloys. Experiments aimed at resolving the various issues noted in the previous section.

Acknowledgements

This research was supported by the DOE Office of Fusion Energy Science (Grant # DE-FG03-94ER54275). The authors also explicitly acknowledge the large IEA F82H database developed by Dr. K. Wallin of VTT Laboratory in Finland.

References

[1] G. R. Odette, K. Edsinger, G. E. Lucas, and E. Donahue, *Small Specimen Test Techniques*, V3, ASTM STP 1329, American Society for Testing and Materials (1998) 298.
[2] ASTM E 1921-03, Standard Test Method for Determination of Reference Temperature, T_o, for Ferritic Steels in the Transition Range, *Annual Book of ASTM Standards: Metals Mechanical Testing; Elevated and Low Temperature Tests; Metallography,* V03.01, American Society for Testing and Materials (2003).
[3] G. R. Odette, T. Yamamoto, H. J. Rathbun, M. L. Hribernik, and J. W. Rensman, J. Nucl. Mater. 323 (2003) 313.
[4] G. R. Odette and M. Y. He, J. Nucl. Mater. 283-287 (2000) 120.
[5] G. R. Odette and M. Y. He, J. Nucl. Mater. 307-311 (2002) 1624
[6] G. R. Odette, H. J. Rathbun, J. W. Rensman, and F. P. van den Broek, J. Nucl. Mater. 307-311 (2002) 1011.
[7] H. J. Rathbun, G. R. Odette, and M. Y. He, Proceedings of the International Congress on Fracture 10 (2001) (searchable Elsevier CD format).
[8] H. J. Rathbun, G. R. Odette, M. Y. He, T. Yamamoto, and G. E. Lucas, *Applications of Fracture Mechanics in Failure Assessment*, PVP 462, American Society of Mechanical Engineers (2003) 31.
[9] H. J. Rathbun, G. R. Odette, M. Y. He, G. E. Lucas, and T. Yamamoto, *Size Scaling of Cleavage Toughness in the Transition: A Single Variable Experiment and Model Based Analysis*, NUREG/CR 6790, U.S. Nuclear Regulatory Commission (2004) in press.
[10] P. Spatig, G. R. Odette, E. Donahue, and G. E. Lucas, J. Nucl. Mater. 283-287 (2000) 120.
[11] P. Spatig, E. Donahue, G. R. Odette, G. E. Lucas, and M. Victoria, *Multiscale Modeling of Materials* 2000, MRS Symposium Proceedings 653, Materials Research Society (2001) Z7.8.
[12] M. Sokolov, R. Klueh, G. R. Odette, K. Shiba, and H. Tanaigawa, *Effects of Irradiation on Materials – 21st International Symposium*, ASTM STP 1447, American Society for Testing and Materials (in press) and private communication.
[13] K. Wallin, A. Laukkanen, and S. Tahtinen, *Small Specimen Test Techniques*, V4, ASTM STP 1418, American Society for Testing and Materials (2002) 33.
[14] J.-W. Rensman et al., J. Nucl. Mater. 307–311 (2002) 245.

ON THE EFFECTS OF FATIGUE PRECRACKING ON THE MICROSTRUCTURE AROUND PRECRACK IN 1TCT FRACTURE TOUGHNESS SPECIMEN OF F82H-IEA—H. Tanigawa (Japan Atomic Energy Research Institute), N. Hashimoto, M. A. Sokolov, and R. L. Klueh (Oak Ridge National Laboratory), and M. Ando (JAERI)

OBJECTIVE

The objective of this work is to observe the effects of fatigue precracking on the microstructure around the precrack in 1TCT fracture toughness specimen of F82H-IEA.

SUMMARY

1TCT fracture toughness specimens of F82H-IEA steel were fatigue precracked and sliced in specimen thickness wise for microstructure analysis around the precrack. The microstructure around the precrack was observed by optical microscopy (OM), scanning electron microscopy (SEM), orientation imaging microscopy (OIM), and transmission electron microscopy (TEM). TEM samples around the crack front were prepared by focused ion beam (FIB) processor. The fracture surfaces of tested 1TCT specimens were also observed. OM observation showed that the precrack penetration was straight in the beginning, and then tended to follow a prior austenite grain boundary and to branch into 2 to 3 directions at the terminal. SEM and OIM observations revealed that the both microstructures around the precracks and ahead of the precrack had turned into cell structure, which is the typical microstructure of fatigue-loaded F82H. TEM images and inverse pole figures obtained from the crack-front region confirmed this structure change. Possible mechanisms by which the precrack branching or the cell structure ahead of precracks affects fracture toughness were suggested.

PROGRESS AND STATUS

Introduction

In the current JAERI-DOE fusion collaboration program, the ductile-brittle transition temperature (DBTT) of the reduced-activation ferritic/martensitic steels (RAFs) is to be determined by the master curve (MC) method, in which the DBTT of ferritic steels is characterized in terms of fracture toughness reference temperature, T_o, as defined in the ASTM standard E1921. This method works out when the transition fracture toughness values follow the MC that is usually independent of the type of steels or the type of the specimens once the value is scaled in the proper manner.

The problem with F82H-IEA[1], one of the RAFs being examined in this collaboration, is that some fracture toughness values obtained by 1TCT specimens fell outside tolerance bands of the MC (Fig.1)[2]. There are two potential reasons that could cause this problem: (1) the heat treatment sensitivity of F82H-IEA, and (2) the fatigue precracking. In this study, the latter possibility was investigated.

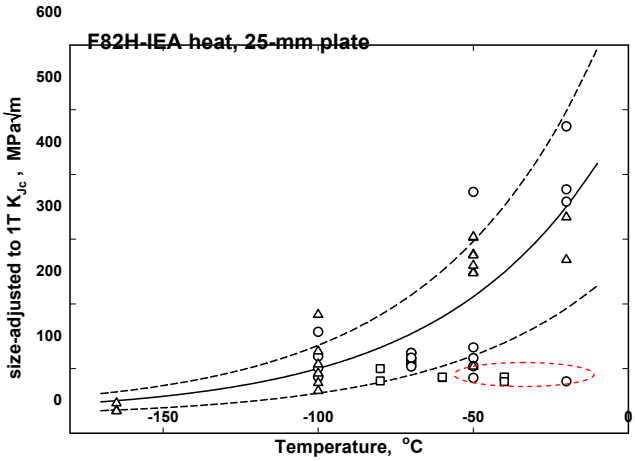

Fig. 1. The MC of F82H-IEA heat. Data points encircled by a broken red line indicate the toughness data which are below the lower tolerance bands of the MC.[2]

Fatigue microstructure of F82H was previously investigated [3,4] on low-cycle fatigue-fractured specimens, and the results revealed that the way that the fatigue crack propagated is that the cyclic

loading causes the lath structure to disappear and a cell structure forms, after which the fatigue crack propagates through the weakest portion of the cell structure. This fact indicates that fatigue precracking on a toughness specimen could induce the same type of microstructure into the region around the crack when the stress level is above the fatigue limit and propagate the crack through the weakest portion. On the other hand, even though ASTM standard E1921 defined the precracking procedure to minimize the effect of the plastic deformation zone on the fracture toughness value, the deformation range was just defined in the region where the stress level is above the yield stress. This could underestimate the effect of fatigue-induced deformation on ferritic/martensitic steels like F82H.

From this point of view, the effect of fatigue precracking on the toughness was investigated based on microstructure observations around the precrack induced in a 1TCT toughness specimen of F82H-IEA.

Experimental

1TCT specimens examined in this study were made from 25mm thick plate of F82H-IEA heat no. 9753, nominally Fe-7.5Cr-2W-0.15V-0.02Ta-0.1C, in wt%. The plate provided had been TIG welded and post weld heat treated at 993K for 1 hr [5]. The specimens were machined in L-T orientation such that loading will be in rolling direction and crack will propagate in transverse direction, and those were precracked as defined in ASTM standard E1921. A precracked and untested specimen was cut by EDM for microstructure examination around the precrack. It was then sliced in specimen thickness wise into 2.5mm thick pieces as shown in Fig.2. Each piece was mechanically polished to remove the EDM-affected zone, and then polished with SiC colloid to remove the effect of mechanical polishing. No electro-polishing was performed in order to conserve the region around the precrack. Fractured 1TCT specimens which showed various fracture toughness values were selected for fracture surface observation. Another specimen was prepared from the grip area of a tested specimen that exhibited a low toughness value. This specimen was polished and etched to perform optical metallography on the section perpendicular to the rolling direction (in plate thickness wise, i.e., specimen thickness wise). This specimen was etched with 8% nitric acid and 1% hydrofluoric acid in water.

Surface observations were performed by optical microscopy (OM) and scanning electron microscopy (SEM) using FE-SEM (Philips XL30). An orientation image microscopy (OIM) system (Tex SEM Laboratories) was used to analyze the grain orientation distribution. The OIM analysis was performed with a resolution of 50 to 150 nm. The specimens for transmission electron microscopy (TEM) were fabricated utilizing the focused ion beam (FIB) processor (Hitachi FB-2000A) with a microsampling system at Japan Atomic Energy Research Institute (JAERI). Further information on the FIB fabrication and these TEM observations can be found in ref. 6.

Results and Discussion

Fig.3 shows the cross sectional OM microstructure through the plate thickness, obtained from one 1TCT specimen with low fracture toughness. The microstructure is uniform thorough the thickness, with no banded structure, as reported by Gelles et.al.[7]. This could indicate that the low-energy fracture has no relation to the band microstructure. Fig.3 shows the fracture surfaces of 1TCT specimens fractured at different conditions. Condition A is for specimens that were tested at 253K or 233K and exhibited low toughness; the value is below the lower tolerance bound of the MC (Fig.4(a) and (b)). Condition B is for a specimen that was tested at 253K and exhibited high toughness; the value is within the tolerance bound of the MC (Fig.4(c)). Condition C is for a specimen that was tested at 173K and exhibited the toughness with the value within the tolerance band of the MC, but the value itself is the same as condition A (Fig.4(d)). On all specimens, the precracked fracture

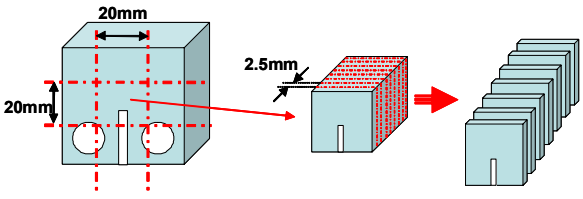

Fig. 2. Specimen preparation procedure for precrack observation on 1TCT specimen.

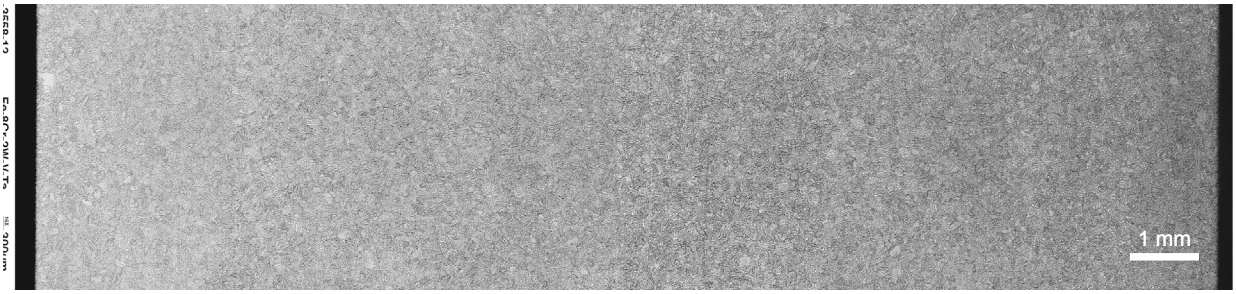

Fig. 3. Optical microstructure of cross section of F82H-IEA 25mm plate obtained from low-energy fractured 1TCT specimen.

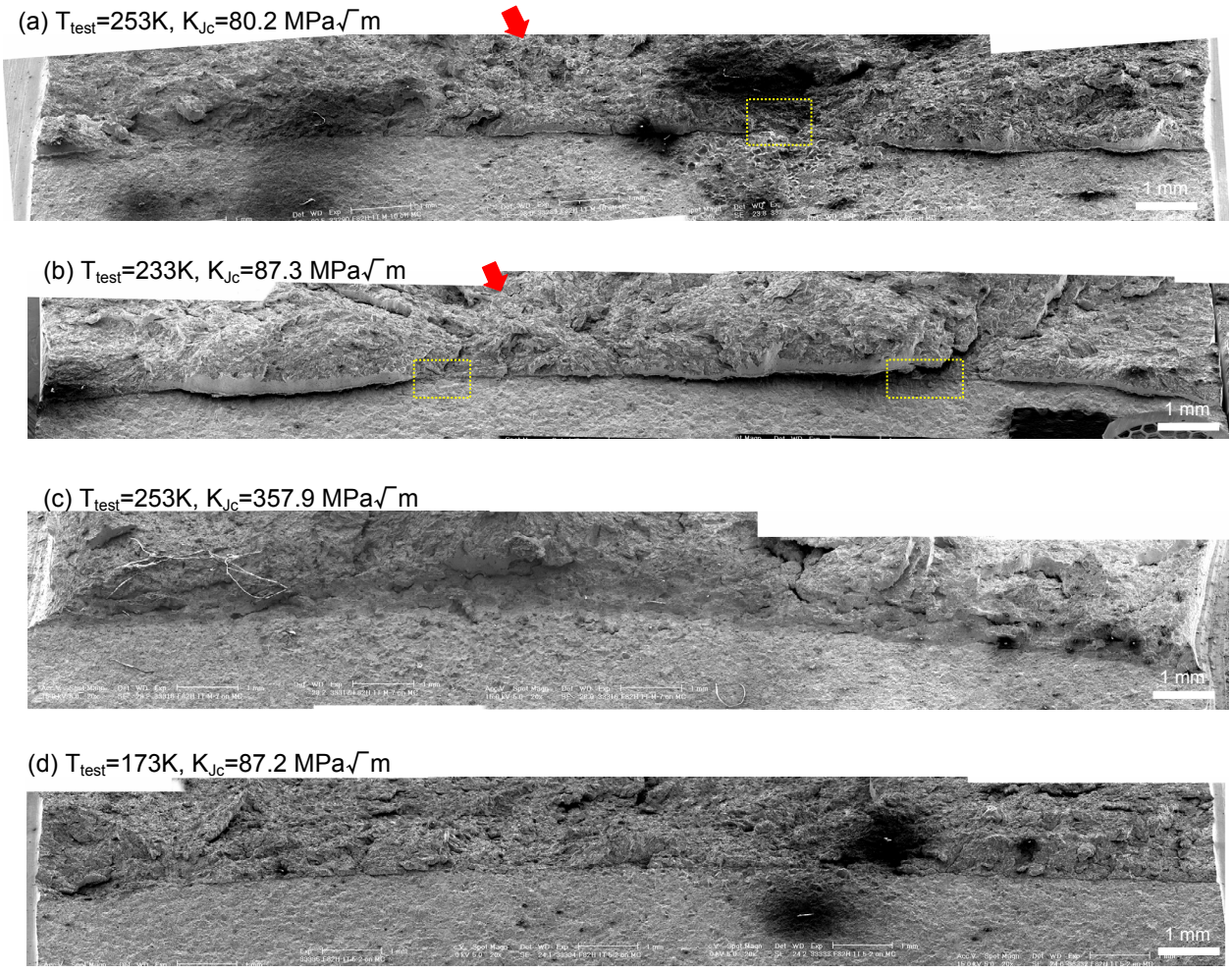

Fig. 4. SEM images of the fracture surface of 1TCT specimens which were tested at various conditions. Specimens were tilted 45 degrees. Images (a) and (b) were the fracture surfaces of the specimens which exhibited low toughness and those values were below the lower tolerance bound of the MC, (c) and (d) were the fracture surfaces of the specimens which exhibited the toughness which values were within the tolerance bound of the MC.

surfaces showed mostly flat and characterless surfaces, but the terminal of the precrack near the middle section showed intergranular fracture surfaces. On the specimen that exhibited low toughness and its value is below the lower tolerance bound of the MC (Fig.4(a), (b)), there is one apparent fracture initiation point (indicated with red arrow). Presence of this trigger point fits very well with premises of the MC methodology. There is also another indication that the fracture may start from very near the pre-crack front which shows inter-granular fracture (region indicated by yellow dashed square in Fig.4(a)), or start from branched crack which was observed beneath the main fracture plane (region indicated by yellow dashed square in Fig.4(b)). The magnified image (Fig.5) of the potential fracture starting point observed in Fig.4(a) shows the continuity from the fatigue pre-crack induced intergranular fracture surface. This might be interpreted as evidence that the fatigue crack which ends up as an intergranular fracture may cause the low-energy fracture.

It is also worth noting that these low-energy fracture surfaces have cracks parallel to the main crack. This might have a strong relationship to the branching of the fatigue precracks which were shown in Fig.6. Fig. 6 shows the pre-crack feature from a different region of specimen thickness. Numbers next to each image indicate the distance from the middle plane of the specimen thickness. These images indicate that the precracks initially propagated straight through the prior austenite grain (PAG), then started to follow the PAG boundary. At the terminal of the precrack, it branched into 2 or 3 cracks. This tendency is quite obvious in the middle section of the specimen.

To investigate the microstructure around the precrack in detail, SEM observations were made on the crack tip on the section +1.2mm from the center. Fig.7 shows back-scattered electron (BSE) images of the crack tip with a schematic drawing of the microstructure. The image shows that the fatigue precrack propagated through the PAG, but began to propagate along the PAG boundaries at its terminal. OIM images shown in Fig.8 suggest that the orientation distribution of the cell structure regions turned to dispersive, and they are different from what is observed on as-prepared F82H. These images indicate the presence of cell structure around the precrack, and this cell structure spread out for 60 μm ahead of crack tip into the direction the maximum shear stress was applied (Fig.8(c)).

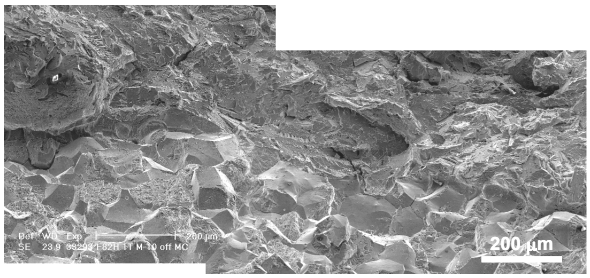

Fig. 5. Magnified image of the fracture initiation point near the precrack front observed in Fig.4(a).

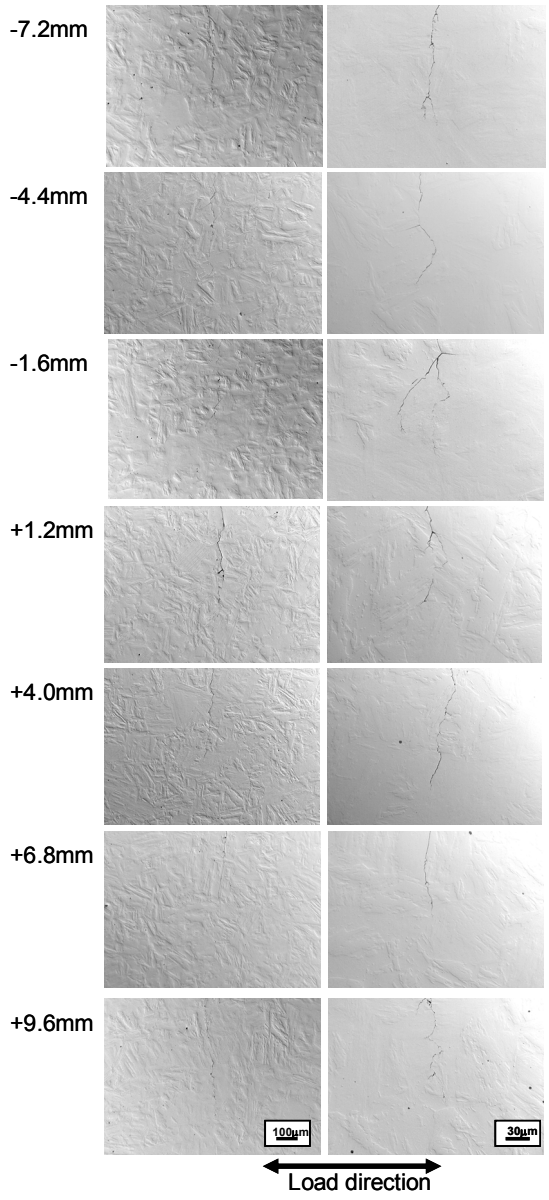

Fig. 6. Precrack features from the different thickness region of 1TCT specimen.

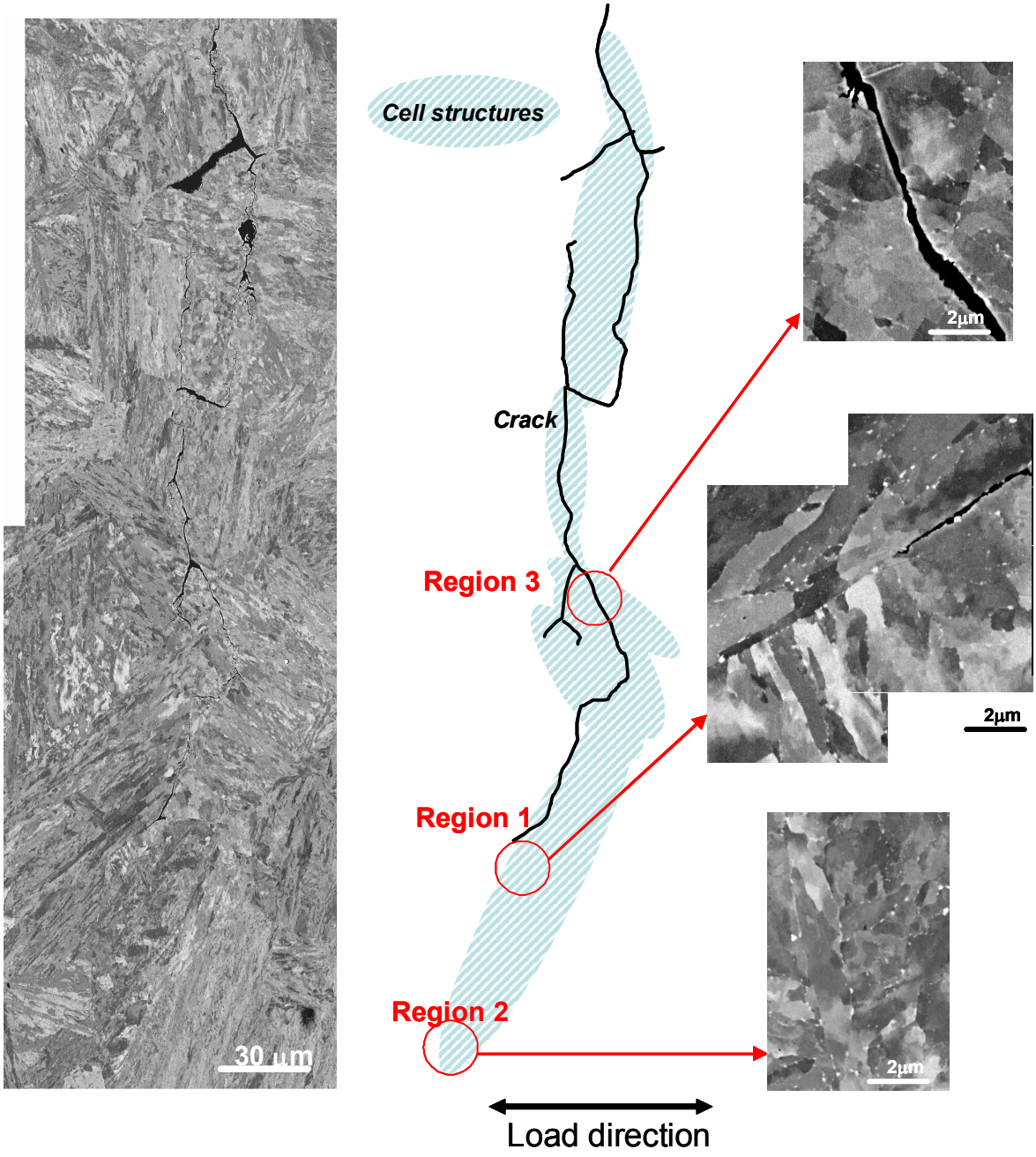

Fig. 7. The BSE images around the pre-crack tip with schematic drawing and magnified images of the microstructure. The specimen was prepared from the section 1.2mm from the middle plane of the 1TCT specimen thickness.

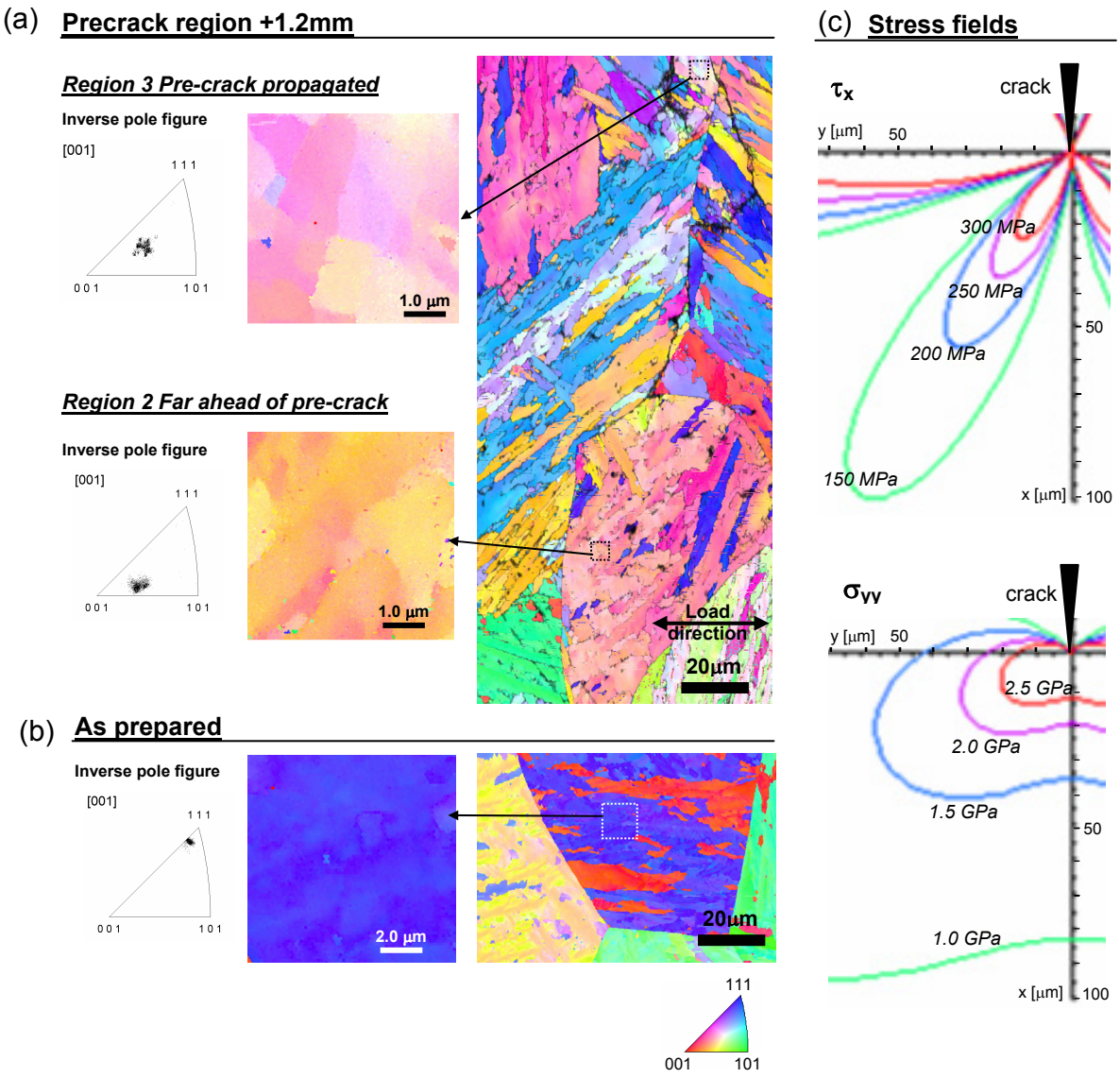

Fig. 8. The OIM images around the precrack tip (a), compared with the as-prepared images (b). Orientation distribution became dispersive as the color variation per unit area increased. Magnified OIM images obtained from precrack propagated region (region3) and ahead of precrack (region2) and as-prepared specimen are also shown with inverse pole figures (IPF) obtained from each magnified area. The calculated stress fields (τ_{xy}, σ_{yy}) for Mode I in a linear elastic, isotropic material is shown in (c) for comparison. No plastic deformation was taken into account. Stress intensity level that was used in the calculation (K = 22.8 MPa$\sqrt{}$m) is the condition at the end of precracking (1TCT, a/W=0.525, P=1270 kg).

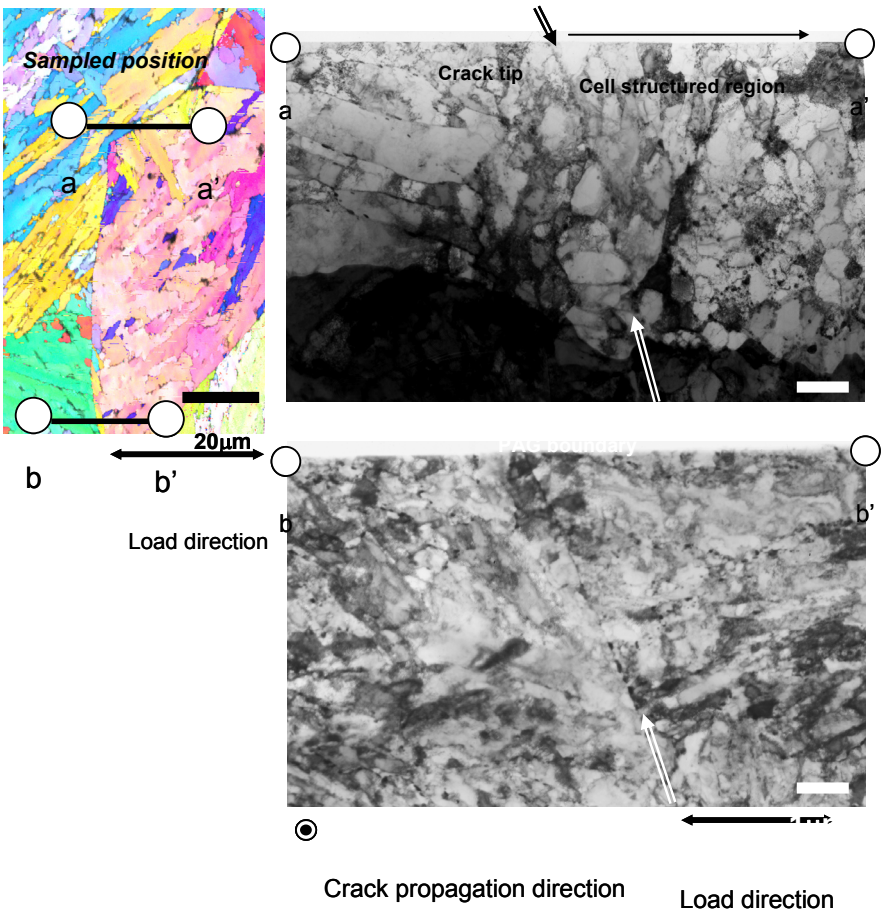

Fig. 9. TEM images of the microstructure at the fatigue precrack tip (a - a'), and the precrack front (b - b').

TEM specimens were sampled from the crack tip region (region 1 in Fig.8) and the region ahead of the crack tip (region 2 in Fig.8) by FIB processor (Fig.9).The specimen sampled from region 2 buckled while thinning, and this indicated the presence of residual stress on this region. Both TEM images confirm the presence of cell structure in each region. It is also worth noting the difference of microstructure between the right side and left side of the PAG boundary in region 1, i.e., the cell structure is distinctive in the right side of the PAG, but the lath structure is still observed on the left side of the PAG, and the crack is propagating along this PAG boundary in the middle of the image.

Fatigue fracture process on F82H-IEA was reported previously [3,4]; i.e., (1) the cell structure is induced in early cycle and then (2) a new cell structure is developed along the PAG boundary, and (3) the cracks propagate thorough the new cell structure cell along the PAG boundary.

Based on this, the fatigue pre-crack development could be interpreted as follows (Fig. 10):

(1) Fatigue-induced cell structure was developed in front of the notch, and the fatigue crack was formed.
(2) While the stress level was high, the fatigue cell structure was induced in front of the crack in a relatively wide range, and the crack continuously propagated in a straight line (Fig.10(a)).
(3) As the stress level was lowered as the crack developed, the fatigue cell structure began to form preferentially in the direction that the maximum shear stress was applied. (Fig.10(b))
(4) The crack began to propagate abruptly, i.e., the crack stopped until the cell structure was developed anisotropically ahead of the crack, then propagated through the weakest region in the developed cell structure, which is usually the PAG boundary. (Fig.10(c))
(5) Processes (3) and (4) were repeated until the fatigue loading was stopped.

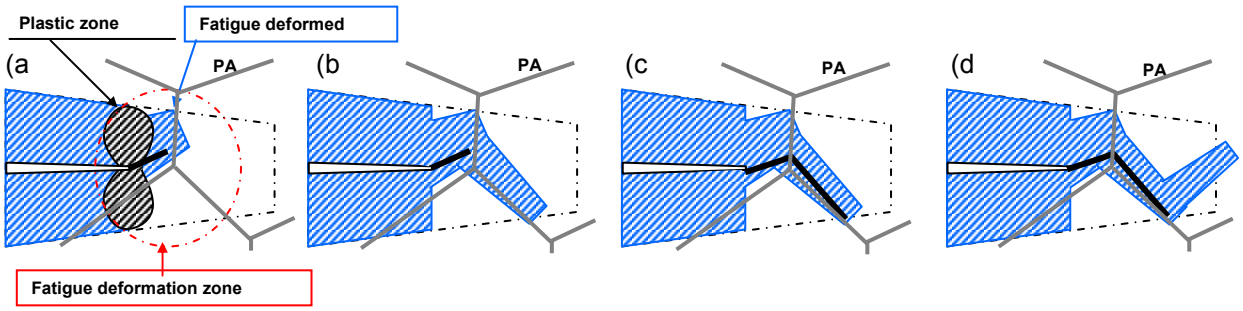

Fig. 10. Schematic drawing of precrack microstructure propagation.

This indicates that if the fatigue precracking process was stopped before the crack propagated thorough the cell structure developed in front of the precrack, then the specimen could have a locally weak (soft) region ahead of the crack (Fig.10(d)). The precrack branching is one of the cases, as the maximum shear stress is generally applied to the two directions ahead of the precrack (Fig.7(c)). This anisotropic cell structure formation in the maximum shear stress direction may cause the crack initiation without large-scale deformation, which was expected at those test temperatures that this low-energy fracture was observed. That is, the crack initiated in this cell structure region ahead of the precrack before the highest constraint region reached the critical condition to initiate the crack.

Although the cell structure could affect fracture toughness, the impact of the fatigue cell structure on the post-irradiation test might be small, because the local cell structure may be eliminated during irradiation. Further, most PIE will be performed at the temperature region where the specimen shows brittle fracture, as it was limited by the small specimen size. The irradiation microstructure development of fatigue cell structure should be examined to make sure of its effect.

The probability of the precrack branching and the scale of the cell structure anisotropically spread out ahead of the precrack tip could have a relation to the size of the PAG. F82H-IEA has large PAGs (~120μm), and consequently the packet, the area with similar crystal orientation, is generally large. This might allow the anisotropic cell structure development ahead of the precrack to occur over a longer distance, as shown in Fig.7 and Fig.8. Precrack branching could happen when the cell structure was equivalently developed enough for the crack propagation into the two directions where the maximum stress was loaded. On the other hand, if the PAG size is small, then the crystal orientation becomes less anisotropic even in a small range of area, and this would decrease the range of anisotropic cell structure development and the possibility of precrack branching. This implies the possibility that the low-toughness fracture value below the lower tolerance bound of the MC would not happen if the PAG size is small. Further fracture toughness experiments in view of this possibility will be conducted in near future.

SUMMARY AND CONCLUSIONS

The microstructure around the fatigue pre-crack of a 1TCT fracture toughness specimen of F82H-IEA steel was analyzed to investigate the cause of the low-energy fracture values that fell out of the tolerance band of the master curve. The pre-cracked 1TCT specimen was sliced through the thickness for various microstructural analyses. The fracture surfaces of tested 1TCT specimens were also observed. The following summarizes the observations and conclusions:

(1) The fracture surfaces of low-energy fractured specimen showed the presence of one apparent fracture initiation point, which fits very well with premises of the MC methodology, and it also showed the possibility that the fracture may start from the terminal of a precrack front which shows intergranular fracture or branched fracture.
(2) The precracks initially propagated straight through the PAG, then started to follow the PAG boundary, and at the terminal of the precrack, it branched into 2 or 3 cracks.

(3) The microstructure ahead of the precrack and around the precrack had turned into cell structure, which is the typical microstructure of fatigue-loaded ferritic/martensitic steels.
(4) It was suggested that the anisotropic cell structure formation ahead of precracks in the direction that the maximum shear stress was applied could cause the low-toughness fracture with values below the lower tolerance bound of the MC.
(5) The possibility that the large PAGs of F82H-IEA provoke the low toughness fracture was indicated.

Acknowledgements

All SEM and OIM analysis were performed at SHaRE Collaboration Research Center at Oak Ridge National Laboratory. This research was sponsored by the Japan Atomic Energy Research Institute and the Office of Fusion Energy Sciences, US Department of Energy under contract DE-AC05-96OR22464 with UT-Battelle.

References

[1] K. Shiba, M. Suzuki, and A. Hishinuma, J. Nucl. Mater. 233-237 (1996) 30.
[2] M. Sokolov et al., to be reported at next semiannual progress report (DOE/ER-0313/36, June 2004).
[3] T. Hirose, H. Tanigawa, M. Ando, and A. Kohyama, Mater. Trans. 43 (2001) 389.
[4] H. Tanigawa, T. Hirose, M. Ando, S. Jitsukawa, Y. Katoh, and A. Kohyama, J. Nucl. Mater. 307-311 (2002) 293.
[5] K. Shiba, R. L. Klueh, Y. Miwa, N. Igawa, and J. P. Robertson, DOE/ER-0313/ 28 (2000) 131.
[6] N. Hashimoto, H. Tanigawa, M. Ando, and M. A. Sokolov, in this progress report.
[7] D. S. Gelles and M. A. Sokolov, DOE/ER-0313/34 (2003) 49.

TEM OBSERVATION AROUND CRACK IN FATIGUE-PRECRACKED 1TCT FRACTURE TOUGHNESS SPECIMEN OF F82H-IEA—N. Hashimoto (Oak Ridge National Laboratory), H. Tanigawa (Japan Atomic Energy Research Institute), M. Ando (JAERI), and M. A. Sokolov (ORNL)

OBJECTIVE

In order to investigate microstructural evolution with crack propagation, transmission electron microscopy (TEM) specimens were prepared from a fatigue-precracked specimen of IEA modified F82H (F82H-IEA) specimens.

SUMMARY

Transmission electron microscopy (TEM) specimens of F82H-IEA were prepared from a middle section of the fatigue-precracked 1TCT specimens and fabricated by using the Focused Ion Beam (FIB) technique in order to investigate microstructural evolution with crack propagation. The TEM specimens, taken from the area around crack, the area of crack tip, and the area in ahead of the crack tip, indicated the presence of cell structure that was generally seen in fatigue-loaded ferritic/martensitic steels. It is possible that this cell structure affects the fracture toughness, however, the effect would be negligible for irradiated specimen due to elimination of the cell structure during irradiation.

PROGRESS AND STATUS

Introduction

To validate the potential of reduced activation ferritic/martensitic steel (RAF) as a structural material for fusion power plants, the strength with adequate toughness after irradiation must be guaranteed. As fusion materials, the RAFs have some advantages, such as superior swelling resistance and excellent thermal properties. However, one of serious disadvantage of RAF is its high ductile-brittle transition temperature (DBTT) after irra
diation.
The DBTT of RAFs could be determined by the master curve (MC) method [1], which categorize in terns of fracture toughness reference temperature. Most of RAF's fracture toughness values tend to be on the MC, however, F82H-IEA has some data points off the MC. One of possible reason of this deviation could be the effect of fatigue precracking.

In this experiment, in order to investigate microstructure around precrack and the contributions of fatigue precracking to DBTT, transmission electron microscopy (TEM) specimens of F82H-IEA were taken from a middle section of the fatigue-precracked 1TCT specimens and fabricated by using the Focused Ion Beam (FIB) processor.

Experimental

The fatigue specimens of F82H-IEA used for this experiment were made by JAERI. The 1TCT specimens were made from 25mm thick F82H-IEA heat plate (Fe-7.5Cr-2W-0.15V-0.02Ta-0.1C, in wt.%), followed by precracking as defined in ASTM standered E1921. TEM specimens were prepared from a middle section of the fatigue-precracked 1TCT specimens and fabricated by using the FIB processor (Hitach FB-2000A) with a microsampling system at Japan Atomic Energy Research Institute (JAERI). There are some advantages of FIB fabrication compared to electro-polishing. First, the optimum sample can be taken from a proper area of bulk specimen. Second, reduction of magnetic field is possible due to reduction of volume by fabrication. The FIB fabricated specimens could be handled just as nonmagnetic materials. The main disadvantage of FIB is that fabrication tends to produce some damage in specimens. In this case, the Low Energy Gun Milling (LEG) mode is effective to remove damage by fabrication, and actually LEG was carried out at JAERI for all specimens after fabrication.

Results and Discussion

Fig. 1 shows the SEM image of crack propagation in a middle section of the fatigue-precracked 1TCT specimen. The precrack propagated downward in the figure. The crack seemed to propagate through prior austenitic grain (PAG) first, and then, propagate along with (PAG) boundaries at the end. Fig. 1 also indicates the cell structure with arrows that formed along and around the crack during the fatigue precracking.

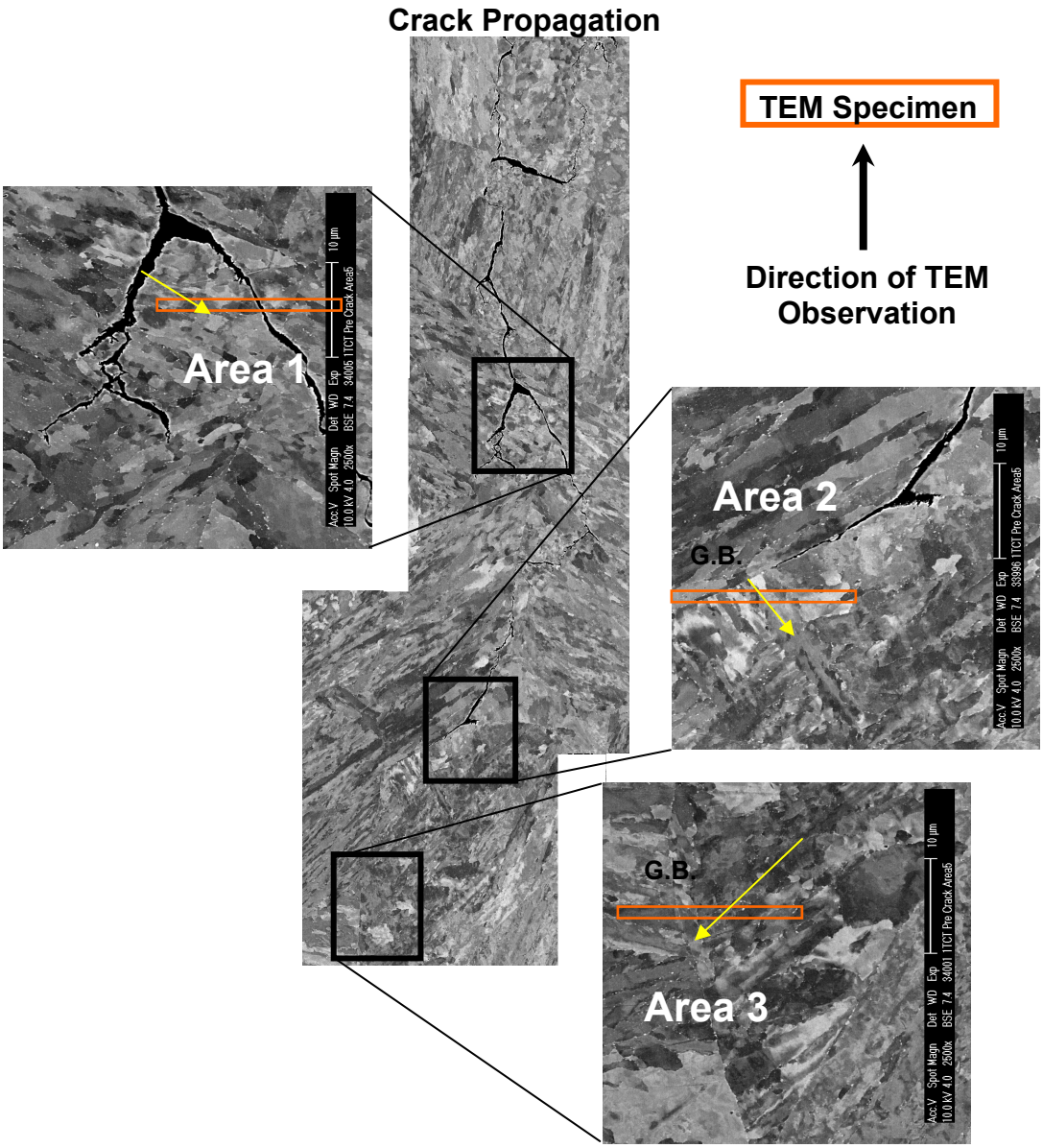

Fig. 1. SEM image of crack propagation in the fatigue-precracked 1TCT specimen. TEM specimens were prepared from three areas as highlighted in this figure. Arrows indicate directions of cell structure development.

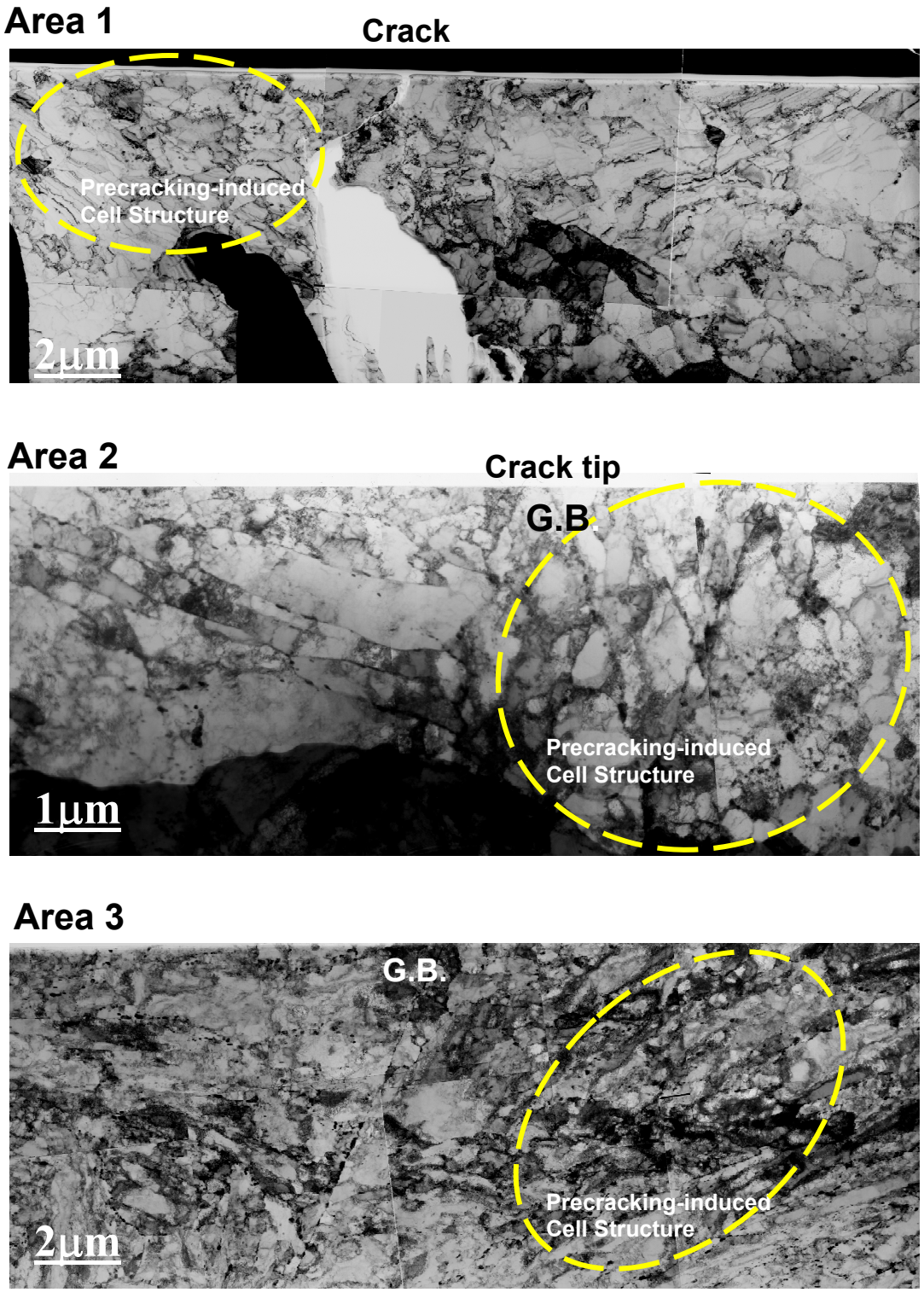

Fig. 2. TEM images sampled from the fatigue-precracked 1TCT specimen. Area 1 includes the crack with cell structure, area 2 taken at the crack tip shows cell structure along with a PAG boundary, and area 3 ahead of the crack tip also shows cell structure coming from the crack tip.

Three of TEM specimens were sampled from the fatigue-precracked 1TCT specimen (Fig. 1); the area 1 which includes the crack, and the area 2 taken at the crack tip with a PAG boundary, and finally the area 3 in ahead of the crack tip with a PAG boundary, as shown in Fig. 2.

Each TEM image showed the presence of cell structure along and around crack. Cell structure formed during fatigue precracking is very different from microstructure of as-prepared specimen. The left side of the crack in the Area 1 indicated lengthwise narrow band of cell structure that grew perpendicularly from the branch of the crack (see arrows in Fig. 1). Also, the right side of the PAG boundary in the Area 2 showed lengthwise narrow band of cell structure from the PAG boundary in front of the crack tip. The cell structure of the right side in the area 3 seemed to be grown from the crack tip into the PAG boundary. It should be noted that the specimen of the area 3 was distorted during fabrication process, indicating the presence of residual stress around this area.

From these results and the information concerning about development of cell structure during fatigue fracture process [2, 3], it could be conformed that stress due to fatigue precracking developed fatigue-induced cell structure and crack. The direction of the development would be a direction the maximum shear stress was applied. The crack would propagate with looking for the best direction for development, such as PAG boundaries and fatigue-induced cell structure in front of the crack tip, till the end of fatigue loading.

The formation of fatigue-induced cell structure might have somewhat of effect on fracture toughness data points off the MC, however, the effect would be negligible for irradiated specimen due to elimination of the cell structure during irradiation.

The possible explanation for the data points off the MC can be found in this progress report [4].

Acknowledgements

This research was sponsored by the Japan Atomic Energy Research Institute and the Office of Fusion Energy Sciences, US Department Energy under contract No DE-AC05-96OR22464 with UT-Battelle, LLC.

References

[1] Sokolov et al., to be published in the next report.
[2] T. Hirose, H. Tanigawa, M. Ando, and A. Kohyama, Mater. Trans. 43 (2001) 389.
[3] H. Tanigawa, T. Hirose, M. Ando, S. Jitsukawa, Y. Katoh, and A. Kohyama, J. Nucl. Mater. 307-311 (2002) 293.
[4] H. Tanigawa et al., in this report.

IRRADIATION CREEP AND SWELLING FROM 400°C TO 600°C OF THE OXIDE DISPERSION STRENGTHENED FERRITIC ALLOY MA957—M. B. Toloczko, D. S. Gelles, F. A. Garner, and R. J. Kurtz (Pacific Northwest National Laboratory),* and K. Abe (Dept. of Quantum Sci. and Energy Eng., Tohoku University, Sendai, Japan)

Extended abstract of a paper submitted to the Journal of Nuclear Materials as part of the proceedings of the 11th International Conference on Fusion Reactor Materials, Kyoto, Japan, December 7-12, 2003.

EXTENDED ABSTRACT

Recently, there has been a growing interest in the use of oxide dispersion strengthened (ODS) ferritic steels for fusion reactor applications. As part of an extensive study performed at PNNL on the ODS steel MA957 [1], irradiation creep tests were performed on pressurized tubes made from MA957 by two different methods. The tubes were made either by gun drilling alone or by a combination of rod drawing and gun drilling. The different fabrication methods were explored because ODS steels have been difficult to form. The pressurized tubes were irradiated in the Fast Flux Test Facility (FFTF) to doses ranging from 40 dpa to 110 dpa at temperatures ranging from 400°C to 600°C. The effective stresses resulting from the pressurization of the tubes ranged from 0 MPa to 175 MPa.

Swelling was estimated from diameter changes of the stress free tubes, and none of the stress-free tubes exhibited any evidence of swelling by this measurement. The observed irradiation creep behavior as a function of dose was similar to previously observed irradiation creep behavior in conventional ferritic-martensitic steels except that at 400°C, there appears to be a slight reduction in irradiation creep rate of MA957 after 80 dpa. The creep behavior below 80 dpa may perhaps represent a creep transient, or the reduction in creep rate above 80 dpa may be due in-part to the method used to manufacture this steel. In comparing the creep behavior of the gun-drilled tubing to the drawn tubing, the creep rates and transients were similar in magnitude, but the gun-drilled tubing was more prone to failure. Most all the gun drilled tubes failed before the last irradiation, but nearly all the drawn tubes survived all the irradiation cycles. An example of this can be seen in Figure 1.

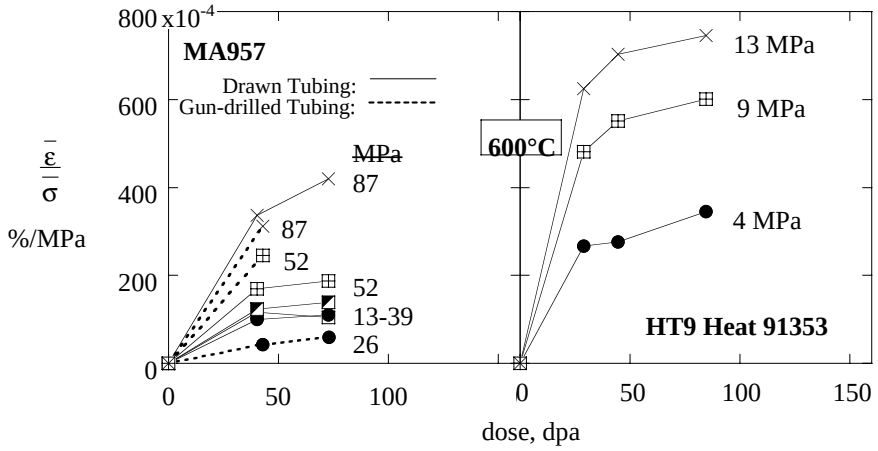

Figure 1. Irradiation creep behavior of MA957 and HT9 at 600°C showing that the drawn MA957 tubes failed less frequently than the gun-drilled MA957 tubes and also showing at this temperature in an irradiation environment that transient creep strain in MA957 is much lower than that for HT9.

*Pacific Northwest National Laboratory (PNNL) is operated for the U.S. Department of Energy by Battelle Memorial Institute under contract DE-AC06-76RLO-1830.

The physical mechanisms which contribute to creep in an irradiation environment can be considered to be due to both irradiation and thermal effects on point defect and extended defect populations and dynamics. The progression of irradiation creep as a function of time is similar to that of thermal creep; there is a creep transient which appears to occur within the first 40 dpa, and then this is followed by steady state creep. The similarity is likely due to the fact that in the temperature range studied here, creep in a thermal environment is a large fraction of the amount of creep which occurs in an irradiation environment [2]. For temperatures from 400°C to 550°C, the observed steady state irradiation creep rates of MA957 were similar to that of HT9. At 600°C, the steady state creep rate of MA957 was unchanged, but the value for HT9 had doubled. The creep rates are shown in Figure 2. At 600°C, it is likely that thermal creep is beginning to strongly dominate the total creep signal, and it is known that ODS steels are more resistant to thermal creep than conventional ferritic-martensitic steels at this temperature [3]. Transient creep strain contributed increasingly to the total irradiation creep strain as the temperature increased from 400°C to 600°C for both MA957 and HT9, and by about 75 dpa at 600°C, the transient creep strain contributed to about one-half the total creep strain in MA957. This can be seen in Figure 1. The total creep strain in MA957 after 40 dpa at 600°C is due almost entirely to transient creep and is about 0.25% strain at 26 MPa, and about 0.9% strain at 52 MPa. The transient values for MA957 were much smaller than that for HT9 as can also be seen in Figure 1.

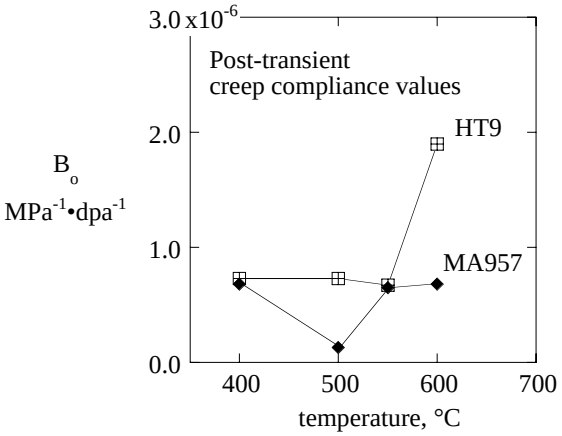

Figure 2. Creep compliance of MA957 (and HT9) as a function of temperature.

MA957 offers no clear advantage over HT9 at temperatures below 600°C. However, from the experimental results, it is clear that MA957 has better creep resistance than HT9 in an irradiation environment for temperatures of 600°C and probably higher. At 600°C, the large contribution of transient creep to the total amount of creep in MA957 is noteworthy, and for doses up to 40 dpa, it makes up essentially all of the total creep strain. The total creep strains at an effective stress of about 52 MPa after 40 dpa at about 600°C are about 0.9%. If better irradiation creep resistance is required, it appears that the next step in improving the irradiation creep resistance of MA957 at 600°C (and probably above) should be aimed at understanding and controlling the creep transient. The reduced failure rate of the drawn tubing also suggests that some effort should be aimed towards defining the processing conditions which provide the best failure resistance.

References

[1] M. L. Hamilton, et al., Fabrication Technological Development of the Oxide Dispersion Strengthened Alloy MA957 for Fast Reactor Applications, Pacific Northwest National Laboratory, PNNL-13168 (February 2000).

[2] M. B. Toloczko, et al., Comparison of Thermal Creep and Irradiation Creep of HT9 Pressurized Tubes at Test Temperatures from ~490°C to 605°C, ASTM STP 1405 (2002) 557-567.

[3] D. K. Mukhopadhyay, F. H. Froes, D. S. Gelles, Development of oxide dispersion strengthened ferritic steels for fusion, J. Nucl. Mater. 258-263 (1998) 1209-1215.

IRRADIATION EFFECTS ON TENSILE PROPERTIES OF HIGH-CHROMIUM FERRITIC/MARTENSITIC STEELS—R. L. Klueh (Oak Ridge National Laboratory)

OBJECTIVE

The objective of this work is to develop an understanding of the effect of irradiation on fracture behavior of reduced-activation ferritic/martensitic steels of interest for fusion applications and to use that knowledge to develop steels with improved properties.

SUMMARY

Tensile specimens of four ferritic/martensitic steels were irradiated at 390-395ºC in the Experimental Breeder Reactor (EBR-II) to 32-33 dpa. The steels were the ORNL reduced-activation 9Cr-2WVTa and that steel containing 2% Ni (9Cr-2WVTa-2Ni), modified 9Cr-1Mo, and Sandvik HT9 (12Cr-1MoVW). The 9Cr-2WVTa and 9Cr-2WVTa-Ni were irradiated after normalizing and tempering some specimens 1 hr at 700ºC and some specimens 1 h at 750ºC; the 9Cr-1MoVNb and 12Cr-1MoVW were tempered 1 h at 760ºC. Based on the change in tensile properties, the results demonstrated the superiority of the 9Cr-2WVTa steel over the two commercial steels. Charpy properties of the 9Cr-2WVTa-2Ni steel were similar to those of the 9Cr-2WVTa steel, indicating no adverse effect of the nickel on the properties after irradiation in a fast reactor around 400ºC.

PROGRESS AND STATUS

Introduction

The 9Cr reduced-activation ferritic/martensitic steels are candidates for applications as first wall and blanket structural materials for future fusion reactors. Displacement damage by neutron irradiation of these types of steel below 425-450ºC hardens the steel lattice, causing an increase in strength and a decrease in toughness. The effect on impact toughness is measured in a Charpy test as an increase in the ductile-brittle transition temperature (DBTT) and a decrease in the upper-shelf energy (USE).

The possible effect of helium on hardening and embrittlement is important because large amounts of transmutation helium will form in the ferritic/martensitic steel first wall of a fusion reactor. Nickel-doped 9 and 12 Cr steels have been irradiated in a mixed-spectrum reactor such as the High Flux Isotope Reactor (HFIR) to study the effect of helium on fracture [1]. Helium (an alpha-particle) is formed in a mixed-spectrum reactor by a two-step transmutation reaction between ^{58}Ni and thermal neutrons in the mixed-neutron spectrum. This technique allows for the simultaneous production of displacement damage and helium in the steel matrix, thus simulating what will happen in a first wall. Results from such irradiation experiments at 400ºC have been interpreted to indicate an effect of helium on embrittlement. This conclusion was based on the comparison of the steels with and without nickel and on the differences between the behavior of the nickel-doped steels in a mixed-spectrum reactor, where considerable helium forms, and in a fast reactor, where little helium forms [1].

More-recent irradiation experiments of nicked-doped 9Cr reduced-activation steels have indicated that the nickel-doped steels hardened more than steels without nickel [2,3]. A 9Cr-2W steel with and without 1% Ni was irradiated in the Japanese Materials Test Reactor (JMTR) to 0.15 dpa at 170ºC, and an increase in the room temperature yield stress of up to 350 MPa was observed for the nickel-containing steel, compared to a 120 MPa increase for the steel without nickel. However, no difference in the strength increases was observed for steels irradiated at 220ºC [2]. Irradiation of the steels to 2.2 and 3.8 dpa at 270 and 348ºC, respectively, in the Advanced Test Reactor (ATR) indicated that the nickel-containing steel hardened about 20% more than the steel without nickel at 270ºC, but strengths were similar after irradiation at 348ºC [3]. Also, a larger shift in DBTT occurred for the nickel-containing steel than the one without nickel when irradiated at 270ºC, but not after irradiation at 348ºC. TEM analysis indicated that nickel refined the size of the irradiation-produced defect clusters, which were more numerous in the nickel-containing steel [3].

These results indicate that the nickel-doping simulation technique should be used below about 300ºC with caution, if at all. The results using nickel doping that most strongly indicated that helium caused an increase in the DBTT above that caused by displacement damage alone were on steels irradiated in HFIR to high fluence at 400ºC [1]. Tensile tests of specimens irradiated under similar conditions gave no indication of hardening due to helium (or nickel) [1]. Also, when the same steels were irradiated at similar conditions in the Fast Flux Test Facility (FFTF), no difference was observed in the embrittlement of the nickel-doped and undoped specimens [4]. Transmission electron microscopy (TEM) studies of nickel-doped steels irradiated in HFIR and FFTF showed that a high density of M_6C formed in the nickel-doped steel but not in the undoped steel [5]. Since the shift in DBTT in HFIR, where helium forms, was larger than in FFTF, where little helium forms, the results were taken to mean that helium caused the shift [1].

In this report, tensile properties are reported for the reduced-activation steel ORNL 9Cr-2WVTa and this steel containing 2% Ni (9Cr-2WVTa-2Ni) after irradiation in the Experimental Breeder Reactor (EBR-II). The commercial non-reduced-activation steels modified 9Cr-1Mo (9Cr-1MoVNb) and Sandvik HT9 (12Cr-1MoVW) steels were also irradiated and tested. In a previous report, the Charpy properties of these same steels irradiated in EBR-II were reported [6].

Experimental Procedure

Compositions and designations of the steels used in this experiment are given in Table 1. In the original Oak Ridge National Laboratory (ORNL) alloy development program for development of reduced-activation steels [7], an 18-kg heat of the electroslag-remelted heat of the 9Cr-2WVTa steel was prepared by Combustion Engineering Inc, Chattanooga, TN. Material from that heat was used as the master alloy to prepare 450-g vacuum arc-melted button heats of 9Cr-2WVTa and 9Cr-2WVTa-2Ni steels. The 9Cr-2WVTa heat was a remelt of the master alloy so that the steels could be compared after similar processing.

Table 1. Chemical composition of the steels tested

Element[a]	9Cr-2WVTa	9Cr-2WVTa-2Ni	9Cr-1MoVNb[b]	12Cr-1MoVW[c]
C	0.098	0.098	0.092	0.20
Si	0.19	0.19	0.15	0.17
Mn	0.39	0.38	0.48	0.57
P	0.014	0.014	0.012	0.016
S	0.003	0.003	0.004	0.003
Cr	8.71	8.55	8.32	12.1
Mo	<0.01	<0.01	0.86	1.04
W	2.17	2.15	<0.01	0.61
Ni	0.02	2.01	0.09	0.51
V	0.23	0.23	0.20	0.29
Nb	<0.01	<0.01	0.06	<0.001
Ta	0.06	0.06		
N	0.016	0.016	0.054	0.027

[a]Balance iron
[b]Modified 9Cr-1Mo steel
[c]Sandvik HT9

The small heats were cast as 25.4 mm x12.7mm x 152 mm ingots, after which they were rolled to 6.4-mm plate and 0.76 mm sheet. The steels were normalized by austenitizing for 0.5 h at 1050ºC in a helium atmosphere and quickly cooled in flowing helium. Specimens were irradiated in two tempered conditions: 1 h at 700ºC and 1 h at 750ºC.

The modified 9Cr-1Mo (9Cr-1MoVNb) and Sandvik HT9 (12Cr-1MoVW) steels were from large commercial-size heats that have been irradiated previously and were included in this experiment as benchmarks for the reduced-activation steels.

Tensile specimens 44.5-mm long with a reduced gage section of 20.3 x 1.52 x 0.76 mm were machined from the 0.76-mm sheet with gage lengths parallel to the rolling direction. Specimens were heat treated after machining. Tests were conducted on irradiated and unirradiated specimens at 400ºC (near the irradiation temperature) in vacuum on a 44-kN Instron universal testing machine at a nominal strain rate of 4×10^{-4} s^{-1}.

Two tensile specimens of each heat and each heat-treated condition were irradiated in the COBRA experiment in EBR-II at temperatures of 390 to 395ºC. Fluence was determined from flux monitors in the irradiation canisters. There was some variation for different specimens, depending on their position in the canisters, but the individual sets of specimens for a given steel and heat treatment were kept together in the canisters and experienced the same irradiation conditions. Specimens were irradiated to 6.7×10^{26} to 6.9×10^{26} n/m^2 (E>0.1 MeV), which produced between 32 and 33 dpa. Helium concentrations were calculated to be between about 3 to 6 appm, depending on the dose and composition (the 6 dpa was for the steel containing 2% Ni).

Results

Irradiated specimens were tested at 400ºC, which is near the irradiation temperature (reported as 390-395ºC). Tensile data for the unirradiated and irradiated steels are summarized in Table 2.

First, the results for the reduced-activation 9Cr-2WVTa steel with and without nickel will be discussed to examine the effect of tempering and the effect of nickel. After that, results for the 9Cr-2WVTa steels will be compared with the commercial modified 9Cr-1Mo (9Cr-1MoVNb) and Sandvik HT9 (12Cr-1MoVW) steels.

Table 2. Tensile data for unirradiated and irradiated steels tested at 400ºC

Steel	Temper	Irradiation	Strength (MPa)		Elongation (%)	
			Yield	Ultimate	Uniform	Total
9Cr-2WVTa	700ºC	Unirradiated	701	758	2.7	9.7
9Cr-2WVTa	700ºC	390ºC/32.6dpa	698	732	1.2	6.5
9Cr-2WVTa	750ºC	Unirradiated	517	595	3.3	11.0
9Cr-2WVTa	750ºC	390ºC/32.6dpa	613	645	1.3	7.1
9Cr-2WVTa -2Ni	700ºC	Unirradiated	707	788	2.7	11.3
9Cr-2WVTa -2Ni	700ºC	390ºC/32.6dpa	649	690	3.4	10.0
9Cr-2WVTa -2Ni	750ºC	Unirradiated	674	787	2.7	8.3
9Cr-2WVTa -2Ni	750ºC	390ºC/32.6dpa	637	699	3.4	10.8
9Cr-1MoVNb	760ºC	Unirradiated	562	636	1.4	4.6
9Cr-1MoVNb	760ºC	395ºC/32.1dpa	612	626	0.7	5.3
12Cr-1MoVW	760ºC	Unirradiated	558	697	1.9	4.3
12Cr-1MoVW	760ºC	395ºC/32.1dpa	720	776	1.7	4.0

<u>9Cr2WVTa and 9Cr-2WVTa-2Ni Steels</u>

Figure 1 shows the yield stress and ultimate tensile stress for the 9Cr-2WVTa and 9Cr-2WVTa-2Ni steels given the different tempers before and after irradiation. There appears to be little effect of irradiation on strength for the 9Cr-2WVTa for the 700ºC temper and on the 9Cr-2WVTa-2Ni for both tempering conditions. There is a small amount of irradiation hardening for the 9Cr-2WVTa after the 750ºC temper.

The effect of irradiation on ductility (Fig. 2) appears to be greater for the 9Cr-2WVTa than the 9Cr-2WVTa-2Ni. For both tempering conditions, uniform elongation of the steel containing nickel increased after irradiation, while that for the steel without nickel decreased. Total elongation of the 9Cr-2WVTa also

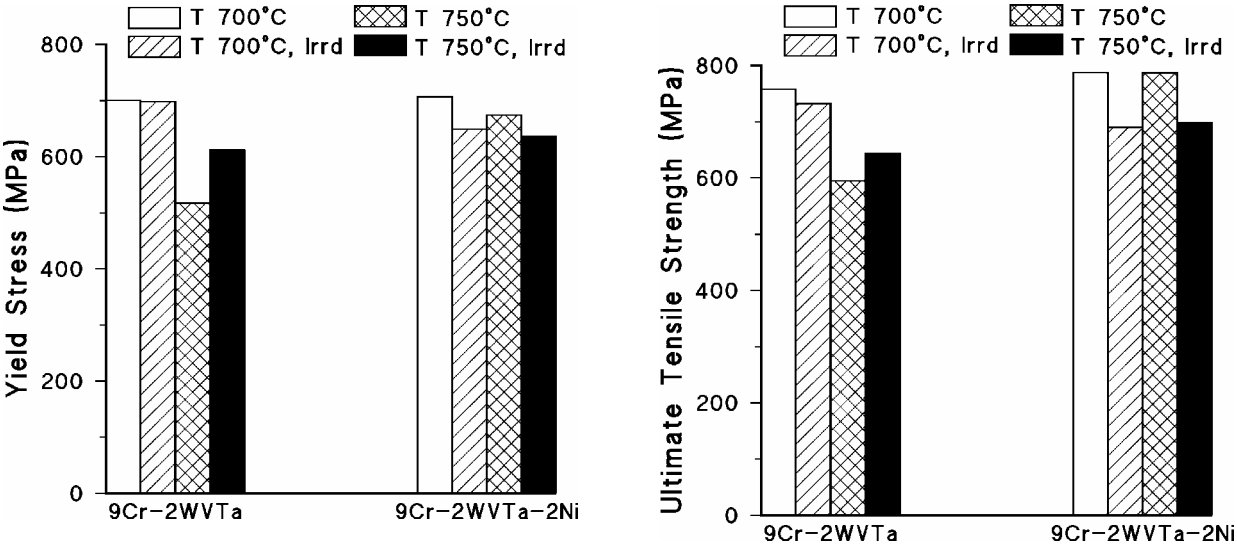

Fig. 1. The yield stress (left) and ultimate tensile strength (right) of 9Cr-2WVTa and 9Cr-2WVTa-2Ni steels for two different tempering conditions before and after irradiation in EBR-II.

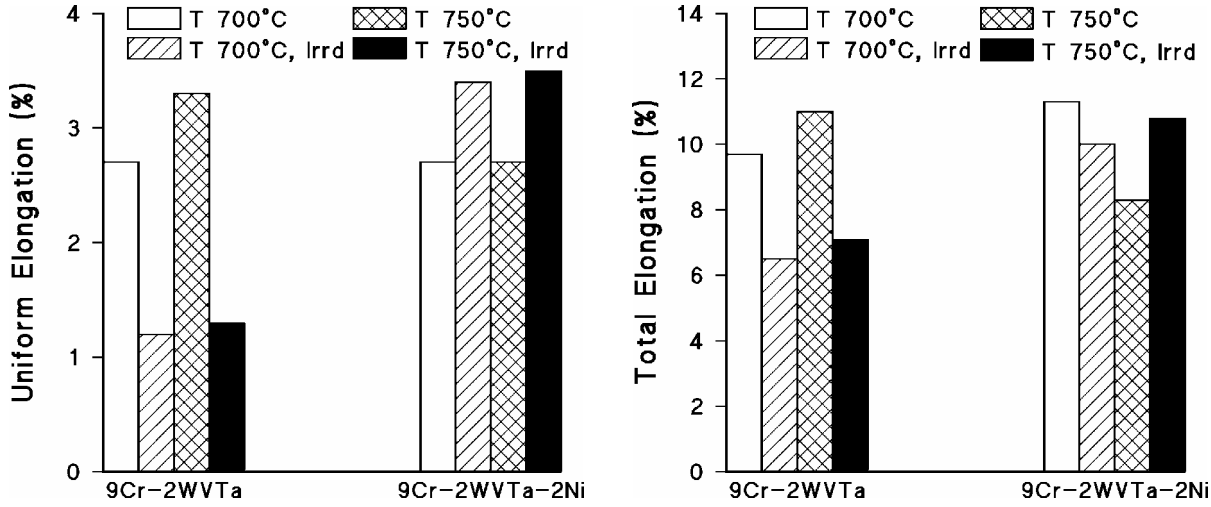

Fig. 2. The uniform elongation (left) and total elongation (right) of 9Cr-2WVTa and 9Cr-2WVTa-2Ni steels for two different tempering conditions before and after irradiation in EBR-II.

Decreased after irradiation for both tempering conditions, but the total elongation for the 9Cr-2WVTa-2Ni decreased slightly for the steel tempered at 700ºC and increased slightly for the steel tempered at 750ºC.

Comparison of Reduced-Activation and Commercial Steels

Tensile properties of the reduced-activation 9Cr-2WVTa and 9Cr-2WVTa-2Ni steels were compared with those of 9Cr-1MoVNb and 12Cr-1MoVW steels. Comparison was for 9Cr-2WVTa and 9Cr-2WVTa-2Ni steels tempered 1 h at 750ºC and the commercial steels both tempered 1 h at 760ºC, the conventional tempering temperature for 9Cr-1MoVNb. In both the unirradiated and irradiated conditions, there is relatively little difference in strength among the steels (Fig. 3) with somewhat more variation in the ductility (Fig. 4).

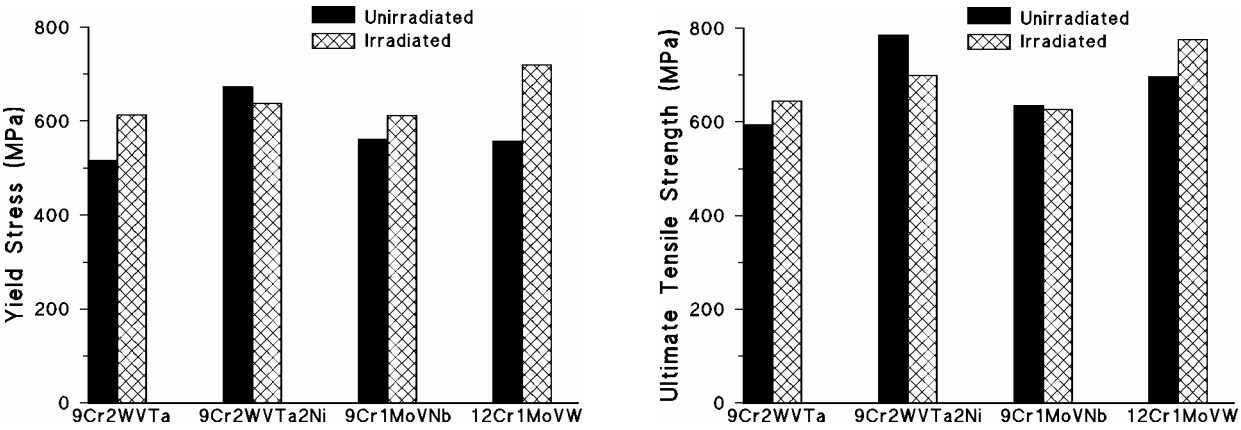

Fig. 3. Yield stress (left) and ultimate tensile strength (right) of unirradiated and irradiated 9Cr-2WVTa, 9Cr-2WVTa-Ni, modified 9Cr-1Mo (9Cr-1MoVNb), and Sandvik HT9 (12Cr-1MoVW) steels.

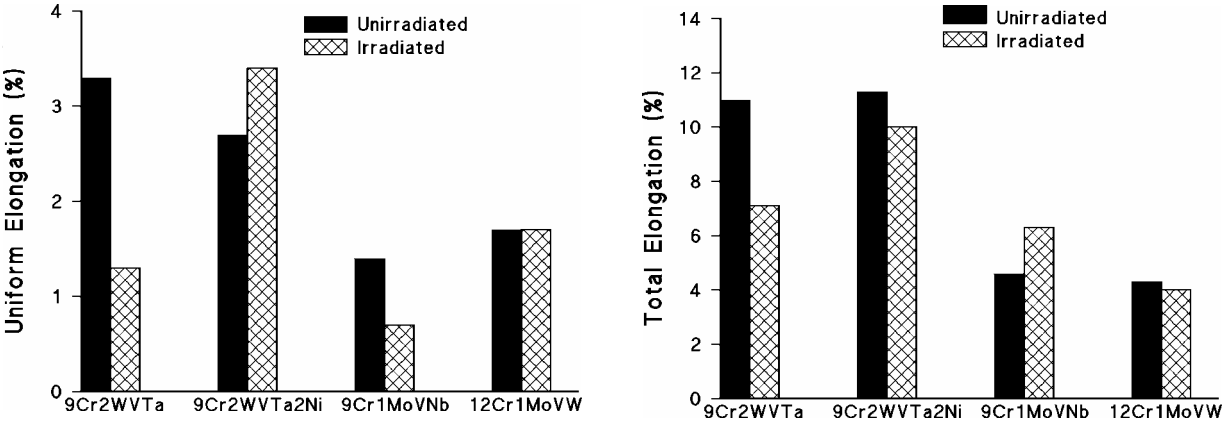

Fig. 4. Uniform (left) and total (right) elongation of unirradiated and irradiated 9Cr-2WVTa, 9Cr-2WVTa-Ni, modified 9Cr-1Mo (9Cr-1MoVNb), and Sandvik HT9 (12Cr-1MoVW) steels.

Both the yield stress and ultimate tensile strength indicate that relatively minor irradiation hardening occurred and, in the case of 9Cr-2WVTa-2Ni, softening occurred (Fig. 3). This is reflected in the ductility (Fig. 4), where the uniform elongation of the 9Cr-2WVTa-2Ni steel and the total elongation of the 9Cr-1MoVNb increased after irradiation. This steel had the highest uniform and total elongation of the four steels after irradiation. The greatest change in ductility was observed for the 9Cr-2WVTa steel, although after irradiation it had ductility as good as or better than that for 9Cr-1MoVNb and 12Cr-1MoVW. The latter steel showed little change in uniform and total elongation after irradiation.

Discussion

It is well known that one effect of adding nickel, an austenite stabilizing element, to a ferritic steel is a reduction in the Ac_1 temperature, the temperature where ferrite begins to transform to austenite when a steel is heated. If the tempering temperature is above the Ac_1, then any austenite formed during tempering will transform to martensite, and such a "normalized-and-tempered" steel will contain untempered martensite. For the commercial steels in the present investigation, it is known that nickel lowers the Ac_1 below the 750ºC tempering temperature [8], and because of the similarity of the commercial and reduced-activation steels it is assumed the Ac_1 for those steels is also below 750ºC.

This is verified because the effect of the presence of untempered martensite can be seen in the unirradiated strength of the 9Cr-2WVTa-Ni by comparing the strengths of this steel after the 700 and 750ºC tempers with the strengths of the steel without nickel (Fig. 1). The unirradiated strengths of the 9Cr-2WVTa-2Ni steel after the 700 and 750ºC tempers are similar, compared a large reduction for the 9Cr-2WVTa tempered a 750ºC relative to that tempered at 700ºC.

As discussed above, the primary reason for irradiating 9Cr-2WVTa-2Ni is that reactions between ^{58}Ni and the thermal neutrons in a mixed-spectrum produce helium, thus providing a method to study helium effects. Irradiation of the steel in a fast reactor, where very little helium forms, provides a control for helium-effects studies. Generally, those studies are made on the steels with and without nickel tempered below the Ac_1 to similar strengths [1]. In the present experiment, the 750ºC temper was used because it was decided to investigate the effect of small amounts of untempered martensite.

The results for the 9Cr-2WVTa-2Ni steel provided the most interesting observations. First, before irradiation, the increased strength of the 9Cr-2WVTa-2Ni after the 750ºC temper is not accompanied by a greatly reduced ductility relative to the 9Cr-2WVTa steel (Fig. 2). Second, a most unusual observation after irradiation was that there was essentially no hardening of the 9Cr-2WVTa tempered at 700ºC and no hardening—actually softening—of the 9Cr-2WVTa-2Ni steel. Despite the relatively small irradiation hardening, the uniform and total elongations of the 9Cr-2WVTa steel decreased, whereas the uniform elongation of the 9Cr-2WVTa-2Ni, the steel containing untempered martensite, actually increased for both tempering conditions, as did the total elongation for the steel tempered at 750ºC. A slight decrease in total elongation was observed for the 9Cr-2WVTa-2Ni steel tempered at 700ºC. The ductility of the nickel-containing steel after irradiation was superior to that of the steel without nickel for all conditions.

This unexpected behavior of the 9Cr-2WVTa-2Ni is also indicated when the 750ºC-tempered steels are compared with 9Cr-1MoVNb and 12Cr-1MoVW steels tempered at 760ºC, where the 9Cr-2WVTa-2Ni was the only steel not hardened, although none of the other three steels hardened significantly (Fig. 3). Likewise the 9Cr-2WVTa-2Ni steel had the best ductility after irradiation. The results for the comparison of the different steels demonstrated the excellent behavior of the reduced-activation 9Cr-2WVTa steel relative to the two commercial steels.

The relatively minor hardening—and softening—was unexpected from previous experiments where these steels were irradiated at ≈400ºC [9-11]. A possible explanation may be found in results from previous studies that found a peak in irradiation hardening with increasing fluence. This effect was observed for reduced-activation steels [12] and for commercial-type Cr-Mo steels [13,14]. The effect for the reduced-activation steels is shown in Fig. 5 [12].

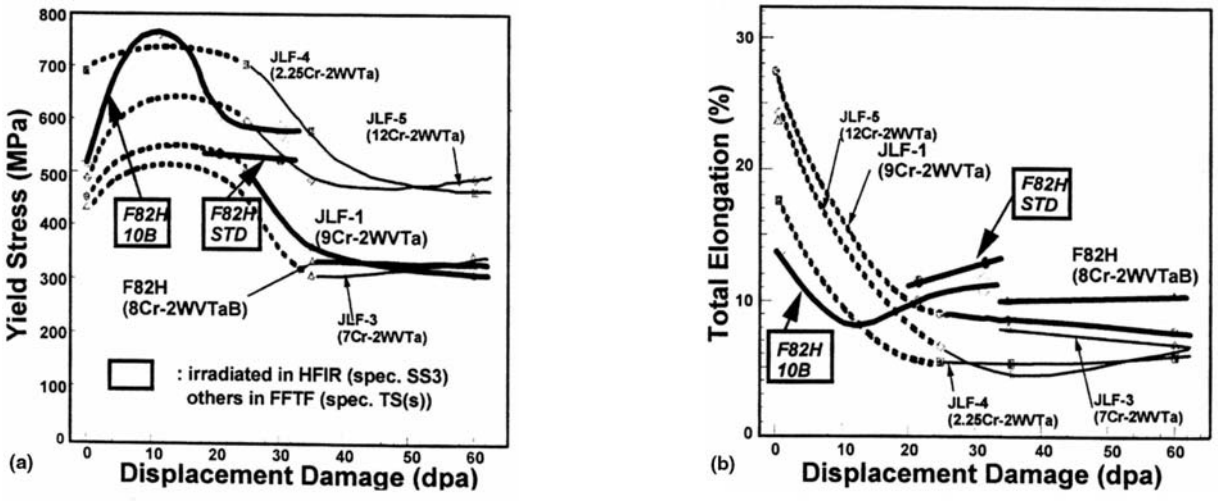

Fig. 5. The (a) yield strength and (b) total elongation as a function of irradiation doses for several reduced-activation steels [11].

The results in Fig. 5 indicate that that the reduction in irradiation hardening with increasing dose begins to approach the unirradiated value near 30 dpa for some of the steels shown, which is similar to the dose of the specimens irradiated in the present experiment that showed this behavior. Total elongation appears to decrease to a plateau around 30 dpa. There is an indication of a minimum in total elongation for one of the steels in Fig 5, but the minimum is indicated somewhere beyond 30 dpa. A possible explanation for the peak in strength is that irradiation-enhanced recovery of the microstructure offsets the irradiation hardening [14].

The positive effect of nickel and the untempered martensite in the irradiated 9Cr-2WVTa-2Ni steel tempered at 750ºC could also be an effect of irradiation-enhanced recovery and, in particular, irradiation-enhanced recovery of the untempered martensite. In this case, the larger rate of recovery of the untempered martensite would partially or wholly offset the irradiation hardening. This assumes that the effect is not due to the nickel, which appears to be a reasonable assumption, since there is relatively little difference in the tensile properties between the 9Cr-2WVTa and 9Cr-2WVTa-2Ni tempered at 700ºC, either before or after irradiation. If this explanation is what is occurring, then one way to improve the irradiation resistance of the reduced-activation 9Cr-2WVTa steel would be to temper above the Ac_1. If the results of the present experiment are then reproduced, a higher-strength steel with less irradiation hardening would result. Since irradiation hardening causes embrittlement, as measured in an Charpy impact test, less embrittlement should occur. The Charpy results previously reported for these steels appear to support this conclusion.

References

[1] R. L. Klueh and D. J. Alexander, J. Nucl. Mater. 187 (1992) 60.
[2] R. Kasada, A. Kimura, H. Matsui, and M. Narui, J. Nucl. Mater. 258-263 (1998) 1199.
[3] A. Kimura, Report of IEA Workshop on Reduced-Activation Ferritic/Martensitic Steels, JAERI-Conf 2001-007, 348.
[4] W. R. Corwin, J. M. Vitek, and R. L. Klueh, J. Nucl Mater. 149 (1987) 312.
[5] P. J. Maziasz, R. L. Klueh, and J. M. Vitek, J. Nucl. Mater.141-143 (1986) 929.
[6] R. L. Klueh and M. A. Sokolov, Fusion Materials Semi-Annual Progress Report for Period Ending June 30, 2003, DOE/ER-0313/34, 63.
[7] R. L. Klueh and P. J. Maziasz, Met. Trans. 20A (1989) 373.
[8] R. L. Klueh, J. M. Vitek, and M. L. Grossbeck, Effects of Radiation on Materials, ASTM STP 782, (American Society for Testing and Materials, Philadelphia, 1982) 648.
[9] R. L. Klueh and J. M. Vitek, J. Nucl. Mater. 132 (1986) 27.
[10] R. L. Klueh and J. M. Vitek, J. Nucl. Mater. 137 (1986) 44.
[11] R. L. Klueh and D. J. Alexander, Effects of Radiation on Materials: 18th International Symposium, ASTM STP 1325 (American Society for Testing and Materials, Philadelphia, 1999) 911.
[12] A. Kohyama, A. Hishinuma, D. S. Gelles, R. L. Klueh, W. Dietz, and K. Ehrlich, J. Nucl. Mater. (1996) 138.
[13] R. L. Klueh and D. J. Alexander, J. Nucl. Mater. 258-253 (1998) 1269.
[14] V. S. Khabarov, A. M. Dvoriashin, and S. I. Porollo, J. Nucl. Mater. 233-237 (1996) 236.

AN ANALYSIS OF THE EFFECTS OF HELIUM ON FAST FRACTURE AND EMBRITTLEMENT OF ≈ 8Cr TEMPERED MARTENSITIC STEELS—G. R. Odette, T. Yamamoto, and H. Kishimoto (University of California, Santa Barbara)

OBJECTIVE

The objective of this research is to assess the effect of helium on fast fracture and irradiation embrittlement of ≈ 8Cr martensitic steels.

SUMMARY

We have assembled the available paired datasets on irradiation-induced increases in yield stress ($\Delta\sigma_y$) and transition temperature shifts (ΔT), in order to assess the potential role of high levels of helium on irradiation embrittlement of ≈8Cr martensitic steels. Both ΔT versus $\Delta\sigma_y$ scatter plots and variations in the hardening-shift coefficient, $C = \Delta T/\Delta\sigma_y$, are used to evaluate potential non-hardening helium embrittlement (NHHE) contributions to ΔT. The available data is limited, scattered, and potentially confounded. However, collectively the database suggests that there is a minimal NHHE up to a few hundred appm. However, a NHHE contribution appears to emerge at higher helium concentrations, estimated to be more than 400 to 600 appm. The NHHE is accompanied by a transition from transgranular cleavage (TGC) to intergranular fracture (IGF). IGF generally occurs only at high $\Delta\sigma_y$. Synergistic combinations of large $\Delta\sigma_y$ and severe NHHE could lead to very large ΔT in first wall and blanket structures at fusion spectrum dose levels above 50 to 75 dpa. Future research will focus on continued collection and analysis of data, participation in new experiments to better address NHHE and developing detailed micromechanical models of helium effects.

PROGRESS AND STATUS

Introduction

Two of the most important issues facing the development of normalized and tempered ≈ 8Cr normalized and tempered martensitic steels for fusion applications are the effects of high levels of transmutation product helium under conditions of simultaneous displacement damage production and irradiation embrittlement. Indeed, it is largely concerns about helium that have motivated the need for the International Fusion Materials Irradiation Facility. Because of the high sink density that act as traps, martensitic steels are generally believed to be relatively immune to helium effects [1,2,3]. However, at high helium levels, a significant population of bubbles forms, with number densities, sizes and spatial distributions that depend on the irradiation temperature and the alloy microstructure. The amount and distribution of helium on grain boundaries is particularly significant [4].

A key manifestation of irradiation embrittlement is an increase in transition temperature (ΔT) for fast fracture, typically measured in sub-sized Charpy V-notch type impact tests. Much attention has been directed at the effect of helium on low temperature fast fracture and embrittlement, and this issue remains a matter of significant uncertainty. One school of thought has asserted that helium plays a dominant role in embrittlement, in some cases even apparently showing a linear correlation between helium concentration and ΔT [5-14]. A contrary view attributes a dominant role to irradiation hardening induced embrittlement, where the hardening is primarily associated with displacement damage. Thus, at least up to some concentration, helium only plays a secondary role [15,16], primarily through its effect on hardening. The sensitivity of hardening to helium generally appears to be modest below very high levels. However, to date it has not been possible to obtain reliable experimental assessment of helium effects on fast fracture in candidate materials at damage rates, doses and temperatures relevant to the first wall and blanket environment. Thus there has been no clear experimental resolution of this issue.

We begin by proposing a framework to better assess the issue of helium effects on fast fracture based on existing data. It is noted that this framework has been used to design a series of experiments that are being conducted as part of the US-Japan collaborative irradiation program in the High Flux Isotope Reactor (HFIR). The framework can be described as follows:

1) "Brittle' fracture occurs in bcc alloys when the elevated normal stress ($\sigma_n = M\sigma_y$) in front of a notch or crack tip exceeds a critical local fracture stress for transgranular cleavage (σ_c^*) or intergranular (σ_{ig}^*) fracture over a critical microstructural volume of material (V*), or $\sigma_n(V^*) \geq \sigma_c^*$. Here σ_y is the yield stress and M is a constraint factor that varies between about 2 to 4 depending on the notch/crack geometry and the alloy strain-hardening rate [16-18].

2) At low irradiation temperatures (< ≈ 375-400°C), and in the absence of high levels of helium, the ΔT is due to irradiation hardening and can be correlated with changes in yield stress ($\Delta\sigma_y$), as $\Delta T = C\Delta\sigma_y$ [15-19]. The value of the hardening-embrittlement coefficient C depends on both $\Delta\sigma_y$ and the elastic cleavage transition temperature and upper shelf energy of a particular unirradiated alloy [17].

3) At high irradiation temperatures (> ≈ 400-425°C) there is typically either little or no hardening, or some degree of softening, with $\Delta\sigma_y \leq 0$ [20]. However, positive ΔT may occur in this temperature regime as the result of reductions in σ^* due to irradiation enhanced thermal aging processes [16,19]. Such non-hardening embrittlement (NHE) processes include precipitation or coarsening of brittle phases, grain boundary segregation of solutes, such as phosphorous, and instabilities in the tempered martensitic substructure [9,16,19-21]. In 8Cr martensitic steels containing significant quantities of tungsten, a primary non-hardening embrittlement mechanism is precipitation of brittle Laves phases on prior austenitic grain boundaries (PAGs). Purely thermal NHE occurs at ≈ 500°C and above; but it appears that radiation enhanced diffusion decreases to lower leg of the time-temperature NHE C-curve to about 400°C or less [16,19]. This is a concern, since combinations of $\Delta\sigma_y$ and NHE may give rise to very large ΔT. Significant NHE is signaled by large, or alternatively, negative (when $\Delta T > 0$ and $\Delta\sigma_y < 0$) values of C and, often, a transition from transgranular cleavage (TGC) to intergranular fracture (IGF).

4) The accumulation of helium and hydrogen on PAGs may also lead to NHE. We will focus on the potential effect of large amounts of helium and NHHE, but in some cases this cannot be distinguished from a corresponding high concentration of hydrogen. The distribution of helium on the grain boundaries is critical. For example, a coarse distribution of large bubbles would be expected to have little effect on ΔT, while a monolayer-type film of boundary would likely be most damaging [16].

5) As noted above, NHE and NHHE are generally associated with a transition from a TGC to IGF local fracture mode. While oversimplified, a conceptual model of the competing effects TGC versus IGF is very useful. The model posits that the TGC continues to be the fracture path of least resistance as long as it has a lower critical stress than that for IGF. Thus, gradual weakening of the PAGs by helium (and/or other mechanisms) would not be reflected in IGF until σ_{ig}^* falls below σ_c^*, where ΔT depends synergistically on both $\sigma_{ig}^* - \sigma_c^*$ (< 0) and $\Delta\sigma_y$. Of course in reality the transition would not be abrupt and the conceptual model is oversimplified.

6) High levels of helium may also contribute an increment of hardening beyond that due to displacement damage alone. However, the incremental hardening appears to be modest up to fairly high concentration [1,19,22-24], at least at lower irradiation temperatur

7) A number of experimental studies have used nickel doping to produce high concentrations of helium by two-stage $^{58}Ni(n_{th},\gamma) \rightarrow {}^{59}Ni(n_{th},\alpha)$ reactions. It is well established that nickel additions result in additional hardening at lower irradiation temperatures [25-28]. This may be due to enhancement of hardening from defect clusters as well as fine scale nickel enriched precipitates. More generally, nickel additions change the transformation temperatures and kinetics in quenched and tempered steels, hence, modifying the overall microstructure. Thus increases in ΔT associated with nickel doping may or may not be due to helium.

8) Doping with boron isotopes (natural boron is 0.2 ^{10}B and ≈ 0.8 ^{11}B) can also be used to produce large quantities of helium from the $^{10}B(n, \alpha)^{6}Li$ thermal neutron reaction. However, the solubility of boron in steels is extremely low, and boron doping is also confounded by: a) the non-uniform distributions, which tends to segregate boron at PAGs and other interfaces and/or to form boride precipitate phases; b) boron's general effects on the microstructure and properties of quenched and tempered alloys; c) boron's role in strengthening grain boundaries; d) the production of equal amounts of transmutant lithium and helium while eliminating boron; d) very rapid transmutation and burn-out of boron at relatively low dpa; and, e) at low doses, excess dpa due to recoils from the n,α reactions.

9) The effects of such confounding factors can be partially mitigated by careful experimental designs. For example, comparisons of ΔT in paired alloys doped with either ^{58}Ni or ^{60}Ni (alternatively ^{10}B or ^{11}B) can help isolate the independent effect of helium.

Since the effects of fusion relevant helium levels on hardening appear to be modest, the major issue is the potential role of helium in NHHE. The framework outlined above has been incorporated in recent experiments. For example, a single variable experiment is being carried out to compare the ΔT, $\Delta\sigma_y$ and C for martensitic alloys doped with ^{58}Ni and ^{60}Ni isotopes as well as natural Ni; and another experiment is planned that will use alloys doped with ^{10}B and ^{11}B isotopes. However, these principles are generally not reflected in past studies. Indeed, most previous experiments did not even include tensile specimens to provide $\Delta\sigma_y$ data as a complement to the ΔT measurements from sub-sized Charpy tests; and even the simple expedient of microhardness measurements to estimate irradiation hardening was rarely exploited. Further, there have been relatively few fractographic studies to characterize the local fracture mode, and any transitions from TGC to IGF in irradiated alloys as a function of helium content.

Nevertheless, it is still possible to analyze existing data to try to detect, and even quantitatively estimate, the potential NHHE by examining the relation between ΔT and $\Delta\sigma_y$ and/or $C = \Delta T/\Delta\sigma_y$. Specifically, C accounts for the primary hardening induced embrittlement and, to first order, resolves many (not all) of the confounding factors. Large increases in C with increasing helium signal a NHHE contribution and vice versa. Of course, even if C appears to increase with helium, NHHE is not assured due to the confounding factors. Further, uncertainties in C must also be considered. Even relatively optimistic estimates of uncertainties of only ±10°C in ΔT and ± 20 MPa in $\Delta\sigma_y$ result mean uncertainties in C of ≈ ±10/ΔT for an actual C = 0.4°C/MPa. Thus a relatively large scatter in C values should be anticipated, particularly at small ΔT, and it is always useful to examine ΔT versus $\Delta\sigma_y$ scatter plots as well as the trends in C. Of course there are other indicators of NHHE. The most significant is the transition from TGC to IGF above some critical level of helium [1,24,29].

Analysis of the Existing ΔT - $\Delta\sigma_y$ Database and the Effects of He

We have assembled available information in cases in which it was possible to obtain reasonably good estimates of pairs of $\Delta\sigma_y$ and ΔT data. The most relevant ΔT data are based on sub-sized Charpy tests [7,8,30-38]. Unfortunately, due to the failure to include tensile specimens in many experiments, such data is limited. Other issues are that the tensile data is confined to tests at the elevated irradiation temperature

(or greater), where the $\Delta\sigma_y$ are smaller than at lower temperatures pertinent to the ΔT measured in sub-sized Charpy tests [20]. Thus when possible, we use $\Delta\sigma_y$ from room temperature tests. In addition to separate tensile (or hardness) tests it is possible to extract dynamic yield stress (σ_{yd}) values from the load-time data provided by instrumented sub-sized Charpy V-notch impact tests. Unfortunately, σ_{yd} information is seldom reported. An exception is the case of a large embrittlement database developed in Germany and summarized in a recent report and papers [7,8,30]. The alloys in these studies contained various amounts of natural B, thus had different levels of helium following mixed spectrum irradiations. Hence, we were able to obtain paired data $\Delta\sigma_{yd}$-ΔT.

There are also pertinent data from for spallation proton irradiations based on so-called small punch (SP) tests that can be used to estimate both irradiation hardening and transition temperature shifts [15,29,39]. However the SP technique is not true fracture tests per se. An effective yield stress (σ_{yp}) and corresponding irradiation hardening ($\Delta\sigma_{yp}$) are evaluated based on the nonlinearities in punch load-displacement curves. An effective transition temperature (T_{sp}) and irradiation induced shifts (ΔT_{sp}) are determined by plotting the integrated load-displacement energy at fracture, measured at the point of a large load drop, as a function of the test temperature. Since SP tests are inherently involve static, low constraint conditions, with small values of M (or ratios of the maximum principal stress relative to the σ_y) the brittle (TGC or IGF) to ductile transition, if any, occurs at temperatures that are much lower than for standard, and even sub-sized, Charpy impact tests; and the corresponding shifts in ΔT_{sp}, due to embrittlement, are also much lower than ΔT. An empirical adjustment of $\Delta T \approx 2.5\Delta T_{sp}$ is used in this report to evaluate ΔT and C [15,29,39-41] Finally, while highly unusual in steels, brittle fracture may also occur in tensile tests with lower bound values of M = 1. As noted above this implies a very low value of the critical brittle fracture stress. However, even in a tensile test M is greater than 1 in the necked region beyond the uniform strain limit. The maximum M increases with necking and can be related to the reduction in area at fracture and the corresponding tri-axial stresses in the necked region.

Figure 1a and b summarizes the very limited available Charpy-tensile test ΔT versus $\Delta\sigma_y$ data with helium variations in nominally similar alloys with and without nickel or boron doping for irradiations at ≈ 300 and 400°C respectively [31-38]. Helium content shown in parenthesis is common for both of Charpy and tensile specimens except for some cases where data for a common condition are not available; in these cases, both values of (Charpy/tensile) specimens are shown. The dashed lines indicate the scatter in the general database for ΔT versus $\Delta\sigma_y$ [19]. Two data sets are for a 9CrMo alloy both undoped and doped with 2%Ni irradiated at 300 and 400°C. The nickel doping results in increases from ≈ 14 to 234 and 33 to 369 appm He in these cases, respectively. Both the doped and undoped alloys fall on virtually the same ΔT versus $\Delta\sigma_y$ line with C = 0.40 °C/MPa at 300°C and C = 0.82 ± 0.02 °C/MPa at 400°C. Thus while the nickel addition increases the $\Delta\sigma_y$ in these cases, there is no independent NHHE effect of either nickel or helium indicated by this data set. The corresponding ΔT for a 9Cr2W alloy doped with 2% nickel irradiated at ≈ 300°C with ≈ 115 appm He falls slightly above the ΔT versus $\Delta\sigma_y$ line for the corresponding undoped steel with ≈ 5 appm helium, with C of 0.44 and 0.32 °C/MPa respectively. However, both are well within the overall ΔT versus $\Delta\sigma_y$ and C scatter band. A generally similar result is found for natural B doped F82H and JLF1 steels irradiated at 300°C, with ≈ 23-40 appm He, compared to undoped alloys with ≈ 3 appm He. These results may suggest a slightly stronger effect of boron compared to nickel doping, with values of ≈ 0.53 and 0.75 (high helium) versus 0.43 and 0.58 (low helium).

Figure 1a and b also show ΔT versus $\Delta\sigma_y$ for 12Cr1Mo Ni-doped and undoped alloys also indicating no effect of helium and the data all fall within the normal scatter bands [36-38]. However, a recent review paper included 300°C data on F82H doped with various isotopes of B showed a systematic increase of C with increasing helium up to 340 appm [42,43]. Thus these results may also suggest a stronger effect of boron compared to nickel doping, perhaps due to B segregation to PAGs. Overall, however, the very the limited nickel and boron doping data show little effect of helium on C up to concentrations ≈ 300 appm.

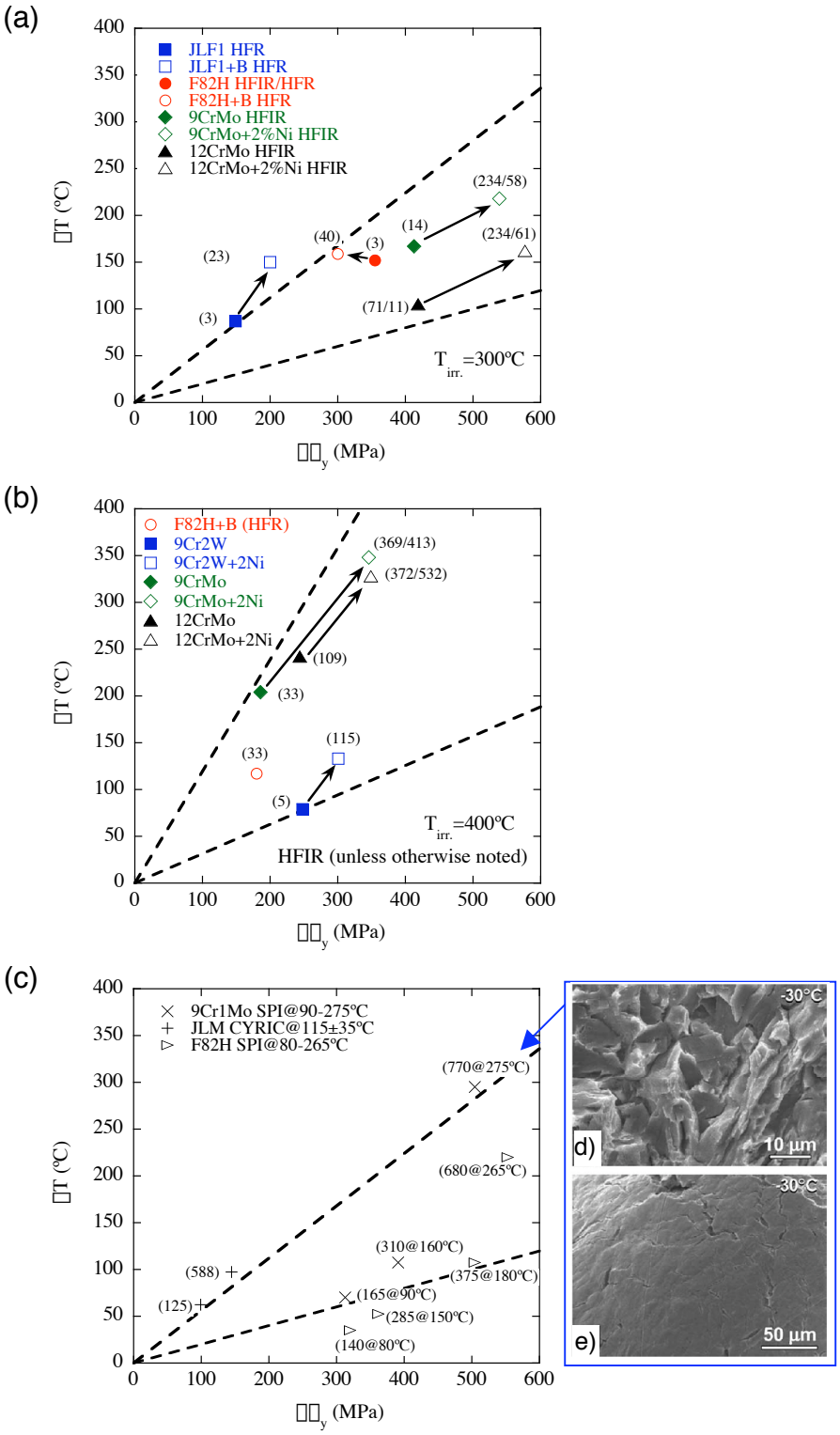

Figure 1. (a) Charpy □T versus tensile □□$_y$ data with helium variations in nominally similar steels with and without B- or Ni-doping irradiated at 300 ºC and (b) at 400 ºC. (c) SP □T_p versus □□$_{yp}$ data with helium variations after SPI along with □T_p versus □□$_{ym}$ data with helium variations. (d) Fracture surface and (e) bottom surface of punch-tested specimen with 770 appm He/9.4 dpa showing the occurrence of IGF from reference 29. [11,19,29,31-38].

Dai and co-workers have reported a nearly linear correlation between the helium level and ΔT for spallation proton irradiations (SPI) of 9Cr1Mo T91 and F82H steels at nominal temperatures between ≈ 90 to 275 °C from ≈ 2.5 to 9.4 dpa producing ≈ 140 to 770 appm He [29,39]. Note the temperatures, He levels and dpa generally increase in tandem. Figure 1c shows plot of this SP ΔT_p versus $\Delta\sigma_{yp}$ data. The helium levels and nominal irradiation temperatures are shown in the parenthesis near each data point. At the intermediate helium levels, the data fall in the lower region of the overall ΔT versus $\Delta\sigma_y$ scatter band for this irradiation temperature range shown by the dashed lines. Jia and Dai also noted the fact that these data fall in the general scatter band of ΔT versus dpa for fission irradiations [39]. However, there is a distinct break in the ΔT_p versus $\Delta\sigma_{yp}$ trend for the data points at 680 appm He in F82H and 770 appm He in T91. Although the corresponding C values are neither particularly high, nor anomalous, the onset of significant amounts of IGF are observed in these cases, suggesting the emergence of a NHE contribution at very high helium levels. Note, IGF is readily observed both on the fracture surfaces and as a network of grain boundary cracks on the bottom surface of the SP disc as shown in the micrographs taken from reference 29. (Figures 3d and 3e.)

Of course, the SPI results based on SP tests do not represent single variable experiments, and interpretations of this should be viewed with considerable caution. For example, high levels of hydrogen and other transmutation products may also play a role in the larger C observed at the highest spallation proton dose, confounding unambiguous conclusions about the effects of helium acting alone. Figure 1c also shows ΔT_p versus $\Delta\sigma_{ym}$ data for 36 MeV α-ion irradiations to 100 and 600 appm He at 115 ± 35 °C based on SP assessments of ΔT_{sp} and hardening evaluated using Vickers microhardness tests ($\Delta\sigma_{ym}$) [15]. In this case, the ΔT_p versus $\Delta\sigma_{ym}$ data fell near the top of the general scatter-band, but there was essentially no effect of helium on the ΔT_p versus $\Delta\sigma_{ym}$ relation.

Another useful source of paired ΔT-$\Delta\sigma_{yd}$ data has been developed by Schneider and co-workers on a variety of steels that 'happen to have' different natural boron contents [7,8,30]. The Schneider database includes mixed spectrum neutron irradiations from 0.2 to 2.4 dpa at temperatures between 250 and 450°C that produce up to ≈ 120 appm helium. Based on empirical plots of ΔT versus helium for subsets of this database various authors [5,6] have also suggested a dominant role of helium on embrittlement. Indeed, fits to the overall database for T < 400°C do result in a weak correlation that would indicate a strong effect of helium, that would, if true, result in an enormous $\Delta T \approx 1080$°C at 1000 appm He. Note, the 450°C data indicates that ΔT decreases with increasing helium, but is excluded from this analysis, since the C are very scattered and, on average, systematically larger than those observed at lower irradiation temperatures, indicating a NHE mechanism that is <u>not</u> related to helium. This is consistent with other observations of increased C at higher temperatures [16], but is not pertinent to the assessment of NHHE. Even restricting the analysis to 400°C or less, the ΔT versus helium data is very scattered and the statistical significance of the apparent correlation is low, with $r^2 \approx 0.21$.

However, a much more significant shortcoming of this sort of analysis is that it neglects the large range of $\Delta\sigma_{yd}$ in the irradiated steels. This masks the combined effects of both differences dose (dpa) as well as the wide range of metallurgical variables representing the various alloys in the Schneider database. Both $\Delta\sigma_y$ and $C = \Delta T/\Delta\sigma_{yd}$, hence the corresponding ΔT, depend on these variables, in a way that is largely independent of either the alloy boron or helium content. Note, C itself also increases with $\Delta\sigma_y$ and depends as the alloy microstructure and unirradiated Charpy properties [14]. At lower irradiation temperatures, $\Delta\sigma_y$ is the most significant factor in controlling ΔT, thus it must be accounted ***<u>before</u>*** attempting to evaluate any potential effects of any other variables.

Notably, three of the alloys with the highest boron contents in the Schneider database also contained significant quantities of nickel (0.66 to 0.92%Ni). At 300°C, the $\Delta\sigma_{yd}$ in these nickel-bearing alloys is higher by an overall average factor of ≈ 1.6±0.25 relative to a set of nominally similar nickel free alloys. Indeed, there is a systematic overall correlation between $\Delta\sigma_y$ and the alloy nickel content. The nicke

sensitivity of $\Delta\sigma_y$ decreases with irradiation temperature, dropping significantly between 350 and 400°C. Figure 2a shows that the ΔT versus $\Delta\sigma_{yd}$ generally fall in the same scatter band as the larger overall database for ≈8Cr tempered martensitic steels as shown by the dashed lines. Figure 2b plots the corresponding $C = \Delta T/\Delta\sigma_{yd}$ as a function of helium content. Least squares fits show an apparently significant effect of higher helium increasing ΔT only for the data for irradiations at 250°C; and in the case, the effect of helium is primarily manifested in the range below 50 appm He. The fits for the largest set of data for irradiations at 300°C show only a weak apparent effect of helium, while at higher temperatures there is a negative association between helium and C. A best fit to all the C data in the Schneider database for irradiations at ≤ 400°C shown by the solid line, indicates a very weak, statistically insignificant, negative effect of helium. These results are not surprising, since all but one data point is below 100 appm helium. The scatter in C is consistent with expectations and the C = 0.41±0.2 MPa/°C, shown by the horizontal dashed lines, are very consistent with the corresponding values for the larger overall ≈8Cr martensitic steels database [16].

Figure 2c re-plots the C versus helium Schneider database along with paired lower-higher helium C values for ≈8Cr alloys from Figures 1a and b shown as heavy solid lines [19]. These data show a generally weak effect of helium on C. Figure 2c also shows the relation between C and helium for the SP test data from Dai and Kasada as heavy dashed lines [15,29]. At lower helium levels the C for the Dia data the C that fall near the lower bound of the scatter band, but they increase with increasing helium in this case, falling above the nominal mean value at the highest in the range of 680 to 770 appm He. Given the atypical nature of the SP test, it is also useful to examine the relative variations of C when the SP data are normalized to a more typical value of 0.4°C/MPa at the lowest helium as shown the dotted lines. The normalized C for the SP tests exceed 1°C/MPa at the highest helium level, consistent with a significant NHHE effect and the observation of IGF.

Another data set published by Henry and co-workers [4] at least indirectly pertinent to the issue of NHE are the results of tensile tests at 25 and 250°C following spallation proton irradiations of a 9Cr1Mo (EM10) steel in various thermo-mechanical treatment conditions at ≈ 260°C to ≈ 9.8 dpa and 750 appm He. The alloy conditions included as-tempered (AT), as-quenched (AQ) and tempered and cold-worked (CW). A strong effect of the alloy thermo-mechanical treatment and test temperature was observed in this dataset. In three cases the specimens failed after considerable deformation at reductions in area (RA) from about 44-48% that were somewhat less than the corresponding RAs of 58 to 68% in the unirradiated condition. The ductility varied with test temperature and thermo-mechanical treatment condition and increased with decreasing σ_y (given in the parenthesis) in the order: AT at 250°C (960 MPa); AT at 25°C (1150 MPa) and CW at 25°C (1220 MPa). The fracture surfaces were a mixture of ductile microvoid coalescence and cleavage with some IGF and transverse cracking. Assuming there is no strain hardening, the average fracture stress in the necked region is on the order of ≈ 2000 MPa consistent with typical values of σ_c^*. Indeed, the principal tri-axial stress would be even higher in the necked region, and this may compensate for some level of strain softening. The AQ alloy tested at 25°C had the largest σ_y of 1320 MPa and lowest ductility with a RA of only 2% and ≈ 100% IGF. Given the small amount of necking prior to fracture it is not unreasonable to assume that $\sigma_{ig}^* = \sigma_y \approx 1300$ MPa, which is much lower than typical values of σ_c^*. This low value may at least in part be due to the high level of helium. This conclusion is supported by the observation that the fracture mode was ≈ 100% ductile microvoid coalescence after neutron irradiations of the AQ alloy to a slightly higher strength $\sigma_y \approx 1330$ MPa. A comparison of the fracture surfaces for the neutron and spallation proton irradiations is shown in Figure 3

Jung and co-workers [44] have reported the results of tensile tests at 25 and 250°C on EM10 and T91 after high-energy α-implantation at 250°C to 0.8 dpa and 5000 appm He that result in an ≈ 0% RA, ≈ 100%IGF and σ_y = 1079 to 1217 MPa. The ductility was much higher and the σ_y much lower after α-implantations at 550°C. The RA was much also lower for tensile tests at 550°C compared to 25

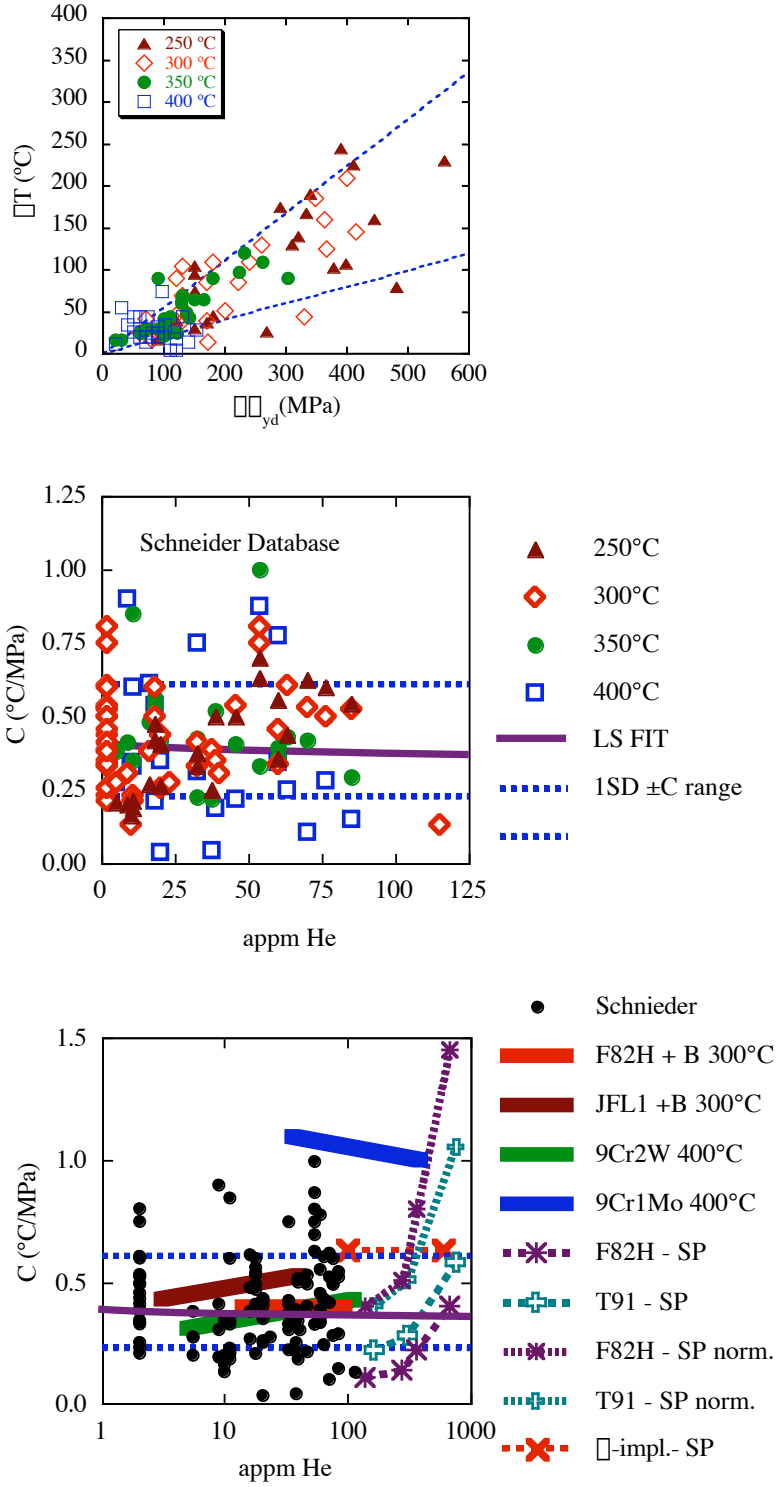

Figure 2. (a) □T versus □□$_{yd}$ from Schneider's database compared to the overall scatterband for martensitic steels irradiations at ≤ 400. (b) C = □T/□□$_{yd}$ for Schneider's database as a function of helium content with a least squares fit line. (c) C values from Schneider database along with paired lower-higher helium C values from Figures 1a and b shown as heavy solid lines [11,19, 30-38].

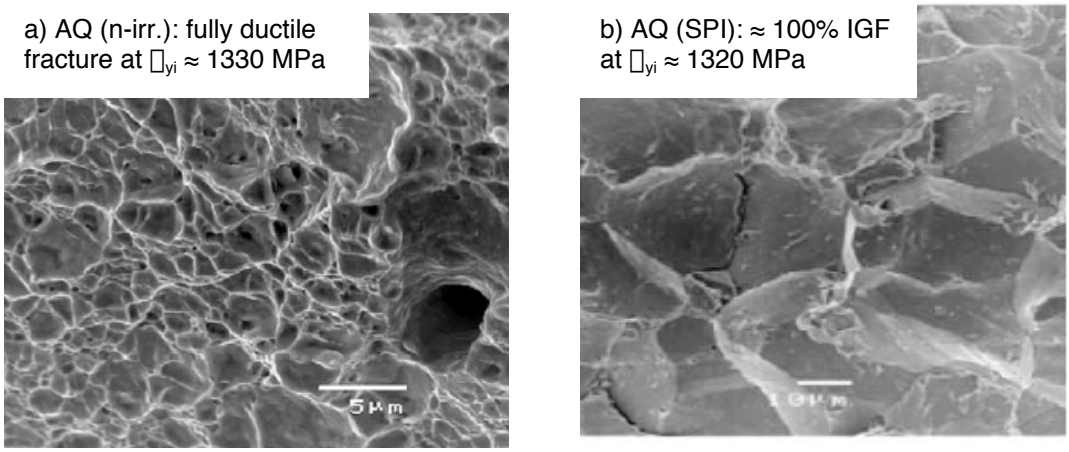

Figure 3. Tensile fracture surfaces of AQ alloy of 9CrMo steel after (a) neutron and (b) spallation proton irradiations to the similar levels of hardening at ≈ 250 ºC showing ductile and IGF, respectively [from reference 4].

While no firm conclusions can be drawn from the tensile data, it is extremely significant that ≈ 100% IGF is observed at normal stress levels in the range of ≈ 1100 MPa (5000 appm He) to 1300 MPa (750 appm He). Further the results suggest that in addition to helium itself, NHE and IGF also depend on both the irradiation and test temperatures. Of course the presence of cracks or notches and/or high loading rates would make materials that are so brittle in a static tensile test even more so in normal fracture tests.

Summary

We have collected and analyzed a variety of data pertinent to the issue of the effect of helium on fastfracture and irradiation embrittlement by evaluating the relation between □T and □□y. The hardening-shift relation was assessed both in terms of □T versus □□y scatter plots and trends in C = □T/□□y. Large values of C, as well as transition from TGC to IGF, at high helium concentrations were used as signatures of possible NHHE. While the data is scattered, and to some degree confounded by uncontrolled variables, the results suggest that up to concentrations several hundred appm, helium has little effect on C or □T. However, at higher concentrations the data is consistent with the hypothesis that accumulation of helium weakens PAG to the point where a NHHE effect emerges as signaled by higher C and IGF. This hypothesis is supported by the results of tensile tests on steels in a high strength AQ-irradiated state or implanted with very high concentrations of helium.

Future Work

Work during the next reporting period will focus on developing models of NHHE embrittlement, analysis of additional data as it becomes available and participation in the implementation of a new series of well-designed irradiations experiments in HFIR that will better address the issue of helium effects on fast fracture and embrittlement. These experiments will include pre-cracked fracture and tensile specimens that are doped with isotopes of nickel and boron that will allow evaluation the effects of up to very high concentrations of helium in alloys that are otherwise very similar. Further, we have initiated discussions with Dr. Y. Dai at PSI about establishing an active collaboration to carry out tensile, hardness and fracture tests on martensitic alloys that have been irradiated with spallation protons at low-to-intermediate temperatures up to very high □□y and concentrations of helium.

Aknowledgements

The authors explicitly acknowledge the extensive research that produced the data analyzed in this report and thank the researches cited in the references for their major contributions to the development of materials for fusion reactors.

References

[1] P. Jung, C. Liu, and J. Chen, J. Nucl. Mater. 296 (2001) 165.
[2] A. Kimura, R. Kasada, K. Morishita, R. Sugano, A. Hasegawa, K. Abe, T. Yamamoto, H. Matsui, N. Yoshida, B. D. Wirth, and T. D. Rubia, J. Nucl. Mater. 307-311 (2002) 521.
[3] A. Hasegawa, H. Shiraishi, H. Matsui, and K. Abe, J. Nucl. Mater. 212-215 (1994) 720.
[4] J. Henry, M.-H. Mathon, and P. Jung, J. Nucl. Mater. 318 (2003) 249.
[5] M. Rieth, B. Dafferner, and H.-D. Rohrig, J. Nucl. Mater. 258-263 (1998) 1147.
[6] R. Lindau, A. Möslang, D. Preininger, M. Rieth, and H. D. Röhrig, J. Nucl. Mater. 271-272 (1999) 450.
[7] H.-C. Schneider, B. Dafferner, and J. Aktaa, J. Nucl. Mater. 295 (2001) 16.
[8] H.-C. Schneider, B. Dafferner, and J. Aktaa, J. Nucl. Mater. 321 (2003) 135.
[9] B. Van der Schaaf, D. S. Gelles, S. Jitsukawa, A. Kimura, R. L. Klueh, A. Möslang, and G. R. Odette, J. Nucl. Mater. 283-287 (2000) 52.
[10] B. Van der Schaaf, *Harde ning and toughness from Radiation and resistance characterization of F82H and Screening Steels*, NRG Petten 20027/99.25387/P.
[11] R. L. Klueh and D. J. Alexander, J. Nucl. Mater. 187 (1992) 60.
[12] R. L. Klueh and D. J. Alexander, J. Nucl. Mater. 218 (1995) 151.
[13] R. L. Klueh, D. S. Gelles, S. Jitsukawa, A. Kimura, G. R. Odette, B. van der Schaaf, and M. Victoria, J. Nucl. Mater. 307-311 (2002) 455.
[14] K. Shiba, M. Suzuki, and A. Hishinuma, J. Nucl. Mater. 233-237 (1996) 309.
[15] R. Kasada, T. Morimura, A. Hasegawa, and A. Kimura, J. Nucl. Mater. 299 (2001) 83.
[16] G. R. Odette, T. Yamamoto, H. J. Rathbun, M. Y. He, M. L. Hribernik, and J. W. Rensman, J. Nucl. Mater. 323 (2003) 313.
[17] G. R. Odette, P. M. Lombrozo, and R. A. Wullaert, ASTM-STP 870 (1985) 841.
[18] G. R. Odette and M. Y. He, J. Nucl. Mater. 283-287 (2000) 120.
[19] T. Yamamoto, G. R. Odette, and H. Kishimoto, Fusion Materials Semiannual Report 7/1 to12/31/2003, DOE/ER-313/34.
[20] L. Schäfer, J. Nucl. Mater. 283-287 (2000) 707.
[21] H. Sakasegawa, T. Hirose, A. Kohyama, Y. Katoh, T. Harada, K. Asakura, and T. Kumagai, J. Nucl. Mater. 307-311 (2003) 490.
[22] L. K. Mansur, J. Nucl. Mater. 318 (2003) 14.
[23] K. Farrell and T. S. Byun, J. Nucl. Mater. 296 (2001) 129.
[24] J. Henry, X. Averty, Y. Dai, P. Lamagnére, J. P. Pizzanelli, J. J. Espinas, and P. Wident, J. Nucl. Mater. 318 (2003) 215.
[25] R. Kasada, A. Kimura, H. Matsui, and M. Narui, J. Nucl. Mater. 258-263 (1998) 1199.
[26] G. R. Odette and G. E. Lucas, Rad. Eff. and Deff. in Solids 144 (1998) 189.
[27] G. R. Odette, G. E. Lucas, D. Klingensmith, B. D. Wirth, and D. Gragg, NUREG/CR-6778 (2002).
[28] G. R. Odette, T. Yamamoto, and D. Klingensmith, Phil. Mag. (2004) (in print).
[29] Y. Dai, X. J. Jia, and K. Farrell, J. Nucl. Mater. 318 (2003) 192.
[30] H.-C. Schneider, B. Dafferner, H. Ries, and O. Romer, Irradiation Programme MANITU: Results of impact tests with the irradiated materials (2.4 dpa), FZKA-6605, Forschungszentrum Karlsruhe (2001).
[31] R. L. Klueh, M. Sokolov, K. Shiba, Y. Miwa, and J. P. Robertson, J. Nucl. Mater. 283-287 (2000) 478.
[32] E. V. van Osch, M. G. Horsten, G. E. Lucas, and G. R. Odette, *Effects of Radiation on Materials: 19th International Symposium*, ASTM STP 1366 (2001) 612.
[33] E. V. van Osch, J. B. M. Bakker, R. den Boef, and J. Rensman, NRG Petten 20023/99.26974/P.

[34] J. Rensman, J. van Hoepena, J. B. M. Bakkera, R. den Boef, F. P. van den Broek, and E. D. L. van Essen, J. Nucl. Mater. 307-311 (2002) 245.
[35] R. L. Klueh and D. J. Alexander, J. Nucl. Mater. 179-181 (1991) 733-736.
[36] R. L. Klueh and P. J. Maziasz, J. Nucl. Mater. 187 (1992) 43-54.
[37] R. L. Klueh and D. J. Alexander, J. Nucl. Mater. 187 (1992) 60.
[38] R. L. Klueh and J. M. Vitek, J. Nucl. Mater. 150 (1987) 272.
[39] X. Jia and Y. Dai, J. Nucl. Mater. 323 (2003) 360.
[40] Y. Ruan, P. Spaetig, and M. Victoria, J. Nucl. Mater. 307-311 (2003) 236.
[41] J. Kameda and X. Mao, J. Mater. Sci. 27 (1992) 983.
[42] S. Jitsukawa et. al., ICFRM-12.
[43] K. Shiba and A. Hishinuma, J. Nucl. Mater. 283-287 (2000) 474.
[44] P. Jung, J. Henry, J. Chen, and J.-C. Brachet, J. Nucl. Mater. 318 (2003) 24

INFLUENCE OF HIGH DOSE NEUTRON IRRADIATION ON MICROSTRUCTURE OF EP-450 FERRITIC-MARTENSITIC STEEL IRRADIATED IN THREE RUSSIAN FAST REACTORS—A. M. Dvoriashin, S. I. Porollo, and Yu. V. Konobeev (Institute of Physics and Power Engineering), and F. A. Garner (Pacific Northwest National Laboratory)*

OBJECTIVE

The objective of this effort is to explore the response of Russian ferritic-martensitic steels to irradiation in various Russian and Kazakh fast reactors, looking for insights on how Western steels of similar composition might behave.

SUMMARY

The microstructure of EP-450 ferritic-martensitic steel was determined after irradiation in BN-350, BOR-60 and BR-10 fast reactors at temperatures in the range 275-690°C. The examinations confirm a high resistance of EP-450 steel to void swelling, but the resistance appears to be lower when the dpa rate is reduced. Depending on irradiation dose and temperature the following was observed: voids (285-520°C), dislocation loops and linear dislocations (275-520°C), α'-phase (285-520°C), χ phase (460-590°C), and M_2X precipitates (460-690°C). It appears that the formation of dislocation loops and α' precipitates at high densities is responsible for the low temperature embrittlement observed in this steel.

PROGRESS AND STATUS

Introduction

Ferritic/martensitic (F/M) steels are known for their high resistance to swelling and relatively low irradiation creep rate, and therefore are attractive as possible fusion candidate materials. The steel EP-450 is used most widely in Russia and other former Soviet states, especially as the reference structural material of hexagonal wrappers and safety control tubes of the BN-600 fast reactor. An effort is underway to compile the microstructural data for this steel, with the main experimental database obtained by examination of hexagonal wrappers from the BN-350 and BN-600 fast reactors and from fuel pin cladding irradiated in BR-10 and BN-350 reactors. BR-10 and BN-600 have relatively high inlet temperatures compared to that of BN-350. BR-10 has the lowest neutron flux, producing ~7 x 10^{-8} dpa/sec, while the other two reactors operate at higher fluxes, producing 1-2 x 10^{-6} dpa/sec. The first preliminary results are presented in this report.

Experimental Details

The compositions of all specimens examined fall within the limits of the EP-450 specification (0.1-0.15C, <0.8Mn, <0.5Si, 0.015S, <0.025P, 11.0-13.5Cr, 0.05-0.30Ni, 1.2-1.8Mo, 0.1-0.3V, 0.3-0.6Nb, wt %). The final heat treatment for hexagonal wrappers of BN-350 and BN-600 reactors subassemblies involves normalization at 1020-1100°C with subsequent tempering at 780-800°C for 1 hr. For fuel pin cladding, however, normalization proceeds at 1050°C followed by tempering at 710°C for 1 hr.

Sections of 15 mm length and 4 mm width were cut out from fuel cladding using a remote milling machine. Then disks of 3 mm in diameter were punched from the segments. For hexagonal wrappers (flat-to-flat distance of 96 mm and wall thickness of 2 mm) sections of size 10×10 mm and 0.8-1.0 mm in thickness were cut from the middle of the faces. Following electrolytic thinning of the sections to a thickness of 0.4 mm, disks of 3 mm in diameter were punched. TEM specimens were prepared by a standard technique of two-jet polishing using the "TENUPOLE" device with electrolyte of 5 vol. % $HClO_4$+

*Pacific Northwest National Laboratory (PNNL) is operated for the U.S. Department of Energy by Battelle Memorial Institute under contract DE-AC06-76RLO-1830.

95 vol. % H_3COOH. Microstructural investigations were carried out at an accelerating voltage of 100 kV using a JEM-100CX electron microscope equipped with a lateral goniometer.

Experimental Results

Void structure

The initial microstructure was similar for both wrappers and tubes, consisting of grains of ferrite (40-50%) and tempered martensite (50-60%), with grain sizes of ferrite and martensite ranging 17-50 microns. Grains in tempered martensite were divided into sub-grains. The dislocation density was ~2×10^{14} m^{-2} in ferritic grains, and ~ 1×10^{15} m^{-2} in martensite.

Both ferrite and martensite contain $M_{23}C_6$ carbides in the matrix and on grain boundaries. The grain boundary occupation by $M_{23}C_6$ was 90-100%, with particle sizes of 0.05-0.50 microns. Inside ferrite grains the carbide sizes ranged from 0.05 up to 0.2 microns, and their concentration in some grains reaches 2×10^{20} m^{-3}. In the tempered martensite $M_{23}C_6$ precipitates were located, as a rule, on sub-grain boundaries, with mean sizes of 0.15-0.3 microns. Carbonitrides such as M (C, N) with mean size of ~1 micron were also observed inside ferrite and martensite grains. Additionally, small plate-like precipitates of M_2 (C, N) were observed in ferrite grains.

The microstructure of the steel changed significantly due to irradiation. Voids, dislocation loops and new precipitates have formed, with size and concentration depending on irradiation conditions. Parameters of voids observed to date are shown in Table 1.

Isolated voids of 4 nm diameter formed after irradiation to 0.5 dpa at the temperature of 285°C in BN-350. Further increases of dose resulted in an increase of void concentration. At irradiation temperatures in the 285 - 460°C range voids are uniformly distributed with no essential difference between grains of ferrite and tempered martensite (Figures 1 & 2). For higher irradiation temperatures the spatial distribution of voids is non-uniform. Generally, voids in ferrite grains are adjacent to precipitates. In grains of tempered martensite they are located mainly on sub-grain boundaries. Voids were not observed at irradiation temperatures above 520°C for the dose range available.

The average swelling rate for the specimens listed in Table 1 is shown in Figure 3. The maximum average swelling rate is ~1×10^{-2} % /dpa in the temperature range 390-410°C. Note that the highest rate is observed at rather low dpa levels in BR-10, rather than at much higher dpa levels reached in BN-350. Remember that BR-10 operates at a much lower dpa rate.

Dislocation structure

Irradiation at temperatures from 275 to 520°C results in formation of dislocation loops as shown in Figure 4. The data on dislocation loops are still being compiled and will be published later, but at this time we can specify the general observations.

Table 1. Parameters of voids observed in neutron irradiated EP-450 F/M steel

Reactor	Sample type	Irradiation conditions		Voids		
		$T_{irr.}$,°C	Dose, dpa	Diameter, nm	Number density, $10^{15}cm^{-3}$	Swelling, %
BR-10	fuel pin	360	9.7	--	0	0
BR-10	fuel pin	395	11	18	0.28	0.1
BR-10	fuel pin	410	10.8	24	0.12	0.1
BR-10	fuel pin	430	9.0	--	0	0
BN-350	fuel pin	285	0.5	4	very low	~0
BN-350	fuel pin	285	3.0	4	very low	~0
BN-350	fuel pin	285	10	4	4	0.01
BN-350	fuel pin	285	21	4	7	0.02
BN-350	fuel pin	355	37	8	2	0.08
BN-350	fuel pin	420	46	18	0.7	0.3
BN-350	fuel pin	315	34	5.5	0.7	0.01
BN-350	fuel pin	380	56	12	1	0.1
BN-350	fuel pin	460	60	7	0.3	0.006
BN-350	fuel pin	595	39	0	0	0
BN-350	fuel pin	690	17	0	0	0
BN-350	wrapper	275	4.7	--	0	0
BN-350	wrapper	275	18.8	3	5	0.003
BN-350	wrapper	305	33.5	5	4	0.015
BN-350	wrapper	415	47	12	2	0.2
BN-350	wrapper	520	18.8	14	0.1	0.01
BN-350	wrapper	280	15	3	2.5	0.005
BN-350	wrapper	352	89	13.5	3	0.6
BN-600	wrapper	345	31	13	1	0.1
BN-600	wrapper	360	<1	4	1	0.003
BN-600	wrapper	365	42	10	0.4	0.03
BN-600	wrapper	360	35	8	0.4	0.02
BN-600	wrapper	365	39	8.5	0.4	0.02
BN-600	wrapper	465	81	--	0	0

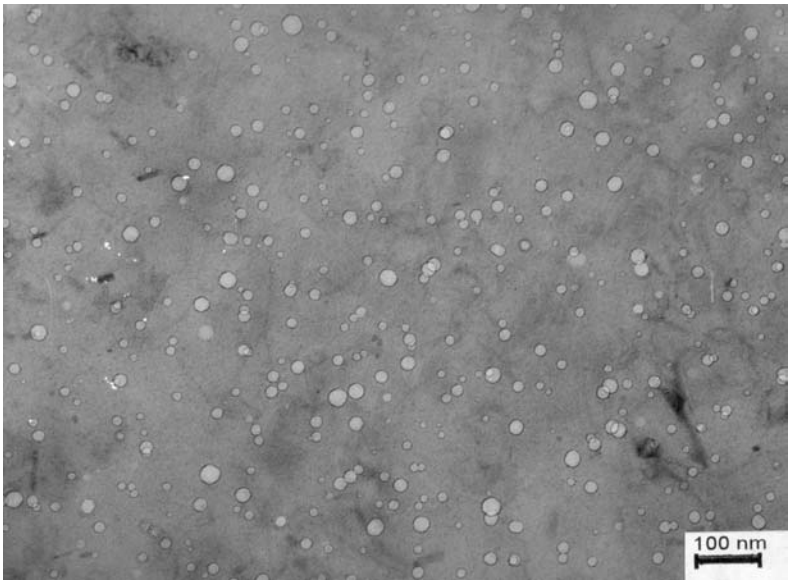

Figure 1. Voids in EP-450 after irradiation in BN-350 to 89 dpa at 352°C.

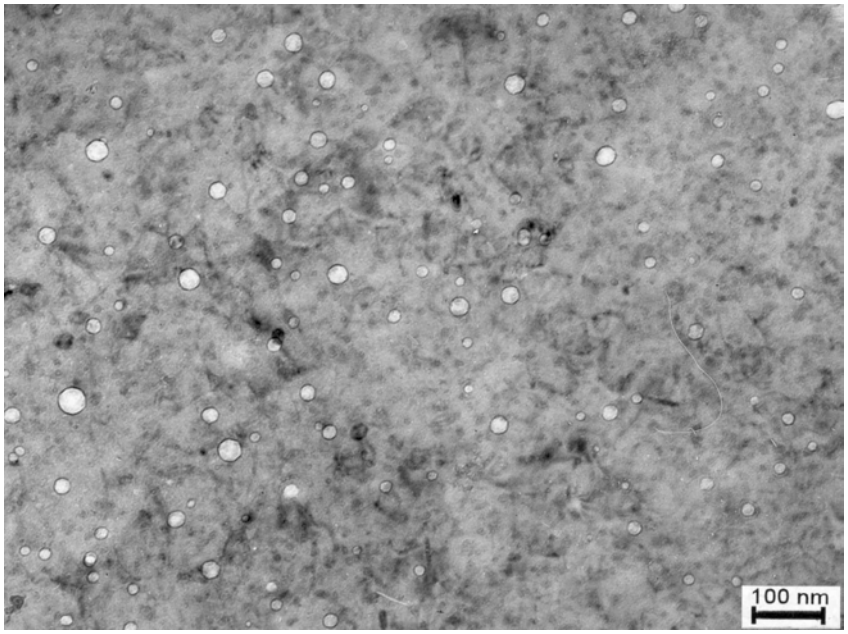

Figure 2. Voids observed in EP-450 after irradiation in BN-350 reactor to 46 dpa at 420°C.

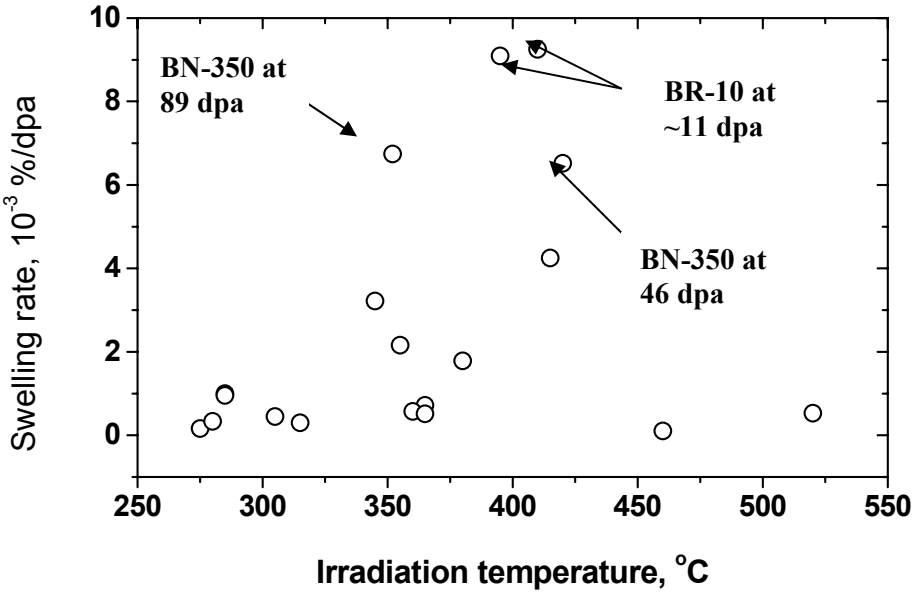

Figure 3. Temperature dependence of the average swelling rate observed in EP-450 with three data points highlighted to show the effect of dpa rate on swelling.

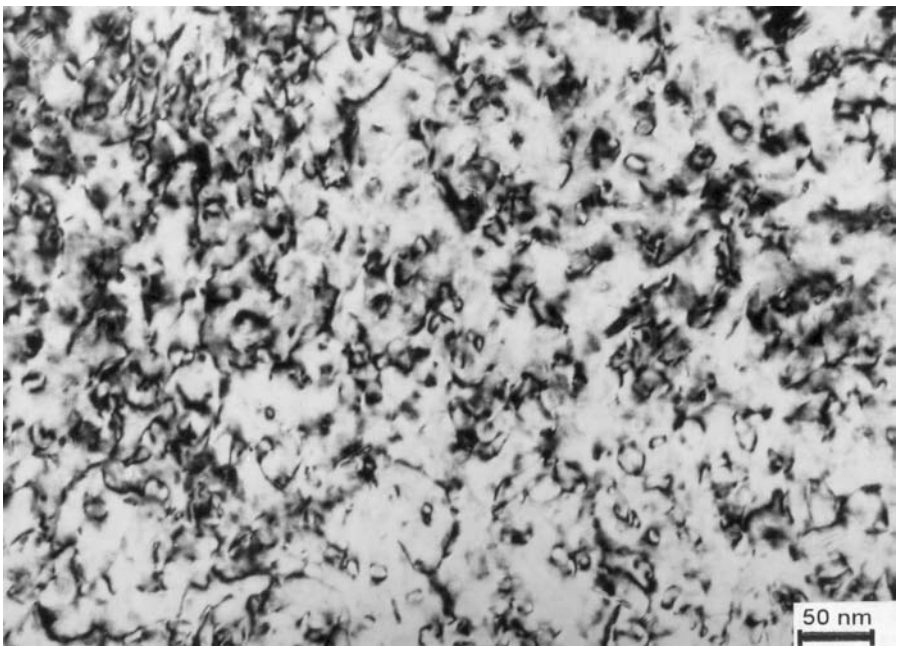

Figure 4. Dislocation structure in ferrite grains of neutron irradiated EP-450 after irradiation in BN-600 to <1 dpa at 360°C.

In ferrite grains both the mean loop diameter and loop concentration are slightly larger than in grains of tempered martensite. The mean loop diameter increases with increasing irradiation temperature. The loop concentration depends on both the temperature and dose. However, the influence of irradiation temperature appears to be more pronounced. Along with dislocation loops, radiation defects in the form of black dots are observed in the steel microstructure at the irradiation temperatures of 275 and 285°C and doses <20 dpa. The dot number density is on the level of ~10^{21} m^{-3} in both ferrite and tempered martensite grains.

In the range 360-520°C dislocation loops interact each with other, as well as with any existing dislocation network. As a result of such interaction, the total dislocation density decreases with increasing temperature. The dislocation structure formed after irradiation at >520°C consists of a dislocation network, the density of which is slightly higher in tempered martensite grains.

Precipitate structure

Formation of new precipitates as well as the transformation of pre-existing precipitates occurs in EP-450 under irradiation. At irradiation temperatures ranging from 275 to 520°C a high concentration (10^{22}-10^{23} m^{-3}) of fine precipitates is observed in both the ferrite and tempered martensite (Figure 5). These precipitates are α' phase (ferrite enriched with chromium) usually formed in these types of steel under neutron irradiation [I-3]. After irradiation to only 3 dpa α' precipitates can be detected as diffuse dots of ~5 nm size.

An increase of irradiation temperature causes increased size of α' precipitates accompanied with simultaneous reduction of concentration. Uniform distribution of these particles is a characteristic feature at temperatures in the range of 275-480°C. At 520°C α' precipitates are observed as islands of small clusters, with concentration $1\times10^{21}m^{-3}$ and mean diameter of 16 nm. In addition, two types of radiation-induced precipitates were observed in ferrite grains, equiaxed precipitates of χ-phase (Figure 6) and rod-like precipitates of M_2X (Figure 7).

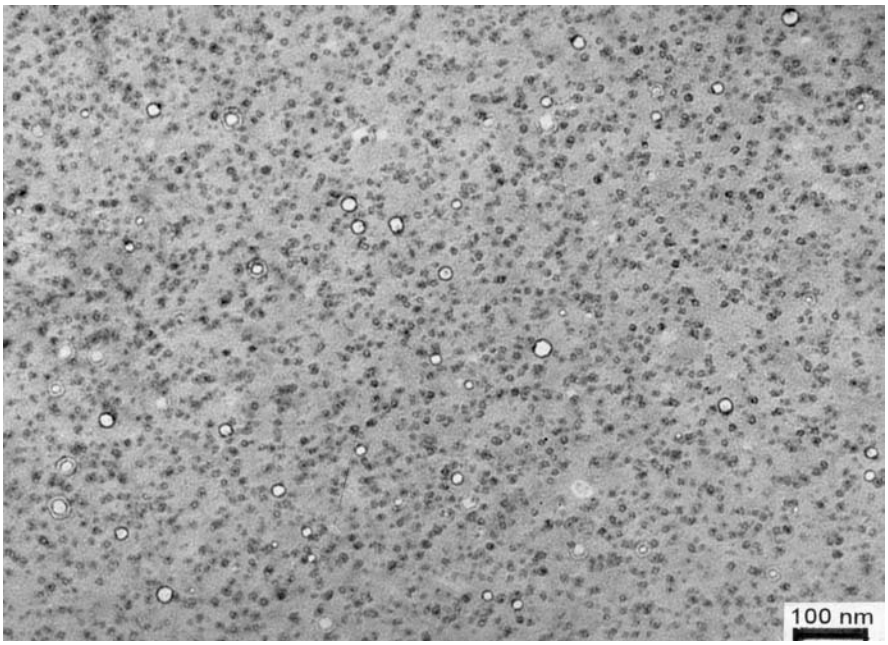

Figure 5. α'-phase precipitates and voids observed in EP-450 irradiated in BN-350 reactor to 56 dpa at 380°C.

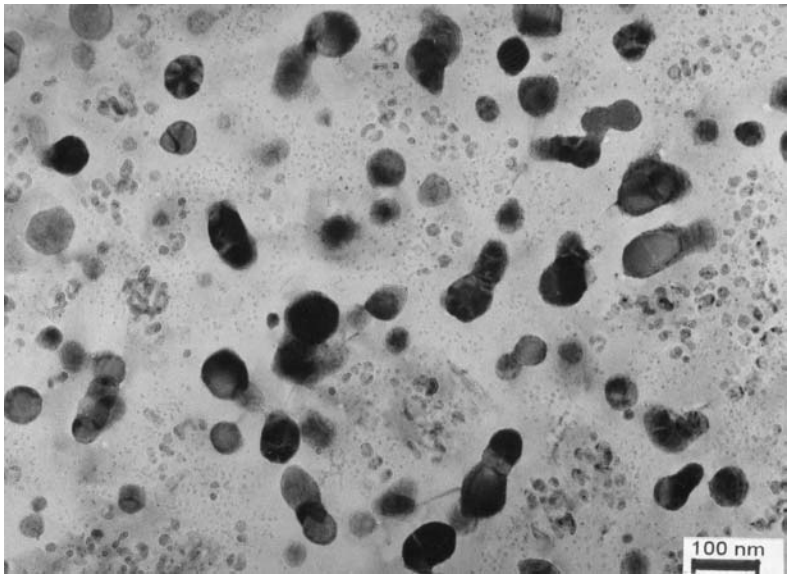

Figure 6. Precipitates of χ-phase in EP-450 irradiated in BN-600 reactor to 81 dpa at 465°C.

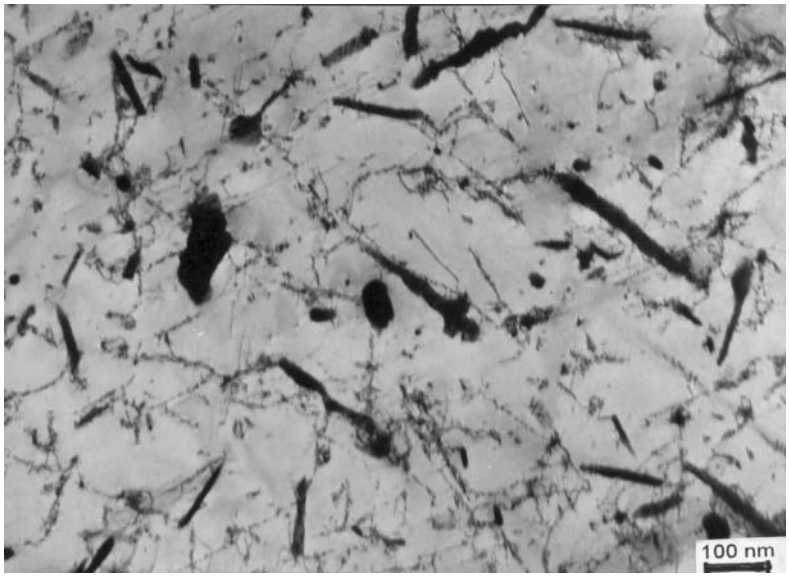

Figure 7. M_2X precipitates observed in EP-450 irradiated in BN-350 reactor to 17 dpa at 690°C.

χ-phase formed in the range 460-590°C, with sizes ranging from 35 to 60 nm that increased with temperature. Their concentration was largest at 515°C and 55 dpa, with a value of 5×10^{20} m^{-3}. M_2X particles formed in the 460-690°C range, with size increasing from 80 to 600 nm with increasing temperature from 460 up to 690°C, but the concentration was constant at ~5×10^{19} m^{-3}.

Irradiation at 510-690°C caused growth of $M_{23}C_6$ on grain boundaries and an increased concentration of carbides on sub-grain boundaries in tempered martensite grains, with the trend increasing with temperature. After irradiation at 690°C blocky precipitates of $M_{23}C_6$ carbides of 100 to 500 nm in size were observed in ferrite grains. In tempered martensite grains additional precipitates did not form, however.

Discussion

Microscopy has confirmed the relatively low susceptibility of the EP-450 steel for neutron-induced swelling in fast reactors. Voids were found in the 275 - 520°C temperature range, but the maximum swelling level at doses to 90 dpa did not exceed 1%.

The maximum average swelling rate of ~1×10^{-2} % /dpa was observed at 395-410°C, but it must be noted that this average is calculated over the entire dose, including that portion associated with the incubation-transition regime. Nevertheless, this maximum rate is much lower than the 2 x 10^{-1} %/dpa maximum swelling rate predicted by Garner and co-workers for ferritic/martensitic steels [4, 5]. It is of interest to note, however, that swelling rate of ~1×10^{-2} % /dpa was observed after irradiation in BR-10 at a rather low displacement rate of 7.6×10^{-8} dpa /s. For comparison, the dose rate in BN-350 and BN-600 is ~ $(1\text{-}2)\times10^{-6}$ dpa /s. Garner and co-workers have predicted that ferritic/martensitic alloys will swell more at lower dpa rates due to a flux-dependent shortening of the transient regime of swelling [4]. They have also explored the competing effects of different He/dpa ratios and dpa rates to influence the duration of the transient regime [6], but in the case of these three fast reactors there are not large differences in neutron spectra and resulting He/dpa ratio.

Previous measurements of mechanical properties of the EP-450 steel have shown that both pin cladding [7] and hexagonal wrappers [8] experience low-temperature irradiation embrittlement. Based on the observations in this paper it appears that the combined effect of dislocation loops and α' precipitates produces the embrittlement of EP-450 steel, especially at lower temperatures where their density is highest. The α' phase, in particular, is known to be responsible for embrittlement during aging and irradiation of chromium steels [9, 10]. It has been particularly established, that the formation of α' is responsible for deterioration of the impact properties of ferritic steels [11].

Conclusions

The microstructure has been studied of EP-450 ferritic/martensitic EP-450 steel after irradiation in three Russian fast reactors when serving as the structural material of hexagonal wrappers and fuel pin cladding at temperatures in the range of 275-690°C up to maximum dose of 89 dpa. It has been shown that radiation-induced microstructural evolution proceeds in a manner which is dependent on irradiation temperature, dpa level and possibly dpa rate. The influence of dpa rate on swelling is of particular interest, leading to earlier and larger levels of void swelling at lower dpa rates, in agreement with the results and predictions of earlier studies. Radiation-induced modification of phase stability was also observed and appears to be strongly related to irradiation temperature.

Acknowledgements

The U.S. portion of this work was jointly supported by the Office of Fusion Energy, and the Office of Nuclear Energy (in support of the Advanced Fuel Cycle Initiative), U.S. Department of Energy, under Contract DE-AC06-76RLO 1830. The Russian data presented in this report was generated earlier in irradiation programs conducted under the sponsorship of the Ministry of Science of the Soviet Union and later evaluated under the sponsorship of MINATOM, of the Russian Federation. The assistance of Natalia A. Brikotnina of Interpreter and Transslation Services to facilitate the discussions and to provide English translations of the various drafts of this work is deeply appreciated.

References

[1] D. S. Gelles, J. Nucl. Mater. 103-104 (1981) 975-980.
[2] D. S. Gelles, J. Nucl. Mater. 148 (1987) 136-144.
[3] D. S. Gelles and L. E. Thomas, Effects of Neutron Irradiation on Microstructure in Experimental and Commercial Ferritic Alloys, Proceedings of Topical Conference on Ferritic Alloys for Use in

Nuclear Technologies, Eds. J. W. Davis and D. J. Michel, Metal Society of AIME, New York (1984) 559-568.

[4] F. A. Garner, M. B. Toloczko, and B. H. Sencer, Comparison of Swelling and Irradiation Creep Behavior of fcc-Austenitic and bcc-Ferritic/Martensitic Alloys at High Neutron Exposure, J. Nucl. Mater. 276 (2000) 123-142.

[5] B. H. Sencer and F. A. Garner, Compositional and Temperature Dependence of Void Swelling in Model Fe-Cr Base Alloys Irradiated in EBR-II, J. Nucl. Mater. 283-287 (2000) 164-168.

[6] F. A. Garner, D. S. Gelles, L. R. Greenwood, T. Okita, N. Sekimura, and W. G. Wolfer, Synergistic Influence of Displacement Rate and Helium/dpa Ratio on Swelling of Fe-(9, 12) Cr Binary Alloys in FFTF at ~400°C, in DOE/ER-0313/33 (December 31, 2002) 122-127; also submitted to J. Nucl. Mater., Proceedings of ICFRM-11.

[7] A. M. Dvoriashin, V. D. Dmitriev, and V. S. Khabarov, ASTM STP 1125 (1992) 1180-1189.

[8] V. S. Khabarov, V. D. Dmitriev, A. M. Dvoriashin, V. V. Romaneev, and E. A. Medvedeva, Mechanical Properties and Microstructure of Neutron-irradiated Ferritic-martensitic Steel, used as Wrapper Material for the BN-350 and BN-600 Fast Reactor, Proc. of Int. Conference “Fast Reactor Core and Fuel Structural Behavior” (Inverness, Great Britain, June 4-6, 1990) 263-267.

[9] T. J. Nichol, A. Datta, and G. Aggen, Metallurgical Transactions 41A, No. 4 (1980) 573.

[10] D. Gilbon, J. L. Seran, and R. Cauvin, ASTM STP 1046 (1989) 5-34.

[11] P. J. Grobner, The 885°F (475°C) Embrittlement of Ferritic Stainless Steels, Metallurgical Transactions 4, No. 1 (1973) 251.

COMPILATION AND PRELIMINARY ANALYSIS OF A IRRADIATION HARDENING AND EMBRITTLEMENT DATABASE FOR 8Cr MARTENSITIC STEELS—T. Yamamoto, G. R. Odette, H. Kishimoto (University of California, Santa Barbara), and J. W. Rensman (NRG, Petten)

OBJECTIVE

The objective of this work is to develop and analyze a database on irradiation hardening and embrittlement of ≈ 8Cr martensitic steels.

SUMMARY

Data on irradiation hardening and embrittlement of 7-9Cr normalized and tempered martensitic steels (TMS) has been compiled from the literature, including results from neutron, spallation proton (SP) and He-ion (HI) irradiations. Limitations of this database are briefly described. Simple, phenomenological-empirical fitting models were used to assess the dose (displacement-per-atom, dpa), irradiation temperature (T_i) and test temperature (T_t) dependence of yield stress changes ($\Delta\sigma_y$), as well as the corresponding dependence of sub-sized Charpy V-notch impact test transition temperature shifts (ΔT_c). The $\Delta\sigma_y$ are similar for SP and neutron irradiations, with very high and low helium to dpa ratios, respectively. The $\Delta\sigma_y$ trends were found to be remarkably consistent with the T_i and dpa hardening-dependence of low alloy steels irradiated at much lower doses. The similar T_i and (low) dose dependence of $\Delta\sigma_y$ and ΔT_c, as well as an analysis of paired ΔT_c-$\Delta\sigma_y$ datasets, show that embrittlement is dominated by a hardening mechanism below about 400°C. However, the corresponding hardening-Charpy shift coefficient, $C_c = \Delta T_c/\Delta\sigma_y \approx 0.38\pm0.18$ is lower than that for the fracture toughness reference temperature (≈ 0.57±0.1), indicating that sub-sized Charpy tests provide *non-conservative* estimates of embrittlement. The C_c increases, or sometimes even takes on negative values, at $T_i \geq 400$°C, indicative of a non-hardening embrittlement (NHE) contribution. Analysis of limited data on embrittlement due to thermal aging supports this conclusion, and we hypothesize that the NHE regime is shifted to lower temperatures by radiation enhanced diffusion. Possible effects of helium on embrittlement are addressed in a companion report.

PROGRESS AND STATUS

Introduction

An important objective for the fusion materials community is to develop a high quality database on the effects of irradiation on the constitutive and fracture properties of 7-9Cr normalized and tempered martensitic steels (TMS). This report focuses on changes in the tensile yield stress ($\Delta\sigma_y$) and irradiation embrittlement characterized by transition temperature shifts (ΔT_c) measured in sub-sized Charpy V-notch impact tests. A high quality database is needed to develop predictive models of the changes in $\Delta\sigma_y$ and ΔT_c (and other properties) as a function of the *combination* of all significant metallurgical and irradiation variables. The metallurgical variables include the start-of-life alloy composition (wt%), microchemistry and microstructure, including the effects of thermo-mechanical processing treatment (TMT). The primary irradiation variables include irradiation temperature (T_i) and the neutron flux (ϕ), energy spectrum [$\phi(E)$] and fluence (ϕt). The neutron irradiation variables and are best represented in terms of the total and rates of production of damaging species, including for displacements-per-atom (dpa), helium, hydrogen and solid transmutation products (appm). Post-irradiation testing and data analysis variables are also significant. For example, $\Delta\sigma_y$ depends on the test temperature (T_t, °C) and $\Delta\sigma_y$ depends on the strain rate ($\dot{\varepsilon}$, s^{-1}). Ultimately a comprehensive and high quality database will be analyzed with physically based, multiscale models [1-3]. Such models will sequentially relate: a) the primary variables to microstructural evolutions; b) the effects of these evolutions on fundamental structure-sensitive constitutive and local fracture properties; c) and the consequences of changes in these fundamental properties to more

complex engineering properties, like ΔT_c (and shifts in fracture toughness reference temperatures) [1-3]. In the interim, simpler phenomenological-empirical models and physically motivated correlations will be used analyze the growing database.

There have been many irradiation studies aimed at contributing to such a database. Among the most notable are the International Energy Agency (IEA) round robin project on the Japanese F82H steel [4,5], as well the large program in Europe currently focusing on various heats of the Eurofer steel [6-8]. There are also other data based on irradiations of TMS with spallation protons (SP), which generate very high levels of helium and hydrogen [9-13]. Other pertinent data includes accelerator based ion irradiations, including with high energy He-ions (HI) [14,15]. In this report, we summarize the preliminary results of an ongoing effort to tabulate and analyze existing $\Delta\sigma_y$ and ΔT_c data on TMS. One objective was to gain a practical, working knowledge of what is required in a mechanical property database to make it functionally useful and of 'high quality'; and to assess the state of the existing data in this context. A second objective was to carry out a simple preliminary analysis to gain insight on the variables that control $\Delta\sigma_y$ and ΔT_c.

Our analysis addresses several specific issues.

- The dpa , T_i, T_t (for $\Delta\sigma_y$) and metallurgical variable dependence of $\Delta\sigma_y$ and ΔT_c.
- The relation between $\Delta\sigma_y$ and ΔT_c to characterize hardening and non-hardening induced embrittlement.
- The reliability of Charpy-based ΔT_c as a surrogate for fracture toughness reference temperature (T_o) shifts (ΔT_o).
- The possible role of irradiation induced or enhanced non-hardening embrittlement (NHE) mechanisms on ΔT_c.

Possible effects of helium on embrittlement are addressed in a companion report [16].

Compilation of the Existing Irradiation Hardening and Embrittlement Data

Detailed descriptions of the development of a computer accessible database will be provided in the future. Most of the data is for neutron irradiations, but we also include a significant body of results of spallation proton (SP) irradiations, which generate from ≈ 60 to 150 appm He/dpa, as well as limited data from high energy He-ion (HI) irradiation studies implanting up to 5000 appm He. Currently, the database consists of 821 entries for determining $\Delta\sigma_y$ and 546 entries for determining ΔT_c. However, not all of the hardening and embrittlement data entries contain sufficient ancillary information to be useful in our analysis.

We first established a set of variables and parameters for each $\Delta\sigma_y$ and ΔT_c entry that are needed in a database for it to be useful. Basically, it is necessary to have comparable baseline and irradiated data and to know the details of[1]: a) the metallurgical variables including alloy composition and TMT processing history; b) the irradiation variables and their history; c) the descriptions of the test procedures and methods used to reduce, analyze and parameterize the data. Of course, it is also important to characterize uncertainties, assumptions and any possible biases in these variables, methods and parameters. There are also often complexities in an experiment that are important to know, such as planned and unplanned variations in T_i. Based on these criteria, it is necessary to conclude that the

[1]Chemical composition, normalizing-tempering temperatures and times, hot/cold work strains; specimen size, geometry, orientation, test temperature, strain rate; irradiation source, dpa dose and dose rate, irradiation temperature, He and H; baseline versus post irradiation tensile (σ_y, σ_u, ε_f, ε_l, ε, RA), Charpy (DBTT, USE, σ_{yd}) – all with uncertainties.

existing data do not yet comprise a high quality and optimally useful database. A partial list of limitations we found is as follows:

- In some cases there was incomplete and uncertain characterization of the alloy and poorly defined pairs of baseline and irradiated data sets.
- Most often there was no indication of uncertainties in key variables, that are known to often be poorly defined, or even biased, particularly T_i.
- Often there is no reported assessment of possible uncertainties or bias in the test measurements and data reduction-parameterization procedures. This is a particular issue for the ΔT_c that often were deduced from a small and, indeed, often insufficient number of specimens.

Due to such limitations, the analysis presented below provides only a systematic, first-iteration assessment of the relations of $\Delta\sigma_y$ and ΔT_c to dpa, T_i, T_t and metallurgical variables. Since many different alloys have been irradiated under very different irradiation conditions it is necessary to reduce the number of independent variables to make the analysis tractable. This is discussed in the next section.

Preliminary Data Analysis [4-15,17-64**]**

We first carry out an analysis involving a minimum number of reduced independent variables. Thus it is necessary first to define broad alloy categories and T_i bins to make the analysis tractable. The lumped data are naturally very scattered, but statistical fits can still be used to establish broad, common trends in $\Delta\sigma_y$ and ΔT_c as a function of dpa, T_i and T_t. Predicted minus measured residual plots, including those for other potential variables not included in the primary fits, can then used to identify inaccuracies and biases in the first-iteration model. The first-iteration model can also be used to adjust the data to a common set of dpa and/or T_i conditions. We divided the alloys into four broad categories: a) F82H; b) Eurofer; c) other 9CrW steels containing 1-2%W; and d) 9CrMo steels containing 0.5 to 1.5%Mo. Except at the lowest and highest irradiation temperatures, the T_i binning, described below, generally ranged from about ±15 to ±25°C around the nominal value. These T_i bins are on the order of the corresponding irradiation temperature uncertainties. In general, the SP irradiation data have larger uncertainties in T_i. The test temperature T_t is also a very important variable. Most often the $\Delta\sigma_y$ data is reported for $T_t \approx T_i$ or $T_t \approx$ 25°C, and sometimes both. The $\Delta\sigma_y$ generally decreases with T_t. Thus, we analyzed available datasets to quantify this effect. However, since there is much more available data, the $\Delta\sigma_y$ results presented in this Section are for nominally $T_t \approx T_{ir}$, except for $T_i < 220$°C, where most of the data is for $T_t \approx 25$°C. In a few cases where only $T_t \neq T_i$ data are available, the data for $T_t \approx T_i \pm 40$ ºC were also included.

Analysis of the $\Delta\sigma_y$ Data [7,9-12,14,17-44]

A useful general fitting expression for $\Delta\sigma_y$ is

$$\Delta\sigma_y = \Delta\sigma_{ys}[1-\exp(-dpa/dpa_o)]^p + \Delta\sigma_o \qquad (1)$$

Here $\Delta\sigma_{ys}$ is a saturation hardening, dpa_o specifies the dose transient prior to saturation, and p is an effective dispersed-barrier hardening exponent. The constant hardening increment, $\Delta\sigma_o$, allows for either a) a very rapid, but saturating, low dose hardening mechanism; or b) a threshold dose for the initiation of hardening. The saturating form of Equation 1 can be physically related to the depletion of solutes, in the case of a precipitation hardening mechanism, or an excluded volume effect in the case of the accumulation of displacement damage-type defects. The initial rate of hardening is characterized by $\Delta\sigma_{ys}/dpa_o^p$.

More complex forms and detailed physical models could be used, but they must be based on comprehensive microstructural observations and more detailed mechanistic understanding and models than are within the scope of this initial report. In the case of simple dispersed barrier hardening with one type, size and strength of hardening feature, and with a number density that initially increases linearly with dose, p ≈ 1/2. This is the so-called Makin and Minter model [45,46]. However, p may deviate from a value of 1/2 for a wide variety of reasons. These include combinations of increases in the size of a fixed number of features, size-dependent feature dislocation obstacle strength, distributions in the number, sizes and strengths of features and superposition of the strengthening contribution of various features. However, in view of the limitations of the present database, and the desire to make cross-comparisons between alloy classes and at different T_i, we sought simplicity and consistency in the first-iteration fitting form, rather than additional complexity. Thus, we fixed a value of p = 1/2 and $\Delta\sigma_o = 0$. Note that this fitting expression has the advantage that low dose data can be used to obtain good estimates the combined $k = \Delta\sigma_{ys}/\sqrt{dpa_o}$ fit parameter, even in the absence of high dose data. Thus broad trends in the $\Delta\sigma_{ys}$ and dpa_o can then be used in such cases to derive a self-consistent model.

Figure 1a to g shows plots of $\Delta\sigma_y$ versus √dpa for T_i bins of: a) 25-220°C (nominal 120°C); b) 250-280°C (nominal 265°C); c); nominal 300°C, d) 300-360°C (nominal 330°C); e) 365-390°C (nominal 380°C); f) 400-440°C (nominal 420°C); g) and > 440°C.[4,7,9-12,14,17-44] The black solid lines are $\Delta\sigma_y = C_\sigma\sqrt{dpa}$ fits for the low dose data (note, $C_\sigma \approx k$) and the black solid-double-dashed lines are the fits for the saturating form given in Equation 1 with p = 1/2 and $\Delta\sigma_o = 0$. The neutron, SP and HI irradiation data are shown as filled symbols, open diamonds and crosses respectively. The symbol colors are used to code the alloy class with red, blue and green for F82H, 9Cr-W and 9Cr-Mo alloys, respectively. The first-iteration fits are for neutron and SP irradiations of all the alloys in each of the nominal T_i bins.

Figure 1a shows the results for $T_i < 220$°C. The majority of the data is for SP irradiations of 9Cr-1Mo steels. The scatter bands for the SP and neutron irradiations overlap. Farrell reported that the heavy purple dashed line shown in Figure 1a, which falls near the top of the SP irradiation scatter band, provides a good fit for both the SP neutron data for irradiations in the High Flux Isotope Reactor at doses between ≈ 0.05 and 1 dpa [34]. The dashed box distinguishes the SP irradiations producing ≈ 150 appm He/dpa from cases with lower He/dpa ratios from ≈ 60 to 80 appm He/dpa. The $\Delta\sigma_y$ data at the higher He/dpa tend to fall on the high side of the SP irradiation scatter band, and hardening continues to a higher dpa in this case. Except for this single high helium SP irradiation data point, however, both the neutron and SP irradiation hardening appears to be saturating at $\Delta\sigma_{ys} \approx 346$ MPa at a low $dpa_o \approx 0.7$ dpa. The single HI irradiation $\Delta\sigma_y$ data point, with a high He/dpa ratio ≈ 6300 appm/dpa, falls substantially above the scatter bands for both the SP and neutron irradiations.

In the case of $T_i \approx 265$°C, shown in Figure 1b, most of the data is for neutron irradiations, except of the highest dose data for SP irradiations to ≈ 9 dpa. The latter was used to fit the saturating form for $\Delta\sigma_y$. Saturation occurs at a higher $dpa_o \approx 4.5$ than for the $T_i = 120$°C irradiations. There is not a large and systematic difference in the $\Delta\sigma_y$ for the various alloys classes. The nominal saturation $\Delta\sigma_{ys} \approx 419$ MPa, is actually slightly higher at 265°C compared to the lowest T_i. The hardening rate for HI irradiations is again substantially higher than for neutrons.

The data shown in Figure 1c is based on a recent set of neutron irradiation $\Delta\sigma_y$ data reported by Rensman [8] for a narrow range of $T_i \approx 300$°C. The data for various T_t have been adjusted to a common value of 300°C using a relation also derived by Rensman [8]. The 9Cr-W data in this case are for various heats of Eurofer. Although limited to doses less than 10 dpa, the 300°C results constitutes a very high quality dataset and can be considered a lynchpin for other parts of the database and analysis. While the dose does not reach saturation levels, the data are sufficient to provide good estimates for both $\Delta\sigma_{ys} \approx 489$ MPa and $dpa_o \approx 6.8$ dpa. As shown below, this $\Delta\sigma_{ys}$ is higher than at any other T_i, but both the $\Delta\sigma_{ys}$ and dpa_o are reasonably consistent with extrapolations of the trends at higher and lower T_i. The heavy dashed

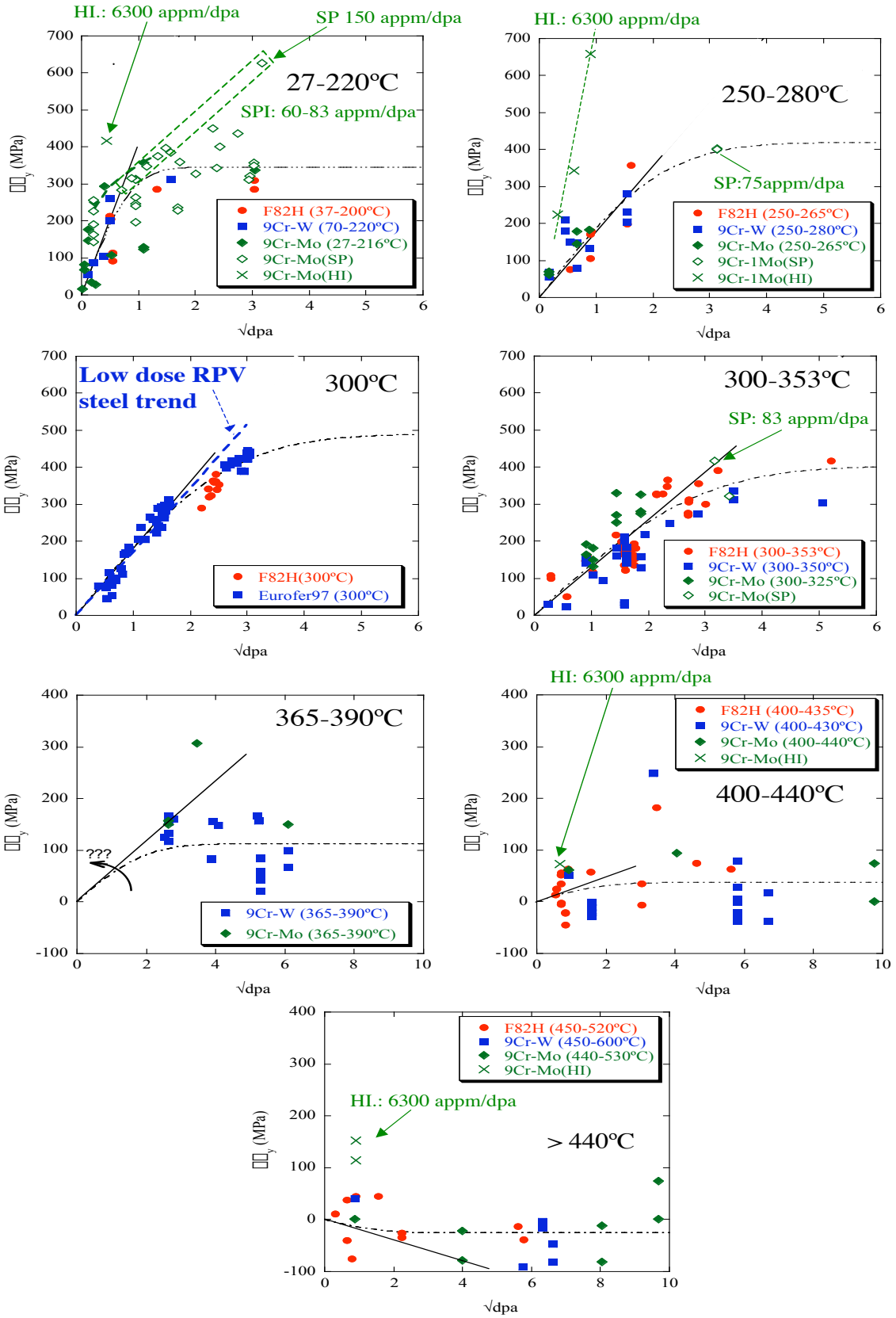

Figure 1. The √dpa dependences of $\Delta\sigma_y$ for the temperature bins, (a) 25-220 ºC, (b) 250-280 ºC, (c) 300 ºC , (d) 300-360 ºC, (e) 365-390 ºC (f) 400-440 ºC and (g) > 440 ºC.[4,7,9-12,14,17-44]

blue line show an extrapolation of the typical hardening predicted for low Cu (< 0.07%) low alloy (C-Mn-Si-Mo-Ni) quenched and tempered bainitic RPV steels irradiated at ≈ 290°C to a much lower maximum dpa of < 0.06 dpa, is in remarkably good agreement with initial $\Delta\sigma_y$ trend for the TMS in the dose range up to a few dpa.

With the exception of two spallation proton irradiation data points the $\Delta\sigma_y$ at T_i = 330°C shown in Figure 1d are for neutron irradiations. Note, this dataset also includes some F82H and Eurofer data previously reported by Rensman. There is an apparent trend towards saturation at a larger dpa_o ≈ 8.0 dpa than at both T_i = 265°C and 300°C. In general the $\Delta\sigma_y$ data for the 9Cr-1Mo alloys fall above the hardening in the F82H and 9Cr-W alloys, with the SP irradiation data lying near the lower bound of the scatter band for this steel class. In this case, the nominal saturation $\Delta\sigma_{ys}$ ≈ 403 MPa is lower than that for both the 265 and 300°C irradiations.

As shown in Figures 1e and f, the data is sparser at $T_i \geq$ 380°C, but, in this case, extend to a significantly higher dpa for the irradiations which were carried out in fast reactors. The $\Delta\sigma_{ys}$ = 112 MPa at T_i = 380°C and = 37 MPa at 420°C are much less than for the lower T_i. There is no low dose data in the transition in these cases to evaluate dpa_o. Thus we used extrapolations of the trend in $\Delta\sigma_{ys}/\sqrt{dpa_o}$ from lower T_i to estimate dpa_o in this case. The $\Delta\sigma_y$ for the 9Cr-1Mo alloys are again higher than for the other steels (note, there is no F82H data at T_i = 380°C). There is a tendency towards modest softening ($\Delta\sigma_y < 0$) at $T_i >$ 440°C. Much higher hardening is observed for the HI irradiations at both T_i = 420 and > 440°C.

Clearly, the reduced variable datasets are highly scattered. However, this is not surprising since, there are both a variety of sources of uncertainty and potential biases in the data, which represent different alloys, irradiation particles and a range of T_i and T_t, within the various data groupings. However, in spite of the scatter, the fits can be used to establish broad trends in the database. Cross-plots of the fitting results as function of T_i are shown in Figure 2. Figure 2a plots the initial hardening rate coefficient $k = \Delta\sigma_y/\sqrt{dpa_o}$, the $\Delta\sigma_y$ at 2 dpa and the saturation hardening, $\Delta\sigma_{ys}$. The T_i-dependence of the $\Delta\sigma_y$ parameters decreases with increasing dose below T_i ≈ 300°C, but remains strong at higher T_i even for $\Delta\sigma_{ys}$. The heavy red dashed lines show a temperature dependence predicted by a relation

$$\Delta\sigma_y(T) = f_T(T)\Delta\sigma_y(T_r) \qquad (2)$$

Here $f_T(T)$ is a function independently derived by Jones and Williams for very low dose irradiation hardening of both C-Mn ferritic and RPV bainitic steels [67]. The reference temperature, T_r, at $f_T(T_r) = 1$ is taken as 300°C. The agreement between the predictions based on data fit for very low dose ferritic and bainitic steel irradiations and the trend for much higher dose $\Delta\sigma_y(T_i)$ data for TMS is striking, and lends considerable confidence to the results of the analysis shown in Figure 2a. Figure 2b shows that saturation dose parameter, dpa_o, increases systematically with increasing T_i up to ≈ 330°C, and then apparently decreases at higher T_i. Due to the paucity and scatter in the data, the estimates of $\Delta\sigma_{ys}$ (at lower T_i) and dpa_o (at higher T_i), are very uncertain, but generally follow systematic and reasonably self-consistent trends.

As noted above, Rensman has suggested that the effect of test temperature and also be treated by a dose-independent adjustment factor, $g(T_t) = \Delta\sigma_y(T_t)/\Delta\sigma_y(25°C)$ that he derived from his T_i ≈ 300°C database [8]. This $g(T_t)$, is shown Figure 3 along with the corresponding $g(T_t)$ for sets of $\Delta\sigma_y(T_t)$ in our database. The data are restricted to $T_t \leq T_i$ + 50°C to avoid excessive damage annealing. The results scatter around the Rensman's $g(T_t)$ but yield a similar mean trend shown by the dashed least squares fit line.

Figure 2 constitutes a first-iteration model for $\Delta\sigma_y(dpa,T_i)$ for $T_i \approx T_t$. Interpolations of the k and dpa_o the between the nominal T_i can be used to adjust the individual data to a common set of conditions. The

results of adjusting the $\Delta\sigma_y$ for the irradiations between $T_i \approx 250$ and 360°C to a common $T_i = T_t = 300$°C are shown in Figure 4. While there is considerable scatter, Equation (1) can be fit to the individual alloy subsets of data. The average $dpa_o \approx 7.7 \pm 2.8$ dpa for 9CrW, 9CrMo and Eurofer 97 was used to fit the F82H data. The standard deviation between the measured and predicted values is ≈ 64, 64, 56 and 54 MPa for F82H, 9CrW, 9CrMo and Eurofer97, respectively. The, adjusted F82H data deviate most from the assumed fitting form. The limited SP irradiation $\Delta\sigma_y$ appear to fall below the neutron irradiation trends, but this is probably an artifact of the analysis. Further refinement of the model, in part based on analysis of the residuals, will be carried out in the next reporting period. In summary, irradiation hardening can be

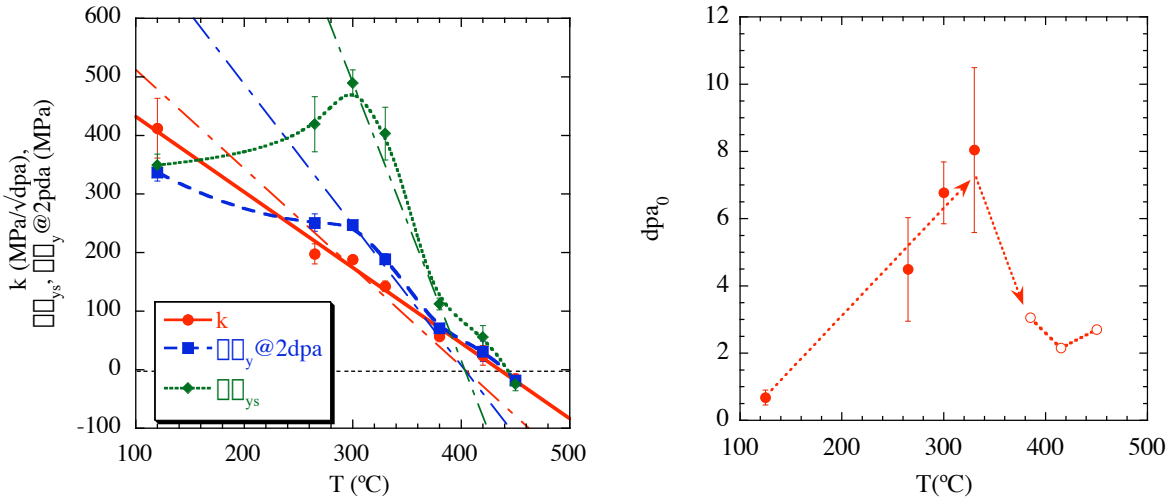

Figure 2. (a) Temperature dependences of the initial hardening rate, k (MPa/√dpa), hardening at 2 dpa, and the saturation hardening, $\Delta\sigma_{ys}$, evaluated from the fits shown in figure 1 a-g. The f_T relations to the various hardening values at 300 ºC are also plotted as the dotted-dash lines. The trends are in excellent agreement with the low dose TMS data and remain a good approximation for $300 < T_i < 400$ ºC. (b) Temperature dependences of the dpa_o. The values for the three higher temperatures (open symbols) were estimated from the linear fit of k shown in (a) and $\Delta\sigma_{ys}$.

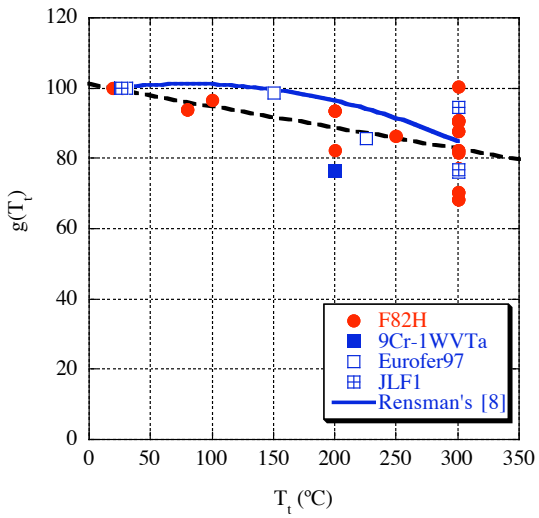

Figure 3. $g(T_t)$ (solid line) from Rensman and the UCSB $\Delta\sigma_y(T_t)/\Delta\sigma_y(25$ ºC) data and fit (dashed line).

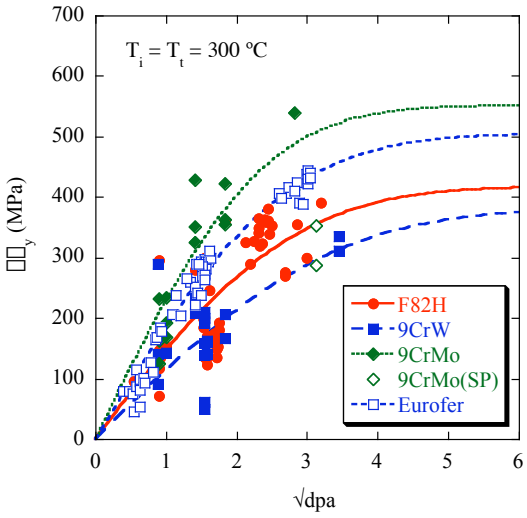

Figure 4. The $\Delta\sigma_y$-√dpa data adjusted common $T_i = T_t = 300$ ºC along with fits for the different alloys

described by a saturating function of the √dpa that is characterized by a saturation hardening, $\Delta\sigma_{ys}$, and a saturation dose parameter, dpa_o. The $\Delta\sigma_{ys}$ peaks at ≈ 490 MPa at $T_i \approx 300°C$. The saturation $\Delta\sigma_{ys}$ depends weakly on T_i at less than ≈ 300 °C, but decreases rapidly at higher temperatures, with softening observed at $T_i > 440°C$. The saturation dose parameter, dpa_o, increases up to ≈ 330°C, but also appears to decreases at higher T_i. The low dose range irradiation hardening trends in the TMS are remarkably similar to those observed for very low dose irradiations of ferritic (C-Mn-Si) and low alloy (C-Mn-Si-Mo-Ni) bainitic RPV steels. The SP $\Delta\sigma_y$ are similar to or less that for neutron irradiations, at least for T_i between 250 and 360°C. The $\Delta\sigma_y$ also decreases with increasing T_t, in a way that can be approximately accounted for with the adjustment factor shown in Figure 3. Finally, there are systematic differences in the $\Delta\sigma_y$ trends for the various alloy classes that will be assessed in more detail in the future.

Preliminary Analysis of the ΔT_c Data [4,7,36-59]

We carried out a similar analysis of ΔT_c as a function of dpa and T_i. However, in this case, the alloy classes were analyzed separately, since there were more significant differences between the various steels and a common T_i binning was not as useful. The data, which in most cases were very scattered, could be reasonably fit using a simpler function

$$\Delta T_c = C_c\sqrt{dpa} \qquad (3)$$

The ΔT_c versus √dpa data and C_c fits are shown in Figure 5a to c [4,7,36-59]. Note, these plots do not include the complete database assembled by Schneider and co-workers [60] on a variety of 9Cr-W steels, including some alloys with Ni additions, as well as F82H. This large database is currently being analyzed great detail. The analysis will be completed during the next reporting period. However, preliminary results, pertaining to the possible effect of He on NHE, are discussed in a companion report [16]. Figure 6 shows a cross plot of C_c from the fits in Figure 5 as a function of T_i. The 9Cr-Mo and F82H alloys show the lowest and highest C_c, respectively, with the 9Cr-W steels generally falling between, but closer to F82H. The T_i dependence of the C_c is in reasonable agreement with the corresponding T_i-dependence of the average hardening rates up to 2 dpa shown as dashed color-coded lines multiplied by $\Delta T_c/\Delta\sigma_y$ conversion factors of = 0.18, 0.3 and 0.36°C/MPa for the 9Cr-Mo, 9Cr-W and F82H, respectively Notably, these values of $\Delta T_c/\Delta\sigma_y$ are much less than the $\Delta T_o/\Delta\sigma_y \approx 0.57\pm0.1$°C/MPa found in for fracture toughness reference temperature shifts [1]. In the case of F82H, a significant ΔT_c persists in the $T_i > 400°C$, when irradiation hardening is minimal or when softening is observed. Note that high, and even negative values, of $\Delta T_c/\Delta\sigma_y$ are also observed in the Schneider database for $T_i = 450°C$.

Figure 7 plots the available paired ΔT_c and $\Delta\sigma_y$ datasets, including results from the preliminary assessment of Schneider database. In the latter case, the $\Delta\sigma_y$ is based on measurements of changes dynamic yield stress. Figure 7a shows the results for $T_i < 400$ and Figure 7b is for $T_i \geq 400°C$. Where possible, the $\Delta\sigma_y$ are for $T_t = 25°C$. However, the $T_t = 25°C$ data is limited for static tensile test measurements of $\Delta\sigma_y$, and the open symbols are for cases when only $T_t \approx T_i$ are available. The lines show the nominal and ± one standard deviations fits for static tensile data only. Note the data with $\Delta\sigma_y < 0$ are not used in these fits. Once again, the data are highly scattered. The fitted $\Delta T_c/\Delta\sigma_y$ are ≈ 0.38±0.18°C/MPa for $T_i < 400$ and 0.75±0.44°C/MPa for $T_i \geq 400°C$ bin. Schneider's database also showed similar trends with $\Delta T_c/\Delta\sigma_y \approx 0.41 \pm 0.17$ °C/MPa for $T_i < 400$ and 0.75±1.07°C/MPa for $T_i \geq 400°C$ bin. These results are consistent with the trends observed for F82H and the 9Cr-W steels in Figure 5, showing that $\Delta T_{ic}/\sqrt{dpa}$ persists above 400°C when $\Delta\sigma_y \approx 0$ or is even < 0. Thus again the $\Delta T_c/\Delta\sigma_y$ for $T_i < 400°C$ are much lower than the $\Delta T_o/\Delta\sigma_y \approx 0.57\pm0.1$°C/MPa for the corresponding fracture toughness reference temperature shifts [1].

These results lead to two very important conclusions:

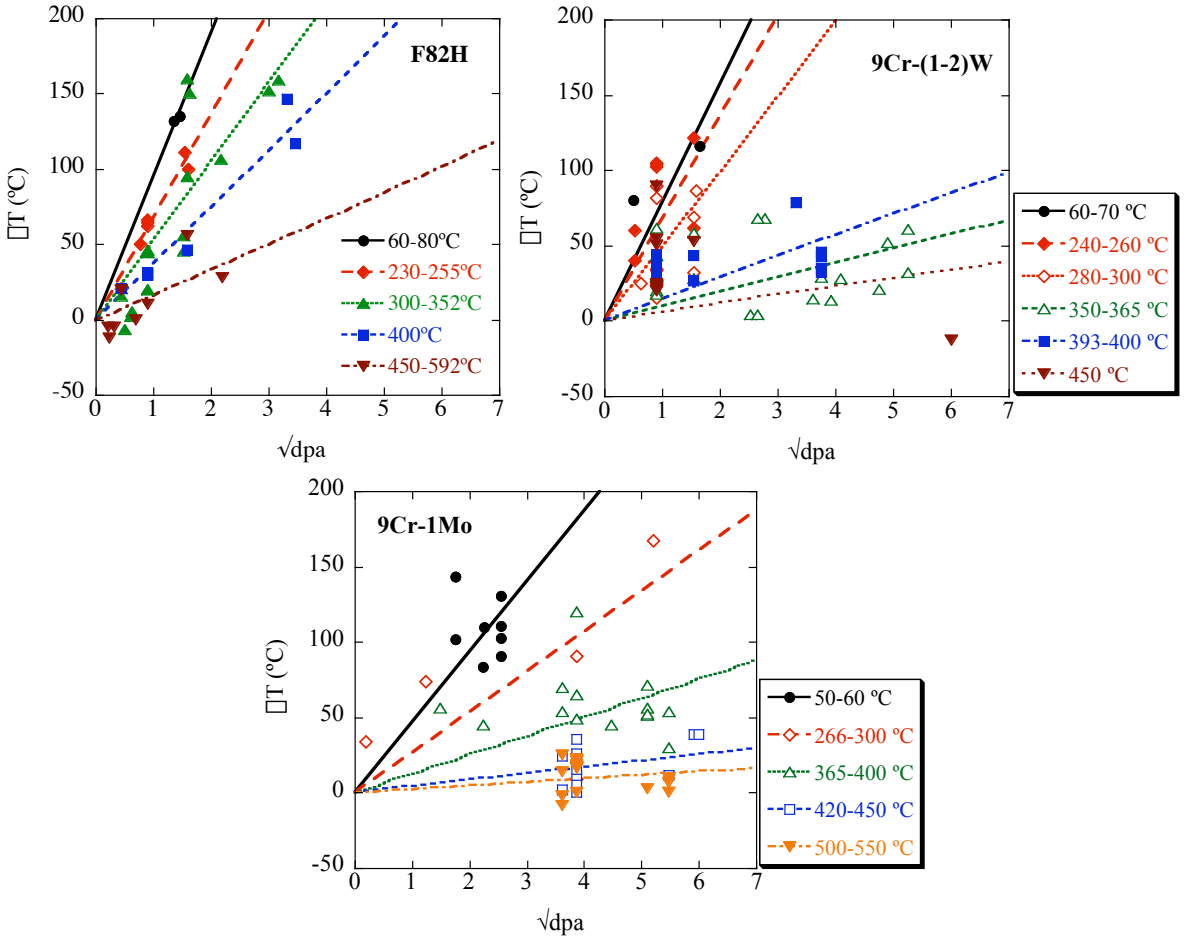

Figure 5. The √dpa dependence of ΔT_c for (a) F82H, (b) 9Cr-W and (c) 9Cr-Mo steels. [4,7, 36-59]

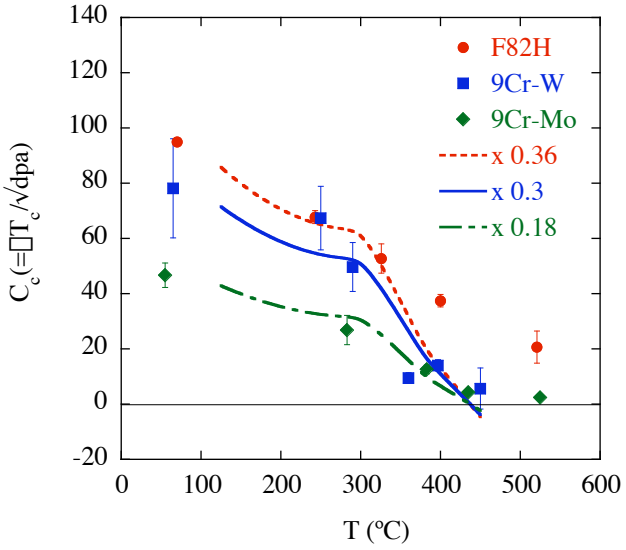

Figure 6. Embrittlement rate C_c vs. temperature of each steel group with accordingly multiplied average hardening rate up to 2 dpa.

- The $\Delta T_c/\Delta\sigma_y$ irradiations at T_i < 400°C are generally less than the corresponding fracture toughness indexed $\Delta T_o/\Delta\sigma_y$ shifts. Thus the ΔT_c from sub-sized Charpy tests are probably non-conservative, and may seriously underestimate the potential of martensitic steels to experience severe irradiation embrittlement. Assuming a nominal $\Delta T_o/\Delta\sigma_y \approx 0.6\pm0.1$°C/MPa and a maximum $\Delta\sigma_y$ = 600 MPa leads to an estimated $\Delta T_c \approx 360\pm60$°C. In a companion report we show that the $\Delta T_c/\Delta\sigma_y$, hence presumably $\Delta T_o/\Delta\sigma_y$ as well, may be even larger for steels containing high levels of He, which would likely result in unacceptable ΔT_o.

- The $\Delta T_c/\Delta\sigma_y$ are larger for irradiations at $T_i \geq 400$°C; and in some cases $\Delta T_c > 0$ for $\Delta\sigma_y < 0$, indicating a contribution of NHE.

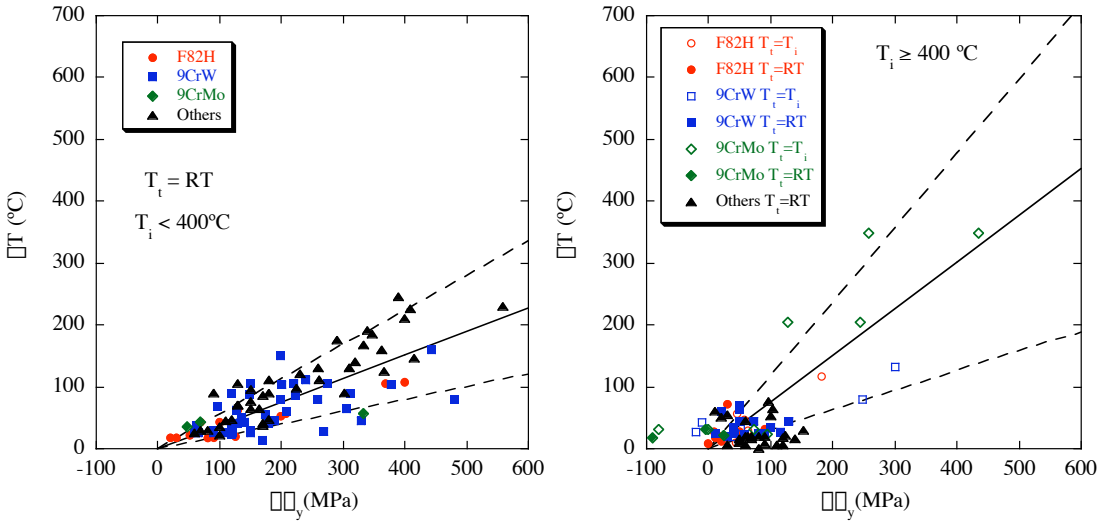

Figure 7. ΔT vs. $\Delta\sigma_y$ plots from paired datasets from (a) T_i < 400 and (b) $T_i \geq$ 400 ºC. [8,15,19,21,25,29,32,36-38,40,41,43,44,46,50,52,54,55,57,59-64]

Non-Hardening Embrittlement

The persistence of ΔT_c to higher temperatures and large or negative values of $\Delta T_c/\Delta\sigma_y$ signal a non-hardening embrittlement (NHE) contribution. There are several potential sources of NHE that occur primarily at higher temperatures under thermal aging conditions, including some that may also be assisted by irradiation:

- Precipitation (Laves) and coarsening (carbides) of brittle grain boundary phases that act as cleavage 'trigger-particle' or brittle grain boundary fracture paths.

- Grain boundary segregation of trace impurities, such as P, and/or depletion of beneficial elements like C.

- Instabilities in the dislocation and lath-packet substructures leading to larger effective subgrain sizes.

- Development of damage, particularly on grain boundaries, in the form of microcracks, gas bubbles and creep cavities. The potential for NHE by high concentrations of helium are discussed in a companion report.

- High concentrations hydrogen is a major source of NHE. One manifestation of such hydrogen embrittlement (HE) in steels is associated with the reduced cohesion of grain boundaries where it is segregated to much higher concentrations than in the bulk. HE is enhanced by high strength levels, hence may be synergistic with irradiation hardening.

NHE due to precipitation and solute segregation can result from by radiation-enhanced diffusion (RED) and radiation induced segregation (RIS). Further, excess fluxes of point defects enhance structural instabilities, like dislocation recovery. In particular, the diffusion controlled, lower leg of a time-temperature ΔT_c C-curve is shifted to lower temperatures by RED. The T_i corresponding to a bulk RED coefficient (D*) under irradiation that is the same as the thermal diffusion coefficient (D_{th}) at the higher aging temperature T_a can be estimated from

$$T_i = T_a\{1-[RT_a/Q_d]\ln(r)\} \quad (4)$$

Here Q_d is activation energy for thermal diffusion and r is the D^*/D_{th} ratio at T_i. Assuming a reasonable value of $r = 10^4$ at a dose rate of $3x10^{-7}$dpa/s and Q_d = 300 kJ/mole, $T_t \approx 405°C$ for $T_a = 600°C$. The NHE kinetics would be further accelerated if irradiation enhances other rate limiting steps like nucleation or dissolution. Note, however, the effects or RED on grain boundary dominated transport processes are likely to be less significant and have not been modeled. Further, NHE associated with RED processes like precipitation are bounded by factors such as solute depletion, or may transform to slower kinetics, like coarsening versus growth of a brittle phase.

The limited data on thermal embrittlement of 7-9Cr martensitic steels [68-72] is summarized in Figure 8 as a plot of ΔT_c versus t_a for various alloys and T_a. Notably, significant ΔT_c are observed for aging ≤ 10000h in the T_a range from 500 to 650°C. As expected, ΔT_c increases with t_a and T_a. The apparently linear increase with t_a and the rather modest T_a-dependence are not understood. This NHE due to thermal aging is probably due to precipitation of brittle Laves (nominally Fe_2W) phases on the grain boundary. Thus, as expected, the alloy JLS-2 with 3%W has a somewhat larger ΔT_c compared to F82H with 2%W. The legend in Figure 8 also shows the equivalent temperature under RED conditions based on Equation 4 and the parameters cited above.

Figure 9 plots an embrittlement time (or inverse rate) parameter $\ln(t_a/\Delta T_c)$ versus T_a for the F82H alloys. The dashed line shows the prediction of Equation 4 and associated parameters described for the effect of RED. The star symbols show the corresponding embrittlement rate for the irradiated data shown in Figure 4 at ≈ 400 and 500°C for a dpa rate of $3.5x10^{-7}$/s (≈ 10 dpa/yr). The NHE data in Figure 9 is in reasonable agreement with the predicted effect of RED, but has a temperature-dependence that is opposite to that predicted by the simple model. In part, this may be due to ignoring a contribution to ΔT_c from irradiation hardening at 400°C and possible softening effect at ≈ 500°C. However, these results do indicate that significant ΔT_c associated with irradiation enhanced NHE processes can be expected at T_i > 400°C. While such NHE may or may not itself be a major problem, it will be likely to interact synergistically with other hardening and NHE mechanisms, potentially producing large ΔT_c.

NHE is most often accompanied by a transition from transgranular cleavage fracture (TGC) to intergranular fracture (IGF) along weakened prior austenitic grain (or other) boundaries. As discussed elsewhere [1], the transition to IGF can be conceptually linked to gradual decrease of a critical grain boundary fracture stress σ_{ig}* to the point where it falls below the critical stress, σ*, for TGF. Developing an IGF ΔT_c model will be pursued during the next reporting period.

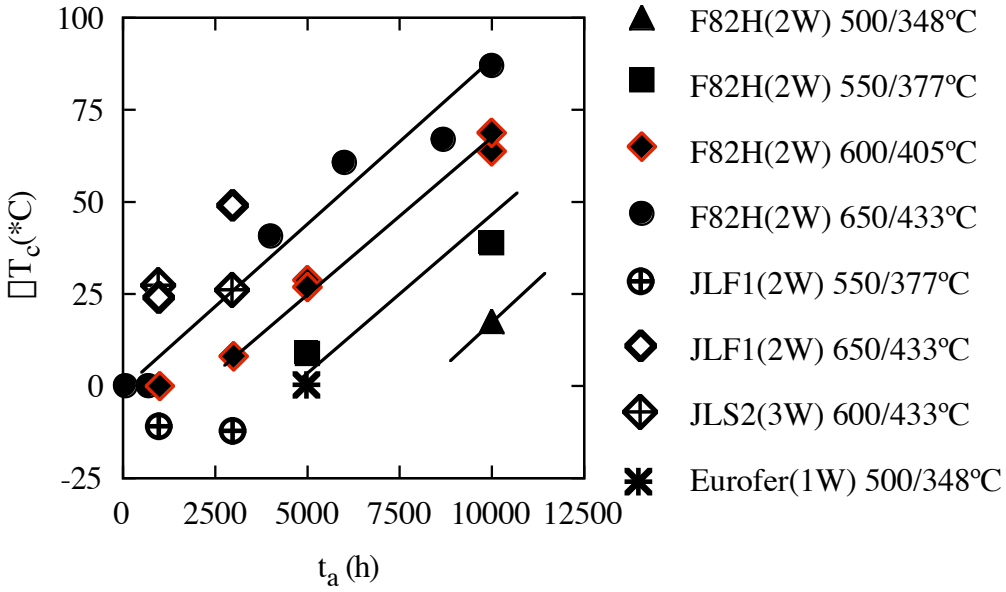

Figure 8. Charpy ΔT_c versus aging time t_a and temperature, T_a [68-72]. The second entries are estimates of the equivalent temperatures accounting for RED, assuming a dose rate of $3x10^{-7}$dpa/s and Q_d = 300 kJ/mole.

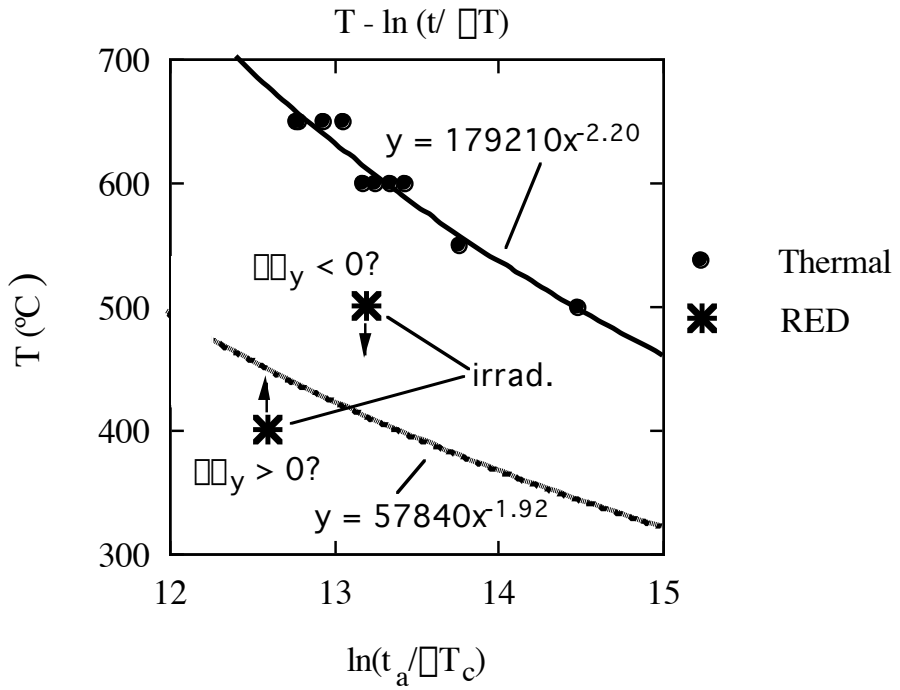

Figure 9. The embrittlement time (or inverse rate) parameter $\ln(t_a/\Delta T_c)$ versus T_a for F82H alloys. The dashed line shows the prediction of Equation 4 and associated parameters described for the effect of RED. The star symbols show the corresponding embrittlement rate for the irradiated data shown in Figure 4 at ≈ 400 and 500°C assuming a dpa rate of $3.5x10^{-7}$/s (≈ 10 dpa/yr).

Discussion, Summary, and Conclusions

This initial report on developing and analyzing a comprehensive database on irradiation effects on the mechanical properties of ≈8Cr TMS should be viewed as a first step and work in progress on a long-term effort. However, the preliminary evaluation of the T_i and dpa-dependence of irradiation hardening, $\Delta\sigma_y$, and embrittlement, ΔT_c, has provided considerable insight that will help guide future research. First, it is clear that the existing database is not sufficient. Future, experiments must strive to avoid uncontrolled variables and confounding variable combinations, as well as providing sufficient detail to be compatible with inclusion in a high quality database. These details should include explicit estimates of uncertainties in key parameters, such as the irradiation temperature, T_i.

In spite of the limitations in the database, however, our analysis provided a first-iteration empirical model of the dpa, T_i and T_t dependence of $\Delta\sigma_y$ and ΔT_c. This model will be refined in the future, but demonstrates that very large $\Delta\sigma_y$ approaching 600 MPa can be anticipated at high dose at T_i around 300°C at lower T_t that are pertinent to embrittlement. There appear to little or no systematic differences between hardening produced by spallation proton (SP) and neutron irradiations with very high and low He/dpa ratios, respectively. Our analysis also shows that embrittlement is dominated by hardening below $T_i \approx 400$°C. The hardening-shift coefficients, $C_c = \Delta T_c/\Delta\sigma_y$, for sub-sized Charpy tests are lower than for fracture toughness reference temperature shifts, ΔT_o. Thus ΔT_c is a *non-conservative* measure of embrittlement. Clearly, future irradiation experiments must focus on establishing a comprehensive ΔT_o database as well as for other fracture toughness properties, like ductile tearing resistance.

Our analysis also suggests that a non-hardening embrittlement (NHE) contribution to ΔT_c occurs at $T_i >$ 400°C. The NHE can be rationalized on the basis of decreases in temperatures normally associated with embrittlement due to thermal aging at temperatures > 500°C, possibly due to radiation enhanced diffusion (RED). While probably not a major issue per se, such NHE may act synergistically with hardening and other NHE mechanisms, such as those due to high concentration of H and He. The potential effects of He on NHE are addressed in a companion report.[16] NHE is generally associated with a transition from transgranular cleavage (TGC) to intergranular fracture (IGF). However, previous fractography studies to characterize such transitions have been very limited and must be a major focus of future work.

Future Research

Research during the next reporting period will focus on continued development and analysis of the database. This includes completing the analysis of the large Schneider ΔT_c database and extending our recent work on developing a database on fracture toughness. We will also continue to develop micromechanical mechanical property models for analysis and application of the growing database. Finally, we will initiate an effort to develop a complementary microstructural database.

Acknowledgements

The authors explicitly acknowledge the extensive research that produced the data analyzed in this report and thank the researches cited in the references for their major contributions to the development of materials for fusion reactors.

References

[1] G. R. Odette, T. Yamamoto, H. J. Rathbun, M. Y. He, M. L. Hribernik, and J. W. Rensman, J. Nucl. Mater. 323 (2003) 313.
[2] G. R. Odette, B. D. Wirth, D. J. Bacon, and N. M. Ghoniem, MRS Bull. (2001) 176.
[3] S. Jumel et al., J. Test. Eval. 30-1 (2002) 37.

[4] K. Shiba, A. Hishinuma, A. Toyama, and K. Masamura, Properties of the reduced activation ferritic steel F82H IEA heat (in Japanese) JAERI-Tech 97-038.
[5] K. Shiba, M. Suzuki, and A. Hishinuma, J. Nucl. Mater. 233-237 (1996) 309.
[6] H. E. Hofmans, Tensile and impact properties of Eurofer97 plate and Bar, NRG Petten 200023/00.381153/P.
[7] J. Rensman, H. E. Hofmans, E. W. Schuring, J. van Hoepen, J. B. M. Bakker, R. den Boef, F. P. van den Broek, and E. D. L. van Essen, J. Nucl. Mater. 307-311 (2002) 250.
[8] J. Rensman, ICFRM11.
[9] K. Farrell and T. S. Byun, J. Nucl. Mater. 296 (2001) 129.
[10] J. Henry, X. Averty, Y. Dai, P. Lamagnére, J. P. Pizzanelli, J. J. Espinas, and P. Wident, J. Nucl. Mater. 318 (2003) 215.
[11] S. A. Maloy, M. R. James, G. Willicutt, W. F. Sommer, M. Sokolov, L. L. Snead, M. L. Hamilton, and F. Garner, J. Nucl. Mater. 296 (2001) 119.
[12] Y. Dai, X. J. Jia, and K. Farrell, J. Nucl. Mater. 318 (2003) 192.
[13] X. Jia and Y. Dai, J. Nucl. Mater. 323 (2003) 360.
[14] P. Jung, J. Henry, J. Chen, and J.-C. Brachet, J. Nucl. Mater. 318 (2003) 241.
[15] R. Kasada, T. Morimura, A. Hasegawa, and A. Kimura, J. Nucl. Mater. 299 (2001) 83.
[16] G. R. Odette, T. Yamamoto, and H. Kishimoto, Fusion Materials Semiannual Report 7/1 to 12/31/2003, DOE/ER-313/34.
[17] A. Kimura, T. Morimura, M. Narui, and H. Matsui, J. Nucl. Mater. 233-237 (1996) 319.
[18] R. Kasada, A. Kimura, H. Matsui, and M. Narui, J. Nucl. Mater. 258-263 (1998) 1199.
[19] P. Spätig, R. Schaublin, S. Gyger, and M. Victoria, J. Nucl. Mater. 258-263 (1998) 1345.
[20] R. Kasada, A. Kimura, H. Matsui, A. Hasegawa, and M. Narui, J. Nucl. Mater. 258-263 (1998) 360.
[21] R. Lindau, A. Möslang, D. Preininger, M. Rieth, and H. D. Röhrig, J. Nucl. Mater. 271&272 (1999) 450.
[22] Y. Dai, S. A. Maloy, G. S. Bauer, and W. F. Sommer, J. Nucl. Mater. 283-287 (2000) 513.
[23] E. V. van Osch, J. V. van Hoepen, J. Boskeljon, and J. Rensman, Tensile Properties of 2.5 dpa 300 °C Neutron Irradiatied RA FM plate, powder HIP and EB and TIG weld, NRG Petten 20023/99.26704/P.
[24] R. L. Klueh and J. Alexander, Effects of Radiation on Materials: 18th International Symposium, ASTM STP 1325, 911.
[25] E. I. Materna-Morris, H.-C. Schneider, B. Dafferner, R. Roll, and O. Romer, Irradiation Influences on Mechanical Properties and Structures of Martensitic Low-Activation Alloys, presented in ICFRM-10.
[26] K. Shiba, JAERI Data Base.
[27] H. Kurishita, H. Kayano, M. Narui, A. Kimura, M. L. Hamilton, and D. S. Gelles, J. Nucl. Mater. 212-215 (1994)730.
[28] F. Abe, T. Noda, H. Araki, M. Narui, and H. Kayano, J. Nucl. Mater. 191-192 (1992) 845.
[29] R. L. Klueh, P. J. Matiasz, and M. Vitek, J. Nucl. Mater. 141-143 (1986) 960-965.
[30] A. Kohyama, H. Matsui, K. Hamada, and H. Simidzu, J. Nucl. Mater. 155-157 (1988) 896.
[31] R. L. Klueh, J. Nucl. Mater. 179-181 (1991) 728.
[32] R. L. Klueh, J. M. Vitek, and M.L. Grossbeck, ASTM STP 782 (1982) 648.
[33] J. Russell Hawthorne, J. R. Reeds, and J. A. Sprague, ASTM STP 870 (1985) 580.
[34] K. Farrell and T. S. Byun, J. Nucl. Mater. 318 (2003) 274.
[35] V. K. Shamardin, V. N. Golovanov, T. M. Bulanova, A. V. Povstyanko, A. E. Fedoseev, Z. E. Ostrovsky, and Yu. D. Goncharenko, J. Nucl. Mater. 307-311 (2003) 229.
[36] V. V. Rybin, I. P. Kursevich, and A. N. Lapin, J. Nucl. Mater. 258-263 (1998) 1324.
[37] A. Alamo, M. Horsten, X. Averty, E. I. Materna-Morris, M. Rieth, and J. C. Brachet, J. Nucl. Mater. 283-287 (2000) 353.
[38] R. L. Klueh, M. Sokolov, K. Shiba, Y. Miwa, and J. P. Robertson, J. Nucl. Mater. 283-287 (2000) 478.
[39] R. L. Klueh, J. J. Kai, and D. J. Alexander, J. Nucl. Mater. 225 (1995) 175.
[40] E. I. Materna-Morris, M. Rieth, and K. Ehrlich, Effects of Radiation on Materials: 19th International Symposium, ASTM STP 1366 (2001) 597.
[41] E. V. van Osch, M. G. Horsten, G. E. Lucas, and G. R. Odette, Effects of Radiation on Materials: 19th International Symposium, ASTM STP 1366 (2001) 612.

[42] J. Rensman, J. van Hoepena, J. B. M. Bakkera, R. den Boef, F. P. van den Broek, and E. D. L. van Essen, J. Nucl. Mater. 307-311 (2002) 245.
[43] J. L. Séran, A. Alamo, A. Maillard, H. Trouron, J. C. Brachet, P. Dubuission, and O. Rabouille, J. Nucl. Mater. 212-215 (1994) 588.
[44] M. A. Sokolov, R. L. Klueh, G. R. Odette, K. Shiba, and H. Tanaigawa, ASTM STP 1447, American Society for Testing and Materials (in press).
[45] R. L. Klueh and D. J. Alexander, J. Nucl. Mater. 233-237 (1996) 336.
[46] M. Rieth, B. Dafferner, and H.-D. Rohrig, J. Nucl. Mater. 258-263 (1998) 1147.
[47] I. V. Gorynin, V. V. Rybin, I. P. Kursevich, A. N. Lapin, E. V. Nesterova, and E. Yu. Klepikov, J. Nucl. Mater. 283-287 (2000) 465.
[48] N. Baluc, R. Schaublin, C. Bailat, F. Paschoud, and M. Victoria, J. Nucl. Mater. 283-287 (2000) 731.
[49] R. L. Klueh, D. J. Alexander, and M. Rieth, J. Nucl. Mater. 273 (1999) 146.
[50] H.-C. Schneider, B. Dafferner, and J. Aktaa, J. Nucl. Mater. 295 (2001) 16-20.
[51] R. L. Klueh and D. J. Alexander, J. Nucl. Mater. 218 (1995) 151.
[52] E. V. van Osch, J. B. M. Bakker, R. den Boef, and J. Rensman, NRG Petten 20023/99.26974/P.
[53] R. L. Klueh and D. J. Alexander, J. Nucl. Mater. 258-263 (1998) 1269.
[54] T. Lechtenberg, J. Nucl. Mater. 133-134 (1985) 149.
[55] R. L. Klueh, J. M. Vitek, W. R. Corwin, and D. J. Alexander, J. Nucl. Mater. 155-157 (1988) 973.
[56] H. Kayano, A. Kimura, M. Narui, Y. Sasaki, Y. Suzuki, and S. Ohta, J. Nucl. Mater. 155-157 (1988) 978.
[57] R. L. Klueh and D. J. Alexander, J. Nucl. Mater. 179-181 (1991) 733.
[58] W. L. Hu and D. S. Gelles, ASTM STP 956 (1987) 83.
[59] R. L. Klueh and D. J. Alexander, J. Nucl. Mater. 187 (1992) 60.
[60] H.-C. Schneider, B. Dafferner, H. Ries, and O. Romer, Irradiation Program MANITU: Results of Impact Tests with the Irradiated Materials (2.4dpa), FZKA6605, Forschungszentrum Karlsruhe (2001).
[61] R. L. Klueh and P. J. Maziasz, J. Nucl. Mater. 187 (1992) 43.
[62] J. L. Séran, V. Lévy, P. Dubisson, D. Gilbon, A. Maillard, A. Fissolo, H. Touron, R. Cauvin, A. Chalony, and E. Le Boulbin, ASTM STP 1125 (1992) 1209.
[63] R. L. Klueh and J. M. Vitek, J. Nucl. Mater. 132 (1985) 27.
[64] E. Lucon, M. Decréton, and E. van Walle, Fusion Engineering and Design 69 (2003) 373.
[65] M. J. Makin, A. D. Whapham, and F. J. Minter, Philos. Mag. 7 (74) (1962) 285.
[66] M. J. Makin and F. J. Minter, Acta. Metall. Mater. 8 (10) (1960) 691.
[67] R. B. Jones and T. J. Williams, ASTM-STP 1270 (1996) 569.
[68] B. Van der Schaaf, D. S. Gelles, S. Jitsukawa, A. Kimura, R. L. Klueh, A. Möslang, and G. R. Odette, J. Nucl. Mater. 283-287 (2000) 52.
[69] B. Van der Schaaf and A. A Tavasoli, Hardening and toughness from radiation and resistance characterization of F82H and Screening Steels, NRG Petten 20027/99.25387/P.
[70] L. Schäfer, J. Nucl. Mater. 283-287 (2000) 707.
[71] H. Sakasegawa, T. Hirose, A. Kohyama, Y. Katoh, T. Harada, K. Asakura, and T. Kumagai, J. Nucl. Mater. 307-311 (2003) 490.
[72] P. Fernandez, A. M. Lancha, J. Lapena, and M. Hernandez-Mayoral, Fusion Engineering and Design 58–59 (2001) 787.

EXTRAPOLATION OF FRACTURE TOUGHNESS DATA FOR HT9 IRRADIATED AT TEMPERATURES 360-390°C—R. J. Kurtz and D. S. Gelles (Pacific Northwest National Laboratory)*

OBJECTIVE

The objective of this task is to provide estimated HT9 cladding and duct fracture toughness values for test (or application) temperatures ranging from -10°C to 200°C, after irradiation at temperatures of 360-390°C. This is expected to be an extrapolation of the limited data presented by Huang[1, 2]. This extrapolation is based on currently accepted methods (ASTM 2003 Standard E 1921-02), and other relevant fracture toughness data on irradiated HT9 or similar alloys.

SUMMARY

Following irradiation in the AC01 test at 360°C to 5.5 x 10^{22} n/cm^2, two HT9 samples tested at 30°C were found to have fracture toughness levels of 28.2 and 31.9 MPa m$^{1/2}$, whereas a third identical specimen tested at 205°C gave 126 MPa m$^{1/2}$. Based on testing of notched tensile specimens from the same irradiation test, the low toughness was a result of brittle fracture. A similar low level of toughness has also been demonstrated in HT9 following irradiation at 250°C and therefore such behavior is reproducible.

Using ASTM Standard E1921-02, which characterizes the fracture toughness of ferritic steels that experience onset of cleavage cracking at instabilities, it has been shown that these data can be analyzed by a Master Curve approach, and that the trend of the fracture toughness over a wider range of temperatures can be estimated. Master Curve analysis shows that toughness will remain low over a wide range of temperatures near 30°C, but will degrade only slightly when temperatures drop below that value. Application of the ASTM Standard methodology did not permit a rigorous, statistically significant determination of the lower bound fracture toughness of HT9 due to the limited data available.

PROGRESS AND STATUS

Introduction

The FFTF project is planning on shipping irradiated sodium-bonded metal fuel pins with HT9 cladding material, to INEEL. These pins are to be shipped in the T-3 Cask, either as full fuel assemblies or loose pins packaged in a liner. The current NRC license does not address this type of fuel packaging. An addendum to the Safety Analysis Report (FFTF-14624), which addresses these changes, has been prepared for acceptance by the DOE/NRC and is to be in compliance with the requirements of 10CFR-71. The structural section of FFTF-14624, addresses the potential for “brittle fracture” of the fuel pins under hypothetical accident conditions (HAC). For cold HAC, a fuel pin temperature of 10°C was estimated. Fracture toughness data [1, 2] relevant to the brittle fracture of the fuel pins consist of 3 data points (one at 205°C and two at 30°C). The planned shipments may be below the temperature range of the test data. Fracture toughness values used in previous evaluations were based on straight-line extrapolation, which are conservative.

Approach

Since the generation of an irradiation effects data base for HT9 fracture toughness that ended about 1989, considerable progress has been made to understand the consequences of irradiation on fracture toughness and to generate a means for extrapolating the available data base. Much of that work is based on the behavior of pressure vessel steels, but it should be directly pertinent for HT9, a “super 12Cr steel” intended for high temperature applications. That body of work has resulted in an ASTM Standard for fracture toughness evaluation, designated E1921-02 and entitled “Determination of Reference

*Pacific Northwest National Laboratory (PNNL) is operated for the U.S. Department of Energy by Battelle Memorial Institute under contract DE-AC06-76RLO-1830.

Temperature T_0, for Ferritic Steels in the Transition Range" [3]. The standard takes note of the fact that at low temperatures, fracture toughness response replicates that of Charpy Impact behavior, and shows a transition from ductile-to-brittle behavior with decreasing temperature. The standard defines the parameters for a Master Curve for a given alloy in terms of a reference temperature, T_0. The Master Curve defines the temperature dependence for fracture toughness in the ductile-to-brittle transition range in the form:

$$K_{Jc(med)} = 30 + 70 \exp [0.019(T - T_0)], \text{ MPa } m^{1/2}. \ldots . (1)$$

where $K_{Jc(med)}$ is the median value for fracture toughness at a given temperature, T, in units of MPa $m^{1/2}$. All materials, irradiation conditions, test conditions and specimen geometries will behave similarly and can be fit with the adjustable parameter T_0. Therefore, data generated with different specimen geometries can be converged, and different material heat treatments and irradiation conditions may result in correspondingly different values for T_0. Using this approach, it should be possible to estimate HT9 fracture toughness values for test (or application) temperatures ranging from -10°C to 200°C, after irradiation at the 360-390°C temperature range given data obtained at room temperature and 205°C.

HT9 Data Base

An HT-9 fracture toughness data base has been generated primarily by F. H. Huang and co-workers as part of the Department of Energy National Cladding and Duct (NCD) and Fusion Reactor Materials (FRM) Programs with more recent contributions from UCSB [1, 2, 4-6]. The NCD program was intended to qualify HT9 as a duct and fuel cladding material for fast breeder reactor applications, and the FRM program followed with the intention of expanding the data base to lower irradiation temperatures and to include weldments. The standard specimen geometry used by Huang is shown in Figure 1, with B at 2.54 mm, W at 11.94 mm and diameter at 16 mm. Specimens were fatigue pre-cracked to a total crack length of about 6 mm leaving an uncracked ligament of about 6 mm. The thickness selected corresponds to that of a standard FFTF duct. Specimens had electrodes attached so that a crack length measurement could be obtained from each specimen tested using a potential drop technique.

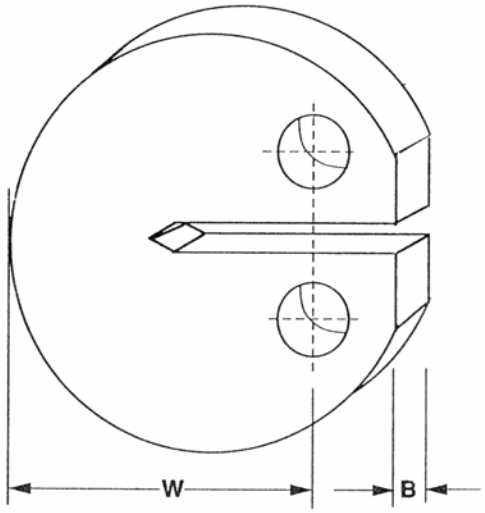

Figure 1. Specimen geometry used by Huang.

The Huang data base for HT9 base metal along with the UCSB bend bar data is shown in Figure 2. {Where K_C values were measured, they have been converted to J_C values using the relation $J_c=K_c^2/E$ where E is the elastic modulus.} The data base contains both unirradiated and irradiated specimens, the former shown with solid symbols and the latter with crossed or open symbols. From Figure 2, the behavior for unirradiated specimens shows low values of fracture toughness at very low temperatures due to brittle fracture, and a strong dip in toughness at ~300°C due to interstitial impurity hardening associated with dynamic strain aging.

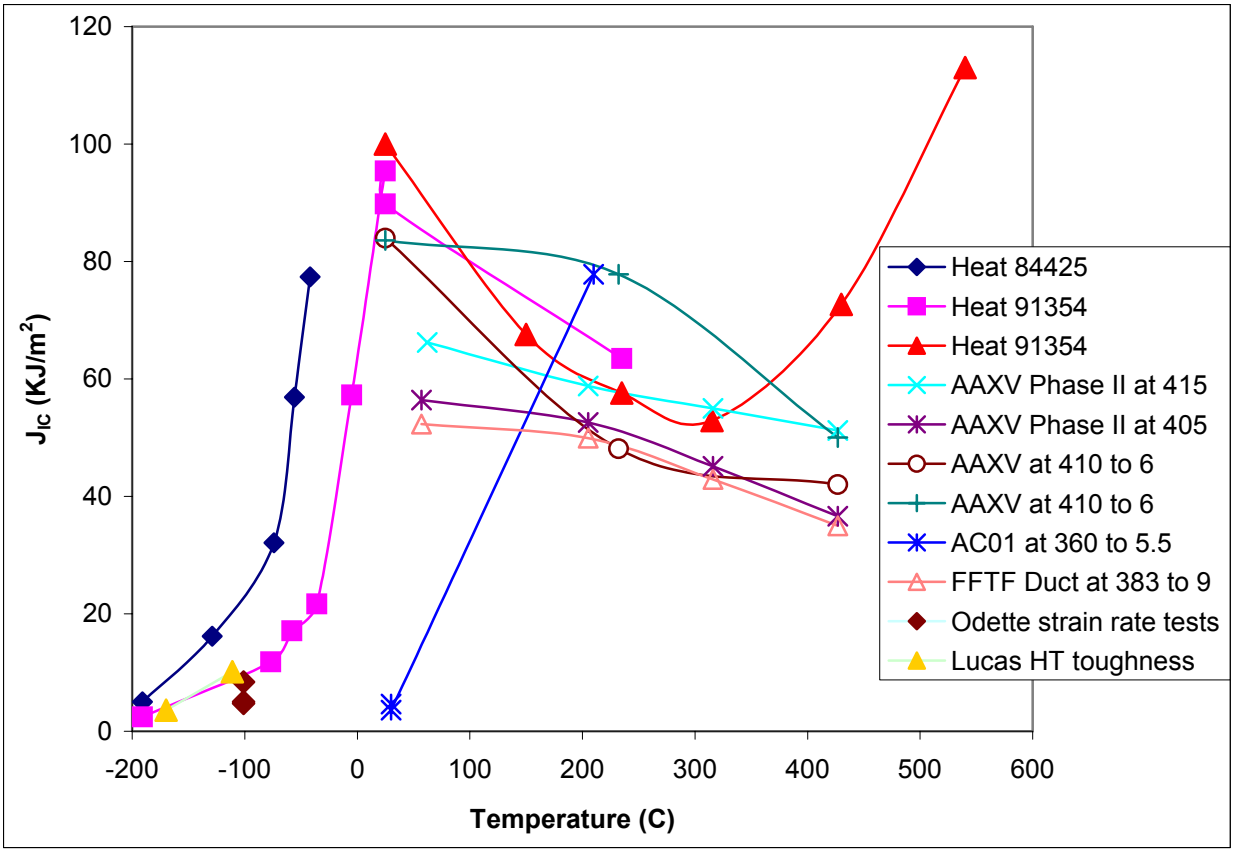

Figure 2. HT9 fracture toughness data base generated by Huang and co-workers. Unirradiated conditions are denoted by filled solid data points.

Irradiation at temperatures of 390°C and higher is found to cause only minor changes in toughness whereas irradiation at 360°C, based on the AC01 test gave two measurements on the order of 5 KJ/m^2 when tested at room temperature. Therefore, irradiation at temperatures below 390°C can result in large reductions in fracture toughness. Similar behavior was reported in support of the FRM program. [7] There it was found that following irradiation at 250°C to low dose, the fracture toughness at room temperature was also 5 KJ/m^2. However, those results were not included in Figure 2 because toughness levels reported for unirradiated conditions were approximately four times those of Huang, and the differences were attributed to a different, softer tempering treatment (780°C/2h verses 740-760°C/1h for Huang). Such high toughness levels should make it very difficult to obtain valid measurements on miniature specimens. Also, it can be noted that independent measurements showed toughness levels on the order of 100 KJ/m^2 for HT9 at room temperature after a tempering treatment of 780°C/2.5h, in agreement with the Huang data but in disagreement with the FRM data [8].

Fracture toughness measurements have also been made for HT9 weld metal and heat-affected-zone (HAZ) specimens. The results are shown in Figure 3, in comparison to the unirradiated base metal data. The temperature dependence at high temperatures was somewhat different, but toughness values remained high following irradiation at 390°C or higher.

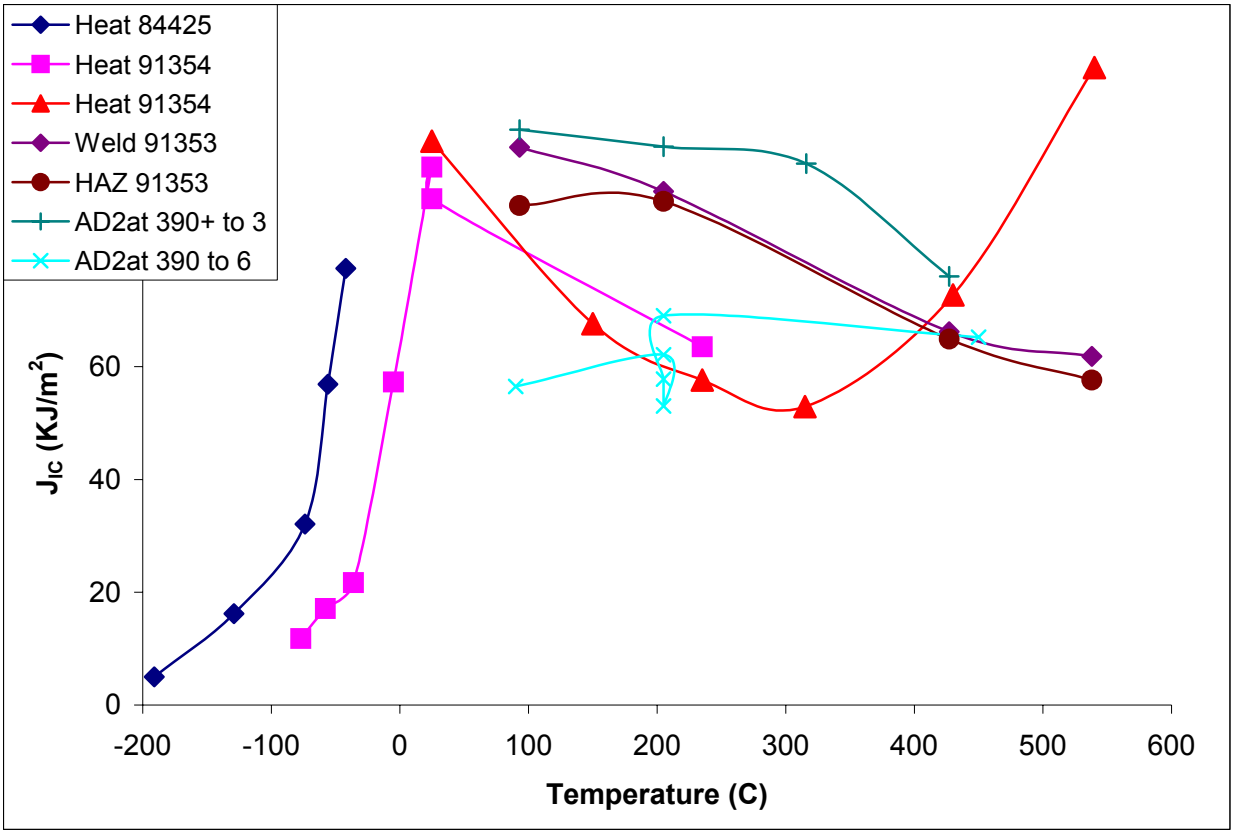

Figure 3. Fracture toughness response in HT9 weld specimens.

Therefore, some fracture toughness data exists for HT9, including testing following irradiation. Measurements of fracture toughness on the order of 5 KJ/m^2 do occur in unirradiated samples tested at temperatures below 0°C, as well as in specimens irradiated at 250 and 360°C when tested at room temperature. The fracture appearance for unirradiated samples with low fracture toughness was brittle, but fractography was not performed on irradiated samples showing low fracture toughness. However, a notched tensile specimen irradiated under identical conditions at 360°C and tested at room temperature was shown to have a brittle appearance [1]. Therefore, it is likely that the fracture toughness levels on the order of 5 KJ/m^2 for irradiated specimens are a result of an irradiation induced ductile-to-brittle transition.

Analysis

The ASTM Standard, E1921-02, covers the determination of a reference temperature, T_0, that characterizes the fracture toughness of ferritic steels, which experience the onset of cleavage cracking at elastic, or elastic-plastic instabilities, or both. The specific types of steels covered are those with yield strengths ranging from 275 to 825 MPa. The temperature dependence of fracture toughness is assumed to conform to a standard shape known as the Master Curve (Equation 1). The Master Curve is indexed to a reference temperature, T_0. Variations in material properties such as heat treatment and irradiation history are characterized by temperature shifts. The standard places requirements on specimen size and the number of replicate tests needed to reliably determine T_0 and, therefore, the temperature dependence of the fracture toughness for a given metallurgical condition. The specimen remaining ligament must be sufficiently large to ensure that a condition of high crack-front constraint exists at fracture in order to obtain valid fracture toughness measurements. The maximum K_{Jc} capacity of a specimen is given by:

$$K_{limit} = [(Eb_0\sigma_{ys})/30(1-\nu^2)]^{1/2} \qquad (2)$$

where E is Young's modulus, b_0 is the remaining ligament, σ_{ys} is the material yield strength at the test temperature, and is ν Poisson's ratio. A minimum of six tests is needed at a single test temperature in order to satisfy statistical requirements of the standard. More than six tests may be needed if the testing is performed over a range of temperatures. All of the results are normalized to a standard specimen thickness of 25.4 mm. The standard includes a size effect adjustment, as follows:

$$K_{Jc(x)} = K_{min} + [K_{Jc(o)} - K_{min}](B_o/B_x)^{1/4} \qquad (3)$$

where:

$K_{Jc(o)} = K_{Jc}$ for a specimen size B_o,
B_o = gross thickness of test specimens (side grooves ignored),
B_x = gross thickness of prediction (side grooves ignored), and
K_{min} = 20 MPa $m^{1/2}$.

However, the application under consideration in this study is for cladding and duct where thicknesses do not exceed 2.54 mm, and the data available that has been generated by Huang is for a specimen thickness of 2.54 mm. Note that greater thickness results in higher values of T_0 and therefore lower values of toughness at a given temperature.

The relevant fracture toughness data used for estimating T_0 is presented in Table 1. Note that none of the data sets satisfy statistical requirements for the number of replicate tests since multiple test temperatures were used. Also note that tests performed at –191°C (italicized values in Table 1) were excluded from the analysis since these tests fell outside the acceptable temperature range for T_0 determination. Values of E, σ_{ys}, and ν used to compute the K_{Jc} measurement capacity of the disc compact tension specimen utilized by Huang were obtained from Spatig et al., [9] an IEA data base report, [10] and Zinkle, et al [11]. The temperature dependence of the elastic properties are plotted in Figure 4 and the yield strength in Figure 5. Calculation of K_{limit} values shows that none of the specimens violated dimensional requirements, but it should be noted that at high fracture toughness the values of K_{Jc} that meet the requirements of Eq. 2 may not always provide a unique description of the crack-front stress-strain fields due to some loss of constraint caused by excessive plastic flow. This condition may be more prevalent in materials with low strain hardening characteristics.

Values for T_0 have been estimated for four sets of HT9 data, three unirradiated conditions and one condition following irradiation. These analyses are shown in Figures 6 through 9. Figure 6 shows Master Curve analysis for Heat 84425 from [4] which gives T_0 at –25.5°C. Figure 7 shows Master Curve analysis for a different heat of HT9, 91353, from [4] which gives T_0 at 34.1°C. Figure 8 shows Master Curve analysis for heat 84425 tested at a higher strain rate of $3.2x10^{-2}$ from [4] (and not plotted in Figure 2) which gives T_0 at 33°C. Applying the same criterion to the AC01 test data, Figure 9 shows Master Curve analysis for heat 91354 irradiated at 360°C [1-2] which gives T_0 at 238°C. It should be noted that the confidence bounds presented in Figures 6 through 9 are tied directly to the T_0 values obtained from application of the ASTM analysis methodology, but none of the data sets satisfy ASTM statistical requirements so these curves may not bound the data.

Discussion

The ASTM Standard E1921-02 for Master Curve analysis of ductile-to-brittle fracture toughness behavior was developed after an irradiation effects data base for HT9 was generated. The Standard recommends that tests be replicated six times in order to estimate a median K_{Jc} because extensive scatter among replicate tests is expected. The recommended test temperature for those tests is one giving a toughness of ~100 MPa $m^{1/2}$, but testing over a range of temperatures is allowed, given the understanding that the uncertainty in T_0 determination increases as the toughness level decreases (i.e., more specimens are

Table 1. Fracture Toughness Data for Unirradiated and Irradiated HT9 Used to Determine T_0

T, °C	E, MPa	σ_{ys}, MPa	J_c, KJ/m^2	K_{Jc}, MPa m$^{1/2}$	$K_{Jc(1T)}$, MPa m$^{1/2}$	K_{limit}, MPa m$^{1/2}$
Heat 84425						
-191	*228*	*1099*	*5*	*35*	*29*	*234*
-129	225	806	16.2	63	44	199
-74	222	643	32.1	88	58	177
-56	221	608	56.9	117	75	171
-42	220	589	77.4	136	85	168
Heat 91353						
-191	*228*	*1099*	*2.43*	*25*	*23*	*234*
-77	222	650	11.8	53	39	178
-58	221	612	17.1	64	45	172
-36	220	582	21.7	72	49	167
-5	218	562	57.3	117	74	164
25	216	556	95.4	150	93	162
25	216	556	89.8	146	91	162
Heat 84425 (high strain rate)						
-191	*228*	*1099*	*2.5*	*25*	*23*	*234*
-74	222	643	11	52	38	177
-58	221	612	17	64	45	172
-36	220	582	22	73	50	167
-6	218	562	57	116	74	164
25	216	556	97	151	94	162
Heat 91354						
30	216	1095	-	32	27	227
30	261	1095	-	28	25	250
210	206	568	-	126	80	160

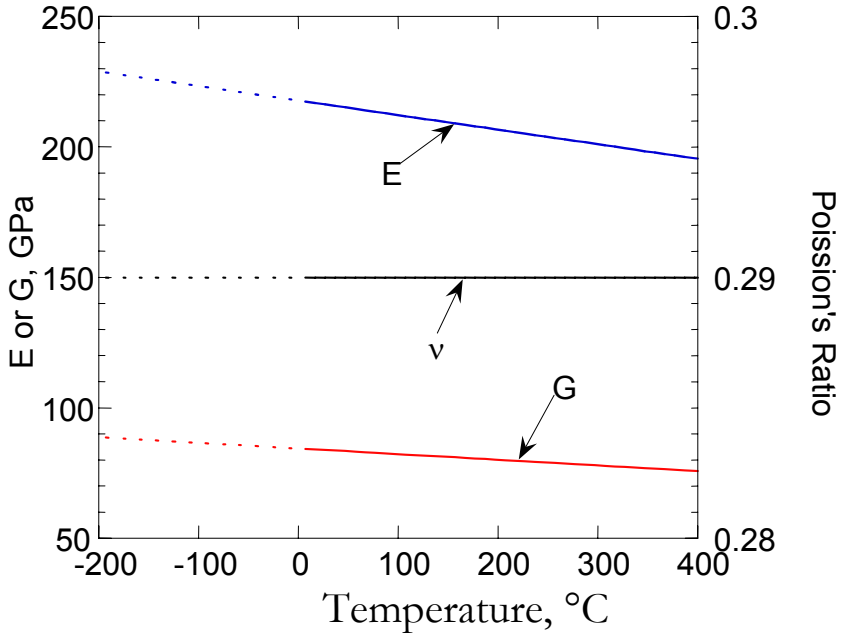

Figure 4. Temperature dependence of Young's modulus (E), shear modulus (G) and Poisson's ratio (ν).

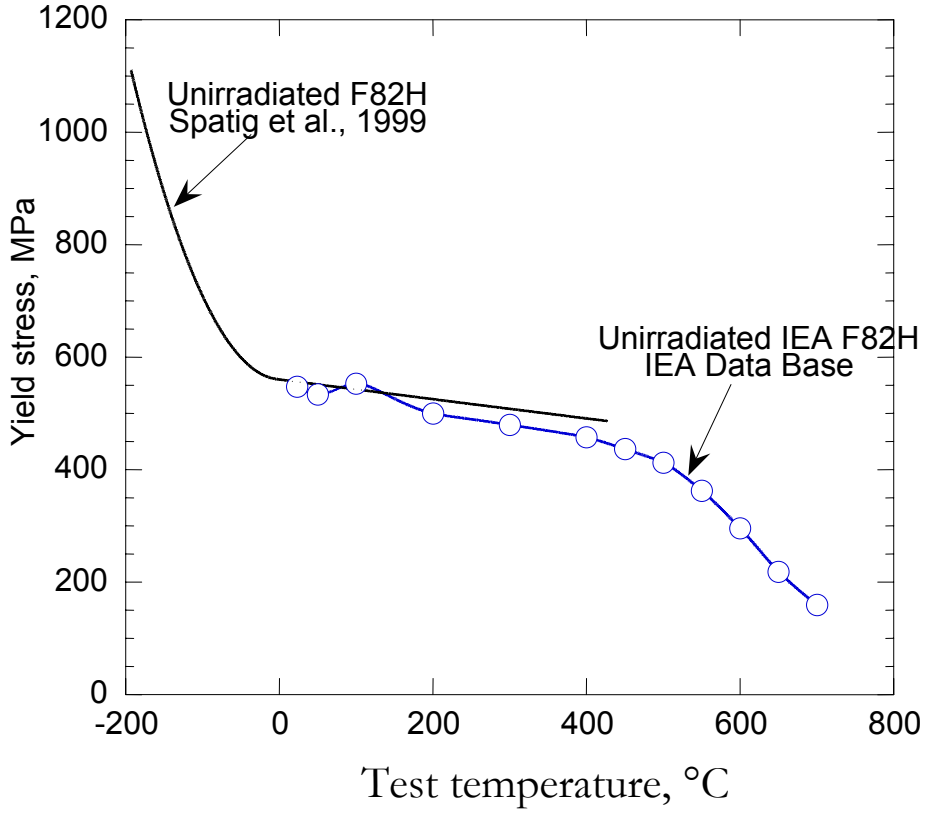

Figure 5. Temperature dependence of the 0.2% offset yield strength for F82H.

required to reliably compute T_0). Therefore, insufficient data has been obtained by Huang to satisfy ASTM Standard criterion for HT9 duct irradiated at 360°C to 5.5 x 10^{22} n/cm^2. Nonetheless, extrapolation of available data from the AC01 test may be justifiable in the spirit of the Standard, and a Master Curve should be a better estimate of fracture toughness over the temperature range -10°C to 200°C than a straight line extrapolation of the data points, shown in Figure 2, would provide. The Master Curves presented in Figures 6 through 9 show the trend of the HT9 fracture toughness as a function of temperature, but they cannot give precise lower bound fracture toughness values due to the data base limitations mentioned above.

Fracture toughness behavior for HT9 duct and cladding can be estimated based on the ASTM standard using Equation 3. As the cladding to be shipped has a thickness of 0.559 mm (0.022”), corrections for K_{Jc} can be obtained and a value for T_0 estimated. Results are shown in Figures 10 for duct and in Figure 11 for cladding with T_0 estimated at 203 and 178°C, respectively. Comparison of Figures 10 and 11 reveals that below room temperature, the curves are effectively identical, but the data points at 30°C are shifted up, from 28 and 32 to 32 and 37 or about 15%.

However, it is not clear that such an approach is valid for very thin samples. Therefore, it is perhaps best to expect that toughness in thin sections should increase but the actual magnitude estimated by the standard for going from duct to cladding geometries of 15% may be low.

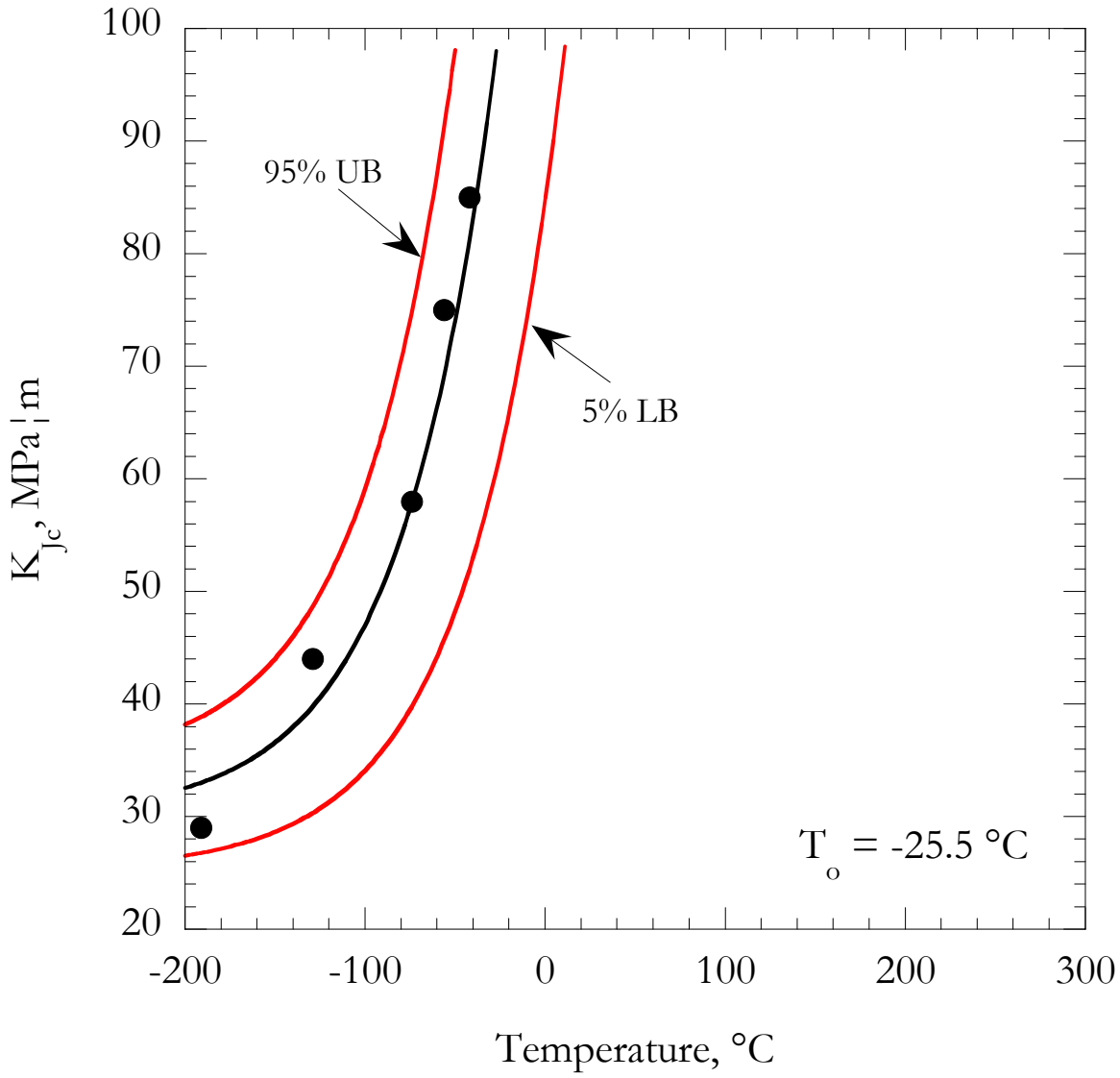

Figure 6. Heat 84425 Master Curve with thickness adjustment to the ASTM Standard of 25.4 mm. This material is unirradiated. The calculated reference temperature, T_0, is –25.5°C. The predicted median curve is shown in black with the measured values plotted as filled circles. Upper (95%) and lower (5%) bounds on the median curve are shown in red.

A concern can be raised that the fluence obtained in the AC01 experiment of 5.5 x 10^{22} n/cm^2 (E>0.1MeV) was insufficient to reach saturation. If this were the case, then irradiation to higher fluence might result in further degradation of fracture toughness properties. This concern can be countered in two ways. Sufficient Charpy impact data exists to show that impact energy changes saturate by 3 x 10^{22} n/cm^2 [12]. As behavior is qualitatively similar between Charpy impact and fracture toughness, it is therefore likely that saturation in toughness degradation has been achieved by 5.5 x 10^{22} n/cm^2. However, the Master Curve approach emphasizes that once a material has been embrittled so that response is brittle, and then fracture toughness will degrade little more.

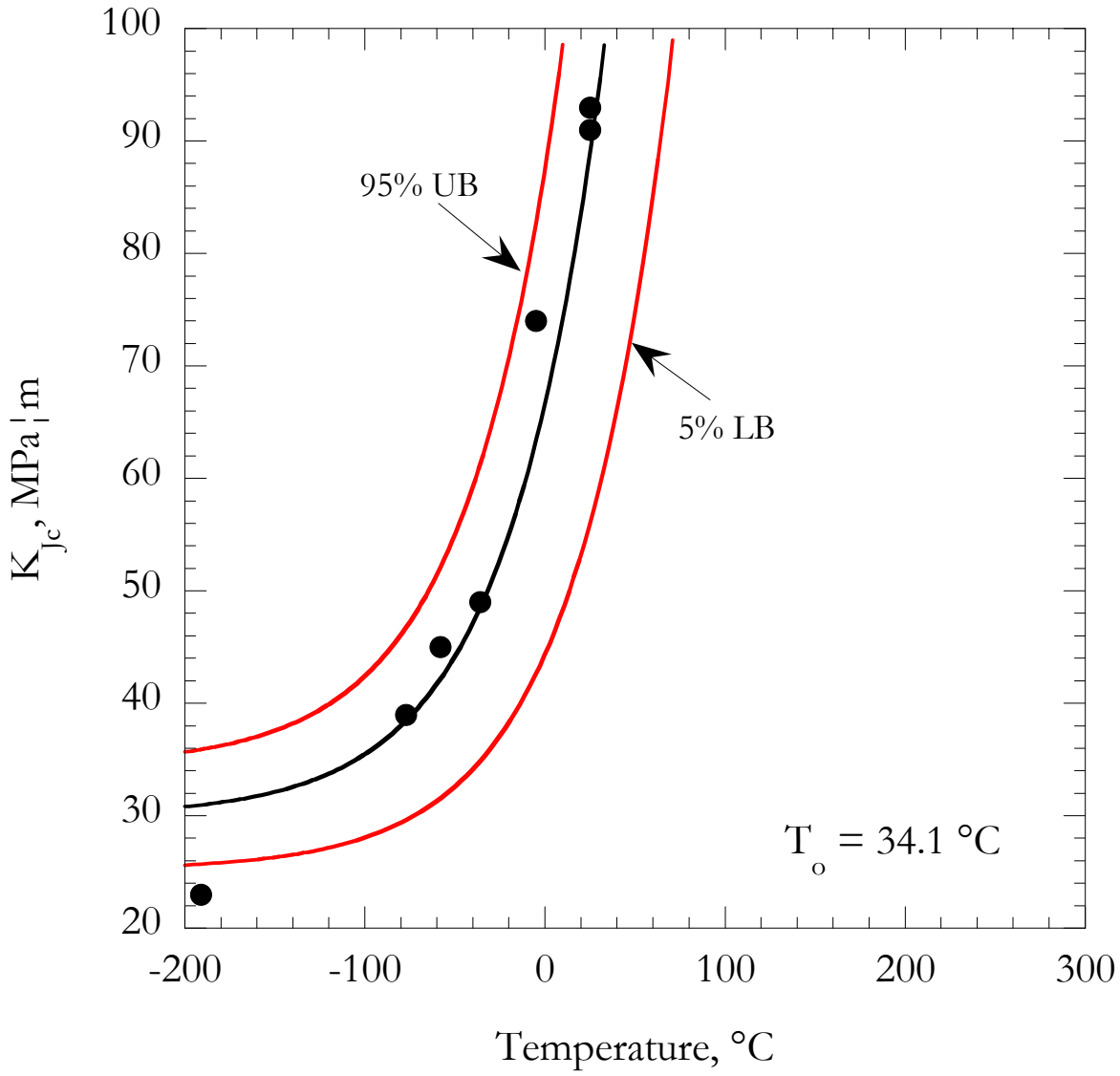

Figure 7. Heat 91353 Master Curve with thickness adjustment to the ASTM Standard of 25.4 mm. This material is unirradiated. The calculated reference temperature, T_0, is 34.1°C. The predicted median curve is shown in black with the measured values plotted as filled circles. Upper (95%) and lower (5%) bounds on the median curve are shown in red.

It is worthwhile to emphasize the consequences of Master Curve analysis. Extrapolation of toughness data due to brittle fracture both above and below the test temperature of 30°C results in only minor further changes in toughness. For example, from Figure 10 for the case of an HT9 duct irradiated at 360°C to 5.5 x 10^{22} n/cm^2, the median fracture toughness expected at 30°C is 33 MPa m$^{1/2}$. The temperature at which the median value drops to 30 MPa m$^{1/2}$ is –200°C, but at 100°C, the median toughness is only 40 MPa m$^{1/2}$. Therefore, toughness degradation is insensitive to temperature fluctuations anticipated during shipment. However, in comparison, linear extrapolation of the AC01 data gives misleading predictions.

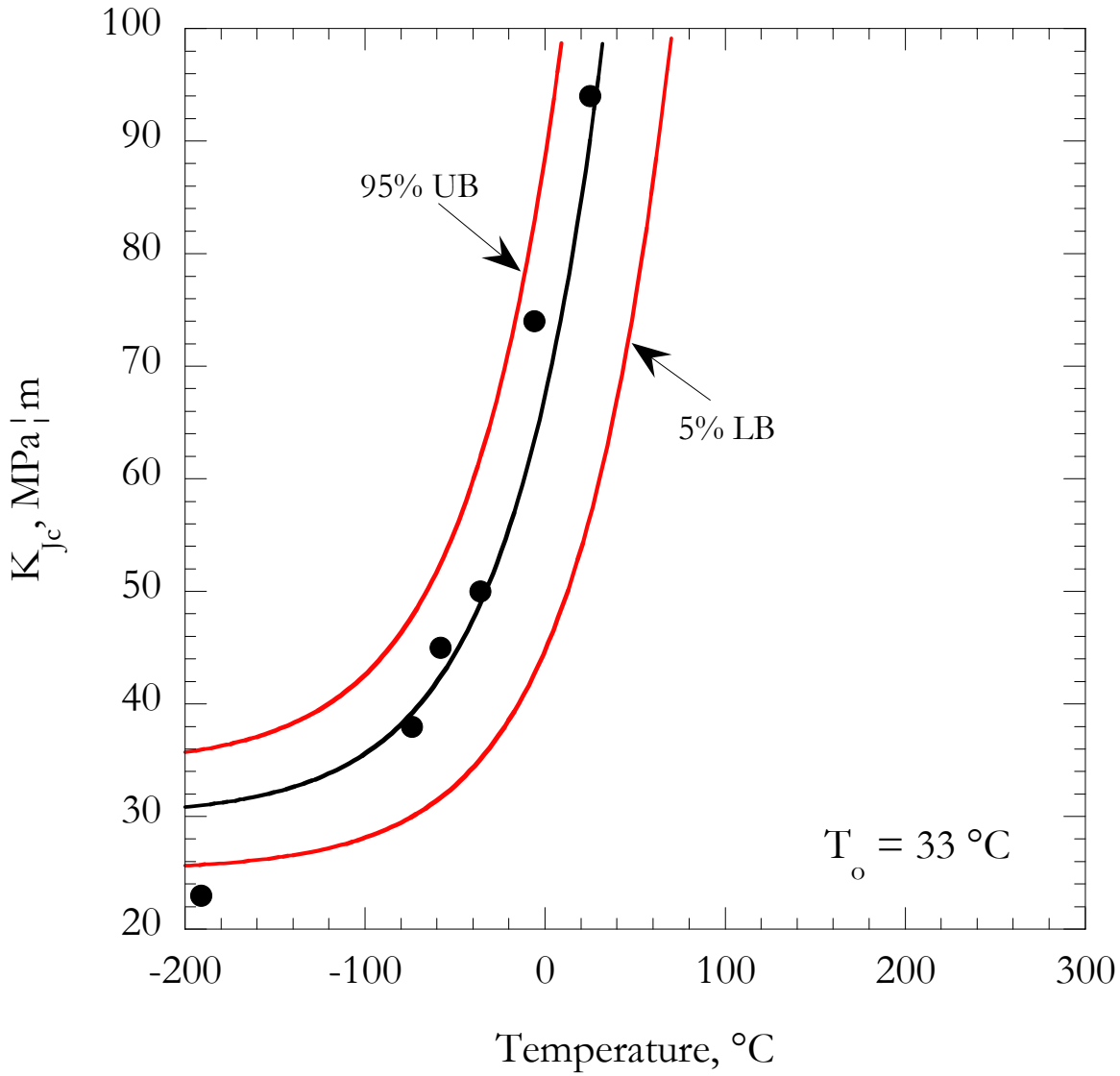

Figure 8. Heat 84425 (tested at high strain rate) Master Curve with thickness adjustment to the ASTM Standard of 25.4 mm. This material is unirradiated. The calculated reference temperature, T_0, is 33°C. The predicted median curve is shown in black with the measured values plotted as filled circles. Upper (95%) and lower (5%) bounds on the median curve are shown in red.

We have attempted to estimate the difference in toughness between HT9 ducts and HT9 cladding based on the ASTM Standard E 1921-02. An improvement on the order of 15% is predicted at 30°C, with less improvement at lower temperatures. However, we suspect that these procedures do not apply to such thin material, and recommend further analysis be performed.

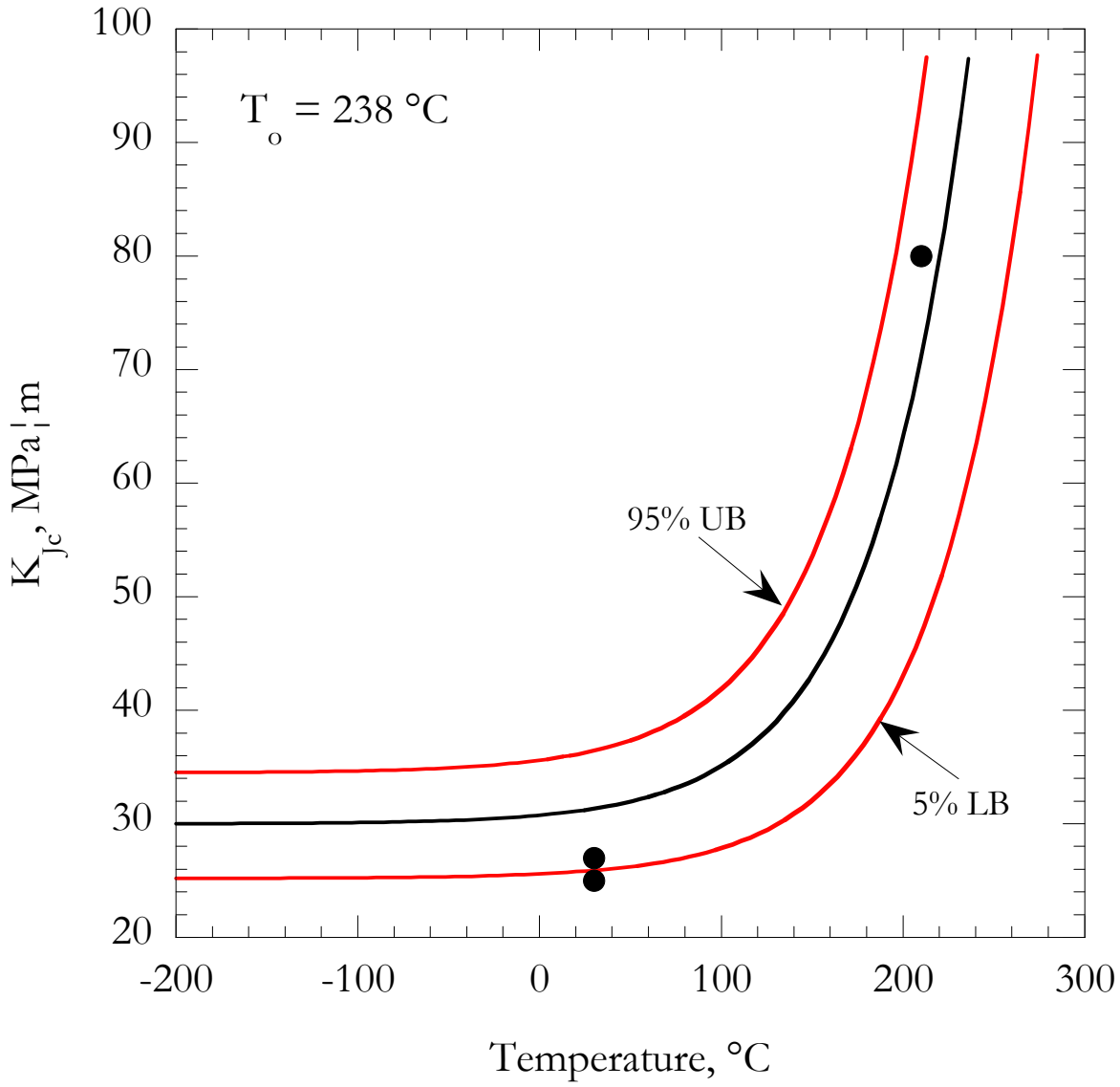

Figure 9. Heat 91354 Master Curve with thickness adjustment to the ASTM Standard of 25.4 mm. This heat was irradiated at 360 °C to 5.5 x 10^{22} n/cm^2 (E>0.1MeV). The calculated reference temperature, T_0, is 238°C. The predicted median curve is shown in black with the measured values plotted as filled circles. Upper (95%) and lower (5%) bounds on the median curve are shown in red.

Conclusions

Following irradiation in the AC01 test at 360°C to 5.5 x 10^{22} n/cm^2, two HT9 samples tested at 30°C were measured to have fracture toughness levels of 28.2 and 31.9 MPa m$^{1/2}$, respectively, whereas a third identical specimen tested at 205°C gave 126 MPa m$^{1/2}$. Based on testing of notched tensile specimens from the same irradiation test, the low toughness was a result of brittle fracture. A similar low level of toughness has also been demonstrated in HT9 following irradiation at 250°C and therefore such behavior is reproducible.

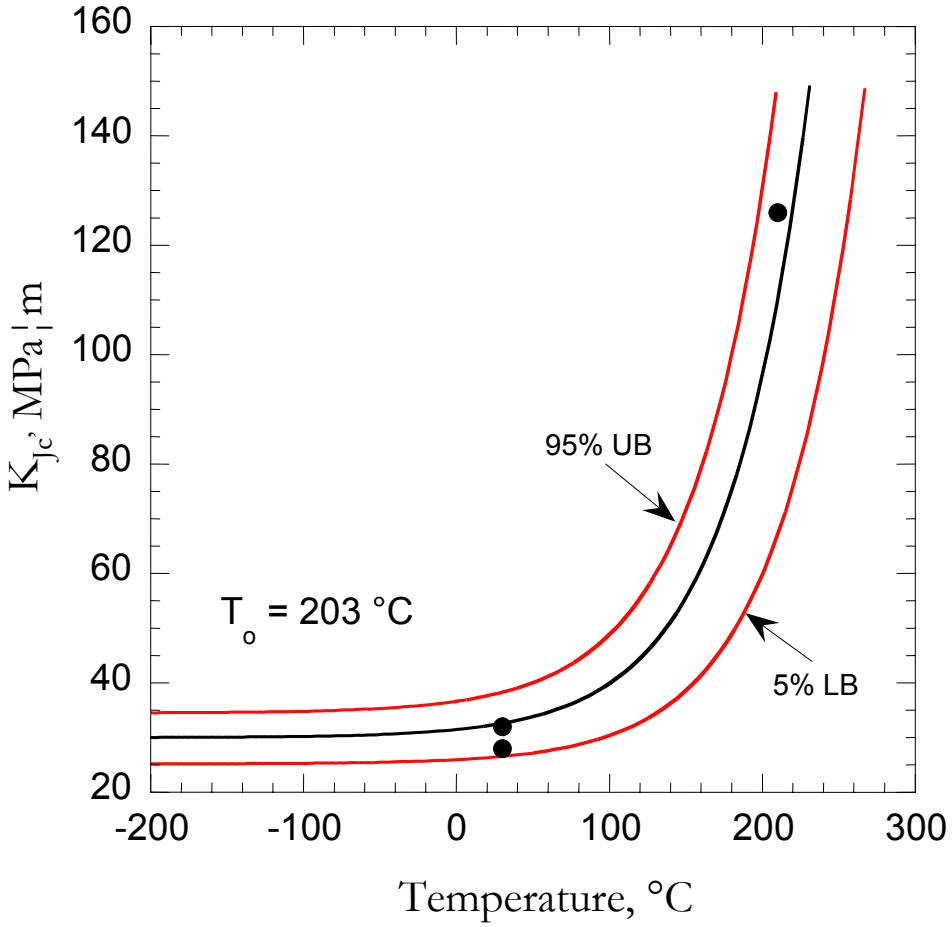

Figure 10. Heat 91354 Master Curve without thickness adjustment to the ASTM Standard of 25.4 mm. This heat was irradiated at 360 °C to 5.5 x 10^{22} n/cm^2 (E>0.1MeV). The calculated reference temperature, T_0, is 203°C. The predicted median curve is shown in black with the measured values plotted as filled circles. Upper (95%) and lower (5%) bounds on the median curve are shown in red. Note the curves shown in this figure are not strictly in accordance with the ASTM Master Curve analysis since this analysis applies only to specimens 25.4 mm thickness.

Using ASTM Standard E1921-02 which characterizes the fracture toughness of ferritic steels that experience onset of cleavage cracking at instabilities, it has been shown that these data can be analyzed by a Master Curve approach, and that the trend of the fracture toughness over a wider range of temperatures can be estimated. Master Curve analysis shows that toughness will remain low over a wide range of temperatures near 30°C, but will degrade only slightly when temperatures drop to –10°C. Application of the ASTM Standard methodology did not permit a rigorous, statistically significant determination of the lower bound fracture toughness of HT9 due to the limited data available.

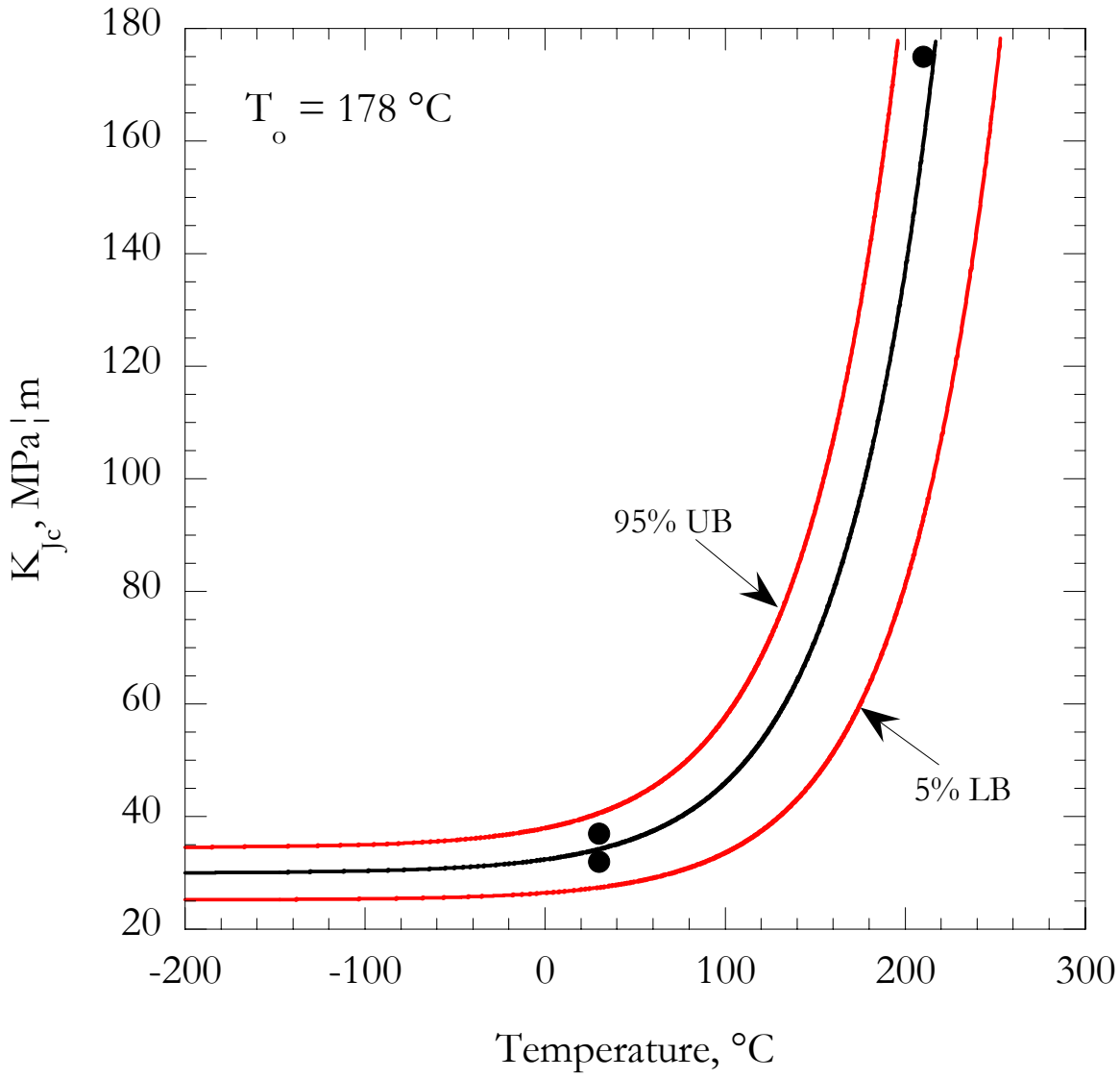

Figure 11. Heat 91354 Master Curve with thickness adjustment from 2.54 mm to 0.559 mm to estimate the fracture toughness of HT-9 fuel cladding. This heat was irradiated at 360°C to 5.5 x 10^{22} n/cm^2 (E>0.1MeV). The calculated reference temperature, T_0, is 178°C. The predicted median curve is shown in black with the measured values plotted as filled circles. Upper (95%) and lower (5%) bounds on the median curve are shown in red. Note the curves shown in this figure are not strictly in accordance with the ASTM Master Curve analysis since this analysis applies only to specimens 25.4 mm thickness.

Future Work

The effort will be continued as opportunities become available.

References

[1] F. H. Huang, in Effects of Radiation on Materials: 15th International Symposium, Eds. R. E. Stoller, A. S. Kumar, and D. S. Gelles, ASTM STP 1125 (1992) 1267-1286.

[2] F. H. Huang, Fracture Properties of Irradiated Alloys (Avante Publishing, 1995) 285-310.

[3] ASTM 2003 Standard E 1921-02 in Annual Book of ASTM Standards, Vol. 03.01.
[4] F. H. Huang and M. L. Hamilton, Fusion Reactor Materials Semiannual Progress Report for the period ending March 31, 1989, DOE/ER-0313/6 (1989) 161-175.
[5] G. R. Odette, G. E. Lucas, R. Maiti, and J. W. Sheckherd, J. Nucl. Mater. 133-134 (1985) 849.
[6] G. E. Lucas, H. Yih, and G. R. Odette, J. Nucl. Mater. 155-157 (1988) 673.
[7] D. J. Alexander, J. E. Pawel, M. L. Grossbeck, A. F. Rowcliffe, and K. Shiba, in Effects of Radiation on Materials: 17th International Symposium, Eds. D. S. Gelles, R. K. Nanstad, A. S. Kumar, and E. A. Little, ASTM STP 1270 (1996) 945-970.
[8] J. R. Hawthorne, Alloy Development for Irradiation Performance Quarterly Progress Report for the period ending December 31, 1980, DOE/ER-0045/5 (1981) 127-141.
[9] P. Spatig, G. R. Odette, G. E. Lucas, and M. Victoria, Fusion Reactor Materials Semiannual Progress Report for the period ending June 30, 1999, DOE/ER-0313/26 (1999) 83-95.
[10] IEA Data Base on Material Properties of F82H (2002).
[11] S. J. Zinkle, J. P. Robertson, and R. L. Klueh, Fusion Reactor Materials Semiannual Progress Report for the period ending June 30, 1998, DOE/ER-0313/24 (1998) 135-143.
[12] W. L. Hu and D. S. Gelles, in Effects of Radiation on Material Properties: 13th International Symposium, Eds. F. A. Garner, C. H. Henager, Jr., and N. Igata, ASTM STP 956 (1987) 83-97.

NANOFEATURE DEVELOPMENT AND STABILITY IN NANOSTRUCTURED FERRITIC ALLOYS—

M. J. Alinger and G. R. Odette (University of California, Santa Barbara) and D. T. Hoelzer (Oak Ridge National Laboratory)

OBJECTIVE

The objective of this study was to use small angle neutron scattering (SANS) to characterize nanofeatures (NFs) in nanostructured ferritic alloys (NFAs) and to explore the factors that control their formation and evolution.

SUMMARY

Ferritic alloys containing a high density of nanoscale clusters of Y-Ti-O exhibit superior creep strength as well as potential for high resistance to radiation damage. Small angle neutron scattering (SANS) was used to characterize the sequence-of-events and the necessary ingredients for the formation of nanoclusters (NCs) during processing, as well as their thermal stability during high temperature aging. Mechanical alloying (MA) dissolves Y_2O_3 in the master alloy Fe-Cr-W powders. A large population of 1-2 nm NCs precipitate during subsequent high temperature consolidation. The NC sizes increase and their volume fractions and number densities decrease with increasing the consolidation temperature. Both Ti and Y are necessary for NC formation at higher temperatures. The NCs in MA957 are stable during aging at 1150°C for times up to 243 h, but systematically coarsen at 1200°C. The NCs coarsen rapidly and become unstable at higher aging temperatures. Variations in the alloy hardness are consistent with differences in the NC sizes and number densities.

PROGRESS AND STATUS

Introduction

A promising approach to achieving high creep strength, radiation damage resistant alloys is to create a very high density of fine-scale features that act as dislocation obstacles, serve as the dominant nucleation site for small helium bubbles and promote vacancy-interstitial recombination. A high density of coherent, nm-scale Y-O-Ti nanoclusters (NCs) are produced by mechanical alloying (MA) Fe-Cr-Ti powders with Y_2O_3 followed by hot consolidation [1-5]. However, the detailed character of the NC, the sequence-of-events and necessary ingredients in their formation, their stability during long-term high temperature irradiation service, and their effect on mechanical properties are not well understood. Such understanding is necessary to develop optimized properties and less costly processing paths.

Thus we seek to develop a basic understanding of the mechanisms that control the NC evolutions during processing and service, and to characterize their corresponding relations to mechanical properties. The NCs were characterized by small angle neutron scattering (SANS) and the results were compared to Vicker's microhardness measurements. A transmission electron microscopy (TEM) study of a subset of alloy-conditions in this paper is described in a companion paper [6].

Experimental Procedure

The alloy-condition codes, compositions, consolidation processes and temperatures of the powders and alloys characterized in this study are presented in Table 1. Gas atomized master alloy powders contained ≈14-wt% Cr, 0 and 0.4-wt% Ti and 0 and 3-wt%W were MA with and without 0.25-wt% Y_2O_3 by SPEX ball milling in argon for 8 hours. The milled powders were then consolidated by hot isostatic pressing (HIPing) at 200 MPa for 3 h at 850, 1000 and 1150^{o}C. Milled and un-milled powders were also annealed at these conditions. *Single variable* measurements were carried out by fabricating powders and consolidated alloys that served as baseline controls for a specified composition or processing variable. Thus, un-milled, milled, milled-annealed powders and consolidated alloys established the effects of the sequence of

processing steps. Likewise, for example, 14Cr-0.25Y_2O_3-3W powders and consolidated alloys served as the baseline controls for alloys with 14Cr-0.25Y_2O_3-0.4Ti-3W to evaluate the effect of Ti.

Table 1. Alloy IDs, chemical compositions and the consolidation processes and temperatures

Alloy ID	Alloy Element (wt%)						Consolidation	
	Cr	Al	Ti	Mo	W	Y_2O_3	Process	Temperature (^oC)
MA957	14	-	1	0.3	-	0.3	Hot Ext.	1150
J12YWT	13	-	0.4	-	3	0.25	Hot Ext.	1150
PM2000	20	5.5	0.5	-	-	0.5	Hot Ext.	1150
U14Y	14	-	-	-	-	0.25	HIP	850, 1000,1150
U14YT	14	-	0.4	-	-	0.25	HIP	850, 1000,1150
U14YW	14	-	-	-	3	0.25	HIP	850, 1000,1150
U14YWT	14	-	0.4	-	3	0.25	HIP	850, 1000,1150
U14WT	14	-	0.4	-	3	-	HIP	850, 1000,1150

Measurements were carried out with a λ = 0.5nm neutron beam on the 8m SANS instrument (NG1) at the National Institute of Standards and Technology with a maximum scattering vector, q ≈ 0.3 nm^{-1}. A strong ≈ 1.7T magnetic field permitted measuring both nuclear, $d\Sigma/d\Omega(q)_n$, and magnetic, $d\Sigma/d\Omega(q)_m$, neutron scattering cross sections, where

$$\frac{d\Sigma}{d\Omega}(q,\phi)=\frac{d\Sigma}{d\Omega}(q)_n+\sin^2\phi\frac{d\Sigma}{d\Omega}(q)_m. \quad (1)$$

Here, ϕ is the angle with respect to magnetic field direction. Subtraction of parasitic counts and normalization of the sample counts, transmissions and masses to a water standard were carried out to measure the absolute $d\Sigma/d\Omega(q,\phi)$ that were averaged over specified detector q and ϕ ranges, typically at ϕ = 0±30, 45±15 and 80±10, and used to evaluate the magnetic-to-nuclear scattering ratio (M/N).

The scattering cross sections for the features associated with the variable of interest, $d\Sigma/d\Omega_f$, were determined by subtracting the control cross section (see reference 7 for a detailed description of the SANS data reduction and analysis procedures). For example, subtracting the $d\Sigma/d\Omega$ for U14WT from that for U14YWT was used to assess the effect of Y_2O_3. The $d\Sigma/d\Omega(q,\phi)$ specify the average size (<r>), size distribution ($\Delta r/r$), volume fraction (f) and number density (N) of scattering features. For features with a specified size (r)

$$\frac{d\Sigma}{d\Omega}(q)=NV^2\left(\rho_f-\rho_m\right)^2S(qr) \quad (2)$$

Here, ρ_f and ρ_m are the feature and matrix coherent scattering length densities and S(qr) is a form factor that depends on the features shape and size [8]. We determined <r>, f and N by fitting computed $d\Sigma/d\Omega(q)_m$ curves to the $d\Sigma/d\Omega(q)$ data assuming a log-normal distribution, parameterized by mode radius, r_m, $\Delta r/r$, and $d\Sigma/d\Omega(0)_m$ [7]. However, measuring f and N requires *knowledge* of the ρ_f and ρ_m. Assuming the features are primarily Y, Ti and O, ρ_f ≈ 0 and the ρ_m accounted for Cr and other solutes.

The <r>, N, f and M/N were measured for MA957 thermally aged in a gettered argon atmosphere in 50°C temperature (T_a) increments from 1150 to 1400°C for various times (t_a) from 1 to 243 h (depending on T_a). However, good qualitative insight on the effects of composition and processing variables on the UCSB

powders and the as-processed alloys can be simply obtained by comparing the $d\Sigma/d\Omega(\phi = 45\pm15)$ versus q^2 curves. A minimum of 7 indents at a 1000g load was used to measure the Vicker's microhardness, H_v (kg/mm^2).

Results and Analysis

The sequence-of-events in the formation of NCs is revealed in Figure 1a. The $d\Sigma/d\Omega$ versus q^2 plots for the milled U14WT (filled circles) and U14YWT (filled squares) powders are very similar, and have a small slope in the range of $q^2 > 2$ nm^{-2}, indicating that NC features are not present in either case. The slightly higher high q scattering in the U14YWT is indicative of the presence of additional solutes or very small solute clusters. However, HIPing the U14YWT at 850°C (filled diamonds) results in the precipitation of a high number density NCs, indicated by the large bulge in the $d\Sigma/d\Omega$ curve for q^2 between ≈ 1 and 6 nm^{-2}. The corresponding $d\Sigma/d\Omega$ for U14WT, without Y_2O_3, HIPed at 850°C (empty circles) is much smaller in this q-range.

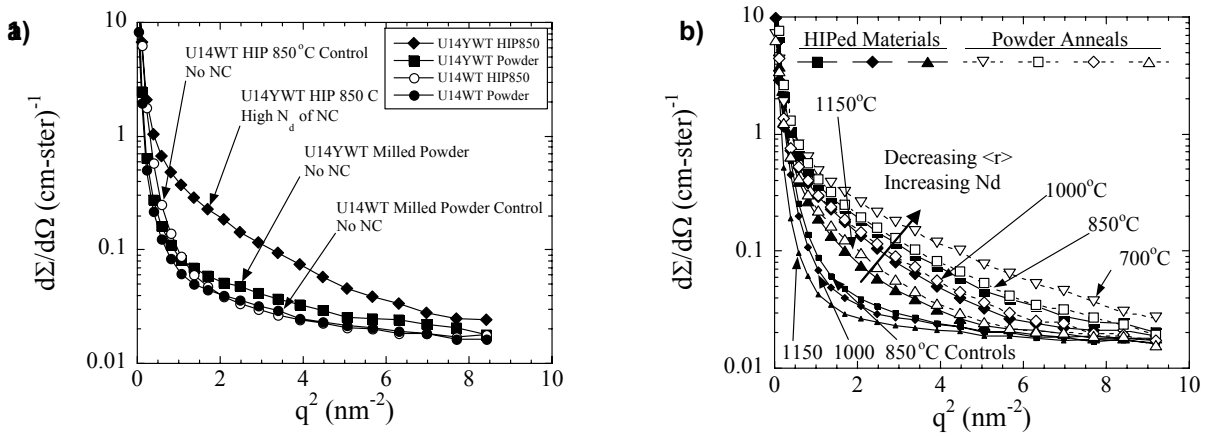

Figure 1. (a) SANS curves for U14YWT showing that mechanical alloying dissolves the Y_2O_3 and that the NCs form during HIP consolidation and (b) the effect of HIP consolidation (closed symbols) and powder annealing (open symbols) temperatures on NC formation in U14YWT.

Figure 1b shows the effect of HIPing (closed symbols) and powder annealing (open symbols) temperatures of 850 (squares), 1000 (diamonds) and 1150°C (triangles) on U14YWT along with U14WT controls (small symbols). The decreases in the magnitude and increases in the slope of the $d\Sigma/d\Omega$ versus q^2 curves indicate that the <r> increases and the N and f decrease with increasing HIPing and powder annealing temperature. Notably, the scattering in the consolidated alloys and annealed powders is very similar. The powder annealed at 700°C (upside down triangles) has the highest scattering and lowest slope, hence, the smallest <r>; however, a quantitative analysis shows that the f and N are slightly smaller in this case compared to the powders annealed at 850°C.

Figure 2a shows the effects of alloy composition on the formation of NCs in alloys HIPed at 1150°C. The U14YW (diamonds) and U14Y (squares) alloys without Ti do not contain NCs. However, a high density of similar NCs form in both the U14YWT (upside down triangles) and U14YT (triangles) alloys with Ti. The general trends are similar at lower HIPing temperatures (not shown), but the importance of Ti is weaker in this case, and NCs are observed in U14YW and U14Y in alloys HIPed at 850°C.

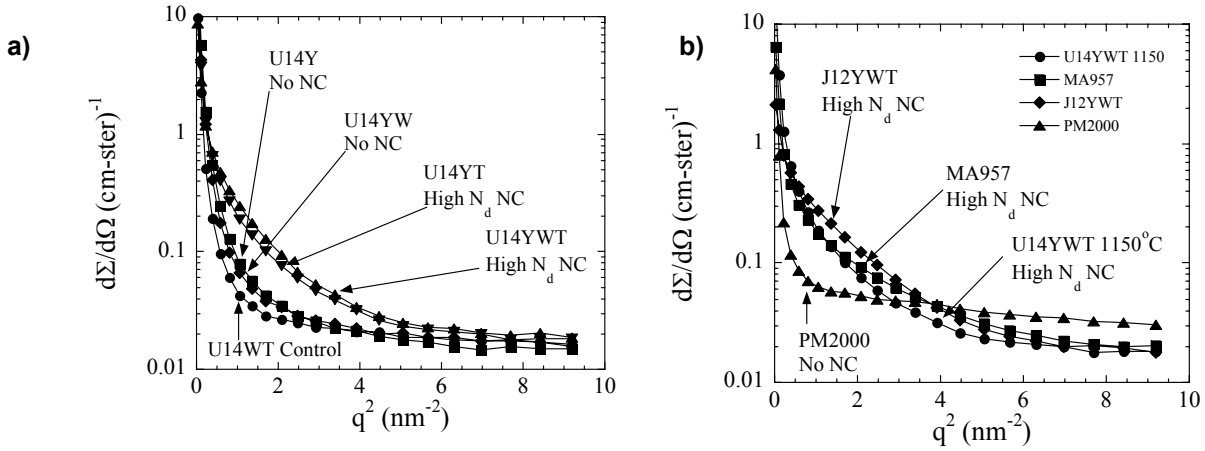

Figure 2. (a) The effect Ti on NC formation for HIPing at 1150°C. (b) Comparison of NC scattering in U14YWT, MA957, J12YWT, and PM2000.

Figure 2b shows that the NCs in U14YWT HIPed at 1150°C (circles) are very similar to those in MA957 (squares) and 12YWT (diamonds). However, the PM2000 (triangles) alloy does not contain NCs. Note, the larger $d\Sigma/d\Omega$ at high q in this case is due to the higher Cr content of this alloy.

We summarize only the most salient results of the quantitative analysis of the thermally aged MA957. Figure 3a shows that N decreases with increasing T_a, accompanied by increases in <r> and decreases in f (not shown). Aging at the processing temperature of 1150°C has little effect, while aging at 1200°C produces a systematic coarsening and a decrease in f by a factor of ≈ 0.7 at a constant M/N. The N and $<r(t_a)>^3-<r(0)>^3$ approximately scale with t_a^{-1} and t_a, respectively, in this case, consistent with a classical bulk diffusion controlled coarsening. In contrast, aging at 1250°C produces a rapid drop in N at 3h. While the NCs are significantly larger in this case, they have a similar f and M/N. Subsequent NC growth occurs at longer t_a occurs at an apparently fluctuating f and constant M/N. The decrease in N and increase $<r(t_a)>^3-<r(0)>^3$ at 1250°C scale with ≈ $t_a^{-0.3}$. At still higher T_a the N continues decrease with large jumps at 3h, again followed by non-classical coarsening scaling with t_a^{-p}, where p << 1 as shown in Figure 3a. Both f, and particularly M/N, are larger at the highest t_a of 1350 and 1400°C. Additional data and analysis is needed to understand this complex behavior. However, in summary, the NCs classically coarsen at 1200°C, undergo a rapid instability at 1250°C and experience another transition at and above 1350°C.

These complex results suggest that there is not one single mechanism controlling the evolution of NCs under high temperature aging. Analysis of the N and $<r(t_a)>^3-<r(0)>^3$ data yields effective activation energies Q_e of ≈ 400 and 300±20 kJ/mole respectively. The value of 300kJ/mole is reasonably consistent with typical values for solute and self-diffusion in iron [9]. Note a much higher, and non-physical, Q_e is indicated by the relative stability of the NCs between 1150 and 1200°C. If we assume that diffusion controlled kinetics the Q_e ≈ 300 to 400 kJ/mole are applicable to lower aging temperatures, pertinent to service conditions, we can estimate the corresponding coarsening rates. Assuming a Q_e of 300 kJ/mole the NC stability at 1150°C after 243h would correspond to $t_a \approx 10^5$h at 800°C. The modest but significant coarsening at 9h and 1200°C would correspond to t_a of 8.3×10^4 to 1.75×10^6 h at T_a = 800°C for Q_e of 300 and 400 kJ/mole, respectively. This suggests that the NCs will be either stable or very stable at expected service temperatures. However, long-time aging studies of aging below the final processing temperature are needed to confirm this conclusion.

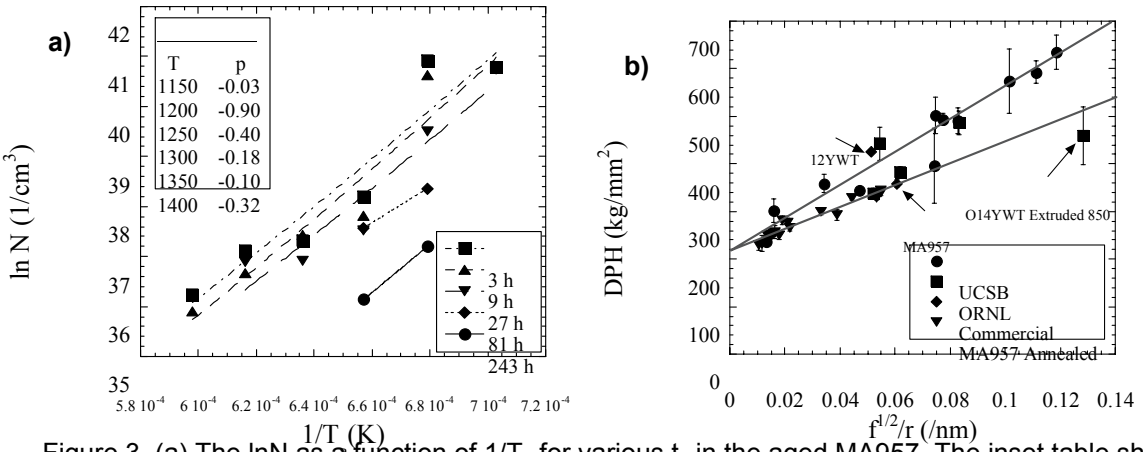

Figure 3. (a) The lnN as a function of $1/T_a$ for various t_a in the aged MA957. The inset table shows the fit parameters, p, for the relation $N = C(T)t_a^p$. (b) The H_v as a function $f^{1/2}/r$ showing two hardening regimes.

Figure 3b plots the H_v, including for some alloy-conditions not explicitly discussed here, versus $f^{1/2}/\langle r\rangle$. The data fall into two hardening rate categories of $\Delta H_v/\Delta[f^{1/2}/\langle r\rangle]$, as indicated by the slopes of the two least square fit lines. The higher hardening rate is generally associated with the alloys containing Y-Ti-O NCs HIPed at 850 and 1000°C and 12YWT. The alloys with a lower hardening rate include the MA957 in both the as-processed and aged conditions, other powders HIPed at 1150°C with and without Ti, as well as powders with Ti that were attritor milled with Y_2O_3 at Oak Ridge National Laboratory. Presumably, most of the hardening is due to NCs. The increase in the yield stress, $\Delta\sigma_y$, due to dispersed barrier obstacles to dislocation slip is given by [10]

$$\Delta\sigma_y \approx 3\alpha Gb/\lambda \approx 1.68\alpha Gb\, f^{1/2}/\langle r\rangle \qquad (3)$$

Here, the 3 is the Taylor's factor, α is the obstacle strength parameter (< 0.8), G and b are the Fe shear modulus (≈ 80 GPa) and Burger's vector (0.25 nm), respectively, and λ is the obstacle spacing on a slip plane, where $1/\lambda = 0.56f^{1/2}/\langle r\rangle$ [10]. Assuming $\Delta\sigma_y$ (MPa) ≈ $3\Delta H_v$ (kg/mm^2) the slopes of the lines in Figure 3b can be used to estimate effective values of α, ≈ 0.33 and 0.5. However, a significant Hall-Petch type contribution from the small grain-subgrain size is also expected. Since the grain/sub-grain size is also influenced by the processing conditions and boundary pinning by the NCs themselves, it is difficult to separate the two contributions to $\Delta\sigma_y$.

Conclusions

The results of this study can be summarized as follows:

-The Y_2O_3 dissolves during mechanical alloying.
-Y-Ti-O enriched NCs precipitate during high temperature consolidation.
-Increasing consolidation temperature results in larger NC sizes and smaller number densities and volume fractions.
-The NCs that form in annealed MA powders are nearly identical to those in HIP consolidated alloys.
-Both Y and Ti are required for the formation of high number density NCs at higher HIPing temperatures.
-The NCs in U14YWT HIP consolidated at 1150°C are similar to those found in MA957 and J12YWT that are extruded at the same temperature.
-The NCs in MA957 are expected to be thermally stable at service temperatures around 800°C.
-There is an excellent correlation between microhardness and the size and volume fraction of the NCs or their spacing on a slip plane.

Acknowledgements

The authors gratefully acknowledge Doug Klingensmith (UCSB) for his contributions to the SANS experiments and Professor Brian Wirth (UC Berkeley) for his help in analysis of the SANS data. We acknowledge the support of the National Institute of Standards and Technology, U.S. Department of Commerce, in providing facilities used in this work. This research was supported by DOE Office of Fusion Energy Science (Grant # DE-FG03-94ER54275) and the INERI DOE Office of Nuclear Energy through a subcontract with ORNL (Grant # 400014112).

References

[1] J. S. Benjamin, Met. Trans. V1N10 (1970) 2943.
[2] S. Ukai, T. Nishida, and H. Okada, J. Nuc. Sci. and Tech. V34N3 (1997) 256.
[3] S. Ukai, T. Nishida, T. Okuda, and T. Yoshitake, J. Nucl. Mater. 258-263 (1998) 1745.
[4] T. Okuda and M. Fujiwara, J. Mater. Sci. 14 (1995) 1600.
[5] M. K. Miller, E. A. Kenik, K. F. Russell, L. Heatherly, D. T. Hoelzer, and P.J. Maziasz, Mater. Sci. and Engr. A A353 (2003) 140.
[6] H. Kishimoto, M. J. Alinger, G. R. Odette, and T. Yamamoto, Journal of Nuclear Materials, submitted.
[7] E. Mader, Ph.D. Thesis, University of California, Santa Barbara (1995).
[8] ILL Neutron Data Booklet, A.-J. Dianoux and G. Lander, Eds., Institut Laue-Langevin (2001).
[9] J. Kucera and K. Stransky, Mater. Sci. and Eng. 52 (1982) 1.
[10] J. W. Martin, Micromechanisms in Particle-Hardened Alloys, Cambridge University Press (1980).

4.0 COPPER ALLOYS

EVOLUTION OF CLEARED CHANNELS IN NEUTRON-IRRADIATED PURE COPPER AS A FUNCTION OF TENSILE STRAIN—D. J. Edwards (Pacific Northwest National Laboratory)* and B. N. Singh (Risø National Laboratory, Denmark)

Extended abstract of a paper submitted to the Journal of Nuclear Materials as part of the proceedings of the 11th International Conference on Fusion Reactor Materials, Kyoto, Japan, December 7-12, 2003.

EXTENDED ABSTRACT

The occurrence of localized deformation via dislocation channeling in irradiated materials continues to present an interesting challenge to the fusion materials community. While this phenomenon has been known for over 40 years [1-4], until recently little progress has been made in understanding the origin of the channels and the variables that influence their formation and propagation. More recent work [5-10] has led to a re-evaluation of how channels are formed and propagate in irradiated materials, as well as in unirradiated materials. Some of the outstanding issues that remain unanswered include how to precisely relate the occurrence of the yield point to the microstructure formed during irradiation, how channels are cleared of defects and leave no dislocation debris behind, and how to account for the increase in stress when no conventional work hardening processes are evident.

As part of a broader set of experiments aimed at studying localized deformation in pure metals, a simple experiment was conducted wherein tensile tests of neutron-irradiated copper were stopped at intermediate strains. The material used in the present investigation was thin (0.3 mm) sheet of oxygen-free high conductivity (OFHC) copper containing 10, 3, < 1 and < 1 ppm, respectively, of Ag, Si, Fe and Mg, respectively. The oxygen content of this copper was found to be 34 appm. Five tensile samples of OFHC copper were irradiated in the DR-3 reactor at Risø National Laboratory. Prior to irradiation, the OFHC copper samples were given a solution annealing treatment of 823K for 2 hours in a vacuum of 10^{-6} torr. The resulting grain size and dislocation density were about 30 μm and ~10^{12} m^{-2}, respectively. The tensile specimens were irradiated at 323K to a dose level of 0.3 dpa (NRT). All specimens were irradiated at a displacement damage rate of ~5 x 10^{-8} dpa (NRT)/s. The specimens were tensile tested at room temperature in an Instron machine at a strain rate of 1.2 x 10^{-3} s^{-1}. One specimen was tested to failure, one specimen loaded to ~90% of the upper yield stress, unloaded and then removed from the test fixture, and the remaining 3 specimens strained plastically to 1.5, 5 or 14.5% elongation, unloaded and then removed from the tensile machine. The full tensile curve and the associated stress-strain curves for the other four samples are shown in Figure 1.

The sample stopped at ~90% of the yield stress exhibited a few narrow channels scattered at random in isolated grains. Defect free zones (DFZ) around grain boundaries were common, and were definitively not diffusion based because the width of the zones varied considerably along the length of an individual grain boundary and sometimes disappeared altogether. A check of the untested sample revealed no such features, indicating the defect zones were a consequence of grain boundary migration or sliding under the high stress reached before yielding. The main mode of plastic strain accumulation was via by dislocation channels initiated at interfacial stress concentrations that then propagated quickly through the grain. Examination of the samples strained to successively higher plastic strains confirmed that new channels continued to form even in the necked region of the failed tensile sample, illustrating that the dense population of defects effectively inhibits the global movement of dislocations to very high plastic strains and stresses. Examples of the progressive formation of slip steps on the surface of strained specimens are shown in Figure 2. These slip steps are thought to correspond directly to individual dislocation channels. The yield point is thought to be related to the initial generation of isolated channels from stress concentrators (not necessarily unpinning of Frank-Read sources), which is then followed by the continual generation of new channels from interfacial stress concentrators as the plastic strain increases to the point of necking and failure. Dislocations are not produced uniformly inside the grains by

*Pacific Northwest National Laboratory (PNNL) is operated for the U.S. Department of Energy by Battelle Memorial Institute under contract DE-AC06-76RLO-1830.

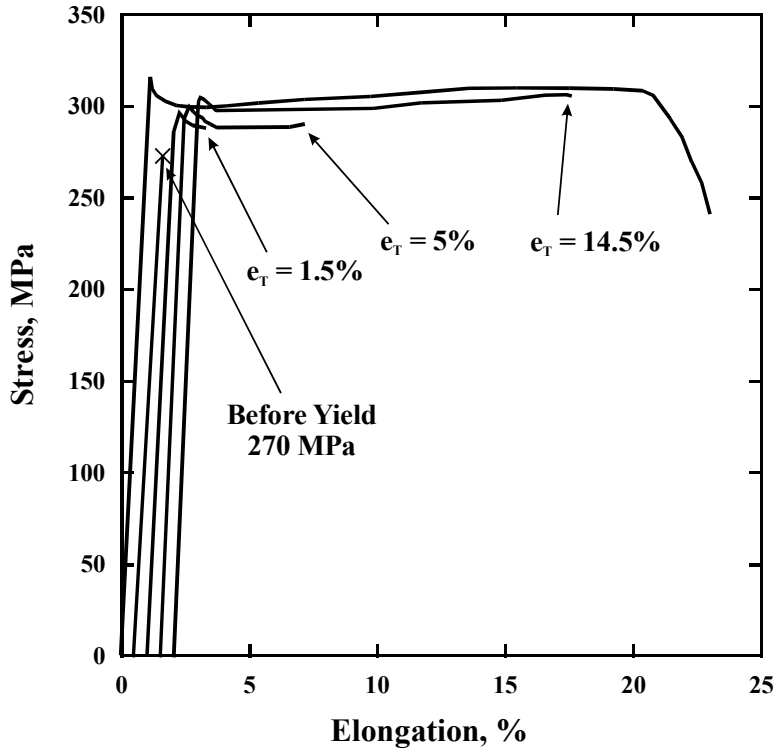

Figure 1. The tensile curves for each of the 5 tested conditions are shown. The stress or strain at which the tests were stopped for each specimen are indicated by the arrows. Note that some variability exists from specimen to specimen, so the yield point varies slightly. Curves are offset for clarity.

deformation, only in dislocation channels. Pre-existing loops and dislocation segments formed during irradiation are able to move and interact over very short distances, however, these dislocations do not appear to play any role in channel formation. The lack of any cell wall formation or general expansion of the DFZs around grain boundaries further testifies that dislocations produced outside of channels cannot move large distances in this irradiation condition. The continued generation of new channels past even the onset of necking subdivides the grains into smaller volumes that rotate and slide with respect to each other, much like subgrains in unirradiated and deformed copper.

Acknowledgements

The present work was partly funded by the European Fusion Technology Programme. The authors wish to thank B. F. Olsen for his technical assistance. D. J. Edwards would like to thank Risø National Laboratory for the support and assistance during his visit. His work was partly supported by the U.S. Department of Energy under contract DE-AC06-76RLO 1830 with the Battelle Memorial Institute at the Pacific Northwest National Laboratory.

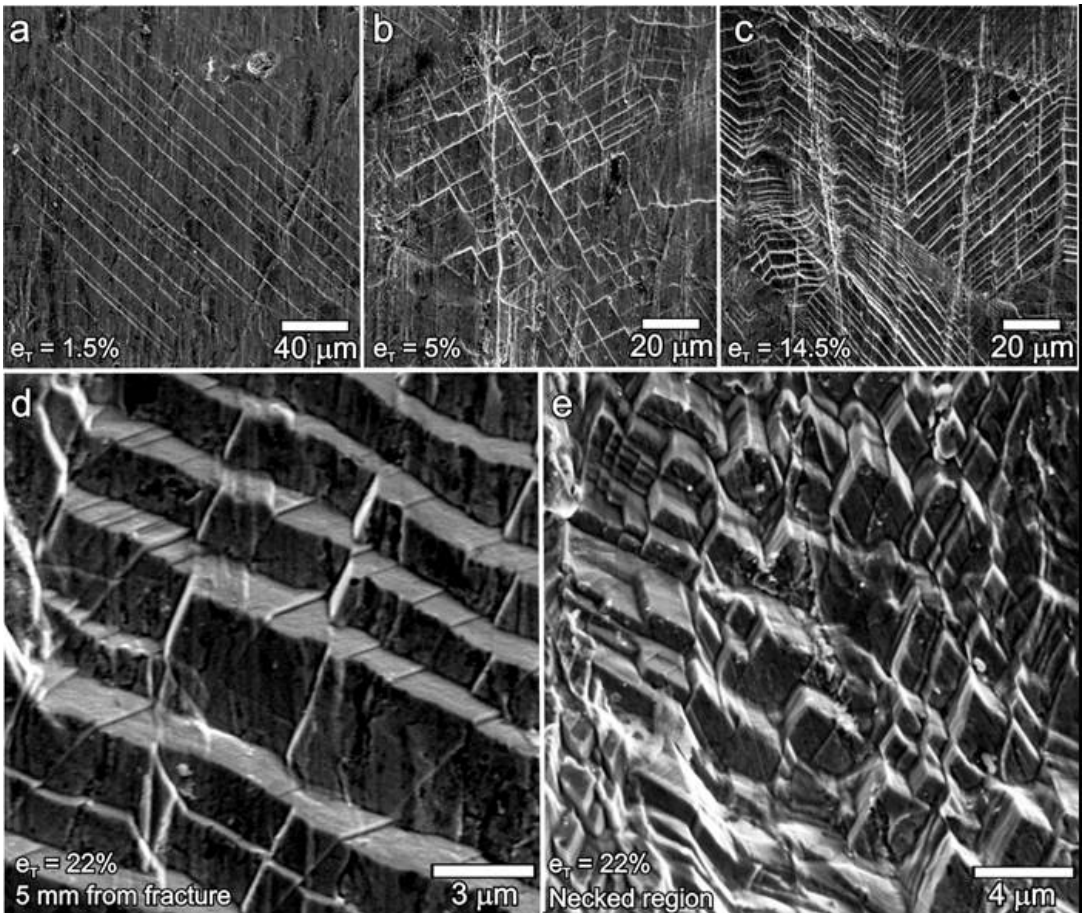

Figure 2. Examples of the slip step evolution as a function of strain are shown. As the plastic strain increases, the density of slip steps in a given grain increases and secondary slip steps begin to arise. In the last two figures (d and e), the crystal has been divided into discrete rectangular volumes that appear to slide with respect to each other. The image in (d) was taken 5 mm from the final fracture, and the image in (e) was taken in the necked region less than 1 mm from the final fracture location.

References

[1] J. Silcox and P. B. Hirsch, Phil. Mag. 4 (1959) 1356.
[2] A. Seeger, in Proc. 2nd UN Int. Conf. on Peaceful Uses of Atomic Energy, Geneva, 6 (Sept. 1958) 250.
[3] B. L. Eyre and A. F. Bartlett, Phil. Mag. 11 (1965) 53.
[4] M. J. Makin, in Radiation Effects (ed. W.F. Sheely), AIME, 37 (1966) 627 (Metallurgical Soc. Conf., Asheville, NC, Sept. 1965), published by Gordon and Breach, Science Publishers, Inc., New York.
[5] M. J. Makin and S. A. Manthorpe, Phil. Mag. 8 (1963) 1725.
[6] B. N. Singh, A. J. E. Foreman, and H. Trinkaus, J. Nucl. Mater. 249 (1997) 103.
[7] M. Victoria, N. Baluc, C. Bailat, Y. Dai, M. I. Luppo, R. Schaublin, and B. N. Singh, J. Nucl. Mater. 276 (2000) 114.
[8] K. Farrell, T. S. Byun, and N. Hashimoto, Mapping Flow Localization Processes In Deformation of Irradiated Reactor Structural Alloys – Final Report, ORNL/TM-2003/63 (2003).
[9] J. S. Robach, I. M. Robertson, B. D. Wirth, and A. Arsenlis, Phil. Mag. 83 No. 8 (2003) 955.
[10] B. N. Singh, D. J. Edwards, and P. Toft, J. Nucl. Mater. 299 (2001) 205.

DISLOCATION DENSITY-BASED CONSTITUTIVE MODEL FOR THE MECHANICAL BEHAVIOR OF IRRADIATED CU—A. Arsenlis (Lawrence Livermore National Laboratory), B. D. Wirth (Department of Nuclear Engineering, University of California Berkeley), and M. Rhee (Lawrence Livermore National Laboratory)

EXTENDED ABSTRACT

Performance degradation of structural steels in nuclear environments results from the formation of a high number density of nanometer scale defects. The defects observed in copper-based alloys are composed of vacancy clusters in the form of stacking fault tetrahedra and/or prismatic dislocation loops that impede the motion of dislocations. The mechanical behavior of irradiated copper alloys exhibits increased yield strength, decreased total strain to failure and decreased work hardening as compared to their unirradiated behavior. Above certain critical defect concentrations (neutron doses), the mechanical behavior exhibits distinct upper yield points. In this paper, we describe the formulation of an internal state variable model for the mechanical behavior of such materials subject to these environments. This model has been developed within a multiscale materials modeling framework, in which molecular dynamics simulations of dislocation – radiation defect interactions inform the final coarse-grained continuum model. The plasticity model includes mechanisms for dislocation density growth and multiplication and for irradiation defect density evolution with dislocation interaction.

The material parameters for the constitutive model were fit to the published stress-strain behavior of unirradiated Cu, with irradiation damage-dependent constants approximated from the initial yield strength of irradiated Cu. We then compared model predictions of the homogeneous constitutive behavior to observed tensile stress-strain behavior of irradiated Cu, for variations of irradiation induced defect density between $4x10^{20}$ and $4x10^{23}$ m^{-3}, with an initial SFT size of 2.5 nm. The general behavior of the homogeneous constitutive model shows that as the defect density increases, the initial yield point increases and the initial strain hardening decreases. Implementation of the final coarse-grained constitutive model into a finite element framework was used to simulate the behavior of tensile specimens. The simulation results compare favorably with the experimentally observed mechanical behavior of irradiated Cu, and reproduce the increased strength, the decreased nominal strain at the ultimate tensile strength, the formation of an initial yield point forms above a critical SFT density of about $2x10^{23}$ m^{-3}, and higher stresses after the ultimate tensile strength for a given strain, as compared to unirradiated behavior.

Future modeling efforts will focus on coupling the constitutive model to a microstructure evolution model to predict the mechanical property changes as a function of irradiation variables and on developing a model for irradiated bcc alloys, which will require a temperature dependent dislocation velocity law to account for the inherent lattice resistance and the material's response to strain localization and the formation of adiabatic shear bands.

Reference

A. Arsenlis, B. D. Wirth, and M. Rhee, submitted for publication in Philosophical Magazine.

5.0 REFRACTORY METALS AND ALLOYS

No contributions.

6.0 AUSTENITIC STAINLESS STEELS

THE STRONG INFLUENCE OF DISPLACEMENT RATE ON VOID SWELLING IN VARIANTS OF FE-16CR-15NI-3MO AUSTENITIC STAINLESS STEEL IRRADIATED IN BN-350 AND BOR-60—N. I. Budylkin, E. G. Mironova, N. M. Mitrofanova, and V. M. Chernov (Bochvar Institute of Non-Organic Materials), S. I. Porollo (Institute of Physics and Power Engineering), T. M. Bulanova, V. K. Shamardin (Research Institute of Atomic Reactors), and F. A. Garner (Pacific Northwest National Laboratory)*

OBJECTIVE

The object of this effort is to determine the parametric sensitivity of void swelling, especially with respect to the effect of atomic displacement rate.

SUMMARY

Recent irradiation experiments conducted on a variety of austenitic stainless steels have shown that void swelling appears to be increased when the dpa rate is decreased, primarily by a shortening of the transient regime of swelling. This paper presents results derived from nominally similar irradiations conducted on six Russian steels, all laboratory heat variants of Fe-16Cr-15Ni-3Mo-Nb-B, with each irradiated in two fast reactors, BOR-60 and BN-350. The BN-350 irradiation proceeded at a dpa rate three times higher than that conducted in BOR-60. In all six steels, a significantly higher swelling level was attained in BOR-60, agreeing with the results of earlier studies.

PROGRESS AND STATUS

Introduction

Earlier studies have shown that the atomic displacement rate is unexpectedly one of the most important variables in determining the onset and magnitude of swelling in austenitic stainless steels [1-11]. In general, a decrease in the dpa rate leads to an onset of swelling at a lower dose, yielding more swelling at a given dpa level than would be attained at a higher dpa rate. One recent study also suggests that a similar sensitivity to dpa rate exists in ferritic alloys [12].

Given the potential impact on the fusion swelling issue, such a surprising and counterintuitive conclusion requires additional data for confirmation, especially with respect to establishing the general applicability of this conclusion as valid for a wide variety of neutron spectra and for different austenitic steels.

This paper presents results derived from irradiations conducted on six Russian steels, each irradiated in two fast reactors. It should be noted that Russian steels used for nuclear service are in general stabilized steels, usually containing titanium or niobium, while comparable steels used for nuclear service in U.S.A. and Japan are usually unstabilized.

Experimental Details

Two of the major test beds for high fluence irradiation in the CIS (Commonwealth of Independent States, formerly states of the Soviet Union) are BOR-60 in Dimitrovgrad, Russia and BN-350 in Aktau, Kazakhstan, operating at nominal power levels of 60 and 350 MW, respectively. Both BOR-60 and BN-350 are sodium-cooled fast reactors, but the latter, now decommissioned, operated at significantly higher neutron fluxes than the former.

Two experimental series are of interest to the subject of this paper. They involve comparative irradiation experiments in the two reactors that were designed primarily to explore material variables that impact swelling. However, since the irradiation conditions were largely the same except for displacement rate,

*Pacific Northwest National Laboratory (PNNL) is operated for the U.S. Department of Energy by Battelle Memorial Institute under contract DE-AC06-76RLO-1830.

these experiments also explored the competition between material variables and differences in displacement rate.

All specimens in both series were in the form of tensile specimens with a total length of 26 mm and a gauge length of 15 mm. The gauge diameter was 3 mm and that of the heads was 6 mm.

The steels investigated were all laboratory heat variants of Fe-16Cr-15Ni-3Mo-Nb-B, with compositions shown in Table 1. These steels are variations of EP-172 steel that is frequently used for nuclear applications in Russia.

Note that there were two experimental alloy series. The first four-alloy series was Fe-16Cr-15Ni-3Mo-0.6Nb-0.6Mn-0.06C-0.008P but varying in silicon content from 0.4 to 1.2 wt%. The second three-alloy series contained the 0.63% silicon variant from the first series and two other alloys where 0.15% titanium either was added to or replaced the 0.6% Nb.

After fabrication, multiple specimens of all six alloys were prepared in the fully annealed condition (50% CW/1080°C for 30 min in argon/air cooling) and irradiated side by side in each reactor while in contact with flowing sodium coolant. In each reactor the specimens experienced similar temperature and dpa levels, but the irradiation proceeded at 5.06 x 10^{-7} dpa/sec in BOR-60 and 1.58x 10^{-6} dpa/sec in BN-350, approximately a factor of three difference in rate. The fluences attained were 11.5 x 10^{22} and 11.9 x 10^{22} n/cm^2 (E > 0.1 MeV), respectively.

The dose reached was 52 dpa in BOR-60 and 53 dpa in BN-350, while the temperatures were 470-480°C in BOR-60 and 490°C in BN-350. All temperatures are calculated with an error of ±15°C. The neutron spectra of the two reactors were very similar at ~4.5 dpa per 10^{22} n/cm^2 (E >0.1 MeV), which ensures that there were no differences in helium generation or other transmutant formation rates.

Following irradiation the specimens were cleaned and their density measured using a CCl_4 immersion technique. Measurements were performed on two (BN-350) to six (BOR-60) nominally similar specimens for each heat. Each specimen was weighed three times to determine the average density. Measurement accuracy was ± 0.2% before irradiation and ± 0.5% in the hot cell after irradiation. In general, there was a rather limited range of swelling variation for nominally identical specimens. Each data point in Figure 1 represents the average of six (BN-350) or eighteen (BOR-60) measurements. For example the swelling of the 0.04% Si specimen in BOR-60 ranged from 19.3 to 22.5%, showing rather good agreement for six nominally identical specimens.

Results

Figure 1 shows that in each case there was a clear effect of composition on the swelling in both series of alloys, but there was more swelling (16-20%) in the BOR-60 experiment conducted at the lower displacement rate, while only 2-7% was reached in the BN-350 experiment at the higher displacement rate.

Another observation is that the relative behavior with composition of each alloy series is somewhat different in the two reactors, indicating that the onset of swelling in response to a given compositional variable can change as competitive and synergistic influences of other environmental variables, such as dpa rate, come into play.

Table 1. Chemical composition in wt% of the EP-172-type steels irradiated in both BOR-60 and BN-350. Nitrogen contents of all steels lie in the range 0.02-0.03 wt%.

Steel #		C	Mn	Si	S	P	Cr	Ni	Mo	Nb	Ti	B
16Cr-15Ni-3Mo-B	1	0.060	0.7	0.40	≤0.015	≤0.015	16.00	15.00	2.90	0.65	-	0.007
	2	0.063	0.7	0.63	≤0.015	≤0.015	16.20	15.20	2.98	0.65	-	0.008
	3	0.062	0.6	0.95	≤0.015	≤0.015	15.50	14.50	2.90	0.65	-	0.008
	4	0.064	0.6	1.22	≤0.015	≤0.015	16.25	15.30	3.00	0.60	-	0.008
	5	0.060	0.5	0.64	≤0.015	≤0.015	16.03	15.06	3.00	0.06	0.15	0.006
	6	0.060	0.6	0.63	≤0.015	≤0.015	16.05	15.08	2.93	0.60	0.15	0.008

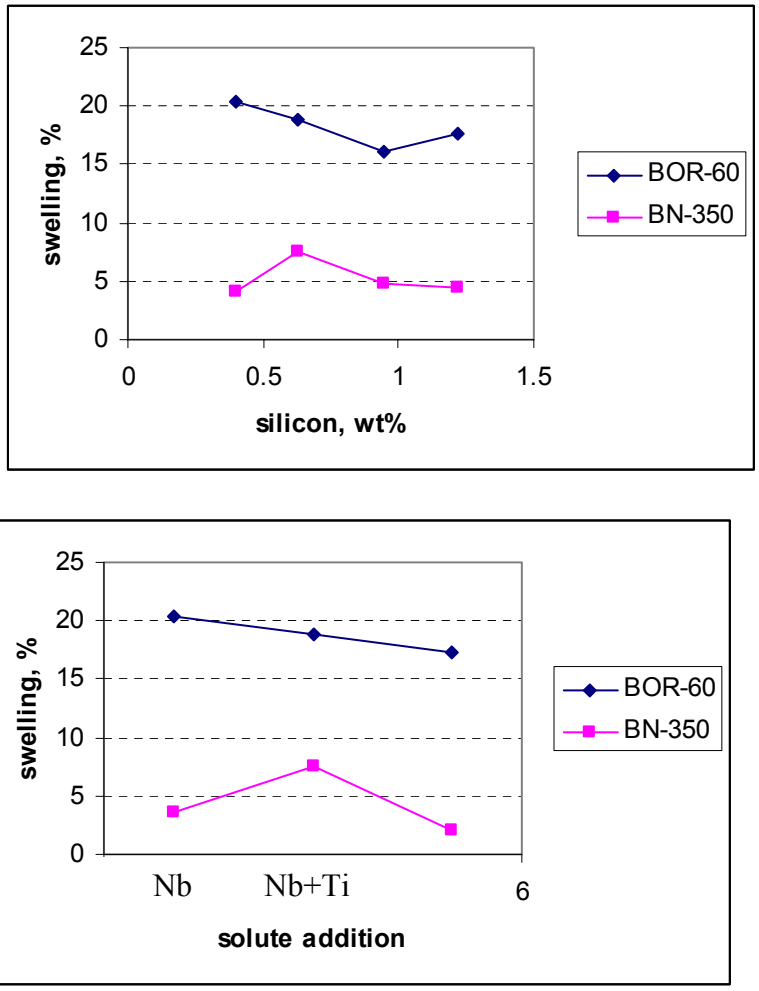

Figure 1. Comparison of swelling measured by density change for the two experimental series irradiated in BOR-60 (470-480°C, 52 dpa, 5 x 10^{-7} dpa/s) and BN-350 (490°C, 53 dpa, 15.6 x 10^{-7} dpa/s).

Discussion

Considering that the two irradiations were conducted in separate reactors, even with nominally similar conditions of temperature, temperature history, neutron spectra and helium generation rate, one can not firmly state based on these data alone that the different dpa rates were the only variable operating to produce the large difference in swelling. However, the very large difference in response between the two irradiations is strongly supportive of an interpretation based on flux-dependent swelling, especially when viewed in the context of the earlier quoted studies [1-11].

While the level of swelling in these experiments appears to be affected by the dpa rate, it is not clear in what stage of the swelling evolution the effect is manifested.

The "flux-effect" studies led by Okita [4, 6, and 7] show that, at least in simple model austenitic alloys, the post-transient steady-state swelling rate is not affected by differences in dpa rate, with the flux sensitivity confined to the transient regime. Okita presents microstructural evidence to support the flux dependency arising primarily from the flux sensitivity of Frank loop evolution and its subsequent transition to a network dislocation.

Conclusions

As data continue to accumulate it appears that austenitic stainless steels irradiated in various fast reactors develop void swelling at accelerated rates as the atomic displacement rate decreases. Synergisms between compositional and irradiation variables operate to produce the observed swelling behavior.

Acknowledgements

The Russian data presented in this report was generated in irradiation programs conducted earlier under the sponsorship of MINATOM and later evaluated under the sponsorship of the Ministry of Science of the Russian Federation. The U.S. portion of this work was jointly supported by the Materials Sciences Branch, Office of Basic Energy Sciences, and the Office of Fusion Energy, U.S. Department of Energy, under Contract DE-AC06-76RLO 1830. The assistance of Natalia Brikotnina of Translation and Interpreter Services to facilitate discussions and to provide the English translation of the Russian draft is gratefully acknowledged.

References

[1] F. A. Garner, Chapter 6: Irradiation Performance of Cladding and Structural Steels in Liquid Metal Reactors, Vol. 10A of Materials Science and Technology: A Comprehensive Treatment, VCH Publishers (1994) 419-543.

[2] D. L. Porter and F. A. Garner, Swelling of AISI Type 304L Stainless Steel in Response to Simultaneous Variations in Stress and Displacement Rate, Effects of Radiation on Materials: Twelfth International Symposium, ASTM STP 870, Eds. F. A. Garner and J. S. Perrin, ASTM, Philadelphia, PA (1985) 212-220.

[3] G. M. Bond, B. H. Sencer, F. A. Garner, M. L. Hamilton, T. R. Allen, and D. L. Porter, Void Swelling of Annealed 304 Stainless Steel at ~370-385°C and PWR-Relevant Displacement Rates, in Proceedings of the 9th International Conference on Environmental Degradation of Materials in Nuclear Power Systems – Water Reactors (1999) 1045-1050.

[4] T. Okita, N. Sekimura, F. A. Garner, L. R. Greenwood, W. G. Wolfer, and Y. Isobe, Neutron-Induced Microstructural Evolution of Fe-15Cr-16Ni Alloys at ~400°C During Neutron Irradiation in the FFTF Fast Reactor, 10th International Conference on Environmental Degradation of Materials in Nuclear Power Systems – Water Reactors (2001) CD format.

[5] T. Okita, N. Sekimura, T. Iwai, and F. A. Garner, Investigation of the Synergistic Influence Of Irradiation Temperature and Atomic Displacement Rate on the Microstructural Evolution of Ion-

Irradiated Model Austenitic Alloy Fe-15Cr-16Ni, 10th International Conference on Environmental Degradation of Materials in Nuclear Power Systems – Water Reactors (2001) CD format.

[6] T. Okita, T. Sato, N. Sekimura, and F. A. Garner, The Effect of Dose Rate on Microstructural Evolution in Austenitic Model Alloys Irradiated with Fast Neutrons, Proceedings of the Fourth Pacific Rim International Conference on Advanced Materials and Processing (PRICM4) (The Japan Institute of Metals, 2001) 1403.

[7] T. Okita, T. Sato, N. Sekimura, F. A. Garner, and W. G. Wolfer, Combined Effect of Temperature, Displacement Rate and Composition on the Neutron-Induced Swelling of Austenitic Alloys, 11th International Conference on Environmental Degradation of Materials in Nuclear Power Systems – Water Reactors (2003) CD format.

[8] V. S. Neustroev, V. K. Shamardin, Z. E. Ostrovsky, A. M. Pecherin, and F. A. Garner, Temperature-Shift of Void Swelling Observed at PWR-Relevant Temperatures in Annealed Fe-18Cr-10Ni-Ti Stainless Steel Irradiated in the Reflector Region of BOR-60, Effects of Radiation on Materials: 19th International Symposium, ASTM STP 1366, Eds. M. L. Hamilton, A. S. Kumar, S. T. Rosinski, and M. L. Grossbeck, American Society for Testing and Materials (2000) 792-800.

[9] S. I. Porollo, Yu. V. Konobeev, A. M. Dvoriashin, V. M. Krigan, and F. A. Garner, Determination of the Lower Temperature Limit of Stainless Steels at PWR-Relevant dpa Rates, Effects of Radiation on Materials, ASTM STP 1447, Ed. M. L. Grossbeck, ASTM International, West Conshohocken, PA (2003) in press.

[10] S. I. Porollo, A. M. Dvoriashin, Yu. V. Konobeev, A. A. Ivanov, S. V. Shulepin, and F. A. Garner, Microstructure and Mechanical Properties of Austenitic Stainless Steel 12X18H9T Neutron Irradiated at Extremely Low Dose Rates, submitted for presentation in Proceedings of the 22nd International ASTM Symposium on Effects of Radiation on Materials, Boston MA (June 2004).

[11] F. A. Garner, N. I. Budylkin, Yu. V. Konobeev, S. I. Porollo, V. S. Neustroev, V. K. Shamardin, and A. V. Kozlov, The Influence of DPA Rate on Void Swelling of Russian Austenitic Stainless Steels, 11th International Conference on Environmental Degradation of Materials in Nuclear Power Systems – Water Reactors (2003) CD format.

[12] F. A. Garner, M. B. Toloczko, and B. H. Sencer, Comparison of Swelling and Irradiation Creep Behavior of fcc-Austenitic and bcc-Ferritic/Martensitic Alloys at High Neutron Exposure, Proceedings of Workshop on Basic Differences in Irradiation Effects Between fcc, bcc and hcp Metals and Alloys, Congas de Onis, Spain, October 15-20, 1998, J. Nucl. Mater. 276 (2000) 123-142.

INFLUENCE OF RADIATION-INDUCED VOIDS AND BUBBLES ON PHYSICAL PROPERTIES OF AUSTENITIC STRUCTURAL ALLOYS—E. N. Shcherbakov, A. V. Kozlov, and I. A. Portnykh (FSUE Institute of Nuclear Materials), Iouri I. Balachov (SRI International), and F. A. Garner (Pacific Northwest National Laboratory)*

OBJECTIVE

The object of this effort is to determine experimentally the effect of radiation-induced microstructural changes on the physical properties of austenitic structural alloys.

SUMMARY

Void swelling in austenitic stainless steels induces significant changes in their electrical resistivity and elastic moduli, as demonstrated in this study using a Russian stainless steel irradiated as fuel pin cladding in BN-600. Precipitation induced by irradiation also causes second-order changes in these properties. When cavities are full of helium as expected under some fusion irradiation conditions, additional second-order changes are expected but they will be small enough to exclude from the analysis.

PROGRESS AND STATUS

Introduction

Void swelling is known to influence not only the dimensional stability of irradiated stainless steels, but also many of its basic physical properties. Recently, there has been a focus in the light water reactor community on measurement of void-induced changes in electrical resistivity, elastic moduli and ultrasonic velocity, and to use these measurements to measure swelling nondestructively [1-3].

Electrical resistivity changes were used earlier in the fusion materials program as a method to estimate the swelling-induced changes of thermal resistivity for high heat flux components [4]. It now appears that nondestructive applications of changes in this and other important physical properties may be useful for stainless steels chosen for use in the fusion energy program. As shown in this study, there are other microstructural contributions to changes in physical properties that must be taken into consideration.

Experimental Details

Fuel element cladding tubes (6.9 mm initial outer diameter and thickness 0.4 mm) constructed from 20% cold-worked austenitic steel of nominal composition 0.1C-16Cr-15Ni-2Mo-lMn that had been irradiated in the BN-600 fast reactor were examined after defueling and cleaning. Specimens of 30 mm length were cut from various areas to obtain a variety of temperatures (430 - 590°C), dose levels (50 to 90 dpa) and swelling values as high as 23%.

The electrical resistivity R was measured for each specimen at room temperature using a technique in which the potential difference between standard and test specimens was determined. The procedure of electrical resistivity measurements was described in detail in [5]. The relative measurement error did not exceed 1%.

To measure Young's modulus E and the shear modulus G an ultrasonic resonant technique was utilized which is based on both excitation of ultrasonic vibrations and measurement of natural frequencies of longitudinal and shear vibrations in the test specimen [6]. The magnitudes of both moduli were calculated based on dynamic elasticity theory using measured values of resonant frequencies and specimen sizes. Measurement error of the moduli did not exceed 1%.

---

*Pacific Northwest National Laboratory (PNNL) is operated for the U.S. Department of Energy by Battelle Memorial Institute under contract DE-AC06-76RLO-1830.

Void swelling *S* was determined from density measurements obtained using a hydrostatic weighing technique.

$$S = (\delta_0 / \delta - 1) \cdot 100\%, \qquad (1)$$

δ_0 and δ are the density in the initial state and after irradiation, respectively, with a measurement error of ± 0.02 g/cm^3.

Results

An earlier report presented the first results on this project, which has now been completed [7]. Results of electrical resistivity measurements and determination of Young's modulus *E* and shear modulus *G* are shown in Figures 1-3. The dependence of these physical properties on void swelling is clearly demonstrated. One can see also some deviations from expected behavior that may reflect experimental problems or may be connected with other structural changes. As radiation-induced structural changes are usually dependent on irradiation temperature the data were separated into two sets: "high-temperature" (>520°C) and "low-temperature" (<520°C).

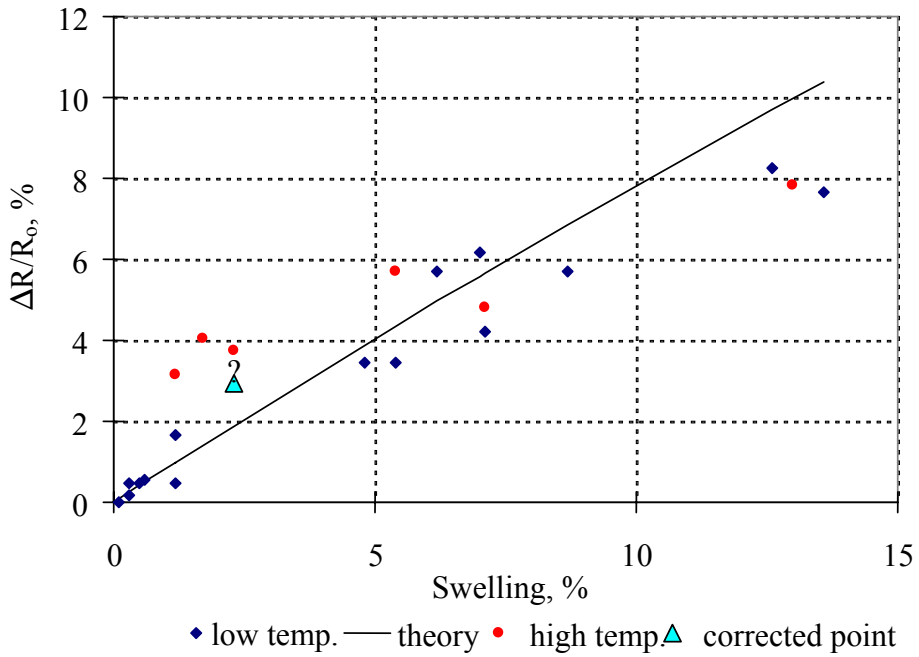

Figure 1. Dependence of relative change in electrical resistivity on void swelling. One point at 2.2% swelling shows the correction that would arise when accounting for nickel segregation into precipitates.

Discussion

As was shown in [6] voids in the two-phase model can be considered as a second phase with zero values of electrical conductivity and elastic modulus. Relative change can are defined in the following analytical expressions assuming an invariance of physical and mechanical properties of the matrix material.

$$\frac{\Delta R}{R_0} = \frac{5 \cdot S}{4 \cdot S + 6} \qquad (2)$$

$$\frac{\Delta E}{E_0} = \frac{1}{(1+S)^2} - 1 \qquad (3)$$

$$\frac{\Delta G}{G_0} = \frac{1}{(1+S)^2} - 1 \qquad (4)$$

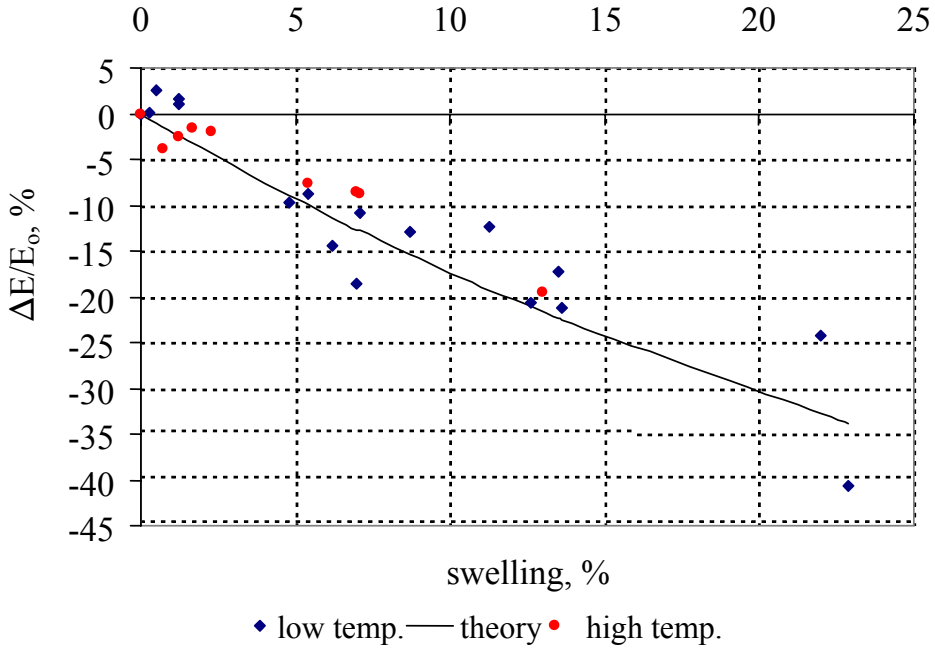

Figure 2. Dependence of relative change in Young's modulus on void swelling.

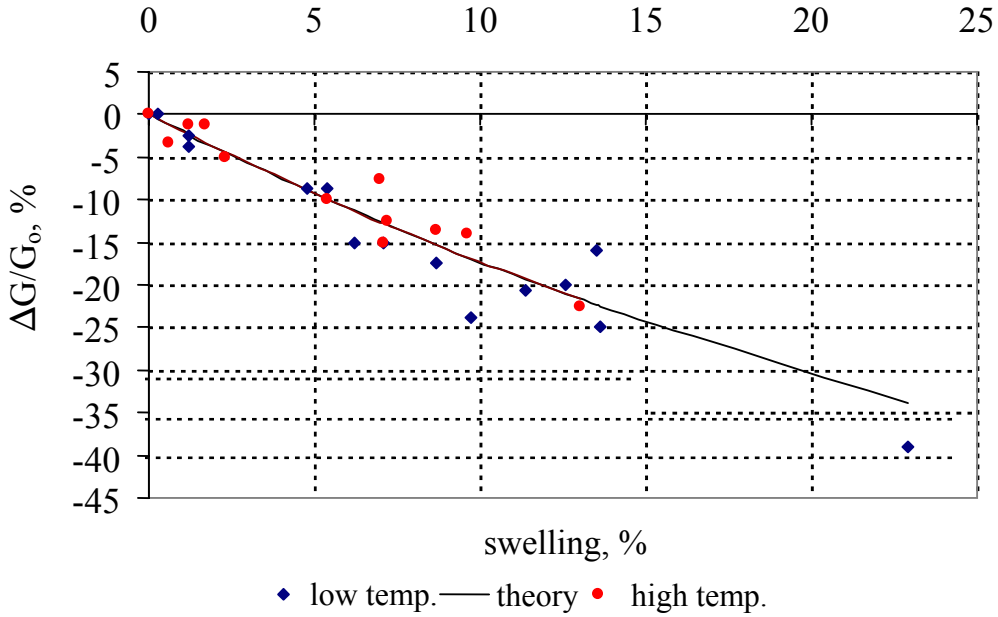

Figure 3. Dependence of relative change in shear modulus on void swelling.

ΔR, ΔE, and ΔG are absolute changes in resistivity and moduli, respectively, and R_0, E_0, and G_0 are the values in the initial state, and swelling S is expressed as a fraction.

Theoretical dependencies of electrical resistivity and elasticity moduli on swelling calculated using equations (1-3) are shown by lines in Figures 1-3. Swelling is confirmed to be the dominant factor in producing changes in these physical properties. At the same time, other structural changes contribute to measured changes in electrical resistivity and elastic moduli. Electrical resistivity in particular is affected, especially, where Figure 1 shows that experimentally determined magnitudes are higher than the void-based prediction at lower swelling and higher irradiation temperatures. Also note that the measured values of resistivity are lower than the prediction at higher swelling.

It is known well that precipitates usually have different densities, ultrasonic velocities and electrical resistivity, but precipitates also change the property of the matrix from which they form, especially by removal of elements that have a strong effect on the electrical resistivity. Let's consider how it is possible to change the electrical resistivity. The main radiation-induced changes in steel are changes in dislocation structure, second-phase precipitates, and change in composition and substitution of neighboring atoms.

When the dislocation density is changed no more than usually observed during irradiation it does not significantly affect electrical resistivity, so this factor can be neglected. Second phases at small volumes can significantly affect electrical resistivity when their specific electrical resistivity is different from the matrix. Phases known to precipitate in this steel under irradiation are $(Fe\text{-}Cr)_{23}C_6$, a phase enriched by Cr, and G-phase which is enriched in Ni at the expense of matrix reduction in this element.

There are no data on specific electrical resistivity of these phases in the literature, but data do exist on various Fe-Cr-Ni alloys in [8] where one can select alloys of Fe-Cr and Fe-Ni close to the considered phases. Based on these reference data it appears that Fe-Cr alloys have electrical resistivities that are relatively independent of Cr content so we can deduce that influence of the $(Fe\text{-}Cr)_{23}C_6$ phase on electrical resistivity of the matrix can be neglected. However, this does not address the removal of carbon from the matrix, which should have some influence to reduce the matrix resistivity. Nor does it address the resistivity contribution of the carbides.

Changing of Ni content in Fe-Ni alloys has a strong influence on electrical resistivity. G-phase is known to contain 42 - 57 % Ni [9] and according to the data on physical properties of high-content Ni alloys [8] the specific electrical resistivity of G-phase can be higher than that of the matrix by ~50 %, based only on this consideration, but this ignores the effect of concentrating Si and Ti in the precipitate and their concurrent reduction in the matrix.

The influence of precipitate phase on electrical resistivity can be included in the two-phase model using the approach of Reference [10], using the electrical resistivity of the G-phase precipitate and steel in its initial state. We obtain the following expression for electrical resistivity.

$$\frac{\Delta R}{R_0} = \frac{5S}{4S+6} + c \times \frac{\Delta\rho}{\rho_0} \times \left(1 + \frac{5S}{4S+6}\right) \times \frac{3}{3 + 2 \times \Delta\rho / \rho_0 \times (1-c)} \quad (5)$$

ρ_0 is the specific electrical resistivity of matrix, $\Delta\rho$ is the difference between electrical resistivity of the phase and matrix, and c is the volume ratio of the phase/matrix.

To estimate the magnitude of the influence of G-phase on electrical resistivity, microscopy examination was conducted on a specimen having 2.3 % swelling, as shown in Figure 4. The volume ratio of G-phase was determined to be 2.2 % in this specimen.

Calculations using Equation 4, in which the corresponding value of the unirradiated specimen was assumed to be the electrical resistivity of matrix, gives an addition of ~1% to electrical resistivity. Therefore, in order to use Equation 2 for estimating swelling from electrical resistivity measurements, it is necessary to adjust the experimental results to account for G-phase formation. We have to shift the experimental value 1% downwards in our case for the test specimen, as shown by the corrected datum shown in Figure 4. We obtain movement toward the curve of ~1% (instead of 2%). This difference is in agreement with accuracy of determination of electrical resistivity.

What changes in this analysis might we anticipate for application of these fast reactor results to fusion-relevant conditions? In this discussion, we ignore the possible effect of helium to change the amount of swelling. We focus only on the possibility that, for a given swelling level, fusion-produced property changes arising from voids or bubbles will be different from that produced in low helium generating spectra found in fast reactors.

The first order effect, if any, must arise from some aspect of the very high helium generation rate characteristic of fusion spectra. It is well known that high helium generation rates tend to "homogenize" swelling, distributing the swelling into a higher density of smaller voids. However, this aspect of high helium generation rates can be ignored, since it is only the total void volume and not its distribution that determines the change in the physical properties [8].

More appropriately, what is the consequence of helium, possibly at high equilibrium values, on void contributions to changes in physical properties? Helium, especially at high pressures, might be expected to decrease the effectiveness of voids to reduce the elastic moduli, and possibly to increase the electrical and thermal resistivity.

Wolfer has examined this possibility for elastic moduli [11]. Gas content can contribute to the bulk moduli but not the shear moduli. Considering the theoretical maximum helium content, the cavity modulus change would be reduced much less than 10%, with most cases resulting in even smaller gas-induced moduli changes.

Since helium is effectively a non-conductor there will be no measurable change in a cavities' ability to resist the flow of electrons. Similarly, the large mass difference between helium and the Fe, Cr, Ni of the

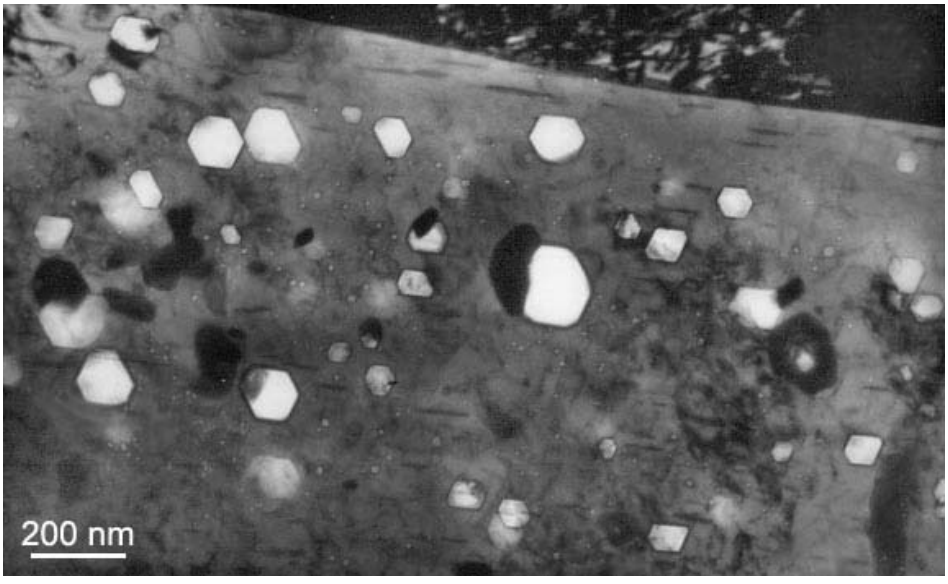

Figure 4. G-phase precipitates and voids observed in an irradiated specimen of 20% cold-worked 0.1C-16Cr-15Ni-2Mo-lMn steel with swelling of 2.3%.

matrix will make heat transfer very inefficient through the voids, yielding no improvement in the thermal conductivity.

Conclusions

Void swelling is the dominant contributor to changes in electrical resistivity and elastic moduli of austenitic steels under high-dose neutron irradiation in fast reactors. Second-order contributions appear to arise from radiation-induced precipitate formation, both directly and indirectly via the effect of precipitation to change the composition of the alloy matrix. It is anticipated that helium-pressurization of cavities in fusion neutron spectra will not appreciably change the influence of cavities on these physical properties, allowing the results of this fast reactor study to be applied without correction to fusion conditions.

Acknowledgements

The Russian data presented in this report was generated in irradiation programs conducted earlier under the sponsorship of MINATOM and later evaluated under the sponsorship of the Ministry of Science of the Russian Federation. The U.S portion of this work was jointly supported by the Materials Sciences Branch, Office of Basic Energy Sciences, and the Office of Fusion Energy, U.S. Department of Energy, under Contract DE-AC06-76RLO 1830. The assistance of Natalia Brikotnina of Translation and Interpreter Services to facilitate discussions and to provide the English translation of the Russian draft is gratefully acknowledged.

References

[1] F. A. Garner, D. J. Edwards, S. M. Bruemmer, S. I. Porollo, Yu. V. Konobeev, V. S. Neustroev, V. K. Shamardin, and A. V. Kozlov, Recent Developments Concerning Potential Void Swelling of PWR Internals Constructed from Austenitic Stainless Steels, PROCEEDINGS, Fontevraud 5, Contribution of Materials Investigation to the Resolution of Problems Encountered in Pressurized Water Reactors (September 23-27, 2002), paper #22, CD format.

[2] I. I. Balachov, F. A. Garner, Y. Isobe, and H. T. Tang, *In-situ* NDT Measurements of Irradiation-induced Swelling in Core Internal Components, Proceedings of ICAPP'03, Cordoba, Spain (May 4-7, 2003), paper 3265.

[3] I. I. Balachov et al., paper 8A.PO.23 in this conference.

[4] D. J. Edwards, F. A. Garner, and L. R. Greenwood, Influence of Transmutation, Void Swelling and Flux/Spectra Uncertainties on the Electrical Properties of Copper and Copper Alloys, J. Nucl. Mater. 212-215 (1994) 404-409.

[5] E. N. Averin, I. M. Kostousov, E. V. Serovikova, and E. N. Shcherbakov, Procedures and Equipment to Study Physical and Mechanical Properties, *VANT Series: Nuclear Techniques and Technology* 3 (1992) 43-51.

[6] A. V. Kozlov, E. N. Shcherbakov, S. A. Averin, and F. A. Garner, The Effect of Void Swelling on Electrical Resistance and Elastic Moduli in Austenitic Steels, *Effects of Radiation on Materials: 21st International Symposium, ASTM STP 1447,* M. L. Grossbeck, Ed., **A**STM International, West Conshohocken, PA (2003), in press.

[7] A. V. Kozlov, E. N. Shcherbakov, S. A. Averin, and F. A. Garner, The Effect of Void Swelling on Electrical Resistance and Elastic Moduli in Austenitic Stainless Steels, in DOE/ER-0313/32 (June 30, 2002), 56-64.

[8] B. E. Neimark, Physical Properties of Steels and Alloys Used in Energetics, Energy, Moscow (1967) (in Russian).

[9] A. F. Rowcliffe and E. H Lee, High Temperature Radiation Damage Phenomena in Complex Alloy, J. Nucl. Mater. 108-109 (1982) 306-318.

[10] B. G. Liphshits, V. S. Karposhin, and Y. L. Linetskiy, Physical Properties of Metals and Alloys, Metallurgy, Moscow (1980) (in Russian).

[11] W. G. Wolfer, The Elastic Properties of Aged Palladium Tritides, Sandia National Laboratory Report SAND90-8253 (December 1990).

CHARACTERIZATION OF STRUCTURAL CONDITIONS OF AISI 316 ANALOG STAINLESS STEEL IRRADIATED IN THE BN-350 REACTOR—O. P. Maksimkin, K. V. Tsai, L. G. Turubarova, and T. Doronina (Institute of Nuclear Physics, Almaty, Kazakhstan), and F. A. Garner (Pacific Northwest National Laboratory)*

OBJECTIVE

The objective of this effort is to explore the response of Russian austenitic steels to irradiation in various Russian and Kazakh fast reactors, looking for insights on how Western steels of similar composition might behave.

SUMMARY

In several recently published studies conducted on a Soviet analog of AISI 321 stainless steel irradiated in either fast reactors or light water reactors, it was shown that the void swelling phenomenon extended to temperatures as low as ~300°C, when produced by neutron irradiation at dpa rates in the range 10^{-7} to 10^{-8} dpa/sec. Other studies yielded similar results for AISI 316. In the current study a blanket duct assembly from BN-350, constructed from the Soviet analog of AISI 316, also exhibits swelling at dpa rates on the order of 10^{-8} dpa/sec, with voids seen as low as 281°C and only 1.3 dpa. It appears that low-temperature swelling at low dpa rates occurs in 300 series stainless steels in general, and during irradiations conducted in either fast or mixed spectrum reactors.

Introduction

In a recently published study it was shown that in annealed 12X18H10T, the Soviet analog of AISI 321 stainless steel, void swelling inhabits a temperature regime with a lower limit just at or above 300°C, when irradiated as a flow restrictor in the BN-350 fast reactor at dpa rates on the order of 10^{-7} to 10^{-8} dpa/s [1]. This study was conducted on an unfueled flow restrictor element removed from the breeder zone of the reactor. Limited comparison of swelling in the same steel following irradiation at comparable dpa rates in several light water reactors confirmed that void nucleation in general is limited to temperatures >300°C [2, 3]. Similar results were recently observed in 316 stainless steel irradiated in Japanese and European PWRs [4, 5].

Previous studies conducted in Western countries could not establish in fast reactors the lower temperature limit of swelling because the inlet coolant temperatures of all second-generation fast reactors in the West are in the range 365-380°C. First-generation Western reactors such as EBR-I and DFR operated with lower inlet temperatures, but these reactors were decommissioned many years ago. In countries of the Former Soviet Union, however, there exist both first and second-generation reactors. One of these, the BN-350 fast reactor in Kazakhstan, was recently decommissioned. It had an inlet coolant temperature of 280°C.

A number of recent studies by Garner and co-workers have shown that void swelling in austenitic stainless steels actually increases at lower dpa rates [6-9], allowing the observation of the lower swelling temperature limit at lower dpa levels. This increase in swelling arises from a decrease in the duration of the transient regime of swelling at lower dpa rates. Both the flow restrictor component and the components from VVERs and PWRs experienced dpa rates that were much lower than those found inside the fueled regions of fast reactor cores.

Another opportunity has recently arisen to provide further confirmation of the lower temperature limit of void nucleation in austenitic stainless steels by examining another component from the BN-350 reactor that was irradiated at low neutron flux.

*Pacific Northwest National Laboratory (PNNL) is operated for the U.S. Department of Energy by Battelle Memorial Institute under contract DE-AC06-76RLO-1830.

Experimental Details

A hexagonal blanket assembly designated H-214(II) was irradiated in the reflector region of the BN-350 reactor, reaching a maximum of 15.6 dpa at an average dpa rate of 4.9×10^{-8} dpa/sec averaged over its lifetime in reactor. During operation time the assembly was moved five times to new positions in the blanket section of the reactor. The hexagonal duct with faces 50 mm wide and 2 mm thick was formed from 08Cr16Ni11Mo3 stainless steel, a Soviet analog of AISI 316 steel, and was produced with the final thermal-mechanical treatment of the duct being 20% cold deformation followed by annealing at 800°C for 1 hour.

The temperature at the bottom of the assembly was 280°C and the temperature at the top of the assembly was 420°C. Due to the thinness of the duct wall, the internal temperature was not raised significantly by gamma heating. Thus, the temperature of the steel is expected to be within 1-2°C of the local coolant temperature.

At the BN-350 site specimens with 10 mm height and 50 mm width were cut from the duct walls at various locations. Subsequent reduction of these specimens was conducted in a hot cell at INP-Almaty for microstructural analysis and microhardness measurements. Plate-shape specimens with sizes of 5×6 mm were prepared for metallography investigations, microhardness measurements and hydrostatic weighing. To display grain boundaries these specimens were subjected to additional mechanical grinding and polishing. Examination techniques employed included optical metallography using a MeF-2 optical microscope and transmission electron microscopy (TEM), using a JEM-100CX electron microscope operating at 100 keV. Microhardness measurements were carried out by the Vickers method on a PMT-3 device provided with a diamond pyramid with an angle of 136°. The density was measured using a hydrostatic weighing technique employing a CEPN-770 electronic balance with methyl alcohol as the working liquid.

Disks of 3 mm diameter for microscopy studies were prepared from ≤300μm sections cut from the mid-section of the duct face. Mechanical grinding and polishing with subsequent electrochemical polishing were used for final preparation of TEM disks. The irradiation conditions for specimens examined to date are shown in Table 1.

Table 1. Fluence and temperature changes over the length of the H-214(II) duct

Distance from midplane, mm	Dose, dpa	dpa rate, 10^{-8} dpa/sec	Temperature, ^{o}C
-1200	0.25	0.08	280
-900	1.27	0.39	281
-500	7.08	2.2	309
0	15.6	4.85	337
+500	6.03	1.87	365

Results and Discussion

Metallography investigations

The microstructure of the outer surface of the duct face revealed through electrolyte etching is shown in Figure 1. Several peculiarities were observed. First, in all specimens the grain sizes were nonuniform to a great extent. Fine grains often were grouped in locations between large-scale grains. Within grains and at their boundaries were observed chains of $Cr_{23}C_6$ carbide inclusions, the quantity and size of which depend on the distance from the midplane of the core. The analysis of grain size distributions (see Figure 2) showed an increase in the fraction of large grains (25-50 μm) with increasing core elevation, and a concurrent decrease in fraction of fine grains (<12 μm).

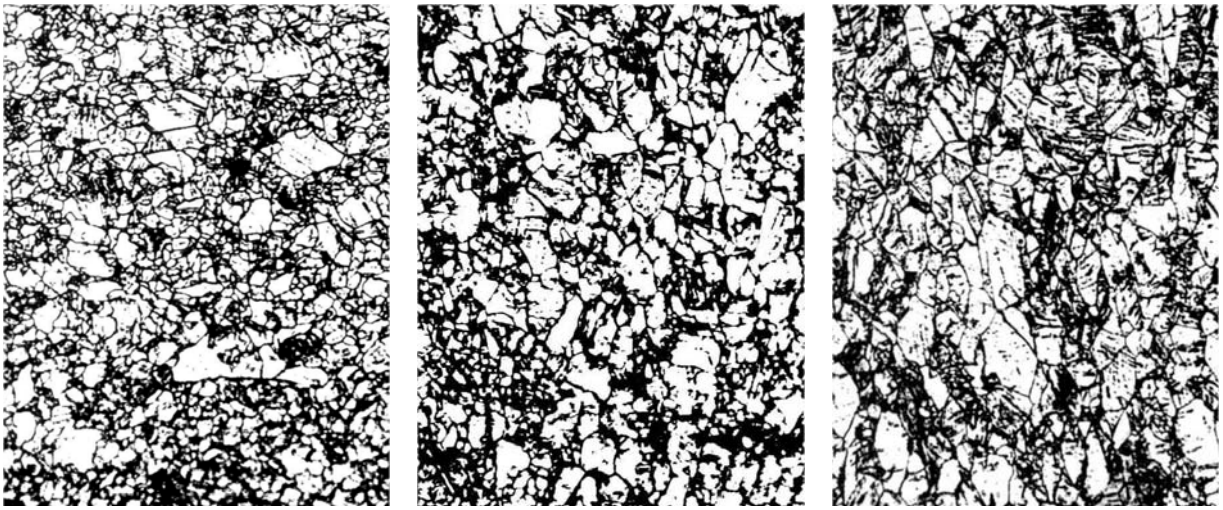

a b c

Figure 1. Microstructure (×200) of AISI 316 –type stainless steel of the H-214(II) duct (BN-350 reactor) sampled at various distances from the midplane of the core (a) –1200mm, (b) –500mm, and (c) +500mm.

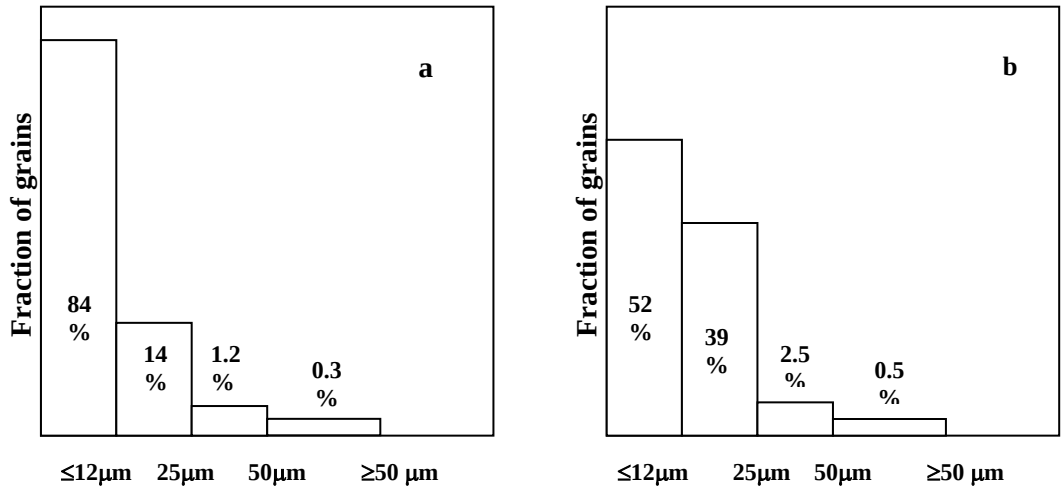

Figure 2. Histograms of grain size distributions for specimens cut at distances of –1200mm (a) and –500mm (b) from midplane.

Electron microscopy

Dislocation loops were observed in the lowest exposure material (0.25 dpa) located a distance of -1200 mm from the midplane, with a concentration of $3\times10^{15}cm^{-3}$, and sizes ≤25 nm (mean loop size was 10.7 nm). At the -900 mm level where the dpa and dpa rates were four times higher, $\sim2\times10^{15}cm^{-3}$ was observed, with sizes 5-40 nm and mean of 15.5 nm. Since the temperature of the two positions was essentially identical this represents an effect of increasing dose to grow larger loops. Thorough investigation of the loops in dark-field mode identified these as Frank loops of interstitial type.

At other higher levels on the duct with higher temperatures the dislocation loop structure and pattern of strains near defects become more intricate with simultaneous increases in both concentration and size distribution of defects.

Figure 3 shows microstructures of specimens when imaged under conditions that allow voids to be visible. Microscopy showed the presence of voids at -900 mm from midplane; where the irradiation temperature was only 280°C, significantly lower than the ~300°C limit reported earlier. The concentration of voids observed at this position is very small but allows us to confirm their presence. From TEM-image analysis microstructural data on voids were obtained (see Table 2).

Table 2. Microstructural data on voids

Distance from midplane, mm	Range for void sizes, nm	Mean void diameter, nm	Void density, $\times 10^{15} cm^{-3}$	Swelling, %
-1200	-	-	no voids	-
-900	< 7	-	some voids	-
-500	10 -15	10.0	0.61	0.04
0	4 -15	8.6	2.57	0.13
+500	10 -35	14.0	0.78	0.16

It should be noted that calculated values of swelling are relatively small, in agreement with earlier published flat-to-flat measurements, proportional to ~1/3 of the swelling, for these positions [10], and the relative change in density (Table 3), the latter calculated using the density value at -1200 mm as a reference zero-swelling state.

Table 3. Data on hydrostatic weighing and microhardness measurements

Distance from midplane, mm	Flat-to-flat size change, % [10]	Density, g/cm^3	$\Delta\rho/\rho$, %	Microhardness kg/mm^2
-1200	0.01	7.972	-	244
-900	0.02	7.961	0.13	286
-500	0.03	7.946	0.3	412
0	0.03	7.947	0.3	380
+500	0.04	7.934	0.4	313

Microhardness measurements

Microhardness results are presented in Table 3. Microhardness was lowest in the bottom-most specimen from the duct (-1200 mm), where temperature and fluence were also lowest, and reaches a maximum at -500 mm. The hardness appears to increase with dpa level and decrease with temperature, as would be expected.

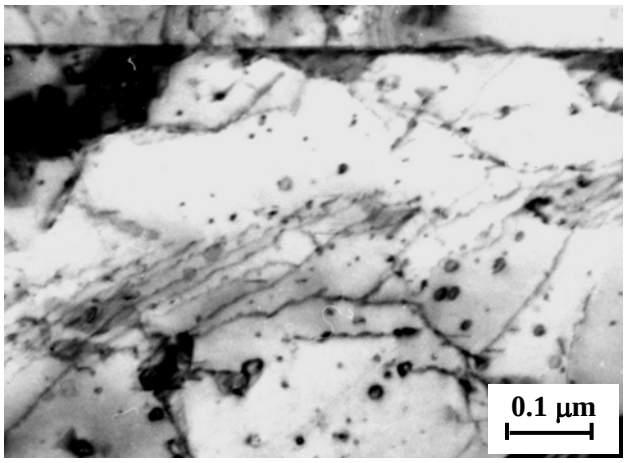

"-1200mm" - No swelling

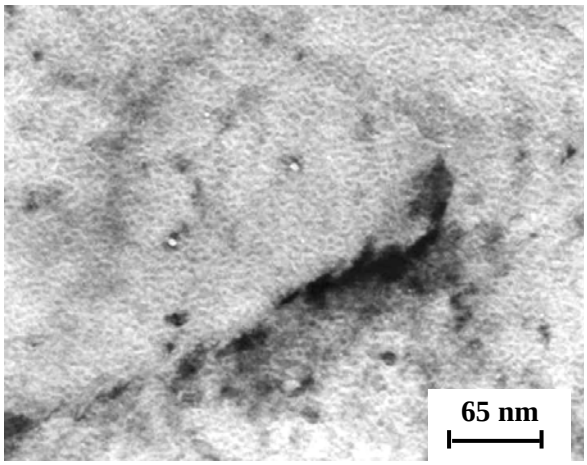

"-900mm"

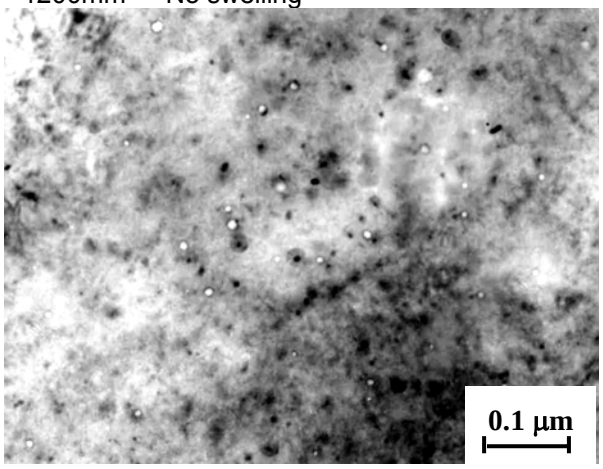

"-500mm"

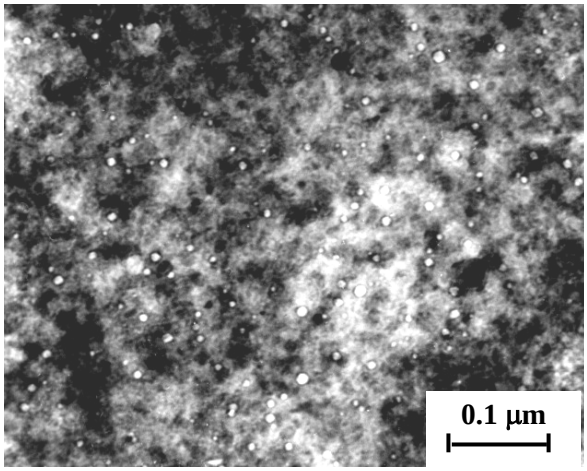

"0mm"

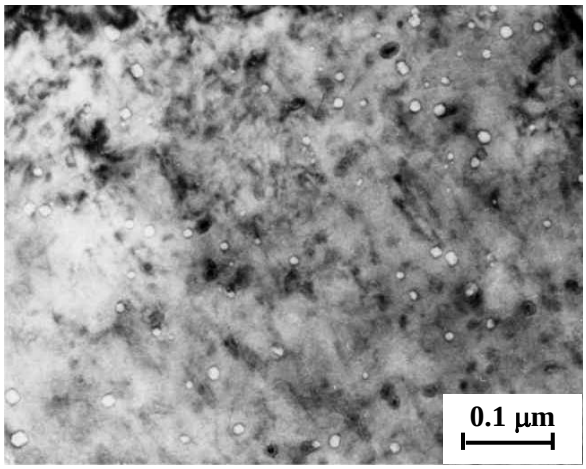

"+500mm"

Figure 3. Microstructure of AISI-316 type steel (H-214(II)) irradiated in the BN-350 reactor at various distances from midplane.

Conclusions

It appears that the irradiation of this steel at low neutron fluxes leads to a recovery process that alters the grain morphology, where the mean grain size increases with temperature and possibly with the total dpa level. This recovery process does not appear to produce deleterious results, however. Concurrently, microstructural evolution proceeds as first Frank loops are produced and then voids at temperatures above 280°C, with measurable increases in resultant hardening.

In agreement with earlier studies voids are observed at very low doses and temperatures in such low flux irradiations, with the first voids observed at a nominal temperature of only 281°C and 1.3 dpa.

Acknowledgements

The Kazakh portion of this work was sponsored by the Ministry of Energy and Mineral Resources of the Republic of Kazakhstan, and under ISTC project number K-437. The U.S. portion of this work was jointly supported by the Materials Sciences Branch, Office of Basic Energy Sciences, and the Office of Fusion Energy, U.S. Department of Energy, under Contract DE-AC06-76RLO 1830. The authors are indebted to Natalia A. Brikotnina of Interpreter and Translation Services for her assistance in the conduct and interpretation of this experiment, and for translation of the original Russian text into English.

References

[1] S. I. Porollo, Yu. V. Konobeev, A. M. Dvoriashin, V. M. Krigan, and F. A. Garner, Determination of the Lower Temperature Limit of Void Swelling of Stainless Steels at PWR-relevant Displacement Rates, 10th International Conference on Environmental Degradation of Materials in Nuclear Power Systems – Water Reactors, CD format.

[2] V. S. Neustroev, V. K. Shamardin, Z. E. Ostrovsky, A. M. Pecherin, and F. A. Garner, Temperature-Shift of Void Swelling Observed at PWR-Relevant Temperatures in Annealed Fe-18Cr-10Ni-Ti Stainless Steel Irradiated at High and Low Dpa Rates in BOR-60, International Symposium on Contribution of Materials Investigation to the Resolution of Problems Encountered in Pressurized Water Reactors (September 14–18, 1998, Fontevraud, France) 261-269.

[3] V. S. Neustroev, V. N. Golovanov, V. K. Shamardin, Z. E. Ostrovskiy, and A. M. Pecherin, Radiation Phenomena in X18H10T Steel Irradiated in Different Reactors under Conditions Close to the Operating Conditions of VVER Internals, Proceedings of 7th Russian Conference on Reactor Material Science (September 8–12, 2003) in press.

[4] K. Fujii, K. Fukuya, G. Furutani, T. Torimaru, A. Kohyama, and Y. Katoh, Swelling in 316 Stainless Steel Irradiated in a PWR, 10th International Conference on Environmental Degradation of Materials in Nuclear Power Systems – Water Reactors, CD format.

[5] N. I. Budylkin, T. M. Bulanova, E. G. Mironova, N. M. Mitrofanova, S. I. Porollo, V. M. Chernov, V. K. Shamardin, and F. A. Garner, The Strong Influence of Displacement Rate on Void Swelling in Variants of Fe-16Cr-15Ni-3Mo Austenitic Stainless Steel Irradiated in BN-350 and BOR-60, in this conference.

[6] D. J. Edwards, E. P. Simonen, F. A. Garner, B. A. Garner, B. A. Oliver, and S. M. Bruemmer, Sensitivity of Microstructural Evolution Due to Temperature and Dose Gradients in Neutron-Irradiated 316SS, J. Nucl. Mater. 317 (2003) 32-45.

[7] T. Okita, T. Sato, N. Sekimura, F. A. Garner, and L. R. Greenwood, The Primary Origin of Dose Rate Effects on Microstructural Evolution of Austenitic Alloys during Neutron Irradiation, J. Nucl. Mater. 207-211 (2002) 322-326.

[8] T. Okita, T. Sato, N. Sekimura, F. A. Garner, and W. G. Wolfer, Combined Effect of Temperature, Displacement Rate and Composition on the Neutron-Induced Swelling of Austenitic Alloys, 11th International Conference on Environmental Degradation of Materials in Nuclear Power Systems – Water Reactors, 2003, CD format.

[9] V. S. Neustroev, V. K. Shamardin, Z. E. Ostrovsky, A. M. Pecherin, and F. A. Garner, Temperature-Shift of Void Swelling Observed at PWR-Relevant Temperatures in Annealed Fe-18Cr-10Ni-Ti

Stainless Steel Irradiated in the Reflector Region of BOR-60, Effects of Radiation on Materials: 19th International Symposium, ASTM STP 1366, Eds. M. L. Hamilton, A. S. Kumar, S. T. Rosinski, and M. L. Grossbeck, American Society for Testing and Materials (2000) 792-800.

[10] V. N. Karaulov et.al., Investigation of Short-term Mechanical Properties Change for Materials of Spent Fuel Assemblies Claddings of BN-350 Reactor – Proceedings of the 2nd International Conference on Nuclear and Radiation Physics (October 8–11, 1997, Almaty) 44-54.

7.0 MHD INSULATORS, INSULATING CERAMICS, AND OPTICAL MATERIALS

RECENT PROGRESS IN THE DEVELOPMENT OF ELECTRICALLY INSULATING COATINGS FOR A LIQUID LITHIUM BLANKET—B. A. Pint, P. F. Tortorelli (Oak Ridge National Laboratory, USA), A. Jankowski, J. Hayes (Lawrence Livermore National Laboratory, USA), T. Muroga, A. Suzuki (NIFS, Japan), O. I. Yeliseyeva (G. V. Karpenko Physico-Mechanical Institute NASU, Ukraine), and V. M. Chernov (Bochvar Institute of Inorganic Materials, Russia)

To be published in the Journal of Nuclear Materials as Proceedings of the 11th International Conference on Fusion Reactor Materials, December 2003, Kyoto, Japan.

OBJECTIVE

The objective of this task is to assess the long-term, high-temperature compatibility of high electrical resistance coatings with lithium at high temperatures. Electrically insulating coatings on the first wall of magnetic confinement reactors are essential to reduce the magnetohydrodynamic (MHD) force that would otherwise inhibit the flow of the lithium coolant. Experimental and theoretical work is being conducted on bulk ceramics to determine resistivity, basic lithium compatibility and maximum-use temperatures of candidate ceramics such as Er_2O_3 and Y_2O_3.

SUMMARY

There are very few candidate MHD coating materials since Li dissolves most oxides and many carbides and nitrides do not have sufficient electrical resistivity for this application. The past few years have seen great changes in the research emphasis and strategy for MHD coatings. Problems with CaO have led to a focus on new candidates with low cation solubility in Li, such as Y_2O_3 and Er_2O_3. Coatings of these materials are being fabricated by a variety of processing techniques and the resistivity and microstructure characterized. Progress is being made in the development of MHD coatings, but as yet no coatings have shown sufficient compatibility with Li. Electrical resistivity results from Y_2O_3 coatings as-deposited and after exposure to Li are presented. Self-healing and in-situ coatings are being investigated based on CaO from Li-Ca and Er_2O_3 from Li-Er. Anticipated problems with defects in ceramic coatings, either as-fabricated or due to tensile cracking, suggests that the most viable coating strategy will have to be multi-layered. An outer metallic layer will prevent Li from wetting cracks in the inner ceramic insulating layer and also limit interaction between the ceramic and Li. Whether the MHD coating is single- or dual-layered, processing issues will need to be addressed before the issue of compatibility can be answered.

PROGRESS AND STATUS

Introduction

In all alloy - liquid metal (e.g. Li and Pb-Li) blanket concepts for a deuterium/tritium fueled fusion reactor where a strong magnetic field is used to contain the fusion plasma, a magnetohydrodynamic (MHD) pressure drop is developed when the electrically conductive lithium flows across the magnetic field lines. To minimize the MHD resistance to flow, it is necessary to have an insulating barrier to decouple the liquid metal and the alloy structure. The coatings must be thin, durable and electrically resistive.[1-3] Perhaps the most difficult material requirement for a Li self-cooled blanket is compatibility with Li at temperatures up to ≈700°C.[4,5] Because of the relative stability of Li_2O, most electrically-resistive oxides readily dissolve in Li.[6,7] Therefore, only a few materials are candidates for this application. Over the past few years, there has been a considerable shift in emphasis in this topic as the underlying compatibility issues have been reevaluated and new candidate materials have been tested in bulk form and fabricated as coatings for further experiments. The development of a viable MHD coating is particularly relevant for

concepts that use vanadium structural alloys because of the good compatibility of vanadium alloys with liquid lithium but their susceptibility to embrittlement by oxygen and hydrogen in other environments such as helium.[8-11]

Shift in Research Emphasis

Both theoretical calculations and experiments over the past 40 years have shown that there are relatively few materials that meet both the Li compatibility and electrical resistance requirements.[1,3,6,7,12-16] Recent reviews have emphasized CaO and AlN as the most attractive candidate materials.[2,3] However, more recent work has shown that the these materials may not be viable.[17,18]

Over the past decade, CaO has been extensively investigated as a candidate coating material.[2,3,14,19] One of its attractive features is its high solubility in Li which suggests that it might be possible to have a self-healing coating. However, thermodynamic calculations and recent experimental work[17] on bulk CaO specimens have proven that CaO cannot perform adequately at 600°-800°C in static Li tests, Figure 1. A mass loss of ≈3mg/cm^2 is equivalent to a 10µm loss of material. Thus, the high mass losses at these temperatures are unacceptably high for a thin coating. An even higher dissolution rate (0.085µm/h) was observed for single crystal CaO in Li-2.8at.%Ca at 600°C.[18] Results for coatings formed on V-4Cr-4Ti with different oxygen preloading showed a lower dissolution rate when tested under the same conditions at 600°C.[18] However, the dissolution rates were sufficient to remove a significant fraction of the coating after 1000h and suggested a coating lifetime of <3000h at 600°C, Figure 2. Because of its poor high temperature compatibility, the CaO coating development program in the U.S. has recently been concluded.

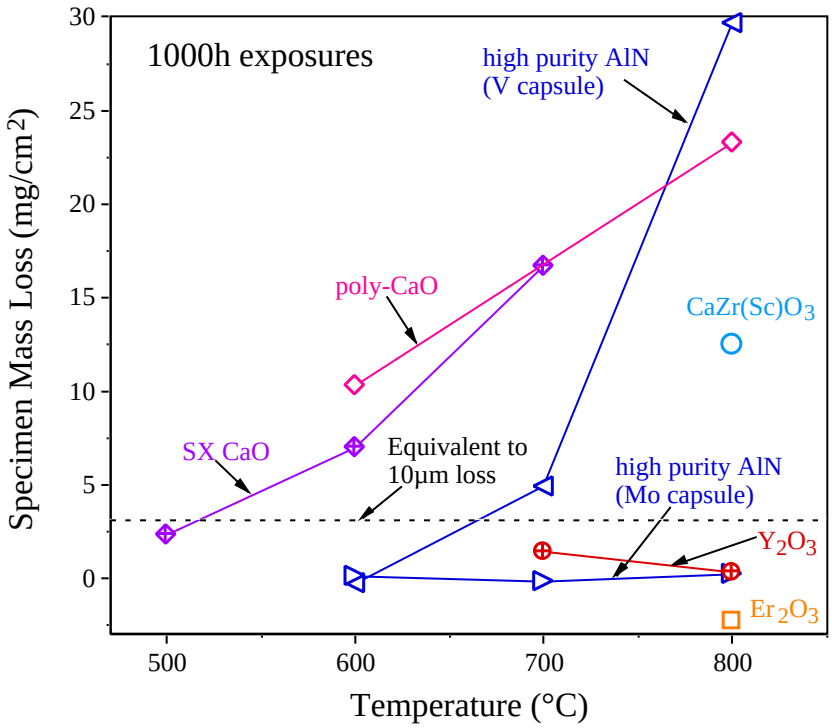

Figure 1. Mass losses for some candidate oxide and nitride materials after 1000h at various temperatures. The results for poly-crystalline and single crystal CaO show severe dissolution above 500°C. The dashed line shows the mass loss associated with the loss of ≈10µm of coating in a 1000h exposure.

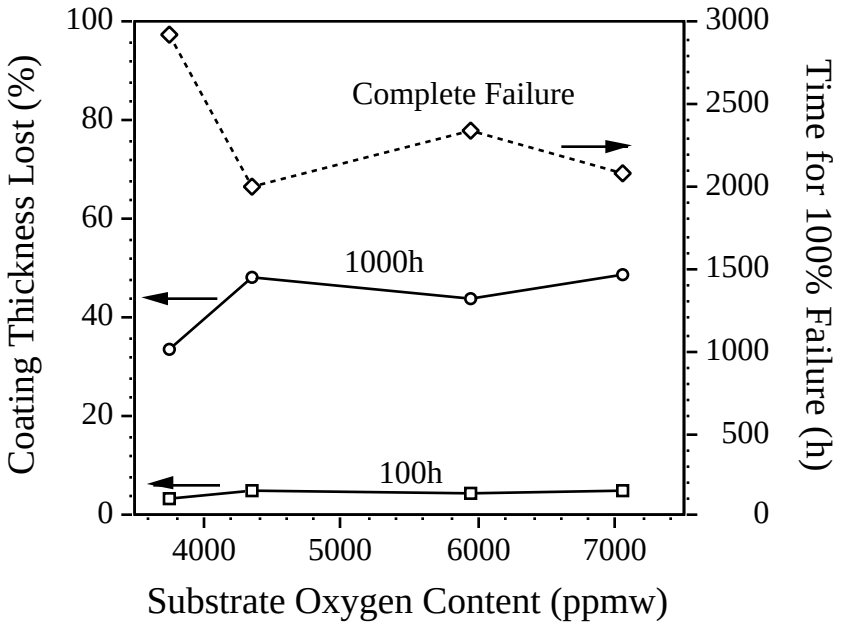

Figure 2. Performance of CaO coatings in Li-2.8at.%Ca at 600°C as a function of oxygen in the V-4Cr-4Ti substrate. Based on the experimentally observed dissolution rate, the percentage of the coating lost with time was calculated as well as the time to complete failure.[18]

Screenings studies initially indicated that CaO was a promising candidate. However, the thermodynamic calculations examined the reaction:

$$CaO + 2Li <-> Ca + Li_2O \qquad [1]$$

and assumed that the Li was saturated with oxygen. Because CaO has a lower free energy of formation than Li_2O, CaO should be stable in Li under these conditions. However, in a flowing system with a temperature gradient this is an unrealistic assumption as the saturation concentration varies considerably with temperature[17] such that if the lithium were saturated at the highest temperature, Li_2O would precipitate out at the lowest temperature and the lithium would no longer be saturated at the highest temperature. A more relevant reaction is for dissolution of the components into lithium until the following equilibrium is reached in solution:

$$CaO = Ca(Li) + O(Li) \qquad [2]$$

Theoretical calculations showed that the equilibrium solubility of Ca in Li increased dramatically with temperature,[17] which was consistent with the high dissolution rates observed experimentally.

The other candidate that has been extensively studied as a coating is AlN.[2,3,20-23] Nitrides are generally more compatible with Li because nitrides of Li are far less stable than Li_2O. However, AlN is one of only a few nitrides with high electrical resistivity. A number of experiments have shown good Li compatibility up to 600°C. However, in higher temperatures capsule tests,[17,23] the behavior was very sensitive to the capsule material, Figure 1. With a Mo capsule, very little mass change was noted after 1000h at 800°C. When a vanadium alloy capsule was used, the mass losses were much higher, Figure 1. The same behavior was observed for high purity (0.04%Y) and ultra-high purity AlN.[17,23] The effect can be understood based on the dissolution equilibrium equation for AlN:

$$AlN = Al(Li) + N(Li) \qquad [3]$$

The vanadium alloy capsule getters N from the Li during the exposure preventing the Li from becoming saturated with N and thus stopping the dissolution. With capsule made from Mo, which does not form a stable nitride, the Li becomes saturated with N and the dissolution stops. Thus, the use of AlN appears problematic because uncoated vanadium alloy channel walls could getter N from the Li. A further complication is that it is extremely difficult to make AlN without oxygen contamination. Any Al_2O_3 formed during coating fabrication would be readily dissolved by Li. Initial Li exposures of AlN coatings at 500°C have shown poor performance.[21]

This combination of experimental results and thermodynamic analyses suggests a new strategy for selecting possible MHD coating materials. Since elements (e.g. Ca) which are highly soluble in Li may be more susceptible to dissolution at high temperature, oxides with cations that have a low solubility in Li will likely have better compatibility. Therefore, more emphasis is now being placed on Y_2O_3 and Er_2O_3 as candidate materials for coating development.

In-situ Coatings

Despite the observed problems with CaO compatibility at higher temperatures, the concept of a self-healing coating is still attractive. An in-situ technique would more easily allow coating of complex components. Therefore, the Li-CaO concept as well as Li-Er_2O_3 are currently being examined to develop an understanding of the issues related to the processing and use of in-situ coatings. Based on earlier experimental work for vanadium alloys exposed to Li-0.5%Ca at 700°C,[24] the process of CaO formation and degradation on vanadium alloys is being modeled.[25] According to the in-situ model in Figure 3, oxygen from the substrate can react with Ca in the Li to form a CaO outer layer. However, this requires balanced fluxes of Ca in the metal and O from the metal which are difficult to achieve. As oxygen is removed from the substrate, Ti-rich oxide particles dissolve. Eventually, some Ca and Li becomes incorporated into the metal while V and Ti can become incorporated into the oxide. This process degrades the coating and the metal. Another scenario involves the deposition of a CaO layer before exposure to Li-

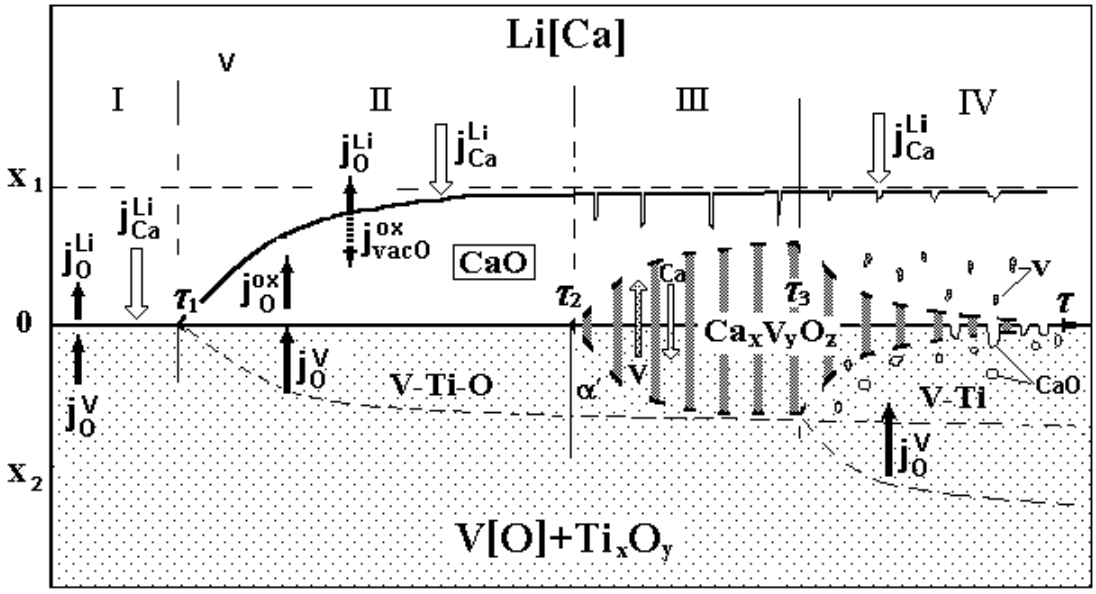

Figure 3. Schematic of the competing processes for the in-situ formation of a CaO layer on a vanadium alloy as a function of time from left to right.[25]

Ca. In this case, similar problems eventually develop as oxygen is removed from the substrate and V and Ti are incorporated into the oxide.

Because of the observed problems with CaO, in-situ Er_2O_3 coatings also are being explored.[26] Vanadium alloys preloaded with oxygen were exposed to Li-0.006at.%Er at 600°C. Figure 4 shows the Er-rich oxide layer formed on the surface. However, the measured O/Er ratio was 2-2.5 due to the incorporation of V, Cr and Ti impurities in the layer. Initial resistance measurements at room temperature showed adequate electrical resistivity when the process was optimized. More work will be required to further optimize this process and characterize the properties and compatibility of coatings made by this process.

Results From New Coatings

Because of the initial positive results on bulk Y_2O_3 and Er_2O_3, the next step was to fabricate coatings of these materials for further characterization and testing. In the U.S., Y_2O_3 coatings were deposited by an electron-beam assisted, physical vapor deposition process (EB-PVD) on V-4Cr-4Ti substrates. The coatings were 12.5µm thick and had a faceted surface microstructure typical of the EB-PVD process, Figure 5a. For coating evaluations, the figure of merit is the change in coating resistivity at 700°C after exposure to Li. The coating must maintain adequate resistivity in order to warrant further testing. In order to avoid oxidation of the vanadium alloy substrate, the electrical resistance was measured in a vacuum. This initial set of coatings showed relatively low resistivity compared to literature values and values measured on a sintered Y_2O_3 specimen using the same equipment, Figure 6. Similar to the testing procedure used for bulk ceramics,[17] the coated specimens were exposed to lithium in sealed vanadium alloy capsules for 100-1,000h at 700° and 800°C. After exposure, performance has varied from little change in resistivity and microstructure to complete loss of the coating. The electrical resistance measured after 3, 100h cycles at 800°C (cooling to room temperature between each cycle) was higher than the as-received coatings. However, after 1000h at 800°C, a degradation in the resistivity was

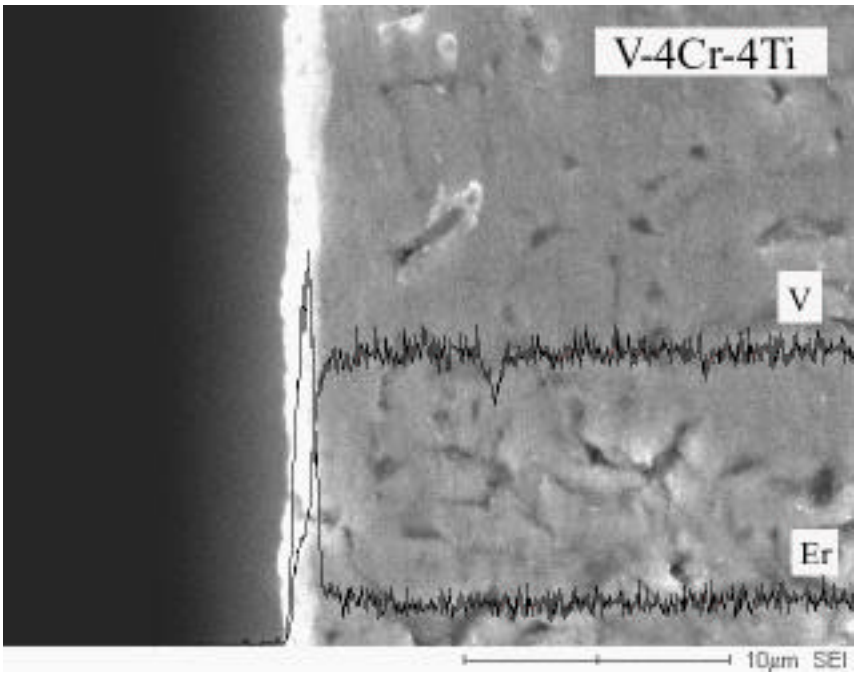

Figure 4. SEM image and EDS line element scan of a cross section of V-4Cr-4Ti oxidized for 6h and annealed for 16h at 700°C, then exposed in Li doped with Er for 300h at 600°C.[26]

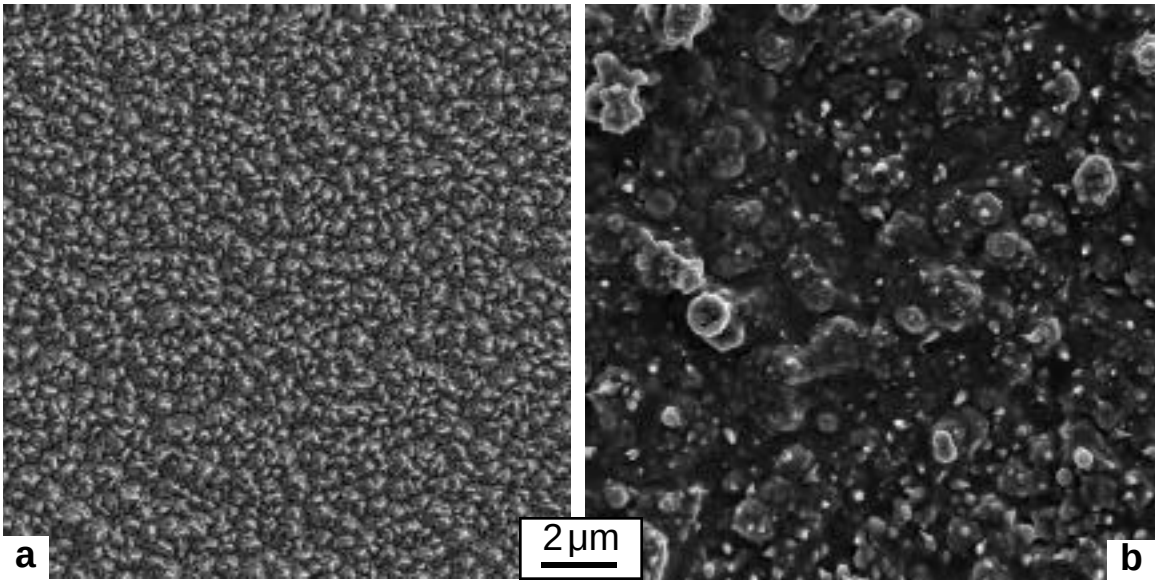

Figure 5. SEM secondary electron plan view images of EB-PVD Y_2O_3 coatings (a) as-received and (b) after exposure to Li at 800°C for 1000h.

observed. X-ray diffraction results showed an exact match with Y_2O_3 for the as-received coatings. With increasing exposure time and temperature, the Y_2O_3 peaks began to disappear and $LiYO_2$ peaks and unidentified peaks were observed. The surface morphology of the coating changed significantly after exposure, for example, Figure 5b. Oxide particles containing Ti and Y were observed on the coating

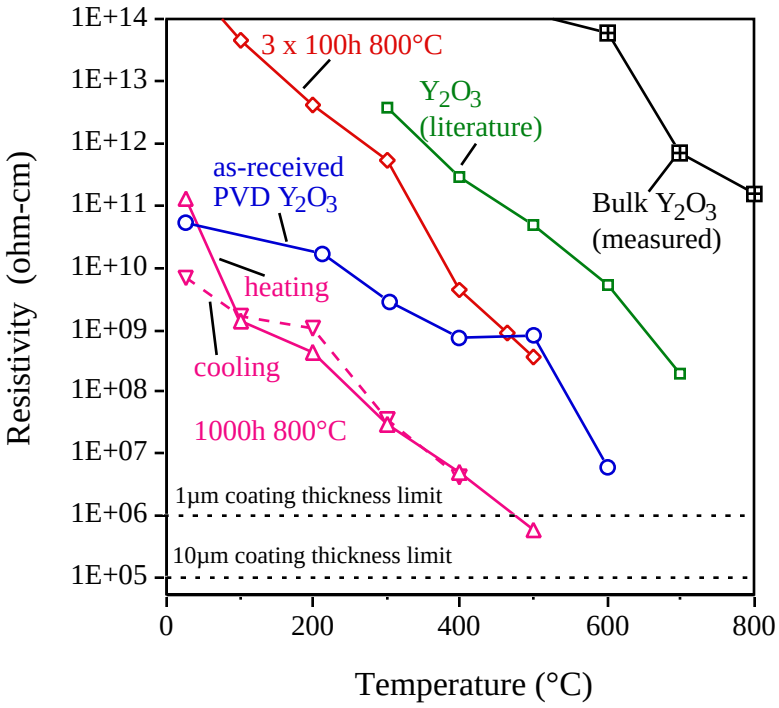

Figure 6. Resistivity as a function of temperature for EB-PVD Y_2O_3 coatings before and after exposure to Li at 800°C. Literature and measured values for bulk Y_2O_3 were much higher.

surface using Auger electron spectroscopy. After a 2000h exposure at 800°C, the coating was destroyed. Exposures at 700°C on a second set of coatings typically showed a complete loss of the coating. Previous work that examined the compatibility of Y_2O_3 and Y_2O_3 coatings in Li found the formation of a $LiYO_2$ layer at the Y_2O_3-Li interface after exposure at 500°C.[27,28] Although the current results on Y_2O_3 coatings show a potential compatibility problem, additional work is needed on coating development to further study the phenomenon as well as the role of coating microstructure on the reaction with Li.

In Japan, research programs are characterizing the properties and microstructure of AlN, Y_2O_3 and Er_2O_3 coatings made by RF sputtering and vacuum arc processes.[29,30] Processing issues need to be separated from those associated with compatibility in Li. Therefore, it is important to have high quality, well characterized coatings prior to testing in Li. For example, the crystallinity and purity of AlN coatings is being characterized.[29] Post-fabrication anneals at 400° and 700°C were used to improve the crystallinity. Annealing lowers the resistivity of the coatings but they retain sufficient resistance for this application. The coatings contain 3-10at.% O which probably contributes to their poor performance in Li at 500°C.[29]

Radiation-induced conductivity effects are being explored using 14MeV neutron irradiation of bulk ceramics specimens and AlN and Y_2O_3 coatings.[30] The increases in conductivity were proportional to the neutron flux but were such that the degradation of the resistivity under irradiation were within allowable limits for the V/Li blanket system.

Coating compatibility testing has not proceeded beyond static capsule-type testing. In order to truly demonstrate compatibility, testing in a thermal gradient will be necessary in order to evaluate the effects of temperature and mass transfer.[31] For example, previous results for Y_2O_3 showed only limited dissolution in static Li testing at 1100°C[12] but complete dissolution in flowing Li in 109h at 1143°C due to mass transfer or erosion.[32] A set of metrics for coating performance has been developed.[33] When coatings are able to meet these metrics in static tests, more extensive thermal convection loop testing will begin.

Effects of Coating Defects

The required properties and effects of defects in MHD coatings have been considered previously.[34-36] A recent analysis of the minimum properties and maximum defect density allowable[37] has caused a reassessment of the MHD coating strategy. Theoretical calculations suggest that only extremely small defect densities of through thickness defects can be tolerated because Li readily wets oxides in the temperature range of interest.[17] Therefore, it is expected that any crack will fill with Li, greatly increasing the effective conductivity of the coating system. (Even in the absence of a defect, Li has been observed to change the conductivity of oxides by interdiffusion at room temperature.[38]) With MHD coating thicknesses expected to be 5-10μm, it is highly unlikely that coatings could be fabricated with virtually no through thickness cracks. High quality bulk ceramics typically will have defects on the order of 10μm.[39] Even if a coating could be fabricated without cracks, tensile loading of the vanadium alloy substrate will cause cracks to form normal to the stress direction with a uniform spacing[40] that is generally expected to be 10-100 times the coating thickness based on data from the literature for standard properties of oxide films.[41,42] Therefore, unless there are no significant tensile loads on the coated vanadium alloys, through-thickness cracks would be expected every 1mm or less in a 10μm thick MHD coating. These cracks should wet with Li rendering the coating virtually useless.

Current Paradigm

Because of the anticipated defects in the insulating layer, it is suggested that the MHD coating will need to incorporate an outer, protective, metallic layer to prevent Li from entering cracks in the insulating layer.

The potential need for an outer layer has been recognized for some time.[1] Most likely, this layer would be vanadium or a vanadium alloy and could be up to 100μm thick.[43] A dual layer MHD coating system will need to be carefully assessed. Rather than a deposited coating, the outer layer could be free standing. A dual-layer coating will be more difficult to fabricate but will change the necessary compatibility metrics for the ceramic insulating layer. It also may preclude the in-situ or self-healing coating concepts, as lithium will no longer be in direct contact with the ceramic. However, some level of compatibility will be required so that a minor breach in the metallic outer layer will not immediately result in dissolution of the inner layer. For a dual-layer system, Y_2O_3 may be an adequate insulator candidate since the observed degradation was due to a solid state reaction to form $YLiO_2$. The amount of degradation will be limited to the amount of Li able to penetrate the outer layer. A minor leak would only have a limited effect on the ceramic layer.

With a thin metallic layer in contact with Li, there is some concern about the compatibility of vanadium and its alloys with Li. Degradation of the relatively thin outer layer by mass transfer or dissolution would have to be minor. There is some conflict about this issue as some investigators have reported rather high dissolution rates for vanadium alloys in flowing Li.[44,45] However, other work has shown good compatibility and low solubility of vanadium in Li.[46,47] As with a single layer system, this issue will need to be addressed by compatibility studies of a dual-layer system in a temperature gradient.

References

[1] Y. Y. Liu and D. L. Smith, J. Nucl. Mater. 141-43 (1986) 38.
[2] D. L. Smith, K. Natesan, J. H. Park, C. B. Reed, and R. F. Mattas, Fusion Eng. Design 51-52 (2000) 185.
[3] D. L. Smith, J. Konys, T. Muroga, and V. Evitkhin, J. Nucl. Mater. 307-311 (2002) 1314.
[4] E. E. Bloom, J. Nucl. Mater. 258-263 (1998) 7.
[5] D. L. Smith, M. C. Billone, S. Majumdar, R. F. Mattas, and D.-K. Sze, J. Nucl. Mater. 258-263 (1998) 65.
[6] J. E. Battles, Intern. Mater. Rev. 34 (1989) 1.
[7] R. J. Lauf and J. H. DeVan, J. Electrochem. Soc. 139 (1992) 2087.
[8] H. D. Röhrig, J. R. DiStefano, and L. D. Chitwood, J. Nucl. Mater. 258-63 (1998) 1356.
[9] K. Natesan and W. K. Soppet, J. Nucl. Mater. 283-287 (2000) 1316.
[10] B. A. Pint and J. R. DiStefano, J. Nucl. Mater. 307-311 (2002) 560.
[11] B. A. Pint, J. R. DiStefano, and P. F. Tortorelli, Fusion Sci. Technol. 44 (2003) 433.
[12] D. Elliott, D. Cerini, and L. Hays, Supporting Research and Advanced Development, Space Programs Summary 37-41, Vol. IV, Jet Propulsion Laboratory, Pasadena, CA (Oct. 1966), 124.
[13] R. N. Singh, J. Amer. Ceram. Soc. 59 (1976) 112.
[14] J. H. Park and T. F. Kassner, J. Nucl. Mater. 233-237 (1996) 476.
[15] P. Hubberstey, J. Nucl. Mater. 247 (1997) 208.
[16] P. Hubberstey and T. Sample, J. Nucl. Mater. 248 (1997) 140.
[17] B. A. Pint, J. H. DeVan, and J. R. DiStefano, J. Nucl. Mater. 307-311 (2002) 1344.
[18] J.-H. Park, K. Natesan, and R. Mattas, Argonne National Laboratory, unpublished results from teleconference (Aug. 2002).
[19] K. Natesan, M. Uz, and S. Wieder, J. Nucl. Mater. 283-287 (2000) 1277.
[20] K. Natesan, C. B. Reed, D. L. Rink, and R. C. Haglund, J. Nucl. Mater. 258-263 (1998) 488.
[21] T. Terai, A. Suzuki, T. Yoneoka, and T. Mitsuyama, J. Nucl. Mater. 283-7 (2000) 1322.
[22] T. Yoneoka, T. Sakurai, T. Sato, and S. Tanaka, J. Japan Inst. Metals 66 (2002) 384.
[23] A. Suzuki, T. Muroga, B. A. Pint, T. Yoneoka, and S. Tanaka, Fusion Eng. Design, 69 (2003) 397.
[24] O. I. Yeliseyeva, V. M. Chernov, and T. V. Tsaran, J. Nucl. Mater. 307-311 (2002) 1400.
[25] O. I. Yeliseyeva, V. M. Chernov, T. V. Tsaran, M. M. Potapenko, and D. L. Smith, these proceedings.
[26] Z. Yao, A. Suzuki, T. Muroga, and K. Katahira, these proceedings.

[27] T. Terai, T. Yoneoka, H. Tanaka, A. Suzuki, S. Tanaka, M. Nakamichi, H. Kawamura, K. Miyajima, and Y. Harada, J. Nucl. Mater. 233-237 (1996) 421.
[28] T. Mitsuyama, T. Terai, T. Yoneoka, and S. Tanaka, Fusion Eng. Design 39-40 (1998) 811.
[29] A. Sawada, A. Suzuki, T. Terai, and T. Muroga, these proceedings.
[30] T. Tanaka, A. Suzuki, T. Muroga, F. Sato, T. Iida, and T. Nishitani, these proceedings.
[31] J. H. DeVan, J. Nucl. Mater. 85-86 (1979) 249.
[32] L. Hays, NASA Tech. Report 32-1233, JPL, Pasadena, CA (Dec. 1967).
[33] B. A. Pint and J. R. DiStefano, DOE-ER-0313/32 (2002) 87.
[34] L. Bühler, Fusion Eng. Design 27 (1995) 650.
[35] S. Malang, H. U. Borgstedt, E. H. Farnum, K. Natesan, I. V. Vitkovski, Fusion Eng. Design 27 (1995) 570.
[36] A. Y. Ying and A. A. Gaizer, Fusion Eng. Design 27 (1995) 634.
[37] D.-K. Sze et al., these proceedings.
[38] J. W. Lee and S. I. Pyun, J. Power Sources 119 (2003) 760.
[39] P. F. Becher, private communication (2003).
[40] D. C. Agrawal and R. Raj, Acta Metall. 37 (1989) 1265.
[41] J. R. Nicholls, D. J. Hall, and P. F. Tortorelli, Mater. High Temp. 12 (1994) 141.
[42] M. Schütze, Mater. High Temp. 12 (1994) 237.
[43] D.-K. Sze, private communication (2003).
[44] Ch. Adelhelm, H. U. Borgstedt, and J. Konys, Fusion Tech. 8 (1985) 541.
[45] O. K. Chopra and D. L. Smith, J. Nucl. Mater. 155-157 (1988) 683.
[46] V. A. Evtikhin, I. E. Lyublinski, and A. V. Vertkov, J. Nucl. Mater. 258-263 (1998) 1487.
[47] S. N. Votinov et al., J. Nucl. Mater. 233-237 (1996) 370.

8.0 BREEDING MATERIALS

No contributions.

9.0 RADIATION EFFECTS, MECHANISTIC STUDIES, AND EXPERIMENTAL METHODS

THE EFFECTS OF INTERFACES ON RADIATION DAMAGE PRODUCTION IN LAYERED METAL COMPOSITES—H. L. Heinisch, F. Gao, and R. J. Kurtz (Pacific Northwest National Laboratory)*

Extended abstract of a paper submitted to the Journal of Nuclear Materials as part of the proceedings of the 11th International Conference on Fusion Reactor Materials, Kyoto, Japan, December 7-12, 2003.

OBJECTIVE

The objective of this research is to use molecular dynamics modeling to explore the effects of interfaces on cascade-producing radiation damage in nanolayered metal composites and to assess the resistance of these composites to damage by neutrons in fusion devices.

PROGRESS AND STATUS

Introduction

Multilayered composites consisting of many alternating metal layers, each only nanometers thick, possess enormous strength, approaching theoretical limits. These materials also display unexpectedly high thermal and mechanical stability [1]. Their unique properties derive from the operation of deformation mechanisms that do not occur in conventional metallic materials and are a result of the large internal interfacial areas and high coherency strains of the nanolayered metals. The enormous interface area to volume ratio of these materials may also positively affect their resistance to radiation damage, making them potentially useful materials for applications in fusion reactors.

As a first step in assessing the response of such materials to irradiation, we have begun studying the effects of typical interfaces on primary damage production. Atomic-scale molecular dynamics (MD) simulations of displacement cascades have been performed near bilayer interfaces of layered Cu and Ni, one of the systems for which nanolayer composites have been produced in the laboratory by physical vapor deposition techniques.

For very thin layers the interfaces are coherent, and each layer is in compression or tension as necessary to maintain coherency of the lattice parameter across the interface. At larger layer thicknesses, it is energetically favorable for misfit dislocations to form in the interface to reduce or eliminate the coherency stresses at some distance from the interface (on the order of half the misfit spacing), and the interfaces are referred to as “semi-coherent.” When the two metals have the same crystal structure, e.g. face centered cubic for Cu and Ni, a cube-on-cube layering scheme results in the formation of misfit dislocations (Lomer-Cottrell <110>{100} dislocations lying on the (100) Cu/Ni interface plane) in a regularly spaced network, the spacing of which depends on the mismatch of their lattice constants.

We have studied the nature of cascade damage in both coherent and semi-coherent Cu-Ni bilayer models by simulating cascades from 5 keV recoil atoms originating at varying distances from the interface in both the Cu and Ni layers. Although 5 keV recoils are quite small compared to those from fusion neutrons, they are of sufficient energy to display the essential elements of cascade damage for this initial study, and they fit within a model of convenient size, about 110,000 atoms total. The model consists of a rectangular volume containing two rectangular sub-volumes of approximately equal numbers of Cu and Ni atoms, respectively, oriented with their respective (100) faces parallel. The present semi-coherent model with periodic boundaries is oriented such that an a/2<110> misfit dislocation along the x-direction is centered in the (010) Cu/Ni interface, and two transverse a/2<110> misfit dislocations along the z-direction intersect it at the edges of the model cell. See Figure 1.

*Pacific Northwest National Laboratory (PNNL) is operated for the U.S. Department of Energy by Battelle Memorial Institute under contract DE-AC06-76RLO-1830.

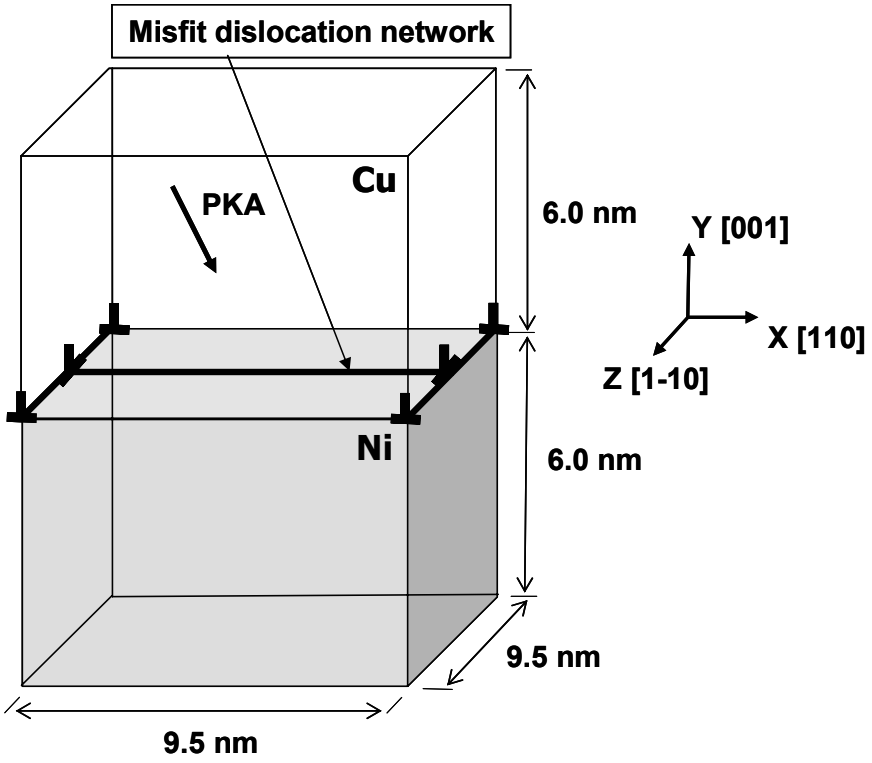

Figure 1. The orientation and approximate dimensions of the computational model for the semi-coherent Cu/Ni model, which contains a network of misfit dislocations along <110> directions in the [010] interface. The coherent Cu/Ni model has the same orientation and dimensions as the semi-coherent model, but with no misfit dislocations. Coherency is maintained by applied stresses along the X and Z directions.

Interatomic potentials for Cu-Cu, Ni-Ni and Cu-Ni interactions were based on the embedded atom potentials of Voter and Chen [3], with the universal potential of Ziegler et al. [4] spline-fitted to the pair potential at small interatomic separations. In all cases the model was equilibrated at a temperature of 100 K prior to starting the cascade simulations. In this initial study of cascade-induced displacement damage, a total of twelve cascades were simulated one at a time in each of the coherent and semi-coherent models. In a separate study, the effects of multiple cascades in the same sample were also investigated. Up to four cascades were produced sequentially in the same model, and the damage was recorded as a function of "dose."

In the post-cascade analysis, vacancies and interstitials were identified in terms of the occupation of initial lattice sites, and atomic mixing due to cascades was determined by counting the number of atoms of type A in the material of type B. In this paper we refer to atoms of type A occupying a lattice site of type B, and vice versa, as "antisite" defects. In all cases the numbers of atoms and lattice sites of each type were conserved in the model. The defect configurations were analyzed in each case after the cascade had cooled sufficiently near to 100 K, and such that the numbers of defects did not change, a total simulated time of about 15-20 ps.

Results

Considering all twelve cascades in the coherent interface model, the average number of defects produced per cascade was about the same in each of the Ni and Cu layers. See Table 1. The average

Table 1. Defect production in Ni and Cu layers by 5 keV cascades near coherent and semi-coherent Cu/Ni interfaces. The average numbers of vacancies (V), self-interstitial atoms (SIA) and anti-site defects for 12 cascades in each interfacial model are shown. Also shown are the numbers of defects not associated with the misfit dislocations (MFD).

Model	Ni			Cu		
	V	SIA	Cu in Ni	V	SIA	Ni in Cu
Coherent	6	5	9	4	5	10
Semi-coherent	18	8	11	6	15	21
Semi-coherent (excluding defects on MFD)	9	4	-	5	2	-

numbers of residual vacancies, self interstitial atoms (SIA) and anti-site defects were about the same in the Cu layer as in the Ni.

In the semi-coherent model the defect production is somewhat different from the coherent model (Table 1). About twice as many total point defects are produced in the semi-coherent case as compared to the coherent case. Also, the relative numbers of vacancies and SIA in the Cu and Ni layers are different. There are about twice as many SIA as vacancies in Cu and about twice as many vacancies as SIA in the Ni. Also, there are about twice as many antisite defects in Cu as in Ni. In all cases both the numbers of Cu and Ni atoms and the balance between vacant sites and interstitial atoms are conserved.

A striking feature of the cascade damage near the semi-coherent interface is the formation of stacking fault-like defects associated with the misfit dislocations. See Figure 2. These are most likely related to a property of the misfit dislocations in the Cu-Ni interface: under applied tensile stresses the misfit dislocations dissociate along close packed {111} planes projecting into the Cu layer. Moreover, given sufficient layer thickness and the appropriate applied stresses, the misfit dislocation array dissociates into a three-dimensional array of stacking fault pyramids [2]. In our simulations, during the cascade cooling process, after most of the in-cascade recombination has occurred, areas of stacking fault can be observed emanating into the Cu layer from various places along the misfit dislocation, as if the misfit dislocation is locally dissociating. These areas disappear and reappear with time as thermal equilibrium is approached. After complete cooling, some vacancy clusters reside at the misfit dislocation in stacking fault tetrahedra (SFT) -like configurations. SIA clusters are also observed to form in pyramidal structures at the misfits. SFT-like defects associated with the misfit dislocations appear as part of the damage in nearly all the cascades in the semi-coherent case. It is interesting to note in Table 1 that the numbers of vacancies and SIA in the semi-coherent interface that are not associated with (or trapped at) the misfit dislocations are about the same as the total numbers of defects produced by cascades in the coherent case.

In Table 2 we also compare the defect production in the coherent and semi-coherent Cu-Ni bilayers with the numbers of defects produced by 5 keV cascades in perfect bulk Ni and Cu respectively, as reported by Bacon et al. [5]. On average, about 35% fewer defects are produced in the coherent case than in the pure metals. On the other hand, in the semi-coherent case about 50% more defects are produced than in the pure metals, of which about half are those associated with the misfit dislocations. This comparison with cascades in pure metals should be considered with some caution because it results from a small number of highly variable cascades that were initiated in a variety of locations in the highly stressed, inhomogeneous Cu/Ni bilayer models.

The effects of multiple 5 keV cascades on defect production were also studied in both the coherent and semi-coherent models. Four cascades, starting from different locations, were introduced sequentially into the same model at intervals of 10-20 ps. This was repeated with different cascades four times, and

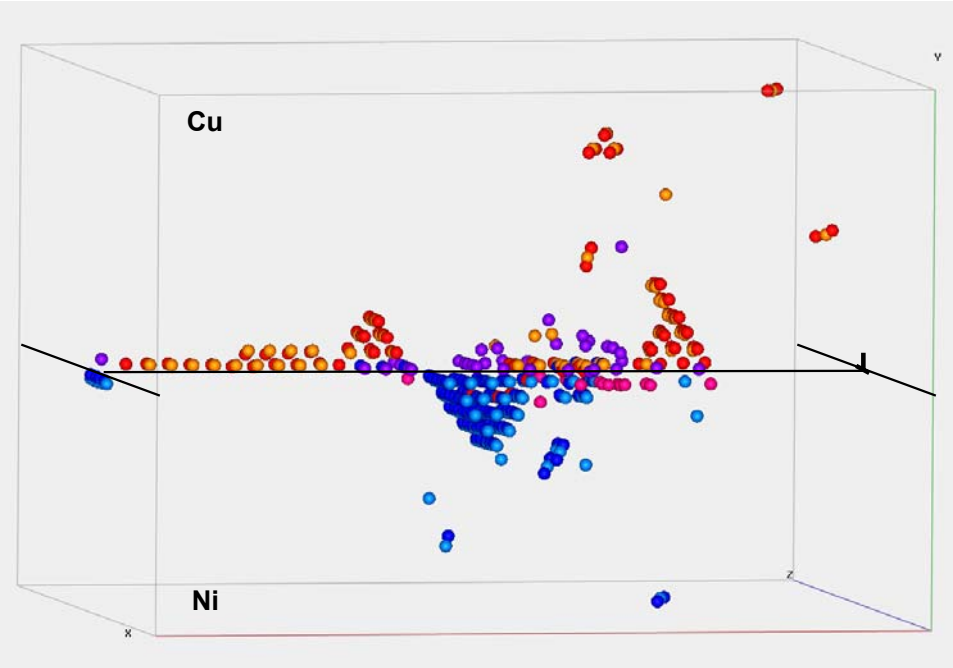

Figure 2. Defects resulting from a 5 keV cascade in the semi-coherent Cu/Ni model. In the Cu layer vacant sites are yellow, displaced atoms are red, and a Ni atom in a Cu lattice site is purple. In the Ni layer vacant sites are light blue, displaced atoms are dark blue, and a Cu atom in a Ni lattice site is dark pink. Interstitials are depicted as two displaced atoms on either side of the vacant site they share. Longer strings of alternating vacant sites and displaced atoms along the z-direction [1-10] in Cu are more highly strained single interstitials forming in tetrahedral shaped clusters along the misfit dislocation. In the Ni layer the triangular-shaped defect cluster attached to the misfit dislocation is a stacking fault "pyramid" of vacancies.

Table 2. Comparison of total defects from 5 keV cascades in layered Cu/Ni models with the average defect yields from 5 keV cascades in pure Cu and pure Ni (Bacon et al. [5]). The average numbers of vacancies (V), self-interstitial atoms (SIA) and total defects for 12 cascades in each interfacial model are shown.

Model	V	SIA	Total (V+SIA)	Total Antisite Defects
Coherent	10	10	**20**	19
Semi-coherent	23	23	**46**	32
Semi-coherent (excluding defects on MFD)	14	6	20	
Pure Cu	17	17	34	
Pure Ni	14	14	28	
Average of pure Cu and Ni			**31**	

the results were averaged for each type of interface. The results are displayed in Figures 3 and 4. For the coherent interface, Figure 3, the numbers of vacancies and SIA increase fairly uniformly with dose in both the Cu and Ni. The numbers of anti-site defects increase with dose at a much higher rate than the numbers of vacancies and SIA in both the Cu and Ni, tending toward saturation at the higher doses. In the semi-coherent case, Figure 4, the numbers of anti-site defects increase faster with dose than the vacancies and SIA, but at different rates in the two materials. As in the single cascades, the SIA in Cu and vacancies in Ni are present in greater concentration than the SIA in Ni and vacancies in Cu, and their numbers continue to increase at a somewhat higher rate with dose. There is some indication of saturation, or at least very slow growth, in the numbers of vacancies and SIA with dose, and overall the atomic mixing is less in the semi-coherent case.

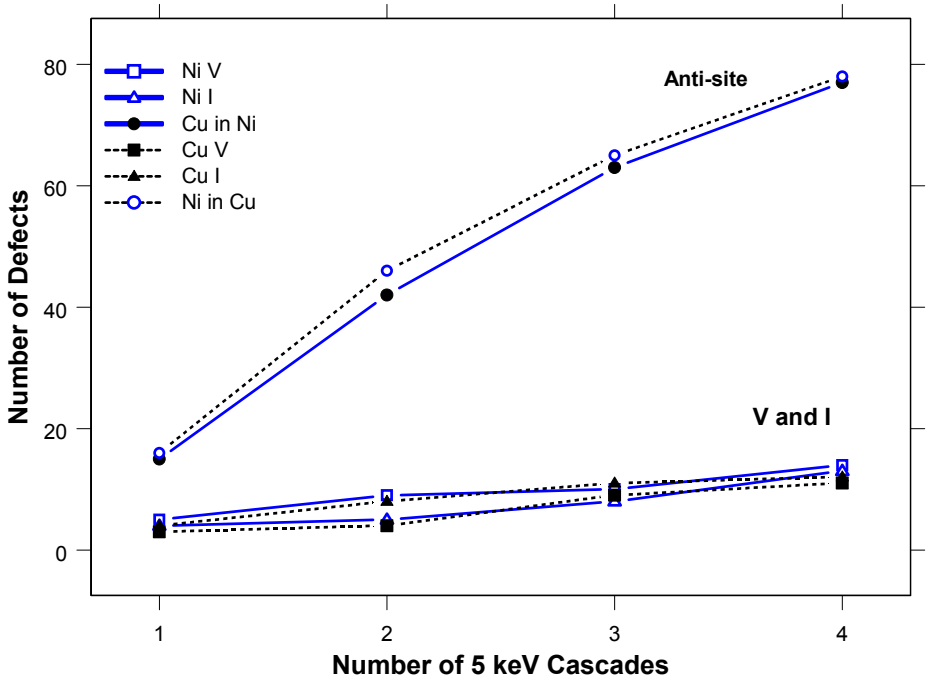

Figure 3. The numbers of residual defects as a function of dose (the number of successive 5 keV cascades in the same sample) for the coherent model. The separate curves are for NiV, the numbers of vacancies in the Ni layer, NiI, the numbers of interstitials in Ni, Cu in Ni, the numbers of Cu atoms in Ni sites, and likewise for the defects in the Cu layer.

Discussion and Conclusions

There are clear differences in defect production for the coherent and semi-coherent interfaces, and in both cases the defect production differs from that in the respective perfect pure metals. In the coherent composite both sides accumulate damage of the same type at the same rate, but fewer vacancies and SIA are produced than in the pure metals. In addition, atomic mixing is substantial, increasing with dose much faster than the numbers of vacancies and SIA. However, the mixing appears to saturate with dose. Since coherent interfaces are stable only for composites with very thin layers (less than about 5 nm in the Cu-Ni system), significant mixing of the Cu and Ni layers by prolonged irradiation could change the material properties significantly.

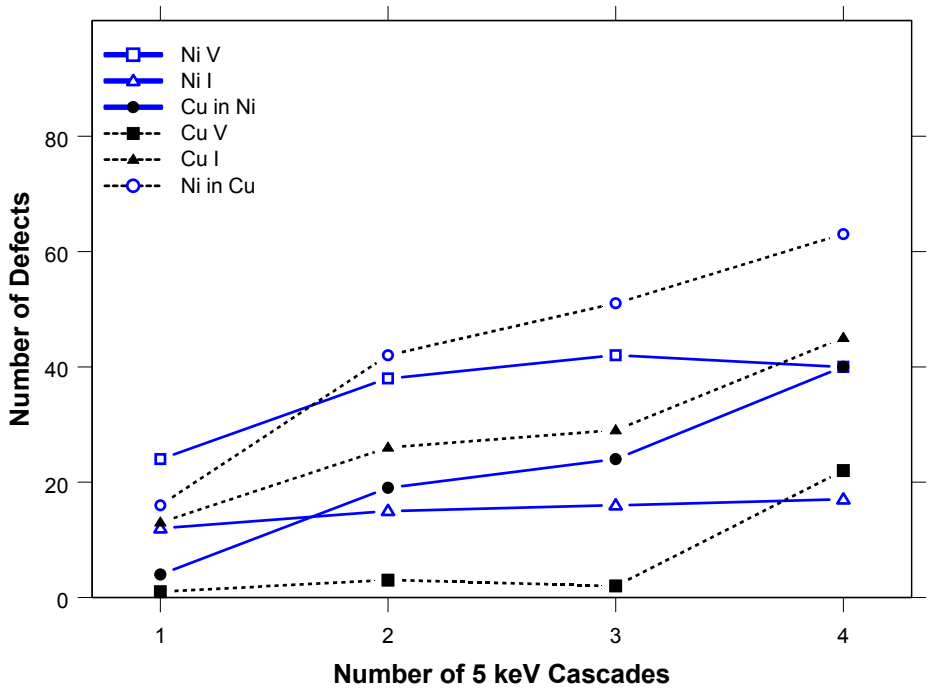

Figure 4. The numbers of residual defects as a function of dose (the number of successive 5 keV cascades in the same sample) for the semi-coherent model. The separate curves are for NiV, the numbers of vacancies in the Ni layer, NiI, the numbers of interstitials in Ni, Cu in Ni, the numbers of Cu atoms in Ni sites, and likewise for the defects in the Cu layer.

In the semi-coherent composite more defects are produced than in the coherent case, although about half of the defects in the semi-coherent case are directly formed at the interface and are associated with the misfit dislocation. It is not yet clear how the defects associated with the misfit dislocations will affect the subsequent behavior of the material. In the semi-coherent case the numbers and types of radiation-induced defects are different in Cu and Ni layers. It is premature to try to predict the overall effects of the asymmetry in defect production between the Cu and Ni layers on the properties of irradiated nanolayer Cu-Ni composites, especially when based solely on the properties of the primary damage state after 20 ps, since the migration energies and transport properties of defects in these systems is unknown.

The Cu-Ni composite system was chosen for these initial cascade studies because it is easily characterized and modeled, and the radiation damage phenomena can be compared with similar studies in the pure metals. Samples of Cu-Ni, Cu-Ag and Cu-Nb composites, as well as Cu-stainless steel composites, exist and will be included in irradiation experiments. Modeling radiation damage in the more complicated systems will undoubtedly reveal quite interesting effects.

Acknowledgements

The authors are indebted to Erik Carl for assistance with cascade simulations and to R. G. Hoagland and C. H. Henager, Jr. for valuable discussions. This work was supported by the Office of Fusion Energy Sciences of the U.S. Department of Energy under contract DE-AC06-76RLO1830.

References

[1] A. Misra, J. P. Hirth, and H. Kung, Phil. Mag. A 82 (2002) 2935.
[2] R. G. Hoagland, T. E. Mitchell, J. P. Hirth, and H. Kung, Phil. Mag. A 82 (2002) 643.
[3] A. F. Voter and S. P. Chen, Proc. of Mat. Res. Soc Symp 82 (1987) 175; A.F. Voter, Phys. Rev. B 57 (1998) R13985.
[4] J. F. Ziegler, J. P. Biersack, and U. Littmark, The Stopping and Range of Ions in Matter, Volume 1, (New York, 1985. Pergamon).
[5] D. J. Bacon, F.Gao, and Yu. N. Osetsky, J. Nucl. Mater. 276 (2000) 1.

MULTISCALE MODELING OF RADIATION DAMAGE IN FE-BASED ALLOYS IN THE FUSION ENVIRONMENT—B. D. Wirth (Department of Nuclear Engineering, University of California Berkeley), G. R. Odette (University of California, Santa Barbara), J. Marian (California Institute of Technology), L. Ventelon (University of California, Berkeley), J. A. Young and L. A. Zepeda-Ruiz (Lawrence Livermore National Laboratory)

EXTENDED ABSTRACT

Ferritic alloys represent a technologically important class of candidate materials for plasma-facing first wall structures in future fusion energy facilities. Predicting their in-service performance requires a detailed understanding of the mechanisms of defect accumulation and microstructure evolution. The physical processes involved in radiation damage are inherently multiscale and hierarchical, spanning length and timescales from the atomic nucleus to meters and picosecond to decades. In this paper, we present a multiscale modeling methodology to describe the accumulation of radiation damage and the corresponding effects on material microstructure and property degradation within the fusion energy environment. Selected results from atomic scale investigation are presented in the paper, focusing on (i) the mechanisms of self-interstitial dislocation loop formation with Burgers vector of a <100> in Fe relative to Vanadium, (ii) He transport, (iii) the interaction between He and small self-interstitial clusters in Fe, and (iv) dislocation – helium bubble interactions in fcc Al.

The results illustrate a range of phenomena occurring during irradiation in the fusion environment that require further investigation and incorporation into evolution models.

1. MS simulations in Fe and V show that dislocation loop clusters of SIA are lowest energy with **b**=a/2<111>. However, loops with **b**=a<100> in Fe are closer in energy than anticipated by dislocation theory, allowing for the possibility of a<100> metastable loops.
2. a<100> junctions can form between intersecting a/2<111>-type dislocation loops in both V and Fe. In V, the junctions are thermally unstable and rapidly dissolve as the loops rotate to form a single a/2<111> dislocation loop. In Fe, the junction is stable over an intermediate temperature regime and can propagate, leading to a single a<100> dislocation loop.
3. Atomistic simulations of substitutional He diffusion in Fe within the framework of the multiple frequency diffusion analysis of Le Claire [27] reveals an activation energy of 0.65 eV. The simulations reveal that He is strongly delocalized in a di-vacancy – He complex and that substitutional He can jump into a second nearest neighbor vacancy with an activation energy of 0.66 eV.
4. MD simulations of the interactions between substitutional He and SIA in Fe, reveal strong interactions leading to SIA-V recombination and the kick-out of He to an interstitial position. The simulations indicate strong trapping and apparent immobility of a interstitial He – substitutional He complex, as well as the strong trapping of relatively small a/2<111> SIA clusters by both substitutional and interstitial He, with a calculated binding energy of 1.5 eV between a 6-SIA and interstitial He.
5. MD simulations of the interaction between an edge dislocation and under-pressurized He bubble in Al reveal a critical shear stress of about 35 MPa, with a bypass mechanism that involves the local annihilation and re-nucleation of dislocation segments, producing a shear step in the bubble.

Reference

B. D. Wirth, G. R. Odette, J. Marian, L. Ventelon, J. A. Young, and L. A. Zepeda-Ruiz, submitted for publication, ICFRM-11 proceedings, to be published in Journal of Nuclear Materials.

INFLUENCE OF PKA DIRECTION, FREE SURFACES, AND PRE-EXISTING DEFECTS ON CASCADE DAMAGE FORMATION—R. E. Stoller, S. G. Guiriec (Oak Ridge National Laboratory)

OBJECTIVE

The objective of this work is characterize primary damage formation in irradiated structural materials, including the impact of all the various irradiation, material, and experimental conditions that may influence defect formation.

SUMMARY

Primary cascade damage production in iron has been extensively investigated by molecular dynamics, and average defect production parameters, such as the total number of stable point defects, in-cascade defect clustering fractions, and in-cascade cluster size distributions have been derived. However, preliminary results indicated several factors could alter “normal” cascade evolution and lead to quite different defect production behavior. Further investigations of three such factors have been carried out: (1) primary knock-on atom (PKA) direction, (2) nearby free surfaces, and (3) pre-existing effects. Results of the investigation confirm these factors can significantly impact cascade damage formation. The effects include enhanced defect survival for PKA directions that lie in close-packed {110} planes, increased point defect clustering and larger defect clusters for cascades initiated near a surface, and reduced defect survival in simulation cells containing defects. The origin and implications of these effects are discussed relative to the interpretation of certain experimental observations and parameters used in other modeling studies.

PROGRESS AND STATUS

Introduction

The use of molecular dynamics (MD) simulations to investigate the evolution of atomic displacement cascades has provided a detailed understanding of primary radiation damage formation in irradiated materials [1-10]. In particular, increased computational capability has enabled this method to be used to obtain a statistically meaningful cascade database for iron [1,5]. Representative values have been derived for several measures of primary damage, including: the number of stable point defects (interstitials and vacancies) created, the number of these stable defects that cluster directly during the cascade event, and the size distribution of these in-cascade defect clusters. For convenience when comparing different materials and cascade conditions, the number of displacements obtained from the standard NRT model [11,12] is often used as a normalizing factor for the number of defects produced and in clusters. This convention is followed in the present work.

Although the iron cascade database in the literature is relatively large, a number of factors have been identified that can cause cascade evolution, and hence defect production, to deviate from the average behavior exhibited in the database. Three of these factors are: PKA direction [3,13], presence of a nearby surface [8,9,14], and pre-existing defects (such as cascade debris) in the simulation cell [15,16]. In some cases, the results just referenced exhibited rather significant differences from the typical MD cascade that is carried out in an atomic simulation cell that contains perfectly crystalline material. However, in other cases the results were either ambiguous, limited in their parameter range, or an insufficient number of simulations were done to establish statistical significance. Since displacement cascades are stochastic events, the quantitative impact of any cascade variable can only be determined by a systematic study with “enough” events to capture inherent statistical variations in their behavior [1,5]. The objective of the current investigation is to establish the degree to which these three factors influence cascade evolution and defect formation by carrying out additional simulations and extending the range of the previous work to higher PKA energies and temperatures. Since the methods and models used have been discussed in detail in previous publications, [1-5,13,14] only a brief description is included here.

Application of MD Simulation Method

MD simulations were carried out using the code MOLDY and a modified version of the Finnis-Sinclair potential [3,17,18]. Periodic boundary conditions were imposed on a constant pressure ensemble of atoms. The simulation cell size varied from 16,000 atoms for the low-energy investigations of PKA direction effects, to 250,000 atoms for the 10 and 20 keV simulations employed to evaluate the impact of free surfaces and pre-existing damage. The iron cascade database mentioned above served as the basis for comparison with the new simulations [1,5].

Results of MD Simulations

Influence of PKA Direction

A fairly dramatic effect of PKA direction was observed at low cascade energies during an earlier analysis of the complete cascade database [1, 13]. In order to avoid lattice effects such as channeling and directions with particularly low or high displacement thresholds, MD cascade simulations are typically carried out using a high index PKA direction. For example, most of the simulations in the database discussed in Ref. [1] were generated using a [135] PKA direction. A preliminary evaluation of PKA direction effects using 1 keV cascades indicated that mean values obtained with [135] PKA should be representative of the average behavior at this energy [4]. However, analysis of a large number of 300 eV simulations found that stable defect production was significantly above the average when the PKA direction lay in the close-packed {110} planes. For example, some cascades initiated with a [114] developed completely within a single plane. The planar channeling effect resulted in greater separation of vacancies and interstitials and therefore less in-cascade recombination.

It was expected that this effect would not persist to higher energies where the higher kinetic energies would tend to kick recoils out of the {110} plane. However, when the energy dependence of this enhanced defect formation was explored using simulations at 100K, and it was somewhat surprisingly found that the increased defect survival was detected at energies as high as 2 keV. The ratio of the defect survival using [114] to that using [135] was 1.59, 1.12, 1.28, 1.15, and 0.995 for cascade energies of 0.3, 0.5, 1.0, 2.0 and 5.0 keV, respectively [13]. In order to obtain further information on the potential for this phenomenon to influence defect production, additional simulations have been carried out at 600 and 900K to see if increased atomic thermal motion would act to minimize the planar channeling.

Some of the results of 600 and 900K simulations are shown in Figs. 1a and 1b, respectively. This figure compares stable defect formation as a function of energy for the [114] and [135] PKA directions, where the error bars in the figure are the calculated standard errors of the mean values. The error bars are somewhat larger than in the 100K comparisons shown in Refs. [1 and 13] because the number of cascades at each condition is smaller. However, it seems clear that there is no systematic deviation between the two PKA directions at either temperature. Even at 300 eV, where the effect was strongest in 100K cascades, the impact is small at 600K. Additional simulations are underway to improves the statistical comparison in Fig. 1, and to provide data for comparison at additional energies.

Influence of Free Surfaces

A previous publication describes the motivation for concern about the influence of a nearby free surface on cascade evolution, and results obtained from a series of 10 keV cascades were presented [14]. The primary interest is to provide an explanation for the lower yield of visible defects from MD cascades simulations as compared to the results of thin foil ion irradiations that are carried out in a transmission electron microscope. The 10 keV simulations exhibited a clear effect on both total stable defect production and in-cascade clustering for cascades initiated at or near a free surface [14]. However, the largest vacancy and interstitial clusters formed were still too small to be observed by TEM.

Therefore, additional simulations have been carried out using 20 keV cascades, an energy where point defect clustering is increased and larger clusters have been observed in the existing database. The new simulations were carried out using the same method discussed in Ref. [14]. A free surface was created by

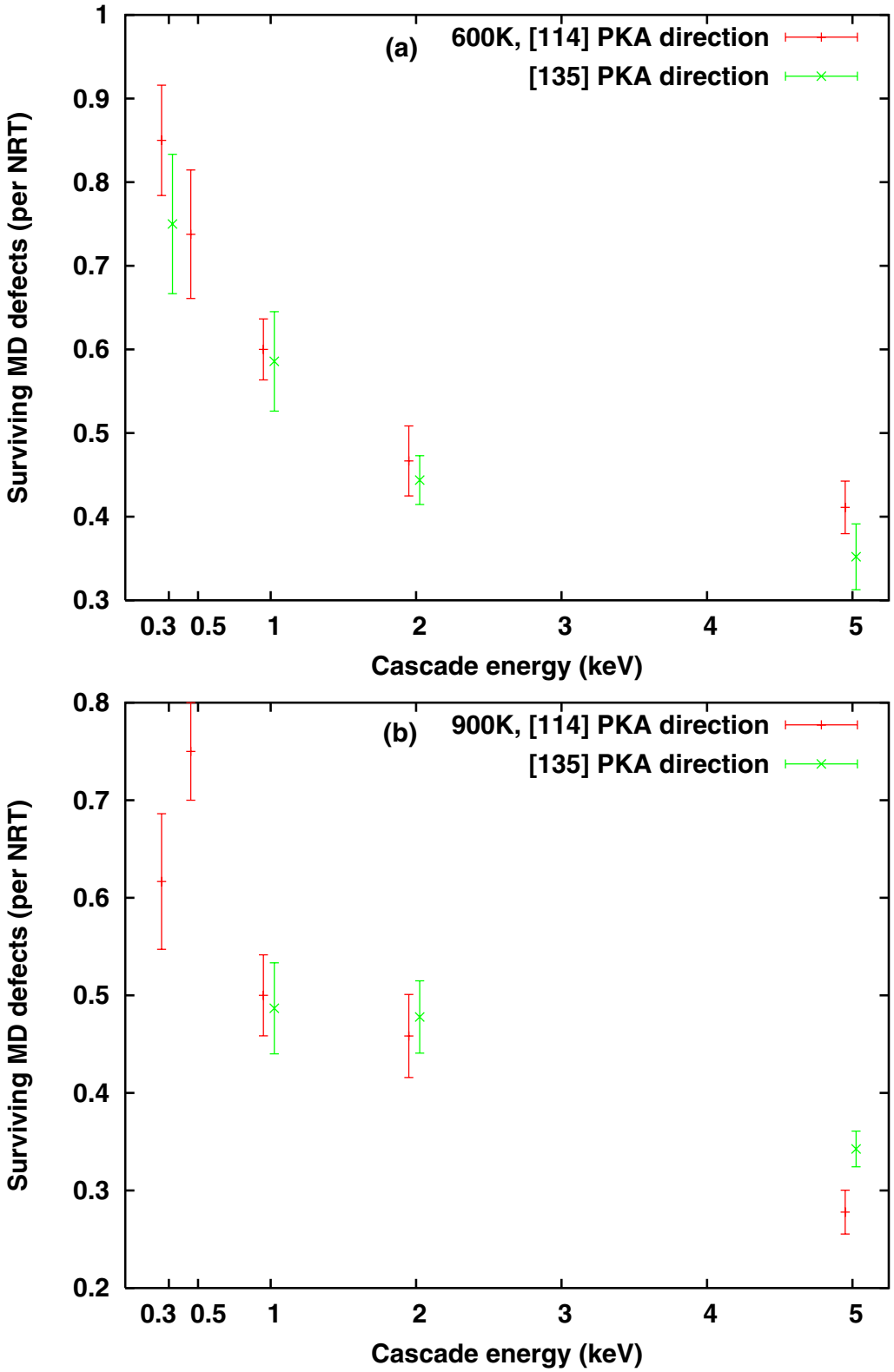

Fig. 1. Energy dependence of the PKA direction effect on stable point defect formation at (a) 600K and (b) 900K.

removing 5 layers of atoms from one surface of a $(50a_o)^3$ atom cell, containing 250,000 atom sites. Periodic boundary conditions are otherwise imposed. Eight simulations were carried out at 100K in which all the PKAs selected were surface atoms. Several PKA directions were used, with each of these directions slightly more than 10˚ off the [001] surface normal. The results of these simulations can be compared with the 10 "bulk" cascades conducted previously in which cascades were initiated near the simulation cell center.

The number of surviving point defects (normalized to NRT displacements) is shown in Fig. 2a for both the bulk and surface cascades, with error bars indicating the standard error of the mean. The results are similar to those observed at 10 keV. The average number of stable interstitials produced by the surface cascades is not significantly different than for the bulk cascades, with the mean value shifted slightly higher for the 20 keV surface cascades, whereas it was slightly lower for the 10 keV case. However, there is a substantial increase in the number of stable vacancies produced, and the change is clearly significant. As discussed previously, the number of surviving interstitials and vacancies is no longer equal for cascades initiated at the surface. Interstitials can be lost to the surface by two mechanisms; sputtering or the diffusion of interstitials and small glissile interstitial clusters to the surface. Reducing the number of interstitials leads to a greater number of vacancies surviving since less recombination can take place.

The results for in-cascade clustering shown in Fig. 2b are also similar to the 10 keV simulations, i.e. no significant change in the fraction of interstitials in clusters (~0.18/NRT) while the in-cascade vacancy fraction (based on the 4th-nearest-neighbor criterion [4]) increased from ~0.06/NRT to 0.25/NRT. Moreover, the vacancy cluster size distribution changed dramatically, with larger clusters produced than were observed at 10 keV. The size distributions obtained for bulk and surface cascades are shown in Fig. 3a and b for vacancy and interstitial clusters, respectively. The largest vacancy cluster observed in the bulk cascades contained only six vacancies, while the surface cascades had clusters as large as 21 vacancies. This latter size is near the limit of visibility in TEM, with a diameter of almost 15 nm. The change in the interstitial cluster size distribution was less dramatic.

Influence of Pre-existing Damage

A cascade energy of 10 keV and a temperature of 100K was chosen for this study to expand the range of previous work carried out using 1 keV simulations in copper [15] and 0.40, 2.0, and 5.0 keV simulations in iron [16]. The 10 keV cascade energy is high enough for some in-cascade clustering to occur, is near the plateau region of the defect survival curve, and initiates a limited degree of subcascade formation. For these conditions, the database contains two independent sets of cascades, 7 in a 128k atom cell and 8 in a 250k atom cell that provide a basis of comparison. A cell size of 250k atoms was used for the cascade simulations with pre-existing damage.

Simulations were carried out to investigate three different types of pre-existing damage. The first involved the as-quenched debris from a 10 keV cascade in perfect crystal. A total of 30 vacancies and interstitials were present, including one di-interstitial and one 7-interstitial cluster. The second case was similar, but the vacancies were rearranged to obtain a 6-vacancy void and a 9-vacancy loop. Some additional interstitial clustering occurred when the modified configuration was equilibrated, so that it contained four di-, one tri-, and one 8-interstitial cluster. This starting configuration is shown in Fig. 4. The third configuration contained only a single 30-vacancy void. Eight simulations were carried out starting with different initial PKAs and a <135> PKA direction. The same set of PKAs were used for all three defect configurations, with the PKA location such that it was aimed at the center of the defect field.

The influence of pre-existing damage on the number of stable defects formed in 10 keV cascades is shown in Fig. 5a, where results from the three defect configurations are compared with those obtained in perfect crystal. Results for the fraction of interstitials in clusters are shown in Fig. 5b. The variation between two sets of perfect crystal simulations is provided for comparison. Both defect survival and interstitial clustering results are summarized in Table 1. As expected, substantial variation was observed between the different simulations for any given pre-existing defect configuration, but a significant reduction in the average defect formation was observed for the two configurations most typical of cascade debris. A slight increase (that

may not be statistically significant) in stable defect production was observed when an otherwise perfect crystal contained a small void. Only the second defect configuration (Fig. 4) lead to a significant change in interstitial clustering.

Table 1. Summary of defect production results from cascades with pre-existing damage

	survival fraction (per NRT)	standard error	interstitial cluster fraction (per NRT)	standard error
Perfect crystal (128k and 250k atoms)	0.336	0.0137	0.170	0.0155
Defective crystal				
30 i,v: cascade debris, with 1 di- and 1 7-interstitial cluster	0.260	0.0214	0.179	0.0119
30 i,v: cascade debris with 4 di-, 1 tri-, and 1 8-interstitial cluster; 6-vacancy void, 9-vacancy loop	0.279	0.0258	0.110	0.0191
30-vacancy void only	0.370	0.0288	0.190	0.0188

Discussion and Conclusions

A fairly complete picture of displacement cascade evolution in bulk, perfect crystal iron has been obtained through extensive simulation studies during the past several years. The work reported here is intended to illustrate the impact of three cascade conditions that deviate from the average behavior displayed in the overall cascade database. These are: PKA direction effects, the influence of free surfaces, and the impact of pre-existing defects or cascade debris. In each case, the results reported here extends the range of previous work by the current authors and others.

Higher cascade energies and temperatures have been used to investigate the trends obtained at 100 K and lower energies. The intent is to determine the overall significance of these effects to the average defect production parameters that are used in the damage source terms of kinetic microstructural models. The influence of a planar channeling effect was observed in low energy cascades (up to 2 keV) at 100K for PKA directions that lie in the close-packed {110} planes in bcc iron. This phenomenon has now been investigated in MD simulations up to 5 keV at temperatures up to 900K. Although dramatic differences are observed between cascades that exhibit planar channeling and “normal,” more isotropic cascades, the overall impact of PKA direction on average defect formation in any practical sense appears to be limited. The maximum energy where an effect was seen at 100K was 2 keV, and at 600 and 900K essentially no effect was observed even in 300 eV cscades.

In the case of surface-influenced defect formation, a sufficient number of 20 keV iron cascades were completed to statistically evaluate variations between these and bulk cascades. Relative to cascades initiated far from the free surface, stable vacancy defect production increased for surface-influenced cascades, while the number of surviving interstitials was nearly unchanged. The difference between the number of surviving vacancies and interstitials arises from sputtering and surface absorption of mobile interstitial defects. The fraction of vacancies contained in clusters increased substantially for cascades initiated at the surface, and larger vacancy clusters were formed. The impact on defect clustering increases with cascade energy, and are reaching the limit of TEM visibility in the 20 keV simulations reported here. These results have implications for interpreting experiments in which cascade defect production is observed *in-situ* using transmission electron microscopy

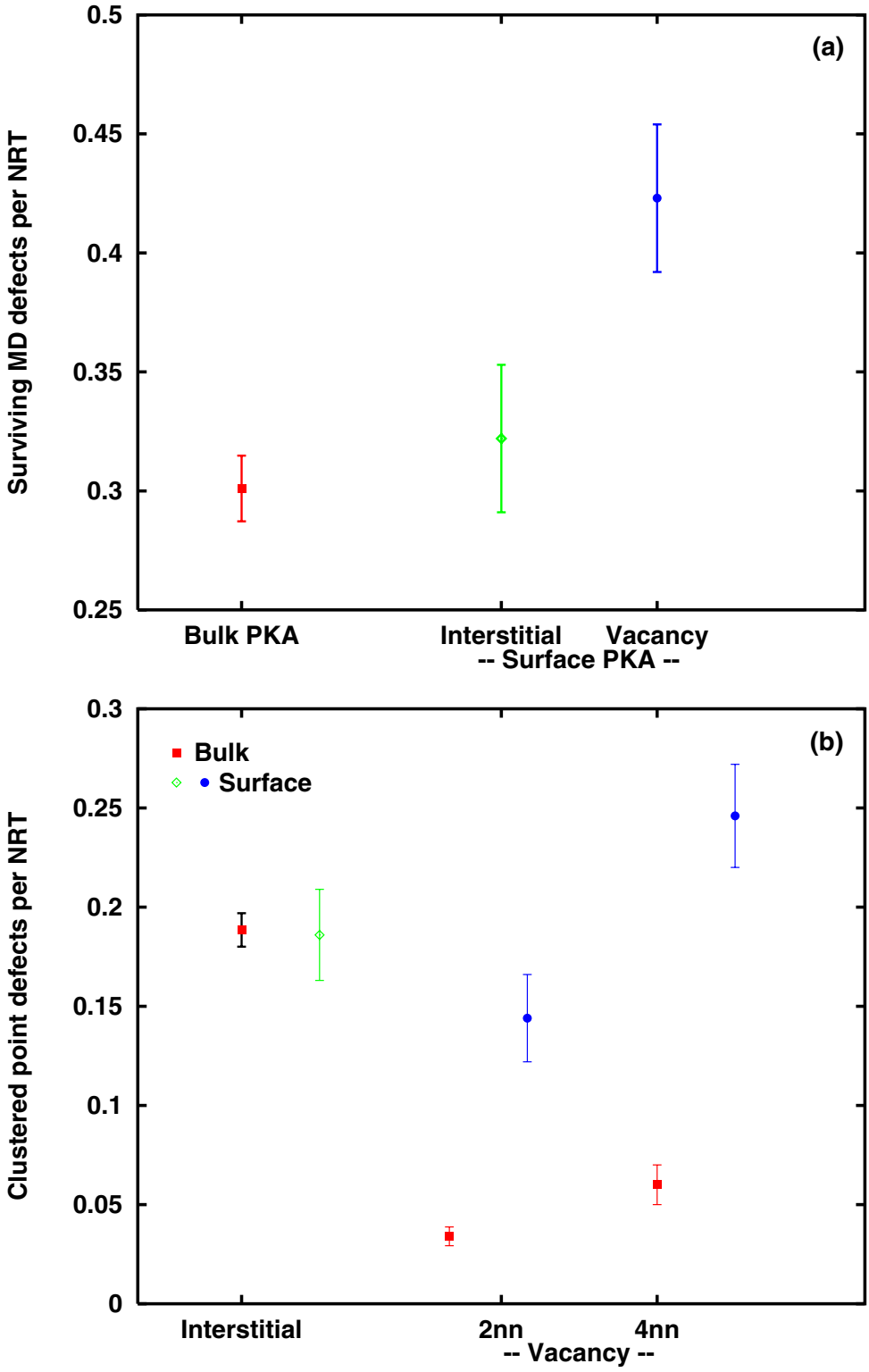

Fig. 2. Comparison of defect production parameters obtained in 20 keV cascades at 100K for cascades initiated by a PKA near the center (bulk) and at the free surface of the simulation cel: (a) average stable defect production (per NRT) and (b) clustered point defect fraction (per NRT).

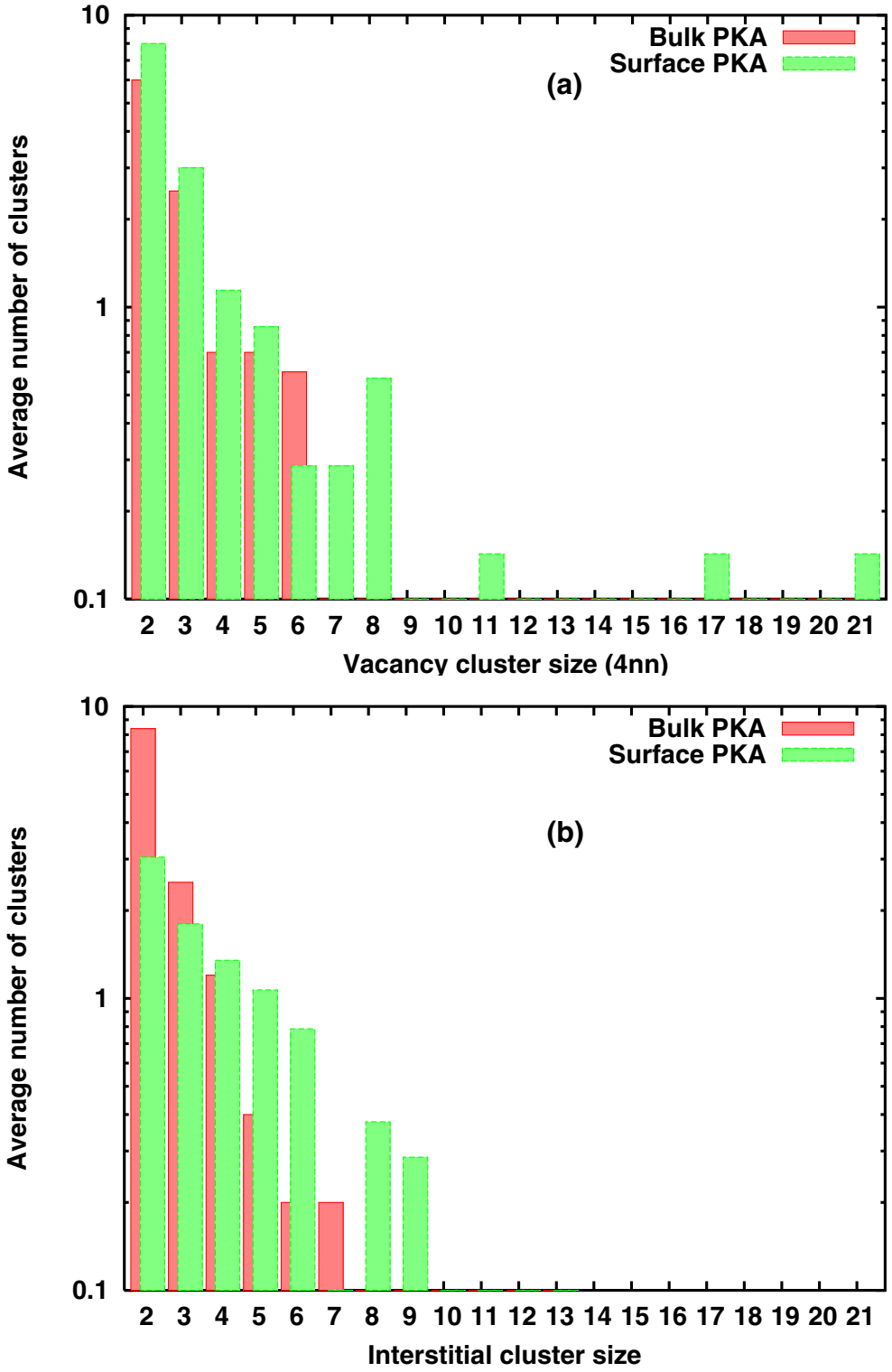

Fig. 3. Comparison of in-cascade point cluster size distributions in 20 keV, 100K cascades initiated by a PKA near the center (bulk) and at the free surface of the simulation cell: (a) vacancy clusters and (b) interstitial clusters.

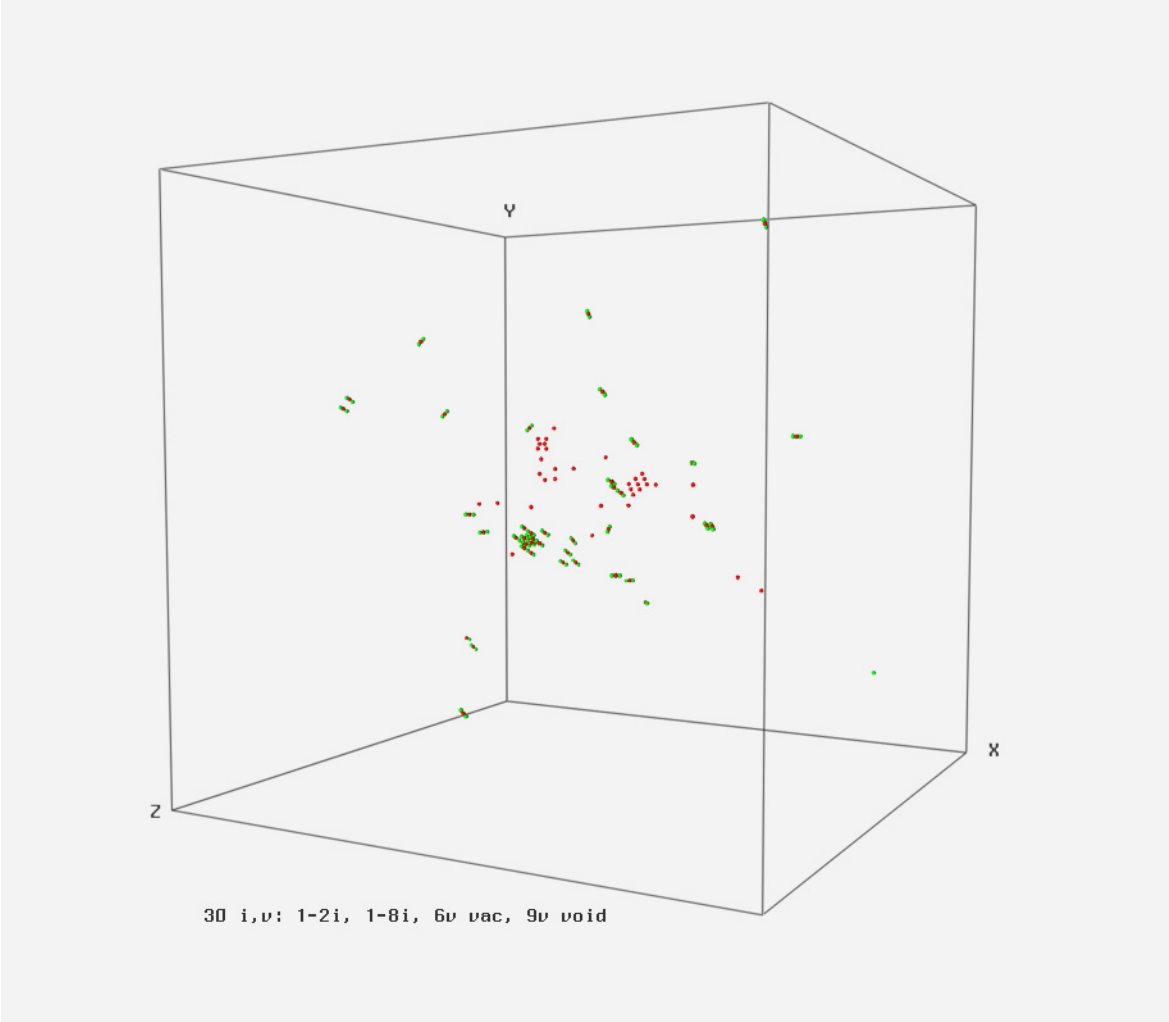

Fig. 4. Second pre-existing defect configuration for 10 keV displacement cascades (see text).

Although the approach in this investigation of pre-existing damage effects was slightly different, the results are generally consistent with the previous studies by English, et al. [15] and Gao, et al. [16]. In both cases, the authors observed substantial reductions in defect production when a cascade was initiated in material containing defects. The reductions in defect production observed in this study (Fig. 5 and Table 1) are somewhat smaller. This difference may partially be due to the higher cascade energy employed here (10 keV vs. 0.4 to 5 keV); but the statistical nature of cascade damage production is also a factor. A number of cascades were carried out in the work of Gao, et al., and the results were analyzed as a function of the distance between the center of mass (COM) of the new cascade and that of the pre-existing damage. A good correlation was found between this spacing and the number of defects produced, and their results provide a trend based on individual cascades as a function of COM distance. In the work reported here, the distance between the cascade origin and the pre-existing damage was nearly the same for all of the simulations. However, the morphology developed in each of the 8 cascades was quite different, so the COM spacings also varied. The average behavior for a fixed initial separation can not be directly compared to the earlier results. Because of the reduced defect survival observed in defective material, these results and the earlier work suggest that the possibility of developing a fluence-dependent cascade survival efficiency for use in kinetic radiation damage models should be investigated.

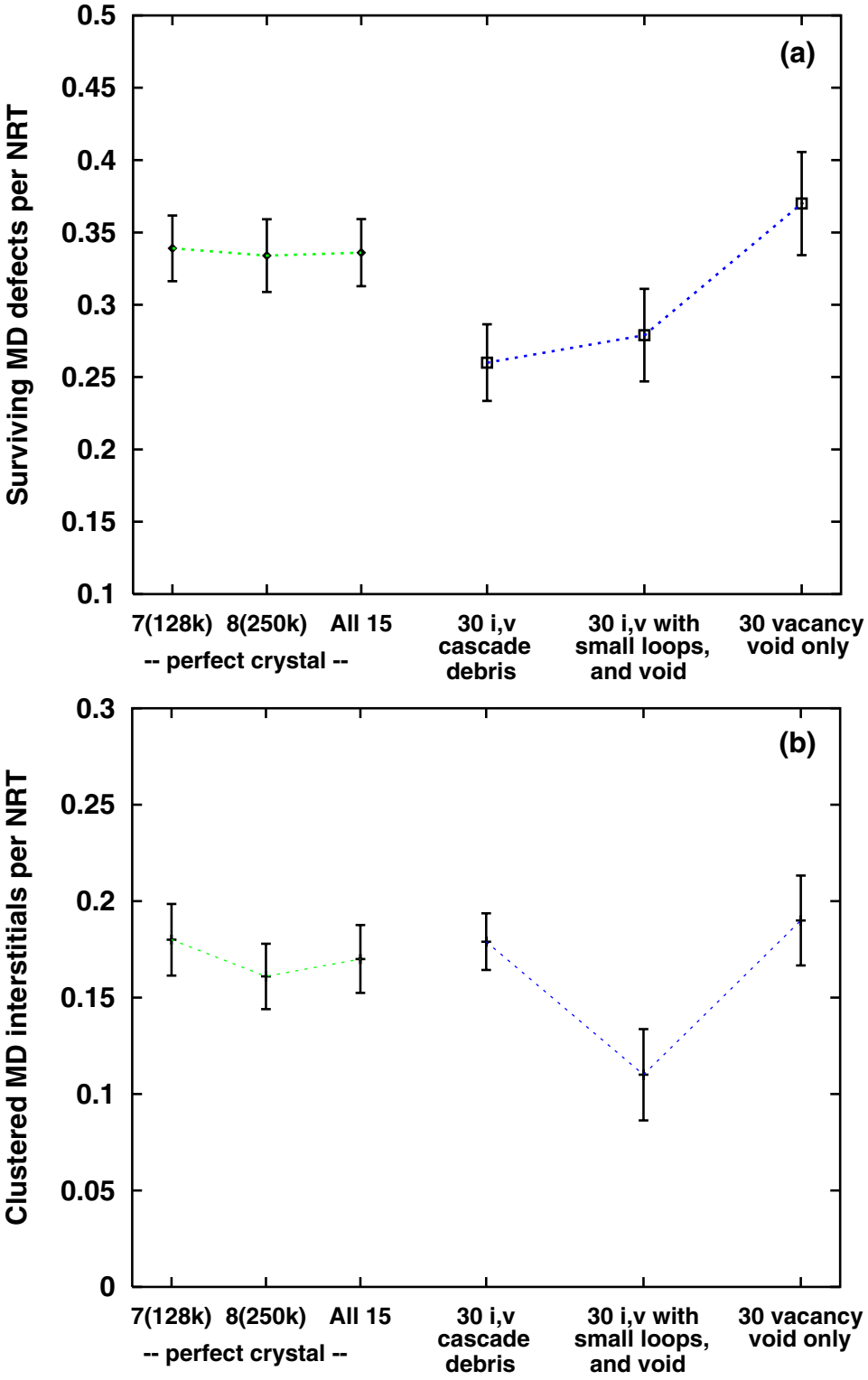

Fig. 5. Comparison of defect formation parameters in perfect and defective simulation cells: (a) total point survival and (b) interstitial clustering.

Acknowledgements

Research support for S. G. Guiriec was provided at ORNL during an internship for the Master of Engineering, Institut Supérieur des Matériaux du Mans (ISMANS), Le Mans, France.

References

[1] R. E. Stoller and A. F. Calder, J. Nucl. Mater. 283-287 (2000) 746-752.

[2] W. J. Phythian, R. E. Stoller, A. J. E. Foreman, A. F. Calder, and D. J. Bacon, J. Nucl. Mater. 223 (1995) 245.

[3] A. F. Calder and D. J. Bacon, J. Nucl. Mater. 207 (1993) 25-45.

[4] R. E. Stoller, G. R. Odette, and B. D. Wirth, J. Nucl. Mater. 251 (1997) 49-69.

[5] R. E. Stoller, J. Nucl. Mater. 276 (2000) 22-32.

[6] D. J. Bacon, F. Gao, and Y. N. Osetsky, J. Nucl. Mater. 276 (2000) 1-12.

[7] M. J. Caturla, N. Soneda, E. Alonso, B. D. Wirth, T. Diaz de la Rubia, and J. M. Perlado, J. Nucl. Mater. 276 (2000) 13-21.

[8] K. Nordlund and R. S. Averback, J. Nucl. Mater. 276 (2000) 194-201.

[9] M. Ghaly and R. S. Averback, Phys. Rev. Let. 72 (1994) 364.

[10] K. Nordlund, J. Keinonen, M. Ghaly, and R. S. Averback, Nature 398 (1999) 48.

[11] M. J. Norgett, M. T. Robinson, and I. M. Torrens, Nucl. Engr. and Design 33 (1975) 50-54.

[12] ASTM E521, Standard Practice for Neutron Radiation Damage Simulation by Charged-Particle Irradiation, Annual Book of ASTM Standards, Vol. 12.02, American Society of Testing and Materials, West Conshohocken, PA.

[13] R. E. Stoller, The Influence of PKA Direction on Displacement Cascade Evolution, Microstructural Processes in Irradiated Materials, Eds. G. E. Lucas, L. L. Snead, M. A. Kirk, and R. G. Elliman, Materials Research Society, Pittsburgh, PA, 650 (2001) 3.5.1-3.5.6.

[14] R. E. Stoller, J. Nucl. Mater. 307-311 (2002) 935-940.

[15] A. J. E. Foreman, W. J. Phythian, and C. A. English, private communication, unpublished.

[16] F. Gao, D. J. Bacon, A. F. Calder, P. E. J. Flewitt, and T. A. Lewis, J. Nucl. Mater. 276 (1996) 47-56.

[17] M. W. Finnis, MOLDY6-A Molecular Dynamics Program for Simulation of Pure Metals, AERE R-13182, UKAEA Harwell Laboratory, Harwell, UK, 1988.

[18] M. W. Finnis and J. E. Sinclair, Phil. Mag. A 50 (1984) 45-55, and Erratum, Phil. Mag. A 53 (1986) 161.

DISLOCATION INTERACTIONS WITH VOIDS AND HELIUM BUBBLES IN FCC METALS—J. A. Young (Lawrence Livermore National Laboratory), B. D. Wirth (Department of Nuclear Engineering, University of California Berkeley), J. Robach, and I. M. Robertson (University of Illinois, Urbana-Champaign)

EXTENDED ABSTRACT

The formation of a high number density of helium bubbles in FCC metals irradiated within the fusion energy environment is well established. Yet, the role of helium bubbles in radiation hardening and mechanical property degradation of these steals remains an outstanding issue. In this paper, we present the results of a combined molecular dynamics simulation and in-situ straining transmission electron microscopy study, which investigates the interaction mechanisms between glissile dislocations and nanometer helium bubbles. The molecular dynamics simulations, which directly account for dislocation core effects through semi-empirical interatomic potentials, provide fundamental insight into the effect of helium bubble size and internal gas pressure on dislocation interaction and bypass mechanisms.

The results demonstrate the use of the latest simulation and experimental techniques to probe the underlying mechanisms governing the mechanical properties of irradiated metals. Reasonable agreement between experiments and simulations are found for the critical shear stress of under pressurized He bubbles in FCC metals. The internal pressure of the bubbles influences the critical shear stress as well as the dislocation interaction and bypass mechanism. Low (under-pressurized) pressure He bubbles are bypassed by dislocation annihilation and re-nucleation, as is the case for bare voids, resulting in a shear step of **b** in the bubble. Dislocation interaction with high pressure bubbles, which are greater than the equilibrium He pressure, depends strongly on the defect structure at the bubble matrix interface. Future work will further examine the effect of internal gas pressure, as well as the effect of dislocation morphology and the geometry of the dislocation/obstacle interactions.

Reference

J. A. Young, B. D. Wirth, J. Robach, and I. M. Robertson, submitted for publication, ICFRM-11 proceedings, to be published in Journal of Nuclear Materials.

THE EFFECTS OF GRAIN BOUNDARY STRUCTURE ON BINDING OF He IN Fe—R. J Kurtz and H. L. Heinisch, Jr. (Pacific Northwest National Laboratory)*

Extended abstract of a paper submitted to the Journal of Nuclear Materials as part of the proceedings of the 11th International Conference on Fusion Reactor Materials, Kyoto, Japan, December 7-12, 2003.

EXTENDED ABSTRACT

Atomistic computer simulations were used to explore the effect of grain boundary (GB) structure on the binding energy of He in Fe. Symmetrical tilt GBs spanning a range of GB energies and excess volumes were examined. While symmetrical tilt GBs represent only a small fraction of the GB character distribution in actual materials, the present results span a wide range of GB properties, and therefore are likely relevant to more complex GB structures.

Most of the details pertaining to the methodology used in the calculations of the atomic arrangements of GBs have been described in detail elsewhere [1, 2]. The model consists of a two part computational cell, rectangular in shape. One part, Region I, contains movable atoms embedded in a semi-rigid part, Region II. The GB approximately bisects the model as shown in Figure 1. Equilibrium, ~0 K, structures are obtained via relaxation using molecular dynamics with an energy quench. The two grains are free to move and undergo homogenous displacement in all three directions and this movement occurs during the relaxation via a viscous drag algorithm. Periodic border conditions are employed in the *x* and *z* directions. Four symmetric tilt GBs were studied in this work, all a common <101> tilt axis. The four GBs were $\Sigma 3$ {112} $\Theta = 70.53°$, $\Sigma 11$ {323} $\Theta = 50.48°$, $\Sigma 9$ {114} $\Theta = 38.94°$, and $\Sigma 3$ {111} $\Theta = 70.53°$. The interatomic potential used in this research has been described in detail previously [3].

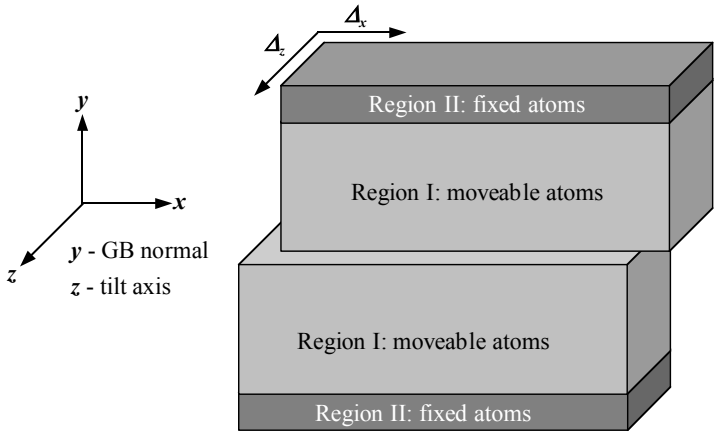

Figure 1. Model geometry used in GB simulations. Models are periodic in the *x* and *z* directions. Δ_x and Δ_z are translation vectors parallel to the grain boundary plane.

An energy distribution function was generated for each boundary by dividing the GB into a large number of slices and computing the excess potential energy E_{xs}/A for each slice, which is

$$\frac{E_{xs}}{A} = \frac{\Sigma\left(E_{gb} - E_p\right)}{L_z w} \qquad (1)$$

where E_{gb} is the potential energy of an atom in the GB model, E_p is the potential energy of an atom in a perfect crystal, L_z is the thickness of the model parallel to the tilt axis and w is the slice width. The

*Pacific Northwest National Laboratory (PNNL) is operated for the U.S. Department of Energy by Battelle Memorial Institute under contract DE-AC06-76RLO-1830.

summation is performed over all atoms in a slice. The GB energy per unit area, γ_{gb}, can be determined by integrating the energy distribution function over several repeat periods. Table 1 lists γ_{gb} for the four boundaries examined here. The GB energies are generally quite large relative to free surface energies. For the Fe potential employed here the free surface energies γ_{100}, γ_{110} and γ_{111} are 1.81, 1.58 and 2.00 J/m^2, respectively. It should be noted that the calculated free surface energies are slightly low relative to experimentally measured values for Fe, which are typically in the neighborhood of 1.6 – 2.3 J/m^2.

Table 1. Grain boundary energy and excess volume for the four symmetric tilt boundaries considered in this study. The tilt axis is <101>.

Σ	GB Plane	γ_{gb}, J/m^2	V_{gb}/A, nm
3	{112}	0.30	0.007
11	{323}	1.00	0.022
9	{114}	1.40	0.036
3	{111}	1.51	0.041

Another important property is the volume expansion normal to the GB plane. This quantity is determined by calculating the excess volume per unit area of GB. Excess atomic volumes were determined from the relation

$$\Omega_{xs} = \Omega_v - \Omega_p \qquad (2)$$

where Ω_v is the Voronoi volume of an atom in the GB model and Ω_p is the atomic volume of an Fe atom in a perfect, unstrained lattice. The Voronoi volume is the volume of a polyhedron whose faces are perpendicular bisectors of the lines connecting an atom to its nearest neighbors. The atomic volume for Fe in this study is 0.01178 nm^3. The excess volume, V_{gb}, in a rectangular patch of GB of area, A, is computed from

$$\frac{V_{gb}}{A} = \frac{\sum \Omega_{xs}}{L_x L_z} \qquad (3)$$

where L_x is the length of the GB perpendicular to the tilt axis. In order to properly compute V_{gb}/A a sufficiently large volume of material must be chosen to account for excess volume variation in the GB plane and normal to it. In this work we computed values of Ω_{xs} for atom planes parallel to the GB until it was essentially zero. Furthermore, values of L_x and L_z were selected to include several repeat periods in those directions so that an accurate estimate of the GB excess volume could be obtained. Table 1 gives V_{gb}/A for the GBs investigated in this study. Note there is good correlation between the GB energy and excess volume.

Binding of He to GBs was explored by insertion of a single He atom in either a substitutional or interstitial location, and then relaxing the simulation block. Both atomic displacements of Region I atoms and rigid-body translations of the two grains were allowed during the relaxation. Since the excess volume varies significantly in the GB core a large number of different starting positions for the He atom were examined. Binding energies at a particular site α (either substitutional or interstitial) in and near the GB core were determined from the equation

$$E_B^\alpha = E_{gb}^\alpha - E_{gb} - E_f^\alpha \qquad (4)$$

where E_{gb}^α is the energy of the GB with a He atom at site α, E_{gb} is the energy of the GB without a He atom, and E_f^α is the formation energy of a He atom at site α in bulk Fe. In Figure 2 the substitutional or interstitial He binding energy is plotted as a function of distance from the Σ3 {111} GB. Also shown in Figure 2 is the distance dependence of the excess volume normal to the GB plane. Three observations may be made from this plot. First, the binding energy of substitutional He is considerably smaller than interstitial He, indicating that interstitial He will be strongly trapped by vacancies in the GB. Relative to the bulk, interstitial He is very strongly bound to the GB, a result similar to the findings of Baskes and Vitek in Ni [4]. Second, the binding energy for both substitutional and interstitial He atoms approaches zero at a

distance of about 0.7 nm from the GB. Similar results were obtained for the other GBs investigated in this study. This "capture radius" depended on GB properties. The Σ3 {112} GB, with the lowest GB energy and V_{gb}/A, gave a capture radius of only ~0.3 nm. Third, the He binding energy is highly non-uniform in the GB core. There appears to be a rough correspondence between the distance dependence of the He binding energies and the excess volume, but this is certainly not unequivocal. As shown in the plot in Figure 3, there is an excellent correlation between the maximum binding energy for both substitutional and interstitial He and the GB excess volume.

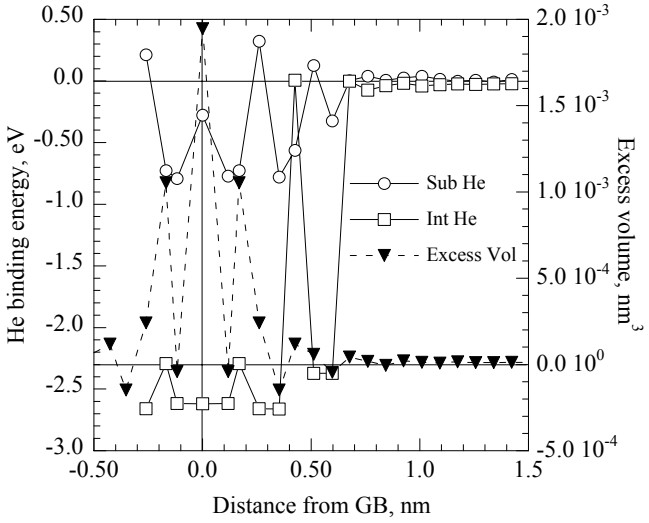

Figure 2. Dependence of excess volume and He binding energy on distance from the GB plane.

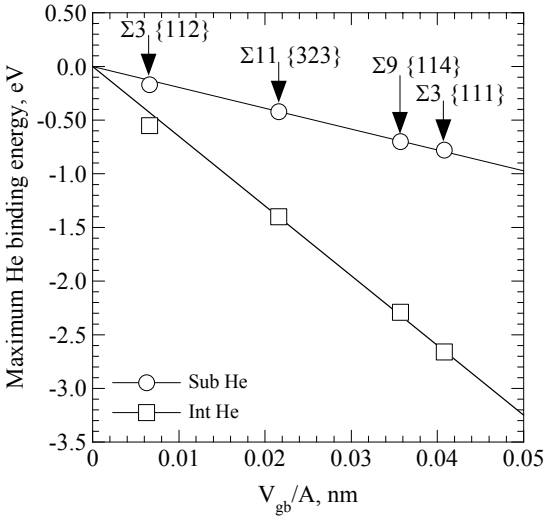

Figure 3. Dependence of the maximum He binding energy on GB excess volume.

Conclusions

The results show that both substitutional and interstitial He atoms are bound to all of the GBs studied. Interstitial He is more strongly bound (E^i_{gb} ~0.5 to 2.7 eV) to the GB core than substitutional He (E^s_{gb} ~0.2 to 0.8 eV). The maximum binding energy of He was found to increase linearly with GB excess volume. The capture radius for a He atom varied from ~0.3 to 0.7 nm and also depended on GB

properties. Lastly, the He binding energy varied significantly within the GB core and approximately corresponded to the variation in atomic excess volume normal to the GB plane. Further work is needed to investigate the effect of multiple He atoms and vacancies on binding to GBs. In addition, migration of He along the GB is an important transport mechanism that will be the subject of a future atomistic study.

References

[1] R. J Kurtz, R. G. Hoagland, J. P. Hirth, Phil. Mag. A79 (1999) 665.
[2] R. J Kurtz, R. G. Hoagland, J. P. Hirth, Phil. Mag. A79 (1999) 683.
[3] K. Morishita, R. Sugano, B. D. Wirth, T. Diaz de la Rubia, Nucl. Inst. and Methods in Phys. Res. B 202 (2003) 76.
[4] M.I. Baskes, V. Vitek, Met. Trans. A 16A (1985) 1625.

DISLOCATION-STACKING FAULT TETRAHEDRON INTERACTION: WHAT WE CAN LEARN FROM ATOMIC SCALE MODELING—Yu. N. Osetsky, R. E. Stoller, and Y. Matsukawa (Oak Ridge National Laboratory)*

OBJECTIVE

The objective of this study is to understand atomic-scale details of interaction of a moving dislocation with Stacking Fault Tetrahedra (SFTs) in irradiated and aged fcc metals.

SUMMARY

Stacking fault tetrahedra (SFTs) are formed under irradiation of fcc metals and alloys with low stacking fault energy. The high number density of SFTs observed suggests that they should contribute to radiation-induced hardening, and, therefore, taken into account when estimating mechanical properties changes of irradiated materials. The central issue is describing the individual interaction between a moving dislocation and an SFT, which is characterized by a very fine size scale on the order of a few to one-hundred nanometers. This scale is amenable to both in-situ TEM experiments and large-scale atomic modeling. In this paper we present results of an atomistic simulation of dislocation-SFT interactions using molecular dynamics (MD). The MD simulations modeled an edge dislocation interacting with SFTs with different sizes and at different temperatures and strain rates. The results are compared with observations from in-situ deformation experiments in which several interactions between moving dislocations and SFTs were observed. It is demonstrated that in some cases the simulations and experimental observations are quite similar, suggesting a reasonable interpretation of experimental observations. Other cases, when modelling does not reproduce experimental observations, are also discussed and the importance of strain rate, dislocation nature and specimen surface effect are indicated.

Introduction

Stacking fault tetrahedra (SFTs) are common defects induced by different treatments, such as irradiation, ageing after quenching and deformation, in metals with a low level of stacking fault energy (SFE) [1-3]. In many cases these defects are mainly responsible for strengthening, hardening and plastic instability during deformation. Interactions between dislocations moving through the population of the existing SFTs is in the basis of these effects and therefore it is important to understand their mechanisms. Three different approaches, namely experiment, continuum theory and atomistic modeling, are currently used to study the details of dislocation – SFTs interactions. The experimental techniques employ in-situ experiments in which the specimen subjected to transmission electron microscopy (TEM) is deformed simultaneously. Provided the resolution is high enough, many important details of the interaction can be revealed in such experiments [4,5]. The disadvantage of the experimental methods is low spatial and time resolution, of about few tens of nm and one image per 1/30 sec. This limits observation of only large defects and very low rate of deformation. The continuum theory approach can be used to investigate dislocation-dislocation type reactions which can be applied to SFTs that are large enough to be described as a set of stair rod dislocations [6]. This approach can be applied to large SFT, with an accuracy limited to the details of the dislocation-dislocation interaction considered at continuum level. Temperature and strain rate effects cannot be studied with this approach. And finally, atomic scale modelling can be formally used to investigate all aspects of dislocation-SFT interactions [7,8,9]. The main limitation of atomic-scale simulation is the total time of the interaction because it is limited by a few nanoseconds. Nevertheless, modern atomic-scale models can be used to obtain valuable information on dislocation-SFT interactions, which in some cases can be compared directly with in-situ experiments. In the present paper we report first results of an extended programme of atomic-scale modelling of dislocation dynamics in the environment of high density of small, less then ~6nm, SFTs which are formed under irradiation by energetic particles. This study is part of a multi-scale materials modeling program aimed understanding the effects of irradiation on the mechanical properties of fusion materials.

---

*Paper submitted to the Journal of Nuclear Materials.

Model

Interactions between a moving edge dislocation and SFT have been studied using the atomistic model developed in ref. [10]. The model was applied for two, qualitatively different, conditions namely statics, e.g., zero temperature, and dynamics, e.g., finite temperature and strain rate. The first approach allows investigation of the equilibrium state of a system containing a dislocation and an obstacle at a certain strain. Only this type of atomic-scale modeling can be compared directly with the continuum dislocation dynamics, and this can be used for parameterization of dislocation-obstacle interaction mechanisms. The second approach allows investigation of temperature and strain rate effects, which are far beyond the continuum theory. The main advantage of the model developed in ref. [10] is that stress-strain dependences, and therefore the critical resolved shear stress (CRSS), can be obtained under different conditions. In the present work we have simulated fcc crystal of size 46.0 x 35.5 x 25.7 nm along the $[1\bar{1}0]$, $[11\bar{2}]$ and $[111]$ axes respectively and containing about 3,5 million mobile atoms interacting via a many-body potential parameterized for copper in [11].

The edge dislocation with initial Burgers vector of $\frac{1}{2}[1\bar{1}0]$ and a (111) glide plane was first introduced, then relaxed. During relaxation the dislocation dissociated into two Shockley partials separated with a stacking fault of about 3nm of width. Staking fault tetrahedra of size from 2.5nm to 4.1nm where then created in the vicinity of the dislocation so that the dislocation glide plane intersects the SFT at different levels. In static modeling at T=0K, strain was incrementally increased by 10-4 per step with the following relaxation of the system to the minimum of potential energy. In dynamic modelling at T>0K strain rate in the range (2-10)x106s-1 was applied. For the crystals simulated such strain rate results in dislocation velocity from ~3 to ~40 m/s. More details on model crystal loading can be found in ref. [10]. Stress-strain dependences, the dislocation and the SFT configurations were analyzed and visualized during both types of modeling.

Due to space limitations we present here only the results obtained for the case of 4.1nm SFT containing 136 vacancies. This SFT was cut by a moving dislocation at different levels schematically presented in Fig. 1 where h is the distance between the dislocation glide plane and the SFT base. Note that the height of the tetrahedron is equal to ~3.34nm.

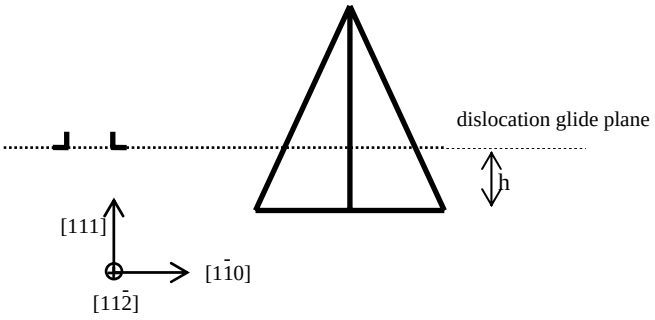

Fig. 1. Schematic view of dislocation-SFT interaction geometry.

Results

An example of stress-strain curves obtained for the case h=0.96nm at different temperatures is presented in Fig. 2. One can see that the critical resolved shear stress, which is the maximum stress level in each curve, depends strongly on temperature. It drops from ~253MPa at T=0 to 148MPa at T=10K and to ~75MPa at T=300K. Note that a significant drop occurs at very low temperatures implying that even very small atomic vibrations significantly assist the dislocation in penetrating through the SFT.

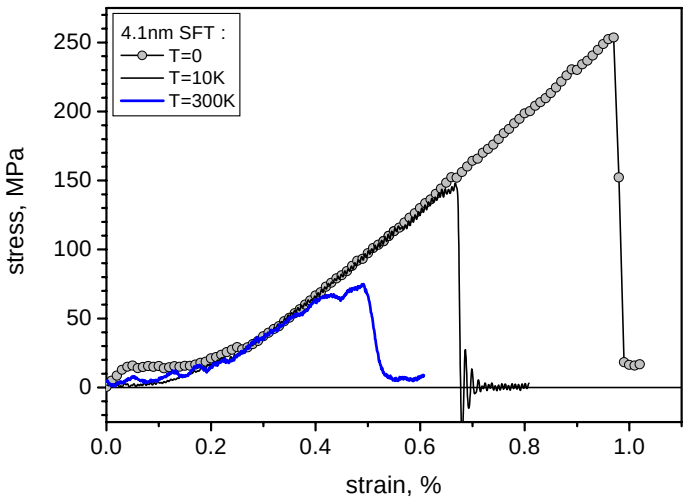

Fig. 2. Applied stress as function of strain in crystal at T=0, 10 and 300K containing a dislocation gliding through a row of 4.1nm (136 vacancies) SFT at h=0.96nm

The stress-strain behavior depends also upon h as shown in Fig. 3 for T=10K where h starts at -0.48nm (just below the SFT base) for curve 1 and ends at h=2.40nm for curve 7. The maximum CRSS, 182MPa, was observed for the case h=0, e.g., when the dislocation glide plane coincides with the SFT stacking fault. It is interesting to note that the CRSS is rather low for the first case on Fig. 3, when the dislocation glide plane is just below the SFT's stacking fault. The dependence of the CRSS versus h is presented in Fig. 4. The overall conclusion is that the CRSS increases as the dislocation glide plane approaches the SFT base inside the SFT volume. At this position dislocation is more strongly pinned and the critical leaving angle decreases. The example of the dislocation configuration at critical stress, σ=148MPa, for the case h=0.96 at 10K is presented in Fig. 5. The grey circles indicate atoms with high potential energy and a low coordination number, therefore belonging to the dislocation core. The shape of the dislocation (circles) and stacking fault area (small crosses) are readily seen, and it is clear that estimationg the critical angle is rather difficult due to dissociation of the dislocation.

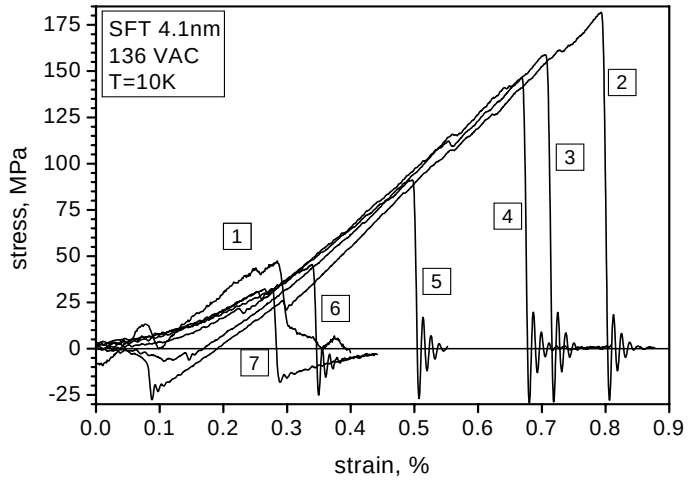

Fig. 3. Applied stress as function of strain in crystal at T=10K containing a dislocation gliding through a row of 4.1nm SFT at different h: 1 – h = -0.48nm, 2 – h=0, 3 – h = 0.48nm, 4 – h = 0.96nm, 5 – h = -1.44nm, 6 – h = 1.92nm and 7 – h = 2.4nm.

The position of the dislocation as it hits the SFT defines also the structural change of the SFT. In other words, the mechanism of the dislocation-SFT interaction depends on the geometry of the interaction. Thus, if the dislocation hits the SFT close enough to its vertex, the SFT may not be damaged – the upper part of the SFT is shifted when the leading partial dislocation pulls away but after the trailing partial dislocations leaves the SFT it recovers its perfect configuration by a collective shift of the corresponding atoms above the glide plane. Note that such a recovery of the SFT was observed when distance between the glide plane and the vertex is $\leq$ 1.5nm. If it is larger the SFT can be damaged in different ways depending on h. Some configurations of SFTs after interaction with the dislocation are presented in Fig. 6. In these figures the size of the cube box is 13a (a=0.3615nm is Cu lattice parameter) and the grid size is 1a. In general the damage to an SFT includes formation of two ledges of opposite sign on two faces. An I-type ledge is created on the face where the leading partial dislocation entered the SFT and a V-type ledge is created

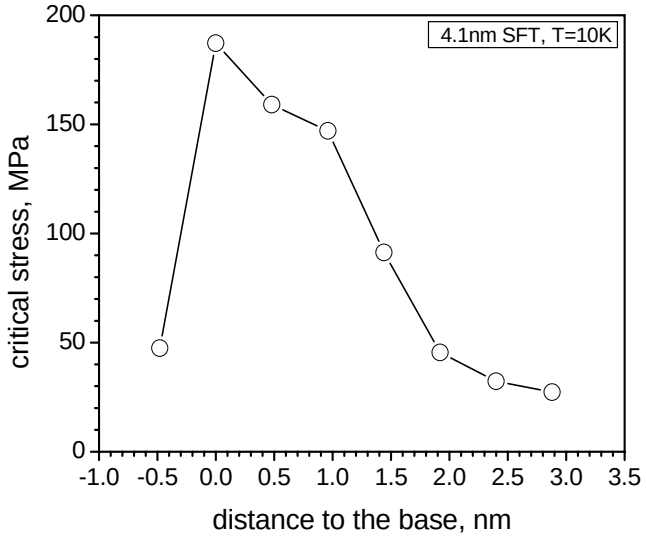

Fig. 4. Dependence of the value of critical resolved shear stress against distance between the dislocation glide plane and the base of a 4.1nm SFT simulated at T=10K.

on the face where the trailing partial dislocation left it. The detailed configuration of ledges depends on h as it can be seen in Fig. 6b-c.on h as it can be seen in Fig. 6b and c. The case h=0, when the whole upper part of the SFT was shifted relatively the stacking fault of the lower base, can be interpreted as a creation of the minimum size ledges (see Fig. 6d).

Experimentally observed formation of channels cleared from radiation-induced

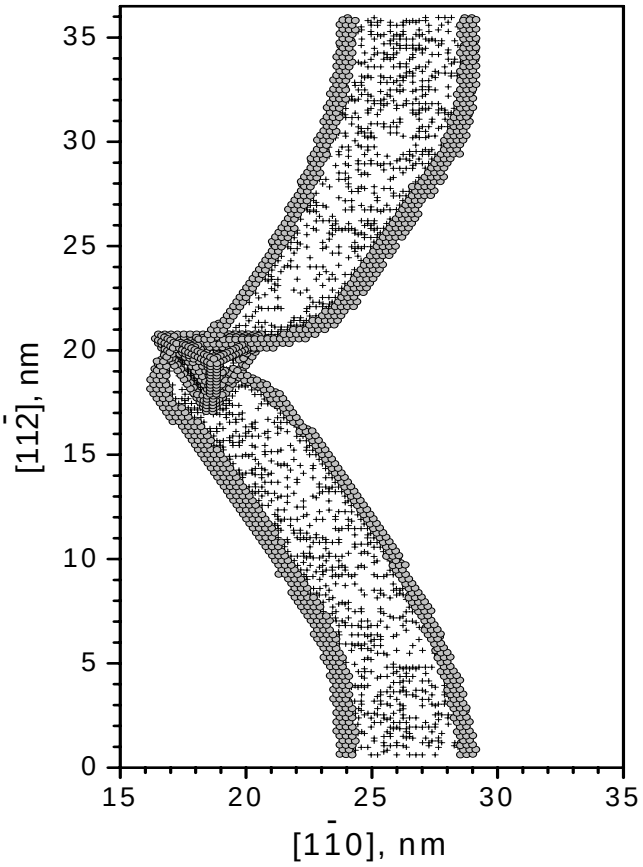

Fig. 5. Dislocation line in the (111) slip plane at the critical stress for 4.1nm SFT cut at h=0.96nm at T=10K. Gray circles are atoms with high energy and low coordination number, little crosses are atoms which are definitely in HCP environment.

defects is characterised by many dislocations formed from the same source gliding in the same and close slip planes [12]. That means the same obstacle, i.e. SFT, can be cut many time by dislocations in the same and/or close slip planes. We have investigated such cases and found that the result again depends on h. For large h, e.g., when slip plane is close to the vertex, SFT cannot be damaged and it restores perfect configuration after every dislocation passes through. In the case of small h, when ledges can be formed, the SFT can be broken into pieces separated proportionally of the number of dislocations passed. An example of configuration of a 2.5nm SFT, containing 45 vacancies, after multiply dislocation cut is presented in Fig. 7.

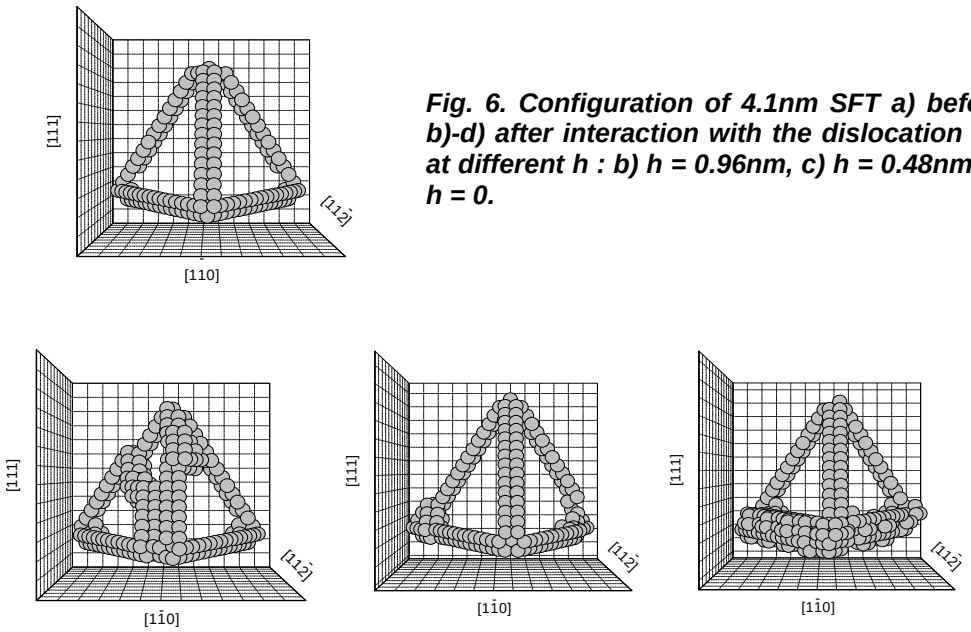

Fig. 6. Configuration of 4.1nm SFT a) before and b)-d) after interaction with the dislocation gliding at different h : b) h = 0.96nm, c) h = 0.48nm and c) h = 0.

The first dislocation, Fig. 7-1 (the number of the configuration in Fig. 7 indicates how many dislocations passed through), created a pair of ledges described above whereas next dislocations shift the upper part of the SFT towards the Burgers vector direction. In the case described the dislocations move from the right to the left. The forth dislocation separates completely a small perfect SFT containing 21 vacancies and a 24 vacancies cluster with two parallel stacking faults, one of which is the former SFT base and the other one is created due to interaction. We did not identify the structure of the lower cluster but it is definitely that of low binding energy and, therefore, should be either dissociated or transformed, e.g., to Frank loop, depending on time and temperature. It is interesting to note that the upper part of the SFT is undamaged and this is consistent with experimental TEM observations during in-situ deformation of quenched and annealed gold [5].

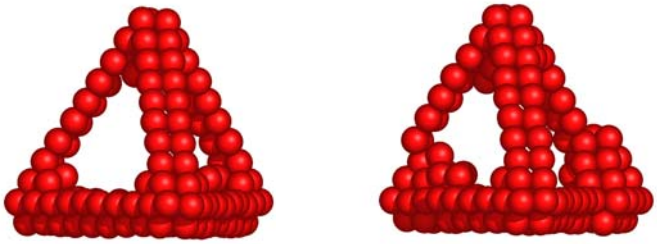

Fig. 7. Configuration of 2.5nm (45 vacancies) SFT 0) before and 1)-4) after interactions with the dislocation gliding through its centre. The number near each configuration indicates how many time the dislocation passed through.

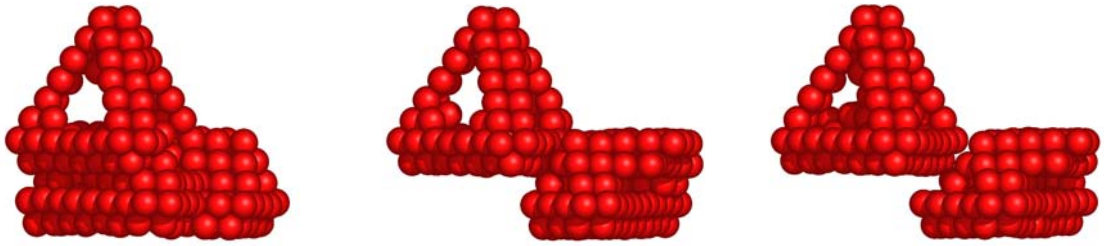

Conclusions and Future Work

Interaction between a moving edge dislocation and stacking fault tetrahedra of size from 2.5 to 4.1 nm has been studied at atomic scale by molecular dynamics and statics techniques. It was found that the critical resolved shear stress depends strongly upon the geometry of the interaction and the crystal temperature. In general, CRSS decreases at higher temperature and larger distance, h, between the dislocation glide plane and the SFT base parallel to it. Depending on h, the SFT can be damaged, or not. The damage includes creation of two ledges of opposite signs on the SFT's faces cut by the moving dislocation. Creation of ledges decreases the SFTs stability and can serve as an initiation of their dissolution. The latter is observed commonly in in-situ deformation TEM experiments [4,5]. However, more detailed study is necessary for a full understanding of the atomic-scale mechanisms involved. Note, that in general the damage of SFTs depends on its size and structure. Thus a significant damage of 2nm SFT by an edge dislocation was reported in [8] and a complete absorption of overlapping non-perfect SFTs, formed in high-energy displacement cascade modeled in Cu, was observed in [13]. At least two other feature of SFT-dislocation interaction 1) TEM contrast of the SFT changes when dislocation approaches and it is restored when dislocation passes through and 2) when the lower (relatively to the slip plane in Fig. 1) part of an SFT disappears due to interaction whereas the upper one remains undamaged, were experimentally observed in gold [5] and are consistent with MD studies reported here.

We admit that the SFTs studied here are more related to irradiation conditions, when the maximum of size distribution function is related to about 2.5nm, than to in-situ experiments, when the size of observed SFTs is of the order 25-50nm. Such a considerable difference in size can lead to a difference in the mechanism of dislocation-DFT interaction. Nevertheless, we conclude that some mechanisms described here are consistent with the available in-situ observations. More atomic-scale studies are necessary to clarify effects involved in plastic instability and creation of cleared channels in irradiation and non-irradiation conditions. Particularly, those for a) screw dislocations, b) SFTs of larger size, when dislocation-SFT reaction may become closer to a dislocation-(stair rod) dislocation reaction, c) lower strain rates, when the time of the interaction became long enough to involve diffusion mechanisms and d) thin film conditions (as in in-situ TEM experiments where the specimen thickness is about 100nm), when the slow moving dislocation may serve as a channel for defect (vacancy) transport to close strong sinks, e.g., surface.

References

[1] B. N. Singh and S. J. Zinkle, J. Nucl. Mater. 206 (1993) 287.
[2] J. Silcox and P. B. Hirsch, Philos. Mag. 4 (1959) 72.
[3] M. Kiritani, Mat. Sci. Eng. A 350 (2003) 1.
[4] J. S. Robach, I. M. Robertson, B. D. Wirth, and A. Arsenlis, Philos. Mag. 83 (2003) 955.
[5] Y. Matsukawa and S. J. Zinkle, these proceedings.
[6] M. Hiratani, H. M. Zbib, and B. D. Wirth, Philos. Mag. A82 (2002) 2709.
[7] B. D. Wirth, V. V. Bulatov, and T. Diaz de la Rubia, J. Eng. Mater. Tech. 124 (2002) 329.
[8] Yu. N. Osetsky, D. J. Bacon, B. N. Singh, and B. Wirth, J. Nucl. Mater. 307-311 (2002) 852.
[9] Yu. N. Osetsky and D. J. Bacon, In: Mesoscopic Dynamics in Fracture Process and Strength of Materials, IUTAM Symposium Proceedings, July 2003, Osaka, Kluwer Academic (2003) in press.
[10] Yu. N. Osetsky and D. J. Bacon, Modelling Simul. Mat. Sci. Eng. 11 (2002) 427.
[11] G. J. Ackland, G. Tichy, V. Vitek, and M. W. Finnis, Philos. Mag. A 56 (1987) 735.
[12] M. Victoria, N. Baluc, C. Bailat, Y. Dai, M. I. Luppo, R. Schaublin, and B. N. Singh, J. Nucl. Mater. 276 (2000) 114.
[13] B. D. Wirth, V. V. Bulatov, and T. Diaz de la Rubia, J. Eng. Mater. Tech. 124 (2002) 329.

KINETIC MONTE CARLO SIMULATIONS OF DISLOCATION DECORATION AND RAFT FORMATION IN BCC-IRON UNDER CASCADE IRRADIATION— M. Wen, N. M. Ghoniem (Department of Mechanical and Aerospace Engineering, University of California, Los Angeles), and B. N. Singh (Risø National Laboratory, Denmark)

OBJECTIVE

Radiation-induced microstructural and compositional changes in metals are governed by the interaction between point and clustered defects and the internal microstructure. The objective of this computational study is to investigate the inhomogeneity and segregation of point defects, damage accumulation by diffusion and interaction, and the resulting dislocation decoration and formation of rafts of interstitial clusters. A new Kinetic Monte Carlo (KMC) computer code has been developed, with explicit representation of the influence of elastic interaction between microstructure features. Results of computer simulations are utilized to discuss the general conditions for experimentally observed dislocation decoration and formation of rafts.

SUMMARY

Under neutron irradiation, primary defect clusters of both self-interstitial atom (SIA) and vacancy type are directly produced in displacement cascades, which have been confirmed by experiments as well as molecular dynamics simulations. The highly mobile SIA clusters play a crucial role in the development of characteristic microstructures, such as rafts of SIA clusters and dislocation decoration, and the corresponding radiation hardening behavior [1]. We have developed a new approach to KMC simulations to investigate the segregation and accumulation of point defects at the atomic scale with incorporating the elastic interaction between defect clusters and microstructures by using the elastic representation of point defects due to Kröner [2]. The decoration of dislocations by SIA clusters and the formation of rafts in bcc-iron are modeled in detail, and the general conditions for the occurrence and development of both features have are discussed. We also present results of SIA cluster density as a function of irradiation dose, using cluster size distributions, cascade frequency, and individual cluster dynamic parameters obtained from molecular dynamics simulations. Good agreement is found between the results of our present KMC simulations and experimental observations. The one-dimensional motion of glissile SIA clusters and the interaction between defects and microstructures are shown to be the main cause for appearance and development of characteristic microstructures. It is demonstrated that KMC computer simulation is a valuable tool in studying defect kinetics and microstructure evolution, taking into account many different microscopic mechanisms and covering very different time and length scales.

PROGRESS AND STATUS

Introduction

Under neutron irradiation, primary defect clusters, which are directly produced in displacement cascades, play an important role in microstructural evolution and property changes in irradiated materials. Small interstitial loops can further re-organize to make up patches (or rafts) at elevated temperatures [3], and dislocations are often observed being heavily decorated by SIA clusters in the form of small interstitial loops [1]. Rafts of SIA loops and decoration of dislocations with loops have become a crucial issue for understanding radiation hardening under cascade damage conditions. It has been experimentally observed that in the deformation process of metals and alloys under cascade damage conditions, an increase in the upper yield stress without dislocation generation occurs, and is followed by an immediate yield drop and plastic instability. A ‘cascade induced source hardening’ (CISH) model has been proposed by Singh et al. [1] and applied to explain the experimental observation of yield drop. Huang and Ghoniem [4] investigated the interaction dynamics between sessile SIA clusters and dislocations in terms of elastic interactions with various SIA cluster densities, the spatial and size distributions of clusters, and the

orientation distribution of individual Burgers vectors by using the method of parametric dislocation dynamics (PDD) simulations.

In the study of radiation damage MD simulations using semi-empirical embedded-atom method (EAM) interatomic potentials have played a very important role in understanding the details of defect production in displacement cascades, and in understanding the dynamics of point defect and defect cluster diffusion. Radiation damage, however, includes a vast range of irradiation effects, such as production and diffusion of point defects, and their interaction with microstructures, which take place over time and length scales that span many orders of magnitude. MD techniques are inapplicable to deal with microstructure evolution in irradiated materials due to their limitation of time and length scales. Kinetic Monte Carlo (KMC) simulations, on the other hand, provide another option to perform atomic-level modeling of defect kinetics and microstructure evolution over relevant length and time scales. KMC has been used to investigate the local short-term intra-cascade annealing of individual cascades [5], as well as low dose defect accumulation [6]. In the present work, KMC techniques are used to study key aspects of microstructure evolution under irradiation: the inhomogeneity and segregation of point defects, and damage accumulation by diffusion and interaction, and the resulting dislocation decoration and formation of rafts of interstitial clusters.

Model

The basic ideas behind KMC simulations have been comprehensively described in the literature, e.g. [7, 8]. In our work, microstructure evolution of the cascade-induced defect clusters is accomplished by a KMC procedure in which one reaction is executed at one site during each time step. The jump frequency for a possible jump of a defect cluster, i, to take place is given by: $r_i = \omega_0 \exp(-E_i / k_B T)$, where ω_0 is the pre-exponential factor of the defect cluster, k_B the Boltzmann constant, E_i the 'effective' activation energy for jumps of the cluster, and T is the absolute temperature. The probability of selecting an event is simply equal to the rate at which the event occurs relative to the sum of all possible event rates. At each KMC step, one event denoted by m is randomly selected from all possible M events, as follows:

$$\frac{\sum_{i=0}^{m-1} r_i}{\sum_{i=0}^{M} r_i} < \xi_1 < \frac{\sum_{i=0}^{m} r_i}{\sum_{i=0}^{M} r_i} \tag{1}$$

where r_i is the rate at which event i occurs ($r_0 = 0$) and ξ_1 is a random number uniformly distributed in the range [0, 1]. Once an event is chosen, the system is changed correspondingly, and the list of events that can occur at the next KMC step is updated.

The reciprocal of an atomic jump probability per unit time is the residence time for a defect cluster that moves by that specific type of jump. Since the jump probabilities of all the different types of jumps are independent, the overall probability per unit time for the system to change its state by any type of jump step is just the sum of all the possible specific jump type probabilities, and so the residence time that would have elapsed for the system in a specific configuration is the reciprocal of this overall jump probability: $\Delta t = 1 / \sum_{i=0}^{M} r_i$. For random uncorrelated processes, this is a Poisson distribution. If ξ_2 is a random number from 0 to 1, the elapsed time for a particular transition is given by: $\Delta t = -\ln \xi_2 / \sum_{i=0}^{M} r_i$.

The system is then advanced to the final state of the chosen transition and the process is repeated. The expression for Δt is rigorous, and a derivation is also provided by [8]. In our KMC simulations, the elastic interaction is incorporated. The influence of other defects and the external stress on one SIA or vacancy cluster is given by the stress field σ_{ij}. By applying the infinitesimal dislocation loop approximation for SIA clusters, the work necessary to form the loop characterized by normal $\mathbf{n}$, Burgers vector $\mathbf{b}$ and area δA in

the stress field σ_{ij} is SIA cluster interaction energy E_{int}, and is given by: $E_{\text{int}} = \int_V \sigma_{ij}^{(1)} \varepsilon_{ij}^{(2)} dV$, in which $\sigma_{ij}^{(1)}$ is the stress arising from the first dislocation and $\varepsilon_{ij}^{(2)}$ the strain originating in the other. For the present study, the second loop (defect cluster) is assumed to be infinitesimal, the interaction energy can be simplified to [9]: $E_{\text{int}} = \delta A^{(2)} n_i^{(2)} \sigma_{ij}^{(1)} b_j^{(2)}$, where $n_i^{(2)}$ is the unit normal vector to the defect cluster habit plane of area $\delta A^{(2)}$. The total cluster activation energy is then given by: $\widetilde{E}_m = E_m + \Delta E_{\text{int}}$, where E_m is the activation energy in a perfect crystal structure and can be obtained by either experiments or MD simulations, and ΔE_{int} the difference in the interaction energy of an defect cluster placed at two neighboring equivalent position in the crystal. The numerical method developed by Ghoniem [10], and Ghoniem and Sun [11] was employed in our simulation to evaluate the interaction between small defect clusters and slip dislocation loops. A computation cell of 100 × 100 × 100 nm^3 is taken with periodic boundary conditions. For the purpose of studying dislocation-cluster interaction, a slip dislocation loop lying on the [1 0 1] plane, with Burgers vector **b** = [-1 1 1] / 2 is introduced into the simulation box.

Results

Dose dependence of defect density

Doses up to 5.21 × 10^{-3} dpa were simulated at a damage rate of 5 × 10^{-8} dpa/s, and damage accumulation was observed as a function of dose. Fig. 1 shows the SIA cluster density as a function of dose up to 5.21 × 10^{-3} dpa with considering recombination, as well as of dose up to 1.48 × 10^{-3} dpa without recombination centers. In addition, SIA clusters containing more than 100 interstitial atoms (diameter > 3 nm) are counted as visible clusters, and the corresponding cluster density is calculated and compared with the experimental results for bcc Fe irradiated at ~70°C in the HFIR rector at Oak Ridge National Laboratory to displacement dose levels in the range of 10^{-4} to 0.72 dpa [12].

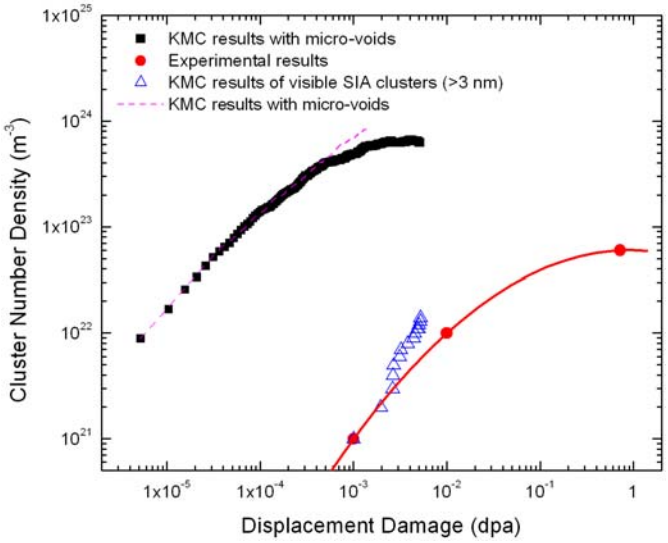

Fig. 1. SIA cluster densities as a function of accumulated dose for bcc iron irradiated at 300 K under cascade irradiation at 5 × 10^{-8} dpa/s. Simulation results are compared to experimental data from TEM observation of iron irradiated in HFIR [12].

At the initial stages of irradiation (dpa < 10^{-4} dpa), the cluster density increases almost linearly with damage dose. The increase in cluster density is then slowed down, when the dose level is higher than 10^{-4} dpa and lower than about 3 × 10^{-3} dpa. Cluster density approaches a saturated value and does not change much beyond a dose level of 3.5 × 10^{-3} dpa. At very low dose, cluster densities of both interstitials and vacancies are rather low, and the chance that one interstitial cluster could get close

enough to another interstitial or vacancy cluster so that they can feel each other in terms of elastic interaction is rather small. Because of the 1D motion of SIA clusters, the recombination cross-section with vacancy clusters produced as well as the agglomeration cross section with other interstitial clusters are small. Theoretically, there are only two mechanisms by which a SIA cluster could change its diffusion direction: either by thermal activation or by the interaction with other defects or microstructures. The effect of thermal activation can be rule out here because our simulation is carried out at constant room temperature. At low damage dose level, the big distance between clusters makes the interaction between them weak. This hardly affects the migration of SIA clusters, resulting in a linear increase of cluster density with dose.

When the damage builds up to a certain level, say 10^{-4} dpa in our simulations, the simulation box becomes crowded. Newly introduced interstitial clusters as well as existing mobile clusters have higher probability of encountering one another and interacting with each other. The events of recombination and agglomeration would occur more frequently than at the early stage of irradiation. Consequently, these reactions slow down the increase in the number of SIA clusters within the simulation box. Once the damage accumulates to some extent, 3.5×10^{-3} dpa in our simulation, the number of interstitial clusters that annihilate or form larger clusters reaches dynamic equilibrium with clusters produced by new cascades. Thus, the density of clusters in the simulation box reaches its saturation level. Vacancy clusters, i.e. micro-voids in our simulation, have significant influence on the density of interstitial clusters. As we can see in Fig. 1, at a dose level lower than 5×10^{-4} dpa, the difference between the cases of including micro-voids and no micro-voids was is distinct. But the difference increases as the dose increases, and at a dose of 1.5×10^{-3} dpa, the cluster density of the micro-voids free case is about 50% higher than that of the case with micro-voids. This indicates that the existence of vacancy clusters considerably reduces the density of mobile interstitial clusters, and that recombination plays an important role in microstructural evolution.

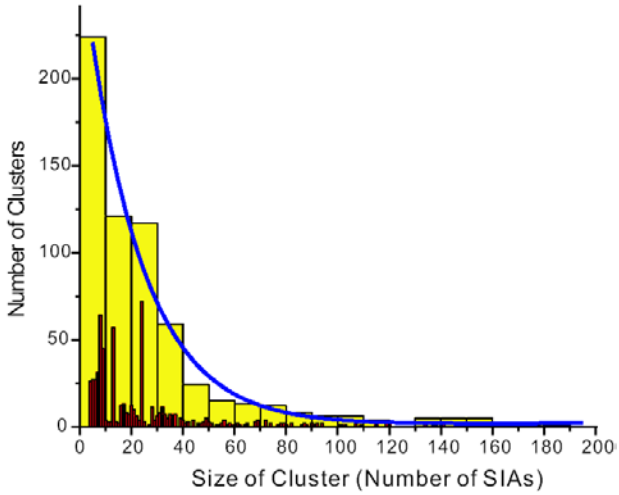

Fig. 2. Size distribution of SIA clusters at a dose level of 5.21×10^{-3} dpa. The red slim bar is the number of clusters of a certain size (fine resolution), and the yellow thick bar are the total number of clusters within a certain range of sizes (coarse resolution).

Although the number density of SIA clusters reaches steady state after 3.5×10^{-3} dpa, the size of clusters continues to increase with increasing dose. In order to compare the results from our simulations with experimentally measured cluster densities, it is necessary to assume a minimum size that can be resolved in the experiments. A value between 1.5 and 2 nm in diameter is quoted in the literature as the minimum size resolved by TEM [13]. For the infinitesimal dislocation loop approximation adopted here, the relationship between radius of the loop (R) and the number of defects (N) is $N = \sqrt{2}\pi R^2 / a_0^2$ for a bcc material, where a_0 is the lattice parameter. A radius of 1.4 nm corresponds to approximately 100 defects in bcc iron. Considering visible interstitial clusters as those with more than 100 interstitial atoms, we

extracted the total 'visible' cluster density from our simulations, as we show in Fig. 1. We can see that the fraction of 'visible' interstitial clusters obtained in the simulations presented here is larger than experimental measurements at high doses, but is still in good agreement. The number of SIA clusters as a function of cluster size at dose of 5.2×10^{-3} dpa is demonstrated by the histogram in Fig. 2. More than half of the total interstitial clusters consist of more than 30 defects though small clusters consisting of less than 10 SIAs still have the highest value for one single section. It can be expected that distribution of Fig. 2 will shift towards the bigger cluster size as damage accumulates.

Characteristics of decoration and raft formation

The main feature of the present KMC simulations that is different from previous work is that the elastic interaction between defects and microstructure is included. Distinct spatial heterogeneity features of damage accumulation under cascade irradiation, such as dislocation decoration and raft formation, can actually be studied. With regard to dislocation decoration, except for a direct encounter of a mobile SIA cluster with a dislocation, clusters will generally be trapped in a region of strong attractive elastic interaction. As expected, at very low dose levels (< 10^{-4} dpa), the probability that a dislocation finds a cluster in the attractive region, and can thus affect the motion of the cluster is rare. Thus, the decoration phenomenon does not occur in the early stage of irradiation. The decoration process builds up quickly with increasing dose, and at 3×10^{-4} dpa, the dislocation has attracted a group of interstitial clusters trapped in its neighboring area. The microstructure configuration of interstitial clusters at 1.3×10^{-3} dpa is shown in Fig. 3(a) where the decoration by interstitial clusters along the dislocation line has become very significant. The accumulation of glissile interstitial clusters near the dislocation is further intensified at dose of 5.2×10^{-3} dpa as shown in Fig. 3(b). When an extremely mobile one-dimensionally migrating interstitial cluster passes through the neighborhood of a pre-existing dislocation, it will feel the influence of the strain field of the dislocation. As long as the defect/dislocation interaction is attractive and the distance is small enough, the interaction of the defect with the stress field of the dislocation could be so strong that the cluster cannot escape from within the attractive zone by thermally activated random walk. Once an interstitial cluster is trapped into the strain field of a dislocation, it rotates its Burgers vector to accommodate to the strain field of the dislocation, and migrates along the direction of lowest energy barrier.

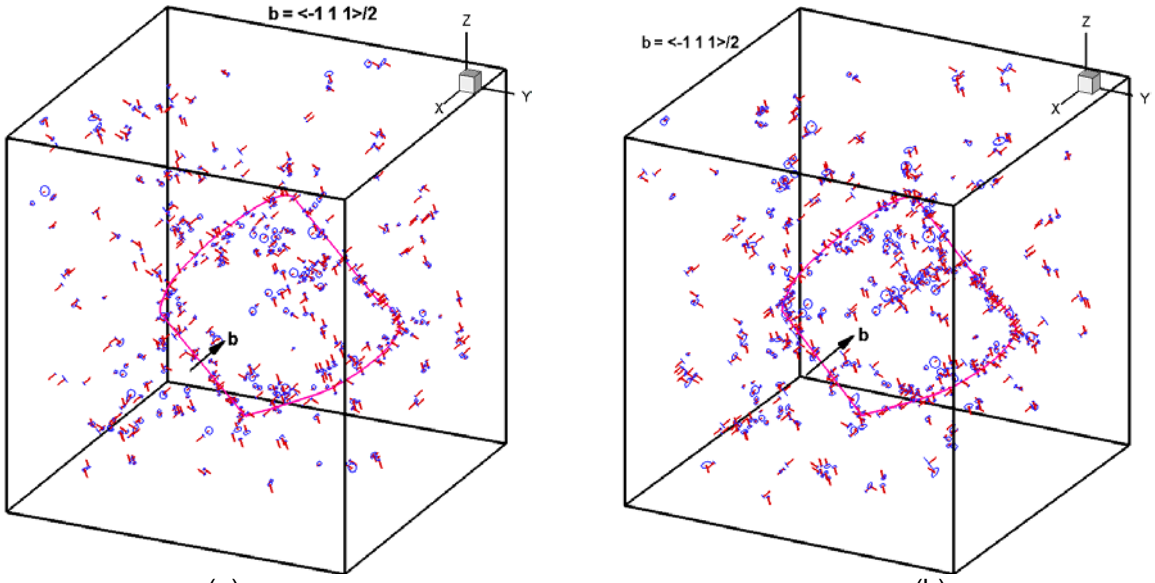

Fig. 3. Snap-shots of the microstructure of interstitial clusters at: (a) 1.3×10^{-3} dpa, where the decoration by interstitial clusters along the dislocation line can be clearly seen; (b) 5.2×10^{-3} dpa, where the accumulation of glissile interstitial clusters near the dislocation is further intensified.

Using dislocation dynamics simulation, Ghoniem et al. [14] investigated the elastic interaction between nano-size prismatic loops and grown-in dislocation loops in bcc Fe and fcc Cu. Their calculation shows that the iso-energy surface for bcc iron has a maximum width around the edge component of the dislocation. Our simulations show a good agreement with their results. It can be clearly seen in Fig. 3 that the pure edge components of the slip dislocation gets more SIA clusters trapped in its vicinity than the mixed character segments. Due to the influence of the strain field of the dislocation, the majority of the decorating clusters have changed their Burgers vector to parallel to the Burgers vector of the dislocation. Trapped clusters can still serve as sinks for glissile clusters, and increase their size by agglomeration before they make a Burgers vector rotation and finally get absorbed by the dislocation. With the accumulation of clusters along the dislocation line, a repulsive force field is gradually built up against further cluster trapping.

Another major striking feature of microstructure evolution under cascade induced irradiation damage is the formation of SIA cluster rafts. This type of frequent experimental observation is also demonstrated here. Fig. 4 shows a configuration of rafts of interstitial clusters forming at a dose level of 1.8×10^{-3} dpa. The Burgers vectors of the clusters making up the raft are parallel to each other, which is in agreement with the experimental observation. When an interstitial cluster approaches another one, the two are subject to the influence of the strain field of each other. If the interaction between them is attractive and strong enough to overcome the energy barrier for directional change, clusters will comply with the interaction between them in terms of adjusting the relative positions and orientations. This scenario is similar to the pinning of clusters, which has been demonstrated in our earlier work [15]. The nature of the configuration of pinning clusters is still glissile, which has been observed in our simulations. The development of this pinning process eventually leads to formation of an extended stable complex that consists of a group of SIA clusters lying on parallel planes. As the number of clusters within a complex increases the mobility of the complex as a whole decreases. The decrease in the mobility of individual clusters can be attributed to the elastic interaction between member clusters within one complex. Such strong interaction prevents clusters from breaking the strain field of others and jumping away. The complex of clusters can grow further, attracting more glissile cluster with the same Burgers vector, thereby creating a raft of SIA clusters.

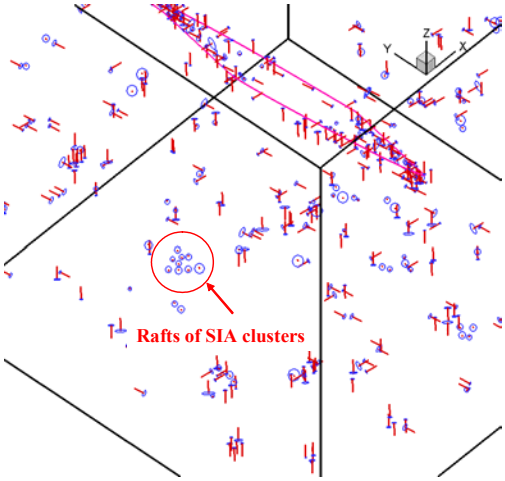

Fig. 4. A close view of the configuration of a raft of interstitial clusters formed at a dose level of 1.8×10^{-3} dpa.

There are two key factors that play an important role in the process of damage accumulation and resultant dislocation decoration and raft formation: (1) the one-dimensional motion of glissile SIA clusters created in displacement cascades, and (2) the interaction between glissile defects and the microstructure. The restriction of diffusion of SIA clusters to 1-D leads to a reduction in the reaction rate with other defects, because one dimensionally moving clusters are able to travel in the atmosphere of randomly

distributed lattice defects through larger distances than those 3-D moving ones. Consequently, the possibility that such SIA clusters annihilate at extended sinks such as pre-existing dislocations and grain boundaries increases. Our simulation demonstrates that even at a fairly low dose of 1.3×10^{-3} dpa a clear decoration phenomenon has already taken place in the vicinity of the pre-existing dislocation loop.

The energy barrier for directional change is a crucial quantity in controlling when, how and in what extent the dislocation decoration and raft formation occur. It determines the maximum range for the elastic interaction that could be strong enough to surpass the barrier and thereby leads to Burgers vector change, as well as the trapping region in the vicinity of dislocations and clusters. In other words, the interaction between defects and microstructure contributes to dislocation decoration and the formation of rafts in terms of changing the diffusivity and the characteristics of mixed 1D/3D migration. Our present simulations suggest that raft formation could be achieved just by prismatic glide of glissile interstitial clusters under the condition of one-dimensional migration combined with strain-field-induced Burgers vector changes. A necessary condition for pronounced formation of rafts of glissile clusters is that the group of clusters having the same Burgers vector is big enough to trap a single glissile cluster in the strain field formed by the group and prevent any trapped cluster from de-trapping or Burgers vector change before it is immobilized by other clusters in the same group. Our simulations indicate that small rafts containing two or three clusters are still mobile; more specifically, these small patches still perform one-dimensional migration. With the size of a patch increasing, the mobility of the whole patch decreases, and a raft consisting of more than five clusters is virtually immobile. Due to thermal activation or interaction with other defects, an interstitial cluster trapped in the outer region of a raft may break loose from the strain field of the raft, and thus gets de-trapped from the raft.

Conclusions

A new approach of KMC simulations, which incorporates elastic interaction between various microstructures, has been developed. The approach is used to investigate the spatial inhomogeneity and segregation of point defects, as well as damage accumulation under cascade irradiation in bcc iron. KMC results have been validated by comparison with experimental observations, including dislocation decoration and raft formation, and the dose dependence of defect density. KMC simulations proved to be a valuable tool in modeling defect kinetics and microstructure evolution at the atomic-level, taking into account many different microscopic mechanisms and covering very different time and length scales.

The importance of glissile SIA clusters produced in displacement cascades has been demonstrated to play a decisive role in irradiation-induced microstructural evolution. The decoration of dislocations by SIA clusters and the formation of rafts have been modeled in detail. The one-dimensional motion of glissile SIA clusters and the interaction between defects and microstructure are shown to be the main cause for the appearance and development of rafts and dislocation decorations. At a rather low dose around 1.0×10^{-3} dpa, a large portion of the initially glissile clusters is trapped around slip dislocation loops (the majority of them are distributed along edge components) and become nearly immobile. The high concentration of SIA loops around slip dislocations results in an extremely inhomogeneous spatial distribution. Our simulations show a clear picture of how SIA clusters are attracted to dislocations to decorate and lock them in place. The simulations show good agreement with experimental observations, at least qualitatively. In addition, for the first time our KMC simulations demonstrate the formation of rafts of glissile clusters with the same Burgers vector. It is suggested that raft formation could be achieved just by prismatic glide of glissile interstitial clusters under the condition of one-dimensional migration combined with strain-field-induced Burgers vector changes. Dose dependence of defect density was investigated quantitatively, using characteristic cluster size distributions, cascade frequency and individual cluster dynamic parameters. The results for visible clusters show fairly good agreement with experimental measurements.

Acknowledgements

This work was supported by the U.S. Department of Energy, Office of Fusion Energy, Grant Number DE-FG02-03ER54708 with UCLA.

References

[1] B. N. Singh, A. J. E. Foreman, and H. Trinkaus, J. Nucl. Mater. 249 (1997) 103
[2] C. Teodosiu, Elastic Models of Crystal Defects (Springer-Verlag, New York, 1982), 287.
[3] J. L. Brimhall and B. Mastel, Radiat. Effects 3 (1970) 203.
[4] J. Huang and N. M. Ghoniem, J. Comp. Mater. Sci. 23 (2002) 225.
[5] H. L. Heinisch and B. N. Singh, J. Nucl. Mater. 251 (1997) 77.
[6] H. L. Heinisch and B. N. Singh, J. Nucl. Mater. 271-272 (1999) 46.
[7] A. B. Bortz, M. H. Kalos, and J. L. Lebowitz, J. Comput. Phys. 17 (1975) 10.
[8] C. C. Battaile and D. J. Srolovitz, J. Appl. Phys. 82 (1997) 6293.
[9] F. Kroupa, in Theory of Crystal Defects, Proceedings of the Summer School held in Hrazany in September 1964, Ed. B. Gruber (Academia Pub. House of the Czechoslovak Academy of Sciences, Prague, 1966), 275.
[10] N. M. Ghoniem, J. Eng. Mater. Tech. 121 (1999) 136.
[11] N. M. Ghoniem and L. Z. Sun, Phys. Rev. B 60 (1999) 128.
[12] M. Eldrup, B. N. Singh, S. J. Zinkle, T. S. Byun, and K. Farrell, J. Nucl. Mater. 307-311 (2002) 912.
[13] B. N. Singh and S. J. Zinkle, J. Nucl. Mater. 206 (1993) 212.
[14] N. M. Ghoniem, B. N. Singh, L. Z. Sun, and T. Diaz de la Rubia, J. Nucl. Mater. 276 (2000) 166.
[15] N. M. Ghoniem, S. H. Tong, J. Huang, B. N. Singh, and M. Wen, J. Nucl. Mater. 307-311 (2002) 843.

MODELING THE BRITTLE-DUCTILE TRANSITION IN FERRITIC STEELS—S. J. Noronha and N. M. Ghoniem (University of California, Los Angeles)

OBJECTIVE

To model the brittle-ductile transition in terms of basic dislocation mechanisms; so that a) the effect of irradiation and consequent microstructural change on DBTT can be predicted, b) to estimate the plastic work done theoretically from the dynamics of dislocations around the crack-tip and c) to the explain the physical basis of master-curve hypothesis.

SUMMARY

The crack tip plastic zone is represented using an array of dislocations emitted from the crack-tip plasticity on loading. The dislocations emitted shield the crack-tip, thereby enhancing the applied stress intensity for fracture from the Griffith value. The stress intensity at fracture is thus a function of the dislocation distribution around the crack tip. This distribution in effect is controlled by the mobility and nucleation energy of dislocations. The method is used to simulate the case where microcracks in the plastic zone of the macrocrack initiate cleavage fracture.

PROGRESS AND STATUS

Introduction

It is now a well-accepted fact that cleavage in ferritic steels in the lower shelf and near the transition temperature is controlled by the microcracks originated in the precipitates. We model the system using a microcrock in the field of macrocrack, both emitting dislocations and generating plastic zone. We outline the details of the model and the calculation procedure in the next section. The results obtained are described in the following section. We also compare our predictions with experimental results reported in the literature. Finally we discuss possible improvements to our model.

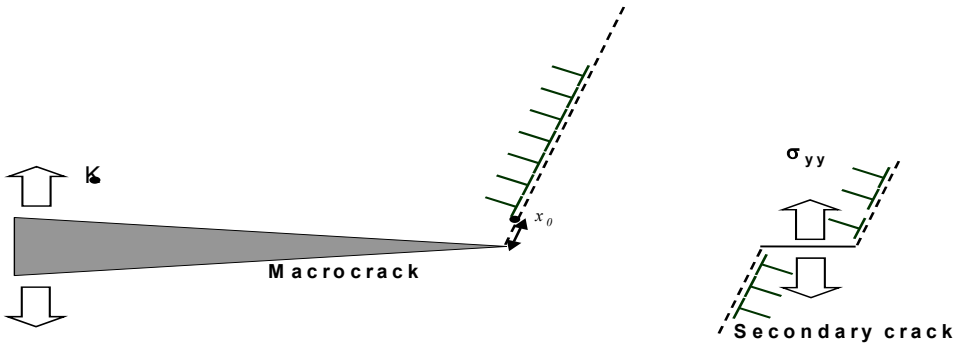

Fig. 1. The geometry of crack and dislocations used in the 2D coupled macrocrack-microcrack simulation model.

Model and Method of Calculation

The geometry of the 2-d model used is shown in Fig. 1. A semi-infinite crack (macrocrack) with a finite crack (microcrack) situated ahead of it in its crack plane is loaded. A dislocation

source is assumed to exist at a distance x_0 from, and situated on the slip plane passing through, each crack tip. The value of x_0 used in simulation is *10b*, where *b* is the burgers vector; the slip plane is oriented at an angle of 70.5^0 to the crack plane. A dislocation is emitted when the resolved shear stress on a dislocation at x_0 is greater than τ_f. Where τ_f is the friction stress used and is chosen to be equal to $\sigma_y/\sqrt{3}$, where σ_y corresponds to the uniaxial yield stress at a given temperature. The temperature dependence of fracture toughness is then obtained by inputting the corresponding friction stress value. The resolved shear stresses are obtained using expressions based on derivations for semi-infinite crack [0] and finite crack [0]. The emitted dislocations move along the slip plane away from the crack tip, and the stress at the source increases until another dislocation is emitted. (For each positive dislocation emitted, a negative one is assumed to move into the crack.) In the case of microcrack, the sources on opposite sides of the crack are at equivalent positions x_o and operate simultaneously. (This ensures that no net Burgers vector remains in the crack). Dislocations are assumed to move with a velocity v given by

$$\mathrm{v}_{x_i} = \left(\frac{\left|\tau_{x_i}\right|}{\tau_0} \right)^m \mathrm{v}_0 \left(\frac{\left|\tau_{x_i}\right| - \tau_f}{\tau_{x_i}} \right) \qquad (1)$$

for $\left|\tau_{x_i}\right| > \tau_y$ and v = 0 for $\left|\tau_{x_i}\right| < \tau_f$. The computations were carried out with m = 2.67 and v_0 = 4.5 x 10^{-10} ms^{-1}, appropriate to the velocities of screw dislocations in iron at 273K [0]. During the simulation, the applied stress intensity is increased in small increments and the positions of dislocations are determined. It is found that the dislocations reach near equilibrium positions. It should be noted that with the dislocations in near-equilibrium positions, the temperature and strain-rate dependence of K_F, the numbers of dislocations emitted at fracture, and the plastic zone size are determined only by the temperature and strain-rate dependence of the yield stress, σ_y.

The emitted dislocations shield the crack from external load by compressive stresses they exert at the crack tip. The shielding stress intensity factor for each dislocation (K_D) is calculated at each crack tip. The expressions for semi-infinite were used from [0] and that for finite crack from [0] and the total net shielding stress intensity factor is obtained by summation. The fracture criterion for this model is a critical crack-tip stress intensity of the microcrack. Thus, when $k = K_{IC}$, cleavage fracture of the matrix is assumed to occur; the applied load at the macrocrack, K_A then gives the critical loading for fracture propagation K_F and the microscopic cleavage fracture stress (σ_F) is the net stress due to the macrocrack field and the array of dislocations emitted from it.

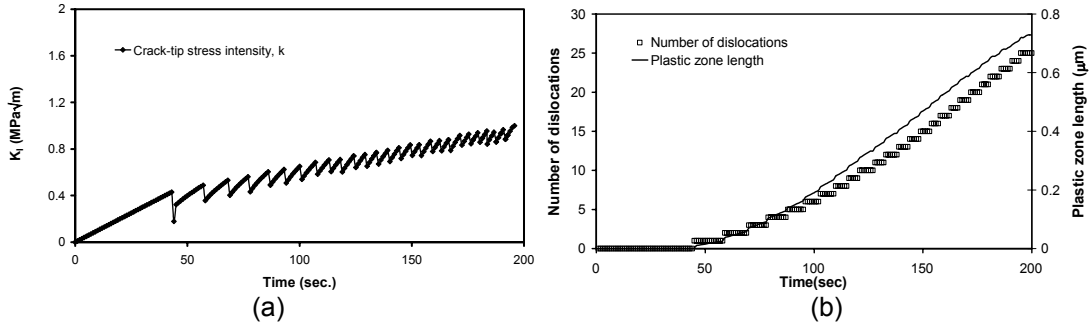

Fig. 2(a). The stress intensity at the micocrack tip and as a function of simulation time; crack size=1μm, yield stress=800 MPa; (b) The number of dislocations and the plastic zone length as a function of simulation time; crack size=1μm, yield stress=800 Mpa.

Results and Discussion

A typical behavior of the crack tip stress intensity at the microcrack(k) while it is loaded is shown in Fig. 2a. The fracture criterion in this case is k reaching a critical value (chosen as 1 MPa$\sqrt{m}$, an approximate value for pure cleavage to occur in Fe). Each drop in the curve corresponds to the dislocation emission at the crack-tips. The emitted dislocations shield the crack and enhance the stress required for cleavage. The amount of shielding (K_D) can be interpreted as the *plastic work during crack propagation*. In this case, the microcrack size is 1μm, the yield stress is 800 MPa and the rate of loading, dK/dt = 0.01 MPa$\sqrt{m}$ s^{-1}. Fig.2b shows the number of dislocations and length of the plastic zone developed at the microcrack tip with the progress in simulation.

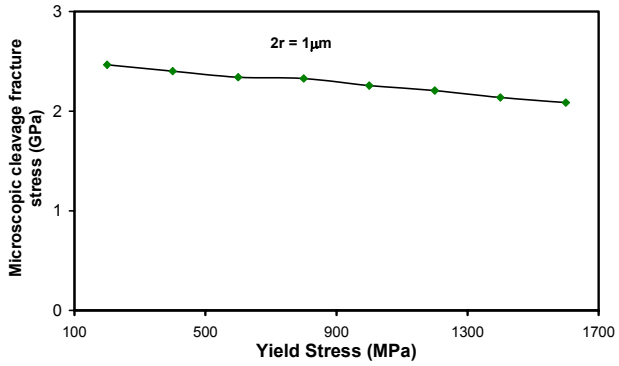

Fig. 3a. The stress at the particle at fracture as a function of yield stress.

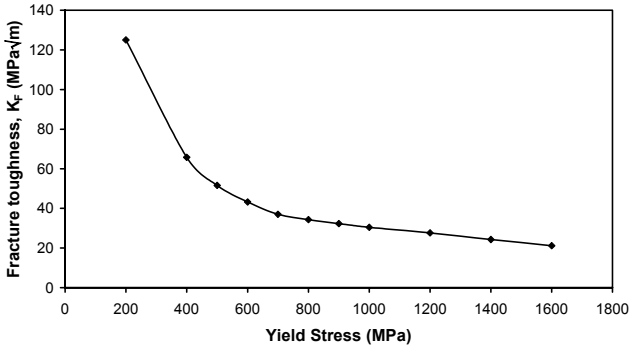

Fig. 3b. The fracture toughness as a function of yield stress, the criterion of fracture is the critical crack-tip stress intensity of the microcrack.

A microcack of size 1μm is placed at a distance of 10μm from the macro crack tip (10μm is the average distance obtained in [4] with which we compare our results). Fig. 3a shows the variation of microscopic cleavage fracture stress (σ_F) (that is the net stress due to the macrocrack stress field and the dislocation array developed at the macrocrack at fracture) as a function of yield stress is less than 10% consistent with the experimental observations. Fig. 3b shows the macroscopic fracture toughness, K_F as a function of yield stress. There is sharp increase in the fracture toughness at low yield stresses, which correspond to the transition from brittle to ductile behavior. However this sharp upturn is not captured when we map the fracture toughness as a function of temperature, since the variation of yield stress at or near the transition-temperature region is found to be weak. In Fig.3c portion of the fracture toughness curve in Fig.3b is mapped to temperature using experimental yield stress [4] to obtain the brittle-ductile transition curve. We can see that model fits well to experim-

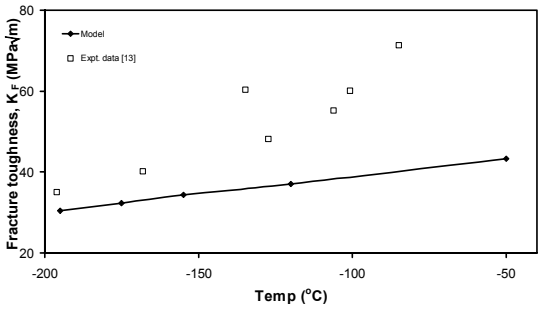

Fig. 3c. The fracture toughness values from above Fig. (5a) mapped to temperature and the experimental fracture toughness.

ental results at lower shelf fracture toughness; however it does not predict the sharp upturn at the transition. Note, the yield stress range to which we could map the data is very narrow (600-100MPa), due to the unavailability of data for a broader temperature range. Also our model does not consider dislocation multiplication, which will have significant effect at lower yield stress or high temperature regime.

Conclusions and Outlook

The, 2-d dislocation dynamics is used to study the crack system involved in the fracture of ferritic steels; a macrocrack with microcracks ahead of it. The dynamic interaction between dislocations emitted from both macrocrack and microcrack has been included. The crack-tip behavior and the predicted brittle to ductile transition have good agreement with experiment at the low temperature region. However the model does not predict the sharp upturn near the transition temperature. It should be noted that our simulations do not involve dislocation multiplication processes, which become significant at higher temperatures near the transition temperature. This draw back could be overcome by carefully devising local rules using 3D dislocation simulations, which is now in progress.

Acknowledgements

This work was supported by the U.S. Department of Energy, Office of Fusion Energy, Grant Number DE-FG02-03ER54708 with UCLA.

References

[1] V. Lakshmanan and J. C. M. Li, Mat. Sci. Engin. A104 (1988) 95.
[2] S. Wang and S. Lee, Mat. Sci. Engin. A130 (1990) 1.
[3] H. Saka, K. Nada, and T. Imura, Crystal Lattice Defects 4 (1973) 45.
[4] R. O. Ritchie, J. F. Knott, and J. R. Rice, J. Mech. Phys. Solids 21 (1973) 395.
[5] S. J. Noronha, J. Huang, and N. M. Ghoniem, Journal of Nuclear Materials (accepted).

MD AND KMC MODELING OF THE GROWTH AND SHRINKAGE MECHANISMS OF HELIUM-VACANCY COMPLEXES IN FE—K. Morishita, R. Sugano (Institute for Advanced Energy, Kyoto University), and B. D. Wirth (Department of Nuclear Engineering, University of California Berkeley)

EXTENDED ABSTRACT

A multiscale modeling approach, which is based on atomistic simulations, was applied to investigate the growth and shrinkage mechanisms of helium–vacancy (He–V) clusters in Fe. Molecular dynamics (MD) simulations with empirical interatomic potentials were used to determine energies for the formation and dissociation of clusters as a function of their size and He density. Both the number of He atoms and vacancies in a cluster ranged from 0 to 20. The dissociation energy of clusters showed a strong dependence on the He density, rather than the cluster size, indicating that the growth and shrinkage of clusters strongly depend on the He density.

A kinetic Monte Carlo (KMC) model has been developed to simulate the long-time cluster behavior, using the binding and dissociation energies obtained from MD. The KMC simulations indicated that He stabilizes He–V clusters by suppressing thermal vacancy emission and by promoting thermal self-interstitial Fe atom emission. A preliminary KMC simulation to investigate the migration behavior of He–V clusters is also presented. The diffusion of a He–V cluster depends on the size and lifetime of the cluster, and therefore depends on the He density and cluster size.

Reference

K. Morishita, R. Sugano, and B. D. Wirth, Journal of Nuclear Materials 323 (2003) 243.

NUCLEATION AND GROWTH OF HELIUM-VACANCY CLUSTERS IN IRRADIATED METALS. PART II. A GROUPING METHOD FOR AN APPROXIMATE SOLUTION OF TWO DIMENSIONAL KINETIC EQUATIONS DESCRIBING EVOLUTION OF POINT DEFECT CLUSTERS TAKING INTO ACCOUNT BROWNIAN MOTION OF THE CLUSTERS—S. I. Golubov, R. E. Stoller, S. J. Zinkle (Oak Ridge National Laboratory)*

OBJECTIVE

The objective of this work is to develop kinetic models describing the nucleation and evolution of radiation-induced defect clusters. Current work includes the modification of a previously-developed grouping method used to obtain a solution for the two dimensional kinetic equations describing gas assisted vacancy cluster formation in irradiated materials. The new model can account for the coalescence of clusters driven by Brownian motion.

SUMMARY

Nucleation, growth and coarsening of point defect clusters or secondary phase precipitates are of interest for many applications in solid-state physics. As an example, clusters nucleate and grow from point defects (PD) in solid under irradiation. In typical nucleation, growth and coarsening problems, a master equation (ME) is constructed that summarizes the large number of equations needed to describe the evolution process. When only the mobility of point defects and their reactions with the clusters are taken into account the ME takes the form of a differential equation known as the continuity equation in cluster size space. A new grouping method was developed by Golubov et al. for both the one-dimensional ME, which describes evolution of dislocation loops under irradiation or ageing, and the two-dimensional ME, which describes gas-assisted nucleation of voids or bubble formation in irradiated metals [1, 2]. However it has been shown that mobility of the clusters (e.g. He-vacancy) leading to coalescence, may play a key role in their evolution, particularly in the case of annealing of He implanted metals. The ME in the case becomes of the integro-differential type which complicates the numerical solution. The coalescence of clusters has been treated by different calculation methods (see e.g. [3-9]) but it has not been subjected to any specific grouping method of the type just described and this work intends to fill this gap. In the present work, the grouping method proposed by Golubov et al. [1] for the two-dimensional ME is generalized to take into account the coalescence of the clusters. An application of the method to the problem of helium bubble evolution which takes place during annealing of He implanted stainless steel is presented.

PROGRESS AND STATUS

Introduction

Precipitation of helium introduced into metals by (n,α) reactions that occur in fission and fusion reactors influence microstructure evolution materials. It has been established that helium atoms assist the nucleation and growth of cavities in irradiated materials leading to swelling and mechanical properties changes. The literature contains several partial treatments of the problem where both coarsening mechanisms, namely Ostwald ripening (see discussion in [1]) and bubble migration and coalescence [3-9] have been considered. However an accurate treatment of the second mechanism problem is complicated and most previous work has been done in a semi-quantitative way [7,13,14]. When calculating bubble coalescence under annealing conditions, it has commonly been assumed that bubbles maintain mechanical equilibrium during their evolution, which may not be the case. Moreover, very little has been done to calculate bubble evolution while taking into account both coarsening mechanisms simultaneously. It has been shown [1] that for the case when cluster evolution is driven by only mobility of point defects, the simplest and accurate grouping method may be obtained when size distribution function (SDF) within

---

*The work has been done in collaboration with A. M. Ovcharenko and C. H. Woo (Department of Mechanical Engineering, The Hong Kong Polytechnic University, Hong Kong).

a group is approximated by a linear function. Such an approximation maintains the identity of the grouped ME with the original one, while satisfying the conservation laws for both the total number of clusters and the total number of point defects accumulated in the clusters. However the calculation of bubble coalescence has not been subjected to any specific grouping method of the type mentioned. It appears that the grouping method developed in [1] can be generalized to take into account bubble migration and coalescence and this is the objective of the present work. It has been shown that in the framework of a generalized grouping method describing the evolution of the cluster SDF equal accuracy can be obtained for the general case when the evolution is driven simultaneously by cluster interactions with mobile point defects, and by Brownian motion of the clusters.

Master Equation

To describe the evolution of He-vacancy clusters driven by reactions with mobile point defects and Brownian motion of the clusters, the following ME has to be solved in the two-dimensional phase space of x, m

$$\frac{df(x,m,t)}{dt} + \nabla_x J_x(x,m,t) + \nabla_m J_m(x,m,t) = \frac{df(x,m,t)}{dt}_{|BM}, \tag{1}$$

where $f(x,m,t)$ and $J_x(x,m,t), J_m(x,m,t)$ are the SDF (the number density of clusters containing *x* vacancies and *m* He atoms) and fluxes of clusters in *x* and *m*-spaces, respectively. The fluxes are determined by the reactions of clusters with point defects

$$\begin{aligned} J_x(x,m,t) &= P_x(x,m,t) f(x,m,t) - Q_x(x+1,m,t) f(x+1,m,t), \\ J_m(x,m,t) &= P_m(x,m,t) f(x,m,t) - Q_m(x,m+1,t) f(x,m+1,t), \end{aligned} \tag{2}$$

where the coefficients $P_x(x,t)$, $Q_x(x,m,t)$, $P_m(x,t)$, and $Q_m(x,m,t)$ are the reaction rates for capture (*P*) and evaporation (*Q*) between the mobile point defects and clusters leading to a change in the cluster of size x and m, respectively.

The right hand side of the Eq. (1) represents the rate of change of the SDF caused by Brownian motion and coalescence. It may be expanded as follows:

$$\begin{aligned} \frac{df(x,m)}{dt}_{|BM} &= -f(x,m) \sum_{\substack{x'\geq 1, x'\neq x \\ m'\geq 0, m'\neq m}} \Lambda_{xm,x'm'} f(x',m') - 2f^2(x,m)\Lambda_{xm,xm} + \\ &\sum_{\substack{x'\leq x-2 \\ m'\leq m}} \sum_{\substack{x''\leq x-2 \\ m''\leq m}} \Lambda_{x'm',x''m''} f(x',m') f(x'',m'') \delta(x-x'-x'') \delta(m-m'-m'') = 0. \end{aligned} \tag{3}$$

In Eq. (3) $\Lambda_{x'm',x''m''}$ is the collision cross section between the clusters containing x', m' and x'', m'' vacancies and He atoms and $\delta(x)$ is the Kronneker delta. In the case of Brownian motion $\Lambda_{x'x'',m'm''}$ may be written in the following form:

$$\Lambda_{x'm',x''m''} = \left(48\pi^2/\Omega^2\right)^{1/3} \left[(x')^{1/3} + (x'')^{1/3}\right] \left[D_{x'm'} + D_{x''m''}\right], \tag{4}$$

where Ω is the atomic volume, $D_{x'm'}$ and $D_{x"m"}$ are diffusion coefficients of size x', m' and $x", m"$ clusters. The first term on the right hand side of Eq. (3) describes the rate of decrease in number density of size x, m clusters via collision of the clusters with all other clusters except the x, m clusters. The second term describes coalescence of two x, m clusters. Note that a multiplier of 2 takes into account that the coalescence of the clusters leads to the disappearance of two clusters of the same size. The third term describes the formation of x, m clusters via collisions between smaller clusters which satisfy the equations:

$$x = x' + x", \; m = m' + m". \tag{5}$$

The ME in the form of Eq. (1) leads a set of rate equations for clusters of each size in the range of practical interest. It has already been pointed out [1,2] that for practical purposes it is necessary to consider clusters containing such a large number of point defects (or atoms) that the numerical solution of Eq. (1) becomes difficult. The grouping method developed in [1] permits the number of equations needing to be greatly thus providing a tool which can be useful for numerical solution of Eq.(1). Below the grouping method generalized to take into account coalescence of clusters is presented.

The Grouping Method

Following [1], the cluster SDF is divided into a series of groups with widths $\Delta x_i = x_i - x_{i-1}$, $\Delta m_j = m_j - m_{j-1}$, which include the clusters of the sizes

$$\begin{aligned} &x = x_{i-1} + k, \; \left(k = 1, .., \Delta x_i\right), \\ &m = m_{j-1} + n, \; \left(n = 1, .., \Delta m_j\right), \end{aligned} \tag{6}$$

respectively. The subscript i indicates the number of a group in $x-$space and the subscript j indicates the number of a group in $m-$space. Thus each group consists of $n_{i,j} = \Delta x_i \Delta m_j$ numbers of clusters of different sizes and is defined by the double index "*ij*".

Follow [1] let us approximate $f(x, m, t)$ by a linear function within a group i, j of the type

$$f_{i,j}(x, m) = L_0^{i,j} + L_{1x}^{i,j}(x - < x >_i) + L_{1m}^{i,j}(m - < m >_j). \tag{7}$$

where <> denotes the average number of vacancies and He atoms in the group of clusters. As can be seen from Eq. (7) each group of clusters is defined by three coefficients, $L_0^{i,j}, L_{1x}^{i,j}, L_{1m}^{i,j}$. Thus, the kinetic equation for the grouping method is formulated as a set of three equations for the coefficients in each cluster group. It has been shown [1] that in the case where evolution of the clusters is driven by only reactions between clusters and point defects, the equations for $L_0^{i,j}, L_{1x}^{i,j}, L_{1m}^{i,j}$ are given by

$$\frac{dL_0^{i,j}}{dt} = \frac{1}{\Delta x_i}\left[J_x(x_{i-1}, < m >_j) - J_x(x_i, < m >_j)\right] + \frac{1}{\Delta m_j}\left[J_m(< x >_i, m_{j-1}) - J_m(< x >_i, m_j)\right]. \tag{8}$$

$$\frac{dL_{1x}^{i,j}}{dt}=-\left(\frac{\Delta x_i-1}{2\sigma_i^2\Delta x_i}\right)\left\{\ J_x(x_{i-1},<m>_j)+J_x(x_i,<m>_j)-2J_x(<x_i>-\frac{1}{2},<m>_j)\ \right\}$$
$$+\frac{1}{\Delta m_j}\left\{\ \left[J_m(<x>_i+1,m_{j-1})-J_m(<x>_i,m_{j-1})\right]-\left[J_m(<x>_i+1,m_j)-J_m(<x>_i,m_j)\right]\ \right\}. \quad (9)$$

$$\frac{dL_{1m}^{i,j}}{dt}\Big|_{PD}=-\left(\frac{\Delta m_j-1}{2\sigma_j^2\Delta m_j}\right)\left\{\ J_m(<x>_i,m_{j-1})+J_m(<x>_i,m_j)-2J_m(<x>_i,<m>_j-\frac{1}{2})\ \right\}$$
$$+\frac{1}{\Delta x_i}\left\{\ \left[J_x(x_{i-1},<m>_j+1)-J_x(x_{i-1},<m>_j)\right]-\left[J_x(x_i,<m>_j+1)-J_x(x_i,<m>_j)\right]\ \right\}. \quad (10)$$

where σ_i^2,σ_j^2 are the dispersions of cluster sizes in the group, which are given by

$$\sigma_i^2=\frac{1}{\Delta x_i}\left[\sum_{\alpha=x_{i-1}+1}^{x_i}\alpha^2-\frac{1}{\Delta x_i}\left(\sum_{\alpha=x_{i-1}+1}^{x_i}\alpha\right)^2\right],$$
$$\sigma_j^2=\frac{1}{\Delta m_j}\left[\sum_{\alpha=m_{j-1}+1}^{m_j}\alpha^2-\frac{1}{\Delta m_j}\left(\sum_{\alpha=m_{j-1}+1}^{m_j}\alpha\right)^2\right]. \quad (11)$$

For the case when Brownian motion of clusters takes place, the SDF is changed in accordance with the right hand side of Eq. (1). Thus, the final form of the kinetic equations in the framework of the grouping method has the form

$$\frac{dL_0^{i,j}}{dt}=\frac{dL_0^{i,j}}{dt}\Big|_{PD}+\frac{dL_0^{i,j}}{dt}\Big|_{BM},$$
$$\frac{dL_{1x}^{i,j}}{dt}=\frac{dL_{1x}^{i,j}}{dt}\Big|_{PD}+\frac{dL_{1x}^{i,j}}{dt}\Big|_{BM}, \quad (12)$$
$$\frac{dL_{1m}^{i,j}}{dt}=\frac{dL_{1m}^{i,j}}{dt}\Big|_{PD}+\frac{dL_{1m}^{i,j}}{dt}\Big|_{BM}.$$

To derive the rates $\frac{dL_0^{i,j}}{dt}_{|BM}, \frac{L_{1x}^{i,j}}{dt}_{|BM}, \frac{L_{1m}^{i,j}}{dt}_{|BM}$, the two following assumptions are made:

(a) diffusion coefficients of all clusters within a group are equal to each other

(b) collision of any cluster within a group *pq* with any cluster within a group $p'q'$ creates a cluster, which belongs to a single group *ij* satisfying the following inequalities

$$x_i-1<\left(<x>_p+<x>_{p'}\right)\le x_i,$$
$$m_j-1<\left(<m>_q+<m>_{q'}\right)\le m_j. \quad (13)$$

The first assumption leads to a simple situation in which the collision rates of any particular size cluster within a group with any size cluster within another group are equal to each other. As a result, clusters of all different size inside a group coalesce with the same rate, i.e. they can be considered as a bunch of single size clusters. Since the cross section for cluster coalescence is proportional to the product of the cluster densities, which are determined by the zero order coefficients $L_0^{i,j}$ only ($N_{i,j} = L_0^{i,j}\Delta x_i \Delta m_j$), the rate equation for the coefficient can be written similarly to that of Eq. (3):

$$\left(\frac{dL_0^{i,j}(t)}{dt}\right)_{\text{int}} = -\left(L_0^{i,j}(t)\right)^2 \Lambda_{ij,ij}\Delta x_i \Delta m_j - L_0^{i,j}(t)\sum_{k,n}\Lambda_{ij,kn}L_0^{k,n}(t)\Delta x_k \Delta m_n + \frac{1}{\left(\Delta x_i \Delta m_j\right)}\sum_{p,q}\sum_{p'q'}\Lambda_{pq,p'q'}L_0^{p,q}(t)L_0^{p',q'}(t)\Delta x_p \Delta m_q \Delta x_{p'}\Delta m_{q'}. \quad (14)$$

The only difference being that instead of the Kronneker delta in the last term on the right hand side, the indexes *pq* and $p'q'$ have to satisfy Eq. (13). The first term on the right hand side of Eq. (14) describes the rate of decrease of number density of the *ij* group clusters via collision of the clusters with all other clusters except clusters of same group. The second term describes coalescence of the *ij* group clusters with clusters in same group. Note that a multiplier of 2 accounts for coalescence of the clusters that leads to the disappearance of two clusters of the same group. The third term describes the formation of x, m clusters in *ij* group via collisions of clusters from smaller size groups.

In order to derive equations for the two other coefficients, $L_{1x}^{i,j}(t), L_{1m}^{i,j}(t)$, one needs to calculate the rate of change of the total number of *x* and *m* type defects accumulated in the group fed by the coalescence. These are given by [1]

$$S_{i,j} = \left(L_0^{i,j} < x >_i + L_{1x}^{i,j}\sigma_i^2\right)\Delta x_i \Delta m_j,$$
$$M_{i,j} = \left(L_0^{i,j} < m >_j + L_{1m}^{i,j}\sigma_j^2\right)\Delta x_i \Delta m_j, \quad (15)$$

Taking into account the assumption (a) mentioned above, it is clear that coalescence of the *ij* group clusters described by the first and second terms on the right hand side of Eq. (14) does not change the coefficients $L_{1x}^{i,j}(t), L_{1m}^{i,j}(t)$ since the change of values $S_{i,j}, M_{i,j}$ is fully described by the change of the coefficient $L_0^{i,j}$. However this is not the case for coalescence described by the third term on the right hand side of Eq. (14) since a sum of the average sizes of pq and $p'q'$ groups is not equal to the average size of resulting *ij* group. Taking into account conservation of the total number of *x* and *m* type of defects accumulated in pq , $p'q'$ and *ij* cluster groups, one can find the following equations for these coefficients:

$$\left(\frac{dL_{1x}^{i,j}(t)}{dt}\right)_{BM} = \frac{1}{\left(\Delta x_i \Delta m_j\right)\sigma_i^2}\sum_{p,q}\sum_{p',q'}\left\{\Delta x_p \Delta m_q \Delta x_{p'} \Delta m_{q'} \right.$$
$$\left.\Lambda_{pq,p'q'} L_0^{p,q}(t) L_0^{p',q'}(t)\left(< x >_p + < x >_{p'} - < x >_i\right)\right\}, \tag{16}$$

$$\left(\frac{dL_{1m}^{i,j}(t)}{dt}\right)_{BM} = \frac{1}{\left(\Delta x_i \Delta m_j\right)\sigma_j^2}\sum_{p,q}\sum_{p',q'}\left\{\Delta x_p \Delta m_q \Delta x_{p'} \Delta m_{q'} \right.$$
$$\left.\Lambda_{pq,p'q'} L_0^{p,q}(t) L_0^{p',q'}(t)\left(< m >_q + < m >_{q'} - < m >_j\right)\right\}.$$

Note that similar to Eq. (14), the indexes *pq* and $p'q'$ in Eqs. (16) have to satisfy Eq. (13). Thus, the set of equations (14) and (16) complete the description of evolution of the cluster SDF caused by coalescence within the group method. Equations (12), (14) and (16) together with Eqs. (8)- (10) describe the evolution of SDF within the group approximation taking into account both point defects and cluster mobility. To illustrate the applicability of the method, these equations have been used to calculate the evolution of He bubbles taking place during ageing in pre-implanted stainless steel [10]. Note that the grouping method presented above can be used for both irradiation and ageing, so the calculations presented here consist two parts: (1) implantation of He atoms in the material and (2) annealing of the He-implanted material.

Evolution of He Bubbles Under Irradiation and Annealing

Model description

In order to use the grouping method to describe the evolution of He-vacancy clusters one needs to specify the fluxes $J_x(x,m,t), J_m(x,m,t)$, the diffusion coefficient for the Brownian motion of the clusters, and to set up the equations for mobile point defects with initial and boundary conditions. In Ref. [1] it was shown that for the case where concentrations of 3-D diffusing PDs, $C_v(t), C_i(t)$, are measured in atomic fractions, the rates $P_x\left(x,t\right)$ and $Q_x\left(x,m,t\right)$ in Eq. (2) may be written as follows

$$P_x(x) = wx^{1/3} D_v C_v(t),$$
$$Q_x(x,m) = wx^{1/3}\left[D_i C_i + D_v \exp\left(-E_v^b(x,m)/kT\right)\right] = Q_x^i(x,m) + Q_x^v(x,m), \tag{17}$$

where $w = \left(48\pi^2/\Omega^2\right)^{1/3}$, D_v, D_i are the diffusion coefficients of 3-D diffusing vacancies and interstitials, $E_v^b(x,m)$ is the binding energy of vacancy with a cluster of size *x* containing m gas atoms, k_B is the Boltzmann constant, and T is absolute temperature. The binding energy in Eq. (17) is given by

$$E_v^b(x,m) = E_v^f - \frac{\alpha}{x^{1/3}} + \left(\frac{m}{x}\right) Z\left(\frac{m}{x}, T\right) k_B T, \tag{18}$$

where E_v^f is the vacancy formation energy, $\alpha = 2\gamma\left(4\pi\Omega^2/3\right)^{1/3}$ and γ is the surface energy. The compressibility factor, $Z(T, m/x)$, is computed using the expression derived by Manzke and Trinkaus [11,12]

$$Z(T,m/x) = (1-\rho)\left(1+\rho-52\rho^2\right) + \frac{b}{V_m}\rho(1-\rho)^2 + Z_m\rho^2(3-2\rho), \tag{19}$$

where

$$\begin{aligned}
&\rho = \left(\frac{V_m}{\Omega}\right)\frac{m}{x},\\
&V_m = 56\mathrm{T}^{-1/4}\exp(-0.145\ \mathrm{T}^{1/4}),\\
&Z_m = 0.1225\ V_m\mathrm{T}^{\,0.555},\\
&b = 170\mathrm{T}^{-1/3} - 1750\mathrm{T}^{-1}.
\end{aligned} \tag{20}$$

In Eq. (20) V_m is the He atomic volume is measured in cubic angstroms. Note that Eqs. (20) is written assuming that the volume of the cluster containing *x* vacancies, *V*, is equal to $V = x\Omega$.

In the second Eq. (2) $P_m(x,m,t)$ is the rate of helium absorption by an x,m cluster and $Q_m(x,m,t)$ is the rate of helium resolution from the clusters. The coefficients $P_m(x,m,t)$ and $Q_m(x,m,t)$ are used here in the simple form similar to that for vacancies in Eq. (17). Thus, in the present calculations $P_m(x,m,t)$ and $Q_m(x,m,t)$ are computed as:

$$\begin{aligned}
&P_m(x) = wx^{1/3}D_{He}C_{He},\\
&P_m(x) = wx^{1/3}D_{He}\exp\left(E_{res}/k_BT\right),
\end{aligned} \tag{21}$$

where $C_{He}(t)$ and D_{He} are the concentration and diffusion coefficient of He atoms by the interstitial mechanism, E_{res} is an activation energy for helium resolution from the clusters. Taking into account Eqs. (17) and (21), the evolution of mobile defect concentrations $C_v(t), C_i(t), C_{He}(t)$ may be presented as follows

$$\begin{aligned}
\frac{dC_v}{dt} = &\left\{G_v + Q_m(1)f(1,1,t) + Q_x(2,0)f(2,0,t) + \right.\\
&\left.\sum_{x=2}^{\infty}\sum_{m=0}^{\infty}Q_x^v(x+1,m)f(x+1,m,t) + D_vC_{v0}Z_v\rho_d\right\}\\
&-\left[\mu_RD_iC_iC_v + \mu_R^{He}D_{He}C_{He}C_v + D_vC_vZ_v\rho_d + P_x(1)f(1,0,t) + \sum_{x=1}^{\infty}\sum_{m=0}^{\infty}P_x(x)f(x,m,t)\right],
\end{aligned} \tag{22}$$

$$\frac{dC_i}{dt} = G_i - \mu_R D_i C_i C_v - D_i C_i Z_i \rho_d - \sum_{x=2}^{\infty} \sum_{m=0}^{m_{\max}} Q_x^i(x) f(x,m,t) - Q_x^i(1) \sum_{m=1}^{m=m_0} f(1,m). \tag{23}$$

$$\begin{aligned} \frac{dC_{He}}{dt} &= \left\{ G_{He} + \sum_{x=2}^{\infty} \sum_{m=1}^{m_{\max}} Q_m(m) f(x,m,t) + \sum_{m=1}^{m=m_0} \left[Q_m(m) + m Q_x^i(1) \right] f(1,m) \right\} \\ &- \left[\mu_R D_{He} C_v C_{He} + D_{He} C_{He} Z_{He} \rho_d + \sum_{x=2}^{\infty} \sum_{m=0}^{m_{\max}-1} P_m(x) f(x,m,t) + P_m(1) \sum_{m=1}^{m=m_0-1} f(1,m) \right], \end{aligned} \tag{24}$$

where G_v, G_i, G_{He} are the generation rates of vacancies, self interstitial atoms (SIAs) and He atoms, respectively, μ_R is the coefficient describing the recombination reaction between SIA and vacancy, Z_v, Z_i are the capture efficiencies of dislocations for vacancies and SIAs, respectively, ρ is the dislocation density, C_{v0} is the thermal equilibrium vacancy concentration, m_0 is the maximum number of He atoms associated with a single vacancy (see e.g. [15-17]). The generation rates vacancies and SIAs are given by

$$\begin{aligned} G_v &= G_{NRT}(1-\varepsilon_r), \\ G_i &= G_{NRT}(1-\varepsilon_r), \end{aligned} \tag{25}$$

where G_{NRT} is the generation rate calculated using the NRT model, and ε_r is a fraction of the point defects recombined during cooling phase of cascades.

The migration of the clusters is assumed to be caused by mass transport on the bubble surface (see e.g. Ref. [18])

$$D_{ij} = \frac{3}{2\pi} D_S \left(\frac{\Omega^{1/3}}{< r >_i} \right)^4, \tag{26}$$

where $D_S = D^{(0)} \exp(-E_S / k_B T)$ is the surface diffusion coefficient, $< r >_i$ is the mean radius of the *ij* group of cluster, and $< r >_i = \left(\frac{3\Omega}{4\pi} < x >_i \right)^{1/3}$.

Eqs. (8)-(10), (12), (14) and (16)- (26) have been used to calculate He bubble evolution in a stainless steel under irradiation and annealing.

Experimental data and parameters used in the calculations

As discussed in Ref. [10], specimens of model austenitic alloy P7 (Fe-17Cr-16.7Ni-2.5Mo) were implanted with a 10 to 50 appm He at room temperature and subsequently annealed for one hour at temperatures between 600 and 900°C. The temperature during implantation was <200°C and the He implantation level in specimens used for the annealing varied between 32 and 47 appm. Helium bubble data obtained after one-hour annealing are summarized in Table 1.

Table 1. Summary of bubble microstructures observed after 40 appm helium implantation in solution-annealed P7 and subsequent annealing for one hour [10]

Helium implanted (appm)	T (^{o}C)	Bubble density ($10^{21}m^{-3}$)	Average bubble radius (nm)	Swelling
32	600	-	-	
44	700	8.25	0.82	$1.82*10^{-5}$
37	750	6.33	1.09	$3.2*10^{-5}$
47	800	6.66	1.57	$9.7*10^{-5}$
41	900	2.15	1.99	$6.7*10^{-5}$

As can be seen from the table, bubbles remained invisible after annealing at 600^{o}C. At higher temperatures bubble evolution follows normal coarsening, i.e. the average size of bubbles increases and density decreases with increasing annealing temperature. Note that the small increase in bubble density between 750 and 800^{o}C probably is a result of the higher level of implanted helium in the specimen used for annealing (see calculated helium content at this temperature in Table 1 in [10]).

It is interesting to note that swelling (see last column in Table 1) at all temperatures is very close to that introduced during helium implantation (about $4.0*10^{-5}$ assuming that all implanted He atoms survived in a He-vacancy cluster). Thus one may conclude that He emission from bubbles at all temperatures is low

The calculations in the present work have been done to illustrate the capability of the grouping method. Thus to simplify calculations the implantation temperature is chosen to be 100^{o}C and the helium implantation level is considered to be equal to 40 appm in all specimens. Accordingly, the He implantation parameters used in our calculations are summarized in Table 2.

Table 2. The He implantation parameters in solution-annealed P7 used in the calculations

Helium generation rate, G_{He}	$2.0*10^{-3}$ appm/s
Implantation temperature	100^{o}C
Displacement rate during implantation, G_{NRT}	$5.0*10^{-7}$ dpa/s
Implantation time	$2.0*10^{4}$s
Displacement dose	$1.0*10^{-2}$ dpa
Helium implantation level	40 appm

The calculations have been performed in two steps:

1. Helium pre-implantation regime, which is described by the concurrent processes of Frenkel pair production and He implantation
2. Calculations of bubble evolution during thermal annealing at a given temperature to predict the microstructure obtained.

The initial conditions for the mobile defects and boundary conditions for the SDF for step 1 have the following form:

$$
\begin{aligned}
&C_v(t)_{|t=0} = C_{v0}, \\
&C_i(t=0)_{|t=0} = C_{He}(t)_{|t=0} = 0, \\
&f(x,m,t)_{|t=0} = C_{v0}\delta(x-1)\delta(m), \quad (x \geq 1), \\
&f(x=1,0,t) = C_v(t), \quad f(x=\infty,m,t) = 0.
\end{aligned}
\tag{27}
$$

In addition, it is assumed that the smallest clusters (x=1) are immobile and can be filled with up to 4 helium atoms (see e.g. Ref. [15-17]). Material parameters used in the calculations are given in Table 3.

Table 3. Parameters used in the calculations

Recombination fraction, ε_r	0.75
Effective displacement rates, $G_{NRT}(1-\varepsilon_r)$	$1.25 * 10^{-7}$ dpa/s
Helium generation rate, G_{He}	$2.0*10^{-3}$ appm/s
Recombination coefficients, $\mu_R = \mu_R^{He}$	$5.0*10^{+20}$ m^{-2}
Atomic volume, Ω	$1.15*10^{-29}$ m^{-3}
Vacancy diffusion coefficient, D_v pre-exponentional factor migration energy	 $8.0*10^{-05}$ m^2/s 1.40 eV
SIA diffusion coefficient, D_i pre-exponentional factor migration energy	 $8.0*10^{-06}$ m^2/s 0.15 eV
He atom diffusion coefficient, D_{He} pre-exponentional factor migration energy	 $8.0*10^{-06}$ m^2/s 0.15 eV
Dislocation density, ρ_d	10^{13} m^{-2}
He resolution energy, E_{res}	2.3 eV
Surface energy, γ	(3.4-1.4*T/1000) J/ m^2
Dislocation capture efficiency for vacancies, Z_v	1.00
Dislocation capture efficiency for SIAs, Z_i	1.25
Dislocation capture efficiency for He atoms, Z_{He}	0
Rate of radiation resolution, A	0
Surface diffusion coefficient, D_S pre-exponentional factor, $D^{(0)}$ migration energy	 $(1.6*10^{-6}$-$8*10^{-5})$ m^2/s 1.40 eV

Results

Cluster evolution during implantation

As mentioned above, the first step in the calculations is to use the set of equations for the SDF formulated above within the grouping method to calculate helium implantation at 100°C with the irradiation parameters given in Table 1. Since the implantation temperature is below recovery stage three, vacancies at this temperature are immobile. The evolution of He-vacancy clusters therefore is driven by the mobility of interstitial He and self interstitial atoms. The calculations are carried to a dose of 10^{-2} dpa where the He concentration reached a level of 40 appm. It is found that all He atoms are accumulated in clusters of the smallest size *x= 1*. The SDF obtained during the calculations is used as input to the subsequent calculations of cluster evolution during annealing at temperatures of 600° C and above.

Cluster evolution during annealing at 600°C

As can be seen from Table 1, helium bubbles have not been found in specimens annealed at 600° C for one hour. Thus, the calculations of annealing at this temperature could be used to test the efficiency of different mechanisms and parameters used for causing cluster evolution. The calculated results for the number density and average size of the clusters obtained for different values of the cluster mobility are presented in Figs. 1 and 2. The upper curves in Fig.1 correspond to the total number density of the clusters, and the bottom ones correspond to the number density of visible clusters, i.e. clusters with radius larger than 0.5 nm.

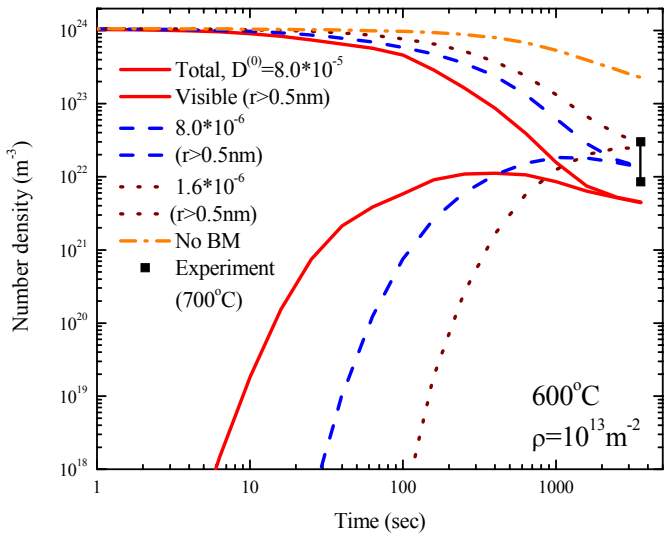

Fig. 1. Calculated time dependence of the bubble density obtained for annealing at 600°C at different magnitudes of bubble diffusivity.

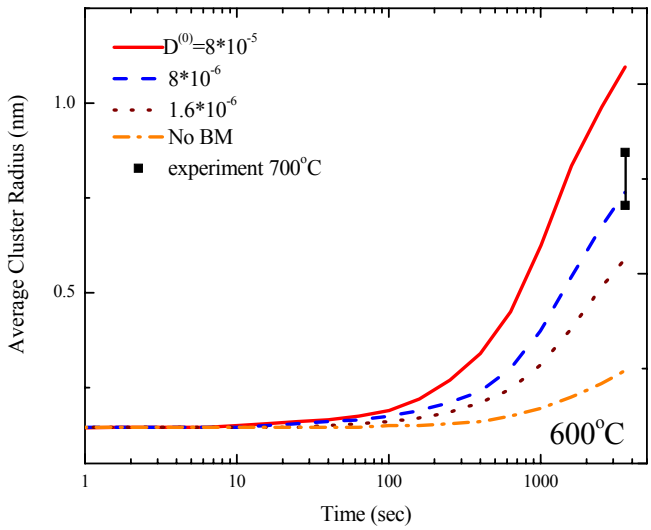

Fig. 2. Calculated time dependence of the average bubble radius obtained for annealing at 600°C with different values of bubble diffusivity.

It can be seen from the Figs. 1 and 2 that in the case where the cluster mobility is not taken into account (marked on the plot as “No BM”) there is very limited cluster evolution. This is related to the fact that without Brownian motion the driving force for cluster evolution is emission of He atoms from the clusters which is very inefficient at this temperature. Thus, one may conclude that cluster mobility under annealing is the main driving force for cluster evolution. As reference points on Fig. 1 and 2, the measured values of bubble density and size after annealing at 700°C are also presented. Comparing the calculated results with the reference points in Fig. 2, one may conclude the calculation results obtained for $D^{(0)} = 1.6*10^{-6} m^2 / s$ agrees with the observations since in this case the bubble size is too small to be detected by TEM.

The calculated size distribution functions of bubbles after annealing for one hour at 600°C for different values of cluster mobility are presented in Figs. 3a, 3b and 3c.

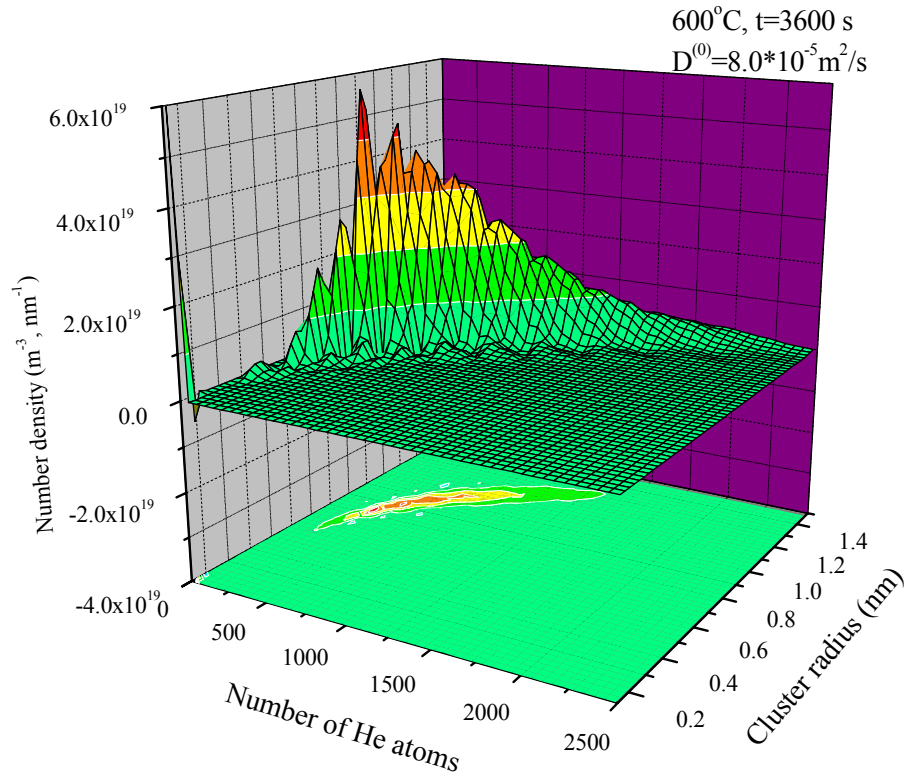

Fig. 3a. Size distribution function of gas bubbles for simulated annealing for one hour at 600°C with the pre-exponential factor equal to 8.0*10^{-5} m^2/s.

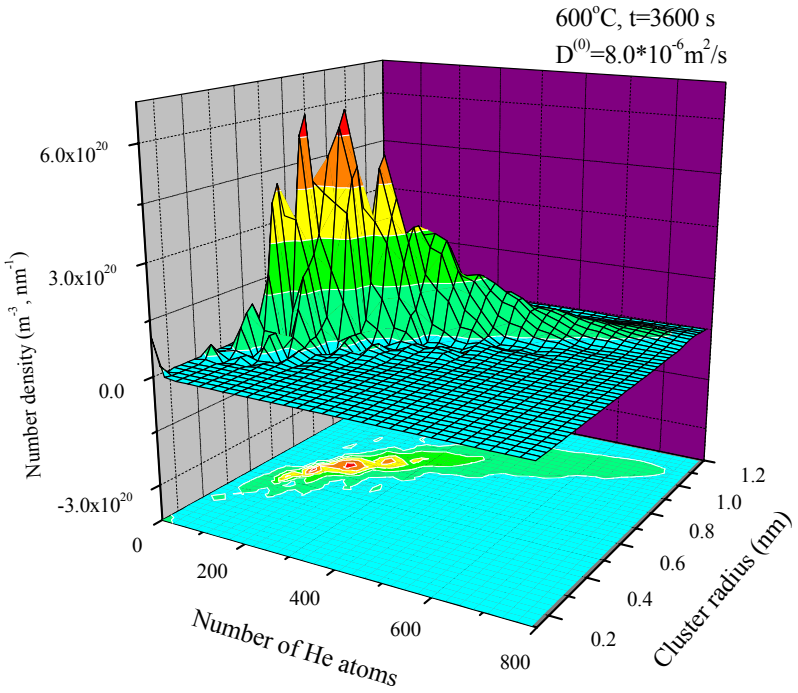

Fig. 3b. Size distribution function of gas bubbles for simulated annealing for one hour at 600°C with the pre-exponential factor equal to $8.0*10^{-6}$ m^2/s.

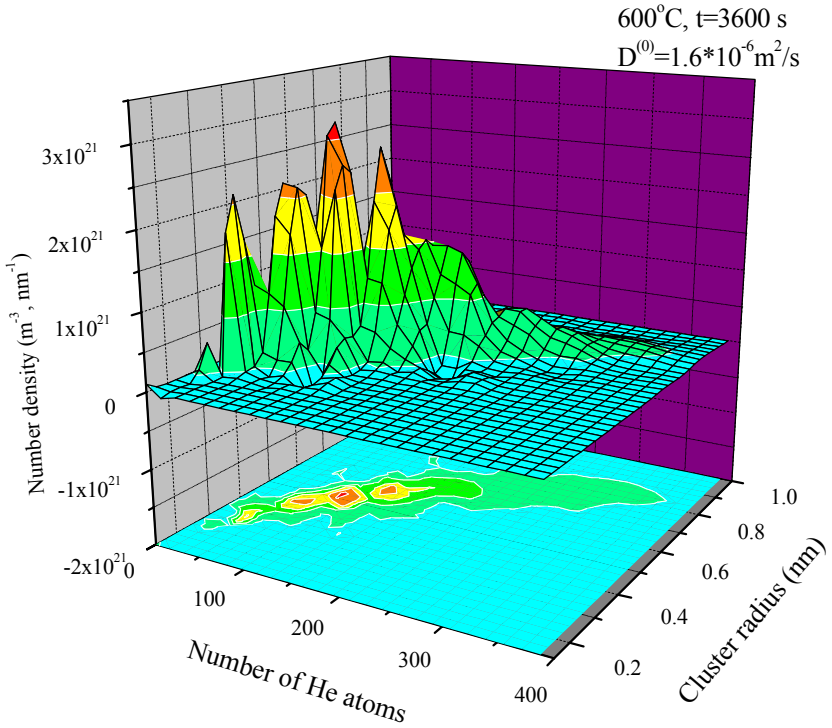

Fig. 3c. Size distribution function of gas bubbles for simulated annealing for one hour at 600°C with the pre-exponential factor equal to $1.6*10^{-5}$ m^2/s.

As can be seen from Fig. 3, the shape of the SDF in all cases is quite similar; all clusters are concentrated along a certain trajectory in *x,m*-space. Close analysis shows that along this trajectory, the gas pressure in the clusters is nearly constant, i.e. all clusters are over- pressurized with respect to the equilibrium value caused by surface tension ($2\gamma / r_{cl}$). Such a situation may be rationalized by taking into account that when coalescence of clusters is the main mechanism of cluster evolution, the total number of vacancies and He atoms accumulated in clusters are conserved keeping the ratio $< m > / < x >$ inside clusters close to a constant. This in turn leads to constant pressure inside the clusters. As a result, the mean cluster size does not follow the law $< r > \sim t^{1/5}$, which is predicted for the case when all bubbles are considered to be in equilibrium. The actual increase in bubble size is found to be slower (about $< r > \sim t^{1/8}$) because there is a lack of vacancies to produce a more rapid size increase. This shows that models for bubble evolution under annealing condition suggested in the past (see e.g. Ref. [3-6]), which considered the process as an evolution of equilibrium bubbles only, are not valid in the case under consideration. Note that a similar situation is likely to be valid at all annealing temperatures up to 900°C since, as pointed out above, the total volume of bubbles after annealing in all cases is close to that introduced in the crystal during helium implantation.

Note that the one-dimensional SDF, $f(x)$, which is normally measured with TEM, can be easily calculated by using the two-dimensional SDF by summation over the parameter *m*, $f(x) = \sum_m f(x,m)$.

An example of the one-dimensional SDF, which corresponds to the two-dimensional SDFs presented in Fig. 3, is presented in Fig. 4.

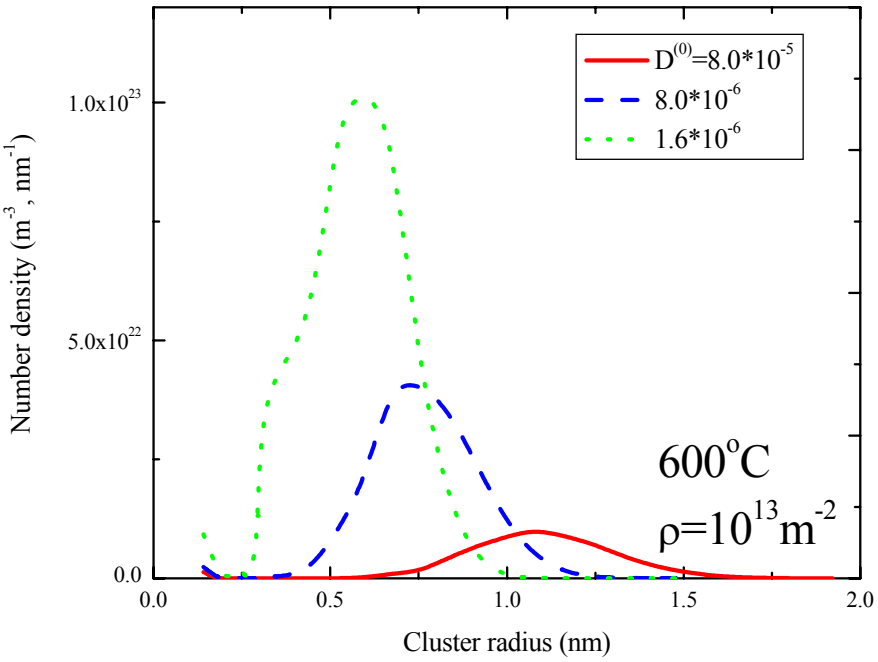

Fig. 4. One-dimensional size distribution function of gas bubbles, which corresponds to that presented on Fig. 3 calculated by summation over the parameter *m*, $f(x) = \sum_m f(x,m)$.

Cluster evolution during annealing at 700°C

Calculations of the He-vacancy cluster evolution during annealing at 700°C have also been performed for different values of the cluster diffusivity. The time evolution of SDF for $D^{(0)}$=8.0*10^{-6} m^2/s is presented in Figs. 5 for annealing times of 400 (a), 1600 (b) and 3600 (c) seconds. As can be seen from the plots, the evolution of bubbles exhibits the same trend as was found for an annealing temperature 600°C. The SDFs located in *x,m* – space follow a certain trajectory, which is the region where all clusters are over-pressurized.

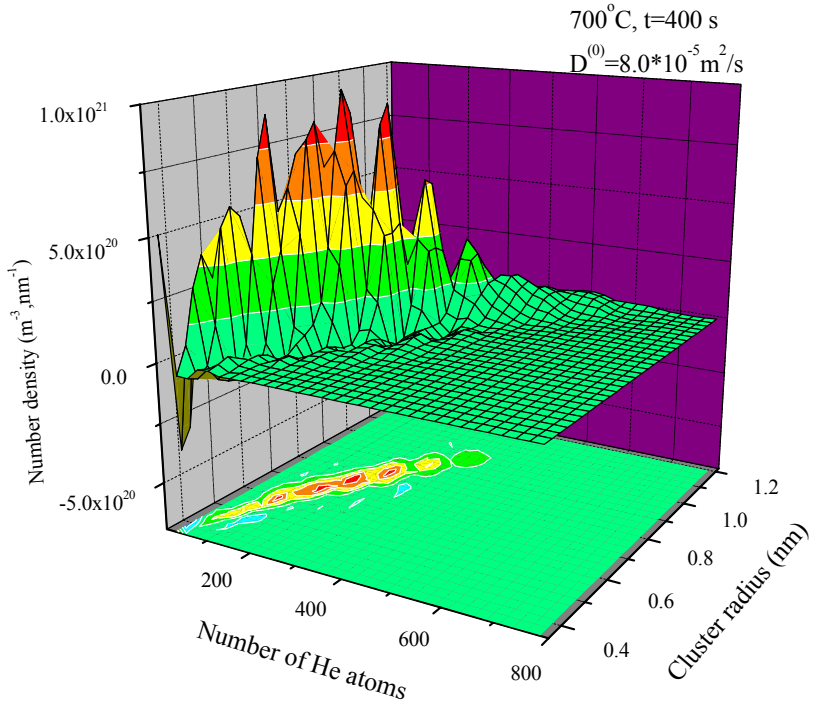

Fig. 5a. Size distribution function of gas bubbles at 700°C calculated under annealing for 400 sec with the pre-exponential factor equal to 8.0*10^{-6} m^2/s.

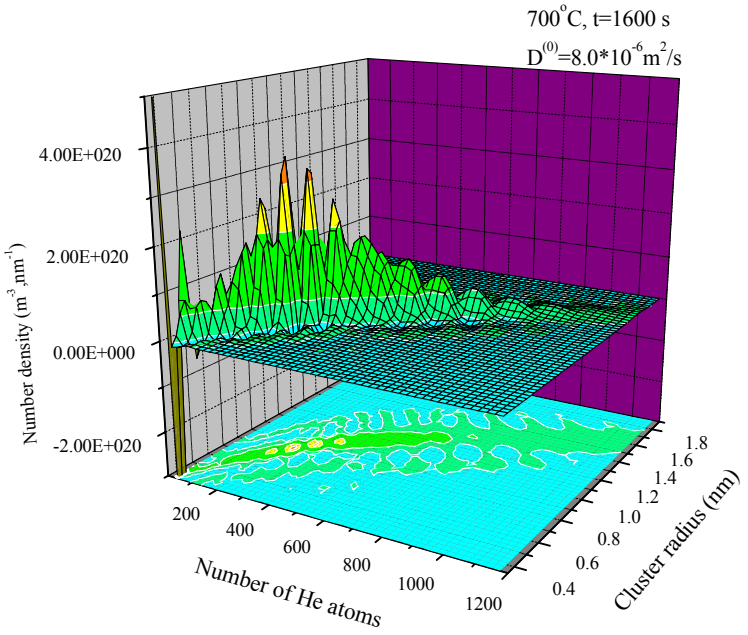

Fig. 5b. Size distribution function of gas bubbles at 700°C calculated under annealing for 1600 sec with the pre-exponential factor equal to $8.0*10^{-6}$ m^2/s.

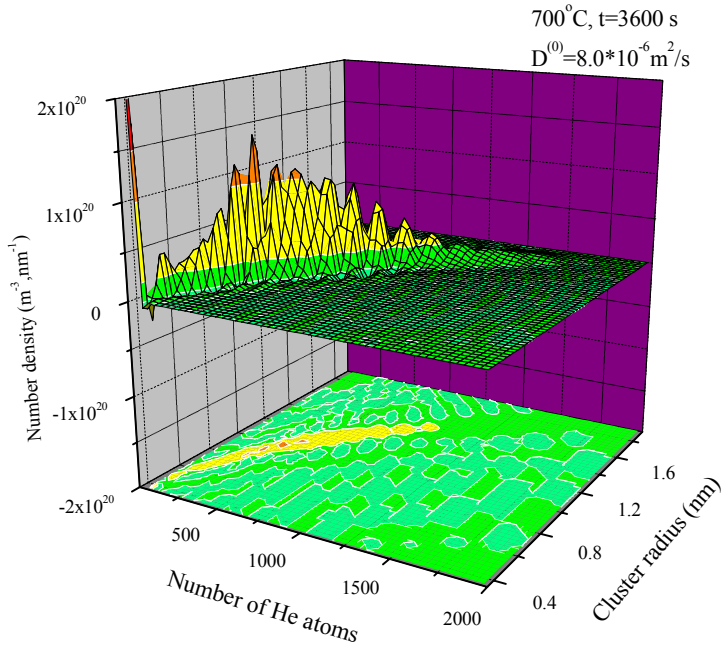

Fig. 5c. Size distribution function of gas bubbles at 700°C calculated under annealing for 3600 sec with the pre-exponential factor equal to $8.0*10^{-6}$ m^2/s.

The calculated results for number density and average size of clusters obtained with the different cluster nobilities are presented in Fig. 6 and 7. Similar to Fig. 1, the upper curves in Fig. 6 correspond to the total number of clusters, whereas the lower curves correspond to the density of visible clusters (r>0.5 nm). As can be seen from the plots the calculated results obtained with the smallest value of cluster diffusivity, ($D^{(0)}$=1.6*10^{-6}m^2/s), fit the experimental data for both the density of the clusters and their size. Thus, one can conclude that the calculated results obtained for $D^{(0)}$=1.6*10^{-6}m^2/s agree reasonably well with the experimental observations in the temperature range of 600-700^{0}C. The calculations of bubble evolution during annealing at temperatures 800 and 900^{0}C are still in progress.

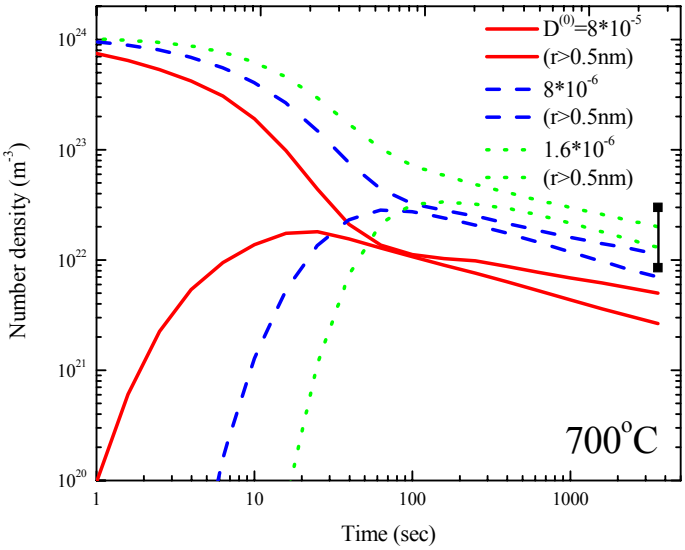

Fig. 6. Time dependence of the bubble density during annealing at 700^{O}C as calculated with different values of the bubble diffusivity.

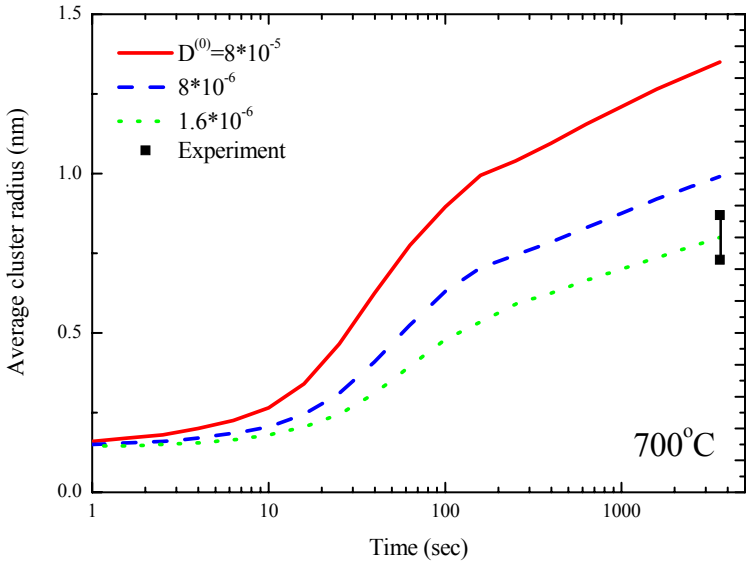

Fig. 7. Time dependence of the mean bubble radius during annealing at 700^{O}C as calculated with different values of the bubble diffusivity.

Conclusions

A grouping method for an approximate solution of two dimensional kinetic equations describing the evolution of point defect clusters has been developed that takes into account Brownian motion of the clusters. It can be used to describe gas-assisted nucleation of voids, bubbles or secondary phase precipitates. It may be shown that the method can be easily generalized for ME of higher dimensionality.

The method was used to describe bubble evolution taking place during annealing in helium implanted (40 appm) austenitic steel, were it was found that that Brownian motion of the clusters is the main mechanism driving He-vacancy cluster evolution during annealing in the case under consideration. Surface diffusion provides a mechanism for cluster mobility, which leads to reasonable agreement between the calculated results and experimental observations for bubble evolution, at least in a temperature range of 600-700^{0}C.

References

[1] S. I. Golubov, R. E. Stoller, and S. J. Zinkle, Fusion Materials Semiannual Progress Report for Period Ending December 31, 2002, DOE/ER-0313/33, U.S. Department of Energy, 155.
[2] S.I. Golubov, A. M. Ovcharenko, A. V. Barashev, and B. N. Singh, Philos. Mag. Series A. 81, No. 3 (2001) 643-658.
[3] E. E. Gruber, In: Radiation-Induced Voids in Metals, Eds. J. W. Corbet and L. C. Iannielo, USAEC-CONF.71061, Albany (1972) 663.
[4] G. W. Greenwood and M. V. Speight, J. Nucl. Mater. 10 (1963) 140.
[5] M. V. Speight, J. Nucl. Mater. 12 (1964) 216.
[6] E. E. Gruber, J. Appl. Phys. 15 (1967) 243.
[7] P. J. Goodhew and S. K. Tyler, Proc. of the R. Soc. of Lond. A377 (1981) 151.
[8] A. J. E. Foreman and B. N. Singh, J. Nucl. Mater. 141-143 (1986) 672.
[9] V. F. Chkuaseli, J. Nucl. Mater. 188 (1992) 258.
[10] R. E. Stoller and G. R. Odette, Radiation Induced Changes in Microstructure: 13th International Symposium (Part I), ASTM STP 955, Eds. F. A. Garner, N. H. Packan, and A. S. Kumar, ASTM, Philadelphia (1987) 371.
[11] R. Manzke, W. Jäger, H. Trinkaus, G. Crecelius, and R. Zeller, Solid State Communications 44, No. 4 (1982) 481.
[12] H. Trinkaus, Rad. Effects 78 (1983) 189.
[13] B. N. Singh and H. Trinkaus, J. Nucl. Mater. 186 (1992) 153.
[14] H. Trinkaus and B. N. Singh, J. Nucl. Mater. 323 (2003) 229.
[15] Van Veen, Mater. Sci. Forum 15-18 (1987) 3.
[16] W. D. Wilson, C. L. Bisson, and M. I. Baskes, Phys. Rev. B 24 (1981) 5616.
[17] B. Adams and W. G. Wolfer, J. Nucl. Mater. 106 (1989) 235.
[18] D. R. Olander, Fundamental Aspects of Nuclear Reactor Fuel Elements, TID-26711-P1, (1976) 236.

10. DOSIMETRY, DAMAGE PARAMETERS, AND ACTIVATION CALCULATIONS

IMPACT OF TRANSMUTATION ISSUES ON INTERPRETATION OF DATA OBTAINED FROM FAST REACTOR IRRADIATION EXPERIMENTS—L. R. Greenwood and F. A. Garner (Pacific Northwest National Laboratory)*

OBJECTIVE

The object of this effort is to determine the effect of in-reactor spectral variations on displacement effectiveness and transmutation/dpa ratio for typical materials of interest to the fusion community.

SUMMARY

The subject of fission-fusion correlation is usually cast in terms of reactor-to-reactor differences, but recently the fusion community has become aware of the impact of differences within a given surrogate facility, especially in constant time experiments when different dose levels are attained in different positions of one reactor. For some materials, it is not safe to assume that in-reactor spectral variations are small and of no consequence.

This point is illustrated using calculations for fusion-relevant materials that were irradiated in the Fast Flux Test Facility – Materials Open Test Assembly (FFTF-MOTA) over a wide range of in-core and out of core positions spanning more than two orders of magnitude in dpa rate. It is shown that although both the neutron spectrum and flux changes, the spectral effectiveness factor, dpa/10^{22} n/cm^2 (E > 0.1 MeV), remains remarkably constant over this range. The transmutation rate per dpa varies strongly with reactor position, however.

PROGRESS AND STATUS

Introduction

The use of surrogate irradiation facilities, especially fission reactors, to simulate fusion environments requires that attention be paid to the trade-offs and penalties associated with the differences in neutron spectra and fluxes between the two environments. A variety of mixed spectrum reactors, such as the High Flux Isotope Reactor (HFIR), and fast reactors, such as FFTF and the Experimental Breeder Reactor (EBR- II) have been used to simulate fusion reactor environments. Although these facilities have very different neutron spectra, the concept of displacements per atom (dpa) has generally been very successful in correlating material effects between different reactors. However, some caution is needed since transmutation effects can be very different not only between facilities, but more importantly within a given reactor environment due to neutron spectral variations. Frequently, data are derived from various positions in a given reactor, each at a different dpa rate. If the radiation-induced property change of interest depends not only on the accumulated dpa level, but also on the dpa rate and/or transmutation-induced changes in composition, it is not valid to treat the data derived from such “constant time” experiments as representing the response to a single variable. For instance, it has recently been shown that constant time FFTF-MOTA experiments on void swelling of Fe-Cr-Ni alloys which do not transmute strongly, are significantly impacted by differences in dpa rate [1, 2]. In some cases the effect of dpa rate can overwhelm the impact of the dpa [3]. However, other fusion-relevant materials such as Cu, W, Re and V are known to transmute strongly, even in fast reactor spectra, requiring that the influence of spectral variations be examined more closely.

We have previously used the concept of the spectral effectiveness factor to characterize the neutron spectra. This factor is simply the number of dpa produced by the neutron fluence above 0.1 MeV in units

---

*Pacific Northwest National Laboratory (PNNL) is operated for the U.S. Department of Energy by Battelle Memorial Institute under contract DE-AC06-76RLO-1830.

of 10^{22} n/cm^2. However, in irradiations involving materials with relatively high thermal or epithermal neutron cross sections, transmutation may be so sensitive to small changes in the neutron spectrum that transmutation effects may be significant even though the spectral effectiveness factor shows little change. This point is easily illustrated by comparisons of spectral effectiveness factors with transmutation rates for various materials irradiated at different locations in FFTF-MOTA assemblies.

Results and Discussion

Irradiations in FFTF

MOTA irradiation experiments were conducted in FFTF from 1983 through 1992. Calculations discussed in this paper were derived from reactor dosimetry measurements performed in the MOTA-2A experiment which was conducted from January 1990 to March 1991 for a total of 299.7 effective full power days (EFPD) at an average power level of 291 MW and for the MOTA-2B experiment from May 1991 to March 1992 for 203.3 EFPD. Irradiation histories for all of the FFTF experiments have been previously published [4]. Reactor dosimetry capsules were placed at various elevations in all of the MOTA experiments. Each capsule contained a number of monitors that were analyzed to determine reaction rates which were used to determine the neutron fluence spectrum at each point in the MOTA assemblies. The measurements and adjusted neutron spectra for the MOTA-2A and -2B experiments were published previously [5, 6]. The adjusted neutron fluence spectra were used to determine the neutron fluences, dpa, and transmutation values shown in this paper. Neutron spectra are shown in Figure 1 for above core, midplane, and below core positions in the MOTA-2A experiment. The neutron spectra are softer at the out of core positions and the increased neutron flux in the epithermal region can produce enhanced transmutation rates, as discussed later. The neutron spectra in the below core (-62.9 cm) and above core (+66.6 cm) locations have more lower-energy neutrons, compared to that of in-core locations, especially in below core locations. This difference produces essentially the same dpa per fast neutron but very different transmutation rates in each location.

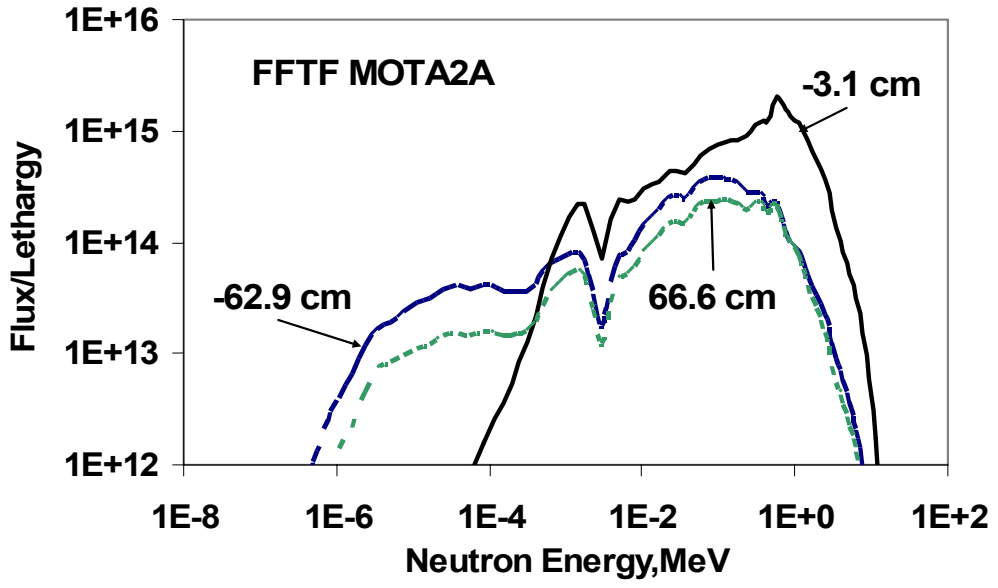

Figure 1. Neutron flux spectra are shown at the below core (-62.9 cm), level 3 (-3.1 cm), and above core (66.6 cm) positions in the FFTF MOTA-2A and 2B assemblies. Note the increased epithermal flux at out-of-core positions, especially below core.

Transmutation and spectral effectiveness ratios

The dpa in 304 stainless steel as well as spectral effectiveness factors, defined by the ratio of the dpa produced by the neutron fluence above E > 0.1 MeV are shown for V, Cu, W and 304 stainless steel in Figure 2. Note that although the dpa rates are changing nearly two orders of magnitude, as shown in Figure 3, the spectral effectiveness factor is rather constant. The scatter in the ratio is most likely due to uncertainties and variations in the local neutron fluence spectra. The dpa values for various elements depend on the threshold energies and generally decrease with the mass of the recoil atom.

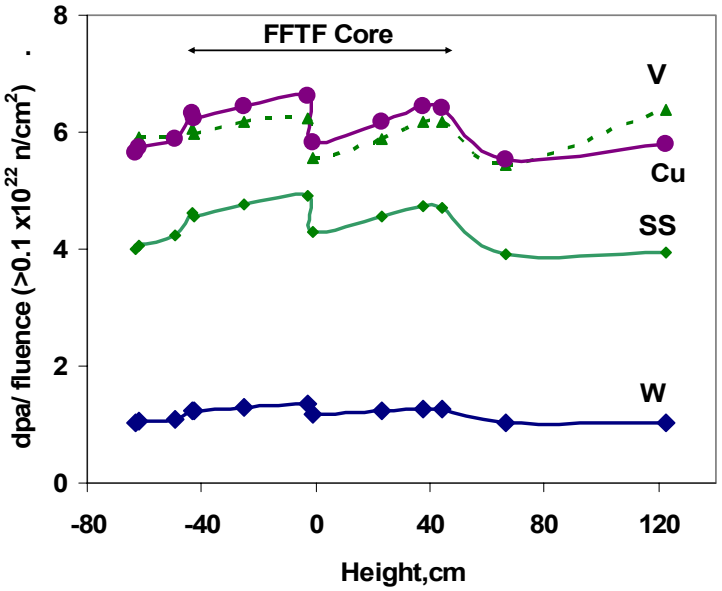

Figure 2. The spectral effectiveness factors for 304 stainless steel, V, Cu, and W in terms of dpa per 10^{22} n/cm^2 (E > 0.1 MeV) as a function of height in FFTF MOTA-2A. Note that the ratio is nearly constant in spite of significant dpa, flux and spectral changes.

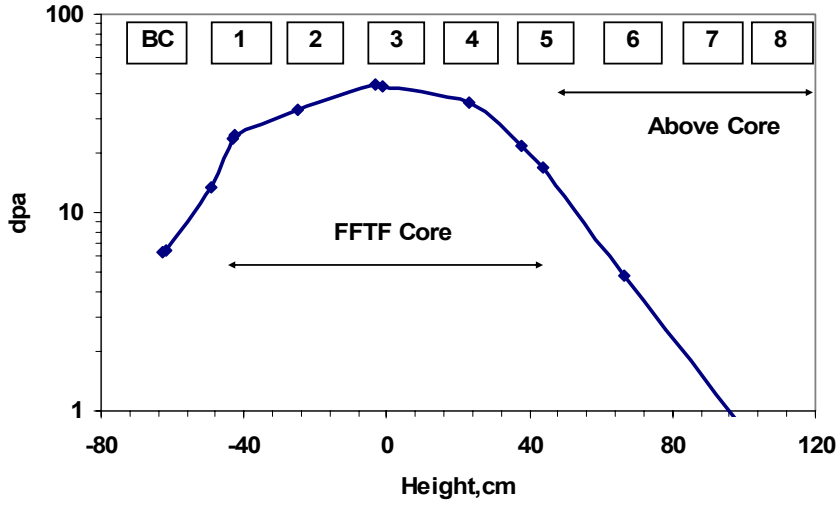

Figure 3. Dpa variation for 304 stainless steel as a function of axial position in MOTA-2A. The MOTA capsule positions where irradiations are conducted in, below and above core are shown at the top of the figure.

Transmutation rates were calculated by integrating neutron activation cross sections from ENDF/B-VI over the adjusted neutron flux spectra, such as those shown in Figure 1, as determined by neutron dosimetry measurements [5, 6]. The transmutation rates show significant differences at different elevations in the MOTA assemblies, as shown in Figures 4-5. This effect is most pronounced for elements that have significant epithermal neutron cross sections for transmutation, as shown for the transmutation of Re to Os and the burnup of boron in Figure 4 (top). Similar dramatic differences are shown for the transmutation of V to Cr and W to Re in Figure 4 (bottom). The transmutation effects are shown as a function of dpa in Figure 5 which shows that samples having the same dpa exposure can have very different levels of transmutation. Figure 6 shows that the He to dpa ratio for the alloy Fe-15Cr-16Ni similarly shows a significant difference between the below core and above core positions due to the extra helium produced by the well-known Ni-58, Ni-59 reaction series [7], arising from the increase of epithermal neutrons in the below core position.

Impact of Transmutation on the Interpretation of Materials Experiments

The impact of transmutation on materials experiments must be carefully evaluated since transmutation can lead to significant changes in materials that may well be more important with respect to a material property than the displacive effects of irradiation. Such effects have been shown in previous publications for Cu [8, 9], V [10, 11], Re [12], W [13], Mo and others [14, 15]. In some cases such as in V and Re, the transmutation leads to significant changes in lattice parameter, obscuring accurate measurement of void swelling. In another case, the production of Cr in V leads to an acceleration of swelling relative that of pure V.

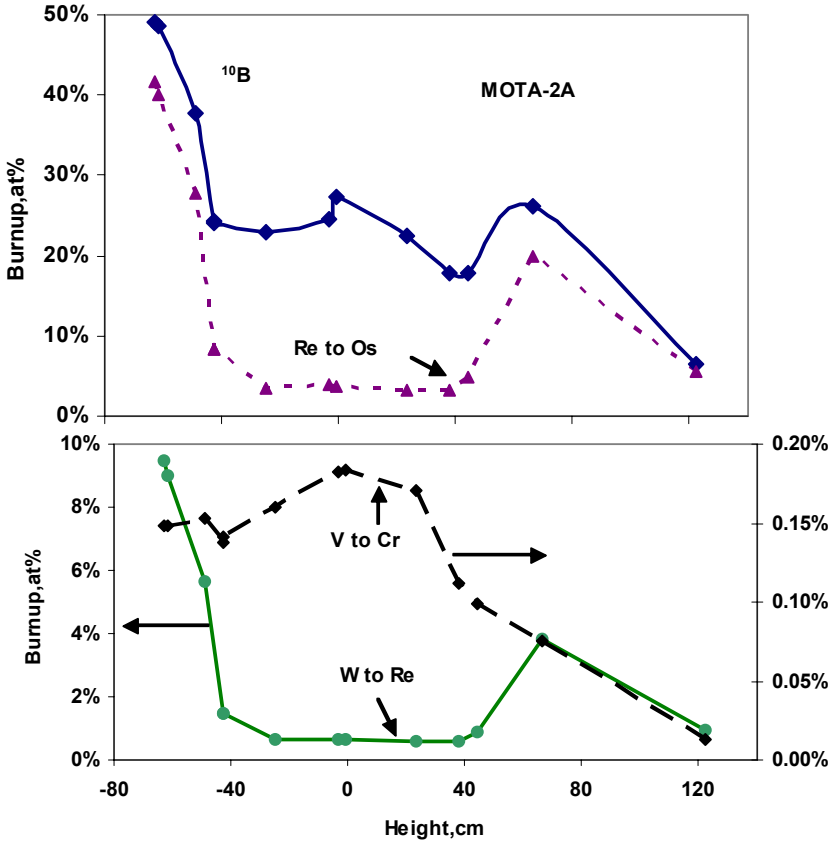

Figure 4. Burnup of ^{10}B and transmutation of V to Cr, Re to Os, and W to Re and Ta as a function of height in the FFTF MOTA 2A experiment.

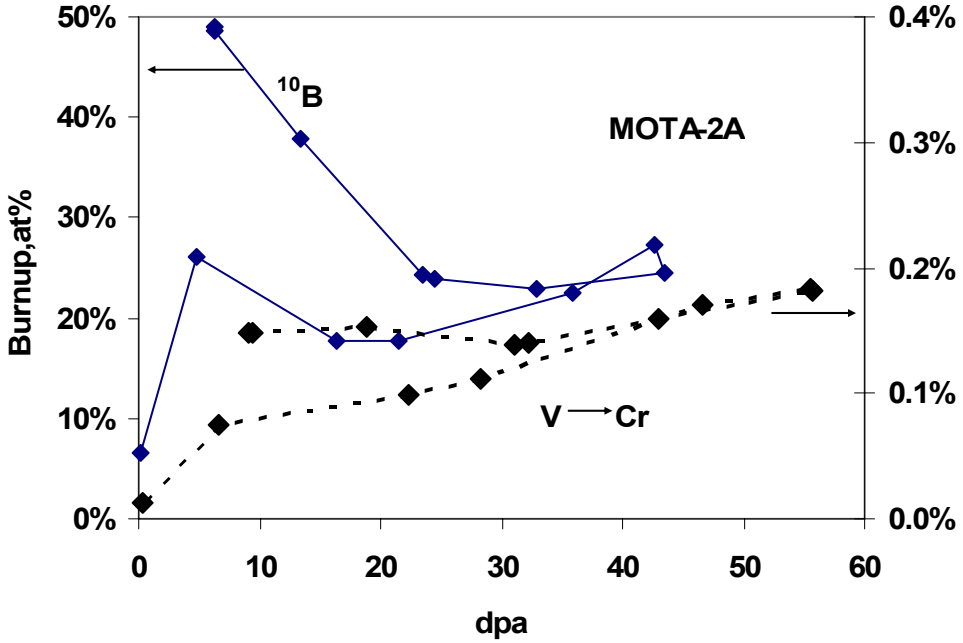

Figure 5. Burnup of ^{10}B and transmutation of V to Cr as a function of dpa in the FFTF MOTA 2A experiment. For boron the dpa level used is that of the stainless steel in which the boron was dissolved.

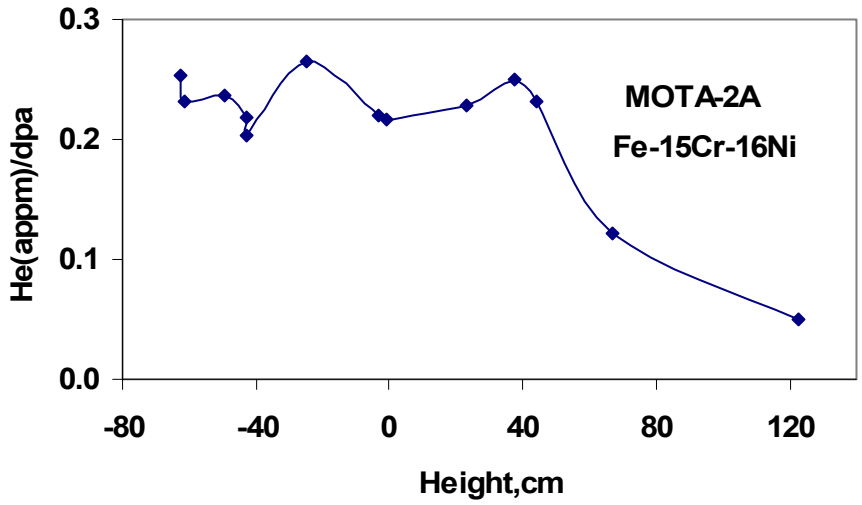

Figure 6. He/dpa ratio for Fe-15Cr-16Ni as a function of height in the FFTF MOTA- 2A experiment. The increased helium generation rate at below core positions, compared with that above core, arises from the ^{59}Ni reaction.

In other cases the effect of two spatially dependent variables such as dpa rate and transmutation rate can compete in opposite directions so as to obscure the action of either one. A good example is provided in another paper concerning swelling of simple Fe-Cr alloys [16]. Whereas a strong effect on swelling of dpa rate differences between in-core regions of EBR-II and FFTF was previously observed on swelling of Fe-Cr binary alloys, no effect of dpa rate was observed when the experiment was conducted only in FFTF [17, 18]. In this case the progressive spectral softening near the edge of the FFTF core leads to lower helium generation rates, unlike the behavior shown in Figure 6 for nickel-bearing alloys. Therefore, the tendency for lower dpa rates to shorten the transient regime of swelling is countered by the concurrent lower helium generation rates, producing an apparent independence of swelling on dpa rate.

Conclusions

Consequently, caution is required in the interpretation of experiments conducted at different dpa rates in the same reactor since transmutation effects may invalidate the assumption that the dpa and dpa rate are the only significant variables operating in such experiments.

Acknowledgements

This work was supported by the Office of Fusion Energy, U.S. Department of Energy, under Contract DE-AC06-76RLO 1830.

References

[1] T. Okita, N. Sekimura, F. A. Garner, L. R. Greenwood, W. G. Wolfer, and Y. Isobe, Neutron-Induced Microstructural Evolution of Fe-15Cr-16Ni Alloys at ~400°C During Neutron Irradiation in the FFTF Fast Reactor, 10th International Conference on Environmental Degradation of Materials in Nuclear Power Systems – Water Reactors (2001), CD format.

[2] T. Okita, N. Sekimura, T. Sato, F. A. Garner, and L. R. Greenwood, The Primary Origin of Dose Rate Effects on Microstructural Evolution of Austenitic Alloys during Neutron Irradiation, J. Nucl. Mater. 307-311 (2002) 322-326.

[3] F. A. Garner, N. I. Budylkin, Yu. V. Konobeev, S. I. Porollo, V. S. Neustroev, V. K. Shamardin, and A. V. Kozlov, The Influence of DPA Rate on Void Swelling of Russian Austenitic Stainless Steels, 11th International Conference on Environmental Degradation of Materials in Nuclear Power Systems – Water Reactors (2003), CD format.

[4] A. M. Ermi, L. R. Greenwood, and H. L. Heinisch, Irradiation Parameters for the FFTF Materials Open Test Assemblies from 1983 to 1992, Fusion Reactor Materials Semiannual Progress Report, DOE/ER-0313/18.

[5] L. R. Greenwood and L. S. Kellogg, Neutron Dosimetry for the MOTA-2A Experiment in FFTF, Fusion Reactor Materials Semiannual Progress Report, DOE/ER-0313/12 (1992) 49-53.

[6] L. R. Greenwood and L. S. Kellogg, Neutron Dosimetry for the MOTA-2B Experiment in FFTF, Fusion Reactor Materials Semiannual Progress Report, DOE/ER-0313/16 (1994) 49-53.

[7] L. R. Greenwood, D. W. Kneff, R. P. Skoronski, and F. M. Mann, J. Nucl. Mater. 122-123 (1984) 1002.

[8] F. A. Garner, H. R. Brager, and K. R. Anderson, Neutron-Induced Changes in Density and Electrical Conductivity of Copper Alloys at 16 to 98 dpa and 430°C, J. Nucl. Mater. 179-181 (1991) 250-253.

[9] D. J. Edwards, F. A. Garner, and L. R. Greenwood, The Influence of Transmutation, Void Swelling and Flux/Spectra Uncertainties on the Electrical Properties of Copper and Copper Alloys, J. Nucl. Mater. 212 (1994) 404-409.

[10] F. A. Garner, L. R. Greenwood, B. A. Loomis, S. Ohnuki, and N. Sekimura, Influence of Flux-spectra Differences on Transmutation, Dimensional Changes and Fracture of Vanadium Alloys, J. Nucl. Mater. 233-237 (1996) 406-410.

[11] S. Ohnuki, H. Takahashi, K. Shiba, A. Hishinuma, J. E. Pawel, and F. A Garner, Influence of Transmutation on Microstructure, Density Change and Embrittlement of Vanadium and Vanadium

Alloys Irradiated in HFIR, J. Nucl. Mater. 218 (1995) 217-223.
[12] F. A. Garner, M. B. Toloczko, L. R. Greenwood, C. R. Eiholzer, M. M. Paxton, and R. J. Puigh, Swelling, Irradiation Creep and Growth of Pure Rhenium Irradiated with Fast Neutrons at 1030-1330°C, J. Nucl. Mater. 283-287 (2000) 380-385.
[13] J. Megusar and F. A. Garner, Response of Dynamically Compacted Tungsten to Very High Fluence Neutron Irradiation at 423-600°C in FFTF, J. Nucl. Mater. 258-263 (1998) 940-944.
[14] F. A. Garner and L. R. Greenwood, Recent Progress in Fusion Reactor Materials Studies: Focus on Transmutation and Radioactivation Aspects, Invited Overview Paper for Materials Transactions, Japan Institute of Metals 34 No. 11 (1993) 985-998.
[15] F. A. Garner and L. R. Greenwood, Neutron Irradiation Effects on Fusion or Spallation Structural Materials: Some Recent Insights Related to Neutron Spectra, in Radiation Effects and Defects in Solids 144 (1998) 251-283.
[16] F. A. Garner, L. R. Greenwood, T. Okita, N. Sekimura, D. S. Gelles, and W. G. Wolfer, Synergistic Influence of Displacement Rate and Helium/dpa Ratio on Swelling of Fe-(9, 12)Cr Binary Alloys in FFTF at ~400°C, accepted for publication in J. Nucl. Mater., Proceedings of ICFRM-11.
[17] F. A. Garner, M. B. Toloczko, and B. H. Sencer, Comparison of Swelling and Irradiation Creep Behavior of fcc-Austenitic and bcc-Ferritic/Martensitic Alloys at High Neutron Exposure, J. Nucl. Mater. 276 (2000) 123-142.
[18] B. H. Sencer and F. A. Garner, Compositional and Temperature Dependence of Void Swelling in Model Fe-Cr Base Alloys Irradiated in EBR-II, J. Nucl. Mater. 283-287 (2000) 164-168.

11. MATERIALS ENGINEERING AND DESIGN REQUIREMENTS

No contributions.

12. IRRADIATION FACILITIES AND TEST MATRICES

ASSEMBLY OF THE MFE-RB-17J EXPERIMENT—A. L. Qualls, K. R. Thoms, D. W. Heatherly, and R. G. Sitterson (Oak Ridge National Laboratory)

OBJECTIVE

The objective of this work is to irradiate mostly vanadium alloy specimens in direct contact with lithium at temperatures of 450°C, 600°C and 700°C in a europium-shielded RB position of the High Flux Isotope Reactor (HFIR). Some steel and ceramic specimens are included but are isolated from the primary lithium bath.

SUMMARY

The 17J experiment is currently in the final stages of assembly in preparation for irradiation in a shielded RB position. The basic features of the design and assembly process are described. The specimen holders were loaded with specimens, filled with lithium, and then assembled into the experiment capsule, which will soon be connected to the control instrumentation.

PROGRESS AND SUMMARY

Design Description

In the MFE-RB-17J irradiation experiment three axially stacked specimen holders are contained within a common inner containment housing, which is itself contained in an outer containment housing. Figure 1 shows the arrangement of the inner housing. The two upper holders are made from the molybdenum alloy TZM and the lower holder is made from stainless steel. The holders are designed to irradiate three sets of metallurgical and ceramic test specimens in lithium baths at 700°C, 600°C and 450°C, in order from top to bottom within the experiment.

The holders are axially separated and loosely held together by stainless steel spacers, which are approximately 2-cm in length. Nine thermocouples and four temperature control gas lines, which are 0.020” in diameter, are passed from the top of the experimental region past the holders through axial grooves in the outer surface of the holders. Three thermocouples are assembled into a group at the bottom of each specimen holder and inserted upward into a thermocouple well that extends from the base of the holder into the specimen assembly and lithium bath.

Assembly

The test specimens were grouped by layer into vanadium baskets that fit inside each specimen holder over the holder thermocouple well. The baskets consist of a base, an outer cylindrical foil and a top cap, all of which are perforated to allow lithium to flow unobstructed through the specimens. Each specimen holder was assembled by loading the specimens into the specimen basket one layer at a time according to a pre-planned specimen loading arrangement. A separation disk was inserted after each specimen layer to ensure that specimens do not shift downward during transportation and operation. After the specimens were loaded into the basket the top cap was installed onto the top of the basket outer cylinder and tack welded into place.

The internal volumes of the holders and the total volume of the specimen basket assembly were carefully measured to determine the amount of lithium required to cover the top of the specimens when in the holder. The lithium level is carefully controlled so that the resulting pressure increase due to the change in volume of the lithium during operation will not cause the sealed specimen holders to fail.

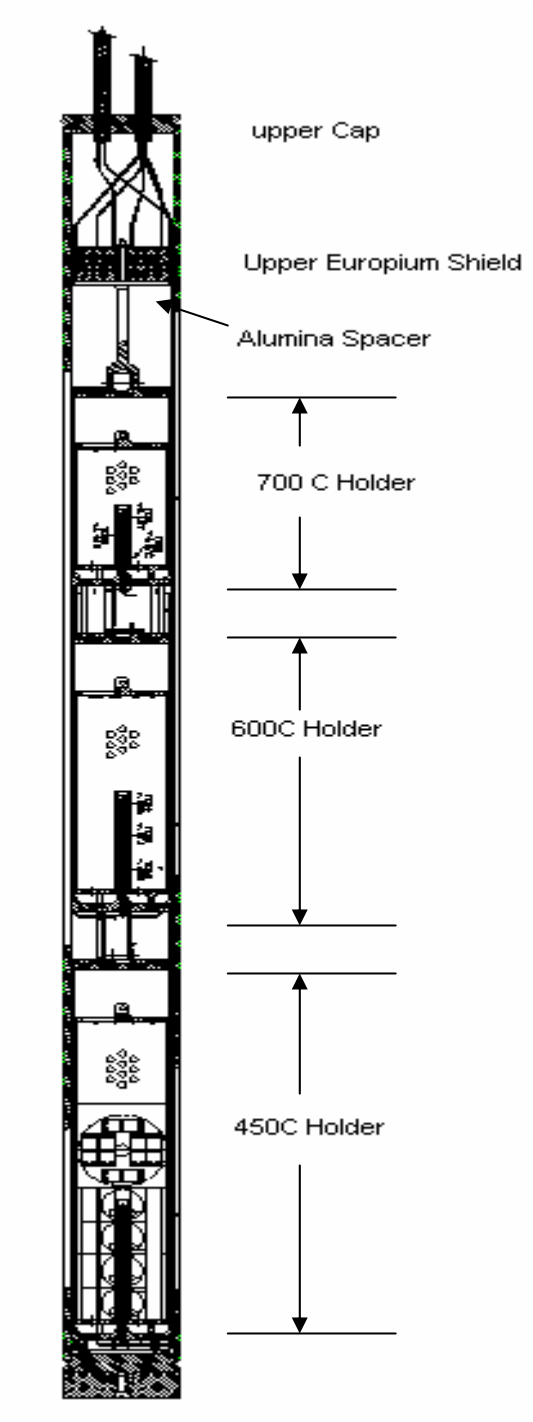

Figure 1. View of the MFE-RB-17J inner housing containment showing three specimen holders stacked axially and shielded by an upper europium shield. The inner housing is sealed with a welded top cap and the instrument leads are passed through penetrations which are sealed with specially designed braze configurations.

Once the amount of lithium required for each holder was determined, the holders, specimen baskets and the lithium were loaded into an argon-filled glove box which contained a specially fabricated, electrically heated furnace. Each holder was loaded into the furnace and the required amount of solid lithium was dropped into the holder. The holder and lithium were heated by controlling the electrical current flowing through a pair of heaters in the furnace until the lithium temperature was approximately 300°C, the point at which the lithium will wet the specimen surfaces as they are slowly lowered into the holder.

The furnace is equipped with a fixture for carefully lowering the specimen basket assembly into the molten lithium because it is important to prevent the lithium from being forced upward along the inner surface of the holder and contaminating the holder sealing cap welding surfaces. After the specimen baskets were successfully loaded into the holders, they were transferred to and welded in a separate atmospherically controlled welding glovebox. The holders were evacuated and backfilled with helium at one atmosphere of pressure prior to the installation and welding of the sealing caps.

The three completed specimen holders were assembled into a loosely connected stack and the experimental capsule was assembled around it. Instrumentation leads were routed from the top of the experimental assembly, through penetrations in the outer and inner housing caps to their termination points below the three specimen holders. The inner housing was inserted over the specimen holders and instrument leads from the bottom of the assembly and the inner housing upper cap was welded in place. The instrument leads were brazed into the upper cap penetrations using a specially designed brazing configuration that ensures braze material completely encases the leads in the penetration over a length of approximately 1 cm. The outer capsule housing was assembled over the inner capsule assembly and the second set of penetrations were sealed creating a third containment around the lithium in the experiment.

Operation

The assembled capsule will be operated in a europium-shielded RB position. The capsule and liner will generate approximately 65 kilowatts of heat due to nuclear interactions during normal steady state operation. The heat is removed from the capsule outer containment by reactor primary coolant water flowing over its outer surface at a rate of approximately 20 GPM.

The temperatures of the three holders are controlled independently by adjusting the thermal conductivity of the mixtures of inert gases flowing between the holders and the inner housing, which effectively controls the temperature difference from the holder to the inner housing. Gas supply lines can feed helium, neon or argon or a mixture of either helium and neon or helium and argon to the plenums below the three holders. Gas from lower holders become part of the mixture for upper holders, so while the temperature of the zones can be independently controlled, they are dynamically coupled. The complexity of the temperature control system makes it difficult to automatically control the holder temperatures, therefore the temperature control for the experiment will be performed manually by an operator.

A helium gas supply line, referred to as a Purge line, is routed to the lower holder lower plenum at the base of the inner housing. Helium flows through this line during the experiment passing upward past the specimen holders and out an effluent line open at the top of the inner containment. The purge line remains open at all times and the flow is increased in response to detected off-normal operating conditions while all other gas flows are stopped, guaranteeing that holder temperatures decrease.

Gas flow transmitter and control valves (FTCVs) in the Materials Irradiation Facility No. 5 (MIF5) Instrument Cabinet regulate the gas flow rate from pressurized sources through the gas supply lines. The use of neon and argon can be selected independently for the three holders at the instrument cabinet. If helium is to be mixed with the neon or argon, then this mixing occurs at the instrument cabinet.

The maximum amount of flow that can be achieved through a gas line is dependent upon the FTCV design limit (200 SCCM) unless the flow resistance through the gas supply line is too large to permit full FTCV flow for the available pressure differential. Flow testing suggests that flow restriction is not a significantly limiting factor for the lines used in the experiment.

Separate lines supply helium to the region between the inner and outer housing and instrument air to the experimental region above the outer housing upper bulkhead.

Temperature Control

Operating temperatures of the holders are determined by the amount of heat generation within capsule components (which is position and material dependent), the size of the gas gaps between the holders and housings, and the thermal conductivity of the gases in those gaps. The dimensions that determine the size of the gas gap between the specimen holder and the inner housing were based on conservative estimates of the heat generation rates within capsule components. It is planned to operate the experiment with neon and helium mixtures, however if neon cannot produce the desired temperature then argon will be substituted.

The lower specimen holder has the lowest target temperature (450°C). Because the experiment is doubly contained in stainless steel containment housings, experience suggests that it may be difficult to achieve this target temperature. The difficulty in achieving low temperatures is compounded by the fact that molybdenum specimen holders expand less than the stainless steel inner housing as temperatures are increased. This causes the temperature control gas gap for molybdenum holders to actually increase in size as the experiment begins operation. Also, molybdenum suffers from irradiation induced embrittlement when irradiated at 450°C. Because of these considerations the 450°C specimen holder is made of stainless steel with a cold (room temperature) radial gas gap of approximately .002”, which is as small as it can be and still ensure successful assembly.

Heat generation within capsule components throughout the HFIR cycle evolves through a repeatable pattern. The amount of heat produced in those components near the reactor mid-plane (600°C holder) will remain reasonably constant over the course of a cycle, while the amount of heat generated in those capsule components near the end of the experimental region (450°C and 700°C holders) will increase throughout the cycle. In order to maintain a constant temperature within the holders at the ends of the experimental region the gas mixture must gradually become more conductive, that is richer in helium. The thermal conductivity of the gas mixture in the centrally located temperature zones must remain more consistent throughout the cycle. Because the three holders are coupled, periodic gas mixture adjustments will be required in each zone. These adjustments will occur approximately once a day initially but will increase in frequency during the final two or three days of the 22 day cycle.

MFE-RB-17J Specimen Loading List

17J 700°C Level #1 (Begin approximately 12 cm above reactor mid-plane)

DFMB
UN12, UB05, UB12, UB13, UN05, UN13

Vanadium Envelopes
7-1, 7-2, 7-3

Tensile bundles
UY25-UY13, UT25-UT14, UV29-UV10, GK35-BLANK, US10-US29, GN15-GK28, UF09-UG11, UP08-UP33, FKB4-BLANK, FA27-FA26, FKH1-FKH0, FG12-BLANK, T006-TA99, TN90-BLANK, T397-TA90, AV46-BLANK, UR23-UR09, UB48-UE08, TY96-BLANK, TV92-BLANK, FB27-FB14

17J 700°C Level #2 (Begin approximately 14 cm above reactor mid-plane)

Tensile bundles
UM08-UH11, T190-T199, UC06-BLANK, FHF3-FHF2, FF14-FD12, TB99-TB90, TR90-BLANK, TT97-TT90, TX97-TX90, FA42-BLANK,

TEM Tubes
26, 31, 19, 28, 13, 10, 27, 18, 8, 9

Vanadium envelopes
7-4, 7-5, 7-6

Ceramic specimen holders – 3A, 3B

70.1260g total mass of loaded basket

17J 600°C Level #1 (Begin approximately 1 cm below reactor mid-plane)

Tensile Bundles
UC-O4-BLANK, US09-US24, UM07-UN04, UB42-UP04, UV05-UV24, FA36-BLANK, TR86-BLANK, UY06-UY20, UT20-UT09, FB22-FB10, TY80-BLANK, UP19-UP28, FHA5-FHG6, TV86-BLANK, T003-BLANK, TX88-TX89, TT80-BLANK, GK14-BLANK, FB06-BLANK, FKD9-FHG7, TA88-TA80, GK24-BLANK, TB80-TB89, FF09-BLANK, T180-BLANK, UF04-UF07

17J 600°C Level #2 (Begin approximately 2 cm above reactor mid-plane)

Tensile Bundles
T381-BLANK, AV45-BLANK, FK65-BLANK, UR16-UR07

TEM Tubes
7, 12, 23, 30, 6, 17, 24, 5, 25, 16

DFMB
UB11, UN11, UN04, UN10, UB10, UB04

PCBB
UG12, UG10, UF15, UB16, UG14, N17/U-7/UN1, N16/U-6/UN, B12/U-2/UB1, B17/U-7UB1, N15/U-5/UNI, N14/U-4/UNI, B15/U-5/UB1, B14/U-4/UB1

CPS
CA22, CJ98, CJ91, CA26, CJ94, CA23, CA14, CJ90, CA24, CA20, CA27, CJ95, CA15, CA18, CA17

Ceramic Holder 2A, 2B

17J 600°C Level #3 (Begin approximately 4 cm above reactor mid-plane)

PCBB
N13/U-3/UN1, UF16, UF12, UF11, UG11, UG13, UF14, UB13, UF13, N12/U-2/UN1

17J 600°C LEVEL #4 (Begin approximately 5 cm above reactor mid-plane)

Vanadium envelopes
6-1, 6-2, 6-4, 6-5, 6-3, 6-6

Pressurized Tubes
UB00, UB15, UB08, UB12, UB03, UB06, UN19, UN08, UN13, UN12, UN02, UN05, UN17, UB19

101.3325 g Total mass of loaded basket

17J 450°C Level #1 (Begin approximately 17 cm below reactor mid-plane)

DCT
UN18, UN8, UN09, UN14, UN16, UN02, UN05, UN19 (First row of bottom of level #1)
UB01, UB-11, UB16, UB02, UB04, UB10 (Second row of bottom of level #1)

JCVN
RB09, TA25, FB01, RAO7, FA11, FA10, FA07, FA04, FA03, FA09, RB04, FA15, RB01, RB10, RA02, TA06, TN09, TN13, TA04, RB08, TN23, TN01, TN04, TA24, FA13, FB07, TN02

17J 450°C Second Level #2 (Begin approximately 15 cm below reactor mid-plane)

DCT
UB07, UB19 (lower level of level#2),

Ceramic specimen holder 1-B

Tensile Bundles
GN04, GK08 & GK04, FHD0, FA01, FA50 & FA31, TA72 & TA70, FKK2

JCVN
TN05, TN21, TA02, TN08, RA06, TA03, RA08, RB03, TN24, RA10, FB04, RB02, RB07, TN00, FB09, RA05, TA07, TA23, FA06, TN22, TN20, FB10, FB03, TN12, RB05, TN03, TN14, TN07, RA04, FA01, FA05, FB08, TA05, TA01, FA12, RB06, FB05, TN11, TA21, TA08, TA22, FA14, RA01, TN06, RA03, TN10, FB06, FB02, FA02

CPS
CA07, CJ85, CJ80

17J 450°C Level #2A (Begin approximately 13 cm below reactor mid-plane)

TEM Tubes
20, 29, 22, 14, 21, 15, 2, 3, 11, 4, 1

Tensile Bundles
UR00-UR15, UE03-UP15, UB30-UB41, UF00-UGO3, UN09, UW00-UW05, UP27-UP02, UT00-UT19, UD00-UD12, UV04-UV18, UY03-UY00, US00-US19, UC12-UG00, UH00-UM00,FB04 – FB05, TY74, FG01-FHA4, TN79-TN71, FKAO, TB74, TX74-TX77, TW02-TW05

Ceramic specimen holder 1-A

17J 450°C Level #3 (Begin approximately 10 cm below reactor mid-plane)

PCBB
UW07, UF07, UG06, NO1 – UNO, B11/U-11/UB, NO0/U-0/UN0, UG09, BO5/U-5/UB0, N07/U-UN0, UW05, UG04, UG07, UG00, NO4/U-4/UN0, NO2/U-2/UNO, UG01, N10/U-U/N10, BO9/U-9/UB0, BO8/U-B/UB0, NO9/U-9/UN0, BO4/U-4/UB0, NO3/U-3/UN0, UW03, UF02, UG08, UF00, UW01, BO1/U-1/UBO, BO6/U-6/UB0, BO2/U-2/UB0, BO3/U-3/UB0, B10/U-0/UB1, B00/U-0/UB0, B07/U-7/UB0, N08/U-8/UN0, N05/U-5/UN0, N11/U-11/UN, NO6/U-6/UN0, UW00, UW02, UW06, UW04, UG05, UG02, UF01, UF06, UF05, UF08, UF03, UF09, UG03, UF04

Tensile Bundles
FD01, T170, TV78-TV73, TT77, TR71-TR74, AV10, T370-T372

17J 450°C Level #4 (Begin approximately 8 cm below reactor mid-plane)

Pressurized Tubes
UN00, UN20*, UN09, UN16*, UN06, UN07*, UN14, UB02, UB07, UB16, UB22, UB11, UB09, UB05

*center specimens

186.7g total mass of 450°C loaded holder

ASSEMBLY OF THE US-JAPAN JP-26 EXPERIMENT AND START OF IRRADIATION IN THE HFIR—
K. R. Thoms, D. W. Heatherly, S. H. Kim, R. G. Sitterson, R. E. Stoller (Oak Ridge National Laboratory), and H. Tanigawa (Japan Atomic Energy Research Institute, Tokai, Japan)

OBJECTIVE

This work is being carried out under Annex I of the Collaboration on Fusion Materials between the US DOE and the Japan Atomic Energy Research Institute. The JP-26 experiment is one component of the Phase-IV experiments with the goal of elucidating the effects of helium in candidate engineering and model alloys, and verifying the irradiation response of alloy F82H.

SUMMARY

Specimen and capsule parts fabrication for JP-26 was completed. Loading of specimens into specimen holders and assembly of the capsule was completed. The experiment was installed in the target region of HFIR and irradiation began with cycle 398, starting December 11, 2003.

PROGRESS AND STATUS

Introduction

This experiment is being carried out within the framework of the US DOE-JAERI Collaboration on Fusion Materials, Annex I, which is in its fourth phase. The goals of the experiment include the investigation of the effects of helium on microstructural evolution, the impact of helium on fracture properties, and the development of engineering data on the fusion candidate alloy F82H. The specimen matrix for JP-26 has been reported earlier [1]. The goal of this report is to provide a detailed description of the final design of the JP-26 capsule and a detailed list of specimens loaded into JP-26.

Description of JP-26 Capsule

The JP-26 capsule includes 17 specimen holders designed to accommodate 6 types of specimens and irradiate them at 3 temperatures, 300, 400, and 500°C. The specimen types are a small bend bar (deformation-fracture mini-beam, DFMB), a sheet tensile specimen (SS-J3), a subsized pre-cracked Charpy V-notch specimen (0.5-1/3-PCCVN), transmission electron microscopy disks (TEM), atom probe specimens (APFIM), and small multi-purpose coupons (MMPC) that have the same overall dimensions as the APFIM specimens.

An overall layout of the JP-26 experiment is shown in Figure 1, which provides the subcapsule position number, the specimen type being irradiated in that position, the design irradiation temperature, and the distance that the center of the subcapsule is from the HFIR horizontal mid-plane (HMP). Also shown in Figure 1 is the location of neutron dosimeter packages.

Each of the specimen holders is fabricated from oxide dispersion strengthened aluminum (DISPAL). The outside diameters of the specimen holders are sized to provide a precise helium-filled gas gap between the holder and the capsule housing tube necessary to achieve the desired irradiation temperature. Centering tabs, six at each end, are machined into the holders to help assure uniform gas gaps. The inner part of the specimen holder is machined to accommodate the type of specimens being irradiated, and therefore each has a unique geometry. Silicon carbide (SiC) passive temperature monitors are included in each specimen holder. These will be analyzed after irradiation to determine actual irradiation temperature.

A top view and axial cross section of the specimen holders used to irradiate TEM specimens (positions 1, 10, and 17) is shown in Figure 2 (all dimensions in Figures 2 through 5 are in inches). A total of 100

(0.010 in. thick) specimens can be accommodated in these holders along with a single SiC temperature monitor located at the center of the holder. To help identify in which hole the specimens are located a 0.040-in. diameter by 0.040-in. deep hole was drilled in the top of each TEM holder, and the specimen holes are then numbered clockwise starting at this 0.040-in. hole.

The loading configuration for the tensile specimen holders is shown in Figure 3. For a given elevation eight SS-J3 tensile and eight APFIM specimens can be accommodated. Four holders (positions 2, 9, 13, and 16) have one layer of specimens with this configuration, while six holders (positions 3, 5, 6, 7, 11, and 15) have two layers, or 16 tensile and APFIM specimens. A spring pin is placed in the center of the specimen array to apply pressure to the SiC temperature monitors and, in turn, on the tensile specimens to assure good thermal contact with the specimen holder. At each corner two APFIM "tuning fork" specimens are loaded with a corrugated spring to assure that they are also in good thermal contact with the holder. In some of the tensile specimen holders two multi-purpose coupons (MMPC) and spacers that combined have the same overall dimensions as the APFIM specimens were substituted for the APFIM specimens (see loading list).

Subsized pre-cracked Charpy V-notch specimens (0.5-1/3-PCCVN) are loaded into specimen holders shown in Figure 4. Each of these holders (positions 4, 8, and 12) have two layers of specimens for a total of 16 specimens per holder. Two SiC temperature monitors and corrugated springs are placed in the center of the specimen array to assure good thermal contact with the holder.

The DFMB specimens are loaded into one holder (position 14) as shown in Figure 5. There are four layers of specimens with 16 specimens at each level. The outer row of each layer is made up of 12 specimens that are 1.68 mm square, while the inner four specimens are 1.68 x 1.45 mm. A SiC temperature monitor and a corrugated spring are placed in the center of the specimen array, and two corrugated springs are placed in two of the outer rows to assure all specimens are in good thermal contact with the holder. Specimen locations are designated by a C, S, TM, or M, to more precisely identify loading locations (see loading list).

Specimen Loading

The location of each of the nearly 700 specimens in JP-26 is reported in Table 1, which contains a box for each of the 17 specimen holder and 5 dosimeter positions. Because coatings applied to some of the TEM discs required the discs to be loaded in a prescribed manner, the boxes for the TEM specimen holders (positions 1, 10, and 17) have a column labeled "Engr. Face" to indicate which way the engraved face of the specimen was loaded. A total of five neutron dosimeter packages provided by PNNL were loaded into JP-26, one each between positions 1 and 2, 5 and 6, 8 and 9, 13 and 14, and below position 17. The 0.5-1/3-PCCVN specimens (in positions 4, 8 and 12) were all loaded with the notches facing towards the center of the holders. The outer rows of specimens in the DFMB holder (position 14) were loaded with the notches facing outward toward the holder, while the inner four specimens were loaded with their notches facing inward toward the center of the holder.

Future Work

The JP-26 capsule will be irradiated to a peak fluence of 8-10 dpa, which will take approximately 5 HFIR cycles.

References

[1] R. E. Stoller and H. Tanigawa, Fusion Materials Semi-annual Progress Report DOE/ER/0313/34, (June 2003) 142.

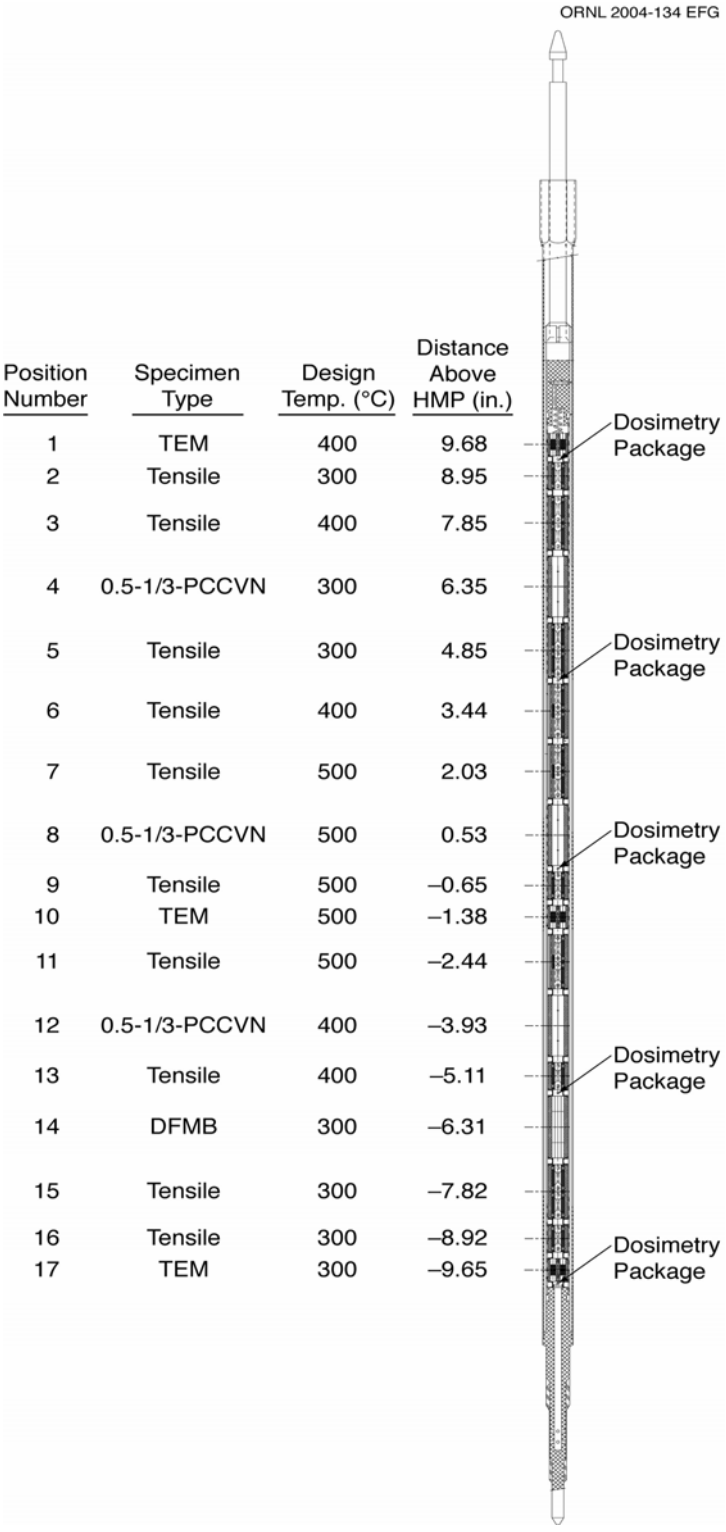

Position Number	Specimen Type	Design Temp. (°C)	Distance Above HMP (in.)
1	TEM	400	9.68
2	Tensile	300	8.95
3	Tensile	400	7.85
4	0.5-1/3-PCCVN	300	6.35
5	Tensile	300	4.85
6	Tensile	400	3.44
7	Tensile	500	2.03
8	0.5-1/3-PCCVN	500	0.53
9	Tensile	500	–0.65
10	TEM	500	–1.38
11	Tensile	500	–2.44
12	0.5-1/3-PCCVN	400	–3.93
13	Tensile	400	–5.11
14	DFMB	300	–6.31
15	Tensile	300	–7.82
16	Tensile	300	–8.92
17	TEM	300	–9.65

Figure 1. Overall layout of JP26 experiment.

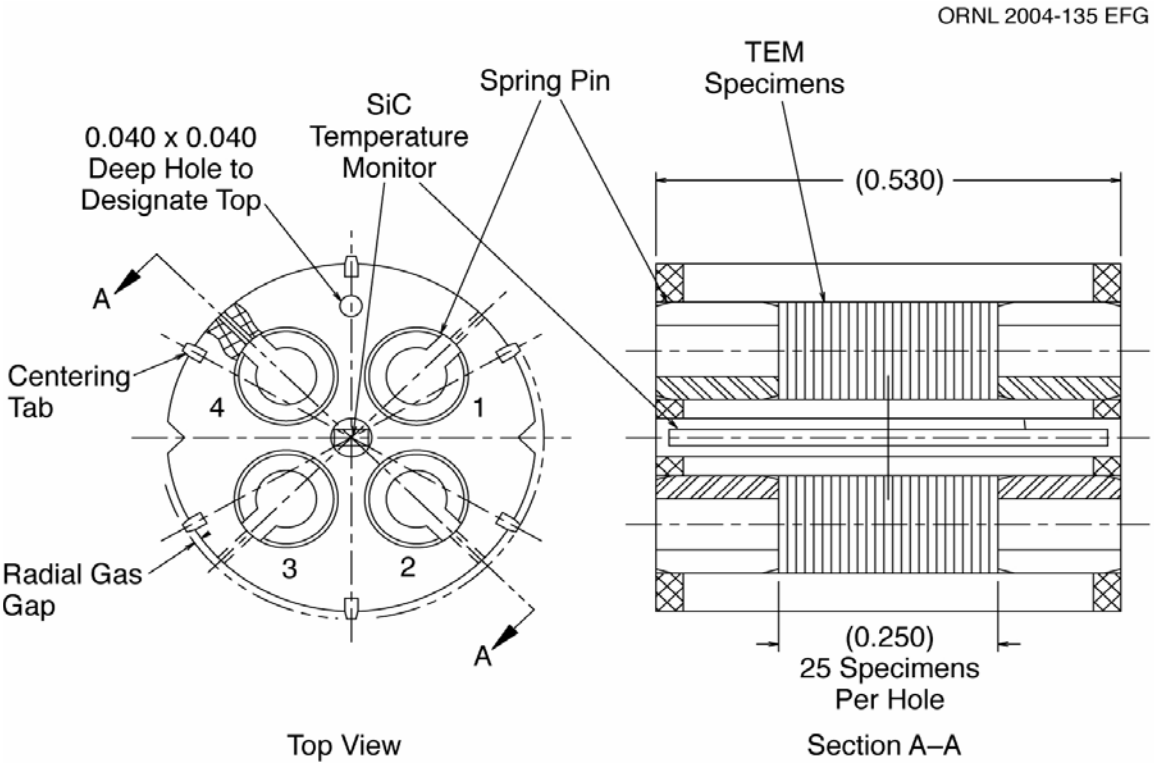

Figure 2. Specimen holder subassembly used in JP-26 for TEM specimens.

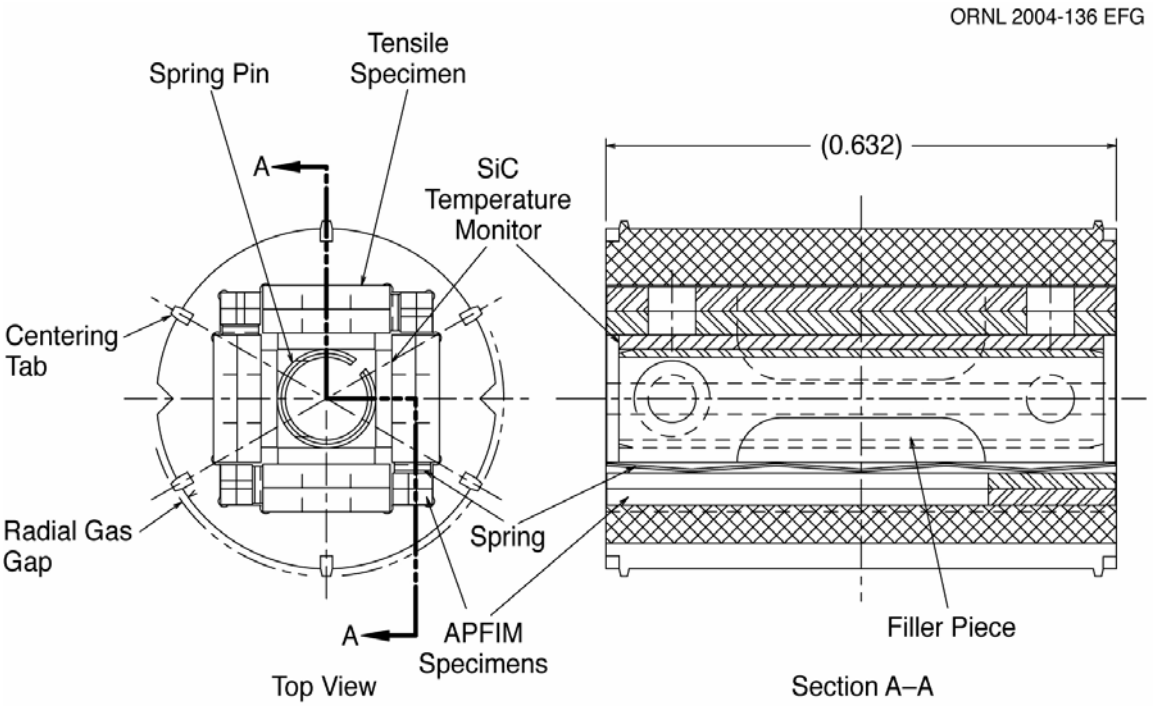

Figure 3. Specimen holder subassembly used in JP-26 for SS-J3 tensile and APFIM specimens.

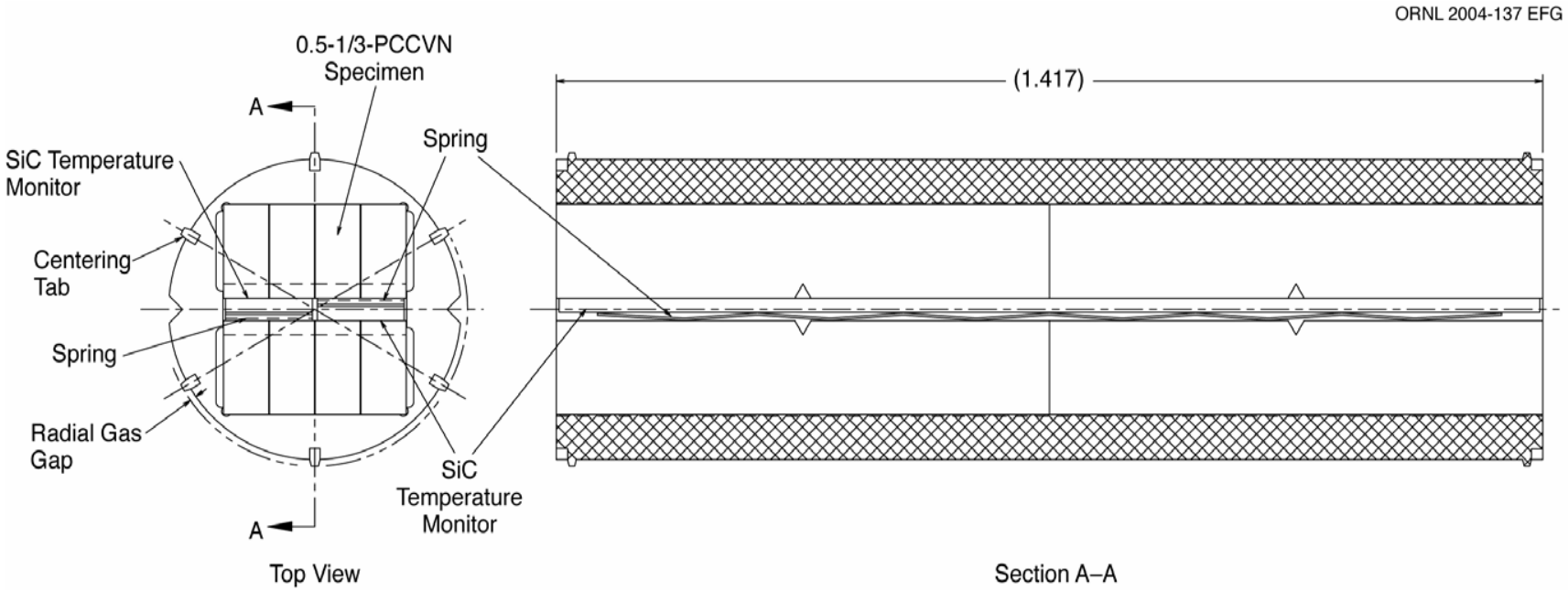

Figure 4. Specimen holder subassembly used in JP-26 for 0.5-1/3-PCCVN specimens.

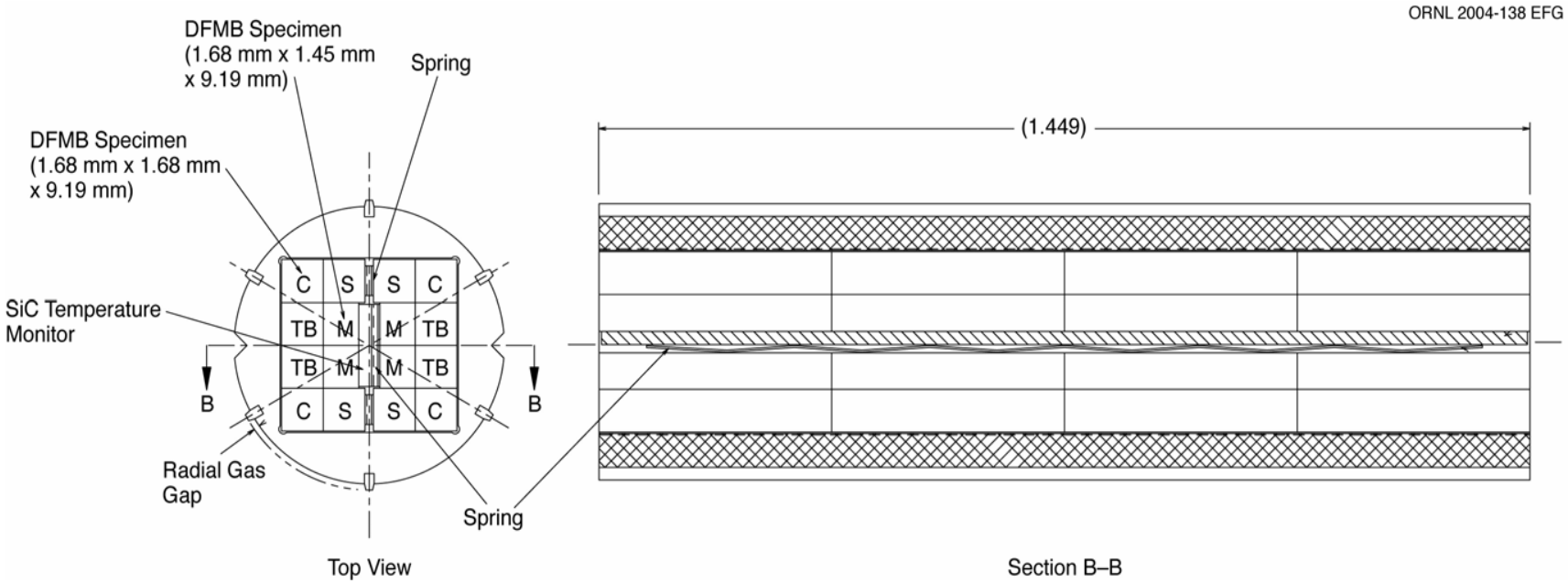

Figure 5. Specimen holder subassembly used in JP-26 for DFMB specimens.

Table 1. JP-26 SPECIMEN & DOSIMETRY LOADING LIST

POS. 1 JP-26		TEM Specimen Numbers								Passive Thermometry in Center Hole
		Hole No.1*	Engr. Face	Hole No.2*	Engr. Face	Hole No.3*	Engr. Face	Hole No.4*	Engr. Face	
BOTTOM	1	**016**	Down	**ZR12**	Down	**ZB10**	Up	**ZS11**	Up	
	2	**ZA15**	Up	**ZN13**	Up	**ZB11**	Up	**ZQ10**	Up	1.
	3	**017**	Down	**ZR13**	Up	**ZC10**	Up	**ZQ11**	Up	
	4	**ZF16**	Up	**012**	Down	**ZC11**	Up	**ZP18**	Up	
	5	**H16**	Down	**ZA12**	Up	**ZD10**	Up	**ZP11**	Up	Ser. #1
	6	**ZF17**	Up	**013**	Down	**ZD11**	Up	**ZR10**	Up	
	7	**H17**	Down	**ZF12**	Up	**ZE10**	Up	**ZR11**	Up	
	8	**UN16**	Up	**H12**	Down	**ZE11**	Up	**K10**	Up	
	9	**R16**	Down	**ZF13**	Up	**ZF10**	Up	**K11**	Up	
	10	**UN17**	Up	**H13**	Down	**ZF11**	Up	**K12**	Up	
	11	**R17**	Down	**UN12**	Up	**001**	Up	**K13**	Up	
	12	**ZH12**	Up	**R12**	Down	**011**	Up	**K14**	Up	
	13	**ZG12**	Down	**UN13**	Up	**H10**	Up	**M10**	Up	
	14	**ZH13**	Up	**R13**	Down	**H11**	Up	**M11**	Up	
	15	**ZG13**	Down	**ZP08**	Up	**blank**		**M12**	Up	
	16	**ZH14**	Up	**ZP13**	Up	**UN11**	Up	**M13**	Up	
	17	**ZG14**	Down	**0150**	Down	**310**	Up	**M14**	Up	
	18	**ZJ12**	Up	**ZA13**	Up	**311**	Up	**N10**	Up	
	19	**ZS14**	Down	**H14**	Down	**R10**	Up	**N11**	Up	
	20	**ZJ13**	Up	**ZA14**	Up	**R11**	Up	**N12**	Up	
	21	**ZS15**	Down	**H15**	Down	**ZG10**	Up	**N13**	Up	
	22	**ZJ14**	Up	**ZF14**	Up	**ZG11**	Up	**N14**	Up	
	23	**ZQ12**	Down	**R14**	Down	**ZH10**	Up	**P10**	Up	
	24	**ZK12**	Up	**ZF15**	Up	**ZH11**	Up	**P11**	Up	
	25	**ZQ13**	Down	**R15**	Down	**ZJ10**	Up	**P12**	Up	
	26	**ZK13**	Up	**015**	Up	**ZJ11**	Up	**P13**	Up	
TOP	27	**ZP16**	Down	**ZP14**	Down	**ZK10**	Up	**P14**	Up	
	28	**ZK14**	Up	**UN14**	Up	**ZK11**	Up			
	29	**ZP17**	Down	**ZP01**	Down	**ZN10**	Up			
	30	**ZN12**	Up	**UN15**	Up	**ZN11**	Up			
	31	**ZA10**	Up	**ZA11**	Up	**ZS10**	Up			
	ed 1, 2, 3, and 4 clockwise starting from 0.040 dia. hole between 2 holes in top of holder									

The spacer between positions number 1 and 2 contains Neutron Dosimeter Number <u>H5</u>

POS. 2 JP-26	SS-J3 Tensile Specimen	APFIM Specimen*	Passive Thermometry
	1. inner **N00**	1. **M02**	1.
	2. outer **K00**	2. **M03**	Ser. #1
	3. inner **N01**	3. **NO2**	2.
	4. outer **K01**	4. **N03**	Ser. #2
	5. inner **P00**	5. **P02**	3.
	6. outer **M00**	6. **P03**	Ser. #3
	7. inner **P01**	7. **(JNCX2)**	4.
	8. outer **M01**	8. **(JNCX2)**	Ser. #4

* Specimen numbers in parentheses are MMPC specimens

POS. 3 JP-26	SS-J3 Tensile Specimen	APFIM Specimen	Passive Thermometry
Top Half	1. inner **R10**	1. **ZQ16**	1. Ser. #17
	2. outer **ZP10**	2. **ZQ17**	
	3. inner **R11**	3. **ZQ22** (notched)	2. Ser. #18
	4. outer **ZP11**	4. **ZQ23** (notched)	
	5. inner **ZR10**	5. **ZR12**	3. Ser. #19
	6. outer **ZQ10**	6. **ZR13**	
	7. inner **ZR11**	7. **ZP12**	4. Ser. #20
	8. outer **ZQ11**	8. **ZP13**	
Bottom Half	SS-J3 Tensile Specimen	APFIM Specimen*	Passive Thermometry
	9. inner **G11**	9. **N10**	5. Ser. #21
	10. outer **G10**	10. **N11**	
	11. inner **G12**	11. **ZQ12**	6. Ser. #22
	12. outer **V11**	12. **ZQ13**	
	13. inner **UA02**	13. **ZQ14**	7. Ser. #23
	14. outer **W10**	14. **ZQ15**	
	15. inner **UA03**	15. **(JNCX2)**	8. Ser. #24
	16. outer **W11**	16. **(JNCX2)**	

* Specimen numbers in parentheses are MMPC specimens

POS. 4 JP-26	.5-1/3 PCCVN Spec.	Passive Thermometry	
Top Half	1. outer **004**	1. Ser. #1	2. Ser. #2
	2. inner **005**		
	3. inner **006**		
	4. outer **007**		
	5. outer **008**		
	6. inner **009**		
	7. inner **00A**		
	8. outer **00B**		
Bottom Half	.5-1/3 PCCVN Spec		
	9. outer **304**		
	10. inner **305**		
	11. inner **306**		
	12. outer **307**		
	13. outer **308**		
	14. inner **309**		
	15. inner **30A**		
	16. outer **30B**		

POS. 5 JP-26	SS-J3 Tensile Specimen	APFIM Specimen	Passive Thermometry
Top Half	1. inner **300**	1. **00D**	1. Ser. #25
	2. outer **000**	2. **00E**	
	3. inner **301**	3. **30D**	2. Ser. #26
	4. outer **001**	4. **30E**	
	5. inner **302**	5. **HOA**	3. Ser. #27
	6. outer **002**	6. **HOB**	
	7. inner **303**	7. **HOC**	4. Ser. #28
	8. outer **003**	8. **HOD**	
Bottom Half	SS-J3 Tensile Specimen	APFIM Specimen	Passive Thermometry
	9. inner **600**	9. **604**	5. Ser. #29
	10. outer **00F**	10. **605**	
	11. inner **601**	11. **HOE**	6. Ser. #30
	12. outer **00G**	12. **HOF**	
	13. inner **602**	13. **HOG**	7. Ser. #31
	14. outer **T00**	14. **BLANK** H & notched	
	15. inner **603**	15. **BLANK** H & notched	8. Ser. #32
	16. outer **T01**	16. **BLANK** H & notched	

The spacer between positions number 5 and 6 contains Neutron Dosimeter Number <u>L8</u>

POS. 6 JP-26	SS-J3 Tensile Specimen	APFIM Specimen	Passive Thermometry
Top Half	1. inner **610**	1. **614**	1. Ser. #33
	2. outer **310**	2. **615**	
	3. inner **611**	3. **ZJ10**	2. Ser. #34
	4. outer **311**	4. **ZJ11**	
	5. inner **612**	5. **ZK10**	3. Ser. #35
	6. outer **312**	6. **ZK11**	
	7. inner **613**	7. **ZN10**	4. Ser. #36
	8. outer **313**	8. **ZN11**	
Bottom Half	SS-J3 Tensile Specimen	APFIM Specimen	Passive Thermometry
	9. inner **01E**	9. **01C**	5. Ser. #37
	10. outer **010**	10. **01D**	
	11. inner **T10**	11. **31C**	6. Ser. #38
	12. outer **011**	12. **31D**	
	13. inner **T11**	13. **ZG10**	7. Ser. #39
	14. outer **012**	14. **ZG11**	
	15. inner **V10**	15. **ZH10**	8. Ser. #40
	16. outer **013**	16. **ZH11**	

POS. 7 JP-26	SS-J3 Tensile Specimen	APFIM Specimen	Passive Thermometry
Top Half	1. inner **V20**	1. **ZG20**	1. Ser. #41
	2. outer **G22**	2. **ZG21**	
	3. inner **V21**	3. **ZQ22**	2. Ser. #42
	4. outer **T21**	4. **ZQ23**	
	5. inner **W20**	5. **ZQ24**	3. Ser. #43
	6. outer **UA04**	6. **ZQ25**	
	7. inner **W21**	7. **ZQ26**	4. Ser. #44
	8. outer **UA05**	8. **ZQ27**	
Bottom Half	SS-J3 Tensile Specimen	APFIM Specimen	Passive Thermometry
	9. inner **620**	9. **ZH20**	5. Ser. #45
	10. outer **02E**	10. **ZH21**	
	11. inner **621**	11. **ZJ20**	6. Ser. #46
	12. outer **02F**	12. **ZJ21**	
	13. inner **622**	13. **ZK20**	7. Ser. #47
	14. outer **02G**	14. **ZK21**	
	15. inner **623**	15. **ZN20**	8. Ser. #48
	16. outer **T20**	16. **ZN21**	

POS. 8 JP-26	.5-1/3 PCCVN Spec.	Passive Thermometry	
Top Half	1. outer **024**	1. Ser. #3	2. Ser. #4
	2. inner **025**		
	3. inner **026**		
	4. outer **027**		
	5. outer **028**		
	6. inner **029**		
	7. inner **02A**		
	8. outer **02B**		
Bottom Half	.5-1/3 PCCVN Spec		
	9. outer **324**		
	10. inner **325**		
	11. inner **326**		
	12. outer **327**		
	13. outer **328**		
	14. inner **329**		
	15. inner **32A**		
	16. outer **32B**		

The spacer between positions number 8 and 9 contains Neutron Dosimeter Number <u>97</u>

POS. 9 JP-26	SS-J3 Tensile Specimen	APFIM Specimen*	Passive Thermometry
	1. inner **320**	1. **02C**	1. Ser. #5
	2. outer **020**	2. **02D**	
	3. inner **321**	3. **32C**	2. Ser. #6
	4. outer **021**	4. **32D**	
	5. inner **322**	5. **624**	3. Ser. #7
	6. outer **022**	6. **625**	
	7. inner **323**	7. **(JNCX2)**	4. Ser. #8
	8. outer **023**	8. **(JNCX2)**	

* Specimen numbers in parentheses are MMPC specimens

POS. 10 JP-26	TEM Specimen Nubers									Passive Thermometry in Center Hole
		Hole No.1*	Engr. Face	Hole No.2*	Engr. Face	Hole No.3*	Engr. Face	Hole No.4*	Engr. Face	
BOTTOM	1	**026**	Down	**ZR22**	Down	**ZB20**	Up	**ZS21**	Up	
	2	**ZA25**	Up	**ZN23**	Up	**ZB21**	Up	**ZQ20**	Up	1.
	3	**027**	Down	**ZR23**	Up	**ZC20**	Up	**ZQ21**	Up	
	4	**ZF26**	Up	**022**	Down	**ZC21**	Up	**ZP19**	Up	
	5	**H26**	Down	**ZA22**	Up	**ZD20**	Up	**ZP29**	Up	Ser. #2
	6	**ZF27**	Up	**023**	Down	**ZD21**	Up	**ZR20**	Up	
	7	**H27**	Down	**ZF22**	Up	**ZE20**	Up	**ZR21**	Up	
	8	**UN26**	Up	**H22**	Down	**ZE21**	Up	**K20**	Up	
	9	**R26**	Down	**ZF23**	Up	**ZF20**	Up	**K21**	Up	
	10	**UN27**	Up	**H23**	Down	**ZF21**	Up	**K22**	Up	
	11	**R27**	Down	**UN22**	Up	**020**	Up	**K23**	Up	
	12	**ZH22**	Up	**R22**	Down	**021**	Up	**K24**	Up	
	13	**ZG22**	Down	**UN23**	Up	**H20**	Up	**M20**	Up	
	14	**ZH23**	Up	**R23**	Down	**H21**	Up	**M21**	Up	
	15	**ZG23**	Down	**ZP28**	Up	**UN20**	Up	**M22**	Up	
	16	**ZH24**	Up	**ZP12**	Up	**UN21**	Up	**M23**	Up	
	17	**ZG24**	Down	**025+**	Down	**320**	Up	**M24**	Up	
	18	**ZJ22**	Up	**ZA23**	Up	**321**	Up	**N20**	Up	
	19	**ZS24**	Down	**H24**	Down	**R20**	Up	**N21**	Up	
	20	**ZJ23**	Up	**ZA24**	Up	**R21**	Up	**N22**	Up	
	21	**ZS25**	Down	**H25**	Down	**ZG20**	Up	**N23**	Up	
	22	**ZJ24**	Up	**ZF24**	Up	**ZG21**	Up	**N24**	Up	
	23	**ZQ22**	Down	**R24**	Down	**ZH20**	Up	**P20**	Up	
	24	**ZK22**	Up	**ZF25**	Up	**ZH21**	Up	**P21**	Up	
	25	**ZQ23**	Down	**R25**	Down	**ZJ20**	Up	**P22**	Up	
	26	**ZK23**	Up	**025**	Up	**ZJ21**	Up	**P23**	Up	
	27	**ZP26**	Down	**ZP20**	Down	**ZK20**	Up	**P24**	Up	
	28	**ZK24**	Up	**UN24**	Up	**ZK21**	Up			
	29	**ZP27**	Down	**ZP25**	Down	**ZN20**	Up			
TOP	30	**ZN22**	Up	**UN25**	Up	**ZN21**	Up			
	31	**ZA20**	Up	**ZA21**	Up	**ZS20**	Up			
*Holes numbered 1, 2, 3, and 4 clockwise starting from 0.040 dia. hole between 2 holes in top of holder										

POS. 11 JP-26	SS-J3 Tensile Specimen	APFIM Specimen	Passive Thermometry
Top Half	1. inner **G20**	1. **H26**	1. Ser. #49
	2. outer **H22**	2. **H27**	
	3. inner **G21**	3. **H28**	2. Ser. #50
	4. outer **H23**	4. **H29**	
	5. inner **H20**	5. **H2A**	3. Ser. #51
	6. outer **H24**	6. **H2B**	
	7. inner **H21**	7. **N20**	4. Ser. #52
	8. outer **H25**	8. **N21**	
Bottom Half	SS-J3 Tensile Specimen	APFIM Specimen	Passive Thermometry
	9. inner **R20**	9. **ZP22**	5. Ser. #53
	10. outer **ZP20**	10. **ZP23**	
	11. inner **R21**	11. **ZQ12** (notched)	6. Ser. #54
	12. outer **ZP21**	12. **ZQ13** (notched)	
	13. inner **ZR20**	13. **ZR22**	7. Ser. #55
	14. outer **ZQ20**	14. **ZR23**	
	15. inner **ZR21**	15. **ZS20**	8. Ser. #56
	16. outer **ZQ21**	16. **ZS21**	

POS. 12 JP-26	.5-1/3 PCCVN Spec.	Passive Thermometry	
Top Half	1. outer **014**	1. Ser. #5	2. Ser. #6
	2. inner **015**		
	3. inner **016**		
	4. outer **017**		
	5. outer **018**		
	6. inner **019**		
	7. inner **01A**		
	8. outer **01B**		
Bottom Half	.5-1/3 PCCVN Spec		
	9. outer **314**		
	10. inner **315**		
	11. inner **316**		
	12. outer **317**		
	13. outer **318**		
	14. inner **319**		
	15. inner **31A**		
	16. outer **31B**		

POS. 13 JP-26	SS-J3 Tensile Specimen	APFIM Specimen	Passive Thermometry
	1. inner **H14**	1. **H18**	1. Ser. #9
	2. outer **H10**	2. **H19**	
	3. inner **H15**	3. **H1A**	2. Ser. #10
	4. outer **H11**	4. **H1B**	
	5. inner **H16**	5. **H1C**	3. Ser. #11
	6. outer **H12**	6. **H1D**	
	7. inner **H17**	7. **ZS10**	4. Ser. #12
	8. outer **H13**	8. **ZS11**	

The spacer between positions number 13 and 14 contains Neutron Dosimeter Number 2F

POS. 14 JP-26	Outer Layer* DFBM Specimens (.066 x .066 x .362)												Inner Layer* DFBM Specimens (.057 x .066 x .362)				Passive Therm.
	C	C	C	C	S	S	S	S	TB	TB	TB	TB	M	M	M	M	
Layer 1 **TOP**	1 **H02a**	2 **H02b**	3 **H02c**	4 **H02d**	5 **00Ca**	6 **00Cb**	7 **00Cc**	8 **00Cd**	9 **30Ca**	10 **30Cb**	11 **30Cc**	12 **30Cd**	1 **H03a**	2 **H03b**	3 **H03c**	4 **H03d**	1. Ser. #1
Layer 2	**H02e**	**H02f**	**H02g**	**H02h**	**00Ce**	**00Cf**	**00Cg**	**00Ch**	**30Ce**	**30Cf**	**30Cg**	**30Ch**	**H03e**	**H03f**	**H03g**	**H03h**	
Layer 3	**H02j**	**H02k**	**H02m**	**H02n**	**00Cj**	**00Ck**	**00Cm**	**00Cn**	**30Cj**	**30Ck**	**30Cm**	**30Cn**	**H03j**	**H03k**	**H03m**	**H03n**	
Layer 4 **BOT.**	**H02p**	**H02q**	**H02r**	**H02s**	**00Cp**	**00Cq**	**00Cr**	**00Cs**	**30Cp**	**30Cq**	**30Cr**	**30Cs**	**H03p**	**H03q**	**H03r**	**H03s**	

* For position designations C, S, TB, and M, see Figure 5.

POS. 15 JP-26	SS-J3 Tensile Specimen	APFIM Specimen	Passive Thermometry
Top Half	1. inner **H06**	1. **ZQ02**	1. Ser. #57
	2. outer **H00**	2. **ZQ03**	
	3. inner **H07**	3. **ZQ04**	2. Ser. #58
	4. outer **H01**	4. **ZQ05**	
	5. inner **H08**	5. **ZQ06**	3. Ser. #59
	6. outer **H04**	6. **ZQ07**	
	7. inner **H09**	7. **ZQ08**	4. Ser. #60
	8. outer **H05**	8. **ZQ09**	
Bottom Half	SS-J3 Tensile Specimen	APFIM Specimen	Passive Thermometry
	9. inner **G00**	9. **ZH00**	5. Ser. #61
	10. outer **V00**	10. **ZH01**	
	11. inner **G01**	11. **ZJ00**	6. Ser. #62
	12. outer **V01**	12. **ZJ01**	
	13. inner **UA00**	13. **ZK00**	7. Ser. #63
	14. outer **W00**	14. **ZK01**	
	15. inner **UA01**	15. **ZN00**	8. Ser. #64
	16. outer **W01**	16. **ZN01**	

POS. 16 JP-26	SS-J3 Tensile Specimen	APFIM Specimen	Passive Thermometry
	1. inner **R00**	1. **ZG00**	1. Ser. #13
	2. outer **ZP00**	2. **ZG01**	
	3. inner **R01**	3. **ZP02**	2. Ser. #14
	4. outer **ZP01**	4. **ZP03**	
	5. inner **ZR00**	5. **ZQ02** (notched)	3. Ser. #15
	6. outer **ZQ00**	6. **ZQ03** (notched)	
	7. inner **ZR01**	7. **ZR02**	4. Ser. #16
	8. outer **ZQ01**	8. **ZR03**	

POS. 17 JP-26	TEM Specimen Numbers									Passive Thermometry in Center Hole
		Hole No.1*	Engr. Face	Hole No.2*	Engr. Face	Hole No.3*	Engr. Face	Hole No.4*	Engr. Face	
BOTTOM	1	**006**	Down	**ZR02**	Down	**ZB00**	Up	**ZS01**	Up	
	2	**ZA05**	Up	**ZN03**	Up	**ZB01**	Up	**ZQ00**	Up	1.
	3	**007**	Down	**ZR03**	Up	**ZC00**	Up	**ZQ01**	Up	
	4	**ZF06**	Up	**002**	Down	**ZC01**	Up	**ZP09**	Up	
	5	**H06**	Down	**ZA02**	Up	**ZD00**	Up	**ZP0A**	Up	Ser. #3
	6	**ZF07**	Up	**003**	Down	**ZD01**	Up	**ZR00**	Up	
	7	**H07**	Down	**ZF02**	Up	**ZE00**	Up	**ZR01**	Up	
	8	**UN06**	Up	**H02**	Down	**ZE01**	Up	**K00**	Up	
	9	**R06**	Down	**ZF03**	Up	**ZF00**	Up	**K01**	Up	
	10	**UN07**	Up	**H03**	Down	**Blank**		**K02**	Up	
	11	**R07**	Down	**UN02**	Up	**000**	Up	**K03**	Up	
	12	**ZH02**	Up	**R02**	Down	**001**	Up	**K04**	Up	
	13	**ZG02**	Down	**UN03**	Up	**H00**	Up	**M00**	Up	
	14	**ZH03**	Up	**R03**	Up	**H01**	Up	**M01**	Up	
	15	**ZG03**	Down	**ZP02**	Up	**UN10**	Up	**M02**	Up	
	16	**ZH04**	Up	**ZP03**	Up	**UN01**	Up	**M03**	Up	
	17	**ZG04**	Down	**005+**	Down	**300**	Up	**M04**	Up	
	18	**ZJ02**	Up	**ZA03**	Up	**301**	Up	**N00**	Up	
	19	**ZS04**	Down	**H04**	Down	**R00**	Up	**N01**	Up	
	20	**ZJ03**	Up	**ZA04**	Up	**R01**	Up	**N02**	Up	
	21	**ZS05**	Down	**H05**	Down	**ZG00**	Up	**N03**	Up	
	22	**ZJ04**	Up	**ZF01**	Up	**ZG01**	Up	**N04**	Up	
	23	**ZQ02**	Down	**R04**	Down	**ZH00**	Up	**P00**	Up	
	24	**ZK02**	Up	**ZF05**	Up	**ZH01**	Up	**P01**	Up	
	25	**ZQ03**	Down	**R05**	Down	**ZJ00**	Up	**P02**	Up	
	26	**ZK03**	Up	**005**	Up	**ZJ01**	Up	**P03**	Up	
	27	**ZP10**	Down	**ZP04**	Down	**ZK00**	Up	**P04**	Up	
	28	**ZK04**	Up	**UN04**	Up	**ZK01**	Up			
TOP	29	**ZP07**	Down	**ZP05**	Down	**ZN00**	Up			
	30	**ZN02**	Up	**UN05**	Up	**ZN01**	Up			
	31	**ZA00**	Up	**ZA01**	Up	**ZS00**	Up			

*Holes numbered 1, 2, 3, and 4 clockwise starting from 0.040 dia. hole between 2 holes in top of holder

The bottom spacer below position number 17 contains Neutron Dosimeter Number <u>E1</u>